

Middle Atmosphere Program

HANDBOOK
FOR MAP
VOLUME 30

Edited by
S. Fukao

ICSU

International Council of Scientific Unions

SCOSTEP

Scientific Committee on Solar-Terrestrial Physics

J. G. Roederer, President
W. I. Axford, Vice President
C. H. Liu, Scientific Secretary

MAP ORGANIZATION

MIDDLE ATMOSPHERE PROGRAM STEERING COMMITTEE

S. A. Bowhill, SCOSTEP, Chairman
K. Labitzke, COSPAR, Vice Chairman
C. H. Liu, SCOSTEP, Secretary

H. S. Ahluwalia, IUPAP
R. D. Bojkov, WMO
A. D. Danilov, COSPAR
J. C. Gille, COSPAR
I. Hirota, IUGG/IAMAP
A. H. Manson, SCOSTEP

T. Nagata, SCAR
R. G. Roper, IUGG/IAMAP
P. C. Simon, IAU
J. Taubenheim, IUGG/IAGA
T. E. VanZandt, URSI
R. A. Vincent, URSI

MAP STANDING COMMITTEES

Data Management -- G. Hartmann and I. Hirota, Co-Chairmen
Publications -- Belva Edwards, Chairman

MAP STUDY GROUPS

MSG-5 Ions and Aerosols, F. Arnold and M. P. McCormick, Co-Chairmen
MSG-8 Atmospheric Chemistry, G. Witt, Chairman
MSG-9 Measurement of Middle Atmosphere Parameters by Long Duration
Balloon Flights, J. E. Blamont, Chairman

MAP PROJECTS

	Coordinator		Coordinator
AMA:	T. Hirasawa	MAC-SINE:	E. V. Thrane
ATMAP:	J. M. Forbes	MAE:	R. A. Goldberg
DYNAMICS:	K. Labitzke	MASH:	A. O'Neill
GLOBMET:	R. G. Roper	NIEO:	S. Kato
GLOBUS:	J. P. Pommereau	OZMAP:	D. F. Heath
GOSSA:	M. P. McCormick	SSIM:	P. C. Simon
GRATMAP:	D. C. Fritts	SUPER CAMP:	E. Kopp
MAC-EPSILON:	E. V. Thrane	WINE	U. von Zahn

MAP REGIONAL CONSULTATIVE GROUP

Europe: M. L. Chanin, Chairman

MIDDLE
ATMOSPHERE
PROGRAM

HANDBOOK
FOR MAP

Volume 30

International School on
Atmospheric Radar

Edited by

S. Fukao

October 1989

Published for the ICSU Scientific Committee on Solar-Terrestrial Physics (SCOSTEP) with financial assistance from the National Aeronautics and Space Administration under the 1988 Middle Atmosphere Program Management Contract and Unesco Subvention 1988-1989.

Copies available from SCOSTEP Secretariat, University of Illinois, 1406 W. Green Street, Urbana, Illinois 61801.

FOREWORD

In the past 15 years, since Woodman and Guillen first obtained echoes from the clear air in the stratosphere and mesosphere with the Jicamarca radar in Peru in 1974, the mesosphere-stratosphere-troposphere (MST) radars (or clear air radars) have developed into the most powerful ground-based technique for probing the atmosphere in this height range. This technique has contributed significantly to the research of atmospheric dynamics, especially small- and medium-scale time-varying dynamical phenomena, such as gravity waves, turbulence, and convections. Recently, the technique has started to provide input to numerical weather prediction experiments.

There are now more than 30 radars of this kind operating in the world and the field is likely to grow in developing countries also. Currently, even commercialized radars are available and have been installed in many countries. Actual and latent demands to learning this new technique are very large, especially among young atmospheric scientists, engineers, and others who want to join this field of research.

Thus, the Radio Atmospheric Science Center of Kyoto University decided to hold an International School of Atmospheric Radar (ISAR) in order to provide a unique learning opportunity for these people. The ISAR was held in Kyoto, Japan, during November 24-28, 1988, prior to the Fourth Workshop on Technical and Scientific Aspects of MST radar held in the same place. The ISAR was organized by S. Kato as Chairman and cosponsored by SCOSTEP, URSI, the Society of Geomagnetism and Earth, Planetary and Space Sciences, and the Meteorological Society of Japan. More than 90 participants attended the ISAR from 17 countries.

This volume of the MAP Handbook includes ten lecture notes presented at ISAR. The notes offer a rather broad, tutorial coverage of the technical and scientific aspects of MST radars, i.e., radar system, control and signal processing, atmospheric waves, practice and applications. We hope that this volume will be a good guide to those who are interested in MST radar techniques which are interdisciplinary in nature.

We would like to thank the ten lecturers for writing the excellent notes. Special thanks are also due to C. H. Liu, J. Röttger, and P. K. Rastogi for giving very helpful suggestions. The expert effort in handling the manuscripts and correspondence by Belva Edwards is greatly acknowledged.

Shoichiro Fukao
Editor

Table of Contents

Foreword, <i>S. Fukao</i>	iii
Table of Contents	v
I. OVERVIEW	
Chapter 1. Historical Aspects of Radar Atmospheric Dynamics, <i>S. Kato</i>	1
II. RADAR SYSTEM, CONTROL AND SIGNAL PROCESSING	
Chapter 2. Radar Principles, <i>T. Sato</i>	19
Chapter 3. Radar Hardware and Control, <i>J. Röttger</i>	54
Chapter 4. Statistical Characteristics of MST Radar Echoes and its Interpretation, <i>R. F. Woodman</i>	114
Chapter 5. Data Acquisition and Processing, <i>T. Tsuda</i>	151
Chapter 6. Spectral and Correlation Analysis with Applications to Middle- Atmosphere Radars, <i>P. K. Rastogi</i>	184
Chapter 7. Target Parameter Estimation, <i>W. K. Hocking</i>	228
III. THEORY, PRACTICE AND APPLICATIONS	
Chapter 8. Gravity Waves and Instabilities in the Lower and Middle Atmosphere, <i>J. Klostermeyer</i>	269
Chapter 9. Applications of MST Radars: Meteorological Applications, <i>M. F. Larsen</i>	299
Chapter 10. Incoherent Scatter Radar Observations of the Ionosphere, <i>T. Hagfors</i>	333

Chapter 1

Historical Aspects of Radar Atmospheric Dynamics

Susumu Kato

Radio Atmospheric Science Center,
Kyoto University, Uji, Kyoto 611, JAPAN

1 Introduction

"Radar" stands for radio detection and ranging. It is well-known that radars were developed during World War II to detect aircraft for military purposes. However, the basic technique for radars was used for the first time by Sir Edward Victor Appleton in his ionosphere research in the 1920s. According to Robert Watson-Watt, "But for Appleton's scientific work, radar would have come too late to have been of decisive use in the Battle of Britain." (Nobel Lectures; Physics, 1964).

The scientific use began mainly after the war under the leadership of scientists working on radars during the war.

There are very many applications of radar techniques now in use. However, we shall below review the history of radar techniques which have been applied only for atmospheric observation. We start with the ionosphere observation by ionosonde symbolizing the earliest history of radar observation and proceed to later developments in the observation by other types of radars as partial reflection, meteor, incoherent scatter radars. As to lower atmosphere observation the historical development will be given mainly about MST radars.

2 Radar Technique Used for the Ionosphere Exploration in Early Days

The basic idea for radars was for the first time in 1924 put forward by Appleton who located the ionized upper atmosphere now known as the ionospheric E region. He worked on an experiment with Barnett who was the first graduate student under Appleton's

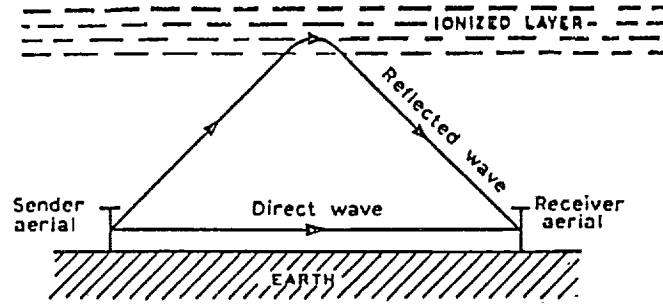


Fig. 1. Appleton and Barnett's experiment in 1924.

guidance at Cambridge (Appleton and Barnett, 1926). It was December 11 in 1924 that they attempted to receive at Oxford radio waves which were transmitted from BBC Station at Bournemouth, a coastal town south west of London. They found, as expected, that the fading pattern maximized repeatedly with the varying radar-wave frequency due to interference between those direct waves which arrived along the ground and those sky waves which were assumed to be reflected from the suspected ionosphere. It is straight forward to obtain the reflection height from the propagation path difference between the direct and sky waves, D , given as

$$m = \frac{D}{\lambda_1} - \frac{D}{\lambda_2} \quad (1)$$

where $\lambda_{1,2}$ are two wavelengths; between these two waves in variation we have m maximum. The arrival direction was identified by a loop and a vertical antenna. This simple system (Fig.1) by Appleton's idea succeeded to determine the E region height as about 100 km, the success which remains as one of his great contributions to the study of upper atmosphere physics leading to his Nobel prize winning in 1947. We see in this Appleton's work the basic idea of radar techniques, especially of FM (Frequency Modulation) type. In 1925 in the U.S.A. Breit and Tuve invented the vertical sounding method which adopts pulse-modulated radio waves to be transmitted vertically, thereby simplifying the system and, since then, being widely used in the world. Thus, the pulsed radar system now in use was established. Appleton worked on theory of the ionized gas (1932). It was found that f_0 the frequency at which radio waves is totally reflected at each height of the ionosphere

is related to the electron density of the ionosphere N at that height as

$$N = \frac{4\pi^2\epsilon_0 m}{e^2} f_0^2 \quad (2)$$

where ϵ_0 is the vacuum dielectric constant and m is the electronic charge and mass; f_0 was found to be 0.75 MHz before dawn in winter. We see that (2) is based on the refractive index n changing relatively to vacuum with the sounding radio frequency f as

$$n^2 = \frac{f^2 - f_0^2}{f^2} \quad (3)$$

which is also applicable for understanding turbulent echoes from the mesosphere in MST radar observations.

Initially, the constant frequency sounding was used, giving the reflection height to vary with time. Note that the virtual height used in this sounding h' is obtained as $h' = \frac{\Delta t}{2}c$ where Δt is the time of the round trip for a radar pulse between the transmitting and the receiving stations, both at the same location and c the light velocity; the pulse traversing the ionosphere on the way is retarded depending on nc , the group velocity, which depends on N on the way given by (2) and (3). In 1930, Appleton initiated to sweep f in order to obtain h' 's versus f , namely, the electron density distribution with height h' 's, the standard ionosphere observation which has routinely in use over the world even now. The ionosphere, however, is probed by this method only in its bottom side lower than the F region peak. The top side remained unknown before the rocket in situ sampling was introduced in the 1950's. The top side sounder on board satellite, based on usual ionosonde techniques, began to supply data of the ionosphere topside on global scale in the 1960's e.g. by the Alouette 1 Satellite as in Fig. 2 (Warren, 1962).

As shown below, in the 1960's novel radar systems were developed for ionosphere observation *i.e.* incoherent scatter radars which enable us to observe the top side ionosphere as well as the bottom side from the ground.

Application of ionosonde observation to ionosphere dynamics is very limited. Quantities available by the observation is the electron density which corresponds to the proving radio wave totally reflected at particular height by (2). We cannot choose certain height for observation unlike in the case of incoherent scatter and MST radars which choose the observing heights by gating the receiver so as to match the time at which echoes from the chosen height arrive. However, some indirect approaches to the dynamical study were attempted as in Fourier-analysing daily variation of ionospheric heights and electron density to find solar and lunar tides (e.g. Appleton and Weeks 1939, Martyn 1947, Rush et al, 1970). Note that the indirect approach depends often on ambiguous mechanisms which connect the dynamics and the observed electron density variation. Ionosphere networks

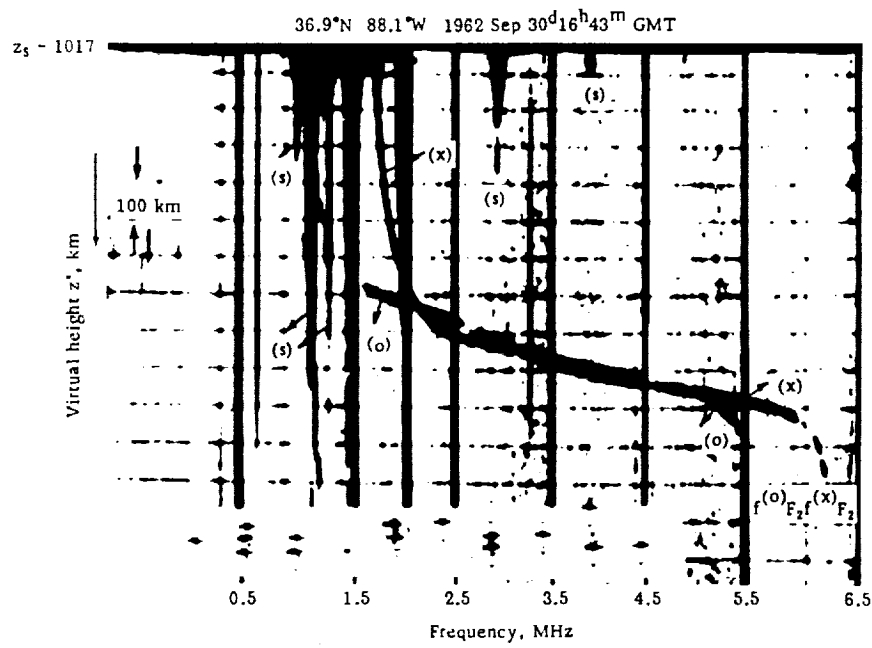


Fig. 2. A topside ionogram for the "quiet" outer ionosphere, obtained with the Alouette 1 satellite at a height $Z_s = 1017$ km.

ORIGINAL PAGE IS
OF POOR QUALITY

local and global are, still now, useful as a source of information regarding the propagation of ionospheric disturbances.

3 Partial Reflection Radar Observation

In the late 1940's, weak echoes were found to be returned from the D region in the height range 75–90 km. Different from usual ionospheric echoes obtained by ionosonde, as mentioned above, the height appeared independent of the frequency range over 1.6–4.0 MHz. In early times the sounding using the weak echoes, understood as partial reflection sounding, was used mainly to measure the D region electron density as based on different absorption between the magnets-ionic ordinary and extraordinary waves of the echoes. We know now that these radar echoes from the mesosphere are utilized for studying mesospheric dynamics. The echoes are now interpreted to be due to, beside partial reflection, the scattering by irregularities of the refractive index for radio waves (See (2)) irregularities which result from atmospheric turbulent mixing of the D region electron density with a height distribution.

Vincent and Belrose (1978) discussed the echoes with 2.66 MHz to vary around 80 km height above which the echoes are less aspect sensitive than those below this height; the echo power spreads in wider angle from zenith in the former than in the latter case. A similar feature was found later for much higher probing frequencies as 50 MHz by Fukao *et al.* in 1979 in their Jicamarca radar experiment. It is still open to question as to how the turbulent mixing of the D region electron density distribution (Fig. 3) can explain this difference around the mesopause. In the field of mesospheric dynamics RRD which stands for partial reflection drift techniques is now regarded as to be important especially for their stable operation for long periods and simple low-cost maintenance of the facility.

The principle of PRD technique is to receive the echo pulse around 2 MHz with its width as 20 μ s by several antennas. Correlations among echoes received at different antennas make it possible to decide the translation velocity of irregularities which cause the diffraction pattern ; the height resolution depending on the pulse width amounts to a few km.

The most sophisticated method, the Full Correlation Analysis, allows the diffraction pattern to be anisotropic changing with time and gives a so-called true velocity. There are many interesting observations of gravity wave and tides by PRD technique by Vincent (1984) and Manson and Meek (1986).

Vincent and Reid (1983) have developed a Doppler radar using MF frequency of this PRD technique, the antenna area having 1 km diameter to produce a 9 °beam-

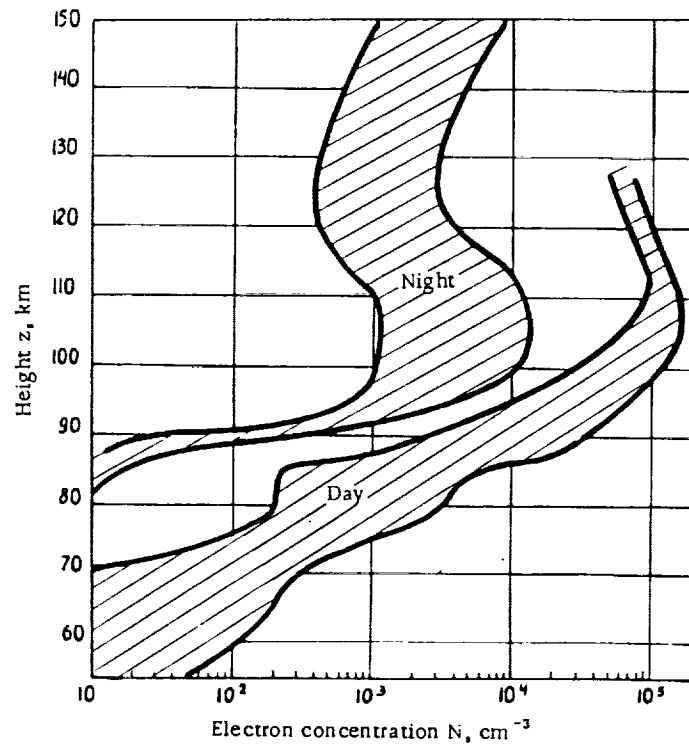


Fig. 3. D region electron density distribution (Al'pert, 1972).

width. They were successful to derive the vertical momentum flux of gravity waves on an interesting idea that two co-planar radar beams steered by an equal angle from zenith are used to measure continuously and simultaneously perturbed winds along the line of sight and the observed velocities squared after being averaged give the vertical momentum flux of horizontal velocity of gravity waves. The deduced flux variation with height seems to suggest a forcing which is consistent with gravity wave theory. This observation technique is now applied to MST radars to other regions of the atmosphere. Details will be discussed in other sessions of the present ISAR course and not be given.

4 Meteor Radar Observation

Meteors impinging on the earth's upper atmosphere produce ionization trails along their path in the height range between 80–100 km depending on their velocity as 10–70 km/s. Appleton in his early observation of the ionosphere has suspected the sudden appearance of the ionization around the E region to be due to meteors. Whilst meteors had been studied by radio methods for astronomical interests before 1960 (McKinley and Millman, 1949) meteor trail movement became a subject of study for observing winds at meteor heights in the 1950s (Manning *et al.*, 1953).

The meteor trail is a column ionization with electron density as $10^{12}/m$; the effective diameter is much shorter than the probing radio-wave frequency, thereby producing coherently scattered echoes over the Fresnel zone along the meteor trail. Meteor trails, with a short life time ($\leq 0.1s$), were expected to move with the local wind. The meteor radar technique is based on this principle and first was used at Stanford, California by Manning who successfully measured winds at meteor heights in the early morning hours in the summer of 1949 to be on the average "125 km per hour with motion's from south-southwest and north the most common" (Manning *et al.*, 1953). It seems interesting to know that he used a rotating radar beam along azimuth to increase the meteor detection frequency with an array of 4 antennas, each changing the phase of the transmitted wave. Later, many (more than 40) meteor radars have been constructed, contributing significantly to the study of winds, called meteor winds, over 80—110 km in heights centered at 95 km where the meteor trail occurs most frequently. The system has been much improved especially in the height resolution which is essential for the study of winds changing rapidly with heights. There are two important improvements; one is the establishment of radio interferometry system to increase the accuracy of the arrival direction of meteor echoes and the other is the use of computers to discriminate echoes on-line. The Kyoto Meteor Radar is one of the standard type of the facility adopting these improvements (Aso *et al.*,

1980). The resolution of elevation angle of the system is 1° averaged over 25° — 70° of elevation angle of the echo arrival direction; this corresponds approximately to 3 km in height resolution.

An advantage of meteor radars over other radars, especially of the standard type, is to be handy in the operation i.e. in unattended fashion suitable for long period observation. The Kyoto Meteor Radar was in operation almost continuously for several years. As done by Meek and Manson (1987) by PRD, the accumulated data made it possible to deduce lunar tides at meteor heights (Tsuda *et al.*, 1981). In general, the facility suits the climatological study of dynamics at meteor heights for atmospheric waves i.e. tides, planetary waves (Tsuda *et al.*, 1988). For obtaining much more data with less height resolution as is required in these dynamical phenomena, the decay height method is used where the principle depends on the measurement of echo decay time i.e. meteor trail life time at each heights which as the molecular diffusion time is calculated using certain model atmosphere as CIRA.

A sophisticated observation of gravity wave was attempted by the Kyoto Meteor Radar. The area at meteor heights illuminated by the radar with an elliptical shape of 100 km in length and 50 km in width, is divided in five strips orthogonal to its major axis. Phase variation of winds from one strip to the next is measured by interferometry, thereby deducing the phase velocity of gravity waves passing in the area (Yamamoto *et al.*, 1986).

The most powerful meteor radar used power as large as 1 MW, receiving tremendous number of echoes (Bowhill *et al.*, 1978). But usual meteor radars receive fairly small number of echoes around dusk, resulting in the overall time resolution of a few hours.

Meteor echoes are also received by both main and side lobes of MST radars and a care must be taken to avoid the echoes which are erroneously detected by the side lobes in wind determination.

5 High Power Radar Observation

In 1958 Gordon pointed out the possibility that a powerful radar can be constructed to be able to detect incoherent scatter echoes by ionospheric free electrons in thermal motion, whereby measuring electron density and electron temperature. His idea was to realize the construction of a radar with "a megawatt transmitter, a 300 meter diameter dish (60 per cent efficiency), a bandwidth of 100 kilocycles matched to the expected Doppler spread, a noise figure of two, 20 decibel signal to noise improvement by averaging pulse, and cable losses of two decibels (Gordon, p.1827, 1958). He further went on saying "The

radar is powerful, but megawatt transmitters are available. The antenna is very large; but since the signal-to-noise does not depend on wavelength, the large area may be obtained with coarse mesh and moderate tolerances by selecting the longest wavelength (about 1.5 meters) consistent with cosmic noise limitations. The antenna may be fixed and pointed vertically". Gordon's idea has introduced in the 1960's the novel powerful ground-based tools called IS (Incoherent Scatter) radars for the study of ionospheric plasma structure and dynamics. The IS radar technique led us in the 1970's to a further development towards MST radar techniques for the study of Mesosphere Stratosphere and Tropospheric dynamics. Before referring to observations of these radars, we have to learn somewhat about how radio waves are scattered in these frequencies where the scatterers are refractive index irregularities, very weak, and filling the entire atmospheric volume illuminated by the radar beams.

We shall follow Villars and Weisskopf in their work on the scattering of electromagnetic waves by turbulent atmospheric fluctuations (1958). The scattered electric field amplitude E_s at a distance R from the scattering volume V ($R^3 \gg V$) is

$$E_s = \frac{\pi}{R\lambda^2} E_0 \left| \int_V d\mathbf{r} \Delta n(\mathbf{r}) e^{i2\mathbf{k} \cdot \mathbf{r}} \right| \quad (4)$$

for back-scattering; λ and \mathbf{k} the radar wavelength and wavenumber respectively; E_0 is the incident wave amplitude. Now n includes neutral-atmospheric effects in addition to that of plasma by (3) as

$$n^2 = 1 + 0.74 \frac{P'}{T^2} + 1.55 \times 10^{-4} \frac{P}{T} - \frac{f^2 - f_0^2}{f^2} \quad (5)$$

where P and P' are the atmospheric and water vapour pressure in the mb and T the temperature. The scattering cross section σ per unit volume per solid angle is

$$\sigma d\Omega = \overline{\Delta n^2} \frac{\pi^2}{\lambda^4} C(2\mathbf{k}) d\Omega \quad (6)$$

where Ω is the solid angle and

$$C(2\mathbf{k}) = \left(\frac{1}{2\pi} \right)^3 \frac{1}{(\overline{\Delta n^2})} \left| \int_V \Delta n(\mathbf{r}) e^{i2\mathbf{k} \cdot \mathbf{r}} \cdot d\mathbf{r} \right|^2 \cong \left(\frac{1}{2\pi} \right)^3 \int_{-\infty}^{\infty} C(\mathbf{r}) e^{i2\mathbf{k} \cdot \mathbf{r}} \cdot d\mathbf{r} \quad (7)$$

where $C(\mathbf{r})$ is the auto-correlation function of $\Delta n(\mathbf{r})$. Thus, by (4) σ is proportional to the spectrum intensity of Δn for $2\mathbf{k}$; the spectrum is the Fourier transform of the auto-correlation function. This implies intuitively that radars pick up as their targets only those irregularities whose size along the radar line of sight is $\frac{\lambda}{2}$ as called Bragg's law in crystal physics.

To ionospheric plasma (4) is given by (3) and (5)

$$\langle \overline{\Delta n^2} \rangle = \left| \frac{\Delta N}{N} \right|^2 \left(\frac{f_0^2}{2f^2} \right)^2 \approx \frac{1}{4} \left| \frac{\Delta N}{N} \right|^2 \left(\frac{f_0}{f} \right)^4 \quad (8)$$

for $f \gg f_0$ thus, by (6)

$$\sigma = (\text{const}) C(2k) \quad (9)$$

i.e. independent of f .

(7) is also applicable to mesosphere observation where free electrons are mainly responsible to the echo scattering.

To the stratosphere and troposphere, the third and second terms in (5) are mainly responsible, respectively. Then, we have by (6)

$$\sigma = (\text{const}) f^4 C(2k) \quad (10)$$

In (9) and (10) "const" is proportional to the mean square fluctuation of each term in (5). Physics to produce refractive index irregularities is different between the regions we observe, i.e. the ionosphere and the lower neutral atmosphere.

In the case of the ionosphere, the scatterers are free electrons in random thermal motion which should produce incoherent scattering. It is expected then that σ is $4\pi r_e^2$ where r_e is the classical electron radius; $\sigma \approx 10^{-28} m^2$ as proved strictly by Fejer in 1960. Bowels (1958) has made for the first time the incoherent scatter experiment using a 41 MHz radio wave, 4-6 MW, 1024 antennas in a $(116 \times 140m)$ area etc. He received echoes as expected by the Gordon's idea in their intensity but not in the Doppler width which was to be due to electron thermal motion equivalent to the F region electron temperature as 10^3 Kelvin in daytime i.e. as large as several ten KHz. What he really obtained was much less than that. Later it was found that if, as in the present case, the probing radar wavelength is much longer than the Debye shielding length which is less than 1 cm in the F region, the Doppler width is mainly due to ions which is in thermal motion of much lower temperature than that of free electrons; the observed Doppler width must be narrower by, at least, 10^{-2} , the mass ratio between electrons and ions. This finding which had not been expected before the experiment opened much more possibilities for this technique so as to be able to observe physical states of ions as well as electrons in the ionosphere. Further, based on close physical coupling between ions and neutral particles due to their similar masses, the thermospheric gas dynamics has also been developed by IS radar observation.

IS radars are regarded in ability as to be rivals and also complements to in situ sampling by rockets and satellites (Evans, 1974). This type of radars was constructed at Arecibo in Puerto Rico and Jicamarca Peru and later at St. Santin in France and Milstone Hill in

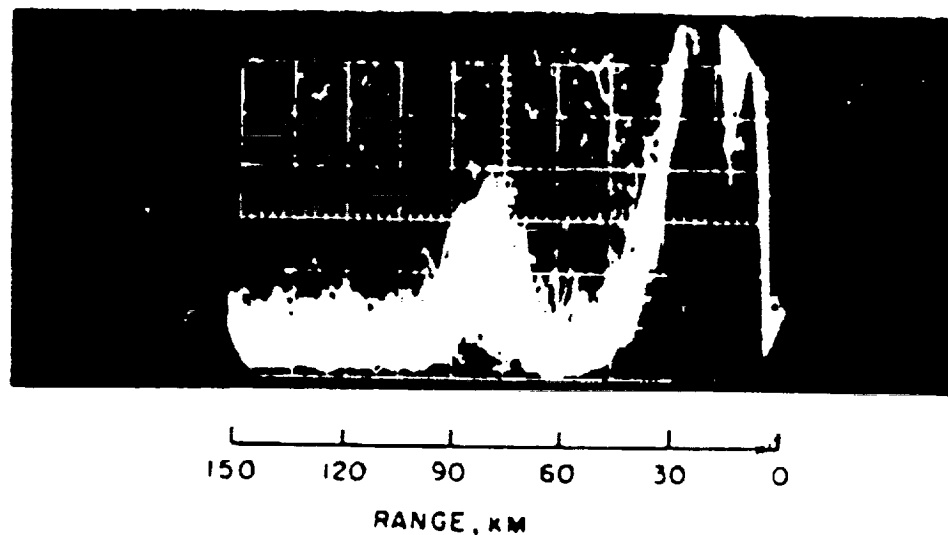


Fig. 4. Observation of a high power radar by Bowles 1958. Note that a strong echo is found around 75 km.

U.S.A. and recently in Scandinavian countries. Details of their contributions will be learned in other sessions.

History shows that sciences enjoy often remarkable progresses through unexpected findings. This is true, as above-mentioned, for IS radars, detecting the observed wide Doppler broadening due to ions. Another finding came unexpectedly around 1970 when the Jicamarca radar, which usually obtained only IS echoes from the ionosphere, detected unknown echoes presumably from the mesosphere. Few seemed to believe Woodman's report on this finding at International Equatorial Aeronomy Conference in Nigeria in 1972. The echoes showed Doppler shifts corresponding to several ten meter per second in velocity. Soon, Woodman and Gullén (1974) identified the echoes with those of scattering due to refractive index irregularities which are caused by turbulence moving with local winds in the mesosphere.

It seems impressive that as in Fig. 4 Bowles in his first IS experiment in 1958 found without noticing any significance intense echoes around a 80 km height. This is an example that scientific significance may vary with time! The finding by Woodman implies the beginning of a novel radar technique to be able to observe mesospheric winds, the MST

technique which enables us to observe the mesosphere, stratosphere and troposphere on the same principle i.e. due to "Clear Air Turbulence (CAT)" echoes in meteorological terms.

We call the mesosphere and stratosphere combined the middle atmosphere which had remained as ignorosphere before 1970, but were required immediate scientific elucidation in the 1970s. This was mainly because of the environmental assessment demanded by threatening pollution by artificial pollutants as Freon, NO_x etc. Under the circumstance, Middle Atmosphere Program (MAP), an internationally cooperative scientific program for the purpose, was planned in the 1970s and realized between 1982-1985. MST radar techniques developed very rapidly just parallelly along the MAP course and played a central role in the program. This is the case even beyond MAP to date.

Let us go back to (9) and (10), the base for MST radar techniques, where $C(2k)$ is now the spectrum of atmospheric turbulence which is known as

$$C(2k) \propto k^{-\frac{11}{3}} \quad \text{or} \quad \sigma = (\text{const})k^{-\frac{11}{3}} \quad (11)$$

and

$$\sigma = (\text{const})k^{\frac{1}{3}} \quad (12)$$

provided that the radar wavelength is within the turbulence inertia subrange; (11) and (12) are applicable, respectively, to the mesosphere, and the stratosphere; (12) is also for the stratosphere. Note that (11) and (12) show the basic principle for designing MST radars; in terms of the radar frequency, the lower the better for the mesosphere, whilst the reverse is true for the stratosphere and troposphere. However, the wave length must always be in the inertia subrange; otherwise, in the viscous range, the spectrum intensity is so weak. The minimum size giving the inertia subrange is approximately several meters in the mesosphere, decreasing monotonously down to 1 cm in the troposphere. Now, the radar wavelength of 5 m is of a fairly standard i.e. 50 MHz. The maximum output is usually 1 MW and the antenna area is 10^4 m^2 or more. By (11) we know that PRD techniques as in Section 4 can use a very weak power as a few kW; the frequency used there ($\sim 2 \text{ MHz}$) is $(1/20)$ which gives 6×10^4 times in the turbulent spectrum intensity to that for 50 MHz of MSP radars by (11). In (11) and (12) σ contains a constant which depends on the height distribution of n implying that as in (5) σ depends on the height distribution of water vapour, air density and electron density. Their distributions are disturbed by turbulence; the turbulent diffusion is the basic process. Villars and Wiskap (1958) failed to notice this process assuming unrealistic air compression by turbulence. The pioneering Booker-Gordon theory (1950) was also unrealistic, resulting in such a σ as virtually independent of k , unlike either (11) or (12).

Atmospheric gravity waves (GW's hereafter) had drawn little interests among meteorologists, say, before 1970. Ionospheric people showed some interests in those events in which GW cause remarkable disturbances named TID (Traveling Ionosphere Disturbance). GW's, which are produced mainly in the troposphere, are so weak that they play no significant role in tropospheric dynamics. However, GW's travel upwards, growing exponentially with the decreasing ambient air density and reaching tens of meters per second in velocity. In the 1970's people began to suspect that GW's may play an important role in the mesosphere. Around the end of the 1970's a theory by Matuno (1982), Holton (1981) and Lindzen (1981) predicted that GW's, after growing to certain degree, tend to break near the mesopause, whereby releasing their momentum against the local wind, working as a dynamic brake. This dynamical brake can explain why winds tend to weaken around a 80 km height as observed; Without this effect, winds should have been indefinitely increased with height. Thus, GW's are regarded as to play an important role in the middle atmosphere general circulation and became one of the most interesting subjects in MAP. Temperature observed by remote sensing techniques from satellite cannot be relevant because of inferior vertical resolution due to the technique and also inferior time resolution due to satellite motion. We need on many occasions 1 km in resolution along the vertical direction and a few minutes in time resolution which can be attained only by MST radars. Among various MST radars now in operation over the globe, that in Japan, named the MU radar to observe both middle and upper atmospheres, is outstanding because it can steer the beam so rapidly by electronic phase-shifting, a characteristics, which makes it possible to measure the GW structure instantaneously within the cone suspended by 30 ° from zenith. There are many studies on peculiar GW behaviors by MST radars. The pioneering works around 1980 owes mainly to Balsley's group in Boulder and Röttger and Max Planck's group in Lindau (e.g. Balsley and Gage, 1980). These works will be discussed elsewhere through the present course.

We have now networks for global observation of the mesosphere dynamics consisting of both MST radars, PRD radars and meteor radars. One of the unique cooperative observations has been done between Kyoto and Adelaide which are located at geographically conjugate points at 35 ° in lat. with respect to the equator. So far, tidal waves have been successfully studied by this cooperation.

There are radars smaller in size mainly for stratosphere and troposphere observation as at Sun-Set near Boulder constructed in the 1970's (e.g. Green *et al.*, 1979); they are ST radars which may replace the conventional routine meteorological balloon observations after distributed at many locations over the globe in future. They are fairly low in cost of construction and can operate continuously and almost unattended.

Rapid progress seen in radar atmospheric dynamics has been successful only by a good cooperation among people of different disciplines especially between ionosphere radio-physicists and meteorological dynamists. This cooperation will be essential for future advancement in this field.

6 Future Radar Observation

Now the atmosphere is found to be one large and complicated system, each part coupling with each others, both horizontally globally and vertically from the ground to the middle and, further, upper atmosphere. Anthropological pollution has become serious problems on atmospheric environments. Under the circumstance we need to understand the atmospheric dynamics increasingly accurately with time. For this purpose, radars will present useful and powerful techniques. These radars must be distributed globally making up an effective and comprehensive network relevant for the purpose.

At present we have none of powerful radars in the equatorial region which is receiving the maximum solar energy input driving almost the whole atmosphere in motion. Interaction of the atmosphere with the ocean there is also important but not well understood. For completing a global radar network the powerful radar construction there is essential. This is the Equatorial Radar Project which has been in planning mainly between Japan and Indonesia. The Indonesian district is the most intensively convecting region together with the equatorial Africa and the Amazon in South America. The MU radar, Adelaide radars (PRD radar), Chung-Li radar (ST radar) and some other radars to come in the Asian Sector will make up a very desirable network with this equatorial radar along the Asian longitude.

The planned system is very ambitious one (Fig. 5), able to measure the entire atmosphere from near the ground to the ionosphere with an excellent resolution with a 300 m diameter of the antenna area and one MW power, beam-steerable by 20 °from zenith. Beside the central radar, there will be meteorological radars together with other supporting facilities. This is the essence of the International Center for Equatorial Atmosphere Research which we desire to be realized in the future. Good Luck for our future!

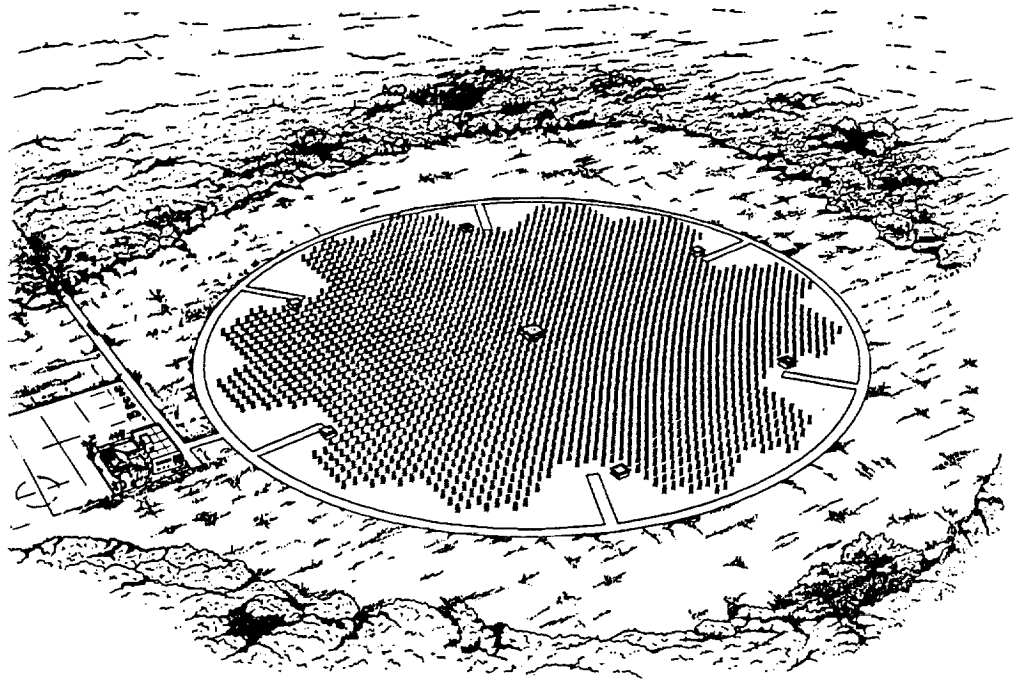


Fig. 5. Artistic view of the equatorial radar.

References

- Al'pert, *Radio wave propagation and the ionosphere*, 1, the ionosphere, 248, (1973, translated from Russian).
- Appleton E. V., *Wireless studies of the ionosphere*, J. Institution. Elect. Engineers., **71**, 642-650, (1932).
- Appleton E. V. and M. A. F. Barnett, *On some direct evidence for downward reflection of electric rays*, Proc. Roy. Soc., (London), **109** 621-641, (1926).
- Appleton E. V. and K. Weekes, *On lunar tides in the upper atmosphere*, Proc. Roy. Soc., **A171**, 171-187, (1939).
- Aso, T., T. Tsuda, Y. Takashima, R. Ito and S. Kato, *Observations of lower ionospheric wind by the Kyoto meteor radar*, J. Geophys. Res., **85**, 177-184, (1980).
- Balsley, B. B. and K. S. Gage, *The MST radar technique: Potential for the middle atmospheric studies*, Rev. Pur. Apple. Geophys., **118**, 459-493, (1980).
- Booker, H. G. and W. E. Gordon, *A theory of radio scattering in the troposphere*, Proc. Inst. Radio Engineer., **38**, 401-412, (1950).
- Bowles, K. L., *Observations of vertical incidence scatter from the ionosphere at 41 Mc/sec*, Phys. Rev. Lett., **1**, 454-455, (1958).
- Bowhill, S., *Private communication*, (1982).
- Breit, G. and M. A. Tuve, *A radio method of estimating the height of the conducting layer*, Nature **116**, 357, (1925).
- Evans, J. V., *Some post-war developments in ground-based radiowave sounding of the ionosphere*, J. Atmos. Terr. Phys., **36**, 2183-2234, (1974).
- Fejer, J., *Scattering of radiowaves by an ionized gas in thermal equilibrium*, Can. J. Phys., **38**, 1114-1133, (1960).
- Fukao, S., T. Sato, R. M. Harper, S. Kato, R. F. Woodman and W. E. Gordon, *Mesospheric winds and waves over Jicamarca on 23-24 May 1974*, J. Geophys. Res., **84**, 4379-4386, (1979).
- Green, J. L., J. M. Warnock, R. H. Winkler and T. E. VanZandt, *A sensitive VHF radar for the study of winds waves and turbulence in the troposphere, stratosphere and mesosphere*, Radar Meteorol. Conf. April 22-24, 1975 Houston, Texas, Amer. Meteor. Soc., 313-315, (1975).

- Gordon, W. E., *Incoherent scattering of radio waves by free electrons with applications to space exploration by radar*, Proc. IRE, **46**, 1824-1829, (1958).
- Holton, J. R., *The role of gravity wave induced drag and diffusion in the momentum budget of the mesosphere*, J. Atmos. Sci., **39**, 791-799, (1982).
- Lindzen, R., *Turbulence and stress owing to gravity wave and tidal breakdown*, J. Geophys. Res., **86**, 9707-9714, (1981).
- Manson, A. H. and C. E. Meek, *The dynamics of the mesosphere and lower thermosphere at Saskatoon (52°N)*, J. Atmos. Sci., **43**, 276-284, (1986).
- Manning, L. A. O., O. G. Villard and A. M. Peterson, *Meteoric echo study of upper atmospheric winds*, Proc. IRE, **38**, 877-883, (1953).
- Martyn, D. F., *Atmospheric tides in the ionosphere II Lunar tidal variation in the F region near the magnetic equator*, Proc. Roy. Soc., **A190**, 273-288, 1947.
- Matsuno, T., *A quasi one-dimensional model of the middle atmosphere circulation interacting with internal gravity waves*, J. Meteorol. Soc. Jpn. **60**, 215-226, (1982).
- McKinley, D. W. R. and P. M. Millman, *A phenomenological theory of radar echoes from meteors*, Proc. IRE **37**, 364-375, (1949).
- Meek, C. E. and A. H. Manson, *Middle atmosphere lunar tides at Saskatoon (52°N, 107°W)*, J. Atmos. Terr., **35**, 445-449, (1987).
- Nobel Lectures: Physics. 1942-1962, pub. for the Nobel Foundation in 1964 Elsevier Pub. Co. Amsterdam-London-N.Y., 1964.
- Röttger, J. and C. H. Liu, *Partial reflection and scattering of VHF radar signals from the clear atmosphere*, Geophys. Res. Lett., **5**, 357-360, (1978).
- Rush, G. M., D. E. St. John and S. V. Venkateswaran, *A unified description of the tidal effects in f^oF_2* , Radio Sci., **5**, 1413-1428, (1970).
- Tsuda, T., S. Kato and R. A. Vincent, *Long period wind oscillations observed by the Kyoto meteor radar and comparison of the quasi-2-day wave with Adelaide HF radar observations*, J. Atmos. Terr. Phys., **50**, 225-230, (1988).
- Tsuda, T., Tani, T. Aso and S. Kato, *Lunar tides at meteor heights*, Geophys. Res. Lett., **8**, 191-194, (1981).
- Villars, F. and V. F. Weisskopf, *The scattering of electromagnetic waves by turbulent atmospheric fluctuations*, Phys. Rev., **94**, 232-240, (1954).
- Vincent, R. A., *Gravity wave motions in the mesosphere*, J. Atmos. Terr. Phys., **46**, 119-128, (1984).

- Vincent., R. A. and J. S. Belrose, *The angular distribution of radio waves partially reflected from the lower ionosphere*, J. Atmos. Terr. Phys., **40**, 35–47, (1978).
- Vincent, R. A. and I. M. Reid, *HF Doppler measurement of mesospheric gravity wave momentum fluxes*, J. Atmos. Sci., **40**, 1321–1333, (1983).
- Warren, E. S., 1962 *Radio Wave Propagation and the ionosphere* by Y. L. Al'pert 1, the ionosphere, p. 40, (1973, Translated from Russian)
- Woodman, R. F. and A. Gullen, *Radar observations of winds and turbulence in the stratosphere and mesosphere*, J. Atmos. Sci., **31**, 493–505, (1974).
- Yamamoto, M., T. Tsuda and S. Kato, *Gravity waves observed by the Kyoto meteor radar in 1983—1985*, J. Atmos. Terr. Phys., **48**, 597–1985, (1986).
- Yamamoto, M., T. Tsuda, T. Sato, S. Fukao and S. Kato, *A saturated inertia gravity wave in the mesosphere observed by the middle and upper atmosphere radar*, J. Geophys. Res., **92**, 11993–11999, (1987).

N 9 1 - 2 6 6 1 5

Chapter 2

RADAR PRINCIPLES

Toru Sato

Radio Atmospheric Science Center
 Kyoto University, Uji, Kyoto 611, Japan

1 Introduction

Radar is a general technique, which has a wide range of variability depending on the type of targets to be measured. A radar can be designed to measure a bullet, while another may observe a planet. The radio frequency spectrum employed also spreads out over many decades.

The target of radars described here is the earth's atmosphere. More precisely, it is so called *clear air echoes* from the earth's atmosphere produced by fluctuations of atmospheric index of refraction. We will refer this kind of radar as the *atmospheric radar* here. There is also a category of radar called *weather radar*, which observes precipitation as its principal target. Although much is common, in principle, to the weather radar and the atmospheric radar, we do not discuss the former here. Those who are interested in weather radars are referred to standard text books such as Battan (1973) or Doviak and Zrnić (1984).

It is possible for powerful weather radars to observe the clear-air echoes. Actually, the name clear-air echo is given in the history of development of the weather radar to classify echoes from unknown targets. Above mentioned text books also discuss about the clear-air echoes in some details, but the major difference between their approach and ours is simply that we discuss radars specially designed to observe the clear-air echoes. As we will see later, this difference affects the choice of frequency, requirement on the sensitivity, and the way data are processed. As a consequence, these two types of radars often look surprisingly different.

Weather radar usually use frequencies of SHF band (3–30 GHz), while atmospheric radars make use of much lower HF (3–30 MHz), VHF (30–300 MHz), or UHF (300 MHz–3 GHz) bands. Antenna size of weather radars is a few to about ten meters in diameter, but an atmospheric radar may require a diameter of more than a hundred meters, depending

on its target region. Operational atmospheric radars have antennas with diameter of 10–300 m. Weather radars cover a wide horizontal area of up to several hundred kilometers in radius by scanning their antenna with low elevation angle. Most of atmospheric radars, in contrast, observe narrow angular range around the zenith, but with larger vertical coverage than the weather radars. The hardware of atmospheric radars is examined in detail in a separate chapter.

It should be noted that the atmospheric radars can, at least in principle, and often in reality, also observe precipitation echoes, which is one of important applications of the atmospheric radars.

Atmospheres of other planets can be, in principle, observed by a similar way as those discussed here. However, the extremely large distance between the radar and the target will cause many problems peculiar to such an application. It is also possible to design a radar to observe clear-air echo on board the vehicles such as ships, airplanes, and satellites. Additional Doppler shifts due to motion of the vehicles will be one of major problems, as well as the problem of size limitations, in such cases.

In the following sections, basic characteristics of echoes are examined, and important concepts concerning techniques of the atmospheric radar are introduced.

2 The Target

One of important features which make the atmospheric radar unique and different from other kinds of radars is that it observes basically transparent earth's atmosphere. We examine here the nature of the atmosphere as a target of radar.

2.1 Vertical Structure of the Atmosphere

The target of the atmospheric radars is the entire earth's atmosphere which extends from the ground (or ocean surface) to the upper boundary of the atmosphere which is usually defined as the highest region rotating together with the earth, whose height ranges from 20,000 km to 40,000 km. Of course, this upper boundary has not yet been observed by means of radar, and only a few of existing radars can observe the atmospheric region above 1,000 km height, most of others with much poorer sensitivity. The lowest observable height, which is usually limited by the switching speed from transmission to reception, ranges from a few hundred meters to several kilometers.

The atmosphere shows a significant variation in its nature even within this limited height range of 0-1,000 km. The largest distinction is between neutral and ionized atmospheres, which are roughly separated by a height of around 100 km. Below this height, the atmosphere is treated as a neutral fluid, while ionized plasma plays an important role above it. These two regions had long been studied independently, and it was widely understood only recently that both can be studied with the same principle.

The other common way of dividing regions is the one based on the vertical structure of atmospheric temperature. Figure 1 shows a typical temperature profile, which is a model profile of mid-latitude equinox taken from the U. S. standard atmosphere (1976). The right ordinate shows the atmospheric pressure in millibars. The atmosphere is classified into 4 regions of troposphere, stratosphere, mesosphere, and thermosphere in ascending order of height.

The troposphere is characterized by a constant decrease in temperature with height. The lapse rate of the model is 6.5 K km^{-1} . The main heat source for this region is the solar radiation absorbed by the surface of the earth. Temperature ceases to decrease at 10-15 km, at the tropopause. The height of the tropopause has a clear latitudinal variation, being highest in the equatorial region and decreasing with increasing latitude.

The stratosphere is the region in which temperature increases with height. The stable stratification of the air due to positive temperature gradient accounts for the origin of the name of this region. Temperature reaches its maximum of about 270 K around 50 km at the stratopause height. The heat source for this maximum is the absorption of solar

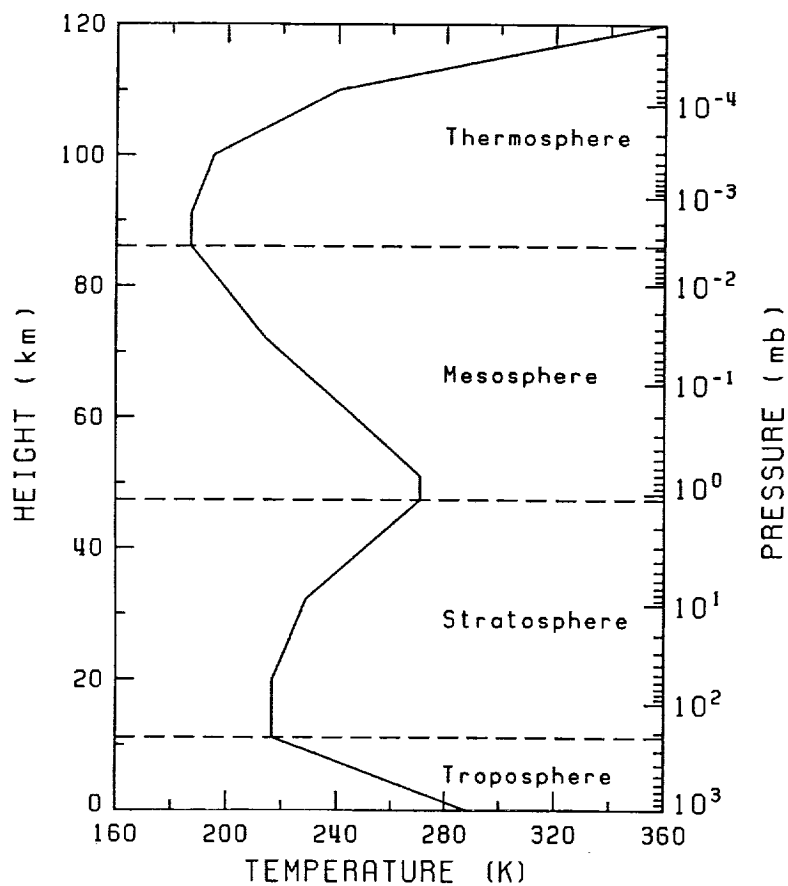


Fig. 1. A model temperature profile for mid-latitude equinox (taken from the U. S. standard atmosphere, 1976).

ultraviolet radiation by ozone.

Temperature decreases again in the mesosphere until it reaches the minimum of 180–190 K at the mesopause height of 80–90 km. The heat balance in this region is determined by the radiative heating of molecular oxygen and infrared radiative cooling of carbon dioxide.

Above 80–90 km, the temperature increases monotonically with height to the limit of 1,000–2,000 K due to radiative heating of atomic oxygen *etc.* This region is called the thermosphere in this nomenclature, but it also corresponds to the ionosphere in the above distinction.

2.2 Radio Refractive Index

Characteristics of the atmosphere seen by radio waves in the absence of liquid water is expressed in terms of the refractive index n . As is the case of optics, n is defined as

$$n = \frac{c}{v}, \quad (1)$$

where c is the speed of light in free space and v is the velocity of the radiowave in the air. Macroscopic changes of n in space cause refraction or reflection, and microscopic changes cause scattering, the latter being of major concern to the atmospheric radar.

Although we are interested in the fluctuations of n from its background, it is important to examine what determines the background n . Major contributions to n at frequencies of HF through UHF bands are expressed approximately as (Balsley and Gage, 1980)

$$n - 1 = \frac{3.75 \times 10^{-1} e}{T^2} + \frac{7.76 \times 10^{-5} P}{T} - \frac{N_e}{2N_c}, \quad (2)$$

where e (mb) is the partial pressure of water vapor, P (mb) is the total atmospheric pressure, T (K) is the absolute temperature, N_e is the number density of electrons, and N_c is the critical plasma density.

The first term represents the contribution from water vapor. As is well known, the water molecule has a dipole moment, which varies with frequency. At extremely high frequency of visible light, only the polarized electric field of the water molecules counts for the refractivity. At lower frequencies of radiowave, the water molecules are not only polarized but they also reorient themselves rapidly enough to follow the changes of electric field. As a result, the contribution of the water vapor to n is greater for radio than for optical frequencies (Battan, 1973).

Above the tropopause height of 10–15 km, the partial pressure of water vapor becomes negligibly small. The second term due to dry air becomes dominant at this region. Since

the major constituents of the earth's atmosphere, N_2 and O_2 , do not change their mixing ratio largely throughout the middle atmosphere of up to around 100 km, the coefficient stays unchanged. Unlike the first term due to the water vapor, this term is frequency independent, being the same for light and radio waves.

While these two terms concern the neutral atmosphere, the third term gives the contribution from free electrons. This term is negligible below about 50 km, but is dominant at ionospheric heights of above around 80 km. It should be noted here that Eq. 2 gives an approximation valid only when $N_e \gg N_c$, and the effect of the third term is expressed more precisely as

$$n = \sqrt{1 - \frac{N_c}{N_e}}, \quad (3)$$

The critical electron density N_c thus determines the condition with which total (or perfect) reflection occurs in the ionosphere. It is given in MKS units by

$$\begin{aligned} N_c &= \frac{4\pi^2\epsilon_0 m_e f^2}{e^2} \\ &= 1.24 \times 10^{-2} f^2, \end{aligned} \quad (4)$$

where ϵ_0 is the dielectric constant in free space, m_e and e are the mass and the charge of an electron, respectively, and f is the radar frequency (*e.g.*, Stix, 1962). The electron density N_e in the ionosphere usually takes its maximum value of 10^{11} – 10^{12} m^{-3} at 200–400 km height. If N_c is smaller than this maximum, the radiowave is reflected at some height where the condition $N_e = N_c$ is met. Otherwise, the entire energy associated with the radiowave is radiated out of the earth's atmosphere except for a tiny fraction absorbed or scattered by the atmosphere. Under most of ionospheric conditions, N_c is larger than N_e at all heights for frequencies of VHF or higher.

Figure 2 shows a typical variation of these three terms with height. The pressure and temperature are taken from the U.S. standard atmosphere (1976). The saturation pressure is used for the water vapor. The electron density is adopted from Mechtly *et al.* (1972).

2.3 Fluctuations of the Refractive Index

In the absence of total reflection, scattering from fluctuations in the refractive index n dominates the received echo of the atmospheric radar. Statistical fluctuations of the electron density due to random thermal motion of electrons and ions can be strong enough in the ionosphere to cause detectable scattering. This component is called *incoherent scattering* because scattered wave from individual electrons are random in phase, so that

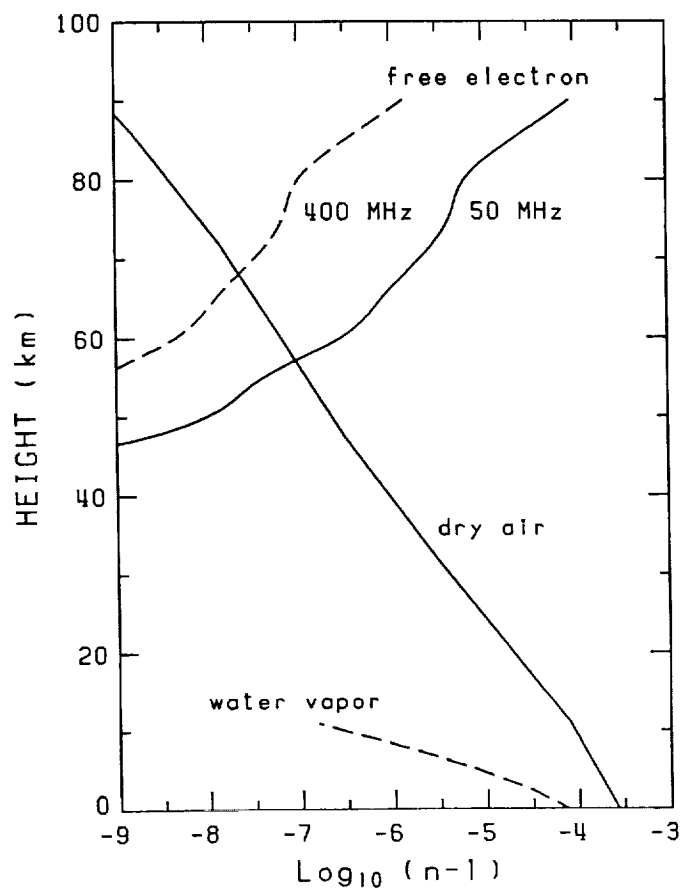


Fig. 2. Typical height profiles of water-vapor, dry-air, and free-electron contributions to the radio refractive index n .

they add up incoherently. Received echo power is then proportional to the number of electrons illuminated by the radar.

Fluctuations due to atmospheric turbulence is known to be the major source of scattering in the lower and the middle atmosphere. This component is often called *coherent scattering* in contrast to the incoherent scattering in the ionosphere. The main difference of the coherent scattering from the incoherent scattering is that the fluctuation of n is caused by macroscopic motion of air parcels, each of which contains a large number of molecules and/or electrons which contribute to the scattered electric field coherently in phase. As a result, the scattered echo power is roughly proportional to the square of the number density of scatterers instead of the linear proportionality of the incoherent scattering. This substantial enhancement in the echo power is the basis for the MST (Mesosphere Stratosphere Troposphere) radars being able to observe the neutral atmosphere with a relatively small system compared to powerful incoherent-scatter radars.

A large difference of the atmosphere from other targets of radars is its distributed nature. While usual targets as airplanes, ships, cars, or missiles, which are referred to as *hard targets* based on their physical nature, have clear boundary, which enables identification of the target, it is usually absent in spatial distribution of the echo from the atmosphere. It is thus necessary to distinguish parts of the atmosphere by means of spatial coordinates of direction and range. This type of target is often called as the *soft target*.

A direct consequence of this limitation, for example, is the fact that decreasing the size of identified volume in order to improve spatial resolution results in a decrease in the echo power, and thus a decrease in sensitivity. On the other hand, the rate of decrease of the echo power with increasing range to the target is much slower with the soft target than with the hard target, because the volume, and thus the size of the scatterer, usually increases with increasing range in case of the soft target.

Mathematical relations which determine the strength of the echo are derived in the following section.

3 The Radar Equation

In designing a radar system, we first need to know how strong the echo of interest is. We will derive a relation between transmitted and received power, called the radar equation, for various situations which concern observations with the atmospheric radar.

3.1 The Radar Equation for a Hard Target

Before discussing the scattering from fluctuations in the radio refractive index, let us first examine a simpler case of the scattering from an isolated hard target located in free space. Suppose we transmit radiowave of power P_t out of an omni-directional antenna which radiates the power into all directions with uniform strength. The density of the power P_i passing through a unit area located at a point sufficiently far from the antenna and perpendicular to the direction of propagation is given by

$$P_i = \frac{P_t}{4\pi r^2}, \quad (5)$$

where r is the distance of the point from the transmitting antenna. The antenna used for a radar usually has a strong directivity with which a narrow region can be illuminated selectively. The above equation is thus modified as

$$P_i = \frac{P_t G_t}{4\pi r^2}, \quad (6)$$

where G_t is the *directional gain*, or simply, the *gain*, of the antenna, which is a function of the azimuth and the zenith angles.

We now consider a target located at this point which intercepts the power and scatters it into various directions. The density of the scattered power P_s per unit area at a distance r' from the target is expressed in terms of the *scattering cross section* σ of the target as

$$P_s = \frac{P_i}{4\pi r'^2} \sigma, \quad (7)$$

where σ is defined as an effective area of the scatterer, the power illuminating which area is scattered isotropically. It should be noted that an alternate parameter of the *differential scattering cross section* $\sigma_d \equiv \sigma/4\pi$ which expresses the scattered power per unit area and *per unit solid angle* is also used often, and occasionally the difference is not clearly mentioned.

It is known, for example, that a perfectly conducting sphere with a radius much larger than the wave length of the radar has a scattering cross section equal to its physical cross section (*e.g.*, Skolnik, 1980).

If we receive the scattered power with an antenna which has a capability of collecting all power passing through an *effective area* A_e , the received power P_r is expressed as

$$P_r = P_s A_e L, \quad (8)$$

where L is the loss factor which represents various attenuation of the received signal due to antenna, transmission line, connectors *etc.* By combining Eqs. 6–8, we obtain

$$P_r = \frac{P_t G_t A_e L}{(4\pi r^2)(4\pi r^2)} \sigma. \quad (9)$$

This equation gives the received echo power from a given target by a radar, and hence is called the *radar equation*. We have so far considered a general case in which the transmitting and the receiving antennas are not the same. Although this type of radar, which is called the *bistatic radar*, or the *multi-static radar* in case there are more than one receiving antennas, is used in reality for some applications, it is much more common to use the same antenna both for transmission and reception for simplicity. This type of radar which uses a single antenna is called the *monostatic radar*, and we will limit our discussion below to this type of radars.

The two parameters G_t and A_e used in the above equations seem to indicate, at a first look, distinct properties of an antenna. There is, however, a useful universal relation known between the two (Silver, 1951), which is

$$G_t = \frac{4\pi A_e}{\lambda^2}, \quad (10)$$

where $\lambda = c/f$ is the radar wavelength. Although A_e is a function of direction since G_t is so, it is implicitly assumed that the antenna beam of the radar is pointed to the direction of the target, so that both G_t and A_e take their maximum value.

For a monostatic radar, the radar equation thereby reduces to

$$P_r = \frac{P_t A_e^2 L}{4\pi \lambda^2 r^4} \sigma. \quad (11)$$

This equation gives the basis for radar system design of choosing appropriate transmitter power P_t and effective antenna area A_e for a given target with a scattering cross section σ at a range r .

The minimum detectable power P_r is limited by the noise power P_n which contaminates the received signal from the target. In most cases, the dominant component of the noise is the *white noise* which is defined as a random time series of signal with a uniform frequency power spectrum within the receiver bandwidth B . The power of white noise produced by a resistor at a temperature T and for a given bandwidth B is given by (Dicke *et al.*, 1946)

$$P_n = kTB \quad (12)$$

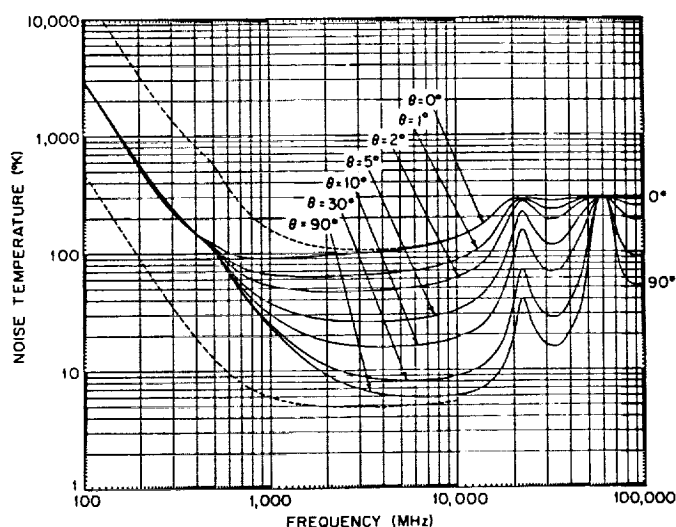


Fig. 3. The sky noise temperature versus frequency (after Skolnik, 1970).

where k is the Boltzmann constant ($= 1.38 \times 10^{-23} \text{ W s K}^{-1}$).

Since this formula can be applied to any type of white noise, it is common to express the noise power of the radar in terms of this equation where T is called the *equivalent noise temperature*. This noise temperature represents all kind of noise sources, and is decomposed as

$$T = T_s L + T_r \quad (13)$$

where T_s is the sky noise temperature due to cosmic, solar, and atmospheric radiation, L is the loss factor, and T_r is the noise power generated by the receiver itself. The sky noise temperature varies largely depending on the radar frequency and also on the direction of the antenna beam. Figure 3 illustrates it versus frequency (after Skolnik, 1970). Solid curves are for various elevation angle θ of the antenna beam direction for geometric-mean galactic temperature, sun noise ten times quiet level, sun in unity-gain side lobe, cool temperate-zone troposphere, and 2.7 K cosmic black body radiation. The upper dashed curve is for maximum galactic noise at the center of galaxy, sun noise 100 times quiet level, zero elevation angle, and other factors the same as for the solid curves. The lower dashed curve is for minimum galactic noise, zero sun noise, and elevation angle of 90° . The maxima at 22 and 60 GHz are due to water-vapor and oxygen absorption resonances.

3.2 The Radar Equation for Distributed Targets

The radar equation derived above applies to a single target. If there are more than one target in the same volume V of the air observed by a radar, the received electric field is expressed as the sum of the electric field components caused by individual scatterers. For a situation where they are random and have no correlation between each other, the total received echo power becomes the sum of the echo power from individual scatterers. In this case, the scattering cross section σ in Eqs. 7, 9, and 11 are simply replaced by $\Sigma\sigma$. If the number of scatterers is very large and if scatterers are distributed uniformly in space, σ increases linearly as V increases. It is thereby suitable to define the *volume reflectivity* η , or the scattering cross section per unit volume as

$$\eta \equiv \frac{d\sigma}{dV}. \quad (14)$$

It should be noted that η has a dimension of $[\text{m}^{-1}]$ unlike the ordinary reflectivity, which is dimensionless.

This situation applies, for example, to the incoherent scattering due to free electrons in the ionosphere observed with a sufficiently high frequency of above about 1 GHz, for which the volume reflectivity is given by

$$\eta = N_e \sigma_e, \quad (15)$$

where σ_e is the scattering cross section of an electron, which is given by

$$\begin{aligned} \sigma_e &= \frac{e^4}{4\pi\epsilon_0^2 m_e^2 c^4} \\ &= 9.98 \times 10^{-29} \quad (\text{m}^2). \end{aligned} \quad (16)$$

The condition 'sufficiently high frequency' is necessary because otherwise interactions between electrons and ions through the Coulomb forces modify significantly the motion of the electrons reacting to the radar wave field. For a sufficiently low frequency of VHF and lower UHF bands, an extra coefficient of 1/2 should be multiplied to the right-hand side of Eq. 15 (Fejer, 1961).

This type of approach based on a microscopic viewpoint is practical only for idealized situations as discussed above. We need to treat the problem from a more macroscopic viewpoint of regarding scattering as due to fluctuations in the refractive index n in order to discuss the cross section of the neutral atmosphere. Here n is a continuous function of space, and represents all of the effects caused by scatterers.

The scattered power P_s produced by small fluctuations of the refractive index Δn is expressed formally as (e.g., Doviak and Zrnić, 1984)

$$P_s = \frac{k^4 P_1}{4\pi^2 r^2} \left| \int_V \Delta n \exp(i2\mathbf{k} \cdot \mathbf{r}) dV \right|^2, \quad (17)$$

where $k (= 2\pi/\lambda)$ is the radar wavenumber, \mathbf{k} is the propagation vector, and \mathbf{r} is the radius vector to a point in the scattering volume. By comparing Eq. 17 with Eq. 7, and applying Eq. 14, we obtain

$$\begin{aligned}\eta &= \frac{k^4}{\pi} C \\ C &= \frac{1}{V} \langle \left| \int_V \Delta n \exp(i2\mathbf{k} \cdot \mathbf{r}) dV \right|^2 \rangle\end{aligned}\quad (18)$$

where $\langle \rangle$ denotes an ensemble average. Although this equation gives a universal expression for the scattering cross section and the volume reflectivity, it is not easy, in general, to perform the integration to determine C . Specific results will be presented in a separate chapter.

For a uniformly distributed target, V is determined by the spatial resolution of the radar. Namely, for a radar with a circular antenna, it is expressed in terms of the half-power beam width of the antenna θ_h in radians, and the size of the range cell Δr , which is examined in the next section, as

$$V = \pi \left(\frac{r\theta_h}{2} \right)^2 \Delta r. \quad (19)$$

The beam width of the antenna has a direct relation with the gain of the antenna G_t because both of these parameters express the degree of concentration of the transmitted power of the radar in space. Probert-Jones (1962) expressed the relation as

$$G_t = \left(\frac{\pi a}{\theta_h} \right)^2, \quad (20)$$

where a is a non-dimensional factor which concerns the non-uniformity of illumination of the antenna. Combining this equation with Eq. 10 we obtain

$$\theta_h = \frac{a\lambda}{D_e} \quad (\text{rad}), \quad (21)$$

where D_e is the effective diameter of the antenna given by $\sqrt{4A_e/\pi}$. For a circular array antenna with uniform excitation for which D_e is roughly equal to the physical diameter of the antenna, $a = 1$ gives a good approximation.

With the aid of Eqs. 10, 19, and 20, the radar equation Eq. 11 can be rewritten for distributed targets as

$$P_r = \frac{P_t A_e \pi a^2 \Delta r L}{64 r^2} \eta. \quad (22)$$

Comparison of this equation with Eq. 11 for a hard target immediately reveals a few of interesting features of the scattering from distributed targets. First of all, the proportionality of the received echo power on the range r is to the square, not to the

forth power as is the case for a hard target. This means that the echo power decreases relatively slowly with increasing r , as mentioned in the preceding section.

Secondly, P_r depends only linearly on the effective antenna aperture A_e . While the A_e^2 factor in Eq. 11 counts for the antenna gain both for transmission and reception, the linear dependence in Eq. 22 can be interpreted that all of the radiated power is intercepted by the distributed scatterers, and thus the antenna gain does not count during transmission. It should also be noted that Eq. 22 does not contain any factor which contains a dependency on the radar frequency. These properties makes the *power aperture product* $P_t A_e$ a good indication of the sensitivity of an atmospheric radar.

Finally, the Δr term in Eq. 22, which does not appear in Eq. 11 means that any attempt to improve the range resolution of an atmospheric radar should be made at an expense of reduced sensitivity.

3.3 The Radar Equation for Specular Echoes

We have so far considered two extreme cases of a single target and uniformly distributed target. Although it is not the purpose of this chapter to get into details of various scattering mechanisms, let us examine a few more cases for which the radar equation takes alternate forms.

The first example is the *Fresnel (or partial) reflection* induced by a horizontal layer which has a slightly different refractive index from that of surrounding air and extends over a sufficiently wide area. This layer can be treated like a planar mirror, but with a small reflectivity ρ for incident electric field (Friend, 1949). Note that ρ here is the reflectivity in an ordinary sense which has no dimension, and has a complex value of $|\rho| \leq 1$.

The derivation of the radar equation for this case is rather simple, because we can consider the case to be a one-way transmission from an antenna to its mirror image located at a distance $2r$, with an extra power loss factor of $|\rho|^2$. Figure 4 shows the situation schematically. The received power is thus given by

$$\begin{aligned} P_r &= \frac{P_t G_t}{4\pi(2r)^2} A_e L |\rho|^2 \\ &= \frac{P_t A_e^2 L}{4\lambda^2 r^2} |\rho|^2 \end{aligned} \quad (23)$$

Although the echo power depends on the range by r^2 like the case of distributed targets, it is proportional to A_e^2/λ^2 like that of a hard target. One of important aspects of the Fresnel reflection is its aspect sensitivity. The above equation assumes that the antenna beam is directed perpendicular to the layer, for which the received echo takes its maximum value.

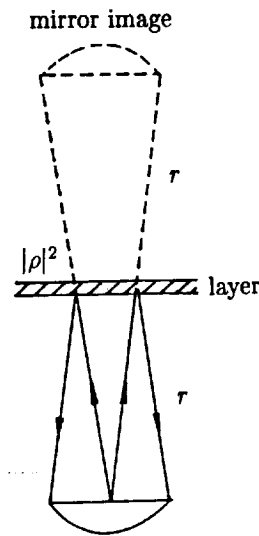


Fig. 4. Equivalent ray path for the Fresnel reflection. The dashed lines denotes the mirror image of the radar due to the layer.

The echo power falls off rapidly as the angle of the antenna beam is changed from this position. The rate of decrease is a function of the beam width of the antenna, and can be readily computed by considering the relation between the transmitting antenna and its mirror image due to the layer. It is not so easy, however, to calculate this function when the layer has some roughness of the order comparable to or larger than the wavelength. Such situation needs a more rigorous treatment based on Eq. 17.

We next examine a case where the scatterer has a linear shape in space. The most important application of such case is the reflection from *meteor trails* which appear at around 100 km height. Meteor trail is a strong localized ionization produced along a path of a meteor caused by the frictional heating when it penetrates into the earth's atmosphere. Since the echo is strong enough to be detected with relatively low sensitivity radars, it has been extensively studied (*e.g.*, McKinley, 1961). There is a category of atmospheric radar called the *meteor radar* which makes use of the meteor echoes to investigate the dynamics of the lower part of the ionosphere.

The scattering element in this case is an electron as is the case for the incoherent scattering for which element the radar equation is given in the form of Eq. 11 by

$$P_{r0} = \frac{P_t A_e^2 L}{4\pi\lambda^2 r^4} \sigma_e. \quad (24)$$

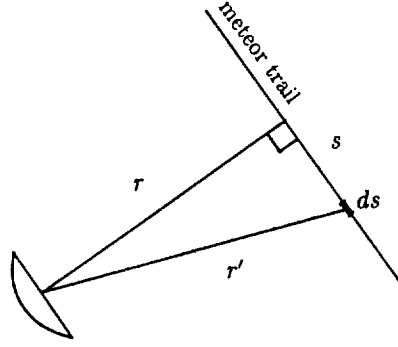


Fig. 5. Coordinates for deriving the effective length l_e for scattering from a meteor trail.

Unlike the case of incoherent scattering where contributions from individual electrons add up randomly, scattered electric fields from electrons aligned in space have a strong coherence. Since the effective diameter of the meteor trail which affects the scattering is shorter than the wavelength of meteor radars, we can safely assume that all electrons are aligned on one line with a *line density* of q_e (m^{-1}). We also assume a straight line without any curvature for simplicity, and that the line is located sufficiently far from the radar.

Electric-field contributions from electrons at distinct points on the line have similar amplitude, but have various phase. We introduce an idea of the *effective length* defined by

$$l_e \equiv \left| \int_{-\infty}^{\infty} \exp\{-i2k(r' - r)\} ds \right|, \quad (25)$$

where r is the distance of the line from the radar, and r' is the range of a line element ds on the line. Figure 5 shows the coordinates. The idea is to represent contributions from all parts of the line which have distinct phases by an effective length in which contributions are assumed to have the same phase at the receiving antenna. By making an approximation $r' - r \simeq s^2/(2r)$ where distance s is measured along the meteor trail from the perpendicular point, we obtain

$$l_e = \sqrt{\frac{r\lambda}{2}}. \quad (26)$$

Since the number of electrons within l_e is $l_e q_e$, and since the electric fields of scattered waves from these electrons have the same phase, the total echo power is given by

$$\begin{aligned} P_r &= (l_e q_e)^2 P_{r0} \\ &= \frac{P_t A_e^2 L}{8\pi\lambda r^3} \sigma_e q_e^2. \end{aligned} \quad (27)$$

This equation has a range dependence of r^{-3} which lies between the cases of a hard target and distributed targets.

3.4 Near Field Correction

In deriving these radar equations, we have assumed that the target is located at a point 'sufficiently far' from the radar without giving any explicit reason or quantitative limit for it. Here we examine how large should be the range r in order that equations we have derived are valid, and what happens within this limit.

The antenna of an atmospheric radar is, whether it is an dish antenna as a paraboloid or an array of Yagi's or half-wave dipoles, designed to form a beam of the transmitted wave as sharp as possible, because it is the condition to maximize the gain G_t and effective area A_e as shown in Eqs. 20 and 21. In order to make the beam sharp, it is essential to produce a planar wavefront over the antenna aperture to the extent as wide as possible. The transmitted wave thereby propagates as a plane wave at a distance near the antenna without changing its outer boundary which keeps the shape of the antenna aperture. As it propagates further, it gradually spreads out into a conical region and finally forms a spherical wave with its center located at the center of the antenna aperture.

The region where the wave can be regarded as a planar wave is called the *near field* of the antenna, while the region where it is a spherical wave is called the *far field*. In another word, the far field is a region from which the antenna can be seen as a point. This condition is stated mathematically that the distance of a target point measured from any point on the antenna aperture falls within a difference sufficiently smaller than the wavelength.

Conventionally, the boundary between the near field and the far field is defined as a range where the cylinder with a diameter equal to the diameter D of the antenna intercepts the cone with an angle θ_h and with its apex located at the center of the antenna as shown in Figure 6. This range r_o is given by

$$r_o = \frac{D^2}{\lambda}, \quad (28)$$

at which the difference of the distance measured from the center and from an outer edge of the antenna aperture becomes $\lambda/8$. As is shown in Eq. 28, r_o is a function of the diameter of the antenna and the radar frequency. The largest value of r_o associated with the existing atmospheric radars is 129 km for the Arecibo UHF radar, which operates at 430 MHz and has an antenna with a diameter of 300 m. All regions of the atmosphere except the upper ionosphere falls within the near field for such case. On the other hand, r_o is much smaller for VHF radars. The MU radar of Japan, for example, operates at

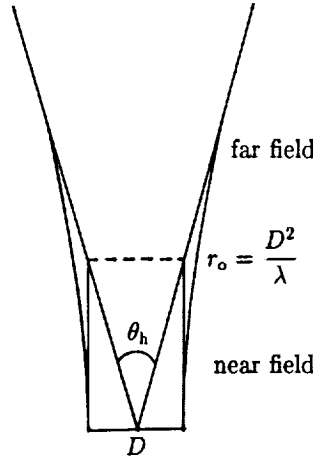


Fig. 6. A conventional definition of the boundary between the near field and the far field.

46.5 MHz and has a 103 m antenna, for which r_o is only 1.6 km. Since the minimum height (or range) that the MU radar can observe is about 1.5 km, the far field condition almost always holds.

In the near field of an antenna, Eq. 6 should be thereby rewritten as

$$P_i = \frac{P_t}{A_e}. \quad (29)$$

Also, Eq. 8 should be modified because the phase differences of the received waves on different parts of the antenna aperture, which differences cause interference and thus reduction of the echo power, is important for the case of the near field. The effective area A_e should then be replaced by an area which represents the effect of adding waves with different phases. This area is obtained by a consideration similar to that of Eq. 26 for the effective length of the reflection from a meteor trail, and is given by $\pi\lambda r/4$. This area also agrees with that of the *first Fresnel zone* which is defined as a zone on a plane in which a wave radiated from a point source arrives with a phase difference of less than $\pi/2$. Figure 7 shows the situation schematically. Thus Eq. 8 becomes

$$P_r = \frac{P_t \pi \lambda r L}{4}. \quad (30)$$

With Eqs. 29 and 30, the radar equation for a hard target Eq. 11 is rewritten as

$$P_r = \frac{P_t \lambda L}{16 A_e r} \sigma. \quad (31)$$

The most striking feature of this equation is that the received power is inversely proportional to the effective area of the antenna, meaning that a smaller antenna gives a stronger

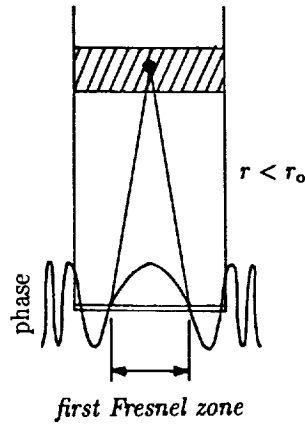


Fig. 7. Scattering due to a hard target within the antenna near field.

echo than a larger one. This is due to the fact that the power density of the transmitted wave is higher for smaller antenna as far as the target is within the near field. It should be noted, of course, that the upper boundary r_0 of the near field also decreases as the size of the antenna is reduced. The other important difference is that the echo power decreases only by r^{-1} with increasing range r in contrast to the very steep r^{-4} decay shown by Eq. 11.

Similarly, the radar equation for distributed targets Eq. 22 can be modified for the case of the near field. Besides the corrections we have made, the scattering volume expressed by Eq. 19 should also be changed as

$$V = A_e \Delta r. \quad (32)$$

Applying Eqs. 14 and 32 to Eq. 31, we obtain the radar equation for distributed targets within the antenna near field:

$$P_r = \frac{P_t \Delta r \lambda L}{16r} \eta. \quad (33)$$

Note that this equation contains no dependence on the antenna size parameter. What Eqs. 31 and 33 tells us is that increasing the size of the antenna in order to improve the sensitivity of the radar works only for targets outside the near field of the antenna.

In section 3.3, we also made an implicit assumption that the effective size of the target for specular reflections, which is determined by phase coherence of the scattered electric field, is smaller than the lateral dimension of the beam at that range. It can be shown that the range at which l_e for the meteor trail becomes the same as the beam size is coincidentally given by r_0 . The \sqrt{r} dependence of l_e thereby verifies the use of Eq. 27 for

$r > r_o$. A similar condition $r > r_o/2$ can be derived for the validity of Eq. 23 for Fresnel reflection by considering the condition that the size of the first Fresnel zone of the mirror image becomes larger than the size of the antenna.

4 Basic Techniques

The radar equation derived in the previous section tells us the intensity of echo, which is essential to estimate the necessary transmitter power and the antenna aperture, but nothing more. In this section, we briefly survey basic techniques used in the atmospheric radar in determining the range of desired target and also in deriving other information concerning the target. Details of individual technique will be discussed in following chapters.

4.1 Pulsed Waveforms

Ranging, or measurement of the range to a target, is one of important functions of radar. We, again, start with the case of observing a hard target. The ranging is made by measuring the time delay of the received echo from the target with respect to the transmitted signal.

As far as the refractive index n satisfies $|n-1| \ll 1$, speed of the radio wave can be well approximated by that in free space as shown by Eq. 1, the error of which approximation is given by Eq. 2. In the lower and the middle atmosphere of below about 100 km, $|n-1| < 10^{-3}$ as shown in Fig. 2, thence the error is negligible for all practical applications. The error becomes larger, however, in the ionosphere of above 100 km depending on the frequency f and the electron density N_e as shown by Eqs. 3 and 4. At a relatively low frequency of 50 MHz, for example, the maximum value of $n-1$ during daytime reaches ~ -0.02 at around the peak height of F2 region of 200–300 km. A care must be taken of this error for an accurate ranging of a hard target above the ionospheric height using lower VHF band. For oblique beam waves, refraction of the ray path is not negligible either under such condition.

Assuming $n = 1$, the range r of a stationary point target is given by

$$r = \frac{c\tau}{2}, \quad (34)$$

where τ is the time delay of an echo. In order to measure this time delay, we need to add some 'feature' to the transmitted wave so that a part of the wave can be identified from others. Although there are a variety of ways to do this, many of which are of practical use, the simplest and most widely used way is to transmit a short pulse of a waveform

$$E(t) = \begin{cases} E_0 \sin(2\pi ft) & (0 \leq t \leq \Delta t) \\ 0 & (t < 0, t > \Delta t) \end{cases}, \quad (35)$$

where E_0 is the amplitude of the electric field of the wave. It should be noted that it is not common to use such an idealized waveform in a real radar because of various restrictions,

so that the amplitude E_o is usually a smoother function of time than this one. When we transmit a pulse of length Δt sec, we receive the echo from this pulse for a duration of Δt sec right after a τ sec of delay. Since we measure the delay in terms of the range according to Eq. 34, this duration is interpreted as if the target has a finite length

$$\Delta r = \frac{c\Delta t}{2} \quad (36)$$

in the radial direction, which length is called the *range resolution*.

It is thereby necessary to reduce Δt in order to improve the range resolution. Unfortunately, however, there is a conflicting relation between the length of the pulse and its frequency bandwidth. For a rectangular pulse waveform of Eq. 35, the half-power frequency bandwidth B is given by

$$B = \frac{0.886}{\Delta t}. \quad (37)$$

Since the receiver should cover this bandwidth, the noise power contaminating the echo increases linearly as increasing B as shown by Eq. 12, thus resulting in a linear decrease of the signal-to-noise ratio, which is, as a consequence, proportional to Δt .

This dilemma can be solved by means of *pulse compression* which allows a radar to utilize a long pulse without sacrificing the range resolution. The basic idea of the pulse compression is to put extra features within the long pulse so that each part of the pulse can be identified, which idea is just the same as the one used above in introducing the pulsed waveform. This is realized, in this case, by applying further modulation to the already pulse-modulated waveform. Among various ways of modulation, binary phase modulation (or coding) is most widely used for the atmospheric radar application. This form of pulse compression is performed by sending N consecutive pulses with the phase of carrier wave 0 or π different from that of the first pulse. The advantage of utilizing only 0 and π of the phase is that they can be interpreted as plus and minus signs of the envelope E_o , so that no special hardware for phase modulation and demodulation is required. Each component pulse of length Δt is referred to as a *sub-pulse* of an N -element coded pulse of length $N\Delta t$. The choice of the time series of phases (0 or π) is a subject of mathematical considerations, and will be discussed in details in a separate chapter (see, for example, Nathanson, 1969, or Skolnik, 1980 for reference).

Here we choose a random phase coding as an example, with which sub-pulses have random and independent phases with each other. The received signal time series from a stationary point target is a weakened and delayed copy of the transmitted time series, which is a series of pulses with a random sequence of signs. We can 'compress' the received signal by displacing sub-pulses to the position of the first sub-pulse with corrected phase,

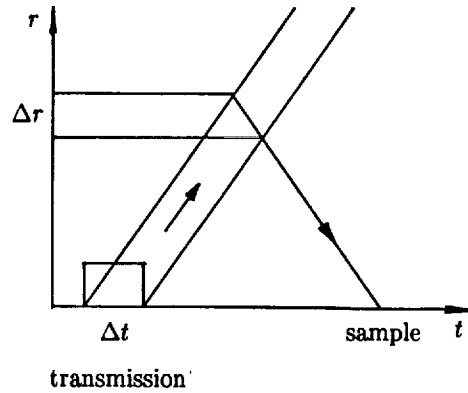


Fig. 8. Time-height section showing the relation of the size of a range cell and the length of a pulse for distributed targets.

and by adding them together. Mathematically, this procedure is expressed as taking the cross-correlation of the transmitted and received time series. This procedure enhances the signal power, which has equal phase for all sub-pulses, by N^2 times, while the statistically independent noise power only by N times, thence the signal-to-noise ratio by N times.

Since the phases of sub-pulses are random, the entire pulse has the same bandwidth as that of each sub-pulse. The range resolution also stays unchanged because the cross-correlation disappears outside an interval of Δt due to random phases between adjacent sub-pulses. As a summary, N -element binary phase compression improves the signal-to-noise ratio by N times compared to a single pulse of length $1/N$, without changing the range resolution.

We now consider the case of distributed targets. If the distribution is uniform with range, the received echo power decreases with the time t after transmission of a pulse as t^{-2} , which simply reflects the r^{-2} dependence of the radar equation through Eq. 34. The object then becomes to determine the nature of the target at a given range, instead of determining the range of the target. The meaning of the range resolution also should be changed from *the ambiguity in determination of the range of a target* to *the radial size of scattering volume which contributes to the echo at a given time*. Actually, the range resolution Δr given by Eq. 36 corresponds to the difference of the range of echoes returned from the leading and trailing edges of a pulse of length Δt at the same time of receiving as shown in the time-height section of Figure 8. It is thereby appropriate to call Δr as the size of a range cell as already quoted in Eq. 19. Echoes from distinct ranges can be obtained by sampling the received signal at an interval of $\sim \Delta t$. A sampling

interval of less than Δt produces overlapping regions between the samples, while a sparse sampling results in missing regions. It is therefore common to sample at an interval just equal to Δt . The sampled time series provides a range (or usually, height) profile of the atmosphere. We should note that the impulsive sampling intended by Fig. 8 does not represent a realistic situation where the receiver has a bandwidth equal to that of the transmitted pulse. In this case, an instantaneous sample of receiver output contains the echo spreads over a duration of Δt . Although this effect broadens the range cell from a rectangular shape of width Δr into a triangular one of width $2\Delta r$, the 'half-power' size of the cell is still given by Δr .

As we have seen, the signal-to-noise ratio is proportional to the length of pulse Δt for the case of a hard target. For the case of distributed targets, we need to take into account the linear proportionality of echo power on Δr as shown in Eq. 22, which represents the number of scatterers in a range cell. The signal-to-noise ratio thus becomes proportional to Δt^2 , setting a severe restriction in improving the range resolution. For example, dividing a single pulse into N sub-pulses with binary phase coding improves the range resolution by N times without sacrificing the signal-to-noise ratio of a hard target, while the same alteration offers the same improvement only at an expense of a reduction of the signal-to-noise ratio to $1/N$ for the case of distributed targets.

4.2 The Doppler Principle

We have so far concentrated our attention only to the echo power. Physical meaning of the echo power is, however, clear only for the case of incoherent scattering from the ionosphere, for which case it can be interpreted in terms of the electron density. It is difficult to make use of the echo power from the lower and the middle atmosphere in a quantitative manner in terms of physical parameters of geophysical interests.

The *Doppler shift* of the echoes, on the other hand, has a great importance for these regions as well as for the ionosphere, because it is directly related to the motion of the target, which is wind. The Doppler frequency shift of echoes from a moving target relative to the radar is given by

$$f_d = \frac{2f}{c} v_d, \quad (38)$$

where v_d is the line-of-sight component of velocity vector \mathbf{v} of the target relative to the radar.

Since the maximum velocity encountered in the atmosphere is on the order of 100 m s^{-1} , $|f_d| < 1 \text{ kHz}$ for any frequency f of less than 1 GHz . A typical value of f_d for 50 MHz band is, for example, around 3 Hz , which corresponds to a line-of-sight velocity of 10 m s^{-1} .

Bandwidth of transmitted pulses is, on the other hand, 100 kHz–1 MHz corresponding to the minimum length of sub-pulses of 1–10 μ s. It is thereby very difficult, if not impossible, to detect such small Doppler shift of a pulse relative to its bandwidth from each received pulse.

Instead, the method of time-series analysis is applied to the series of received signal from consecutive pulses at the same range. If a stationary target is observed, all received pulses should have the same phase relative to the transmitted pulse. It is then interpreted that the received time series has the DC component only, which means that the Doppler shift is zero. Next we suppose that the target is moving at a sufficiently slow speed of v_d in the radial direction so that it does not move out of a range cell into the next one within the period of interest. We examine samples of echoes obtained at the same range cell from adjacent pulses separated by an inter-pulse-period (IPP) of T . Then the phase difference $\Delta\phi$ between the two samples is given by

$$\Delta\phi = 2\pi f_d T = \frac{4\pi f T}{c} v_d. \quad (39)$$

This equation can be applied not only to a hard target but also to distributed targets as far as they move with a mean speed of v_d . The phase difference can be determined from a pair of pulses, while the Doppler frequency shift f_d can be directly derived by a spectral analysis of the time series of samples taken from many pulses.

A limitation of this method arises from the requirement $|\Delta\phi| < \pi$ so that f_d can be determined without ambiguity, together with the one $T > 2r_{\max}/c$ which comes from the restriction that we cannot transmit a new pulse before receiving the echo of the previous pulse from the longest range r_{\max} of interest. By combining these two requirements, we obtain

$$|v_d| r_{\max} < \frac{c^2}{8f}, \quad (40)$$

which gives the condition that both the range and the velocity of a target can be determined unambiguously. Since the quantities on the left-hand side of this equation are limited roughly by $100 \text{ m s}^{-1} \times 100 \text{ km} = 10^7 \text{ m}^2 \text{ s}^{-1}$, this condition is usually satisfied for a frequency of below about 1 GHz, which is the frequency used for atmospheric radars.

Considerations made above assumes that the echo is perfectly correlated in time, which assumption is not valid for the case of the atmospheric radar, where echoes have finite correlation time τ_c due principally to random motion of scatterers within a scattering volume. This correlation time is inversely proportional to the spectral broadening due to the random motion and other observational effects, and given by

$$\tau_c = \frac{b}{\sigma_t} = \frac{bc}{2f\sigma_v}, \quad (41)$$

where σ_f and σ_v denote the standard deviation of the random motion in terms of Doppler frequency and radial velocity, respectively, and b is a numerical coefficient of order unity which is determined by the velocity distribution of the random motion. For a Gaussian distribution, $b = 1.18$.

The value of σ_v differs largely depending on the height, since it is the order of mean thermal motion of ions of more than 1 km s^{-1} in the ionosphere, while it is the mean velocity of turbulent eddies of the order of 1 m s^{-1} in the lower and the middle atmosphere. For ionospheric observation, for which $\sigma_v \gg v_d$, the v_d term in Eq. 40 should be replaced by σ_v , which determines spectral width and thus the minimum sampling interval. It is easily understood that the condition for unambiguous sampling is then no more satisfied, meaning that spectral information of the scatterers must be derived within an interval of order of τ_c . A special technique called *multi-pulse method* was developed for ionospheric observations, and has been widely used (*e.g.*, Farley, 1969).

4.3 Velocity Field Measurements

As shown in Eq. 38, velocity of targets measured by a radar with the Doppler technique is a line-of-sight velocity, which is the projection of velocity vector to the radial direction. We will briefly examine here two distinct techniques of determining the three components of the velocity vector: the *Doppler-Beam-Swing* (DBS) method and the *Spaced-Antenna-Drifts* (SAD) method.

The DBS method makes use of multiple antenna beams each of which is oriented to observe the radial velocity at a different direction. The velocity vector is computed from the line-of-sight velocities from these directions. Here we need to make an assumption that the velocity field is uniform in space over the volume which contains the range cells used to compute a velocity vector. In the atmospheric radar application, it is common to determine a velocity vector from line-of-sight velocities of range cells with the same height assuming the uniformity only in the horizontal plane, so that a height profile of the velocity vector can be obtained. This is because the horizontal velocity is usually much larger than the vertical velocity in the stratified earth's atmosphere, thus making the horizontal uniformity of the velocity field much better than in the vertical direction. Also, the fact that the zenith angle of antenna beams is usually kept within about 30° supports this assumption, in contrast to the case of weather radars, which use almost horizontal beam directions,

The line-of-sight component of the wind velocity vector $\mathbf{v} = (v_x, v_y, v_z)$ at a given

height is expressed as

$$\begin{aligned} v_d &= \mathbf{v} \cdot \mathbf{i} \\ &= v_x \cos \theta_x + v_y \cos \theta_y + v_z \cos \theta_z, \end{aligned} \quad (42)$$

where \mathbf{i} is a unit vector along the antenna beam direction, and θ_x , θ_y , and θ_z are the angle between \mathbf{i} and the x , y , and z axis, respectively. If we measure v_d at three beam directions \mathbf{i}_1 , \mathbf{i}_2 , and \mathbf{i}_3 which do not constitute a plane, we can obtain an estimate of \mathbf{v} as

$$\mathbf{v} = \begin{pmatrix} \cos \theta_{x1} & \cos \theta_{y1} & \cos \theta_{z1} \\ \cos \theta_{x2} & \cos \theta_{y2} & \cos \theta_{z2} \\ \cos \theta_{x3} & \cos \theta_{y3} & \cos \theta_{z3} \end{pmatrix}^{-1} \begin{pmatrix} v_{d1} \\ v_{d2} \\ v_{d3} \end{pmatrix}. \quad (43)$$

If we observe more than three directions, then the estimate of \mathbf{v} can be determined in a least-squares manner, with which the residual given by the following is minimized:

$$\varepsilon_v^2 \equiv \sum_{i=1}^m (v_x \cos \theta_{xi} + v_y \cos \theta_{yi} + v_z \cos \theta_{zi} - v_{di})^2, \quad (44)$$

where m is the number of beam directions. The necessary condition for \mathbf{v} to give the minimum is that partial derivatives of ε_v^2 with respect to all three components of \mathbf{v} are zero:

$$\frac{\partial \varepsilon_v^2}{\partial v_j} = 0 \quad (j = x, y, z). \quad (45)$$

This set of equations can be solved in terms of \mathbf{v} as

$$\mathbf{v} = \begin{pmatrix} \sum \cos^2 \theta_{xi} & \sum \cos \theta_{xi} \cos \theta_{yi} & \sum \cos \theta_{xi} \cos \theta_{zi} \\ \sum \cos \theta_{yi} \cos \theta_{xi} & \sum \cos^2 \theta_{yi} & \sum \cos \theta_{yi} \cos \theta_{zi} \\ \sum \cos \theta_{zi} \cos \theta_{xi} & \sum \cos \theta_{zi} \cos \theta_{yi} & \sum \cos^2 \theta_{zi} \end{pmatrix}^{-1} \begin{pmatrix} \sum v_{di} \cos \theta_{xi} \\ \sum v_{di} \cos \theta_{yi} \\ \sum v_{di} \cos \theta_{zi} \end{pmatrix}, \quad (46)$$

where the summations are taken for $i = 1$ to m .

A special case of this type of multi-beam measurements called the *Velocity-Azimuth Display* (VAD) method, which uses beam directions with a fixed zenith angle θ and uniformly distributed azimuth angles ϕ_i . The line-of-sight velocity v_d of Eq. 42 is then rewritten as

$$v_{di} = v_h \sin \theta \sin(\phi_i + \beta) + v_z \cos \theta, \quad (47)$$

where v_h and β are the amplitude and the direction of the horizontal component of \mathbf{r} , respectively, and given by

$$\begin{aligned} v_h &= \sqrt{v_x^2 + v_y^2} \\ \beta &= \tan^{-1} \left(\frac{v_y}{v_x} \right). \end{aligned}$$

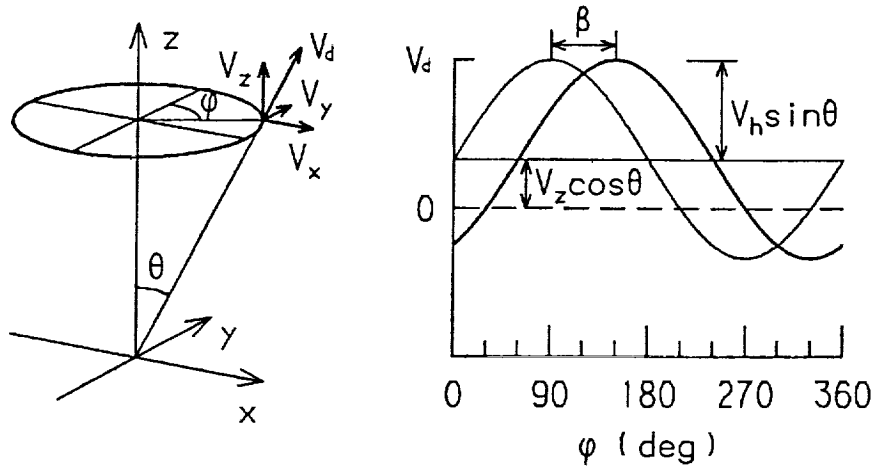


Fig. 9. Coordinates of the Velocity-Azimuth Display method (left panel), and an expected variation of the line-of-sight velocity v_d as a function of azimuth ϕ (right panel).

Figure 9 illustrates coordinates of the VAD method and an expected variation of v_d as a continuous function of azimuth ϕ . The thin curve on the right panel represents a case where the horizontal component of the velocity is toward the x axis, and the thick line shows a general case.

As understood from this illustration, the vertical component of the velocity is indicated by the DC component, and the horizontal component by the amplitude and the phase of the sinusoid. The fitting procedure given by Eq. 46 thereby reduces to fitting a sinusoid with a DC offset to line-of-sight velocities plotted versus azimuth angle. Any inhomogeneity of the velocity field is indicated by deviations of the curve from a sinusoid.

Although there is nothing superior, in a mathematical sense, of the VAD method compared to other choices of beam directions, there are practical advantages which made the method popular: First, this method is suited for radars with a mechanically steered aperture antenna, of which azimuth and zenith angles are often driven separately. This is the case for most of weather radars, although it is not for phased-array antennas with electrical or electronic steering often used for atmospheric radars.

Secondly, quality of data is readily visualized on a display without numerical computations. Systematic error due to an undesired hard target at some direction, for example, can be picked up easily by human intelligence, but it may require an elaborated software for a computer to find it out.

Thirdly, a systematic error due to specular echoes from the vertical direction can be avoided with the VAD method by choosing the zenith angle θ properly. The specular echoes from horizontally stratified layers often dominate over isotropic scattering from turbulence (Gage and Green, 1978, Röttger and Liu, 1978), which make the apparent zenith angle of the antenna beam direction smaller than the physical one for beam directions near the vertical direction. This effect is most prominent for lower stratospheric region, where data from beam directions with small zenith angles must be treated with care (Tsuda *et al.*, 1986).

This caution applies, of course, to all DBS observations. On the other hand, use of too large zenith angle makes the assumption of a uniform velocity field unreliable.

The alternate technique of the Spaced-Antenna-Drifts method makes efficient use of this specular echoes in determining horizontal velocities. It was originally developed to study characteristics of irregularities in the lower ionosphere (*e.g.*, Ratcliffe, 1956), and applied to observations of velocities in the middle atmosphere (*e.g.*, Vincent *et al.*, 1977) and lower atmosphere (*e.g.*, Röttger and Vincent, 1978). Its principle is to measure a spatial correlation of received signal patterns from a reflecting layer with spaced antennas on the ground.

For a given angular pattern of the echo power from the reflecting layer, the spatial correlation function on the ground is given by a two-dimensional Fourier transform of the angular pattern as (Ratcliffe, 1956)

$$\begin{aligned}\rho(x, y) &= \int_{-\infty}^{\infty} \int_{-\infty}^{\infty} W(S_1, S_2) \exp\left(2\pi i \frac{S_1 x + S_2 y}{\lambda}\right) dS_1 dS_2, \\ S_1 &= \sin \theta_1 \\ S_2 &= \sin \theta_2\end{aligned}\quad (48)$$

where $W(S_1, S_2)$ is the power pattern of the echo with respect to the zenith angle θ_1 and θ_2 measured in x - z and y - z plane, respectively. Note that the integrand takes a real value within a range $(-1, 1)$ for S_1 and S_2 . If W is symmetrical with the azimuth angle, which is valid for most of practical cases, Eq. 48 can be rewritten in a polar coordinates (θ, ϕ) as

$$\rho(\alpha) = \int_0^{\infty} \int_{-\pi}^{\pi} W(S) \exp(2\pi i \alpha S \cos \phi) S d\phi dS, \quad (49)$$

where $S = \sin \theta$, and $\alpha = \sqrt{(x^2 + y^2)}/\lambda$ is a distance measured in units of the wavelength. The integral with respect to ϕ is the Bessel function of zero order $J_0(2\pi\alpha S)$ so that

$$\rho(\alpha) = 2\pi \int_0^{\infty} W(S) J_0(2\pi\alpha S) S dS. \quad (50)$$

For randomly distributed irregularities in a thin horizontal layer at a height $z = h$, the power flux in the angular range θ to $\theta + d\theta$ depends only on the antenna pattern of

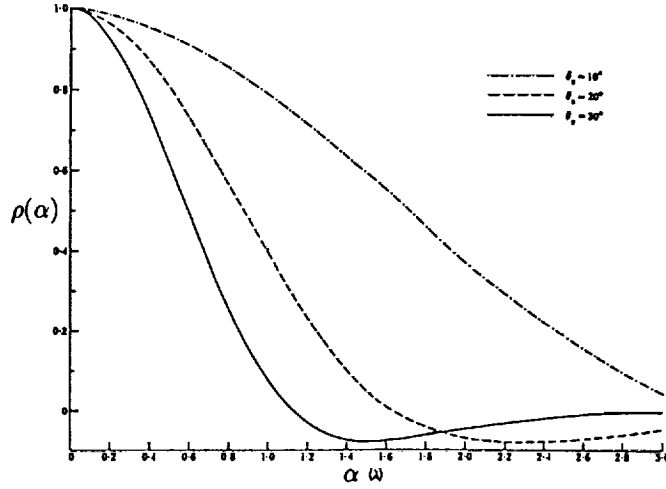


Fig. 10. normalized correlation function $\rho(\alpha)$ between fluctuations recorded by two receivers separated by a distance α . It is assumed that the irregularities are isotropic and randomly distributed, and that both the transmitting and receiving antennas have a pattern of $\exp(-\sin^2 \theta / \sin^2 \theta_0)$ (after Briggs and Vincent, 1973).

the transmitting and receiving antennas, and given by (Briggs and Vincent, 1973)

$$W(\theta)d\theta \propto h^{-2}T(\theta)R(\theta)\sin\theta\cos\theta d\theta, \quad (51)$$

where $T(\theta)$ and $R(\theta)$ are the transmitting and receiving antenna patterns, respectively. Figure 10 draws examples of the correlation function for Gaussian antenna patterns with different width, but assuming the same pattern both for transmission and reception (after Briggs and Vincent, 1973).

We have so far considered the spatial correlation only. As implied by Eq. 41, the received signal is also characterized by its temporal correlation function, which is a Fourier transform of the frequency power spectrum. The spatial and temporal correlations can be treated separately for the case of a stationary pattern, while they are mutually related when the layer, and hence the pattern, has a mean motion. A generalized method called the *full-correlation analysis* was developed by Briggs (1984) in order to retrieve the velocity and other information from such correlation functions. We now introduce the space-time correlation function of the received signal pattern $f(x, y, t)$ on the ground plane:

$$\rho(\xi, \eta, \tau) = \frac{\langle f(x, y, t)f(x + \xi, y + \eta, t + \tau) \rangle}{|f(x, y, t)|^2}, \quad (52)$$

where $\langle \rangle$ means to take an ensemble average, which is often replaced by a temporal average in practical applications. This correlation function represents the statistical relations of the signal pattern at two points with a separation (ξ, η) on the ground and with a time difference of τ . We assume that for a stationary pattern, the correlation function has a form

$$\rho(\xi, \eta, \tau) = \rho(A\xi^2 + B\eta^2 + K\tau^2 + 2H\xi\eta). \quad (53)$$

This assumption implies that the spatial and temporal correlations have the same functional shape, but the shape is arbitrary. Although this is not real in a rigorous sense, it is an acceptable approximation for most of correlation functions at least around their origin.

We next suppose that the pattern is moving at a velocity $\mathbf{V} = (V_x, V_y)$. If we move the coordinates also at this velocity, then Eq. 53 remain unchanged for the moving coordinates. the expression for the stationary coordinates is therefore obtained after a linear transform of coordinates that

$$\rho(\xi, \eta, \tau) = \rho\{A(\xi - V_x\tau)^2 + B(\eta - V_y\tau)^2 + K\tau^2 + 2H(\xi - V_x\tau)(\eta - V_y\tau)\}, \quad (54)$$

which is rewritten as

$$\rho(\xi, \eta, \tau) = \rho(A\xi^2 + B\eta^2 + K\tau^2 + 2F\xi\tau + 2G\eta\tau + 2H\xi\eta). \quad (55)$$

If we have two spaced receivers, we can determine the shape of the cross-correlation as a function of τ for a given set of (ξ, η) . Since Eq. 55 is a function of a second-order polynomial of τ , it is possible to determine three unknowns by fitting it to the measured cross-correlation function. It is thus clear that three spaced receivers, which provides us two sets of independent cross-correlation functions, is sufficient to determine all coefficients in Eq. 55. If we have more than three receivers, we can determine the coefficients in a least-squares manner as is the case of the DBS method.

Once the coefficients are determined, we can retrieve the velocity vector \mathbf{V} from these coefficients. By comparing Eqs. 54 and 55, we obtain

$$\begin{aligned} AV_x + HV_y &= -F \\ BV_y + HV_x &= -G \end{aligned} \quad (56)$$

These equation can be readily solved to give (V_x, V_y) . The vertical component of the velocity vector needs to be determined separately from the Doppler shift of the echo.

An important point which needs to be mentioned is that an apparent velocity V' calculated from the distance between the receivers and the time delay which gives the maximum value of the cross-correlation function does not agree with the true velocity

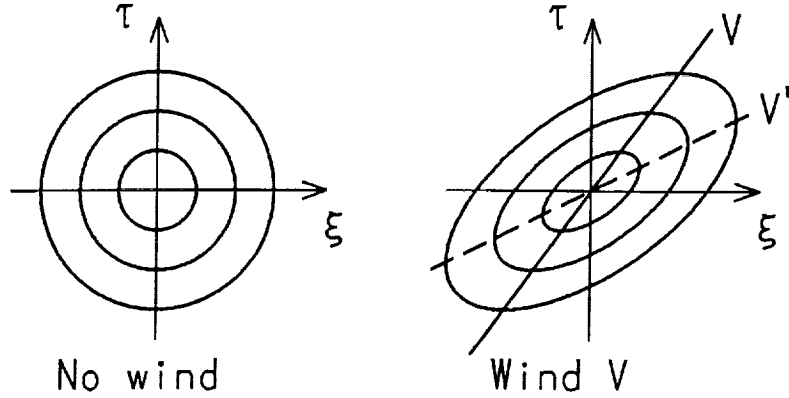


Fig. 11. Contours of equal correlation versus distance ξ and time delay τ . The left panel shows a case with no mean wind, and the right panel is with a uniform wind. The true velocity V estimated with the full-correlation analysis is denoted by the solid line. The dashed line indicates the apparent velocity V' determined from the time delay of maximum correlation.

V of the pattern, which is correctly estimated with the full-correlation analysis. These two time delays coincide when the temporal correlation of the pattern is perfect, which means that the pattern is drifting without evolving with time, while a finite correlation time significantly affects the shape of the cross-correlation function.

Figure 11 illustrates this difference schematically. The left panel shows concentric circles which represent contour lines of equal correlation versus distance ξ along the baseline and the time delay τ for a case of no mean motion. The abscissa and the ordinate are normalized by the correlation distance and the correlation time of the pattern, so that the contours become circles instead of ellipses. If a mean motion of V is added, the contours deform into ellipses as shown in the right panel. Note that the solid line which indicates the true velocity V is drawn by connecting tangential points of the ellipses with horizontal lines as implied by Eq. 54.

Since the cross-correlation function with respect to τ at a distance ξ is given by the values of contours along a line of constant ξ (i.e., a vertical line), V' obtained from its maximum has a slope indicated by the dashed line in the figure, which is drawn by connecting tangential points of ellipses with vertical lines. The difference between the true velocity V and the apparent velocity V' therefore becomes larger as V becomes smaller. One of reasons that the full-correlation analysis is widely used is that it is free from this

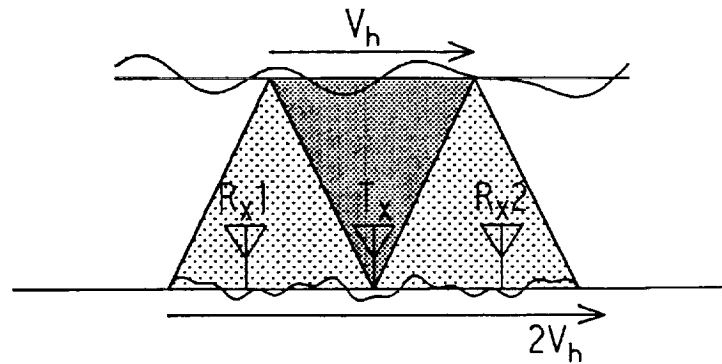


Fig. 12. Motion of a reflecting layer and its echo pattern on the ground.

kind of error.

We should also note that the velocity V we have discussed is the velocity of the pattern on the ground, which is exactly *twice* that of the layer as schematically shown in Figure 12. This is intuitively understood by considering the motion of a shadow of a screen projected on a wall where the light source, the screen and the wall are arranged with equal intervals. It is, of course, possible to derive this relation mathematically by examining the motion of an interference pattern on the ground due to echoes from two or more targets moving horizontally at the same velocity.

From a practical point of view, the DBS and SAD methods have their own advantages and disadvantages which are difficult to compare on the same ground. The advantages of the SAD method are that the complete velocity vector can be determined from a single volume of the target, and that the enhanced specular echoes from the vertical direction can be used efficiently. However, it requires at least three sets of receiving antennas and receivers with equal capability. The DBS method requires, on the other hand, a steerable antenna, which is not necessary with the SAD method. The accuracy of the velocity estimates is known fairly well for the DBS method, while it has not yet been studied in details for the SAD method, which is anticipated to have a variable accuracy depending on the velocity itself.

References

- Balsley, B. B., and K. S. Gage, The MST radar technique: Potential for middle atmospheric studies, *Pure Appl. Geophys.*, **118**, 452-493, 1980.
- Battan, L. J., *Radar Observation of the Atmosphere*, The University of Chicago Press, Chicago, 1973.
- Briggs, B. H., The analysis of spaced sensor records by correlation technique, *Handbook for MAP*, **13**, 166-186, 1984.
- Briggs, B. H., and R. A. Vincent, Some theoretical considerations on remote probing of weakly scattering irregularities, *Aust. J. Phys.*, **26**, 805-814, 1973.
- Dicke, R. H., R. Beringer, R. L. Kyhl, and A. B. Vane, Atmospheric absorption measurements with a microwave radiometer, *Phys. Rev.*, **70**, 340-348, 1946.
- Doviak, R. J., and D. S. Zrnić, *Doppler Radar and Weather Observations*, Academic Press, London, 1984.
- Farley, D. T., Multi-pulse incoherent-scatter correlation function measurements, *Radio Sci.*, **4**, 935-953, 1969.
- Fejer, J. A., Scattering of radio waves by an ionized gas in thermal equilibrium in the presence of a uniform magnetic field, *Can. J. Phys.*, **39**, 716-740, 1961.
- Friend, A. W., Theory and practice of tropospheric sounding by radar, *Proc. Inst. Radio Eng.*, **37**, 116-138, 1949.
- Gage, K. S., and J. L. Green, Evidence for specular reflection from monostatic VHF radar observations of the stratosphere, *Radio Sci.*, **13**, 991-1001, 1978.
- McKinley, D. W. R., *Meteor Science and Engineering*, McGraw-Hill, New York, 1961.
- Mechtly, E. A., S. A. Bowhill, K. P. Gibbs, and L. G. Smith, Changes of lower ionosphere electron concentrations with solar activity, *J. Atmos. Terr. Phys.*, **34**, 1899-1907, 1972.
- Nathanson, F. E., *Radar Design Principles*, McGraw-Hill, New York, 1969.
- Ratcliffe, J. A., Some aspects of diffraction theory and their application to the ionosphere, *Rep. Progr. Phys.*, **19**, 188-267, 1956.
- Röttger, J., and C. H. Liu, Partial reflection and scattering of VHF radar signals from the clear atmosphere, *Geophys. Res. Lett.*, **5**, 357-360, 1978.
- Röttger, J., and R. A. Vincent, VHF radar studies of tropospheric velocities and irregularities using spaced antenna techniques, *Geophys. Res. Lett.*, **5**, 917-920, 1978.

Silver, S., *Microwave Antenna Theory and Design*, McGraw-Hill, New York, 1951.

Skolnik, M. L. (editor), *Radar Handbook*, McGraw-Hill, New York, 1970.

Skolnik, M. L., *Introduction to Radar Systems*, McGraw-Hill, New York, 1980.

Stix, T. H., *The Theory of Plasma Waves*, McGraw-Hill, New York, 1962.

Tsuda, T., T. Sato, K. Hirose, S. Fukao, and S. Kato, MU radar observations of the aspect sensitivity of backscattered VHF echo power in the troposphere and lower stratosphere, *Radio Sci.*, **21**, 971-980, 1986.

Vincent, R. A., T. J. Stubbs, R. H. O. Pearson, K. H. Lloyd, and C. H. Low, A comparison of partial reflection drifts with winds determined by rocket techniques – I, *J. Atmos. Terr. Phys.*, **39**, 813-821, 1977.

Chapter 3

THE INSTRUMENTAL PRINCIPLES
OF MST RADARS AND INCOHERENT SCATTER RADARS
AND THE CONFIGURATION OF RADAR SYSTEM HARDWARE

Jürgen Röttger

EISCAT Scientific Association
P.O. Box 812, S-981 28 Kiruna, Sweden
(on leave from Max-Planck-Institut für Aeronomie, W.Germany)

ABSTRACT

The principle of pulse modulation used in case of coherent scatter radars (MST radars) and incoherent scatter radars (IS radars) is first discussed. Coherent detection and the corresponding system configuration is delineated. Antenna requirements and design are outlined and the phase-coherent transmitter/receiver system is described. Transmit/receive duplexers, transmitters, receivers, quadrature detectors are explained. The radar controller, integrator, decoder and correlator design as well as the data transfer and the control and monitoring by the host computer is delineated. Typical operation parameters of some well-known radars are finally summarised.

1. INTRODUCTION TO PRINCIPLES OF THE ATMOSPHERIC RADAR TECHNIQUE

This tutorial lecture note aims to give a general summary and overview on the MST radar and the incoherent scatter radar technique. With the MST radars the mesosphere, stratosphere and the troposphere are investigated, whereas with incoherent scatter (IS) radars the ionosphere is investigated. It is not intended to present here a review for experts working in this field, but rather to give an overview to newcomers to allow a basic introduction for those who are joining this research field. For more specific technical descriptions of the radar technique in general and the atmospheric radar technique in particular, the reader is referred to other books and articles, such as those by SKOLNIK (1970), HARDY (1972), WILSON and MILLER (1972), BATTAN (1973), GOSSARD and STRAUCH (1983), DOVIAK and ŽRNIC (1984). Very specified descriptions of MST radar techniques can be found in Handbooks for MAP (BOWHILL and EDWARDS, 1983, 1984, 1986), an explicit and useful explanation of the MST and incoherent scatter MU radar was published by FUKAO et al. (1985a,b), and a review of UHF and VHF radar techniques for atmospheric research and wind profiler applications was recently prepared by RÖTTGER and LARSEN (1989). Good overviews on the incoherent scatter radar technique are given by EVANS (1969), BARON (1977) and HAGFORS (1977). Since important features of the MST and IS radar hardware result from certain principles of the basic radar technique, the scattering mechanisms and the data acquisition procedures, these will be briefly outlined in the course of this lecture note, which, however, mainly aims towards the description of radar instrumentation. Further tutorial introductions to the applications of MST and IS radars in atmospheric and ionospheric research can be found in the other articles published in this volume of the Handbook for MAP.

We will describe here the very basic technical principles, which are profound in all radar applications but are usually adjusted according to specific requirements of certain scientific experiments and operational realizations. Some of those are outlined in the following chapters and for more details than given in this tutorial or the in mentioned reviews the reader is referred to the relevant literature summarized in the reference list at the end of this paper.

1.1. Basics of Pulsed Doppler Radars

Usually the MST radars as well as the incoherent scatter radars apply the conventional pulse modulation technique, i.e. a short radar pulse is transmitted as shown in the sketch of Fig. 1, and the backscattered radar echo from a range r (or altitude z) is received after the time t . Sampling the received echoes as function of time then allows to evaluate the echoes from different ranges $r = ct/2$, where c is the propagation velocity of the radar signal, namely the speed of light for the radars operating in the VHF and UHF bands.

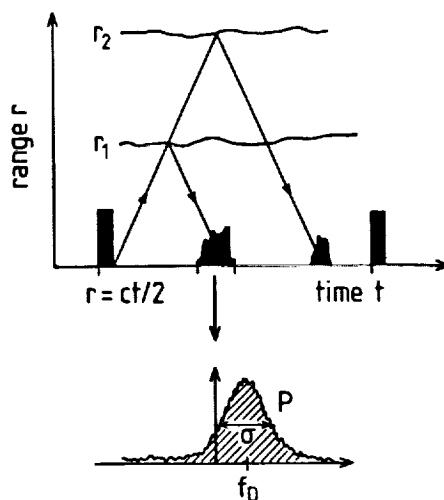


Figure 1. Principle of a pulsed Doppler radar:

A transmitted radar pulse is scattered by some refractive index irregularity at the ranges r . The backscattered radar signal is received after the time of flight t from the ranges $r = ct/2$, where c is the speed of light. Usually the power or Doppler spectrum (as shown in the lower insert) is computed for signals received in certain range gates and the basic parameters total power P , Doppler shift f_0 and the spectrum width σ are deduced. In addition further useful parameters can be determined from the particular shapes of Doppler spectra.

The procedure of pulse radar is described in some more detail in Fig. 2. Let a pulsed electromagnetic wave be transmitted at the time t_1 . The pulse duration of this radar signal shall be δt_1 . For simplification the pulse shape is assumed to be rectangular, but in real applications it may be a smoothed trapezoid or triangle or Gaussian shaped. In a nondispersive propagation medium (at the high frequencies used in the MST and IS radar application the refractive index is very close to one such that dispersion does not have to be considered) the pulse travels with the speed of light c and reaches the range r_a after the time $t_1 = r_a/c$. A target at r_a can scatter or reflect the radar signal in some directions. A small fraction returns to the location of the transmitter, where this radar echo will be received after the time $t_1' = 2t_1 = 2r_a/c$. This yields the basic relation $r = ct/2$, which allows determination of the range of any radar target by measuring the round-trip time t . This relation holds for monostatic radars (transmitter and receiver are at almost the same location). For bistatic radars (with the receiver separated horizontally from the transmitter by a distance comparable to or larger than the ranges to the target) a modified

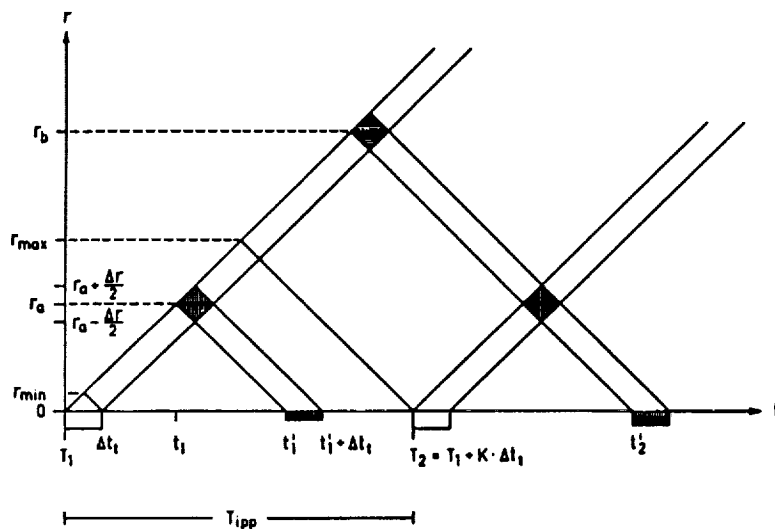


Figure 2. Range-time diagram explaining the main features of pulse transmission and scattering from a volume target at the range r and the reception after a time t (see text for the explanation of the other parameters).

expression has to be applied. Bistatic or multistatic operation will not be discussed in detail here, but is just mentioned for completeness (see Evans, 1969, for more details).

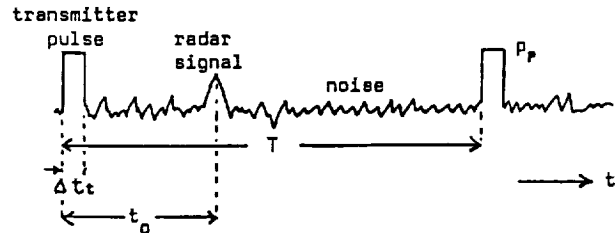
Since the transmitted pulse has a finite duration δt_t , its trailing edge will reach the range r_a at a time $t_1 + \delta t_t$, and reach the receiver at $2t_1 + \delta t_t = t_1' + \delta t_t$. If the radar target is a thin reflecting surface (called discrete, single or hard target scattering), the shape of the received pulse is the replica of the transmitted pulse. Now assume that many scatterers fill all ranges along the radar beam (called soft target or volume scattering). It is then obvious from Fig. 2 that echoes from the range between $r_a - \delta r/2$ and r_a reach the receiver simultaneously at t_1' , and those from r_a to $r_a + \delta r/2$ are received at $t_1' + \delta t_t$. The pulse of duration δt_t , thus, at one time illuminates a volume at r_a extended along a range $\delta r = c \cdot \delta t_t / 2$. This is the range gate or range cell from which the radar echoes are received. Fig. 2 shows that most of the echo power results from the range r_a , and minimum power is received from $r_a \pm \delta r/2$. Thus, the resulting range weighting function of the single range gate centered around r_a is a triangle.

Because of the finite receiver bandwidth (usually matched to the bandwidth of the transmitted pulse) the receiver gate has a finite width in time. The receiver pulse response (given by about the inverse of the receiver bandwidth) distorts the received pulse by smoothing its leading and trailing edges and thus delaying it by about the receiver response time. The transmitter pulse length δt_t , to which the receiver response time is matched, determines the range resolution δr . The instrumental distortions of the radar pulse are not depicted in Fig. 2 to maintain the clearness of survey, but they eventually have to be considered in the final analysis of the radar data.

In radar applications short pulses are normally transmitted periodically, i.e. the n -th pulse follows the $(n-1)$ -th pulse after a specified time. For convenience this time period is set here to be a multiple ($K > 1$) of δt_t . This time $(T_n - T_{n-1})$ is called the interpulse period T_{IPP} , IPP, T_i or just T . Its

inverse is called the pulse repetition frequency $f_{prf} = 1/T_{ipp}$. The off-on-ratio of the transmitter $T_{ipp}/\delta t_t - 1$ determines approximately the range from which radar echoes can be unambiguously received (in units of range resolution). It is more customary, however, to use the ratio $d = \delta t_t/T_{ipp}$, which is called duty cycle or duty factor. The average transmitter power P_a , to be averaged over (more than) one interpulse period, is the product of the duty cycle and the transmitter pulse peak power P_p , i.e. $P_a = d \cdot P_p$. In Table 1 the basic technical terms used in radar applications are summarised.

TABLE 1
DEFINITION OF TECHNICAL TERMS
USED IN ATMOSPHERIC RADAR EXPERIMENTS:



- T = interpulse period (IPP), also T_{ipp}
 $1/T$ = pulse repetition frequency (PRF)
 δt_t = transmitter pulse length (duration)
 P_p = transmitter peak power
 $\delta t_t/T = d$ = duty cycle
 dP_p = average transmitter power
 $r = ct_0/2$ = one-way distance to the radar target

Assume that the radar echo power is due to volume scatter and that isotropic scatterers totally fill the radar beam. Then the received radar echo power P_a is given by the radar equation:

$$P_a = \frac{A P_p \delta r \eta}{8\pi r^2}, \quad (1)$$

where A is the effective antenna area and η is the radar reflectivity.

If the radar echo is due to reflection from a large surface of a refractive index discontinuity, which is stratified perpendicular to the radar wave propagation, the received radar echo power P_r is given by:

$$P_r = \frac{P_p A^2 |g|^2}{4\eta_0^2 r^2} \quad (2)$$

where g is the amplitude reflection coefficient of the surface. For MST radar applications the reflection coefficient can be very small, resulting in partial reflection. In many cases of radar observations scattering takes place, and particularly in ionosphere observations with IS radars the only mechanism is (incoherent) scattering. The partial reflection mechanism is difficult to be distinguished from anisotropic scatter, which both have a pronounced aspect sensitivity (dependence of echo power on beam direction) observed with the long wavelength MST radars. We refer to detailed explanations of these effects, which are for instance outlined in other articles of this book (e.g., HOCKING, 1989).

As compared to radar echoes from single hard targets (e.g. airplanes), where the echo power is proportional to r^{-4} , P_s and P_r are proportional to r^{-2} . This is simply explained by the fact that the volume or the partially reflecting surface or layer of the atmosphere, which is illuminated by the radar beam, is not constant but increases with the square of the range. We particularly have to note the direct dependency of the received signal power on the transmitted peak power P_p and the antenna area A , which means that both these quantities should be optimised. For the reason that the sensitivity of the radars is directly determined by these two parameters, transmitter power and antenna aperture, the quantity "power-aperture product $P \cdot A$ " is used often as the main indicator of the radar capability or sensitivity and it allows a better comparison of measurements done at different radars. Also the term signal-to-noise ratio (SNR), which is the ratio of signal power $P_{s,r}$ and noise power P_n , is used frequently to determine the echo signal strength although this can be misleading because the noise level varies particularly with frequency and antenna look angle, with receiver front-end sensitivity and with loss rates of the antenna and feed systems.

Because in normal radar operations the pulse repetition frequency is kept constant, i.e. the transmitted pulse train is periodic, range-aliasing may occur. This ambiguity is depicted in Fig. 2. At time t_2' an echo of the pulse at T_2 is received from range r_a , and an echo of the pulse at T_1 is received from range r_b . Of course higher order range-aliasing can occur from ranges $r_n = c(t + (n-1)T_{ipp})/2$. Because these echoes return from separate scatter volumes, the echo signals are uncorrelated but still their power accumulates in the same receiver range gate. If no special arrangements (e.g. pulse-coding, frequency changes or non-periodic T_{ipp}) are being made, the maximum unambiguous range is $r_{max} = c \cdot T_{ipp}/2$. The minimum range r_{min} obviously is given by the pulse duration δt_t plus some instrumentally entailed transition time between transmission and reception.

Assume that a bulk motion carries the scatterers or reflectors in the volume at range r . Because of the Doppler effect, the rate of change of phase ϕ of the returned signal is then $d\phi/dt = 4\pi/\lambda_0 \cdot dr/dt$, where λ_0 is the radar wavelength. When V' is the (radial) velocity in direction of the radar signal path, $V' = dr/dt$. The phase change $d\phi/dt$ is the angular Doppler frequency $\Omega_D = 2\pi f_D$, which yields $f_D = -2V'/\lambda_0$. Since the radar signal is pulsed at a frequency f_{prf} , i.e. the radar echo is sampled at a rate T_{ipp} , this yields the maximum Doppler frequency to be resolved by pulse-to-pulse analysis (Nyquist frequency): $f_{Dmax} = f_{prf}/2 = 1/2T_{ipp}$. This corresponds to a maximum radial velocity $V'_{max} = \lambda_0 f_{Dmax}/2$ and $V'_{max} = \lambda_0 c/8r_{max}$. V'_{max} , as defined here, is much larger than any realistic velocity observed in the lower and middle atmosphere.

In cases of large Doppler shift and/or large spectrum widths, i.e. the inverse of the signal correlation time, which are observed for incoherent scatter echoes from the ionospheric E- and F-region, the maximum frequency cannot be resolved by the pulse-to-pulse technique and other means have to be applied. The difference of "coherent signals" observed in MST radar applications and "incoherent signals" observed in IS radar applications is sketched in Fig. 3. For short signal correlation times (shorter than the interpulse period) all samples for the autocorrelation function and the spectrum analysis have to be taken during a single interpulse period (incoherent signal). For long correlation times (longer than the interpulse period) these samples need to be taken during several interpulse periods (coherent signals), which is called "pulse-to-pulse" technique. Details of the corresponding instrumental configurations are discussed in the following Chapter 1.2 and of the data acquisition in Chapter 5.

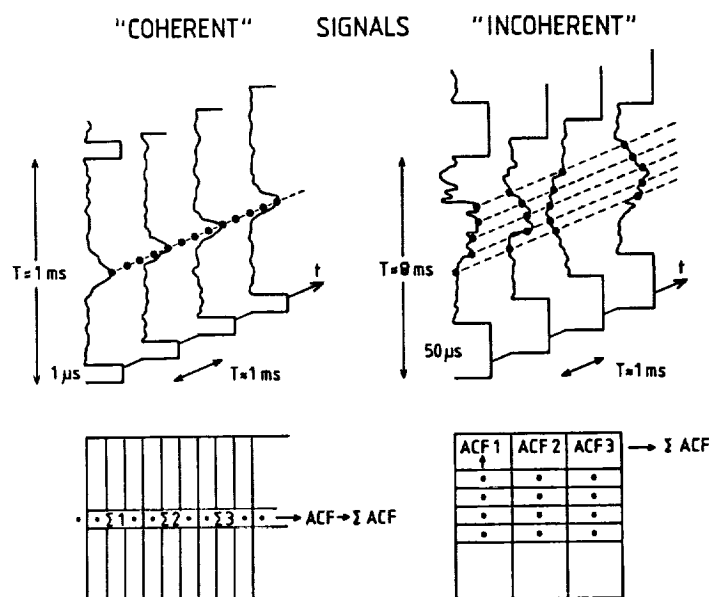


Figure 3. Range-time-amplitude diagrams for coherent (underspread) and incoherent (overspread) signals. The dots mark the sample points, which are used to compute autocorrelation functions ACF. The tables symbolize that for coherent signals coherent integrations ($\Sigma 1, \Sigma 2, \dots$) are performed for fixed range gates over several interpulse periods, then the ACFs are computed which are finally accumulated (ΣACF). This is called "pulse-to-pulse technique". For incoherent signals the ACFs are computed within every interpulse period ($ACF1, ACF2, \dots$) and are accumulated (ΣACF).

1.2. An Overview of Particular Radar Systems

Radars operating in the extended frequency range from MF (medium frequency) to UHF (ultra-high frequency) are used to investigate the structure and dynamics of the troposphere, stratosphere, mesosphere and thermosphere/ionosphere. In Table 2 different kinds of radars and their basic technical parameters are summarized. The MF radars, making use of partial reflection from electron density irregularities, are particularly applied to measure electron density profiles of the ionospheric D-region and lower E-region as well as the horizontal wind velocity in this altitude range, comprising the mesosphere and lower thermosphere. The HF radars (conventionally known as ionosondes) and the ionospheric irregularity scatter radars (somewhat ambiguously also called "coherent radars") are used to study total reflections from the ionosphere and scattering from E- and F-region plasma irregularities. The meteor radars make use of echoes returned from meteor trails to measure wind velocities in the upper mesosphere and lower thermosphere. The mesosphere-stratosphere-troposphere (MST/ST) radars, detecting echoes from turbulence-induced inhomogeneities of the radio refractive index, are applied to investigate winds, waves, turbulence and stability in the indicated altitude regions. Incoherent scatter (also called Thomson scatter) radars, making use of scatter from free electrons, are applied to study the ionosphere and thermosphere. IS radar echoes from the D-region also have long coherence times like MST radar echoes. We concentrate here on the basic principles and applications of the incoherent scatter (IS) and the MST radars, but we note that many principles apply also to the other kinds of radars.

TABLE 2
RADAR METHODS FOR INVESTIGATIONS OF THE LOWER AND MIDDLE ATMOSPHERE
AND THE THERMOSPHERE/IONOSPHERE

Typical operation parameters (approximate)

Radar Method	Frequency Range	Wavelength λ in m	Average Power in kW	Antenna Dimension in λ	Height Region
MF Radar	MF-HF	150-50	0.01-1	1-10	M,L
HF Radar*	HF	300-10	0.01-5	0.5-1	Th/Io
Coherent Radar*	HF-VHF	30-1	0.1-1	5-50	Th/Io
Meteor Radar	HF-VHF	10-6	0.1-10	2-10	M,LT
MST Radar	VHF	6-7	1-100	5-50	M,S,T
Incoherent Scatter Radar	VHF-UHF	1.4-0.25	100-300	100-300	M,LT
ST Radar	VHF-SHF	6-0.1	1-500	10-500	S,T

MF = 0.3-3.0 MHz

HF = 3.0-30 MHz

VHF = 30-300 MHz

UHF = 300-3000 MHz

SHF = 3-30 GHz

* = Ionosonde

M = Mesosphere

S = Stratosphere

T = Troposphere

LT = Lower Thermosphere

Th/Io = Thermosphere/Ionosphere

+ = Irregularity Scatter

The MST radars operate in the lower VHF band around 50 MHz, corresponding to wavelengths around 6 m. Since quasi-vertical antenna beam directions are used, ranges are roughly equal to altitudes. For MST radar observations of the lower and middle atmosphere the range limits r_{max} are between 10-20 km and 100 km. This yields typical pulse repetition frequencies between 10 kHz and 1 kHz. Altitude resolutions from about 1 km down to at least 100 m are required to resolve typical vertical scales in the troposphere, stratosphere and the mesosphere. This corresponds to pulse lengths of about 1-10 μ s. Thus, typical duty cycles are between about 10^{-1} and 10^{-3} . Longer coded pulses are frequently used, which is discussed in Chapter 4.5.

MST radars make use of scattering and reflection from variations of humidity, temperature and electron density, induced by turbulence in the lower and middle atmosphere. Essentially, MST radars can observe: the 3-dimensional wind vector, atmospheric reflectivity and stability, and morphology of turbulence and waves. The continuous measurements with MST radars offer very good quality and quantity middle atmosphere observations of wind velocities. MST radars operate at frequencies around 50 MHz, and therefore are also called VHF radars (VHF = very high frequency band between 30 MHz and 300 MHz). Higher frequency radars mostly cover only the troposphere and stratosphere. Typical peak powers of VHF radars are between 1 kW and 1 MW. Range resolutions down to about 100 m and time resolutions down to some ten second are possible. The antenna arrays with typi-

resolutions down to some ten second are possible. The antenna arrays with typical dimensions of 1000 m² to some 10000 m² point close to the zenith direction. Coherent detection, digital control and data acquisition are mandatory as is described in Chapter 4.

There are basically two methods which are applied by MST radars, in particular to measure velocities, as is sketched in Fig. 4. One method uses a narrow radar beam pointed into various directions and measures the Doppler shift of echoes scattered from irregularities. This method is usually called the "Doppler method" and for this reason these radars are also called "Doppler radars". The other method uses three or more spaced antennas and the received echoes are cross-correlated to determine the drift speed of irregularities and is called "spaced antenna or SA method". Since the irregularities are usually moving with the wind velocity, both methods are capable to measure the wind velocity. Although both methods are basing on the same physical mechanism, in praxis the technical implementation may favour one or the other of these methods. The spaced antenna method can also be applied in the spatial domain radar interferometer mode, which is advantageous for studying the structure of the scattering/-reflecting irregularities. In all these applications a phase-coherent radar system is applied, it is even required for the Doppler and the interferometer method.

3-DIM VELOCITY MEASUREMENTS WITH VHF-RADAR

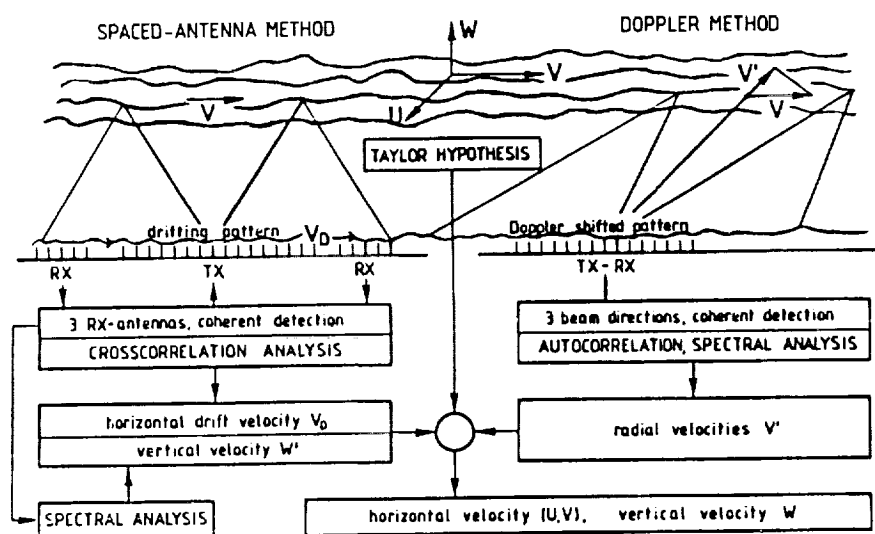


Figure 4. The two principle methods of three-dimensional velocity measurements with monostatic mesosphere-stratosphere-troposphere (MST) radars. These methods are the Doppler method using oblique beams to deduce the horizontal and vertical velocity from the measured radial velocity, and the spaced antenna method applying drifting pattern measurements to deduce the horizontal wind velocity.

The smaller versions of this Doppler radar category, the stratosphere-troposphere (ST) radars operate according to the same principle like the MST radars, but frequently operate on higher frequencies in the UHF band with smaller powers and antenna apertures of several ten square meters only. They are not capable to detect echoes from the mesosphere since either their power-aperture product is too small, yielding too low a sensitivity, or their frequency is so high that their wavelength is in the inertial subrange of refractive index variations such that the scatter echoes are not detectable. These radars apply the Doppler method to measure velocities and are mostly very capable to investigate the lower atmosphere (particularly the troposphere and the boundary layer) with a very good height resolution of some 10 meters or better.

The state of the art of the ST radars and their suitable applicability to measure continuously the wind profiles in the troposphere and the lower stratosphere has attracted wide attention in the meteorological community. As a consequence such ST radars are included into meteorological research networks and particular instrumentation is being designed to allow long-term routine operations of these so-called wind profilers. Since this is a development by industrial companies, we will not discuss these particular designs in the context of this tutorial. A short summary of system specifications of wind profilers, however, can be found in Tables 6 and 7 in Chapter 6.

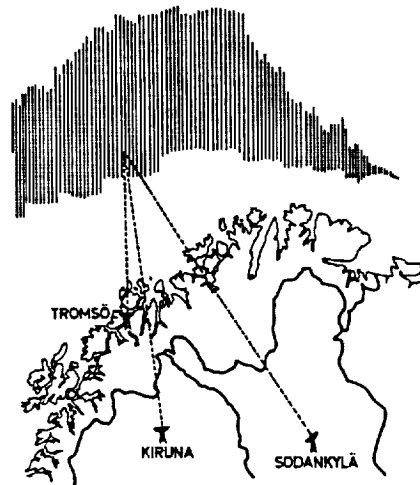


Figure 5. The principle of tri-static incoherent scatter (IS) radar measurements of the auroral ionosphere by the EISCAT UHF system with transmitter and receiver in Tromsø, Norway, and remote receivers in Kiruna, Sweden, and Sodankylä, Finland.

The incoherent scatter radars operate at VHF and UHF frequencies with a much larger power-aperture product than the MST or ST radars. Mostly these radars have large dish antennas or phased arrays occasionally with diameters of several ten to hundred meters. Their peak powers are usually larger than 1 MW, their duty cycle can be up to 12 percent and their fastest interpulse period is mostly not smaller than 1 ms. Pulses as long as 1 ms are used, but frequently amplitude- or phase-coded. Typical altitude resolutions are 0.3 -50 km and time resolutions of some minute to several 10 minutes are achieved. These differences result from the fact that because of the very small volume reflectivity of in-

coherent scatter, the signal-to-noise ratios are mostly well below unity, whereas the SNR is usually much larger than 1 in the MST radar case. The incoherent scatter radars particularly measure electron density, electron temperature, ion temperature and ion velocity in the ionosphere. Fig. 5 shows the tri-static incoherent scatter UHF-radar system of the EISCAT Scientific Association which is operated in northern Scandinavia to study the auroral ionosphere. The tri-static radar configuration is most useful to measure the three-dimensional velocity with the best achievable accuracy. All the IS radars were also used for studies of the stratosphere and the troposphere, although some instrumental constraints had to be considered such as ground clutter, receiver recovery and dynamic range limitations.

A list of these radars is found in Table 9 at the end of this article.

1.3. The Principle of Phase-Coherent Radar Systems

Incoherent or Thomson scatter is caused by fluctuations in the radio refractive index at the radar Bragg wavelength resulting from thermal motions of free electrons in the presence of ions in the ionosphere. Due to these random motions the incoherent scatter signal is widened in frequency and it needs to be sampled fast enough to resolve the complete Doppler spectrum. In the lower ionosphere collisions between ions and neutrals impose the fluctuations of the neutral atmosphere on the plasma and consequently on the electrons. Since these fluctuations, although they can be strong in amplitude, do not contain such high frequency components as the thermal motions, the incoherent scatter signal displays a narrower spectrum, i.e. a longer coherence time in the lower ionosphere. Eventually, the structure of the plasma in the mesosphere (D-region) will be completely governed by the fluctuations due to neutral air turbulence. Instead of incoherent scatter this latter process is called coherent or turbulence scatter. Usually the signal spectrum due to turbulence scatter is much narrower than that of incoherent scatter. In addition to the widening of these signal spectra, they are shifted in frequency if there is a bulk radial velocity of the scattering medium. We would like to explain here that both these scattering processes are being studied with phase-coherent radar systems.

Knowing that fluctuating velocities and radial velocities with quasi-vertical MST radar beams do not exceed several 10 ms^{-1} , the Doppler frequency will barely exceed 10 Hz for MST radars operating at VHF and will be just an order of magnitude larger for UHF. Applying $f_{\text{pr}} > 1 \text{ kHz}$, the MST/ST radar echo will be oversampled, i.e. its phase and amplitude does vary little from pulse to pulse as it was sketched in Fig. 3. This is called a coherent radar echo, in contrast to an incoherent radar echo, which, because of the much shorter correlation or coherence time of the ionospheric scatter medium, randomly changes phase and amplitude from one pulse to the next. Also the velocities in the ionosphere measured with incoherent scatter radars is usually much larger than the velocities in the middle and lower atmosphere, which additionally causes a more rapid change of the phase of the incoherent scatter signals. One does make efficient use of the characteristic coherency of MST radar echoes to improve the data acquisition procedures, which will be discussed in Chapter 4. These differences of the signal coherence times also determine the principle way of the data acquisition structure and instrumentation.

The differences between "coherent signals" detected by the MST/ST radars, used to study the lower and middle atmosphere, and "incoherent signals" detected by the incoherent scatter radars, used to study the ionosphere, is elucidated by the schematics of Figs. 6a and 6b. Since the coherence time, i.e. the inverse of the width of the Doppler spectrum, generally increases from the lower to the middle and to the upper atmosphere (ionosphere) due the increasing variations of

MST-RADAR

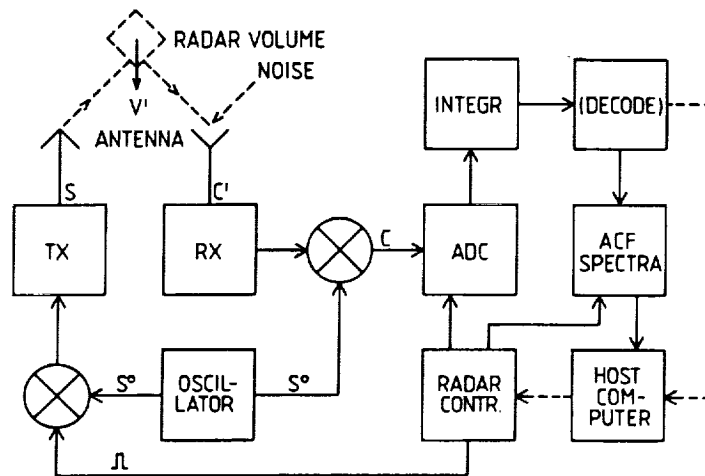


Figure 6a. Block diagram showing the basic configuration of an MST radar system (data acquisition for coherent signals).

IS-RADAR

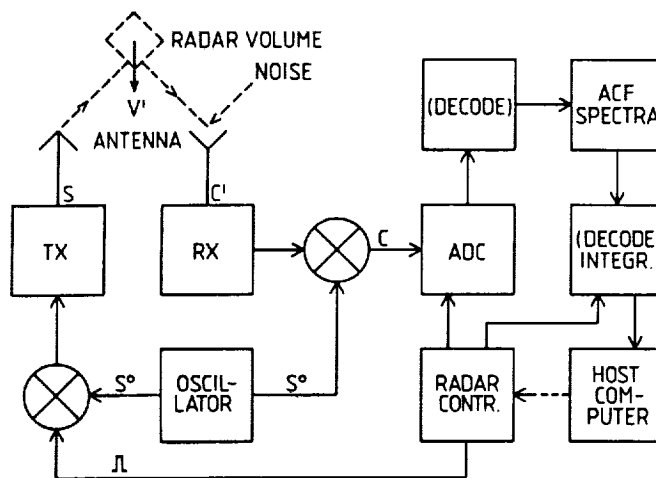


Figure 6b. Block diagram showing the basic configuration of an incoherent scatter radar system (data acquisition for incoherent signals).

the scattering medium. Whereas in the lower atmosphere the coherence time (determined principally by turbulent fluctuations) is generally much longer than a typical interpulse period of an MST/VHF radar of say 1 ms, it is generally much shorter (given by thermal fluctuations) than an interpulse period of incoherent scatter radars. This means that coherent integration and the autocorrelation functions (ACFs) or Doppler spectra are computed on the pulse-to-pulse basis for coherent signals ("pulse-to-pulse technique"). On the other hand, the ACFs have to be immediately computed without coherent integration for each single interpulse period using single long or coded pulses in the case of incoherent signals. The ACFs (from which the spectra are computed) are then postintegrated. The definition of a coherent signal, which we use here, is consequently that the coherence time is much longer than the interpulse period. The incoherent signal is defined by a coherence time which is much shorter than the interpulse period. At some places in the early ionosphere literature the terms under-spread and over-spread signals are used instead of coherent and incoherent signals, respectively. Both kinds of signals anyhow result from the scattering process being coherent in the former and incoherent in the latter case, and both are studied with phase-coherent radar instrumentation.

We notice that the instrumental technique as well as the data acquisition and analysis of the MST radars as well as the IS radars are basically similar, they are well developed, elaborated and fairly mature, although further refinement is always going on. We now will briefly outline the two only striking differences of the instrumental design of these two main radar categories, which result from the coherent and incoherent signal properties and later will discuss particular parts of the instrumental hardware and their principles.

In order to allow the measurement of all signal parameters, particularly the Doppler spectrum, all MST radars and IS radars are phase-coherent. This means that the receiver (RX) and the transmitter (TX) are controlled by or phase-locked to the same main oscillator (see Figs. 6a and 6b). The transmitter radiates through the antenna the electromagnetic signal S , which propagates to the radar volume in the atmosphere or the ionosphere. From there a small fraction of the electromagnetic energy is backscattered to the antenna (which can be a separate or the same antenna, provided that a transmit/receive duplexer can be used). External noise, received by the same antenna and internal receiver noise adds to the atmospheric/ionospheric echo and the total signal plus noise C' is amplified in the receiver and mixed to base band by the same oscillator signal S^0 , which is used to control the transmitter. The resulting base band signal C is converted to a digital series in the analog-to-digital converter (ADC), which is controlled by a series of sample pulses from the radar controller. The radar controller also generates the transmitter modulation and other control pulses.

Following the ADC, the data acquisition procedures are different for MST- and IS-radars as delineated in the Figs. 6a and 6b. This difference results from the different coherence times as described earlier. Because of the long coherence times of echoes from the mesosphere, stratosphere and troposphere, the digital data are usually coherently added in the integrator of an MST radar (Fig. 6a), followed by a decoding procedure if the transmitter pulses are coded (see Chapter 4 for details). These raw, but pre-integrated and/or decoded, data are either directly dumped into the host computer or analyzed in terms of autocorrelation functions or Doppler (Fourier) spectra. The host computer is used to store the raw data together with other operating system parameters and the time, on file or tape, perform an on-line quicklook analysis or some further preprocessing such as computation or post-integration of ACFs or spectra. The host computer also supervises the entire system by loading and starting the radar controller etc. as well as checking the system performance and issuing interrupts in case of system malfunctions. In the case of an incoherent scatter radar

(Fig. 6b) first a decoding has to be performed, then usually ACFs are computed on-line which are post-integrated and then dumped into the host computer. In particular pulse coding schemes also an additional decoding procedure has to be applied after the ACF computation. Otherwise the instrumental design of an IS radar is principally similar to an MST radar.

2. RADAR ANTENNAS

The radiation pattern of MST- and IS-radar antennas has to be carefully designed in order to optimize the wanted atmospheric/ionospheric scatter signal as compared to interfering external influences. These are summarized in the sketch of Fig. 7. It is evident that all the unwanted components, - ground clutter, sea clutter, airplane or satellite echoes, radio interference and scatter received through antenna sidelobes - , have to be properly eliminated or minimized. To achieve a high sensitivity and a reasonable angular resolution the antenna gain should be large and thus the antenna beam width small. The cosmic noise level picked up by the antenna is unavoidable in the low VHF band. In the high VHF and in the UHF band the noise level is not given by the sky noise but by the system noise. This can be minimized by optimum design of the receiver front-end amplifier and adapted data processing.

The antennas of MST- and IS-radars usually consist of an ensemble of single elements which are phase-coherently combined to a large antenna array or are large dish antennas. Usually the dimensions of MST radar antennas are more than several ten radar wavelengths, their gain is mostly exceeding 20 dB, corresponding to a beam width of less than 10 degree. The IS radar antennas usually have antenna gains larger than 40 dB in order to detect the weak incoherent scatter signals. The beam directions can be mechanically or electrically positioned

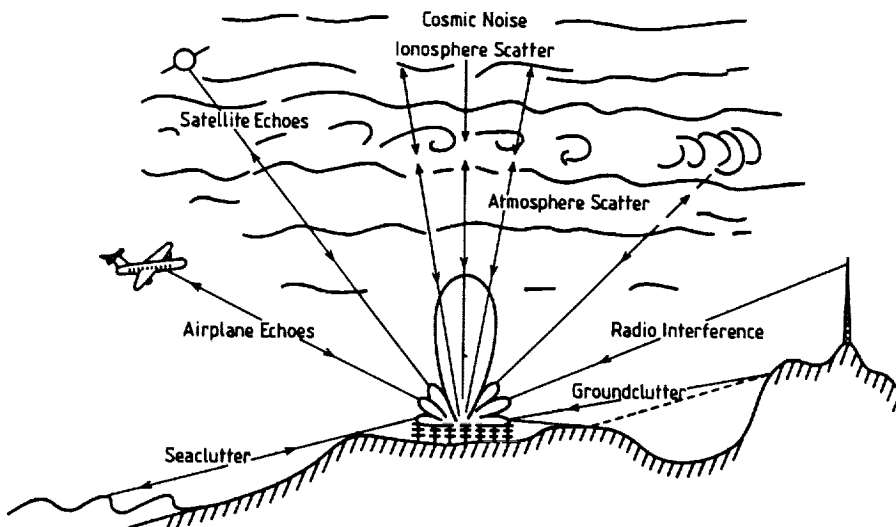


Figure 7. Schematic view of an atmospheric radar in an interference and clutter environment. The radar antenna is depicted here to consist of a phased array of Yagis, but could principally be any other kind of antenna system.

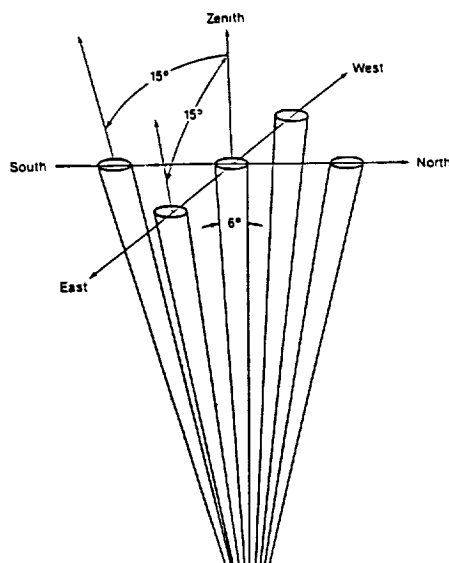


Figure 8. Near-zenith pointing antenna beams of a 403 MHz phased array antenna of an ST radar (after FRISCH et al., 1986).

(e.g., Fig. 8) in order to observe spatial variations of the scatter process and to measure three-dimensional velocity components. The principle of measurements of the velocity components is explained by the schematics of Fig. 9. At a zenith angle δ in the direction of the wave vector k the radial velocity $v = u' + w'$ is measured, which consists of the projections w' of the vertical velocity w and the projection u' of the horizontal velocity u . The combination of the velocities measured in the directions δ and $-\delta$ yields the horizontal and the vertical velocity component. Depending on the requirements to measure all velocity components and their divergence as well as vorticity, more beam directions are necessary. Multi-static radars (e.g., Fig. 5) can also be used to measure the velocity components. The discussion of these possibilities and requirements is out of the scope of this lecture note but can be found elsewhere (see RÖTTGER and LARSEN, 1989, who discuss the applications of MST radars and give further references).

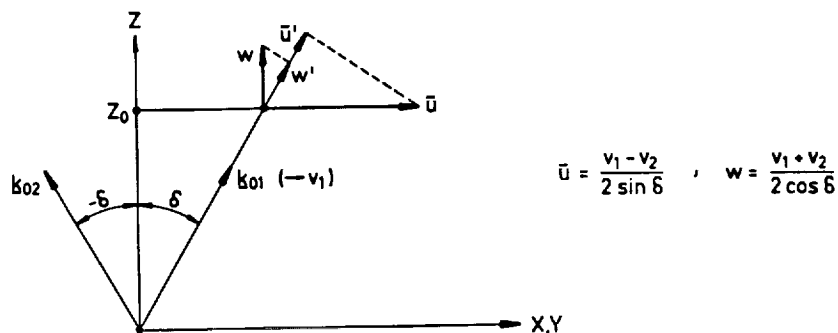


Figure 9. Principle geometry of two antenna beam directions k_{01} and k_{02} at zenith angles δ and $-\delta$ for the deduction of the horizontal velocity component u and the vertical velocity component w . The measured radial velocity components v_1 and v_2 consist of the projections u' and w' of the u and w wind velocity components, respectively.

We now will briefly describe the basic antenna theory in order to allow an understanding of the antenna functions and the design optimization and then will describe some typical antenna systems used in MST radar applications.

2.1. Some Basic Antenna Parameters

The main parameter determining the antenna gain and the corresponding beam width is the size or the area of the antenna, which is also called the antenna aperture. The antenna aperture can be either regarded as a continuous radiator if it is illuminated by an independent feed system, or it can consist of several sub-elements which are electrically fed from a common transmitter source. Both approaches can be basically treated by a similar formalism, which we will explain for the simple case of a line of antenna dipole elements. Assume that N individual antenna elements with equal spacing d are horizontally lined up to form a multi-element array (see Fig. 10). In the array far-field ($r > (Nd)^2/\lambda_0$) the antenna polar diagram is

$$E(\delta) = \sum_{n=1}^N E_n(\delta) \exp(i(\frac{2\pi(n-1)d}{\lambda_0} \sin\delta + \phi_n)), \quad (3)$$

where $E_n(\delta)$ is the pattern of an individual element and ϕ_n is a relative phase placed on this element. Thus, the polar diagram is just the Fourier transform of the spatial aperture distribution. If all the elements have similar $E_n(\delta)$ and ϕ_n , the polar diagram is a function $\sin Nx/\sin x$ with $x = \pi \cdot d \cdot \sin\delta/\lambda_0$. If $d < \lambda_0$, there is only one main lobe at $\delta = 0^\circ$ (for $\phi = 0$). If $d > \lambda_0$, grating lobes at $\delta_g = \arcsin(\lambda_0/d)$ occur, for $E_n(\delta) = \text{const}$ with amplitudes similar to the main lobe. The width of the main lobe is $\delta_s = \arcsin(\lambda_0/Nd)$. In radar applications also the two-way beam width $\delta_s/\sqrt{2}$ is used. If δ_s is small, it is directly proportional to the ratio of the wavelength λ_0 to the aperture dimension Nd . The radiation pattern has minima (nulls in theory) at $\delta_n = \pm n\delta_s$, where $n = 1, 2, \dots, N/2$, and sidelobes occur at $\delta_s = \delta_n \pm \delta_s/2$. If equal weighting W_n is applied to each of the single elements (e.g., $E_n'(\delta) = W_n \cdot E_n(\delta)$, with $W_n = \text{const}$ for all n), the first sidelobe closest to the main lobe is suppressed by 13.2 dB plus the fall-off of the individual element pattern $E_n(\delta)$ at δ_{s1} .

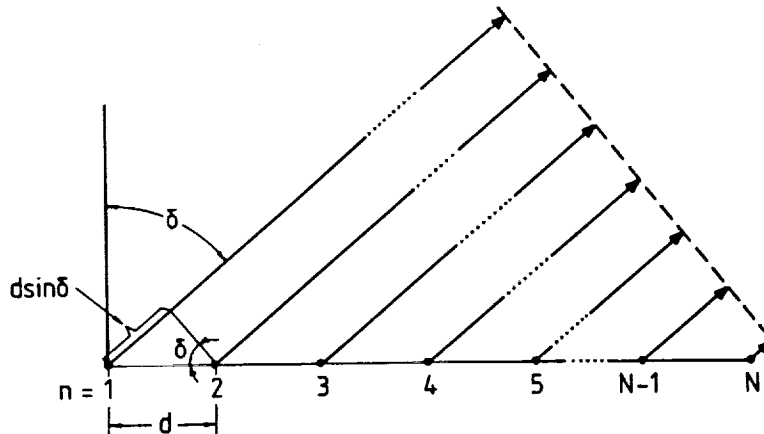


Figure 10. Schematic drawing of wave vectors of a plane wave radiated under a zenith angle δ from N isotropic antenna elements with spacing d .

The antenna pattern, particularly the desired variation of the direction δ_0 of the main lobe, can be changed by applying a linearly progressing phase ϕ_n from element to element, which has to be $\phi_n = 2\pi d(n-1)\sin\delta_0/\lambda_0$. This beam steering should be within reasonable limits of the individual element pattern $E_n(\delta)$ to avoid undesirable degrading of the antenna radiation. Furthermore the effective area of an antenna, which is fixed on the ground, is reduced with larger zenith angles because the illumination changes by $\sin \delta$.

To obtain improved sidelobe suppressions, a tapering of the antenna array can be applied by either changing the weighting function W_n (electrical weighting, i.e. feeding the outer elements of an array with less power than the inner elements), or by using unequal element spacings d_n (spatial weighting, i.e. applying larger spacings for the outer elements of an antenna array). The price one has to pay for the improvement of sidelobe suppression by tapering is always a broadening of the main lobe and lowering of the antenna gain G . Using a triangular weighting, for instance, improves the one-way suppression of the first sidelobe to -26 dB, but widens the main lobe by a factor of 1.44 and reduces the gain by 25%, as compared to uniform weighting. The respective values for a \cos^2 -weighting, which is a good approximation to a Gaussian weighting, are -32 dB, 1.64 and 33%.

These one-dimensional considerations can be extended easily to a realistic two-dimensional radar antenna array by using, instead of d , the projections d' of all element positions onto n axis elongated in the azimuth direction α . The total antenna pattern then can be calculated by (3) for any α and δ . For a real radar antenna we also have to consider that the radiation can be into only one half-sphere. For an array system this means that reflections from the ground, a screen or reflector elements have to be included in the calculations. The antenna gain G is defined as the ratio of the maximum radiation intensity (in the main beam) to the average radiation intensity (averaged over all δ and α). For an antenna array with reasonable sidelobe suppression it is proportional to the antenna area and is given approximately by the inverse of the two orthogonal beam widths δ_B' and δ_B'' (in radians):

$$G = \frac{4\pi A}{\lambda_0^2} \approx \frac{4\pi}{\delta_B' \delta_B''} \quad (4)$$

The effective area A or aperture of the antenna is the product of the physical area of the antenna and the efficiency of its illumination, which for instance may be reduced by tapering. It is noted that A does not include the losses of the antenna elements and its feed system.

The considerations of antenna arrays, consisting of several discrete elements, can generally be extended also to antennas with continuous aperture illumination, such as dish antennas. The aperture A of a phased array or a dish antenna is used to calculate the power-aperture product $P \cdot A$, which defines the sensitivity of an MST radar. Note that P is the effective average power, which is radiated by the antenna, i.e. it is smaller than the output power of the transmitter due to losses in the antenna and feed lines.

This very brief outline is useful for estimating some basic values needed to plan and design a radar antenna system. The minimum requirement for investigations of the troposphere and stratosphere is a power aperture product $P \cdot A = 10^6 \text{ Wm}^2$, where $P = P_A$ is the average transmitter power. We assume that the radar sensitivity is a function of A^k , where $1 < k < 2$ depending on the reflected contribution (see equation (2)). It means that in practice one should favour an extension of the antenna area against an increase of the transmitter power. For a commonly achievable transmitter power $P = 10^3 \text{ W}$, $P \cdot A = 10^6 \text{ Wm}^2$ yields the

dimension of a circular antenna array to be about $Nd \approx 36$ m, and $A \approx 1000$ m². For $\lambda_0 = 6$ m we can obtain a half-power beamwidth $\delta_{\text{HP}} \approx 9^\circ$, and a gain $G \approx 27$ dB. This estimate assumes that the array is optimally filled with elements. A single dipole element over a proper reflector screen has an effective area of about 15 m² (at $\lambda_0 = 6$ m). Thus, about 64 dipoles are needed to fill the array. For a square array with 8x8 elements the resulting spacing is $d \approx 0.75 \lambda_0$, and a grating lobe will not occur. The first nulls are at $\delta_n = \pm 9^\circ$, and the first sidelobes at $\delta_s = \pm 13.5^\circ$. To use such an array to measure reliable velocities, the antenna beam has at least to be steered to a zenith angle $\delta_0 = 9^\circ$ to place a null into zenith direction (minimizes influences of aspect sensitivity). Even then a sidelobe at -4.5° is a problem.

When designing a radar antenna for atmospheric research one has to trade between the choices to optimize the effective aperture or to optimize the side-lobe suppressions. An optimization of the aperture increases the sensitivity, but does not minimize the side lobes. Suppression of sidelobes by tapering attenuates undesirable signals which spoil the estimates of reflectivity and velocity, but it reduces the antenna gain. Principally, any sidelobe effects or their minimization, however, are equivalent to a broadening of the antenna beam. This is generally a minor shortcoming as compared to the tedious procedures to remove sidelobe effects from the signal during the data analysis procedure. As an example of a well optimised MST radar antenna pattern we show in Fig. 11 the antenna diagram in two vertical planes of the mobile SOUSY VHF Radar (from CZECHOWSKY et al., 1984). Note the suppression of near-zenith sidelobes by 25 dB as compared to the main lobe and the grating lobe at 40° .

The radar echo signal is given by the product of the antenna pattern with the spatially varying reflectivity structure of the atmosphere. Thus, knowing the antenna pattern, it should be in principle possible to find the wanted signal parameters which however is generally an ambiguous and time-consuming inversion procedure. For vertically pointing main beams the sidelobe effects are efficiently suppressed if there is anisotropic scattering with maximum aspect sensitivity in zenith direction (e.g., for the 50 MHz MST radars). It follows that sidelobes in such cases are a minor problem for investigations with vertical beams. However, they can be crucial for methods applying off-zenith beams with 50 MHz MST radars. If a sidelobe is pointing towards the zenith a larger power may be received from the vertical than from off-vertical directions when there is an aspect sensitivity due to horizontally stratified scatterers or partially reflecting layers.

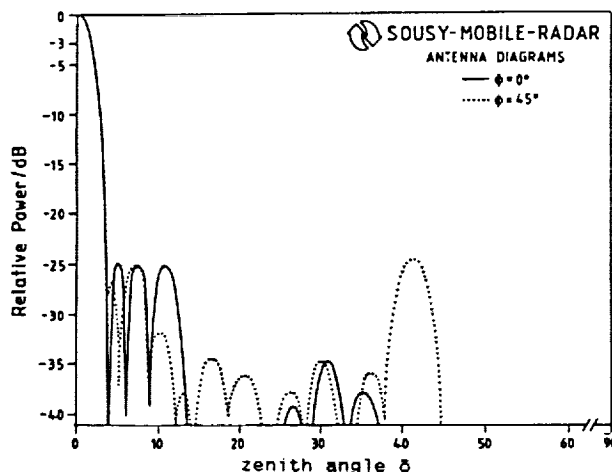


Figure 11. Computed radiation pattern of the mobile SOUSY VHF radar (53.5 MHz) phased array, consisting of 576 Yagi antennas. This antenna system is located on Andoya, Norway. (From Czechowsky et al., 1984).

Also sidelobes at low elevation angles have to be considered since these can cause strong echoes from the non-atmospheric targets in the surroundings of the radar antenna (particularly the ground clutter seen in Fig. 7). The superposition of ground reflected (hatched line in Fig. 7) and direct radiation does very effectively reduce the radiation at grazing angles ($\delta > 85-90^\circ$) since the antenna elements of a phased array are horizontally polarized and the ground-reflected wave then suffers a phase reversal during reflection. This even can suppress low sidelobes of the array pattern which may be regarded as crucial if one would not take into account ground reflections. The location of an MST radar antenna array at a flat ground (extending out to several 100 m) may be sufficient, but a shallow valley generally should be preferred to further suppressing the low angle radiation effects. However, high extending targets, such as radio towers or mountains in the close vicinity, will still cause considerable clutter echoes, even when optimising the antenna array for low angle radiation suppression. For IS radar antennas the criteria of low angle radiation suppression are not so stringent, because ground clutter barely comprises a problem since the ionospheric target regions are usually at much larger ranges. However, for IS radars in auroral regions care has to be taken to suppress coherent echoes from ionospheric irregularities.

2.2. Antenna Types and Feed Systems

MST radars generally operate with quasi-vertical beams, i.e. the zenith angles are smaller than about $20^\circ-30^\circ$. As shown in Fig. 8 usually zenith angles of 15° are chosen. IS radars mostly apply a variety of beam directions, also those very close to the horizon. For MST radar operation linear polarization is sufficient, but circular polarization is needed for incoherent scatter radars since the polarization can change due to dispersion in the ionosphere. Essentially four different types of antenna systems are in use: dish antennas, dipole arrays, coaxial-collinear arrays (COCO) and Yagi arrays. In Fig. 12 we show as an example the 32-m dish antenna of the EISCAT incoherent scatter radar 933-MHz receiving station in Sweden, which can be pointed in all directions by mechanical steering. In Fig. 13 the 200m x 200m MST radar antenna of the Poker Flat Radar in Alaska is shown which has only a few fixed pointing directions to the vertical and at 15° off-vertical.



Figure 12. The 32-m receiving antenna dish of the incoherent scatter radar of the EISCAT UHF (933 MHz) radar system in Kiruna, Sweden.

ORIGINAL PAGE IS
OF POOR QUALITY

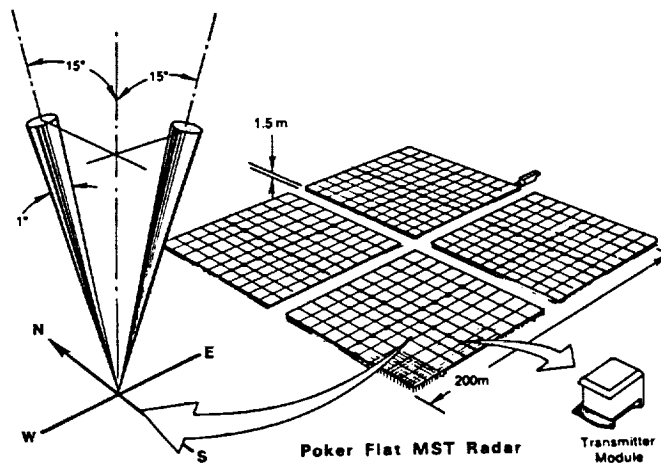


Figure 13. The 200m x 200m coaxial-collinear antenna array of the Poker Flat MST radar in Alaska, operating on 50 MHz with two off-vertical beam directions (from BALSLEY et al., 1980).

Dish or cylinder antennas are rarely used for MST radar applications because of their large dimensions, but they are quite frequently applied in IS radar facilities. Only one or a few elements are applied as primary feed antennas of the dish antennas. The beam steering is done either by moving the position of the feed antenna (e.g., at the Arecibo Observatory (WOODMAN, 1980)) or the entire dish (e.g., at the other UHF IS radars, see Table 9 at the end of this article). This has the advantage that no complicated power distributions and phasing network has to be used to feed the antenna. The EISCAT VHF radar uses a long line feed to illuminate a 120m x 40m dish and allows mechanical steering in one plane and side-steering by phasing in the other plane (HAGFORS et al., 1982). Because of the limited size of the primary feed antennas of dish antennas, the low-angle sidelobe suppression is usually not sufficient, which results in strong clutter echoes, particularly when such antennas are also used for MST radar applications.

Usually the antenna systems of MST radars are phased array antennas consisting of many single elements as can be seen for instance in the lay-out of the antenna system of the MU radar in Japan which consists of 475 crossed Yagi antennas (Fig. 14). In the case of the MU radar modules of four antenna elements are fed by single phase-coherent transmitters, which allows very fast electronic beam steering. In many other cases the individual elements or modules are fed from a single transmitter through a cascading network of cables, hybrids and phase shifters. A relatively simple antenna array is the COCO antenna (coaxial-collinear), which is built in form of an array (see Fig. 15) by using coaxial cable as radiating elements (e.g., BALSLEY et al., 1980). It has the advantage that the feeding of elements in one line is just done by interchanging the inner and outer conductor of a coaxial cable every half wavelength. The earliest application of the COCO antenna can be found at the Jicamarca VHF radar in Peru (see Fig. 16). The outer conductors of the aligned coaxial tube or coaxial cable act as collinear dipoles. The feeding is done from the center of a line, which may typically consist of 16-48 dipoles. Positioning several of these strings or rows in parallel at spacing $d < \lambda_0$, and feeding these by a suitable matching network results in a COCO array (see Fig. 15). The radiation and the loss in a coaxial string comprise some natural tapering, having the intrinsic advantage of

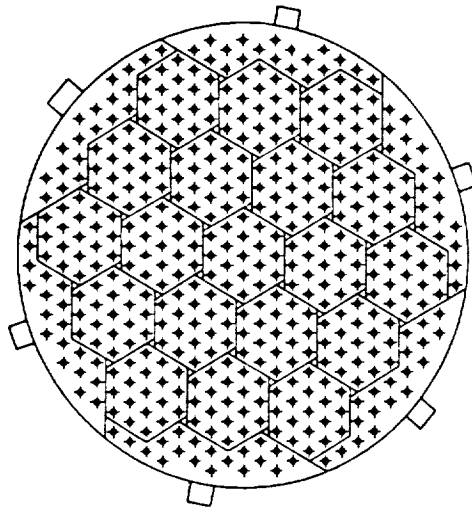


Figure 14. The lay-out of the 475 crossed Yagi-antenna elements of the 46.5-MHz MU radar in Japan (after FUKAO et al., 1985a,b).

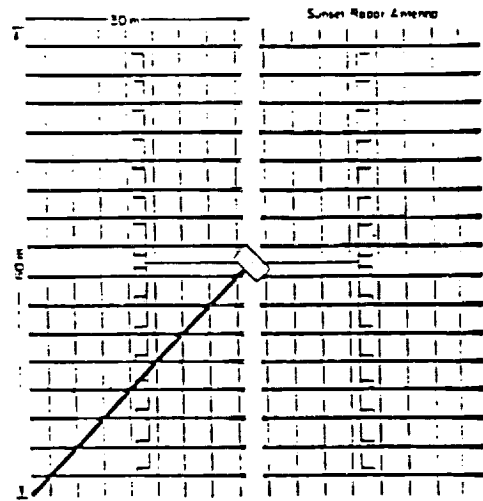


Figure 15. The coaxial-collinear antenna lay-out of the 50-MHz Sunset ST radar in Colorado, USA (from Green et al., 1975).

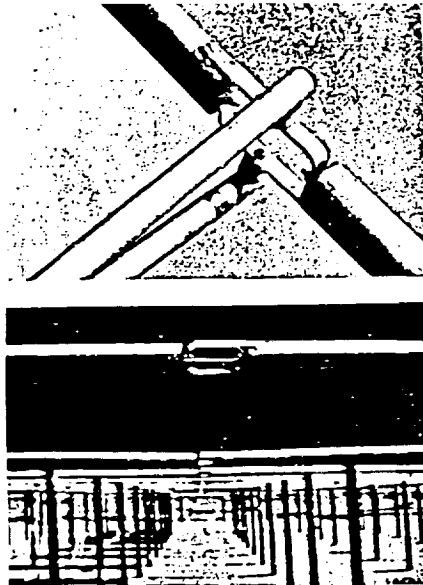


Figure 16. Part of the phased-array antenna of the 50-MHz Jicamarca radar in Peru and a close view of the interchange of inner and outer connector of the coaxial-collinear dipole tubes (from OCHS, 1965).



Figure 17. Yagi antennas and power dividers of the SOUSY-VHF-Radar in West Germany.

ORIGINAL PAGE IS
OF POOR QUALITY

suppressing sidelobes in the plane of the string but the disadvantage of degrading the antenna efficiency. Because of the phase relation along a string is fixed, a beam steering parallel to the COCO string is not possible. Beam steering perpendicular to the string rows is achieved by inserting appropriate phase delays in the cables feeding the parallel rows. The COCO dipoles have to be lined up a quarter wavelength over reflector wires or screens. This antenna type is relatively inexpensive, because coaxial cable is used for antenna elements and the matching network is simple. The successive phasing from one collinear element to the next, however, degrades the bandwidth of this antenna type. Instead of coaxial cable as radiator, half-wave dipoles can also be used which are fed in a properly adjusted phase to form a collinear antenna. The application of collinear dipole lines limits the steerability of an array, and for this reason frequently three antenna arrays are used with three different fixed beam directions (e.g., GREEN et al., 1975; BALSLEY et al., 1980).

Single dipole or Yagi antenna elements (see Fig. 17) are often set up to form a phased array (see Fig. 14 and Fig. 18). They are fed by a cascading network of open wire or coaxial cable systems, when a single transmitter is applied. The cascading is most appropriately done in 2^n branchings ($n = 1, 2, \dots$), as for instance shown in Fig. 19. By these means one can also feed parts of the antenna array with $1/2$, $1/4, \dots$ power to provide tapering without dissipating power (see for instance Fig. 20). The branching is best done in couplers, power dividers or 3dB-hybrids, which prevent RF-power, reflected from a mismatch to return to the transmitter or other antenna elements rather than being dissipated in the resistor port of the hybrid. These hybrid installations also minimize effects due to mutual coupling between the single antenna elements. The coupling can be critical if phase control is applied to steer the antenna beam. The phase shifting, as shown in Fig. 21, is usually inserted close to the final elements, which may also be connected to form modules of 4 or more elements. For continuous beam steering phase shifting has to be done continuously, which mostly is a sensible and difficult procedure particularly when narrow antenna beams are used. The phasing is more easily done by inserting discrete phase delays in steps of $2\pi/16$ with a binary phase shifter, which is shown in Fig. 22. The switching can be achieved by only four relays, allowing phase delays of 22.5° , 45° , 90° and 180° to be inserted in all possible combinations, which are sufficient for commonly applied beam width of several degrees. Another way of phase shifting can be done with hybrids as is shown in the schematics of the later Fig. 32.

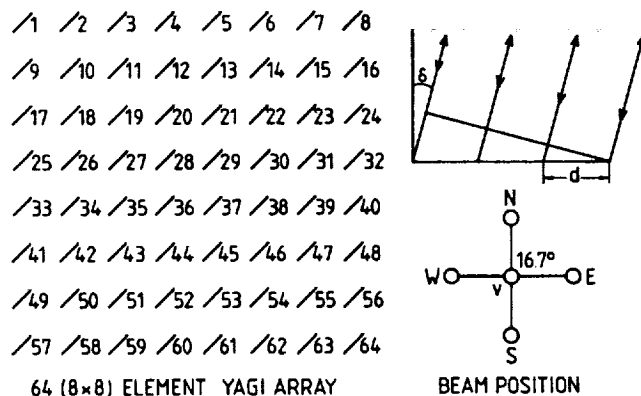


Figure 18. Lay-out of one 64-Yagi-antenna module of the 52-MHz Chung-Li VHF radar in Taiwan (after BROSNAHAN et al., 1984).

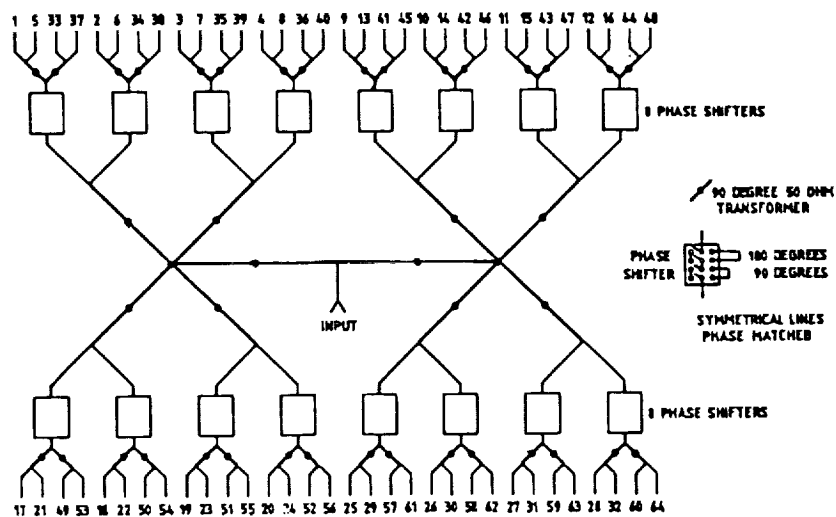


Figure 19. Power divider and beam-steering phase delay (0° , 90° , 180° and 270°) of the Chung-Li VHF radar, allowing five beam positions: vertical ($\delta = 0^\circ$) and north, east, south and west at $\delta = 16.7^\circ$ zenith angle (from BROSNHAN et al., 1984).

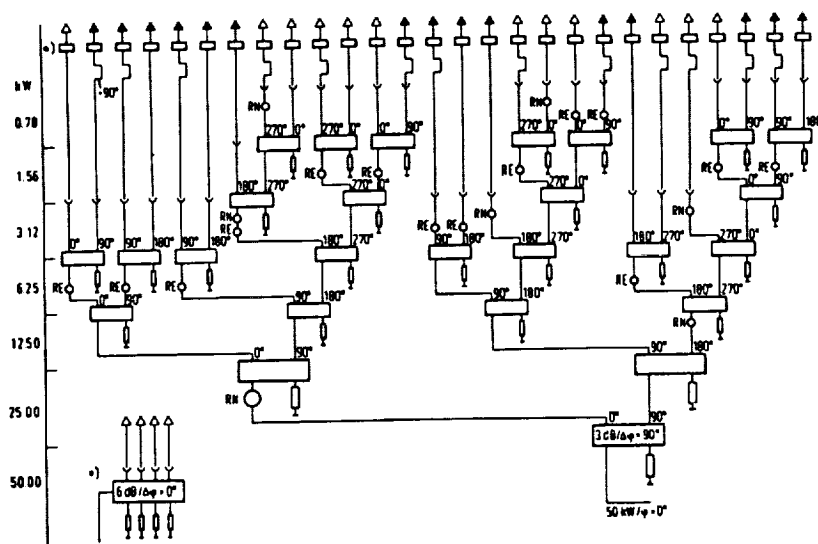


Figure 20. One quarter of the power divider system of the mobile SOUSY VHF radar antenna, allowing for tapering of the antenna elements by staggered power dividing hybrids (from CZECHOWSKY et al., 1984).

Antenna Feed Distribution System

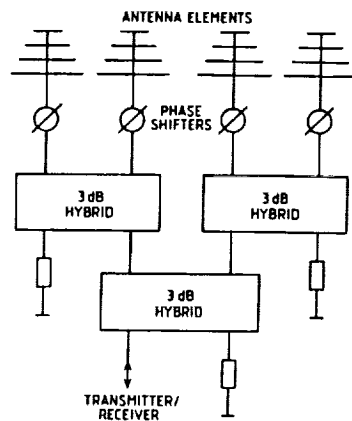


Figure 21. Schematics of a typical antenna feed distribution system using hybrids for power division. The two output ports of a hybrid are phase shifted by 90° with respect to each other. This has to be compensated by the phase shifters, which are also used to insert certain phase shifts for beam steering. The power, which is reflected from the antennas due to an impedance mismatch, is attenuated in the resistor port of the hybrids and does not return through the transmitter-receiver port.

Binary Phase Shifter

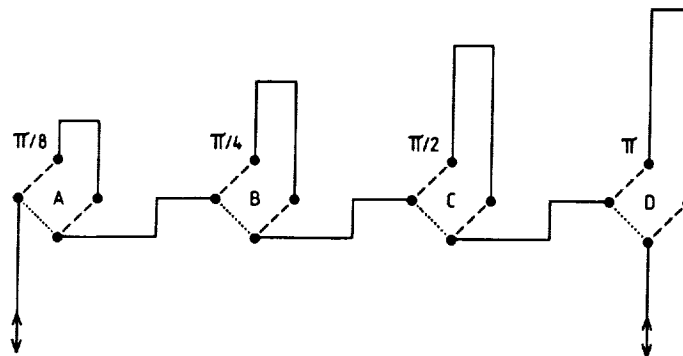


Figure 22. Principle of a binary phase shifter, allowing all the combinations of phases:

Phase shift:		$\pi/8$	$2\pi/8$	$3\pi/8$	$4\pi/8$	$5\pi/8$	$6\pi/8$	$7\pi/8$	π
Phase delay	A:	1	0	1	0	1	0	1	0
(1=on)	B:	0	1	1	0	0	1	1	0
(0=off)	C:	0	0	0	1	1	1	1	0
	D:	0	0	0	0	0	0	0	1

The phases between π and $15\pi/8$ are achieved by keeping the phase delay D in the on-position.

The advantage of Yagi against dipole antenna elements is that no ground screen is needed because of the Yagi reflector. The multi-element structure of a single Yagi allows for a higher gain (improving the filling factor of an array) and a negligible coupling (< -25 dB) between adjacent Yagi antennas in an array. Mostly Yagi antennas can be constructed in such a way that the bandwidth is several Megahertz. The bandwidth limiting factors in a Yagi system essentially are the phase shifters. The losses of a Yagi system are also considerably lower than those of a COCO antenna. However, such a Yagi system is obviously more expensive than a COCO system. The feeding of an array system can be from one transmitter, but also sub-modules can be fed separately by several phase-controlled transmitters (FUKAO et al., 1980). The transmitter phase control can even be used to steer the antenna beam. This, however, needs a similar phase control of the receiver channels.

3. TRANSMIT-RECEIVE SYSTEM

Separate antenna arrays can be used for the transmission and for the reception mode as shown in the graph of Fig. 23. Such an antenna combination was first used with the SOUSY-VHF-Radar for MST measurements with the beam-swinging as well as the spaced-antenna mode, which was added at a later time. For a newly designed radar a combination of the two measurement modes using one antenna for transmission and reception is useful as shown in Fig. 24. While separate antenna arrays allow for sufficient decoupling of the receiver from the transmitter, a fast and highly insulating transmit-receive duplexer (ATR = antenna-transmit-receive switch or duplexer in Fig. 24) has to quickly switch the antenna from the transmitter to the receiver and vice versa, if only one antenna is used. The principle of a duplexer is outlined in Fig. 25. During the transmission phase the pin-diodes are short-circuited and the power at the hybrid output ports is reflected back into the hybrid from where it exits through the antenna port to the antenna. The small leakage through the diodes is combined in phase in the

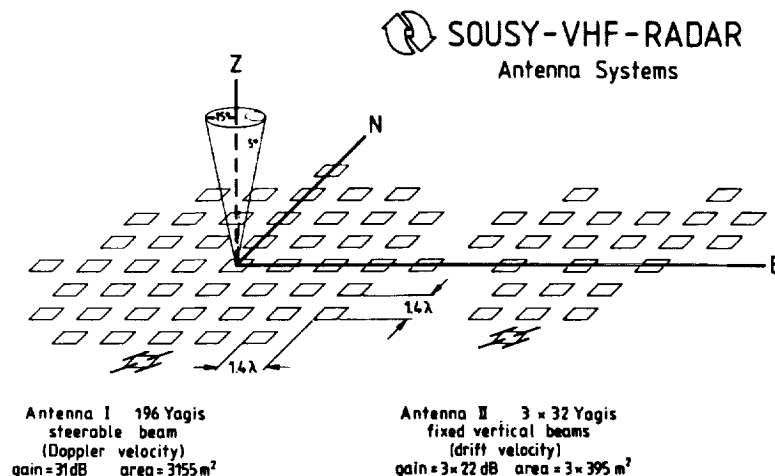


Figure 23. Antenna systems of the SOUSY-VHF-Radar in W.Germany consisting of phased arrays of Yagi-antenna elements. The complete system is designed for beam steering in the Doppler mode with antenna I and in the spaced antenna mode with antenna I and antenna II. For the latter purpose the antenna I is pointed vertical and the separated three subunits of 32 Yagis of antenna II, which are forming a vertical beam also, are used for reception.

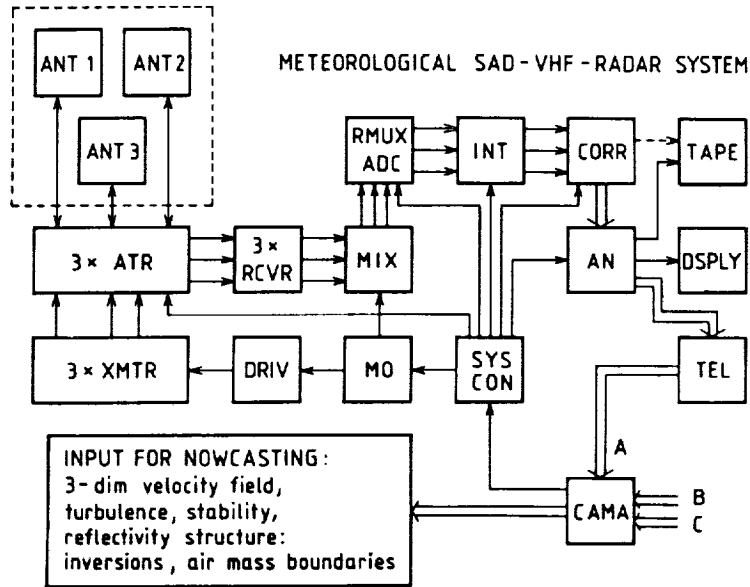


Figure 24. Radar system using three separate receiver-transmitter-antenna modules, which can be operated phase-synchronized to allow beam steering as well as spaced antenna measurements with the same full antenna array. The system is laid out for range multiplexing (RMUX), on-line integration (INT), correlation computation (CORR) and on-line analysis (AN), as well as data telemetry (TEL) and remote control (CAMA). The latter additions of remote control and data transfer are usually needed when such a radar system would be used in operational applications as a wind profiler.

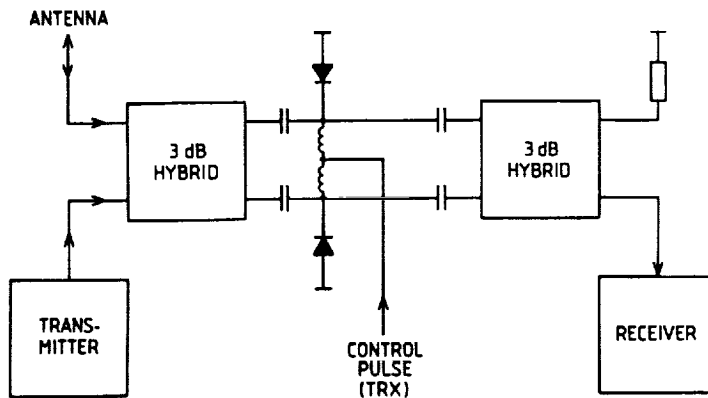


Figure 25. Transmit-receive duplexer (also called T/R switch) using 3-dB hybrids and pin-diode switching.

receiver hybrid and exits through the resistor port. In the reception case the diodes are open and the split power from the antenna is combined in-phase in the receiver hybrid to pass through the receiver port to the receiver input. Any noise, which is still generated in the transmitter during the reception phase is combined into the resistor port of the receiver hybrid. The response and recovery time of the duplexer should be in the order of the range sampling time, i.e. typically less than 10 μ s. To insulate a peak transmitter pulse amplitude of 10^5 W to a fraction of Watt, which will not affect the receiver, the decoupling attenuation has to be better than 60 dB. These specified values can be obtained with the described pin-diode hybrid switch. Other kinds of transmit-receive duplexers, using quarter-wave coax lines or parallel and serial resonance circuits are also used. These are not so suitable because of the resonance circuits, which cause ringing effects and affect the data in the first sample range gates. If circular polarization is applied (in IS radar operations) the duplexer can be replaced by a hybrid, which provides some 30 db decoupling between the transmitter and receiver port. The remaining RF signal leaking through the receiver port is usually attenuated by a so-called receiver protector, which is a fast pin-diode switch disconnecting the receiver input from the hybrid receiver port during the transmission phase. In order to further protect the receiver during eventual malfunctions of the duplexer or the receiver protector the status of these devices is monitored by proper hand-shake and inter-lock systems, which prevent the transmitter to be turned on in case of a failure.

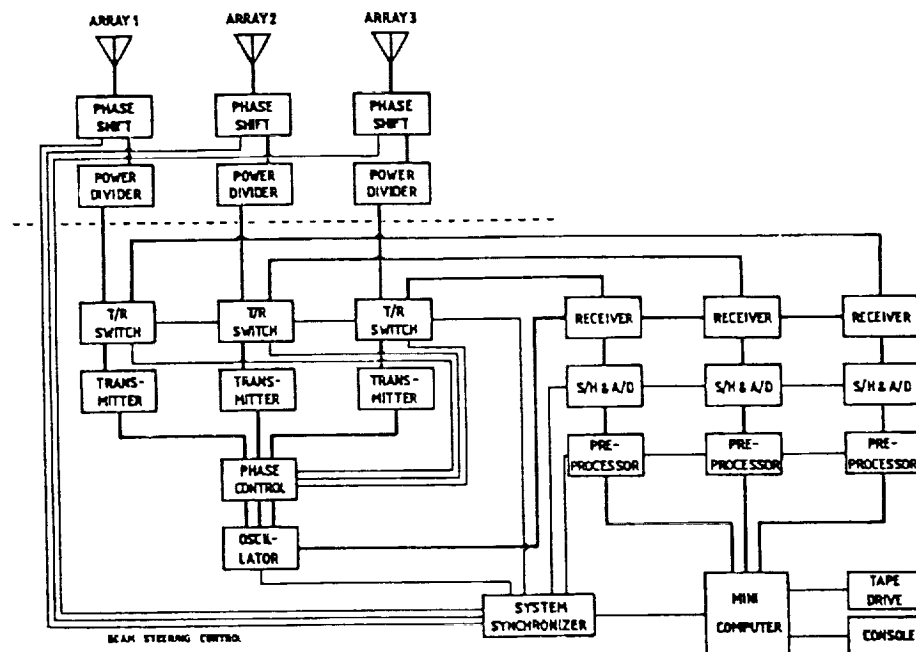


Figure 26. Block diagram of the Chung-Li VHF radar, which bases on the principal lay-out of Fig. 24 (from Brosnahan et al., 1983).

In Fig. 26 a block diagram of the Chung-Li VHF radar is shown, which is a dual-mode radar. Dual-mode means that the radar can be used in the Doppler as well as in the spaced antenna mode (for velocity and interferometer measurements). For the spaced antenna mode it has three separate antenna arrays for reception which are combined in phase for transmission. In the Doppler mode the antenna arrays can be either combined to point into the same direction during transmission and reception, or they can point at the same time into three different directions. The beam steering is done by phase shifters and the power distribution by power dividers, which are made from coaxial cables. The transmit-receive duplexer is called T/R switch (transmit-receive switch) in this diagram. Three transmitters are feeding the three antenna arrays. For providing the essential phase equality at the three antenna arrays, the transmitter drive RF signals are phase-controlled. In order to provide the phase-coherent radar system, the same oscillator controls the transmitters as well as the three receiver channels. Following the sample-and-hold (S/H) circuit and analog-digital converters (A/D) the data are preprocessed, i.e. coherently integrated, and transferred to the mini-computer. From there the data are dumped on tape. By the computer also the radar operation is controlled, particularly by loading the system synchronizer (radar controller) and starting the operation. The system synchronizer also steers the antenna beam directions. We now will briefly describe in more detail some typical sub-units of such a radar system.

3.1. Transmitters, Receivers and Oscillators

In Fig. 27 the principle block diagram of a transmitter is shown. The oscillator generates a continuous wave signal, which is pulse modulated (in amplitude and/or phase) by a fast switch controlled by pulse trains from the radar controller. The switching needs to be done with transition times, which are reasonably faster than the duration of the shortest pulse in single pulse applications or the pulse element in phase coding. Thus the switching of 1- μ s pulse elements needs to be done within 100 ns or so. The pulsed RF signal, usually at a level of several mW, is amplified in driver stages up to peak power levels of several kW. The final amplifier of MST radars usually yields several ten kW peak RF output power. Most frequently vacuum tube amplifiers are applied in the high power stages, which need power supplies with at least 5-10 kV high voltage. Semi-conductor devices needing much lower voltages are now getting in more use,

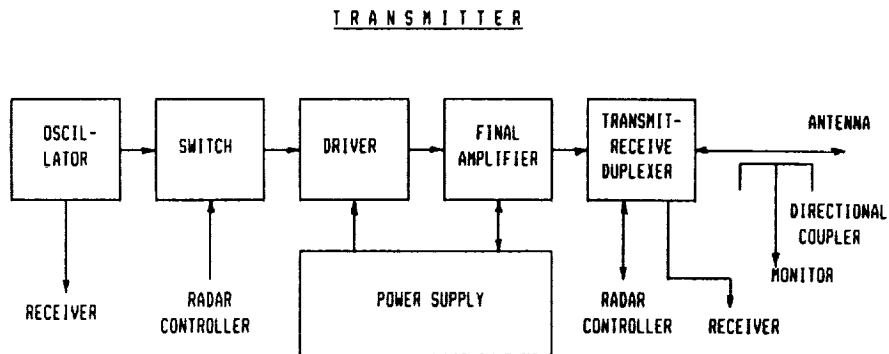


Figure 27. Principle block diagram of a typical MST or incoherent scatter radar transmitter.

particularly when distributed antenna modules are employed instead of one large antenna array. Because of the high output power requirements of more than 1 MW, the incoherent scatter radars apply klystron tubes in the final transmitter stage, which need pulsed power supplies with 50-100 kV high voltage. The high power - high voltage power supplies usually are equipped with a very fast protection switch (a so-called "crow bar"), which discharges the power supply within small fractions of a second in case of a transmitter malfunction to protect the final power amplifier tubes from damage.

Following the final amplifier the transmit-receive duplexer switches the antenna either to the transmitter or to the receiver as described in the last chapter. To allow a measurement of the output power a directional coupler is used after the duplexer output. By measuring the forward as well as the reflected power with two directional couplers the matching (i.e., the voltage-standing-wave-ratio: VSWR) of the antenna is usually monitored. If a phase controller is needed to provide exact phasing of separate antenna arrays, it usually is inserted in the low power stages of the transmitter. Such a device is principally described by the block diagram of Fig. 28. The signal from the transmitter output, measured with the directional coupler, is compared with the local oscillator (LO) reference signal with specified phase (for multiple transmitter beam steering). The phase offset between both these signals is sampled and used to control the phase shifter, which changes the phase of the input signal (RF_{in}). The RF_{out} signal, available with the corrected phase at the output of the phase controller, is then fed to the next amplifier stage in the transmitter.

Usually the local oscillators are more complex because of necessary features, which are outlined in Figs. 29 and 30. For a super-heterodyne receiver, i.e. a multiple mixing of the receiver input signal to one or two intermediate frequencies with subsequent mixing to baseband, a main oscillator in any instance allows for the phase synchronization between these different frequencies (Fig. 29). In case of multi-frequency channel operation, also a set of phase-locked frequencies has to be generated. In practice the transmitter as well as the receiver oscillator signals have to be further processed as shown in Fig. 30. The main local oscillator signal is divided into two signals in the transmitter and the receiver path, respectively. In the transmitter path frequently a phase flip between 0° and 180° is implemented to allow phase coding (phase modulation), followed by the switch to turn on and off the transmitter signal (pulse amplitude modulation). In the receiver path a switch turns off the local oscillator signal during transmission to reduce any feed-through of leakage of the transmitter signal into the receiver. After power dividing of the local oscillator signal one path is phase shifted by 90° to allow baseband mixing to the quadrature components, i.e. real (Re) and imaginary (Im) part of the baseband signal. The control signals (FLP = flip, TXP = transmitter pulse, and LOP = local oscillator protect) are generated by the radar controller (see Chapter 5).

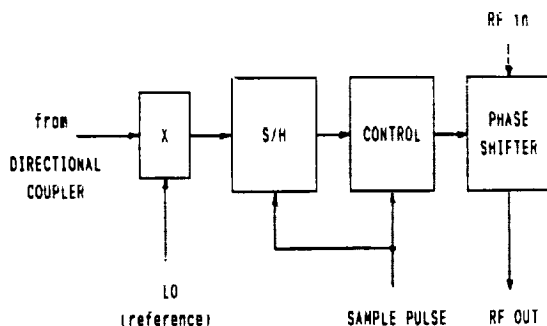


Figure 28. Block diagram of an automatic transmitter phase-controller, which is needed to phase-synchronize multiple transmitters feeding parts of an antenna.

OSCILLATORS FOR SUPERHETERODYNE RECEIVER

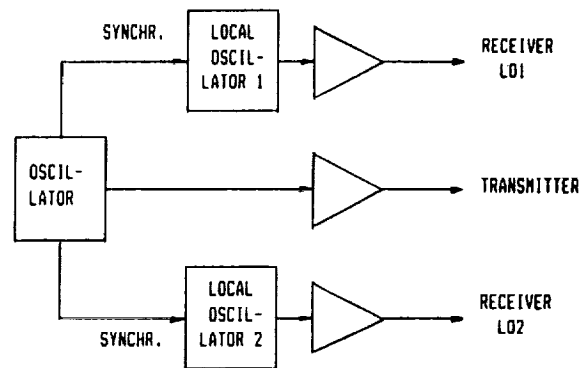


Figure 29. Block diagram of an oscillator circuit for super-heterodyne receivers with two local oscillators LO1 and LO2 and the phase-coherent transmitter oscillator control.

MASTER OSCILLATOR

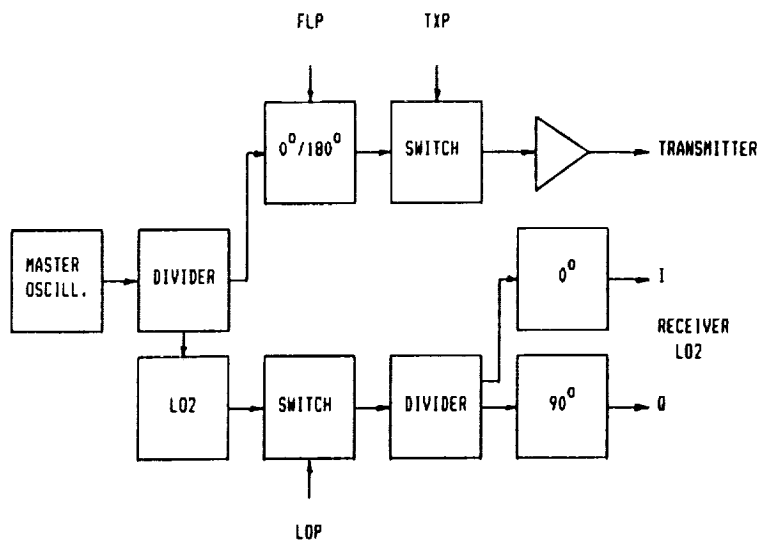


Figure 30. Block diagram of the master oscillator to control the transmitter and the receiver, showing the particular phase shifting and switching circuits for the transmitter and receiver oscillator signals.

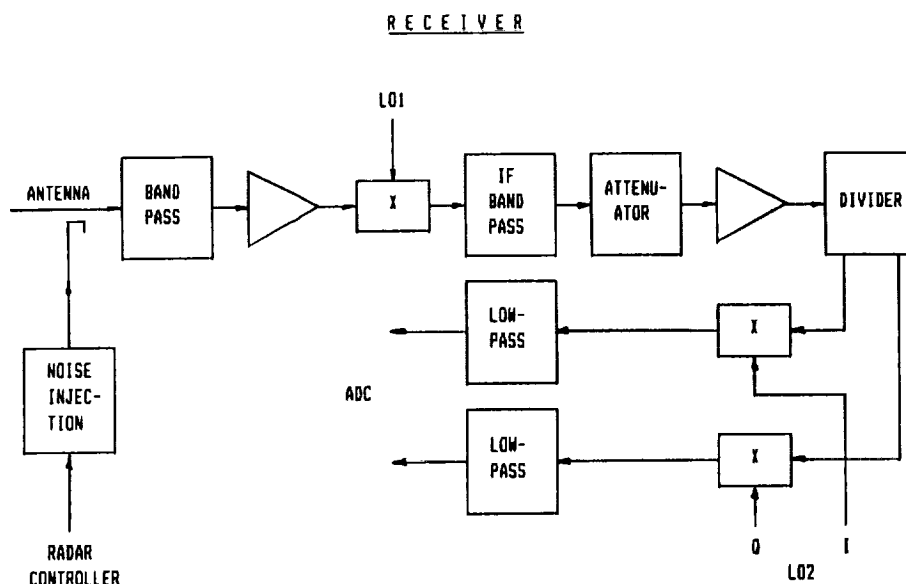


Figure 31. Block diagram of the principle receiver circuitry of MST and IS radars.

The receiver is principally described by the block diagram of Fig. 31. The low-level signal from the antenna (either directly in case of separated transmitter and receiver antennas or via the transmit-receive duplexer in case of a common receiving-transmitting antenna) is fed to the low-noise preamplifier through a band-pass. Frequently also a calibrated noise injection, which is turned on and off by the radar controller, is directly fed into the receiver front end. This is necessary to allow a well calibrated estimate of the receiver amplification factor and thus a deduction of the system temperature and the absolute power of the received signals. In the first mixer the receiver signal is mixed with the signal from the first local oscillator (LO1) to the intermediate frequency (IF). Again a pass-band filter separates the wanted IF from the unwanted mixing products. Before further amplification usually a variable attenuator is implemented to adjust the total amplification of the receiver and thus the output levels for the final baseband mixer and the analog-digital converters. Following the mixing to baseband with the LO2 signal, i.e. the quadrature detection (Re and Im), a lowpass filter is applied which usually should match the signal bandwidth (given by the bandwidth of the transmitted pulse for MST radars and by the bandwidth of the scattering process for IS radars). An example of a low-noise receiver front-end of a UHF incoherent scatter radar, which allows the calibrated noise injection, the reception of circular and elliptical polarization as well as sideband conversion, is shown in Fig. 32. The polarization adaption is achieved by phase changes of the horizontal (H) and the vertical (V) signal components in the polarizer and the sideband conversion by mixing from the upper side (1053.5 MHz) or the lower side (813.5 MHz). Depending on the output from the last hybrid of the polarizer also the sense of rotation of the polarization (left- or right-hand rotation) can be selected.

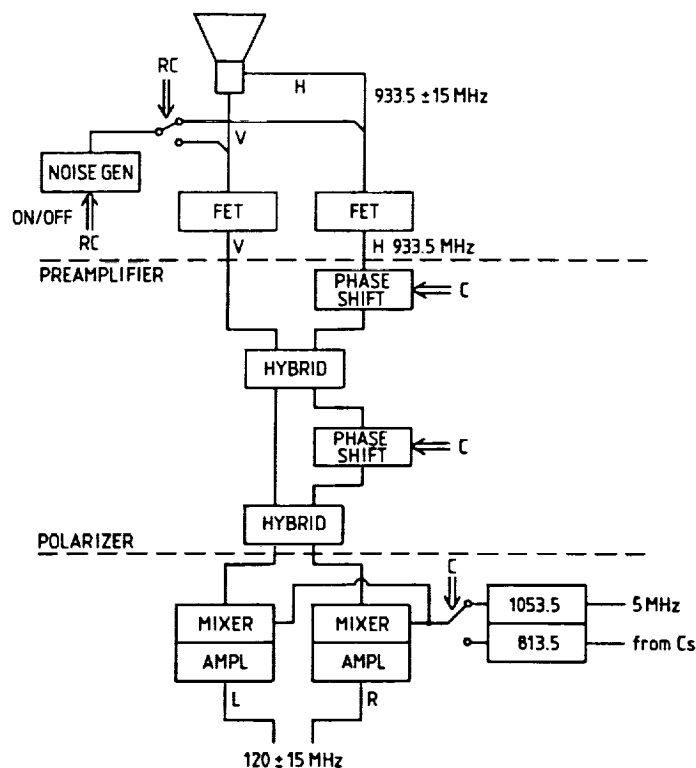


Figure 32. Block diagram of the 933-MHz receiver front-end of the EISCAT incoherent scatter radar receiving stations. The horizontal (H) and vertical (V) components of the signal from the feed horn of the dish antenna are combined by a polarizer (phase shift and hybrids) and mixed to the intermediate frequency 120 MHz. A noise generator, which is switched on and off by the radar controller, injects a calibration signal into the receiver front-ends.

3.2. Examples of Radar Systems

There are some technical system specifications, which principally apply for all atmospheric/ionospheric radar systems. A block diagram of a typical transmitter/receiver system of an MST radar is shown in Fig. 33. It depicts the design of the portable SOUSY Mini-VHF-Radar (46.8 MHz), which was operated at the Arecibo Observatory in 1980. According to individual requirements, many variations and modifications of such a system can be done, but Fig. 33 describes a generally basic design. The 120-MHz signal of the main or master oscillator (MO) is divided by four to obtain a 30-MHz intermediate frequency (IF) which can be modulated (MD) in amplitude (RFC = RE control) and phase (FLP = FLip). This is to provide phase coding and DC-elimination (see Chapter 4 for more details). A similar divider generates the 0° and 90° signals, which are necessary for quadrature detection. The operational frequency 46.8 MHz is generated by mixing (X) with the local oscillator (LO) signal at 76.8 MHz. It is amplified in the transmitter (TX) and fed through the transmit-receive duplexer (TRX) to the antenna. The signal received at 46.8 MHz is gated (RGT = REceiver GAte), amplified in the

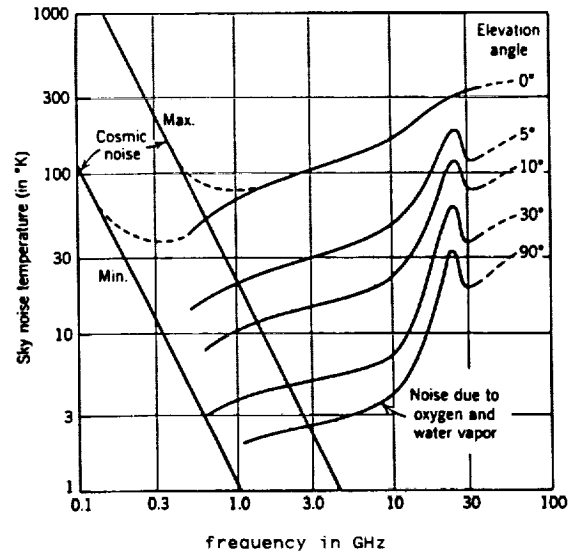


Figure 34. Sky noise temperature as function of frequency and antenna elevation angle (from KRAUS, 1966).

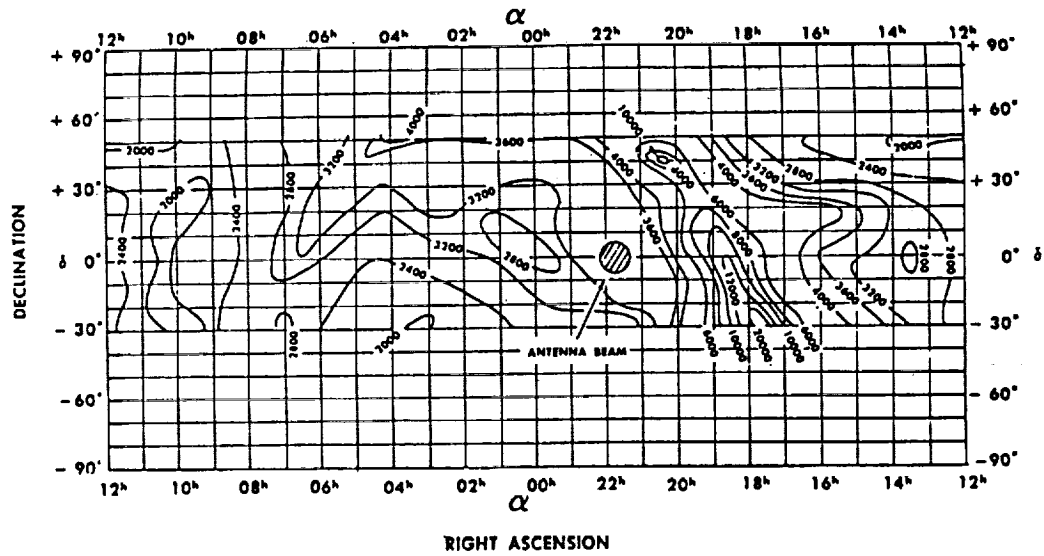


Figure 35. Sky noise map measured as function of declination and right ascension on 64 MHz (after KO, 1958).

needs a continuous monitoring of the transmitter power). However at higher frequencies in the UHF band the sky noise is no more the determining factor as can be seen from Fig. 34. Therefore above several 100 MHz (e.g. in case of the incoherent scatter radars or for the UHF ST radars where the signal-to-noise ratio is usually very low) the receiver frontend has to be carefully designed for lowest equivalent noise temperatures. Usually system temperatures of several ten Kelvin can be achieved at some incoherent scatter UHF radars. The sky noise (from galactic radio sources) changes as function of time of the day and antenna pointing angle as depicted by Figs. 35 and 36 for frequencies of 64 MHz and 53.5 MHz, respectively. This changes the signal-to-noise ratio even if the reflectivity of the radar volumes would be constant. The known variation of sky noise and in particular the well known ephemeris and flux density of point-like radio sources (e.g. Cassiopeia or Cygnus) yield on the other hand a well suited means to calibrate antenna diagrams and antenna gains.

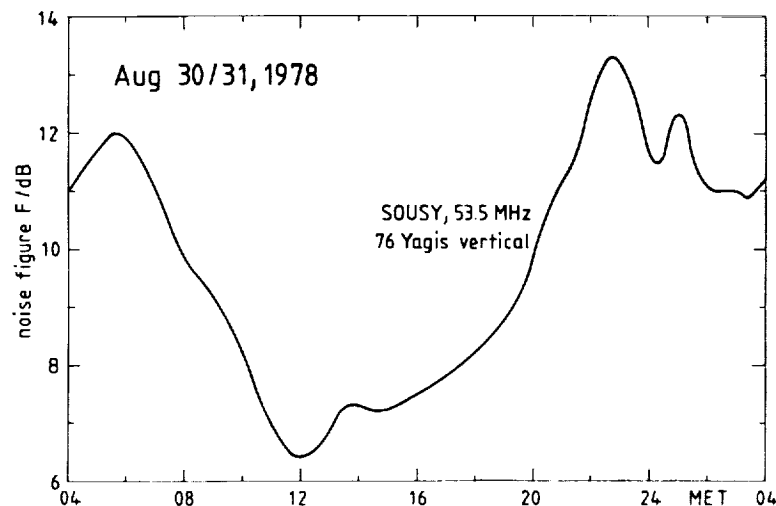


Figure 36. The diurnal variation of sky noise level on 30./31. August 1978 measured at the antenna of the 53.5-MHz SOUSY-VHF-Radar (52°N) in West Germany. The equivalent noise figure of 0 dB corresponds to a system temperature of 290 Kelvin.

In Figs. 37, 38 and 39 we show more block diagrams of three other radars, the Poker Flat MST Radar operating on 50 MHz, the MU radar operating on 46.5 MHz, which is used for MST as well as incoherent scatter observations, and the EISCAT radar systems, which operate as incoherent scatter radars in the 933 MHz and the 224 MHz bands. In Fig. 40 a block diagram of a 915 MHz wind profiler radar and in Fig. 41 the block diagram of the Arecibo bistatic S-band (2380 MHz) CW-radar is shown. The latter radar operates on 2380 MHz in phase-coded continuous wave (CW) mode. The experienced reader will notice several of the basic features in these schematic diagrams which we have mostly outlined in the foregoing chapter. More technical details of these radars should be found in the relevant literature.

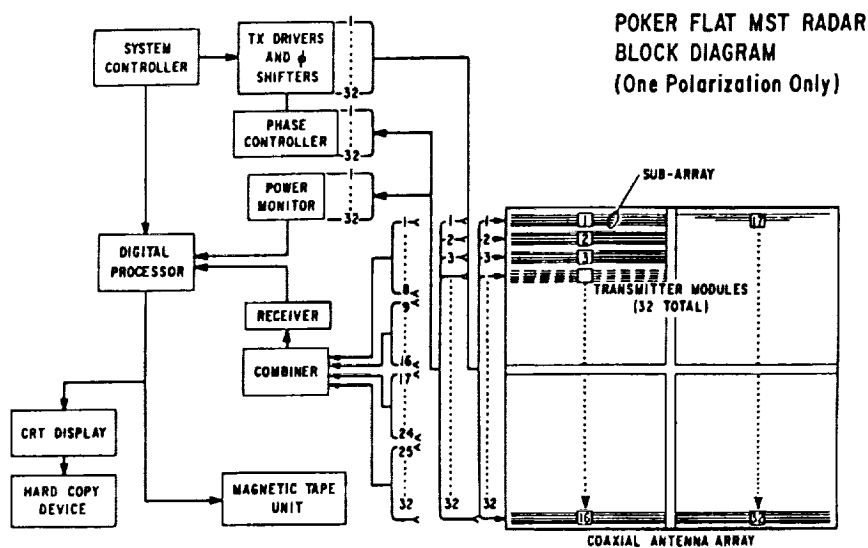


Figure 37. Block diagram of the Poker Flat MST Radar (from BALSLEY et al., 1980).

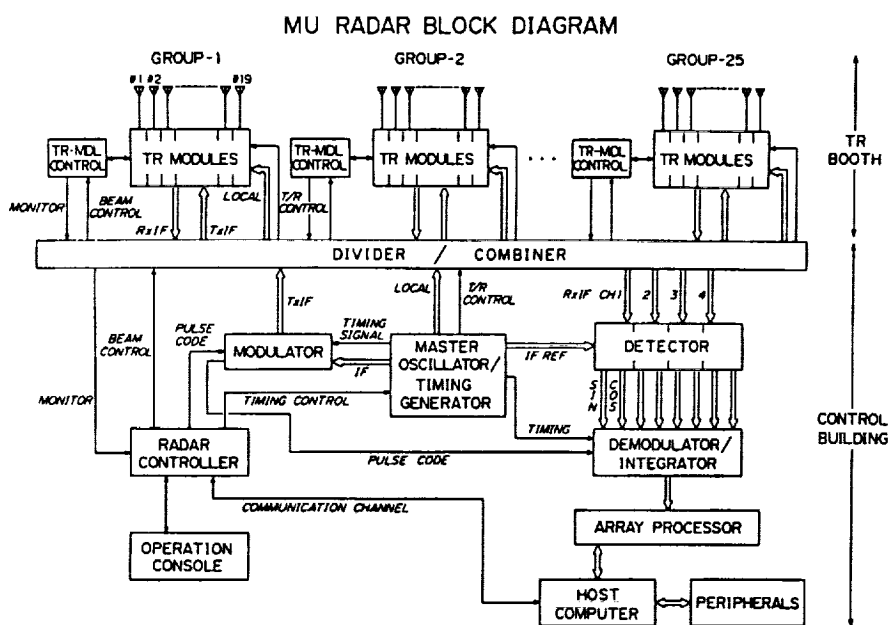


Figure 38. Block diagram of the MU radar in Japan (from FUKAO et al., 1985a,b).

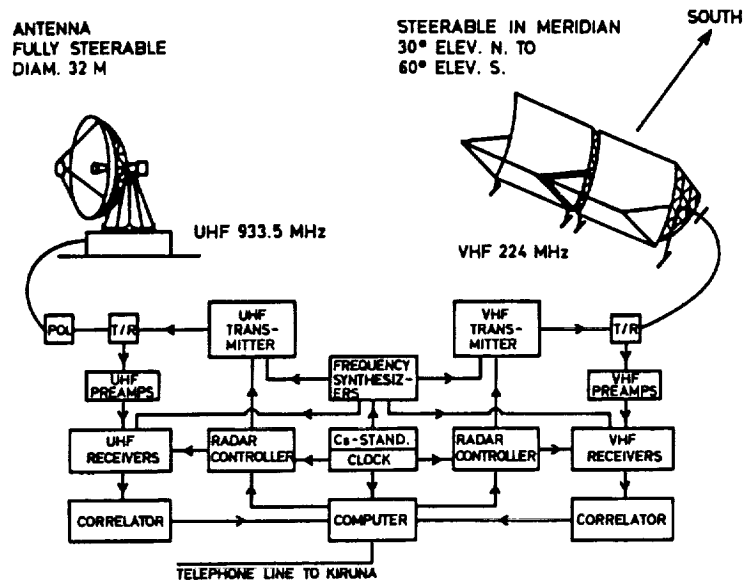


Figure 39. Schematic view and block diagram of the EISCAT UHF and VHF radar system in Tromsø, Norway.

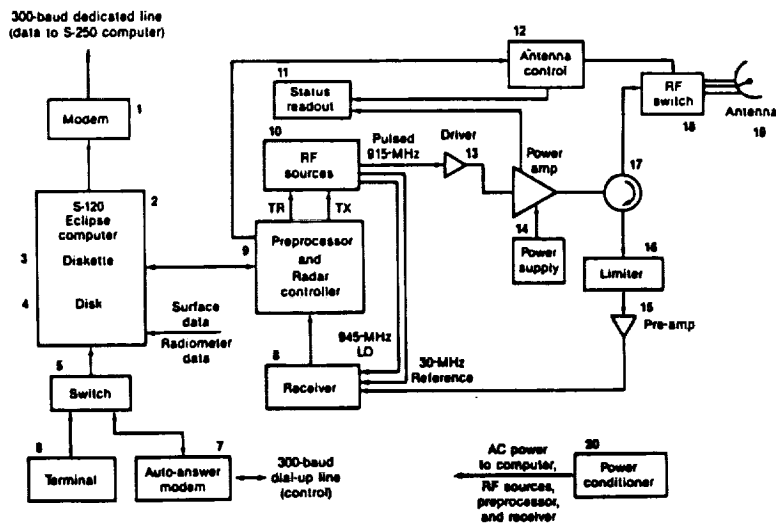


Figure 40. Block diagram of a 915-MHz Doppler radar wind profiler (from FRISCH et al., 1986).

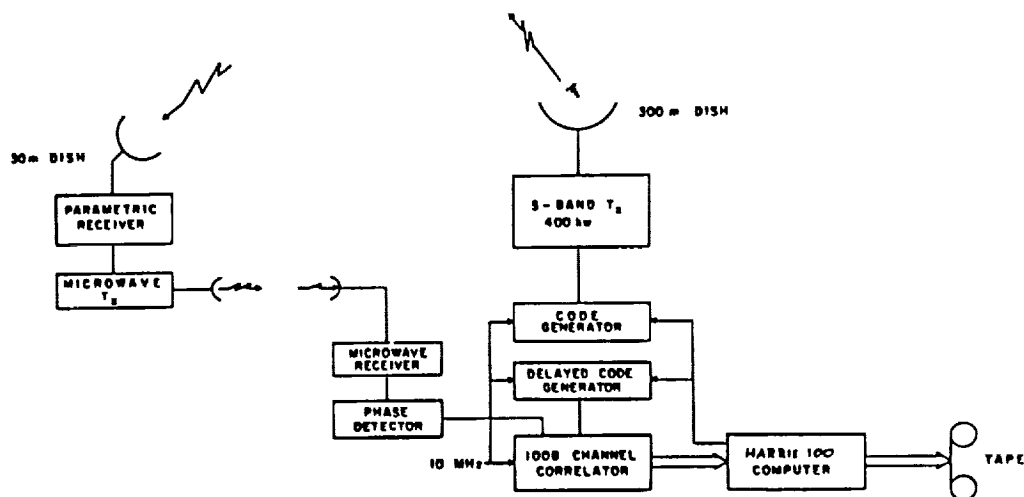


Figure 41. Block diagram of the bi-static S-band (2380 MHz), phase-coded CW (continuous wave) radar system used at the Arecibo Observatory in Puerto Rico for high resolution stratospheric turbulence studies (from WOODMAN, 1980).

4. RADAR SIGNAL ACQUISITION AND PREPROCESSING

The simplified schematics of radar systems, shown in Figs. 6a and 6b, are used for a basic explanation of the radar operation and data-acquisition procedure. After we have briefly explained the lay-out of antennas, transmitters and receivers, in the last chapters we will now explain the formalism of a basic coherent system, the quadrature detection, the digital sampling as well as subsequent data acquisition and phase decoding procedures. For more details see WOODMAN and GUILLEN (1974), RÖTTGER and SCHMIDT (1979), SCHMIDT et al., (1979), CARTER et al., (1980), CLARK and CARTER (1980), SATO and WOODMAN (1982), RASTOGI (1983), for instance. Since these signal processing steps are mostly done in specially designed hardware processors, we now briefly summarize the underlying concepts.

4.1. Coherent Detection

The oscillator generates a signal s^0 at the angular frequency $\Omega_0 = 2\pi f_0$ where $f_0 = c/\lambda_0$ is the center radar operation frequency. A pulse train, generated by the radar controller, imposes a modulation to this signal. After amplification in the transmitter (TX in Figs. 6a and 6b) the radar signal

$$s(t) = a(t) \exp(i(\Omega_0 t + \phi(t))) \quad (5)$$

is transmitted, where $a(t)$ determines an amplitude modulation (by the pulse train) and $\phi(t)$ corresponds to a phase modulation (for coding), and $i = \sqrt{-1}$. $a(t)$ and $\phi(t)$ are slowly varying as compared to $\Omega_0 t$. The radar signal is scattered/reflected from the radar volume and reaches the receiver (RX) via the same or a separate antenna. Additionally, noise (sky noise and interference) is received and adds to the radar echo.

For simplifying the explanation we will assume for a while that the transmitted signal $s(t)$ is not modulated, i.e. $a(t)=\text{const}$ and $\phi(t)=\text{const}$, and the echo results only from a small radar volume at a given range. The echo signal $s'(t)$ plus noise $r(t)$, which are both band-limited because of the scattering process and/or the receiver bandwidth, can be represented by

$$c'(t) = s'(t) + r(t) = a_1(t)\cos \Omega_0 t + ia_2(t)\sin \Omega_0 t,$$

where $a_1(t)$ and $a_2(t)$ are independent Gaussian variables in a pure scattering process. The uncorrelated noise $r(t)$ contributes only uncertainties to these estimates. After linear amplification in the receiver, $c'(t)$ is coherently detected by multiplicative mixing with s^* . After low-pass or post-detection filtering (to eliminate high frequency components $2\Omega_0$, which are generated during the mixing procedure), this yields

$$c(t) = a^*(t)\cos \theta^*(t) + ia^*(t)\sin \theta^*(t),$$

$$\text{where} \quad a^*(t) = (a_1^2(t) + a_2^2(t))^{1/2}/2, \quad (6a)$$

$$\theta^*(t) = \arctan (a_2(t)/a_1(t)).$$

The phase $\theta^*(t) = \Omega_0 t - \theta'(t)$ is given by the Doppler frequency $\Omega_0 = -4\pi V'/\lambda_0$, which is due to the bulk motion V' of the scatterers. The time variable phase $\theta'(t) = \theta(t) + \phi(t)$, where $\theta(t)$ is caused by the fluctuations of the scatterers/reflectors in the radar volume. The amplitude $a^*(t)$ is a measure of the reflectivity of the scattering/reflection process. These latter statements are only valid if the noise contributions are separated from the signal. The coherently detected complex signal (+ noise) can be expressed in the form

$$c(t) = x(t) + iy(t), \quad (6b)$$

where the real part $x(t) = a^*(t) \cos \theta^*(t)$ is called the in-phase component, and the imaginary part $y(t) = a^*(t) \sin \theta^*(t)$ is called the quadrature component. Both components, x and y , are called the quadrature components. The Fourier transform of $c(t)$ is

$$\tilde{X}(\Omega) = \int c(t)\exp(-i\Omega t)dt = \tilde{x}(\Omega) + i\tilde{y}(\Omega),$$

which yields the periodogram $P(\Omega) = \tilde{x}^2 + \tilde{y}^2$; it is often also called power or Doppler spectrum. The measured $P(\Omega)$ is the convolution of the spectrum of the refractive index or the reflectivity fluctuations in the radar volume with the spectrum $P_r(\Omega)$ of the transmitted wave form (for the common case of pulsed transmissions), multiplied by the bandpass characteristics $P_R(\Omega)$ of the receiver. Since $P(\Omega)$ is much narrower than the envelope of $P_r(\Omega)$ and $P_R(\Omega)$ in MST radar investigations, these instrumental effects can mostly be disregarded. However, in incoherent scatter applications the spectrum of the scatter process $P_r(\Omega)$ is mostly wider than the envelope of $P_r(\Omega)$, which leads to the fact that the instrumental effects of receiver and transmitter pulse bandwidth have to be accounted for during the signal analysis.

4.2. Digital Sampling

We now take into account that the signal $c(t)$ results from scattering and reflection in certain altitude ranges. Frequently these signals which originate from scatter or reflection of a transmitted radar signal are called "radar echoes". We now have to note that the transmitted signal is modulated in order to resolve the range from where the radar echoes arrive from. As sketched in Figs. 1 and 2, the echoes from different ranges then occur at different times at the analog receiver output. In order to allow adapted signal processing of

The number of sampling time steps between successive radar transmitter pulses is K , which is also the number of sampled range gates. The interpulse period is $T_{ipp} = K \delta t_s$. The cycle $k = 0, \dots, K-1$ is repeated once with $k' = 0, \dots, K'-1$ with a reversed phase of the transmitter pulse. Both cycles, denoted by k and k' (with $k' \leq K$ and $K' \leq K$), determine one radar cycle $2 \cdot T_{ipp}$ (note that here the radar cycle is two times the interpulse period, because of the introduced phase flip). The serial number of radar cycles is given by $n = 1, \dots, N$. One radar burst is determined by N radar cycles, which last for $t_i = 2N \cdot T_{ipp}$. The generation of all pulse trains, needed to control these cycles of the transmitter and receiver-ADC-integrator system, is done in the radar controller, as described in Chapter 5.

4.3. Coherent Integration and Preprocessing

We will discuss here a standard preprocessing procedure of the pulse-to-pulse technique applied with MST radars. The spectrum which one would obtain for a coherent echo (MST radar) with the sampling rate T_{ipp} is very wide and mostly contains high frequency noise power. The signal power is confined to relatively low frequencies only ($f = 1/\tau_c \ll 1/2T_{ipp}$), where τ_c is the signal coherence time. It is evident therefore that low pass filtering of a coherent signal, done before the spectrum analysis, will not change the signal characteristics but eliminates high frequency noise contributions. The simplest form of low pass filtering is just the complex addition of the signal + noise samples over an interval $t_i \ll \tau_c$. A readily noticed effect of such an averaging over N interpulse periods is the reduction of the number of total samples by a factor $1/N$. We have to note that this processing step of coherent integration cannot be applied for incoherent signal processing, because the signal coherence time is shorter than the interpulse period. This also means that the described DC- and clutter-elimination is not applicable for incoherent signals. The standard procedure of autocorrelation function and spectrum computation, however, is compatible in both applications.

Since the noise (r) and the signal (s) are independent of each other, their quadrature components add to $C_{kn} = C_{kn}^r + C_{kn}^s$, where $C_{kn}^r (= x_{kn}^r + jy_{kn}^r)$ are the quadrature components of the noise and C_{kn}^s those of the signal. A DC-bias can result from a constant, instrumentally introduced voltage at the receiver output C_{kn}^i , or due to radar clutter C_{kn}^c (clutter = echo from a fixed target). All these contributions are additive:

$$C_{kn} = C_{kn}^r + C_{kn}^s + C_{kn}^i + C_{kn}^c.$$

We have to take into account that each radar cycle yields two samples per range gate, namely k and k' . The samples of signal and clutter are shifted by 180° from k to k' , because the phase $\phi(t)$ of the transmitter was flipped by 180° (change $\phi(t)$ by 180° in equations (5) and (6)). This can be accounted for by changing the sign of $C_{k'n}$ when averaging

$$\begin{aligned} C_{k,k'} &= \frac{1}{N} \sum_{n=1}^N (C_{kn} - C_{k'n}) \\ &= \frac{1}{N} \sum_{n=1}^N (C_{kn}^r - C_{k'n}^r + C_{kn}^s - C_{k'n}^s + C_{kn}^i - C_{k'n}^i + C_{kn}^c - C_{k'n}^c). \end{aligned}$$

Since for the instrumental DC-bias $C_{kn}^i = C_{k'n}^i$, it is eliminated by averaging. This is called instrumental-DC elimination (DC = direct current, better to say: constant voltage contribution).

Because of the transmitter phase flip, we find that: $c_{kn}^* = -c_{k'n}^*$ and $c_{kn}^c = -c_{k'n}^c$. Since the noise is independent from one to the next interpulse period, a change in sign of c_{kn}^r does not change its statistical properties. We thus obtain, since $k' = k$:

$$c_k = \frac{2}{N} \sum_{n=1}^N (c_{kn}^r + c_{kn}^* + c_{kn}^c) \quad (7)$$

This averaging, commonly called "preintegration" or better "coherent integration", has become a standard process in MST radar operations. It yields coherently integrated data samples c_{k1} ($l=1, \dots, L$) at the time

$$t_1 = 2 \cdot l \cdot N \cdot K \cdot \delta t_s$$

for the coherent integration period $t_i = 2 \cdot N \cdot K \cdot \delta t_s = 2 \cdot N \cdot T_{ipp}$.

If the summation in equation (7) extends over a time period $t_i = 2 \cdot N \cdot T_{ipp}$, which is much longer than δt_s , the high-frequency noise contribution vanishes. For a coherent integration period $t_i = 2 \cdot L \cdot N \cdot T_{ipp}$, with ($L \gg N$), which is much longer than τ_e , the signal contribution approaches zero since it is fading in amplitude and phase. Only the clutter contribution

$$c_{k1}^c = \frac{1}{L} \sum_{l=1}^L c_{k1}$$

remains, since it is constant in amplitude and phase. This can be used to eliminate the clutter component by means of a digital high pass filter operation: $c_{k1} = c_{k1} - c_{k1}^c$. This operation is called clutter-DC elimination, and is done after the coherent integration.

For the coherent integration given by equation (7), the number N of added samples has to be selected carefully. It is evident that the integration period has to be much shorter than the typical time scale of signal variations due to the fluctuating scatter process as well as due to the frequency changes resulting from the bulk motions of the scattering or reflecting medium. The advantage is, however, that the processing can be made very efficient since only additions (subtractions) but no multiplication of the raw data series with a weighting function are necessary. It is also required that the real part x and the imaginary part y of the detected signal are correctly in quadrature (orthogonal). Ideally they must be phase-shifted by exactly 90° and must have equal amplitudes on the average, otherwise a distortion of the Doppler spectrum results. Accuracies of less than a few degrees phase difference and less than a few percent amplitude difference are tolerable, however, and can be obtained by proper hardware adjustment.

The coherent integration of the quadrature components, formulated by equation (7), is normally done in a digital preprocessor, called adder or integrator. Since this coherent integration is a low pass filter process it can be done also in an analogue filter, such as the clutter elimination which is a notch or high pass filter operation. Obviously the digital processing is much more versatile and flexible. Both analogue and digital preintegration reduce the number of data samples by some orders of magnitude, and compress the huge data flow from the ADCs to make it manageable for the host computer. This is the evident advantage of this preintegration process. We have to note, however, that this coherent integration process loses its advantages for higher frequency (>500 - 1000 MHz) radar applications. The reason is that the signal coherence time is inversely proportional to the radar operating frequency and consequently the coherent integration time has to be reduced. It is often thought that this

process of coherent integration also increases the signal-to-noise ratio since the voltages of the coherent signal but the power of the incoherent noise add. This leads to an improvement of the signal-to-noise (power) ratio by the factor N , since the noise bandwidth is reduced by the factor $1/N$, whereas the signal bandwidth remains unchanged. If one reasonably defines the noise in such a way that its bandwidth is equal to the signal bandwidth (e.g., RÖTTGER and LARSEN, 1989), the coherent integration process only reduces the wide noise bandwidth to the acceptable limit close to the signal bandwidth, and the signal-to-noise ratio does not change by this coherent integration. The advantage of the coherent integration process is still the essential reduction of the number of raw data samples, without giving away information on the signal.

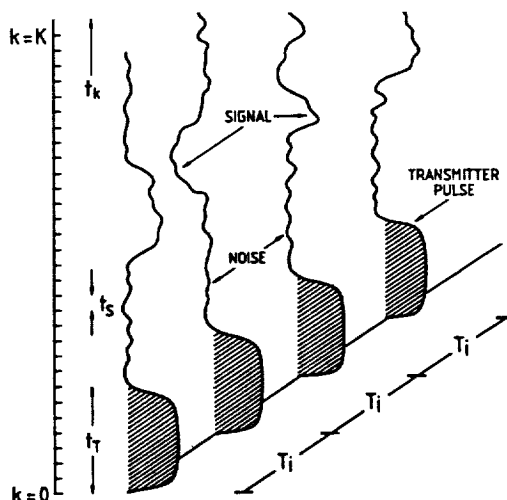


Figure 43. Range-time-amplitude diagram of a long-pulse IS radar modulation and incoherent signals.

This kind of coherent integration used in the pulse-to-pulse technique cannot be applied for incoherent scatter signals, because the signal coherence time is shorter than the interpulse period, and thus the preprocessing needs to be done differently as was principally explained already in Fig. 3. For clearness the same example of an incoherent signal (Fig. 43) is drawn in the same manner as for the coherent MST radar signal (Fig. 42). We notice in Fig. 43 the "incoherence" from one to the next interpulse period, which leads to the fact that the correlation-function and spectrum analysis has to be done within one interpulse period and the ACFs and spectra then are integrated subsequently. The Fig. 43 shows that a fairly long pulse is still needed to obtain samples for the longest lag of the autocorrelation function (ACF) in order to achieve the necessary frequency resolution. This obviously deteriorates the range/altitude resolution. To overcome this problem, so-called multi-pulse modulation is applied, and is explained in Fig. 44. This modulation is most efficiently applied by modulating different frequency channels F1-F6 (within the passband of the transmitter and receiver) in order to fill the gaps between the sub-pulses of this pulse pattern. This increases the average power to the maximum allowable level, but needs a particular multi-frequency channel design of transmitter and receiver. To improve the range resolution further the subpulses can be Barker-coded. Such a multi-pulse multi-frequency Barker-code scheme is successfully used in the EISCAT incoherent scatter radar systems (e.g., TURUNEN, 1986).

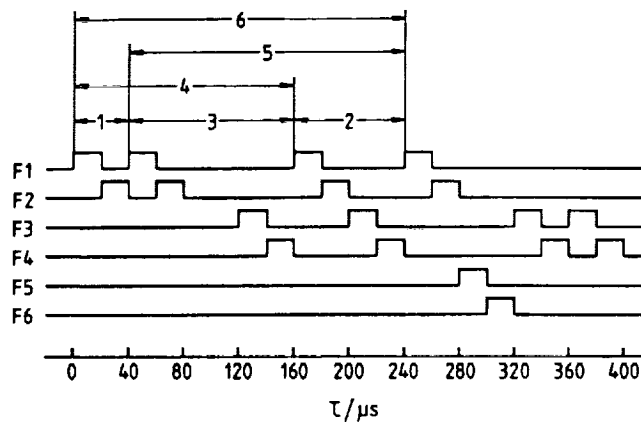


Figure 44. Multi-pulse multi-frequency-channel pulse pattern used in incoherent scatter applications to improve the range resolution and allow measurements of the lag products of the signal autocorrelation function for the temporal lag indices $j = 1$ to 6 (after TURUNEN, 1986).

The application of this modulation scheme as well as the successive "alternating code scheme" has become standard praxis in incoherent scatter work as has the "complementary code scheme" in the MST radar work. We will explain the latter coding scheme after we have briefly outlined some basic formulations of the correlation analysis, which is applied in principle also in the decoding procedures. Again we have to consider that most of the described preprocessing can be done by specially designed digital hardware.

4.4. Correlation and Spectrum Analysis

After the preprocessing by appropriate coherent integration (for coherent signals) or immediate correlation function processing (for incoherent signals) one usually deducts specific signal parameters, such as signal power, Doppler shift and spectrum width. Usually these are the standard parameters in MST applications, whereas in incoherent scatter applications more information is extracted from the spectral shape (see BARON, 1977) by special fitting routines. Before doing this, one has to eliminate the noise which is remaining within the bandwidth given by the signal. The elimination of the noise and further signal processing can be done in the time domain by correlation (covariance) function analysis or in the frequency domain by spectrum analysis. These data processing steps, which follow the hardware preprocessing, can be suitably done by specially designed software in real time in the host computer or off line in separate computers by reading the data from tape. In incoherent scatter applications usually the correlation function computations are done in a special purpose hardware correlator, whereas in MST radar applications the essential preprocessing procedures, which need special hardware, are the coherent integration and decoding. In the latter case further processing to obtain the ACFs or spectra need to be done after the preprocessing.

Since the covariance function and the power spectrum are Fourier transforms of each other, both contain the same relevant information. Depending on the purpose and the feasibility of the analysis, either of both approaches, is used in practice (RASTOGI and WOODMAN, 1974; WOODMAN and GUILLEN, 1974; Hagfors, 1977; RÖTTGER and SCHMIDT, 1979; SCHMIDT et al., 1979; CARTER et al., 1980; CLARK and CARTER, 1980; SATO and WOODMAN, 1980; RASTOGI, 1983).

The complex autovariance function of the quadrature components $c(t)$ is

$$\dot{g}(\tau) = \int c(t) \cdot c^*(t + \tau) dt,$$

where τ is the temporal displacement, and the * denotes the complex conjugate. In digital form

$$R_k(\tau_j) = \frac{1}{L-j} \sum_{l=1}^{L-j} c_{kl} \cdot c_{kl+j}^* = c_{kl} \cdot c_{kl+j}^*, \text{ with } j=0, \dots, J-1 \text{ and } J \leq L,$$

where j is the lag index defining the lag τ_j . For a fixed range k , we find $c_l = x_l + iy_l$, and the covariance function becomes

$$\begin{aligned} R(\tau_j) &= (x_l x_{l+j} + y_l y_{l+j}) + i(x_{l+j} y_l - x_l y_{l+j}) \\ &= R_r(\tau_j) + i R_i(\tau_j), \end{aligned}$$

$$\text{or } R(\tau_j) = |R(\tau_j)| \exp(i(\tau_j)),$$

$$\text{with } |R| = (R_r^2 + R_i^2)^{1/2} \text{ and } \phi = \arctan(R_i/R_r).$$

In radar applications the term correlation function is often used for $R(\tau_j)$ instead of covariance function. The correct definition of the correlation function $\varphi(\tau_j)$ is given by the normalized covariance function:

$$\varphi(\tau_j) = R(\tau_j) / R(0).$$

As well as the autocorrelation function of the series $c(t)$ we also compute cross-correlation functions for two different series, $c_1(t)$ and $c_2(t)$, in the spaced antenna applications and use their modulus in the drift analysis and their phase and amplitude in the interferometer analysis. In a principally similar way also cross spectra are computed from two time series.

The power spectrum is the Fourier transform of $\varphi(T)$, weighted by $W(T)$:

$$P(\Omega) = \int W(\tau) \cdot \varphi(\tau) \exp(-i\Omega\tau) d\tau$$

or in digital form:

$$P_k(\Omega_m) = \frac{1}{J} \sum_{j=0}^{J-1} W_j \cdot R_{kj} \exp(-i\Omega_m j t_i),$$

where W_j is an arbitrary weighting function (e.g., $W_j = J^{-1}$ for all j , etc.) and $\Omega_m = m \pi / J \cdot t_i$; $m = 0, \dots, J$. The length of the integration time interval is $t_i = 2 \cdot N \cdot T_{ipp}$ in the case of a coherent signal. For an incoherent signal, t_i corresponds to the time interval over which lag samples of the ACF are collected.

4.5. Phase Coding

Another preprocessing step which is generally similar to preintegration is the decoding procedure. The principal reason for applying coding/decoding (pulse compression) is to achieve a maximum average power at optimum resolution and maximum unambiguous range. A fairly low duty cycle of 0.1% and hence a low sensitivity would for instance result from using a single pulse of 1 μ s duration

($\delta r = 150$ m) and an interpulse period of 1000 μ s ($r_{\max} = 150$ km). Increasing the pulse length to 32 μ s would increase the duty cycle to 3.2%, but deteriorate the range resolution to 4.8 km. The range resolution of 150 m can still be achieved by phase-coding the transmitter pulse in time (lag) increments of, say 1 μ s. The decoding has to be done by cross correlating the received complex time series c_k (separately for real and imaginary part) with the transmitted code s_m :

$$c_{k*}' = \sum_{m=0}^{M-1} c_{k*+m} \cdot s_m \quad (8)$$

where M is the length of the code and k^* corresponds to the range gate k at lag zero where the correlation function c_{k*}' has a maximum. Thus, the decoding is nothing else but an integration of the signal amplitudes over several range gate samples, which are multiplied by the weighting factor s_m .

The simplest and most versatile phase coding scheme is the binary code, where the phase is flipped between the two states $-1(=0^\circ)$ and $+1(=180^\circ)$. Since here the weights s_m are $+1$ or -1 , the multiplication needed in the decoding process reduces to an addition/subtraction operation. For this reason the decoding can be done in a preprocessor similar to a hardware preintegrator, or the integrator/decoder can even be one unit, as we will outline in Chapter 5. Note that the decoding has to be done for the amplitudes, since these contain the phase information. An advantage in MST radar applications is also that the decoding/integration processes are interchangeable, which reduces the number of operations by about two orders of magnitude (e.g., WOODMAN et al., 1980).

The best codes for radar applications obviously are those where the range sidelobes of the correlation function (8) at $k^* \neq k$ are a minimum. Reasonable sidelobe suppression is achieved with Barker codes, where the phases are flipped in a sequence (e.g., ++++---+--+ for the 13-baud Barker code). The correlation function is 13, 0, 1, 0, 1, 0, 1, 0, 1, 0, 1, 0, 1. The best range sidelobe suppression, achievable with a Barker code, is M^{-1} . The reason is that these sidelobes contain power from other range gates $k^* \neq k$, which cause ambiguities. The sidelobes of the code extend out to ranges $M \cdot \delta t$ on both sides of the center peak. Since the codes cannot be infinitely long, because the minimum range is extended with the length of the code (which obviously increases the minimum range from where echoes can be received), the sidelobe suppression of Barker codes is limited. A good sidelobe suppression is for instance needed if strong echoes occur only in a limited number of range gates.

A better sidelobe suppression can be gained by application of quasi-random codes, which however need decoding before the preintegration as well as to transmit a long series of different code sequences. Also alternating codes appear useful in incoherent scatter applications (e.g., LEHTINEN and HÄGGSTRÖM, 1987). The most suitable codes for MST radar work are the complementary codes (e.g., SCHMIDT et al., 1979), which theoretically have no sidelobes. A complementary code consists of a pair of two code sequences s_1 and s_2 . These have the property that their correlation function sidelobes are exactly equal, but opposite in sign. Normally both code sequences are transmitted at one and the next interpulse period, and the range samples of these two periods are preintegrated and decoded separately. The coherent addition of the decoded sequences then yields the total elimination of the sidelobes ($k^* \neq k$) if the signal is coherent from one to the next interpulse period. The zero lag value $k^* = k$ contains the total signal amplitude. As an example the 8-baud complementary code pair A,B:

$$s_1 = A = ++++---+ \quad \text{and} \quad s_2 = B = +++----+$$

yield the correlation functions:

$$c_1 = 8, -1, 0, 3, 0, 1, 0, 1 \quad \text{and} \quad c_2 = 8, 1, 0, -3, 0, -1, 0, -1$$

and the addition yields:

$$c_1 + c_2 = 16, 0, 0, 0, 0, 0, 0, 0.$$

The peak value of this decoded function at $k^* = k$ is $2M$. There is still the shortcoming of a long code, that it extends the shortest observable range. This can be overcome by transmitting a sequence of a complementary code and a short single pulse in one radar cycle. In Fig. 45 the range-time-amplitude diagram for the simplest 2-baud complementary code with additional phase-flip for instrumental DC-elimination is shown. All these decoding preprocessing steps are most suitably done in a special purpose hardware integrator-decoder. For coding purposes, the hardware radar controller needs to generate the necessary amplitude and phase control pulse trains for the transmitter.

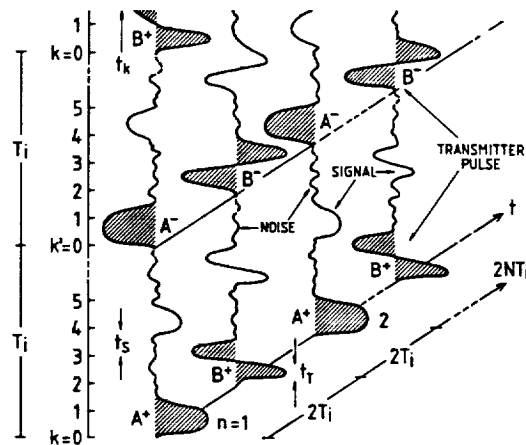


Figure 45. Range-time-amplitude diagram of a two-baud complementary code modulation with DC-phase flip used in MST radar applications.

5. RADAR CONTROL AND DATA ACQUISITION

We will here briefly describe the basic system units which are needed to process the digitized data in terms of coherent integration, correlation function computation and decoding as well as the principle lay-out of a radar controller.

We first describe in Fig. 46 the basic lay-out of an integrator or adder. The data from the ADC are range-gate by range-gate stored into memory. According to equation (7), the data from one interpulse periods are added onto the corresponding data from the successive interpulse period in the arithmetic-logic-unit (ALU). This is recurrently done as long as the integration period is chosen, i.e. the number of interpulse periods preselected for the coherent integration (controlled through the host computer). After the completion of the integration cycle, the coherently integrated data are dumped via the direct-memory-access (DMA) to the host computer.

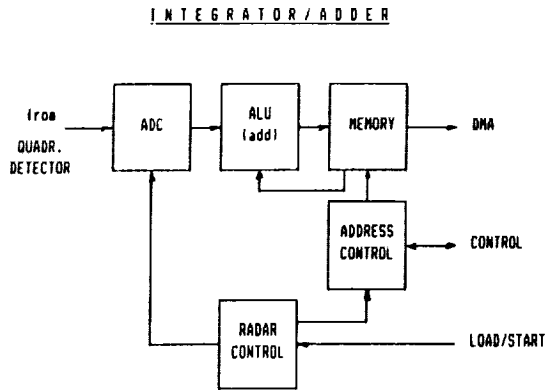


Figure 46. Block diagram of an integrator/adder preprocessor for coherent signal acquisition.

The coherent integration can also be done in the same unit as is used for decoding and the correlation function computation is done. Both the correlation and the decoding operation consist of a multiplication and an addition cycle, where the former needs complex processing and the latter needs to be done for the quadrature components separately. In Table 3 we have outlined the principles of the computation of correlation function, decoding and coherent integration in a graphic form, which should allow better understanding of the hardware configuration sketched in the diagram of Fig. 47.

TABLE 3

COMPUTATION OF CORRELATION FUNCTION, DECODING, COHERENT INTEGRATION

	l=0	1	2	3	.	.	.	L-1	L
j =	(+)	(+)	(+)	(-)	(+)				
J									
J-1									
J-2									
J-3									
.	+	+	+	-	+				
.		+	+	+	-	+			
.			+	+	+	-	+		
2				+	+	+	-	+	
1					+	+	+	-	+

Data Series C_l
(range (k) or time (l))

(A) Correlation Function:

$$R_j = \sum_l C_l \cdot C_{l+j} \quad (\text{lag } j)$$

(B) Decoding:

$$C_l = \sum_m C_{l+m} S_m \quad (l=k)$$

 5-baud Barker code

(C) Integration:

$$C_l = \sum_n C_{l+n} \quad (l=k)$$

The square blocks in Table 3 indicate data samples at range or time gates. The samples in the first row are supposed to be the original data. The hatched part of the diagram indicates data samples which are accessible at a register through which the original data are shifted. The correlation function is computed according to the formula A in Table 3. To compute the zero lag, the range (time) samples of the first (unhatched) row with indices $j=J$ and its replica in the last row $j=0$ are multiplied for each range or time label l , and then all products are summed up over l . To obtain the first lag, the last but one series, which is delayed by one sample with respect to the last row, is multiplied and added in the same way. According to this algorithm all the following lags are computed. In praxis, the last lag is computed first, since the data sample at $j=J-1$ is available first after the original data series had been shifted by one in a shift register (see explanation of Fig. 47 on the next page).

In a very similar way the decoding is performed (formula B in Table 3), since it comprises a cross-correlation function computation which can be performed by the same hardware setup. The only difference to the correlation function computation is, that instead of the data time series the code is used in the delayed data series. In the example of Table 3 a 5-baud Barker code is shown. It is to be noted, that the first completely decoded data point is available only after 5 steps of j at $J-5$, when the 5 bauds of the code are completely existent in the shift register (for longer codes of course the corresponding longer delays have to be considered). The combination (i.e., multiplication and addition according to the formula B) of series $j=J-5$ with $j=J$ yields the decoded value at $l=0$. As another example for instance $j=0$ with $j=J$ yields the decoded sample at $l=3$. Note that a further shift than given by $l=0$ does not allow the

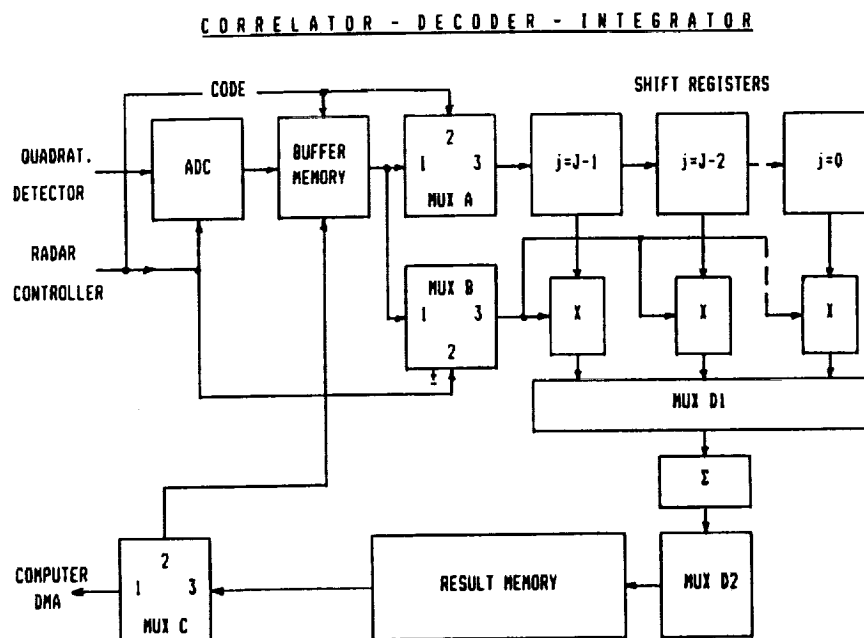


Figure 47. Block diagram of a hybrid version of a correlator-decoder-integrator.

complete decoding unless the data time series $j=J$ is further extended beyond 8 samples in this example. In praxis this means that always a data set has to be available which is longer than a single data series by number L_c , where L_c is the number of bauds in a code minus one. Decoding of complementary codes is done in principally the same way, but as a final step the two cross-correlation functions resulting from the decoding of code s_1 and its complement s_2 have to be added. The coherent integration is simply done, according to formula C in Table 3, in the same hardware processor by just adding the samples for each l (or k) separately over a preselected number of interpulse periods.

We have to note that all these procedures have to be done separately for the real part as well as for the imaginary part of the quadrature components. For convenience we explain only the integration, decoding and correlation function computation for a single component.

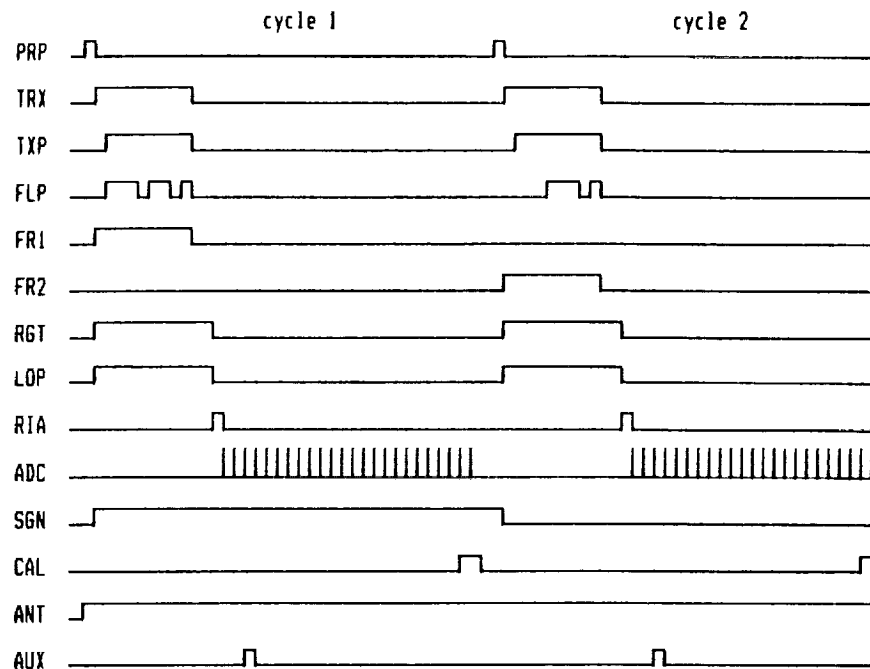
In Fig. 47 we show a block diagram of such a described hybrid "correlator-decoder-integrator". We admit that other realizations may be more practicable, but this layout should show that such a hybrid processor is feasible in principle. The different modes can be understood by following the paths which are selected by different multiplexer positions. In the integrator mode the multiplexer A (MUX A) is connecting ports 1 and 3, multiplexer B ports 2 and 3, multiplexer C ports 1 and 3 and multiplexers D1 and D2 provide that each multiplier is connected to the correct range gate. The data are transferred from the buffer memory to the multipliers, where the sign is changed according to the corresponding phase flip of the transmitter pulse. The multiplier of course could be eliminated if provision would be made to allow also subtractions in the adder. For each range gate the data are added in the accumulator, from where they are multiplexed into the result memory after the specified number of coherent integrations. Depending on the size of the result memory several sets of coherently integrated data are stored and afterwards dumped to the main computer.

For correlation function computations the multiplexers have to be in the positions A: 1-3, B: 1-3 and C: 1-3. The main part of the correlator is the shift register by which the data series is shifted according to the lag indices of the decoding or correlation function. Each data sample of the shifted series is then multiplied with the data sample of the non-shifted data series. For decoding the shifted data series is the code, and for auto-correlation computation the shifted series is the same unshifted data series. After this multiplication the data are accumulated, i.e. summed up, and after completion of the correlation analysis dumped into the result memory from where they are transferred into the host computer. The correct selection of the lag products and their redistribution to the result memory is again provided by multiplexers D1 and D2.

For decoding of the original data series, the multiplexer A is in position 2-3, multiplexer B in position 1-3, and multiplexer C in position 1-3. The original data are existent at the multipliers and according to the position of the code in the shift register, the decoding is performed by multiplication. If the multiplexer A is in position 2-3, B in 1-3 and C in 2-3 a coherently integrated sample set could be also decoded in the same processor and afterwards dumped to the computer. It is noted that also a correlation function computation of decoded as well as coherently integrated data could be possible if the pre-processed data are fed back by multiplexer C in position 2-3 to the result memory. Although the described layout of a multi-purpose integrator-decoder correlator explains the three main processing procedures of MST and IS radars and the solution looks feasible, it may in praxis be more realistic to use three separate units for integration, decoding and correlation function / spectrum analysis.

TABLE 4

RADAR CONTROL



PRP = prepulse (trigger)
 TRX = transmitter-receiver duplex
 TXP = transmitter on
 FLP = phase flip (coding)
 FRI = frequency 1
 FR2 = frequency 2
 ANT = antenna control

RGT = receiver gating on
 LOP = local oscillator protect on
 RIA = reset integrator address
 ADC = analog-digital conversion
 SGN = sign for integration
 CAL = calibration (noise injection)
 AUX = auxiliary

All the timing control of the outlined procedure results from the radar controller or system synchronizer, which of course also generates the control pulses for the transmitter, the receiver and the ADC. A typical example of pulse trains of control pulses, which are generated by the digital radar controller, is demonstrated in the example of Table 4. Following a pre-pulse (PRP), which is used to trigger external control or monitor devices, the transmit-receive duplex (TRX) is switched on, followed by a receiver gate pulse (RGT) and the pulse to turn off the local oscillator (LOP). Then the switch on of the transmitter radio frequency is controlled (RFC), which is phase flipped (FLP) between 0° to 180° for coding. The analogue-digital-converter starts sampling (ADC) after RFC off and the TRX, RGT and LOP have opened the receiver and after the reset of the integrator address (RIA) has taken place. At certain range gates a calibration signal (CAL) is injected. The whole sequence is repeated after one interpulse period when only the phase flip is inverted (for DC-elimination). For application of the complementary coding scheme a second double pulse code (consisting of the complementary pattern) is transmitted, and this radar cycle is repeated N times to yield one radar burst. Additionally, different frequencies

(FR.) and pulses for antenna control (ANT) and other purposes can be generated, which can change from one to the next interpulse period or radar burst. In more advanced systems multichannel receivers and ADCs are used (e.g. spaced antenna parallel processing (e.g. RÖTTGER, 1981)).

The MST radar operation, which is synchronized and which is usually started and stopped by external clock control (in the host computer), takes place in several nested sequences : (1) the radar cycle, i.e. the transmission of one code unit of radar pulses with preselected duration and the sampling of the real and imaginary signal at preselected range gates (e.g. 128). (2) the integration cycle (burst), i.e. the repetition and coherent integration of an externally selected number of radar cycles. (3) record cycle, i.e. the repetition of a preselected number of integration cycles (e.g. 64) to form one total record which is stored in memory. Together with the time and other system parameter information (such as the radar controller program etc.) the data record is then dumped via the computer to file or magnetic tape.

All the control sequences for the radar system are generated by the radar controller, of which a basic block diagram is shown in Fig. 48. The computer loads the instructions, which pulses should be generated and for how long these should be switched on (duration) as well as how many interpulse periods should be coherently integrated, into the radar controller memory. The computer can via the real-time clock start and stop the radar controller. Further interlocks, either via the computer or other fast hardware devices, inhibit under certain failure conditions radar controller pulses in order to protect the radar system from malfunctions or damage if transmitter pulsing would be during the receiving phase.

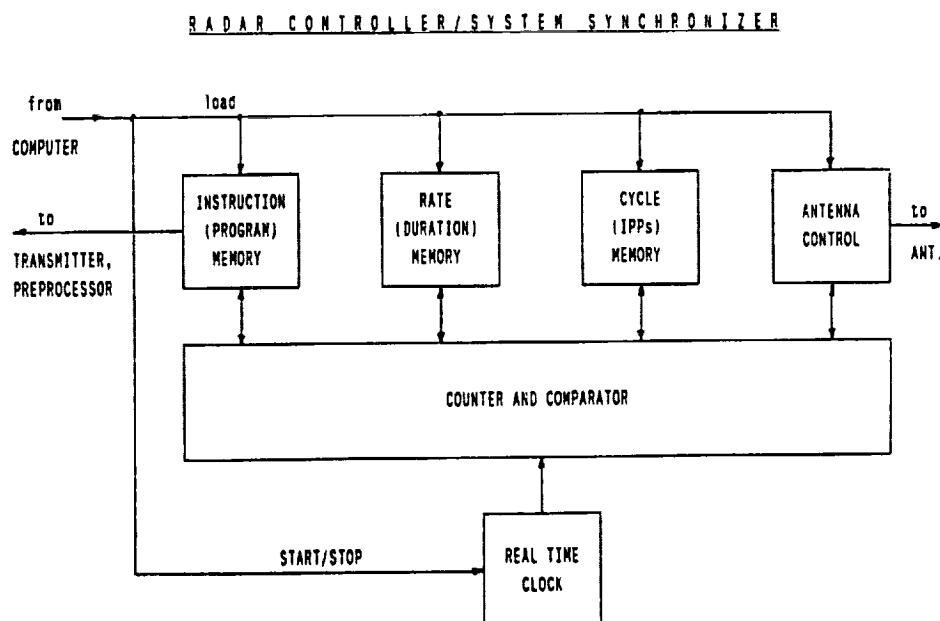


Figure 48. Block diagram of a radar controller or system synchronizer.

It is generally found that 8-bit ADCs are sufficiently matched to the linearity range of the receivers (> 60 dB). If strong clutter signals are present the capacity must eventually be extended to > 12 bit or a range-dependent attenuation has to be used. Applying an 8-bit ADC and a 16-bit integrator allows to add samples from at least $N = 256$ radar cycles in one channel. If more samples would have to be added, the adder and result memory word length would have to be extended. The dump could still be at 16-bit word length if a scaler would be used to scale down the result data according to the number of integrations. The preintegration time for 256 integrations would be $t_i = 2N \cdot T_{IPP} = 128$ ms for $T_{IPP} = 250$ μ s, corresponding to a maximum unambiguous range of 37.5 km and a maximum resolvable radial velocity of 12 ms^{-1} ($f_{\text{max}} = 4$ Hz). Applying a 4-bit complementary code and a 300-m range resolution would result in a transmitter duty cycle of about 3%.

MUFFIN FUNCTIONAL BLOCK DIAGRAM

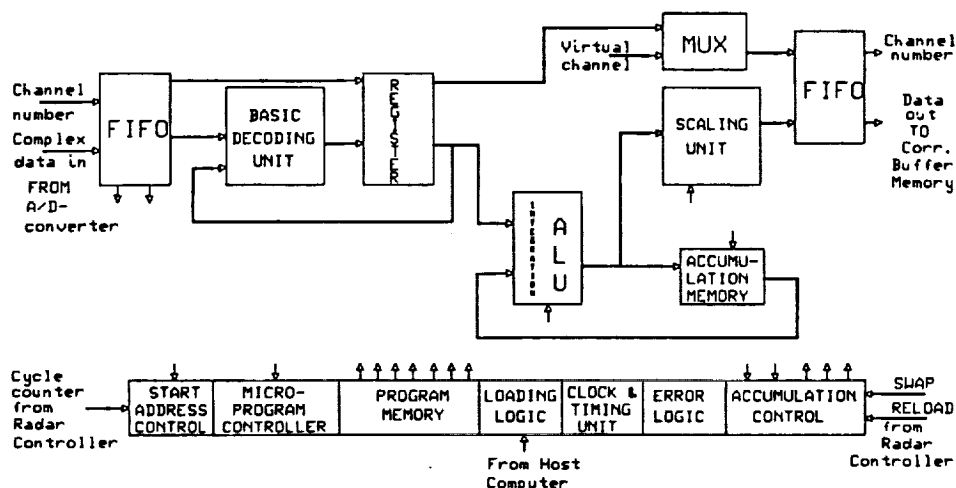


Figure 49. Block diagram of a multi-channel finite-impulse response filter and integrator (MUFFIN) under development as preprocessor for particular coding schemes applied at the EISCAT radars.

There exist many more sophisticated data preprocessing units at several radars and it cannot be in the scope of this lecture to describe those in detail, as it was not possible to line-out all the different variations of the transmitter-receiver-antenna systems. We finally would only like to add the block diagram (in Fig. 49) of a multi-channel finite-impulse-response filter and integrator which is presently under design at the EISCAT radar facilities and shall be used for on-line preprocessing (integration, decoding, correlation computation and radar control) of incoherent scatter and coherent scatter data (POSTILA, 1988, personal communication).

6. AN OVERVIEW ON SOME RADAR SYSTEMS AND THEIR TECHNICAL PARAMETERS

Descriptions of the early VHF radar systems were given by WOODMAN and GUILLEN (1974), GREEN et al. (1975), CZECHOWSKY et al. (1976), RÖTTGER et al. (1978), BALSLEY et al. (1980), and design considerations were summarized by BALSLEY (1978a,b), GAGE and BALSLEY (1978) and BALSLEY and GAGE (1982). More recent developments and technical details were described for instance by CZECHOWSKY et al. (1984), KATO et al. (1984), RÖTTGER (1984), STRAUCH et al. (1984), FUKAO et al. (1985a,b), FRISCH et al. (1986), ECKLUND et al. (1988) and RÖTTGER and LARSEN (1989).

We present in Table 5 the technical parameters of the MU radar (Middle and Upper atmosphere radar) of the Radio Atmospheric Science Center of the Kyoto University (from FUKAO et al., 1985a,b), in Table 6 the basic parameters of a 405 MHz wind profiler radar (from FRISCH et al., 1986), in Table 7 the primary system specifications for an operational wind profiler (from UNISYS, 1987) are repeated, which is supposed to be used in meteorological routine applications. In Table 8 the basic parameters of the EISCAT incoherent scatter radar systems operating in the 933 MHz and 224 MHz bands are summarised. We then display in Table 9 a most complete list of all the MST, ST and incoherent scatter radars as well as some wind profiler systems. Finally we show in Fig. 50 photos of a few well known research radar facilities.

TABLE 5

Basic Parameters of the MU (Middle and Upper Atmosphere) Radar
Operated by the Radio Atmosphere Science Center of the Kyoto University
(from FUKAO et al., 1985a,b)

LOCATION	Shigaraki, Shiga, Japan 134.85°N, 136.10°E
RADAR SYSTEM	monostatic pulse radar; active phased array system
OPERATIONAL FREQUENCY	46.5 MHz
ANTENNA	circular array of 475 crossed Yagis aperture 8330 m ² (103 m diameter)
Beam width	3.6° (one way; half power for full array)
Steerability	steering is completed in each IPP
Beam directions	1657; 0°-30° off-zenith angle
Polarizations	linear and circular
TRANSMITTER	475 solid state amplifiers (TR modules: each with output power of 2.4 kW peak and 120 W average)
Peak power	1 MW (maximum)
Average power	50 kW (duty cycle of 5%) (maximum)
Bandwidth	1.65 MHz (maximum) (pulse width: 1-512 µs variable)
IPP	400 µs to 65 ms (variable)
RECEIVER	
Bandwidth	1.65 MHz (maximum)
Dynamic range	70 dB
IF	5 MHz
A/D converter	12 bits x 8 channels
PULSE COMPRESSION	binary phase coding up to 32 elements. Barker and complementary codes

TABLE 7

System specifications for an operational Wind Profiler Radar
(after UNISYS, 1987)

Maximum height	15.25 km
Minimum height	0.5 km
Vertical range cell spacing	250 m
Maximum horizontal wind	200 mph
Maximum vertical wind	50 mph
Frequency band	400-435 MHz (404.37 std)
Peak power	16 kW
Average power	2200 W
Pulse width (compressed)	2/6.67 μ s
Pulse repetition period	100/153 μ s (nom)
Antenna type	coaxial collinear array
Antenna gain	≥ 32 dB
Sequential beams	vertical, east and north
Sidelobe suppression	-20 to -40 dB
Receiver noise figure	0.5 dB
Signal processor	Digital I and Q
Data processor	MicroVax II
Operating software	higher order language
Fault monitoring	microprocessor control
Two-way data modem	RS-232C landline
Satellite telecon	GOES transmission (401 MHz)
Prime electrical power	115/230 VAC, 50-60 Hz
MTBF (mean time between failure)	≥ 4000 hours
MTR (mean time to repair)	80 minutes
Operational conditions	
Temperature	-40°C to +50°C
Humidity	0-100%
Wind speed	140 mph (185 mph gusts)
Rain	3 inches/hour
Snow	4 feet
Ice	3 inches radial

TABLE 6

Basic Parameters of a 405-MHz Wind Profiler Radar
(from FRISCH et al., 1986)

RADAR	
Frequency	405.25 MHz
Authorized bandwidth	1.00 MHz
Peak power	30 kW
Average power	0.4 kW maximum
Pulse width	1, 3, 9 μ s
Pulse repetition period	100, 150, 300 μ s
Antenna aperture	9 m x 9 m
Antenna pointing	15° off-zenith to north and east
ANTENNA TYPE	
Two-way beamwidth	phased array of Yagi-Uda elements 4.3°
DATA PROCESSING	
Time domain averaging	1 μ s pulse 120 pulses 3 μ s pulse 75 pulses 9 μ s pulse 35 pulses
Spectral average	8 16 24
Maximum radial velocity	± 15.41 ms ⁻¹ ± 16.44 ms ⁻¹ ± 17.62 ms ⁻¹
Spectral resolution (64 points)	0.48 ms ⁻¹ 0.51 ms ⁻¹ 0.55 ms ⁻¹
HEIGHT SAMPLING	
First height	1 μ s pulse 0.4 km AGL 3 μ s pulse 2.4 km AGL 9 μ s pulse 4.0 km AGL
Height spacing	100 m 250 m 870 m
Number of heights	24 24 14

TABLE 8 The EISCAT Radar Facilities (Jan. 1989)

Parameters of the EISCAT UHF system:		Parameters of the EISCAT HF system (Trans on L):	
Transmitter (Trans on L): Peak transmitted power Maximum duty cycle Operating frequencies Pulse widths Rise time Maximum waveform repetition rate Modulations		Receiver: Type of front end System temperature Number of IF channels IF filter bandwidths Detector Post-detection filters on-off, phase-flip, frequency-stop (0°/180°), frequency-stop	
Antennas at all sites (Trans, Lirons, Sodanlyla): Location and height of the UHF antennas above sea level (MSL) (Lirons 50-1500): (Transmitter-receiver) Lirons site: (receiver) Sodanlyla site: (receiver)		Parameters of the EISCAT HF system (Trans on L): Transmitter: Peak transmitted power Maximum duty cycle Operating frequencies Pulse widths Rise time Maximum waveform repetition rate Modulations Antennas: Location Frequency band Azimuth/Elevation Azimuth angle range Elevation angle range Lowest elevation permitted (Trans.) Maximum rate of angular motion Diameter of main reflector Feed system Diameter of subreflector Focal length Polarization Gain (calculated) Aperture efficiency (calculated) Noise contribution (measured) Self-power beamwidth Band of mechanical movement, azimuth and elevation Fresnel zone limit: Rayleigh distance:	
1.6 MW 12.5% (925.5-9.5) MHz, (n=10) 1-10000 Hz 0-1 Hz 1000 Hz on-off, phase-flip (0°/180°), frequency-stop		1.5 MW 6.5% (222.4-2.0) MHz, (n=5, 6, 7, 8) 1-1000 Hz 0-1 Hz 1000 Hz on-off, phase-flip, frequency-stop 89°35'11.9408" N 19°12'12.200" E h = 83.3 m (reference point centre of elevation axis) 228 ± 2.5 MHz 2 panels for transmission, independently movable 40 m 30 m 128 crossed dipoles (32 per panel) 0.5° west of north 5.0° min ⁻¹ 30°-45° north to 30°-90° south of zenith 3200 m 1.7° 0.9° 46 dB 21.3° in steps of 1.25° circular	
Antennas at all sites (Trans, Lirons, Sodanlyla): Location and height of the UHF antennas above sea level (MSL) (Lirons 50-1500): (Transmitter-receiver) Lirons site: (receiver) Sodanlyla site: (receiver)		Receiver: Type of front end System temperature Number of IF channels IF filter bandwidths Detector Post-detection filters on-off, phase-flip, frequency-stop (0°/180°), frequency-stop	
1.6 MW 12.5% (925.5-9.5) MHz, (n=10) 1-10000 Hz 0-1 Hz 1000 Hz on-off, phase-flip (0°/180°), frequency-stop		1.5 MW 6.5% (222.4-2.0) MHz, (n=5, 6, 7, 8) 1-1000 Hz 0-1 Hz 1000 Hz on-off, phase-flip, frequency-stop 89°35'11.9408" N 19°12'12.200" E h = 83.3 m (reference point centre of elevation axis) 228 ± 2.5 MHz 2 panels for transmission, independently movable 40 m 30 m 128 crossed dipoles (32 per panel) 0.5° west of north 5.0° min ⁻¹ 30°-45° north to 30°-90° south of zenith 3200 m 1.7° 0.9° 46 dB 21.3° in steps of 1.25° circular	

0.5°

measured 0.55°
40.0° west of north

I: Combined mode,
all elements aligned,
physical area 5520 m².
II: Split beam mode,
element 1+2 and 3+4
elements aligned,
structure beams as
two independent antennas,
each of physical area 2400 m².

Effective area, broadside, mode I

Circular polarization:
horizontal polarization:
Polarization

Mode I:
(i) Right- and left hand circular,
possibility for polarization
flipping from pulse to pulse
(ii) Linear at ± 45° with respect
to vertical

Mode II:

Left-hand circular (transmission)

Mode I:

0.0° east/west

1.7° north/south

Mode II:

1.2° east/west

1.7° north/south

21.3° east and west of

transmit plane, steps

approximately 1.2°

30° south to 60°

north of zenith

5°/min

solid state
(gain 150 dB)

-250K

0

1.2, 3.0, 18.0 MHz

phase-coherent demodulator

selectable from 12.5 to 100 MHz

in octave steps.

TABLE 9 INCOHERENT SCATTER, MST AND WIND PROFILER RADARS (DEC. 1968)

Radar	Location	Frequency (MHz)	Antenna Gain (dB)	Average Power- Aperture Product (W-m ²)	Altitude Coverage	Beam Directions
Arecibo ¹⁾	Puerto Rico	2380	75 ¹⁾	1-10 ¹⁰ (x)	ST	bistatic
Arecibo ²⁾	"	430	61	6-10 ⁸ (x)	I(M)ST	multi
Arecibo	"	46.8	42	5-10 ⁷	MST	multi
Buckland Park	Australia	54.1	35 ¹⁾	3-10 ⁶	ST	5, SA
Chung-Li	Taiwan/R.O.C.	52	29	1-10 ⁷	ST	5, SA
EISCAT ³⁾	N. Scandinavia	933	48	9-10 ⁷	I(M)ST	multi
EISCAT ³⁾	" Norway	224	43	2-10 ⁸ (x)	I(M)ST	multi N-S
Equatorial Radar ³⁾	Indonesia	47	44	4-10 ⁸ (x)	INST	1441
Fairbanks ³⁾	AL/U.S.A.	≈220	40	1-10 ⁸	ST	5
Flatland	IL/U.S.A.	40.5	27	4-10 ⁶	ST	6
India ³⁾	India	53	36	7-10 ⁸	MST	several
Jicamarca	Peru	49.9	44	1-10 ¹⁰ (x)	INST	several, SA
Willstone Hill ³⁾	WA/U.S.A.	440	46	5-10 ⁷	I(M)ST	several
MU Radar	Japan	46.5	34	4-10 ⁸	INST	1657, SA
Penn State	PA/U.S.A.	49.9	27	9-10 ⁸	ST	2
Penn State	"	405	30	3-10 ⁴	ST	1
Poker Flat ³⁾	AL/U.S.A.	49.9	40	3-10 ⁸	MST	3
Ponape, Christmas	Pacific	49.8	32	5-10 ⁸	ST	1, 3
PROUST	France	935	51 ¹⁾	1-10 ⁸	ST	1, bistatic
Provence	"	45-49	30	5-10 ⁸	ST	several
Sondrestrom ³⁾	Greenland	1290	50	4-10 ⁷	I(M)ST	multi
SOUSY	W. Germany	53.5	31	7-10 ⁷	MST	multi, SA
SOUSY mobile	Norway, etc.	53.5	35	7-10 ⁷	MST	4
Sunset ³⁾	CO/U.S.A.	40.5	24	6-10 ⁸	ST	5
United Kingdom ³⁾	Wales/U.K.	≈50	28	6-10 ⁷	MST	several
Urbana	IL/U.S.A.	40.9	28	2-10 ⁷	MST	several
Wind Profilers	CO, OK/U.S.A.	49.8	27	6-10 ⁸	ST	2
"	"	405	30	3-10 ⁴	ST	2
"	"	915	40	2-10 ⁴	ST	3
Wind Profilers (30) ³⁾	Central U.S.A., etc.	≈404	32	1-10 ⁸	ST	3

¹⁾ operation discontinued ²⁾ in planning or construction phase ³⁾ M = mesosphere, S = stratosphere, T = troposphere
⁴⁾ mostly ionospheric radar ⁵⁾ TX antenna gain in bistatic mode ⁶⁾ (M) = D-region in incoherent scatter mode
⁷⁾ mostly for radar astronomy SA = spaced antenna capability I = ionosphere-thermosphere incoherent scatter

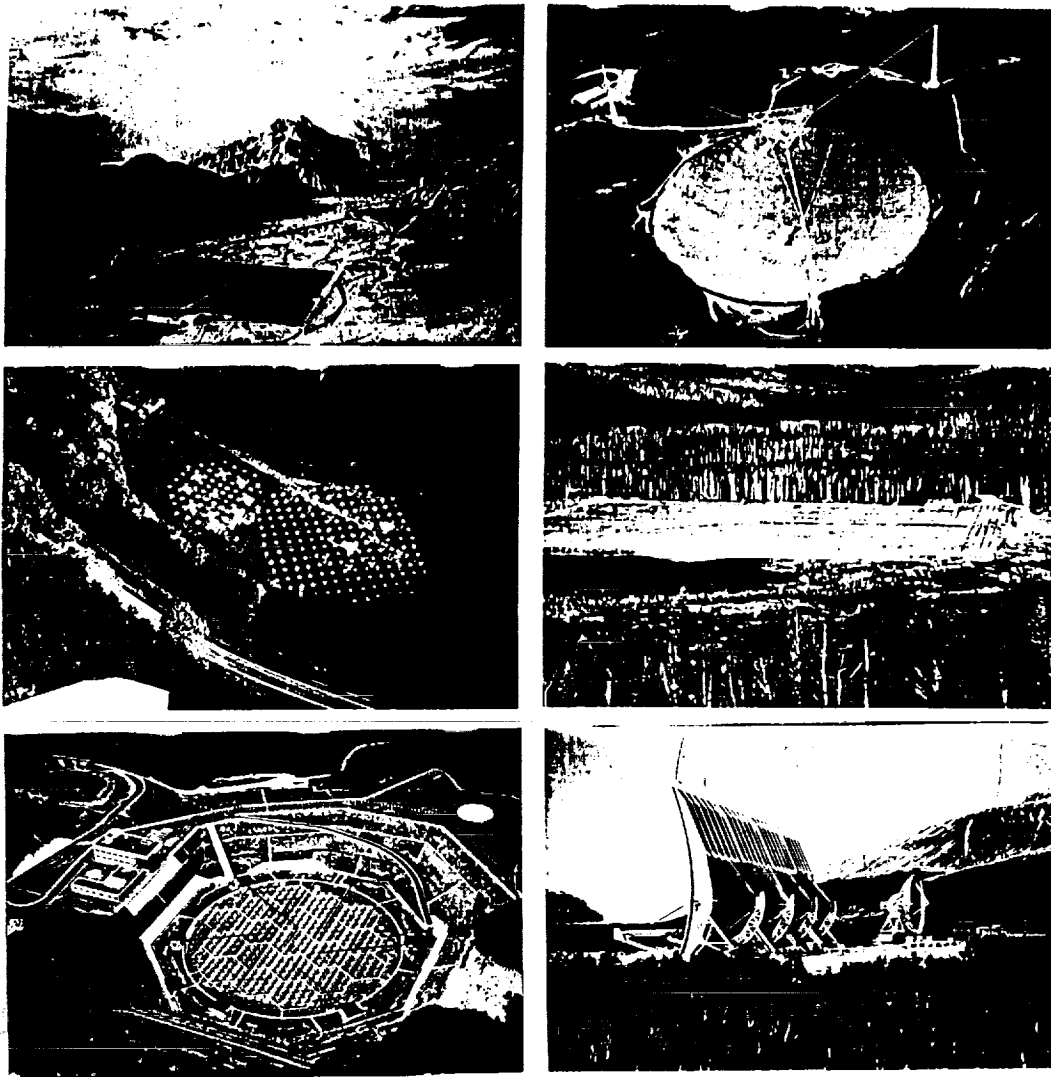


Figure 50. Photos of radar observatories:
Jicamarca/Peru, Arecibo/Puerto Rico,
SOUSY/West Germany, Poker Flat/Alaska,
MU Radar/Japan, EISCAT/Norway.

ORIGINAL PAGE IS
OF POOR QUALITY

REFERENCES

- Balsley, B.B. (1978a), The use of sensitive coherent radars to examine atmospheric parameters in the height range 1-100 km, Preprint Vol. 18th Conf. on Radar Meteorology, 190-193 (publ. by Amer. Meteor. Soc., Boston, MA).
- Balsley, B.B. (1978b), Design considerations for coherent radar systems for probing the troposphere, stratosphere, and mesosphere, Preprint Vol. 18th Conf. on Radar Meteorology, 387-390 (publ. by Amer. Meteor. Soc., Boston, MA).
- Balsley, B.B. and K.S. Gage (1982), On the use of radars for operational wind profiling, Bull. Amer. Meteor. Soc., **63**, 1009-1018.
- Balsley, B.B., W.L. Ecklund, D.A. Carter and P.E. Johnston (1980), The MST radar at Poker Flat, Alaska, Radio Sci., **15**, 213-223.
- Baron, M.J. (1977), The Chatanika radar system, in: Radar Probing of the Auroral Plasma (Proc. of the EISCAT Summer School, 1975; A. Brekke, ed.), 103-141 (publ. by Scandinavian University Books, Oslo).
- Battan, L.J. (1973), Radar Observation of the Atmosphere, The University of Chicago Press.
- Bowhill, S.A. and B. Edwards (Eds.) (1983, 1984, 1986), Handbook for MAP, **9**, **14**, **20** (publ. by SCOSTEP Secretariat, Dept. Elec. Engin., University of Illinois, Urbana, IL).
- Brosnahan, J.W., J.K. Chao and J. Röttger (1983), Chung-Li, Taiwan dual mode (Doppler and spaced antenna) VHF radar: preliminary specifications, Handbook for MAP, **9** (S.A. Bowhill and B. Edwards, eds.), 383-386 (publ. by SCOSTEP Secretariat, Dept. Elec. Engin., University of Illinois, Urbana, IL).
- Carter, D.A., B.B. Balsley and W.L. Ecklund (1980), The Poker Flat MST radar: signal analysis and data processing techniques with examples, Preprint Vol. 19th Conf. on Radar Meteorology, 563-567 (publ. by Amer. Meteor. Soc., Boston, MA).
- Clark, W.L. and D.A. Carter (1980), Real-time scaling of atmospheric parameters from radars using the MST technique, Preprint Vol. 19th Conf. on Radar Meteorology, 599-604 (publ. by Amer. Meteor. Soc., Boston, MA).
- Czechowsky, P., J. Klostermeyer, J. Röttger, R. Rüster, G. Schmidt and R.F. Woodman (1976), The SOUSY-VHF-Radar for tropospheric, stratospheric and mesospheric sounding, Preprint Vol. 17th Conf. on Radar Meteorology, 349-353 (publ. by Amer. Meteor. Soc., Boston, MA).
- Czechowsky, P., G. Schmidt and R. Rüster (1984), The mobile SOUSY Doppler radar - technical design and first results, Radio Sci., **19**, 441-450.
- Doviak, R.J. and D.S. Zrnic (1984), Doppler Radar and Weather Observations, Academic Press, Inc., Orlando, FL.
- Ecklund, W.L., D.A. Carter and B.B. Balsley (1988), A UHF wind profiler for the boundary layer: brief description and initial results, J. Atmos. Ocean. Techn., **5** (in press).

- Evans, J.V. (1969), Theory and practice of ionosphere study by Thomson scatter radar, Proc. IEEE, 57, 496-500.
- Frisch, A.S., B.L. Weber, R.G. Strauch, D.A. Merritt and K.P. Moran (1986), The altitude coverage of the Colorado wind profilers at 50, 405, and 915 MHz, J. Atmos. Ocean. Techn., 3, 680-692.
- Fukao, S., S. Kato, T. Aso, M. Sasada and T. Makihiro (1980), Middle and upper atmosphere radar (MUR) under design in Japan, Radio Sci., 15, 225-231.
- Fukao, S., T. Sato, T. Tsuda, S. Kato, K. Wakasugi and T. Makihiro (1985a), The MU radar with an active phased array system: 1. antenna and power amplifiers, Radio Sci., 20, 1155-1168.
- Fukao, S., T. Tsuda, T. Sato, S. Kato, K. Wakasugi and T. Makihiro (1985b), The MU radar with an active phased array system: in-house equipment, Radio Sci., 20, 1169-1176.
- Gage, K.S. and B.B. Balsley (1978), Doppler radar probing of the clear atmosphere, Bull. Amer. Meteor. Soc., 59, 1074-1093.
- Gossard, E.E. and R.G. Strauch (1983), Radar Observation of Clear Air and Clouds, Elsevier Publ. Comp., Amsterdam.
- Green, J.L., J.M. Warnock, R.H. Winkler and T.E. VanZandt (1975), A sensitive VHF radar for the study of winds, waves and turbulence in the troposphere, stratosphere and mesosphere, Preprint Vol. 16th Conf. on Radar Meteorology, 313-315 (publ. by Amer. Meteor. Soc., Boston, MA).
- Hagfors, T. (1977), Incoherent scatter radar observations, in: Radar Probing of the Auroral Plasma (Proc. of the EISCAT Summer School, 1975; A. Brekke, ed.), 75-101 (publ. by Scandinavian University Books, Oslo).
- Hagfors, T., P.S. Kildal, H.J. Kärcher, B. Liesenkotter and G. Schroer (1982), VHF parabolic cylinder antenna for incoherent scatter radar research, Radio Sci., 17, 1607-1621.
- Hardy, K.R. (1972), Studies of the clear atmosphere using high power radar, in: Remote Sensing of the Troposphere (V.E. Derr, ed.), chapter 14 (publ. by Wave Propag. Lab., NOAA/ERL, Boulder, CO).
- Hocking, W.K. (1989), Target parameter estimation, Handbook for MAP (this issue).
- Kato, S., T. Ogawa, T. Tsuda, T. Sato, I. Kumura and S. Fukao (1984), The middle and upper atmosphere radar: first results using partial system, Radio Sci., 19, 1475-1484.
- Ko, H.C. (1958), The distribution of cosmic radio background radiation, Proc. IRE, 46, 208-215.
- Kraus, J.D. (1966), Radio Astronomy, McGraw-Hill Book Comp., New York.
- Lehtinen, M.S. and I. Häggström (1987), A new modulation principle for incoherent scatter measurements, Radio Sci., 22, 625-634.

- Ochs, G.R. (1965), The large 50 Mc/s dipole array at Jicamarca radar observatory, NBS Rep. 8772 (publ. by National Bureau of Standards, U.S. Dept. of Commerce, Boulder, CO).
- Rastogi, P.K. (1983), Data processing techniques used with MST radars - a review, Handbook for MAP, 9 (S.A. Bowhill and B. Edwards, eds.), 477-488 (publ. by SCOSTEP Secretariat, Dept. Elec. Engin., Univ. of Illinois, Urbana, IL).
- Rastogi, P.K. and R.F. Woodman (1974), Mesospheric studies using the Jicamarca incoherent-scatter radar, J. Atmos. Terr. Phys., 36, 1217-1231.
- Röttger, J. (1981), The capabilities of VHF radars for meteorological observations, ESA SP-165 (Nowcasting: Mesoscale Observations and Short-Range Prediction), 143-148 (publ. by European Space Agency, Paris).
- Röttger, J. (1984), The MST radar technique, Handbook for MAP, 13 (R.A. Vincent, ed.), 187-232 (publ. by SCOSTEP Secretariat, Dept. Elec. Engin., Univ. of Illinois, Urbana, IL).
- Röttger, J. and M.F. Larsen (1989), UHF/VHF radar techniques for atmospheric research and wind profiler applications, in: Radar in Meteorology (D. Atlas, ed.) (to be publ. by Amer. Meteor. Soc., Boston, MA).
- Röttger, J. and G. Schmidt (1979), High-resolution VHF radar sounding of the troposphere and stratosphere, IEEE Trans. Geosci. Electr., GE-17, 182-189.
- Röttger, J., J. Klostermeyer, P. Czechowsky, R. Rüster and G. Schmidt (1978), Remote sensing of the atmosphere by VHF radar experiments, Naturwissenschaften, 65, 285-296.
- Sato, T. and R.F. Woodman (1982), Spectral parameter estimation of CAT radar echoes in the presence of fading clutter, Radio Sci., 17, 817-826.
- Schmidt, G., R. Rüster and P. Czechowsky (1979), Complementary code and digital filtering for detection of weak VHF radar signals from the mesosphere, IEEE Trans. Geosci. Electr., GE-17, 154-161.
- Skolnik, M.I. (1970) (ed.), Radar Handbook, McGraw-Hill, Inc., New York.
- Strauch, R.G., D.A. Merritt, K.P. Moran, K.B. Earnshaw and D. van de Kamp (1984), The Colorado wind-profiling network, J. Atmos. Ocean. Techn., 1, 37-49.
- Turunen, T. (1986), GEN-SYSTEM - a new experimental philosophy for EISCAT radars, J. Atmos. Terr. Phys., 48, 777-785.
- Wilson, D.A. and L.J. Miller (1972), Atmospheric motion by Doppler radar, in: Remote Sensing of the Troposphere (V.E. Derr, ed.), chapter 13 (publ. by Wave Propag. Lab., NOAA/ERL, Boulder, CO).
- Woodman, R.F. (1980), High-altitude resolution stratospheric measurements with the Arecibo 2380-MHz radar, Radio Sci., 15, 423-430.
- Woodman, R.F. and A. Guillen (1974), Radar observations of winds and turbulence in the stratosphere and mesosphere, J. Atmos. Sci., 31, 493-505.
- Woodman, R.F., R.P. Kugel and J. Röttger (1980), A coherent integrator-decoder preprocessor for the SOUSY-VHF-Radar, Radio Sci., 15, 233-242.

Chapter 4

Statistical Characteristics of MST Radar Echoes and its Interpretation¹

RONALD F. WOODMAN
Jicamarca Radio Observatory
Instituto Geofísico del Perú

Introduction

As we shall see later, radar backscattering is produced by fluctuations in the refractive index of the illuminated medium with scale sizes equal to $1/2$ the wave length of the electromagnetic probing wave. The fluctuations are a random process, and so are, consequently, the signals received by the radar. Both have to be characterized statistically. The power of the technique is based on the fact that the statistical parameters that define the signal received are related to the statistical parameters of the medium. This allows us to remote-sense the medium from the ground.

It is important, then, in order to understand the technique, to know the statistical ways of characterizing 1) the fluctuations in refractive index and 2) signals received. The second may be familiar to many of you. The first may not. The second is easier to understand since it is a one dimensional process (time). The first is harder, since involves processes in four dimensions, 3 in space, and 1 in time; on the other hand, it uses extensions of concepts developed originally for one dimension, and should present no difficulties if these one dimensional concepts are understood.

Fluctuations in index of refraction come about mainly as a consequence of atmospheric turbulence. If we are going to use these fluctuations to study the atmosphere, it is important, in order to interpret the signals received, that we understand some of the fundamental concepts related to atmospheric turbulence.

Because of above reasons, we have decided before entering on the main subject of our lecture, that of the characterization of radar echoes and its

interpretation, to review some fundamental concepts in random process statistics and in atmospheric turbulence.

Some statistical concepts

There are two concepts of fundamental importance which should be reviewed: Autocorrelation Function and Frequency Power Spectrum. They are interrelated. One can be defined in terms of the other. Mathematically it is much simpler to define the first, although many find easier to grasp the physical significance of the second.

Given a time series, either as a sequence of numbers in time $s_1, s_2, s_3, \dots, s_i, \dots$, or as a random function of time, $s(t)$, (We will use $s(t)$ for both cases for convenience, unless we want to stress the discrete nature of a sequence), its autocorrelation function is defined as:

$$\rho(\tau) = E[s(t), s(t+\tau)] \quad (1)$$

where $E[\]$ stands for the expectation of its argument. Good estimators of this expectation are:

$$\rho'(\tau) = \overline{s(t)s(t+\tau)}, \quad (2)$$

if the process is stationary, or, under more general conditions,

$$\rho'(\tau) = \overline{s(t)s(t+\tau)}_n. \quad (3)$$

The overbar stands for a time average of duration T , and the brackets stand for averaging over n identical experiments or observations.

The second estimator allows us to evaluate correlation functions even in the case the process is not stationary. When the process is not stationary, we should write $\rho(\tau; t)$, to stress the dependence on t , the time at which the correlation is evaluated.

Let us see what a correlation function means physically. Let us take equation (2) as a good definition (it is, for all practical purposes, if the time T taken for the average is long enough). Fig. 1 show a sample function of the

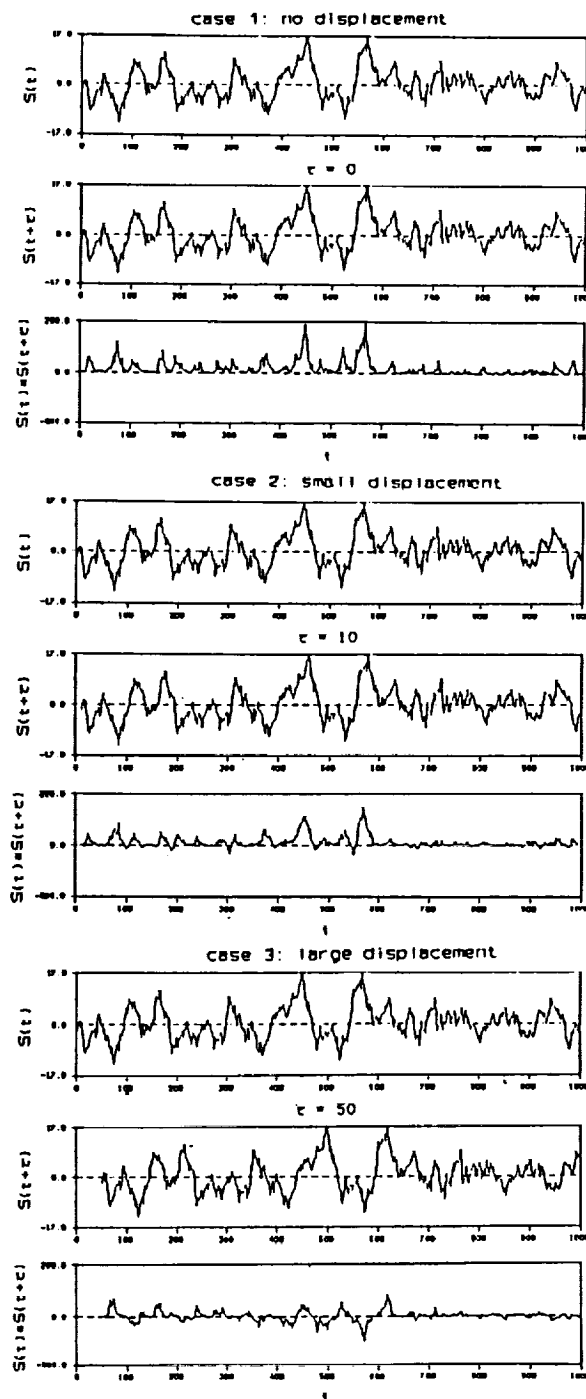


Figure 1 — Three realizations of the $s(t)s(t+\tau)$ process illustrating its eventual contribution to $p'(\tau) = \overline{s(t)s(t+\tau)}$, for $\tau = 0$, small and large.

ORIGINAL PAGE IS
OF POOR QUALITY

random functions $s(t), s(t+\tau)$ and $s(t)s(t+\tau)$ for three displacements, $\tau=0$, $\tau=$ "small" and $\tau=$ "large". When $\tau=0$, we get $s(t)^2$ for the product function, the integral of which corresponds to an estimation of the power of the process, which we use as a reference.

If we increase t by small amount, $s(t)s(t+\tau)$ does not vary much from the $\tau=0$ case, and the integral is slightly smaller than the power. If τ is large enough, it is equally probable for the product to be positive or negative, and the integral is zero.

But, what is small enough and what is large enough? The answer is given by autocorrelation function itself. Note that, between the two τ 's depicted in figure 1, there should be a τ , $\tau_{1/2}$, at which the correlation is equal to $0.5\rho(0)$ and that the correlation function decays from its maximum value to zero in a characteristic time, τ_c . This characteristic time or, alternatively, one derived from the normalized second moment of $\rho(\tau)$, has a ready interpretation and gives us an idea of how fast the process varies. It can be centuries (changes in the global temperature of the earth) or hours (changes in the ambient temperature) or, seconds (changes in the punctual temperature of a turbulent process) or any other time scale. This is the most usual interpretation given to the correlation function. There is more information, of course, besides the power and the characteristic time of the process in the functional shape of the correlation function; for instance, if the shape is oscillatory it tells us that the process is quasi-sinusoidal with a period given by the period of the oscillations. Nevertheless, in many cases, it is sufficient to give only this simple interpretation.

Power spectrum – when defined carefully (e.g. Papoulis, 1965) – is defined as the Fourier Transform of $\rho(\tau)$, namely

$$F(\omega) = 1/2\pi \int_{-\infty}^{\infty} \rho(\tau) \exp(-j\omega\tau) d\tau \quad (4)$$

This is a modern definition. The earlier definition and, in any case, a good interpretative way of looking at it, is that the power spectrum, $F(\omega)$, measures the power density of a process at different frequencies. This means

that, if the process is fed to a bank of filters centered at frequency ω_i , The average power of each filter would be proportional to $F(\omega_i)$, where ω_i is the center frequency of the filter. There are many estimators of $F(\omega)$ which conform to this definition. For instance

$$F'(\omega) = \langle |1/T \int_{-\infty}^{\infty} f(t) \exp(-j\omega t) dt|^2 \rangle_n \quad (5)$$

This is equivalent to getting the Fourier transform of a subset of the sequence, obtain its power (square it) and average many sub-sequences.

Extension to 3-D and time processes

A good example of a three space dimensions and time random process is the temperature or the velocity of a boiling pan of water, or any other turbulent process. These processes are also characterized by its autocorrelation function, $\rho(r, t)$. It is defined in a fashion similar to its one dimensional case. For instance, if we take n to stand for the deviations in density, or the refractive index of a medium, its autocorrelation function is defined as :

$$\rho(r, \tau) = E[n(x, t)n(x+r, t+\tau)] \quad (6)$$

That is, it is the expectation (in practice, the average) of the product of the density at point x at time t , multiplied by the density at a point displaced r from x , at a time τ units later. If the medium is stationary and homogeneous ρ does not depend on x or t . Otherwise, we should write $\rho(r, \tau; x, t)$, since the autocorrelation would be different if measured in a different place or at different time.

As in the case of one dimension, there is a characteristic length, r_c , and a characteristic time, τ_c , much beyond which the autocorrelation is small or zero. If the medium is isotropic, the characteristic length is the same, regardless of the direction of the displacement, r . In this case we can use the magnitude, r , instead of the vector, r . If the medium is anisotropic, there can be as many as three characteristic lengths, one in each major axis direction.

As in the case of one dimension, the characteristic time gives us an idea of

how long we have to wait before the three dimensional structure of a sample process changes significantly. Similarly, the characteristic scale gives us an idea of how far we have to move from a specific point, from which we have taken a snap shot at the process for a second snap shot, taken at the same instant, to differ significantly and yet show some resemblance. The directions of displacement should preferably be taken along the three major axis of the correlation function.

To envision the meaning of statistical anisotropy, let us consider the two dimensional case of the vertical displacement of the surface of a choppy ocean produced by a wind of constant direction. Here, there would be a tendency for the waves, or even swell, to form in with preference in one direction, that of the wind. If we displace ourselves along the crests of the waves, we have to move much further for observational snapshots to look different than if we displace ourselves along the direction of propagation of the waves (direction of the wind). The characteristic lengths in this case are different, being shorter along the direction of the wind.

Again, for the purpose of an introductory interpretation, we have talked about a single parameter per dimension. This is over simplified. One or few parameters does not replace the whole correlation function unless we accompany it with knowledge of its functional shape (e.g. Gaussian, Lorentian, sinusoidal, exponential, etc.), or by a sufficient number of evaluated points.

There is also a counterpart in 3-D processes to the concept of frequency power spectrum. In this case we speak of wave-number-vector (extension of wave-number) power spectrum, or k -spectrum. In an analogous fashion, we define it as the 3-D spatial Fourier transform of the space-time autocorrelation function, $\rho(r, \tau)$, specifically,

$$\phi(k) = 1/(2\pi)^3 \int_{-\infty}^{\infty} \rho(r, 0) \exp(-ik \cdot r) d^3r \quad (7)$$

Note that we have set τ equal to zero. Therefore in this definition, we are performing the displacements in space at the same instant of time, i.e. no time dynamics is included. We could also have used $\rho(r)$ as a symbol for the same concept. Again, its interpretation is similar to the frequency power spectrum. We can interpret $\phi(k)$ as a function which describes the "power" density of the different wave number components of the process. We imagine the process to result from the (Fourier) superposition of different spatial waves with different

directions and wavelengths, each with a power (amplitude squared) given by $\phi(\mathbf{k})$.

There is an important concept in talking about the directional scattering properties of a medium. One talks about the aspect sensitivity of the scatterers. It is a consequence of the anisotropic character of the $\phi(\mathbf{k})$ which characterizes anisotropic turbulent fluctuations. This anisotropy is sometimes better perceived from the shape of the autocorrelation function, $\rho(\mathbf{r})$. In this regard it should be kept in mind that, in any Fourier pair, like $\phi(\mathbf{k})$ and $\rho(\mathbf{r})$, wide functions transform into narrow functions and viceversa. This means that if we have a horizontal, pancake-like spatial autocorrelation function, it transforms into a vertical pencil-like \mathbf{k} -spectrum.

We can relax, above, the restriction for τ to be zero. We would obtain a function, $\phi(\mathbf{k}, \tau)$, which associates certain dynamics to each spatial wave component. Each component will have a characteristic time associated to its life time. This does not mean that the process no longer has power at that particular wave-number vector, but rather that wave component is completely independent of the one observed a few characteristic times, τ_c , ago.

To further complicate matters, we can perform an additional Fourier transformation in time on ρ . We would obtain

$$\Phi(\mathbf{k}, \omega) = (1/2\pi)^4 \int_{-\infty}^{\infty} \rho(\mathbf{r}, \tau) \exp(-j\mathbf{k} \cdot \mathbf{r} - j\omega\tau) d^3\mathbf{r} d\tau. \quad (8)$$

In this case the dynamics of the process, for each wave-number vector, \mathbf{k} , is represented by a superposition of temporal oscillations with frequency ω , and power density $\Phi(\mathbf{k}, \omega)$.

We are not presenting this concepts for purely academical reasons. As we shall see later, the signal statistics of the echoes received in a MST radar are directly related to the spectrum $\phi_n(\mathbf{k}_s, \tau)$ (or $\Phi_n(\mathbf{k}_s, \omega)$) which characterizes the density fluctuations of the medium. Although here, \mathbf{k}_s is no longer a variable but an specific wave-number vector determined by the frequency and geometry of the radar. We should, then, be familiar not only with the mathematical definition of these concepts, but with their physical significance as well. Only then we can attribute physical significance to the results of a MST radar experiment.

We have used the terms stationary and homogeneous. In the theory of random process, they are defined as follows. A process is said to be stationary, if the expectation of any function of its value, or values (for instance $E[s(t)]$ and

$E[s(t)s(t+\tau)]$), is independent of the time of the sample function taken. It is said to be homogeneous, if the expectation is independent of where the values of the sample function are taken.

In the exact context of this definition, the time and physical space have to be infinite in extent. In practice one uses the concept of quasi-stationarity and quasi-homogeneity, in which the "any time" or "any point" implicit in the strict definition is replaced by finite intervals of time and finite regions of space, sufficiently large as to contain a large number of characteristic times and length scales. The assumption of stationarity or homogeneity is considered to be valid if they hold within a particular observation time or region.

For further reading see Papoulis (1965) and Tatarsky (1961).

Some turbulence concepts.

The MST radar depends on turbulence to obtain echoes from the clear atmosphere. It uses turbulence as a tracer of the dynamics of the background atmosphere. Also, since the statistical parameters of the received signal depend on the statistical parameters of the refractive index fluctuations –produced by turbulence–, the radar can also be used to study the turbulence process proper. It is important, then, to understand some of the basics of atmospheric turbulence.

We would like to underline "basics" since turbulence theory is a difficult subject. In fact, as a consequence of its highly non linear behavior, and in spite of all the advances in its mathematical description, we are still not able to predict its behavior, even in a statistical sense.

The meaning of turbulence varies from a general dictionary type definition to controversial and more limited definitions. For us, it suffices to define it as the state of a fluid in which the velocity field is rotational and random in three dimensions and time.

Although some atmospheric physicists envision the existence of two (space) dimensional turbulence in the atmosphere, we will use the term only in a three dimensional context. We are interested in 3-D turbulence with length scales no larger than about a few hundreds of meters in the stratosphere and stable troposphere (non-convective) and a few hundred to slightly above a thousand meters in the mesosphere. We are also occasionally interested in the small scales (meters to hundred of meters) as well as the larger (kilometers)

scales of tropospheric convective turbulence.

For turbulence to exist we need a fluctuating velocity field. Radars, on the other hand, are sensitive to fluctuations in refractive index or, equivalently, fluctuations in density or temperature at constant pressure. Fortunately, in most cases, velocity fluctuations bring about density fluctuations, although this is not always the case.

If we consider a non stratified atmosphere (no gravity) at constant pressure, velocity fluctuations would not produce density fluctuations. Different parcels of air would interchange positions, but since they have the same density, no fluctuations would be produced. But, if a gradient of density exist, for any reason, then, regions of higher density would be brought to regions with lower density and viceversa, producing fluctuations in density and hence in refractive index.

If we stir pure water, for instance, we could not perceive optically any change, but if we mix it with clear syrup, it would produce a whitish fluid (while the emulsion lasts) as a consequence of the light scattering the small scale fluctuations in refractive index are capable to produce.

Mixing in a gravitational stratified atmosphere is slightly more complicated. We have to introduce in this case the concept of "potential density" and "potential temperature".

Let us consider a medium with a constant temperature profile. Under the influence of gravity it would have a density like $\rho = \exp(-z/H)$. If we interchange two parcels of different altitudes adiabatically and in pressure equilibrium, we would cool by decompression the parcel moving up into a lower pressure, and heat the parcel moving down into higher pressure. So, if we stir locally an atmosphere with a constant temperature profile, we end up with fluctuations in temperature, apparently contradicting ourselves. It is more convenient – conceptually and mathematically – to characterize, instead, the state of the medium by the temperature it would have if it were to be brought to sea level adiabatically. This "temperature" is called potential temperature. It is a conserved property of the medium, i.e. it does not change as it is moved adiabatically to other altitudes. In the language of turbulence theory it is said that it behaves as a passive scalar. We can define a potential density in a similar fashion.

For turbulence to produce fluctuations in density or temperature we need a gradient in potential density. Constant potential density backgrounds do not produce fluctuations. When an atmosphere has such profile, we say that the

(actual) temperature has an adiabatic lapse rate (about 1 every 100 meters). The stratosphere has either a constant or positive gradient temperature profile, hence it deviates more from an adiabatic lapse rate than the troposphere. It is potentially capable, then, to produce larger fluctuations for the same mixed layer thickness than the troposphere.

In the mesosphere the refractive index is produced by the density of free electrons. The gradient of both potential and real electron density gradient is positive and hence capable of producing refractive index fluctuations when mixed by turbulence.

Assuming an initial gradient in a passive scalar, one can derive (e.g. Tatarsky, 1961) a quantitative formula relating the standard deviation of the scalar (like potential temperature or potential refractive index) in terms of the original gradient and the depth of the turbulent mixing layer thickness. Assuming further a Kolmogorov power spectrum density law (see below), that is a dependence of ϕ on k of the form $k^{-11/3}$. He derived an expression for the standard deviation of the fluctuations of the form

$$\phi_n(k) = a \cdot 0.033 L_0^{4/3} (\text{grad } n)^2 k^{-11/3} \quad (9)$$

As expected the fluctuation density at any wavelength is directly proportional to positive powers of the original gradient and the scale of the largest mixing eddy, L_0 . "a" is a constant of order unity.

We can also estimate roughly the variance on the velocity field in the following way. If we mix a (stable) gradient in potential density we produce work, since we are moving up potentially heavier and down potentially lighter parcels of air. We need then an energy source. This source comes from shear. Without shear, there is no source and no turbulence. The original shear after turbulence is reduced to very low value due to turbulent viscosity. The excess of kinetic energy resultant from the difference in velocity of the original shear profile and the new constant velocity profile (see fig. 2) has to go into potential energy, result of the work we mention earlier, and the random turbulent kinetic energy. If we assume equipartition of the energy derived from the shear into 4 parts, 3 for the 3 different orthogonal components of the turbulent velocity ($\langle u'^2 \rangle$, $\langle v'^2 \rangle$, $\langle w'^2 \rangle$) and one for the potential energy, and we further assume a normal distribution of velocities, we can derive that the variance of any of the velocity components would be approximately (Woodman and Guillen, 1974; Sato and Woodman, 1982):

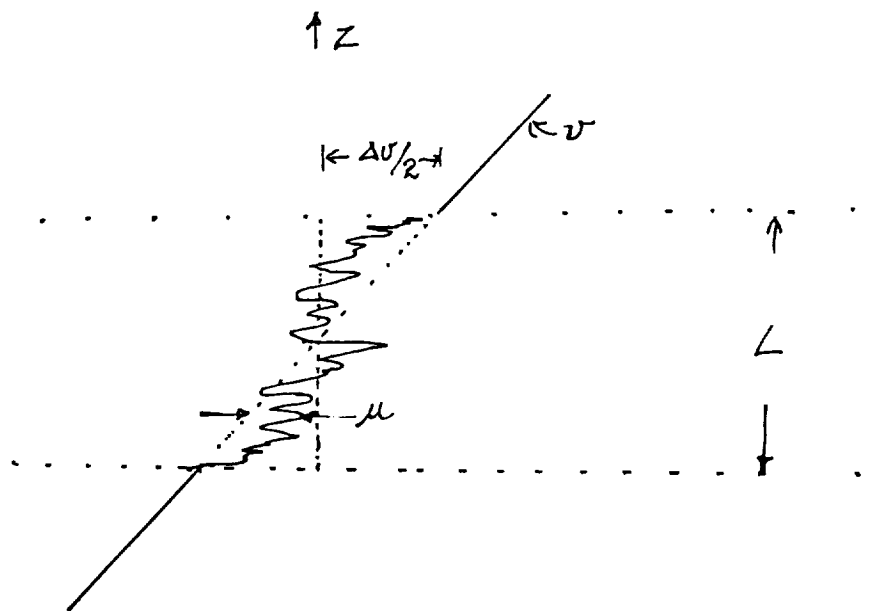


Figure 2 – Schematic profile of the turbulent fluctuating component, u , and its relationship to Δv , the shear component that is randomized by turbulence

$$\langle u'^2 \rangle = 1/48(\Delta v)^2 \quad (10)$$

where Δv is the difference in velocities between the top and bottom of the layered region that went turbulent i.e.

$$\langle u'^2 \rangle = 1/48(L_0 dv/dz)^2 \quad (11)$$

A normal distribution of velocities is a fair assumption, since it parcel of fluid is influenced by the superposition in space and time (velocity is the integral of force) of many independent forces and the limit theorem applies. This is an important additional statistical property of the medium with consequences in the shape of the correlation and spectrum of the signal.

A related subject to that of equations (10) and (11) is that of Richardson's criteria for stability. It says that a layer is unstable if

$$Ri \equiv (g \, d/dz \ln \theta) / (dv/dz)^2 \leq 1/4 \quad (12)$$

The criteria can be interpreted as a condition for turbulence to be energetically possible, namely the available kinetic energy in the shear has to be 4 times larger than the gain in potential energy after the mixing. This is in agreement with above arguments.

Some of these criteria can be used to extract hidden information from MST radar experiments, information that on first thought should not be available. Woodman and Guillen, for instance, using above relations, assuming that the original shears are marginally unstable, and from the measured values of the spectral width, deduced that the turbulent layers in the stratosphere were of the order of 50 meters, even though the resolution of the instrument was 5 km. Sato and Woodman have later validated this arguments by measuring $\langle u'^2 \rangle$ and L_0 with the 150 meter resolution 430 MHz radar at Arecibo.

Richardson's criteria tells us that turbulence is energetically possible, but it does not tell us how it comes about. We need an unstable process that would make small disturbances grow and eventually brake down into the non-linear regime that we call turbulence. One such a process is the Kelvin-Helmholtz instability. The process is analogous to the way wind, blowing on the ocean surface, peaks a particular wave, that which has a phase velocity equal to the

wind velocity, and make it grow until it breaks down. In the atmosphere shear effectively produces a wind that blows with respect to the denser fluid underneath, it peaks a particular gravity (buoyancy) wave, and makes it grow until eventually brake into a billow and this in turn into smaller scale turbulence. The phenomena is confined to the layers within which the process is energetically possible, i.e. were Richardson's criteria is satisfied.

Turbulence is also possible without shear, if the numerator in equation (12), that is if the gradient in potential temperature, is also zero or negative. We then say that the atmosphere is statically unstable. We effectively have a heavier fluid resting on top of a lighter one, a condition that is definitely unstable (Raleigh-Taylor instability).

Both processes mentioned above, Kelvin-Helmholtz and Raleigh-Taylor instabilities, can come about in the atmosphere as a consequence of large amplitude gravity and lower frequency waves in the atmosphere. These waves have a velocity field which is transverse to their \mathbf{k} . Their \mathbf{k} -vector is almost vertical. It is then possible, as the waves grow in amplitude with height, to produce almost horizontal shears that satisfy Richardson's criteria. The slight tilt of the velocity field of the wave is also capable to lift regions of higher (potential) density above regions of lower density, making them statically unstable.

An often quoted and very important conclusion that has come out of turbulence theory is Kolgomorov's wave-number spectrum. It says that within a given range of wave-number values the wave-number power spectra is of the form

$$k^2 \phi(k) \propto k^{-5/3} \quad (13)$$

We have place the k^2 factor on the left hand side to conform with the $-5/3$ power law which is often quoted in the literature. The difference comes from the use of what is referred as the one dimensional (in three dimensions) spectrum, in which the Fourier transformation from \mathbf{r} -space to \mathbf{k} -space is performed by transforming in one dimension integrating along the magnitude of \mathbf{r} .

The range within which this law is valid is called the "inertial subrange". The relationship can be derived on pure dimensional arguments with the assumption that for scales smaller than the primary energy containing scales, but large enough so that molecular viscosity does not play a role, there should be a dimensionless relationship between eddies of different sizes and that they should

be isotropic. The law breaks down at dimensions close to the largest eddy possible, and on the other end, at small dimensions where the inertial forces are comparable to the ones produced by molecular viscosity, i.e. at scales where molecular viscosity becomes important in extracting energy (into thermal) from the eddies. Within the inertial subrange, kinetic energy is cascaded from the larger to the neighboring smaller eddies.

Kolmogorov's law is isotropic and valid for non stratified media. In the case of the gravity stratified atmosphere, Kolmogorov's law is valid for the smaller scales, where potential energy is smaller than kinetic energy. On the larger scale it fails before it reaches the largest scales. The region between the "outer scale" and the inertial subrange, where potential energy is significant is referred to as the "buoyancy subrange". Not only the $-5/3$ power law fails; isotropy is no longer true, gravity, and the unstable phenomena responsible for the larger eddies, have preferred directions which spoil the isotropic symmetry.

The turbulent state of a fluid is often specified by the outer scale, i.e. the size of the largest eddies, and the energy dissipation rate, ϵ (e.g. Hocking, 1983). It can also be specified by the outer scale and the velocity variance, the second being also related to the energy levels involved. Both are theoretically related through the molecular viscosity of the fluid. We prefer the velocity variance for MST radar work, since it involves a radar measurable quantity, as compared to a theoretically derived ϵ , which involves certain assumptions.

For further reading see Batchelor (1953), Tennekes and Lumley (1972), Bolgiano (1968) and Tatarsky

Relationship between radar signals and atmospheric medium statistics

Signal statistics

The usefulness of a MST radar is based on the close relationship there is between the statistics of the signal received and the statistical properties of the atmosphere. It is our intention to show and discuss this relationship, its implications and limitations. Before we get into this task, let us first review the statistical nature of the signals received and ways to characterize their properties.

The experimental setup of an atmospheric radar has been covered by the previous lectures (See also Balsley and Gage, 1980). Regardless of the possible variations of radar systems, it is convenient to think of the signals as a two

dimensional process, but in which both dimensions have units of time. The idea is depicted in figure 3. The figure shows radar signal returns for a sequence of identical pulses. We are showing the signals after filtering and decoding, so we can still talk about identical pulses even if we have used a complementary pulse scheme. In one of the dimensions we have the delay time after the time of pulse transmission. On the other dimension, we have the time of pulse transmission. The process is discrete in this dimension. We can then represent the signal received as $s(t, t')$, where t stands for the (discrete) time at which the pulse was transmitted, and t' the delay time after the pulse. t' is continuous as an analogue output of the receiver, but in practice it is also discretized by the sampling and digital processing. As before we will be careless in differentiating the continuous vs. the discrete representation of signals.

It is convenient to make a change of variables and replace t' by $2h/c$, where h stands for the radar range defined by the delay t' , considering a pulse propagation at the speed of light, c . We can then write $s(t, h)$ to describe the signal, dropping the $2/c$ factor from the notation for convenience. In this way we get around the disturbing dependence on two times as independent variables.

The radar signal is intrinsically a non-stationary time process as a consequence of the non-homogeneous nature of the atmosphere. By writing it in the form $s(t, h)$ we have converted it into multiple (practically) stationary processes in time t , one for each range of interest. We can change our notation once more and write $s_h(t)$ to stress the parametric nature of h . We can now think of h as a label, labeling parallel processes, one for each altitude.

We know how to characterize a random stationary process: by its autocorrelation function. If the echoes come from a (practically) homogeneous turbulence, we can further argue using the limit theorem (sum of many independent contributors) that the process is Gaussian, in which case all the information we can extract from the process is in its autocorrelation function. Gaussian or not, $C_h(\tau)$ is defined as

$$C_h(\tau) = E[s_h(t)s_h(t+\tau)] \quad (14)$$

A good estimator of C_h is $\langle s_h(t)s_h(t+\tau) \rangle_n$ where the average has been evaluated by taking n pairs of sample points. Alternatively, as we have already seen, we can characterize the signals by its frequency power spectrum, $F_h(\omega)$, given by the Fourier transform of $C_h(\tau)$. Good estimates of $F_h(\omega)$ can be obtained from

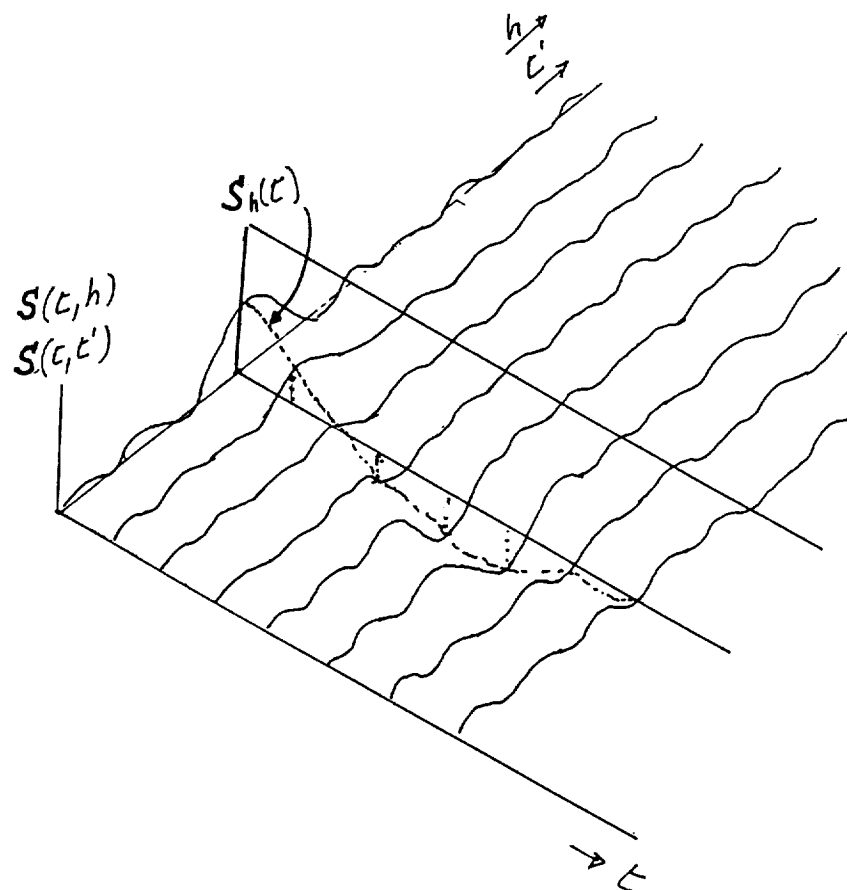


Figure 3 – Two dimensional schematic representation of the radar signals. t is the time of each radar pulse and t'' the radar range delay. The process of interest is $S_h(t)$, i.e. the sampled signal at a given range, h , as a function of the time t of pulse transmission.

discrete Fourier transforms of $C_h(\tau)$ or directly from the sequence by the techniques that will be described later in the lectures.

So far we have considered in the introduction and the discussions above that the radar signals received are real. Indeed they are. We live in a real world. On the other hand, for practical reasons, the signals which originally have a frequency almost equal to the transmitter frequency are converted to base band. To preserve all of the information contained in the original signal we need two converted signals, The so call Q and I components (see lecture on radar hardware). It can be shown (e.g. Woodman and Kohl, 1976) that if we form a complex signal with the Q and I component as real and imaginary component, everything we have say is valid, if we replace $s(t)s(t+\tau)$ by $s(t)s^*(t+\tau)$. We can recover the statistics of the signals before baseband conversion by multiplying the correlation function by $\exp(j\omega_0 t)$, where ω_0 is the transmitter frequency, and then taking the real part. Any complex phase can then be interpreted as a real phase with respect to the transmitter frequency. In particular a Doppler shift in the received signal is manifested as a complex phase of the form $\omega_0 t$ in the converted signal, and as a complex phase of the form $\omega_0 \tau$ in the correlation function.

In the frequency domain, that is in the corresponding frequency power spectra, the effects are simpler , a spectrum of the form $F(\omega-\omega_0)$ is converted to a spectrum of the form $F(\omega)$. A Doppler shift shows as a displacement in both.

A general relationship

In the appendix we have derived a very general relationship between the statistical of a radar signal and the statistics of the fluctuations in density (we could have used the dielectric properties, the temperature, electron density or any other relevant linearly related quantity) of a scattering medium. There, we take the approach of considering the most general conditions the least amount of approximations. Particular cases allow further approximations and specific expressions that one can use in practice to estimate medium parameters or to discuss instrumental effects. It has the advantage of going from the most general to the particular keeping good track of the approximations involved and their limiting implications. Furthermore, it does not take any additional conceptual effort to derive the most general expression, namely

$$C(\tau, t) = \int d^3x d^3r dt' dt'' \chi(t; t', x) \chi'(t+\tau; t'+\tau, x+r) \rho(r, \tau; x) \quad (15)$$

Cumbersome as it looks, because of the variety of arguments, the expression represents linear operations involving only two functions of easy interpretation, χ and ρ . ρ is the space– time autocorrelation function of the fluctuations responsible for the scattering. It characterizes the medium and depends only on the properties and dynamics of the medium. The function $\chi(t; t', x)$ may be called the "instrument function". It can be interpreted as the output of the instrument as a function of time as a consequence of a given arbitrary transmitter output shape (pulsed or continuous) having placed a point scatterer at point x in space, for an instant, at time t' . It is analogous to the impulse response of a system, although here the impulse is in the system characteristics: the scattering density.

The instrument function, χ , includes the pulse shape of the transmitter, any (amplitude, phase or frequency modulation) coding and decoding, match filtering, the geometry of the experiment, the transmitting and receiving characteristics of the antennas and the propagation properties of the medium, including any refraction if necessary. The determination of ρ is a statistical problem related to the physics of the medium. the determination of χ is an electronics and electromagnetics problem. As far as the characteristic of the medium, it includes non homogeneous and anisotropic cases. It is also valid for ionospheric radars including the incoherent scatter technique.

Although not discussed here or in the appendix, the approach can be extended easily to the case the system has two outputs, like in the case of a radar interferometer. We just replace the product of identical χ 's by the product $\chi_a \chi_b$ where the a and b label stand for the outputs of the two antennas, or the two frequencies in a frequency domain interferometer (Kudeki and Stits, 1987)

At the appendix we have derived expressions which include explicitly the transmitter pulse shape, the receiver filter and decoding impulse response, and the antenna pattern. In order to perform some of the integrations and make discussion possible, we have also assumed that the scattering volume, defined by the antenna patterns and the effective pulse width is larger than the characteristic sizes of the fluctuations, although this assumption can be relaxed if necessary. It is possible to reduce the complexity of the expressions further, taking approximations which are valid for specific cases.

The MST case

In the case of MST or clear-air radars it is well justified to assume that the characteristic time of the medium is much larger than that of the pulse and matching filter. In that case we can use equation A.15 and write (with a slight change in notation):

$$C(\tau, h) = \int d^2s dh' K^2(s, h') \phi(k_s(s), \tau; s, h') p(h-h') p^*(h-h'+\tau) \quad (16)$$

It differs from the appendix notation in the use of h' for the range (delay) variable of integration and h for the "range" sampling time. We have also conveniently selected length units such that $c/2$ (half the speed of light) is unity. This allows us to use h and h' for a spatial as well as a time variable. The coordinate system of integration is defined by surfaces of equal delay and an arbitrary two dimensional coordinate, s , in the transverse direction. k is in the direction of h . The directional dependance of ϕ on s is shown explicitly. This dependance is important in the case of anisotropic turbulence and will be responsible for aspect sensitive effects. The possibility of non-homogeneous turbulence is also shown explicitly in the dependance of ϕ on h and s . This is important since it is known that turbulence occurs in layers thinner than the usual range resolution of the radar. The formula is valid for mono-static and bi-static radars, and $K(s, h)$ stand for the product of the transmitter and receiver antenna weighing patterns. The dependance of K in h is usually slow (mainly the inverse of range squared) and can be taken out of the integral.

It is important to stress the fact that k_s is not the variable vector k ; it is a constant vector defined by the vector difference of the incident and the scattered wave number vectors which characterize the incident and scattered electromagnetic wave which leaves the transmitter and arrives to the receiving antenna, respectively. In the case of a backscatter radar it has a wave number twice the corresponding wave number of the illuminating wave, and the same direction.

If we crosscorrelate, as we should, only samples which correspond to the same range, then we have an expression for the auto correlation of the time stationary process $s_n(t)$ we defined above. This is equivalent to restricting the time of the second sample to be at even multiples of the pulse repetition period. In which case, since the filtered pulse function $p(t)$ is periodic, i.e. since $p(t) =$

$p(t+nT)$, we can replace the product of displaced p 's above by $|p(h-h')|^2$.

If we further assume that the medium is homogeneous in the transverse direction \mathbf{s} , we get a simpler but yet very general expression for $C_h(\tau)$:

$$C_h(\tau) = \int d^2\mathbf{s} K^2(\mathbf{s}) \int dh' \phi(\mathbf{k}_s(\mathbf{s}), \tau; h') |p(h-h')|^2 \quad (17)$$

Before we continue with the discussion of this equation it is convenient to make one further approximation, discuss the results and then come back to this more general expression.

If we further assume that we have a homogeneous atmosphere in all directions, and that the antenna has a beamwidth much narrower than the characteristic angular width of any aspect sensitivity which $\phi(\mathbf{k}_s(\mathbf{s}), \tau)$ may present, we can take ϕ out of the integral and write

$$C(\tau) = B \phi(\mathbf{k}_s, \tau) \quad (18)$$

or

$$F(\omega) = B \Phi(\mathbf{k}_s, \omega). \quad (19)$$

The success of radars to study the atmosphere is based on these simple formulae. Even in the case that the approximations behind them are not quite valid, its discussion allows us a first order approximation of the results. We shall discuss the significance of this equation first, and then remove some of the approximations that make it valid.

We will discuss only the implications of the terms ϕ or Φ on above equations. Since both expressions are interrelated, we will most of the time limit our discussions to the time domain expression, i.e equation (18) and extend it to the frequency domain (equation (19)) when desirable. We will not discuss the proportionality term, B , since that is equivalent to a discussion of the radar equation, which we have already seen in the previous lectures.

The first conclusion we can derive from these expressions is that the amplitude and dynamics of the radar signal depends linearly on the amplitude and dynamics of only one Fourier component of the density fluctuations of the medium, that which has a wave-vector equal in amplitude and direction to twice (backscatter case) the wave-vector of the probing electromagnetic wave. In terms of wavelengths, the radar is sensitive only to fluctuations with a wave length half the wavelength of the probing wave and a direction equal to the line

of sight. The radar effectively filters out very sharply all the spatial Fourier components which are not equal to k_x . This wave component is still a random process. Its dynamics is characterized by its temporal correlation function, $\phi(k_x, \tau)$. The signal received has the same dynamics as this particular wave component.

The "power", i.e. the amplitude squared averaged, of the particular wave component of the density fluctuations the radar is sensitive to, is given by $\phi(k_x, 0)$. Therefore the power of the radar signal is proportional to the "power" of the same spatial wave component. Furthermore, if we assume that the k -spectrum follows a Kolmogorov law, we can indirectly infer the power density at other wavelengths.

If the medium is immobile with respect to a frame of reference, in this frame of reference we can show that $\phi(k, \tau)$ is real. This is a consequence of the invariance of $\rho(r, \tau)$ under an interchange of r with $-r$ for any τ . If it were not invariant we would violate our immobile assumption since there would be dynamically a preferred direction. An observer moving with respect to this reference at velocity v would measure instead a correlation function of the form $\rho(r-v\tau, \tau)$, as a consequence of a transformation $x' = x-vt$ in the defining equation (6) for ρ . Using the displacement theorem of Fourier transform pairs, we derive a k -spectrum of the form $\phi(k, \tau)\exp(-ik_x v\tau)$. Replacing this spectral form in equation (18), and remembering that $\phi(k_x, \tau)$ is real, we conclude that the phase slope of the signal correlation is a measure of the projected velocity of the medium with respect to the radar. The projection is along k_x . In terms of the frequency power spectrum $F_n(\omega)$, again using the displacement theorem, we get a new expression, $F_n(\omega-\omega_D)$, where ω_D is, not surprising, the Doppler frequency,

$$\omega_D = k_x \cdot v = (v/2c)\omega_0. \quad (20)$$

Our next step is to show that the characteristic time of the signal correlation is determined by the variance, $\langle w'^2 \rangle$, of the turbulent velocity. This is better shown in the frequency domain. If the scattering volume is larger than the largest eddies, we are sure to have a good sample of all possible velocities within the volume. Normally the eddies are much larger than the wavelength of the fluctuations the radar is sensitive to. We can then divide the scattering volume into many scattering sub-volumes. The signal received would be equal to the sum of each of the contributions of these sub-volumes, each of which would impose a Doppler shift proportional to its averaged projected velocity w' . This projected velocity would not differ much from a corresponding local w' , since we

know from turbulence theory that most of the energy is in the largest scale eddies. Therefore the power frequency distribution (spectrum) of the backscattered signals is going to be distributed in the same way as the probability distribution of w' . Its second moment, σ^2 , would be proportional to the variance of the velocity $\langle w'^2 \rangle$, with the same constant of proportionality as the one which relates the velocity to the Doppler shift, but squared, namely

$$\sigma^2 = \omega_0^2 \langle w'^2 \rangle / 4c^2 . \quad (21)$$

Furthermore, we have mentioned before that from experimental results as well as from limit theorem arguments, we expect the random turbulent velocities to be normally distributed, therefore, we also expect the frequency power spectrum of the radar signals to be distributed likewise.

A normal frequency power spectrum is defined by three parameters: its area(total power), displacement and width; or, alternatively, by its three first moments. It transforms to an autocorrelation function which is also normal, although complex. The three parameters transform into : the amplitude , phase slope and width of the autocorrelation function, respectively. That is all the statistical information either one of them contains, and that is all we should look for in this case. On the other hand we have seen that they are related to very important parameters of the medium. In fact, the relation and importance holds even if normality is not assumed.

Let us come back to the more general equation, (17). The whole expression can be taken as a weighted averages of ϕ , averaged over all ranges weighted by the filtered pulse shape squared, and over all angles weighted by the antenna pattern. In the case of a bi-static arrangement, the averages are taken over surfaces of equal delay ("range") and over appropriate transverse coordinates ("angle").

The pulse function is non-zero for values close to $h-h'=0$, and a depth equal to its width after convolving it with the filter function (similar shape for matched conditions). this means that the range integral is effectively sampling ϕ at $h'=h$, averaging neighboring values within approximately a pulse width.

Similarly, the antenna weighing function is non-zero for values close to the axis of the beams, and a width given by the beamwidth of the antennas.

If the dependance of ϕ on s or h is relatively slow as compared to the width of the weighing functions p^2 and K^2 , an average value of ϕ , representative

of the center point of the sampled scattering volume at range h and center angle of the beam patterns $\mathbf{s} = \mathbf{s}_0$, can be taken out of the integral. The integrand is reduced to the two weighing functions, which integrate to a volume V , as large as the non zero regions of p^2 and K^2 , multiplied by the proportionality constants imbedded in them. The result,

$$C_n(\tau) = b V \bar{\phi}(\mathbf{k}_s, \tau; h), \quad (22)$$

is a proportional expression as the one in (18) and (19), which we have already discussed. We have replaced $\mathbf{k}_s(\mathbf{s}_0)$ by \mathbf{k}_s , where \mathbf{k}_s stands for the corresponding one at the center of the beam. The only difference being the explicit linear dependance on the volume, V , and the averaging nature of the integral operation

An important use of equation (17) is in the evaluation and discussion of broadening of the spectrum, $F(\omega)$, as a consequence of finite beamwidth and wind shear. The evaluation should be done by actually using the equation, and a model of the medium characteristics and the radar system in the integrand. But, it is possible to get a feeling of how the broadening comes about by breaking the integral into the sum of integrals over smaller volumes sufficiently small for equation (18) to be valid. Each subvolume will contribute to the spectrum with comparably shaped spectra but with different Doppler shift, $\mathbf{k}_s \cdot \mathbf{v}$. The Doppler shifts would be different either because \mathbf{k}_s varies in direction within the beamwidth (beam broadening) or because \mathbf{v} varies (shear broadening). The resultant spectrum would be significantly wider if these shifts are larger than the ones produced by the random turbulent velocities. (See Hocking, 1983, for further discussions).

Notice here that it is possible for non isotropic turbulence to have a Φ dependent on \mathbf{s} through its dependance on the direction of \mathbf{k}_s , that is an aspect sensitivity. If the aspect sensitivity is wider than the beamwidth, the radar would be able to resolve it and actually measure the angular dependance, provided of course that the beam is steerable. If the aspect sensitivity is sharper than the beam pattern, then the weighing in the integrand will be performed by the aspect sensitivity function, and the statistics of the echoes will be mainly that corresponding to the most favored aspect angle. The contributing volume will also be correspondingly smaller. (See Doviak and Zmic, 1984, for further discussions).

Something similar would happen if the h dependence of ϕ is smaller than the pulse width. The most important consequence being that the volume would be smaller than that defined by the pulse. Thus, the actual strength of turbulence, $\phi(k)$, would be underestimated if the h dependence of ϕ is not taken into account.

Partial reflection.

So far we have considered only radar echoes that have been produced by random turbulent-produced fluctuations in refractive index. It is possible to have in the atmosphere stratified structure sufficiently large in the horizontal extent as to be considered deterministic for all practical purposes. In fact, the aspect sensitivity that has been measured is so sharp that has let some researchers (Röttger and Liu, 1978 ; Fukao et al, 1979; Gage and Green 1978) to postulate that the echoes are produced by partial reflection from stratified gradients. In this case is more convenient to talk, borrowing from optics, about the reflectivity of the structure, R . It is a coefficient, defined by the ratio of the intensity of the reflected over the incident electromagnetic wave, incident on the structure. A formula often used in the literature to evaluate R is

$$R = \int_{-L/2}^{L/2} \frac{1}{n} \frac{dn}{dz} \exp(-k_z z) dz .$$

Recently, Woodman and Chu, 1988, have shown that the limits, $L/2$, if they fall at points where the integrand has not gone to zero on its own, can introduce artificial discontinuities in the first derivative which overestimate the reflectivity by many orders of magnitude. Nevertheless, partial reflection is possible if step like structure of a fraction of a degree Kelvin exist within a length scale of a meter or so. The existence or not of such a discontinuous structure would have to be established with an independent technique. The aspect sensitivity observed with radars can also be explained in terms of anisotropic turbulence at the edges of the turbulent layers observed with the same technique (Woodman and Chu, 1988).

Characteristics of noise and clutter interference

Radar echo signals are always contaminated, in variable degrees, with sky and receiver noise and echoes from undesirable targets, like mountains, other ground structures, ocean waves, etc.. The latter is referred as clutter. In order to

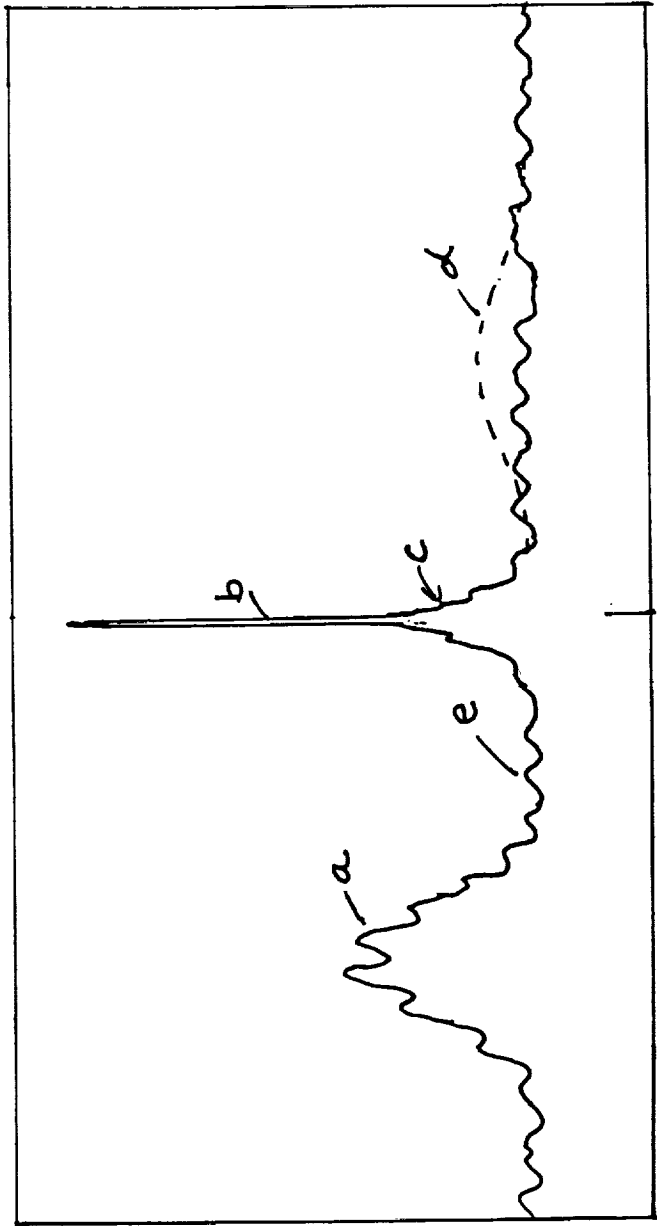


Figure 4 – Schematic plot of a typical VHF MST radar signal showing a) the signal component, b) non-fading ground clutter, c) fading ground clutter, d) possible ocean clutter and e) receiver and sky noise.

properly interpret the desired signals, and be able to discriminate between them and noise or clutter, we need to know the spectral characteristics of the latter as well.

Sky and receiver noise, after passing through the receiver, has a bandwidth determined by the receiver filter. The filter in turn is normally matched to the transmitter pulse width, or Baud width if coded. The pulse width is a small fraction of the pulse repetition period, which also determines the sample time of the sequence $s_n(t)$. Therefore, at this sampling rate, the noise samples are independent. They are also statistically independent with respect to the signal. Hence, the noise contribution to the autocorrelation function of the received signals is a Dirac function centered at the origin. Its contribution to the frequency power spectrum is a flat threshold. It behaves, then as white noise.

The characteristics of ground clutter are the opposite to those of noise. They are very narrow in the frequency domain and wide in the time domain. To first approximation clutter shows as an spectral line in the frequency domain, centered at zero frequency, since it comes from rigid structures with no relative velocity with respect to the radar. At low VHF frequencies, this is practically the case. At UHF frequencies, the reported clutter characteristics (Sato and Woodman, 1981) have two components, an spectral component accompanied by a weaker narrow, but finite, width component both centered at zero frequency. The spectral line comes as in the VHF case from the rigid ground structures, the wider component is believed to come from wind induced motion of tree branches or from phase modulation of the spectral component induced by changes in the effective phase path length between the radar and the target. Both are possible. Changes in the width of this component with different surface wind conditions support them both. Fortunately, except under very windy conditions, the wider component is still a few to several times narrower than the width of the atmospheric echoes and one can discriminate against them (Sato and Woodman, 1981). The task is made easier by its confinement to the center of the spectrum. Under windy conditions, specially when one is interested in the small vertical component, ground clutter is a problem at UHF frequencies.

For those radars near the ocean or large lakes, ocean clutter is a source of interference. It can compete in strength with the atmospheric echoes, specially at the higher ranges. Ocean clutter comes from wavelets on the surface with a wave length equal to half the wavelength of radar. It is Doppler shifted by a frequency corresponding to the phase velocity of the wavelet. These velocities are

of the order of a few meters per second, and hence comparable to the atmospheric velocities we are interested in. This should not surprise us, since the wavelets are excited by matching velocity components the surface wind speed. To make matters worse, ocean clutter echoes have spectral widths which are also comparable to that of the desired echoes (Sato and Woodman, 1982b). Still it is possible to discriminate against them, taking advantage of the predictable frequency shift and their constancy – in amplitude and frequency– as a function of range and time. The problem being limited to those altitudes where the wind profile crosses the value corresponding to the velocity of the wavelets, and only in the case its strength is comparable or weaker to the interference.

REFERENCES

- Balsley, B.B. and K.S. Gage , The MST radar technique: Potential for middle atmospheric studies, *Pure and Applied Geophys.*, Vol.118, P.452–493, 1980.
- Batchelor G.K. , The theory of homogeneous turbulence, Cambridge University press,1953.
- Bolgiano, R., Jr. , Wind and turbulence in the stratosphere, mesosphere and ionosphere (Edited by K. Rawer), North Holland Amsterdam, P.371–400, 1968.
- Doviak, R.J. and D.S. Zrnic, Reflection and scattering formula for anisotropically turbulent air, *Radio Sci.*, Vol.19, P.325–336, 1985.
- Fukao, S., T. Sato, S. Kato, R.M. Harper, R.F. Woodman and W.E. Gordon, Mesospheric winds and waves over Jicamarca on May 23–24, 1974, *J. Geophys. Res.*, Vol.84, P.4379–4386, 1979
- Gage, K.S., and J.L. Green, Evidence for specular reflection from monostatic VHF radar observations of the stratosphere, *Radio Sci.*, Vol.13, P.991–1001, 1978
- Gage, K.S., and B.B. Balsley, On the scattering and reflection mechanisms contributing to clear air radar echoes from the troposphere, stratosphere and mesosphere, *Radio Sci.*, Vol.16, P.1447–1453, 1980
- Gage, K.S., B.B. Balsley, and J.L. Green, Fresnel scattering model for the specular echoes observed by VHF radar, *Radio Sci.*, Vol.16, P.1447–1453, 1981
- Hocking, W. K., R. Rüster and P.Czechowsky, Absolute reflectivities and aspect sensitivities of VHF radio wave scatterers measured with the SOUSY radar, *J. Atmos. Terr. Phys.*, Vol.48, P.131–144, 1986
- Hocking, W. K., On the extraction of atmospheric turbulence parameters from radar backscatter Doppler spectra– I. Theory, *J. Atmos. Terr. Phys.*, 45,89–102,1983.
- Kudeki E. and G. R. Stitt, Frequency domain interferometry: A high resolution radar technique for studies of atmospheric turbulence, *Geophys. Res. Lett.*, 14, 198–201, 1987

- Papoulis, A., Probability, random variables and stochastic processes, McGraw Hill, 1965.
- Röttger, J. and C.H.Liu, Partial reflection and scattering of VHF radar signals from the clear atmosphere, *Geophys. Res. Lett.*, Vol.5, P.357-360, 1978.
- Sato, T. and R.F. Woodman, Fine altitude resolution observations of stratospheric turbulent layers by the Arecibo 430 MHz radar, *J. Atmos. Sci.*, Vol.39, P.2546-2552, 1982(a).
- Sato, T., and R.F. Woodman, Spectral parameter estimation of CAT radar echoes in the presence of fading clutter, *Radio Sci.*, Vol.17, P. 817-826, 1982(b).
- Sato, T., T. Tsuda, S. Kato, S. Morimoto, S. Fukao and I. Kimura, High resolution MST observations of turbulence by using the MU radar, *Radio Sci.*, Vol.20., P.1452-1460, 1985.
- Tatarsky, V. I., Wave propagation in a turbulent medium, McGraw-Hill, 1961.
- Tennekes H. and J. L. Lumley, A first course in turbulence, The MIT press, 1972.
- Tsuda, T., T. Sato, K. Hirose, S. Fukao and S. Kato, MU radar observations of the aspect sensitivity of backscattered VHF echo power in the troposphere and lower stratosphere, *Radio Sci.*, Vol.21, P.971-980, 1986.
- Woodman, R.F. and A. Guillen , Radar observations of winds and turbulence in the stratosphere and mesosphere, *J. Atmos. Phys.*, Vol.31, P.493-505, 1974.
- Woodman, R.F., High altitude resolution stratospheric measurements with the Arecibo 430 MHz radar, *Radio Sci.*, Vol.15, P.417-422, 1980a.
- Woodman R.F., High altitude-resolution stratospheric measurements with the Arecibo 2380-MHz radar. *Radio Science*, 15,423-430, 1980b
- Woodman R. F., Scattering of electromagnetic waves from dielectric density fluctuations, in *Lecture Notes on Incoherent Scatter Techniques*, The Eiscat winter school, Max-Planck Institute für Extraterrestrische Physik, 8046 Garching, München, GFR.
- Woodman, R. F. and Yen-Hsyang Chu, Aspect sensitivity measurements of VHF scatter made with the Chung-Li radar: Plausible mechanisms, *Radio Science*, In Press, 1988.
- Yeh, K. C. and C. H. Liu, Theory of ionospheric waves, Academic Press New York, P.274-276, 1974.

APPENDIX

Scattering of EM Waves from Dielectric Density Fluctuations*

R. F. Woodman
Arecibo Observatory, Arecibo, PR

Radars are used for remote probing of the upper atmosphere. Monostatic and bistatic configurations have been used. The echoes are obtained from the scattering of the illuminating wave by fluctuations in the dielectric properties of the medium under study.

The fluctuations in the local dielectric constant of a medium are direct consequences of fluctuations in the density of the medium or, more properly, on the density of that component or components in the medium responsible for its dielectric behavior, e.g., electron density in an ionized gas, "air" density and water vapor in the low atmosphere, etc.

In the case the medium is in thermodynamic equilibrium, the fluctuations are reduced to a minimum (thermal level). In such a case, and for an ionized plasma, we refer to the technique as incoherent scatter. These fluctuations are never at zero level due to the discrete nature of matter (Summations of delta functions will always produce fluctuations.)

Density fluctuations are statistically characterized by the density space-time correlation function $\rho(r, \tau, \underline{x})$ defined as

$$\rho(r, \tau; \underline{x}) \equiv \langle n(\underline{x}, t) n(\underline{x} + \underline{r}, t + \tau) \rangle \quad (1)$$

where $n(\underline{x}, t)$ is the microscopic random density of the medium at position \underline{x} in space and time t . In (spatially) homogeneous medium ρ is independent of \underline{x} and $\rho(r, \tau) \equiv \rho(r, \tau; \underline{x})$.

Hagfors has treated the problem of how to find $\rho(r, \tau)$ for an ionized medium in thermodynamic equilibrium (or quasi-thermodynamic for the case $T_e \neq T_i$). Farley has described the different techniques for obtaining estimates of $\rho(r, \tau; \underline{x})$ from the scatter echoes.

We shall develop here the functional relationship that exists between the statistical characterization of the signal received in a radar experiment and the fluctuations in the medium characterized by $\rho(r, \tau; \underline{x})$. The fluctuations need not be at the thermal level, so we are not limited to the incoherent scatter problem. We should point out that the usefulness of large radars for the study of the upper atmosphere is not limited to incoherent scatter. Proof of which is found in the large number of papers produced by the Jicamarca Observatory by studying backscatter echoes from E- and F-region irregularities and from turbulent fluctuations in the neutral atmosphere. In fact, some smaller radars are built (STARE, SOUSY and the TS radars) which depend on the enhanced reflectivity produced either by instabilities or turbulence. This could be the case in EISCAT when observing auroral phenomena or the effects of artificial heating. It will also be the case when studying neutral dynamics using backscatter signals from turbulent fluctuations.

Said functional relationships can be found in the literature but it is usually derived from very simplified conditions with assumptions which are not necessarily valid. The derivation is usually heuristic and in many cases difficult to assess the range of validity of the derived expressions. Such approach is, of course, useful for didactic purposes and when the purpose of the paper is on other aspects of the problem. Derived expressions in the literature are usually derived for a specific technique (out of the many described here by Farley) and for specific conditions (e.g., homogeneous media, continuous illumination, slowly varying echoes, narrow pulses, etc.). We shall derive here the functional relationship between the statistical properties of the echoes and the statistical properties of the medium under very general conditions.

*Lecture presented at the M.P.I. EISCAT School, January 1979, Oberstdorf, W. Germany

We shall consider an experimental configuration as depicted in Figure 1. The medium under study is illuminated by an EM wave of frequency ω_0 , modulated by an arbitrary complex signal $p(t)$, scattered EM waves are received at a different location (or at same as a particular case), coherently detected, properly filtered and decoded (if necessary). We are interested in evaluating the complex autocorrelation of the signal received, $O(t)$, i.e.,

$$C(\tau, t) \equiv \langle O(t) O^*(t + \tau) \rangle \quad (2)$$

in terms of the space and time density correlation of the medium.

The signal $O(t)$ is a random process, usually nonstationary, is fully characterized by its time autocorrelation function $C(\tau, t)$. The dependence on t can normally be associated with a given range, h , corresponding to the delay.

We assume: (1) that there is only primary scattering (first Born approximation valid), i.e., the medium is transparent, the illuminating field at a point x within the medium is due to the primary illuminating field and the scattered fields at x are negligible; (2) the system is linear, i.e., if $O_1(t)$ is received for $p_1(t)$ and $O_2(t)$ for $p_2(t)$. The $\alpha O_1(t) + \beta O_2(t)$ is received for an excitation $\alpha p_1(t) + \beta p_2(t)$. The linearity of the propagation in the medium is guaranteed by the linearity of Maxwell equations.

The linearity of the system allows us to evaluate the output signal as the linear superposition of the contributions of each differential volume, d^3x with density $n(x, t)$. This differential contribution can be evaluated in terms of the linear operators depicted in Figure 2. Here we have modeled the propagation of the transmitter to the scattering point by a delay operator with delay $T_1(x)$ and an amplitude factor $K_1(x)$ which represent the effect of antenna gain and other system parameters. The scattered signal is proportional to the local instantaneous (random) density $n(x, t)$ of the medium times the volume d^3x . The dielectric properties of the medium, the receiver, antenna, and other propagation properties are contained in a constant gain (in time) $K_2(x)$. There is a delay block with delay $T_2(x)$, a detector and a filter before we finally get our output from the differential contribution from $n(x, t)$. The filter is characterized by the complex input response $h(t)$ and includes any decoding scheme. Decoding is a convolution operation and can be considered as part of the filter.

The evaluation of the delay functions $T_1(x)$, $T_2(x)$ and the constant terms $K_1(x)$, $K_2(x)$ does not concern us here and are assumed to be known. The output of the system can then be written as

$$o(t, x) d^3x = d^3x \int dt' K(x) p(t' - T(x)) e^{-i \omega_0 T(x)} n(x, t' - T_2(x)) h(t - t') \quad (3)$$

where we have already operated on the "signal" with the delay operators $\delta(t - T_1(x))$ and $\delta(t - T_2(x))$. Here we have used $T(x) = T_1(x) + T_2(x)$ for the total delay and $K(x) = K_1(x) \cdot K_2(x)$. The total signal output is then

$$O(t) = \int d^3x o(t, x) \quad (4)$$

and the autocorrelation, $C(\tau, t) \equiv \langle O(t) O^*(t + \tau) \rangle$, can then be written as:

$$C(\tau, t) = \int d^3x \int d^3x' dt' dt'' K(x) K(x') p(t' - T(x)) p^*(t'' - T(x')) e^{-i \omega_0 (T(x) - T(x'))} \cdot h(t - t') h(t + \tau - t'') \rho[x' - x, t'' - t' - (T_2(x) - T_2(x')); x] \quad (5)$$

It is convenient to write this expression in terms of variables

$$\begin{aligned} \underline{r} &= \underline{x}' - \underline{x} \\ \tau' &= t'' - t' \end{aligned}$$

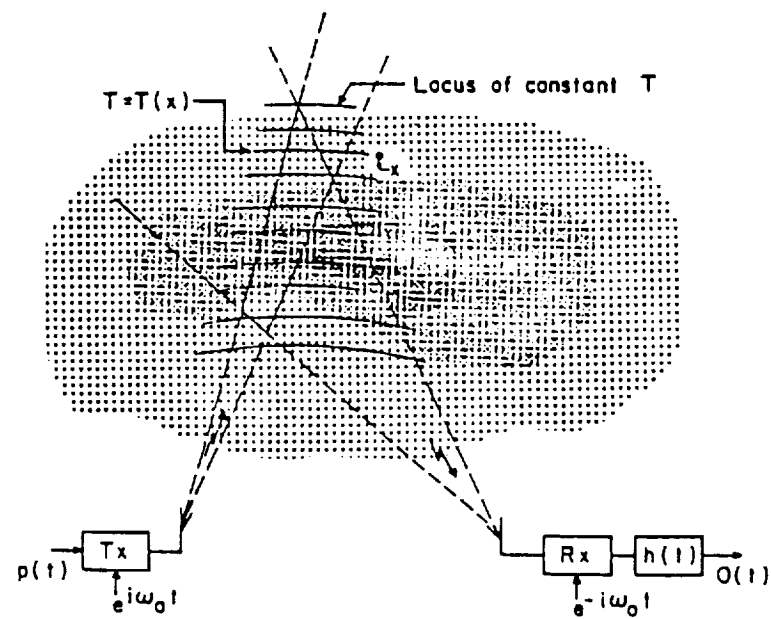


Figure 1.

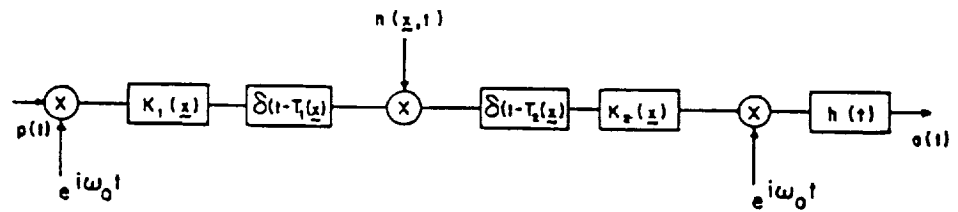


Figure 2.

$$C(\tau, t) = \int d^3x d^3r dt' d\tau' K(\underline{x}) K^*(\underline{x} + \underline{r}) p(t' - T(\underline{x})) p^*(t' + \tau' - T(\underline{x} + \underline{r})) \\ \cdot e^{-i\omega_0(T(\underline{x}) - T(\underline{x} + \underline{r}))} h(t - t') h^*(t + \tau - t' - \tau') \rho[\underline{r}, \tau' - (T_2(\underline{x}) - T_2(\underline{x} + \underline{r})); \underline{x}] \quad (6)$$

This expression is simplified considerably if we take advantage of the fact that in most cases the characteristic length of the density correlation function, r_c , (equal to the Debye length in the I.S. case) is much smaller than the characteristic length of $K(\underline{x})$ and the characteristic length, ct_p , corresponding to the width of the pulse $p(t)$. This allows us to replace $K(\underline{x} + \underline{r})$ by $K(\underline{x})$ and $p(t - T(\underline{x} + \underline{r}))$ by $p(t - T(\underline{x}))$ in the integrand with no appreciable effect on the integral.

Also, the difference in propagation time $T_2(\underline{x}) - T_2(\underline{x} + \underline{r})$ is of the order of r_0/c for points within a correlated volume. This is much smaller than the characteristic time of the decay of the correlation function unless one is dealing with relativistic plasma. Therefore we can ignore this term in the time argument of the correlation function. In addition, the oscillatory nature of the exponential, with a wavelength comparable to the wavelength of the probing wave, makes the integrand unsensitive to any possible long scale structure of the correlation function across the surfaces of constant T .

Furthermore, the almost linear behavior of $T(\underline{x} + \underline{r})$ on \underline{r} for $|\underline{r}| < r_c$ allows us to linearly expand $T(\underline{x} + \underline{r})$ in the exponent around \underline{x} and write:

$$\omega_0 T(\underline{x} + \underline{r}) = \omega_0 T(\underline{x}) + \omega_0 \nabla_{\underline{r}} T(\underline{x}) \cdot \underline{r} = \omega_0 T(\underline{x}) + k(\underline{x}) \cdot \underline{r} \quad (7)$$

where $k(\underline{x}) = k_1(\underline{x}) - k_2(\underline{x})$, and $k_1(\underline{x})$ and $k_2(\underline{x})$ are the local wave number of the incident and scattered wave, respectively. With this approximation we can write:

$$C(\tau, t) = \int d^3x dt' d\tau' K^2(\underline{x}) p(t' - T(\underline{x})) p^*(t' + \tau' - T(\underline{x})) \\ \cdot h(t - t') h^*(t + \tau - t' - \tau') \hat{\rho}(\underline{k}(\underline{x}), \tau'; \underline{x}) \quad (8)$$

where $\rho = (\xi, \tau; \underline{x})$ is the spatial Fourier transform of $\rho(\underline{r}, \tau; \underline{x})$ defined by

$$\rho(\xi, \tau; \underline{x}) = \int d^3r e^{-i\xi \cdot \underline{r}} \rho(\underline{r}, \tau; \underline{x}) \quad (9)$$

Notice that as far as \underline{r} is concerned, \underline{x} can be considered as a constant parameter. Also notice that the output of the experiment depends only on the Fourier component evaluated at a particular set of wave numbers $\underline{k}(\underline{x})$, which for most cases is a constant. It is equal to $2k_1$ in the backscatter case. Equation (8) is the general expression we are after; it involves only two basic assumptions and one approximation regarding the length scale of $\rho(\underline{r})$. It can be used as the starting point for simpler expressions applicable to the particular cases.

Next we consider a few particular cases as illustrative examples.

Case 1. Continuous excitation.

In the case of a cw bistatic experiment, e.g., the French incoherent scatter radar, we have $p(t) = a$, where a is a constant.

In such a case the output of the experiment is time stationary and the correlation function, $C(\tau) \equiv C(\tau, t)$, is given by

$$C(\tau) = a^2 \int d^3x K^2(\underline{x}) \int d\tau' \hat{\rho}(\underline{k}(\underline{x}), \tau', \underline{x}) \phi_{hh}(\tau - \tau') \quad (10)$$

where the second integral is the usual convolution of the correlation function of the input signal to a filter by the autocorrelation function, $\phi_{hh}(\tau)$ of the filter characteristic. The spatial integral represents a weighted average of the contributions of each differential volume, weighted by the beam patterns of the antenna (and the $1/R^2$ dependence). For homogeneous media and constant $\underline{k}(\underline{x}) = \underline{k}$, the spatial integral is independent of ρ and defines a volume, V , and we have

$$C(\tau) = a^2 K^2 V \int \hat{\rho}(\underline{k}, \tau) \phi_{hh}(\tau - \tau') d\tau' \quad (11)$$

The above equations, if expressed in the frequency domain, take an even simpler form where the convolution integral is transformed to a product of frequency functions.

Case 2. Filter time scale smaller than characteristic time of ρ .

In this case the integrand is different from zero for small values of the argument of $h(\bullet)$, i.e., when

$$t \approx t'$$

$$\tau \approx \tau' + t' - t$$

Thus, $\rho(\underline{k}(\underline{x}), \tau'; \underline{x})$ can be taken out of the τ' integral evaluated at $\tau' = \tau$. We can then write (8) as

$$C(\tau, t) = \int d^3 \underline{x} K^2(\underline{x}) \hat{\rho}(\underline{k}(\underline{x}), \tau; \underline{x}) \bar{p}(t - T(\underline{x})) \bar{p}^*(t + \tau - T(\underline{x})) \quad (12)$$

where \bar{p} is defined as

$$\bar{p}(t) = \int dt' p(t') h(t - t') \quad (13)$$

that is the pulse shape passed through the filter or decoder. In optimum designs $h(t)$ is identical to $p(t)$, and $\bar{p}(t)$ is then the autocorrelation of the pulse shape. In multiple pulse experiments the filter is identical to a pulse element of the sequence and $\bar{p}(t)$ is a sequence of autocorrelated pulses.

Surface of constant delay, $T = T(\underline{x})$, can be used as one of the variables of integration (e.g., range in a backscatter case with plane wave fronts) and a suitable set of two transverse coordinates, \underline{s} , for the remaining two. We can then write:

$$d^3 \underline{x} = d^2 \underline{s} c dT \quad (14)$$

where c is the local phase velocity of light taken to be a constant for simplicity, $d^2 \underline{s}$ is a surface differential. Equation (2) then takes the form

$$C(\tau, t) = c \int d^2 \underline{s} \int dT K^2(\underline{s}, T) \hat{\rho}(\underline{k}(\underline{s}), \tau; \underline{s}, T) \bar{p}(t - T) \bar{p}^*(t - T + \tau) \quad (15)$$

Case 3. Backscattering from a (quasi-) homogeneous and isotropic medium.

This case illustrates the effect of decoding and filtering on the dependence of the autocorrelation function. The assumptions involved allow us to replace $\hat{\rho}(\underline{k}(\underline{x}), \tau'; \underline{x})$ by $\hat{\rho}(\underline{k}, \tau')$ and to take it out of the spatial integral. For quasi-homogeneous cases we can take $\hat{\rho}(\underline{k}, \tau; \underline{x})$ with the value it has at the center of the volume, which corresponds to the particular delay \bar{t} of the measurement. Therefore we will write $\rho(\underline{k}, \tau')$ to extend the generality.

We can also perform the spatial integral in terms of the variables \underline{s} and T . Only $K^2(\underline{x})$ is a function of \underline{s} and we can perform the integral with respect to this variable. If K^2 is a factor which

groups all the dimensional factors in $K^2(x)$ then the spatial integral gives us $K^2A(T)$, where $A(T)$ is an equivalent area defined by the s dependence of the beam pattern. On most cases of interest $A(T)$ is a slowly varying function of T , slower than the pulse length and can be taken out of the integral evaluated at the sampling delay t . Considering the above we write equation (8) as

$$\begin{aligned} C(\tau, t) &= CK^2A(t) \int d\tau' d\tau' dT \hat{\rho}_i(k, \tau') p(t' - T) p^*(t' + \tau' - T) h(t - t') h(t + \tau - \tau' - t') \\ &= CK^2A(t) \int d\tau' \hat{\rho}_i(k, \tau') \int d\tau' h(t - t') h^*(t - t' + \tau - \tau') \int dT p(t' - T) p^*(t' + \tau' - T) \end{aligned} \quad (16)$$

or

$$C(\tau, t) = CK^2A(t) \int d\tau' \hat{\rho}_i(k, \tau') \phi_{pp}(\tau') \phi_{hh}(\tau - \tau') \quad (17)$$

where $\phi_{pp}(\tau)$ is the autocorrelation function of the pulse shape and $\phi_{hh}(\tau)$ the autocorrelation function of the filter and decoding system.

Illustrative Examples

In order to gain a better understanding of the significance of the formulas derived for cases 2 and 3, we have constructed Figures 3 and 4, respectively, corresponding to two often used pulse schemes. Case 1 does not need an illustration since in this case the spectrum of the signal received is just the product of the spectrum of the medium with the systems filter characteristics.

Figure 3 depicts the different shapes of the functions involved for a double-pulse experiment, in a backscatter mode, in which two narrow pulses are sent, τ_s apart. In this case the experiment provides information on the correlation function $\hat{\rho}_i(k, \tau')$, at only one delay, $\tau = \tau_s$, corresponding to the pulse separation. In practice the correlation function is evaluated only at this delay. To obtain the value of the correlation function at other delays, another pair of pulses is sent with the proper spacing.

Notice that $C(\tau, t)$ is different from zero only in the vicinity of τ_s , the useful part, and in the vicinity of $\tau = 0$ corresponding to a power measurement. Such power measurement is not useful since it contains not only the contribution from the desired height but also the "self-clutter" contribution from $t - \tau_s$, as illustrated in the two-dimensional plot of $\bar{p}(t - T) \bar{p}^*(t - T + \tau)$.

Multiple pulse schemes can be illustrated in a similar fashion, the main difference being that several correlation delays can be estimated in a single sequence and that the self-clutter is larger and coming from several different altitudes.

Figure 4 illustrates the case in which a long pulse (as compared to the medium correlation times) is sent. The receiver impulse response is narrow and considered square for the sake of simplicity. Two effects are clear from the picture, the medium correlation function is multiplied by a triangular function, $\phi_{pp}(\tau)$, and the result convolved with a narrower function, $\phi_{hh}(\tau)$, given by the self-convolution of the filter input response.

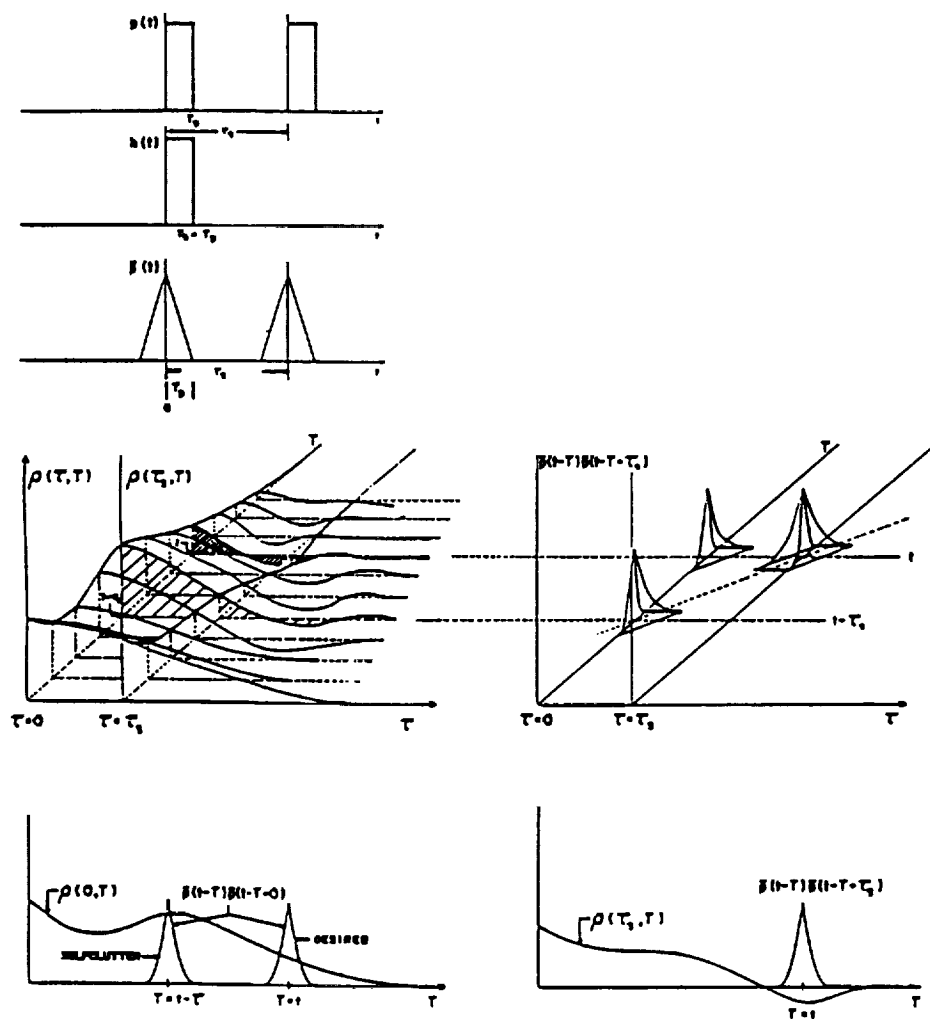


Figure 3.

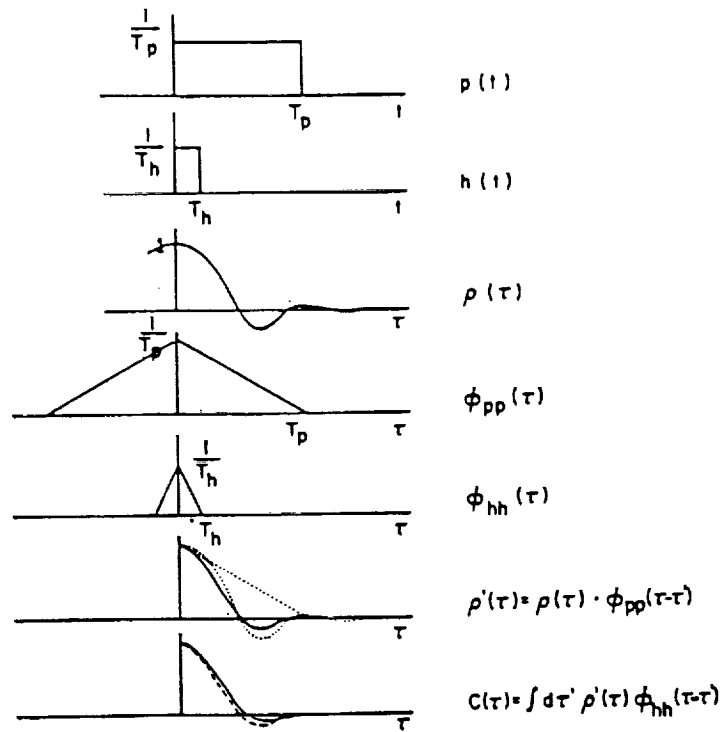


Figure 4.

N 9 1 - 2 6 6 1 8

Chapter 5

Data Acquisition and processing

Toshitaka Tsuda

Radio Atmospheric Science Center, Kyoto University

1 INTRODUCTION

This chapter is devoted to describing fundamental methods of signal processing used in normal MST radar observations. Complex time series of received signals obtained in each range gate are converted into Doppler spectra, from which the mean Doppler shift, spectral width and signal-to-noise ratio (SNR) are estimated. These spectral parameters are further utilized to study characteristics of scatterers and atmospheric motions.

Since it is beyond a scope of this note to describe general techniques developed in radar engineering, readers are encouraged to study a comprehensive textbooks on modern radar techniques such as *Cook and Bernfeld* [1967], *Barton* [1976], *Skolnik* [1981]. Fundamental and advanced techniques of digital signal processing are also summarized by *Gold and Rader* [1969] and *Bendat and Piersol* [1971].

Detailed descriptions of clear air radars operating at frequencies ranging from VHF to a microwave are given by *Gossard and Strauch* [1983] and *Doviak and Zrnić* [1984]. General MST radar techniques are also reviewed by many authors [e.g., *Gage and Balsley*, 1978].

2 RECEIVER HARDWARE

Fig. 1 schematically shows the simplified structure of an MST radar system and the flow of received signals. A VHF or UHF sine wave carrier generated by a stable oscillator is modulated by a rectangular pulse with a width of a few microseconds. This is commonly called a pulsed continuous wave (CW). The transmitted radio wave is backscattered toward the radar. The radar echo is fed to a receiver system through a TR-switch that protects the receiver from damage caused by the high power of the transmitter during the transmission. The received RF signal, which is usually a replica of the transmitted signal, is pre-amplified by a radio frequency (RF) amplifier. The RF signal is mixed with a coherent local (LO) signal and is down-converted to an intermediate frequency (IF) signal.

After maximizing the peak-signal-to-noise power ratio in the IF amplifier, the IF signal is detected by a quadrature detector, which produces a time series of sine and cosine components of the received signal. The detected signal is finally converted to digital signal by an analogue-to-digital (AD) converter, then transferred to a digital signal processing system.

The pulse may be compressed by phase modulation, which is decoded before or after the AD conversion by an analogue or digital correlator, respectively.

3 MATCHED FILTER

The IF-amplifier is generally regarded as a filter with gain, which should be designed to maximize the peak signal-to-noise power ratio SNR_P . Note that the peak signal power defined here corresponds to the maximum instantaneous power, and not to the integrated signal power within the bandwidth. Thus, the SNR_P is not equal to the SNR, which is a

ratio of the integrated signal power to the integrated noise power within the bandwidth. The latter is used in later sections.

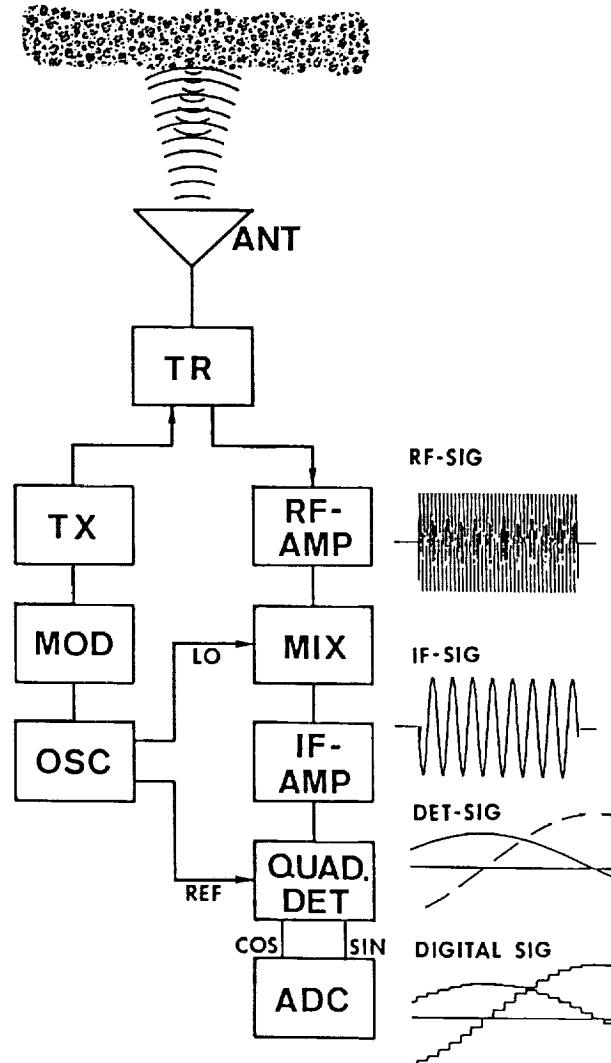


Fig. 1. Block diagram of a typical MST radar system, together with signal waveforms.

Fig.2 shows typical frequency spectra of a pulsed CW signal with a width (duration) τ and of noise. The former is approximated by

$$\left(\frac{\sin(2\pi\hat{f}/2)}{2\pi\hat{f}/2}\right)^2 \quad (1)$$

where \hat{f} is a frequency normalized by $1/\tau$, while the noise can be considered to be white, i.e., its intensity is statically independent of frequency. Although the received signal contains many Fourier spectral components, the receiver amplifies only components that are within a finite bandwidth.

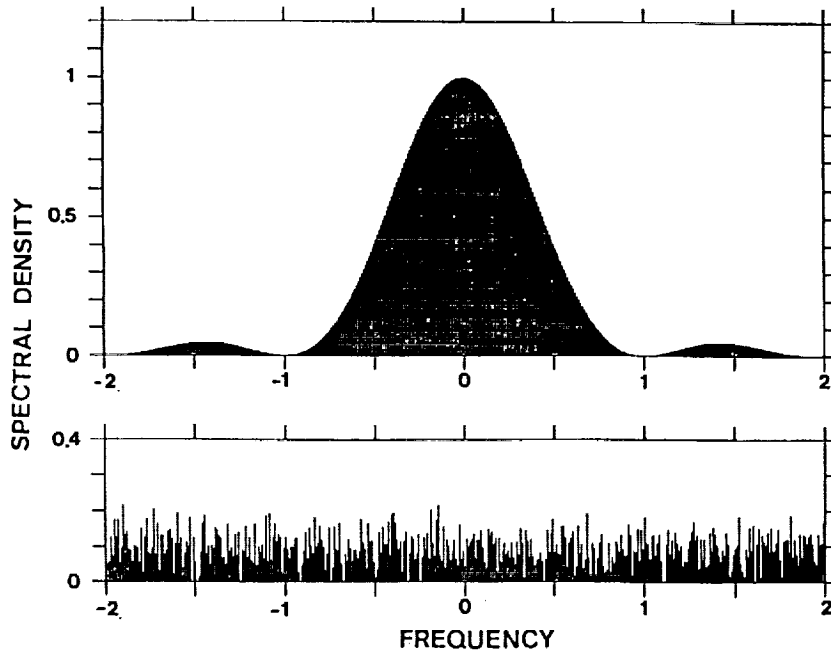


Fig. 2. Frequency spectrum of a pulsed CW signal (top panel) and white noise (bottom panel). The frequency is normalized by the inverse of the rectangular pulse width.

Fig. 3 shows the integrated power of the signal and noise spectra shown in Fig. 2 as a function of double-sided bandwidth B . Since noise spectral density is distributed uniformly in the frequency range of the signal, the integrated noise power is proportional to the receiver bandwidth B . On the other hand, the signal power increases rapidly when B is small, then approaches a constant value as B becomes larger.

When B is considerably narrower than the bandwidth occupied by the signal, the signal energy is not effectively detected by the signal processing, although the noise energy is reduced. On the other hand, if B is wide compared with the signal bandwidth, extraneous noise is introduced by the excess bandwidth, which lowers the output SNR_P. Thus, there is an optimum bandwidth depending on the signal spectrum.

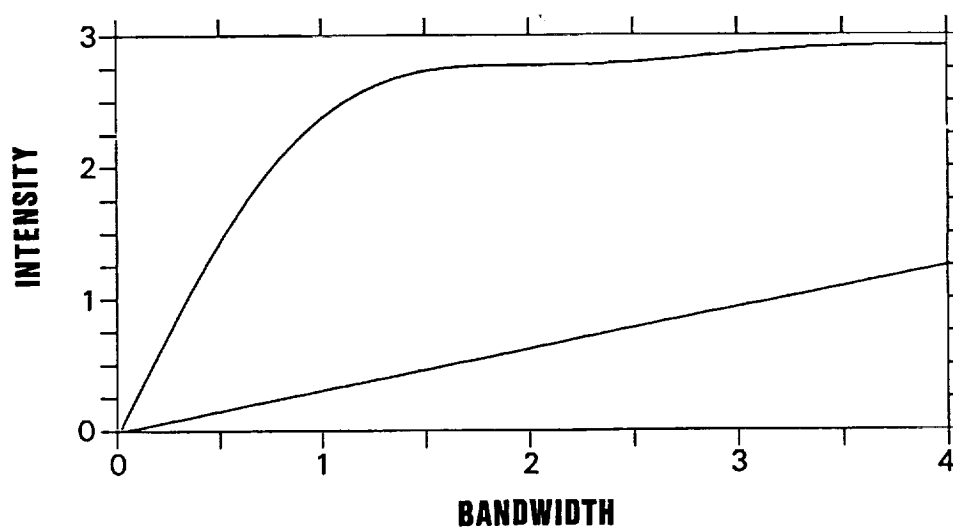


Fig. 3. Integrated power of the signal (upper curve) and noise (lower curve) spectra shown in Fig. 2. The bandwidth is a double-sided frequency range.

The optimum filter is obtained by applying a matched filter design [e.g., *Barton, 1976; Skolnik, 1981*], which is generally defined as a network whose frequency-response function is matched to the pre-filter signal spectrum in order to maximize SNR_p .

The frequency-response function of the IF-amplifier $H(f)$ specifies the relative amplitude and phase of the output signal with respect to the input when the input is a pure sinusoid. For a received signal voltage spectrum $S(f)$, $H(f)$ for the matched filter can be expressed as

$$H(f) = G_a S^*(f) \exp(-i2\pi f t_d) \quad (2)$$

where G_a and t_d are the gain of the network and the time delay. $H(f)$ is the complex conjugate of the signal spectrum except for a phase shift due to the time delay.

As a result, the normalized amplitude spectrum of the matched filter, which corresponds to the filter passband characteristics, is the same as the amplitude spectrum of the signal, but the phase spectrum of the matched filter is the negative of the phase spectrum of the signal plus a phase shift proportional to frequency. By using phase spectra $\phi_S(f)$ and $\phi_H(f)$ for the signal and matched filter, respectively, Eq. (2) can be rewritten as follows:

$$\begin{aligned} |H(f)| &= |S(f)| \\ \phi_H(f) &= -\phi_S(f) + 2\pi f t_d \end{aligned} \quad (3)$$

Specification of the optimum receiver characteristics involves the frequency-response function and the shape of the received waveform, which is usually a replica of the transmitted signal spectrum. The transmitted signal spectrum is usually tapered from the spectrum of a rectangular pulsed CW in order to suppress harmonics and spurious transmission. Therefore, the matched filter design largely depends on the transmitter characteristics.

It is often impractical to construct the exact matched filter. If the signal wave form

is a rectangular pulsed CW, to simplify the filter hardware the matched filter for the IF-amplifier is approximated by a band-pass filter (BPF). The optimum IF bandwidth B_{IF} is the order of $1/\tau$. More precisely, it can be shown that B_{IF} should be $1.4/\tau$ for the optimum rectangular filter.

4 OUTLINE OF A DIGITAL PROCESSING SYSTEM

Fig. 4 shows the flow of the signal processing for a digital signal transferred from the receiver. This processing can be done either in real-time or in an off-line computation, depending on the capability of the system-installed computer system.

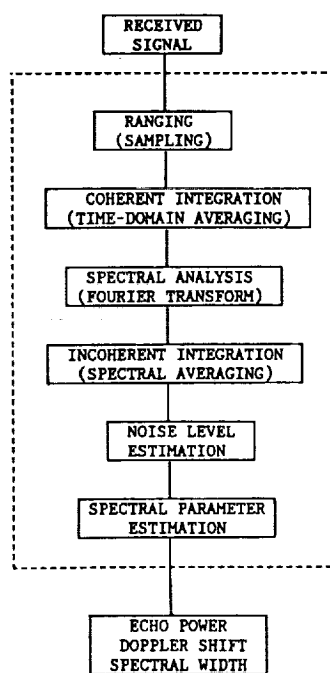


Fig. 4. Flow diagram of a typical digital signal processing system.

The sampled digital signal is arranged as a function of a round-trip time from transmission to reception, which is generally called ranging, and is coherently integrated in order to increase a signal-to-noise ratio SNR. The complex time series of the received signal is Fourier transformed into Doppler spectra. After incoherently averaging the Doppler spectra, the noise level is estimated. Spectral parameters such as the SNR, mean Doppler shift and spectral width are estimated from the Doppler spectra. They are usually stored in a mass storage system for further analysis of radar reflectivity, wind fields and turbulence parameters.

5 RANGING

For a monostatic pulse radar, the distance, or range R to the scatterer from the radar becomes

$$R = \frac{cT_R}{2} \quad (4)$$

where c is the speed of light $c = 3 \times 10^8$ m/s, and T_R is the time interval between the pulse transmission and detection. The denominator 2 appears in (4) because T_R corresponds to the round-trip time interval for radio wave propagation over the range R . In convenient units (4) becomes

$$R(\text{km}) = 0.15T_R(\mu\text{s}) \quad (5)$$

Fig. 5 schematically shows a time-height chart between the range and the round-trip time interval for a radar echo. The interval t_{IPP} between successive pulse transmissions is called the inter-pulse-period (IPP), and the corresponding frequency is called the pulse repetition frequency (PRF). Normally MST radars are operated with uniform IPP, which is, for an example, set equal to 1 ms in Fig. 5. H_m in Fig. 5 is defined as $ct_{IPP}/2$.

The SNR is linearly dependent on the average transmitted power in the IPP. Therefore, in order to increase the SNR, the IPP should be as short as possible when the pulse length and peak transmitting power are fixed. On the other hand, a sufficient length of time must elapse after a pulse is transmitted in order to receive all of the radar echoes before the transmission of the next pulse. Thus, the IPP is determined primarily by the longest range at which targets are expected.

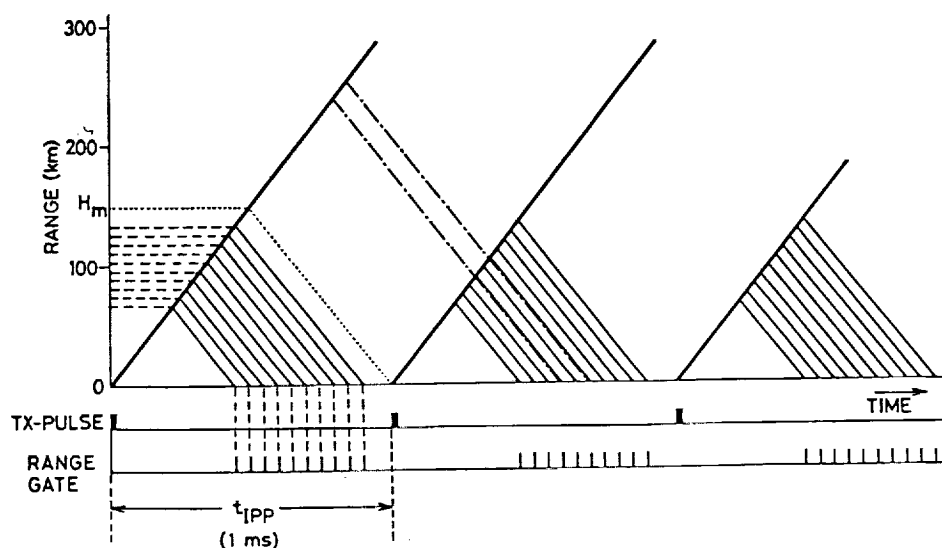


Fig. 5. Time-height chart for MST radar observations when when IPP is 1 ms. Thick and thin solid lines correspond to propagation of transmitted and scattered radiowaves, respectively. The received signal is sampled 10 times with equally spaced range gates as indicated by the dash lines. The dot-dash lines show a second-time-around echoes due to ionospheric scattering.

If the IPP is too short, echo signals from some targets might arrive after the transmission of the next pulse, as indicated by the dot-dash lines in Fig. 5. These echoes from a range greater than $ct_{IPP}/2$ are received during the same interval that as echoes from targets nearer than $ct_{IPP}/2$ return echoes from the next pulse. As a result, instead of their actual range R , they appear to have a range $R - H_m$ or R minus a multiple of H_m .

This ambiguity in the ranging is called a range aliasing. Signals that arrive after the transmission of the next pulse are generally called second-time-around (or multiple-time-around) echoes. The range H_m is called the maximum unambiguous range, beyond which targets appear as second-time-around echoes.

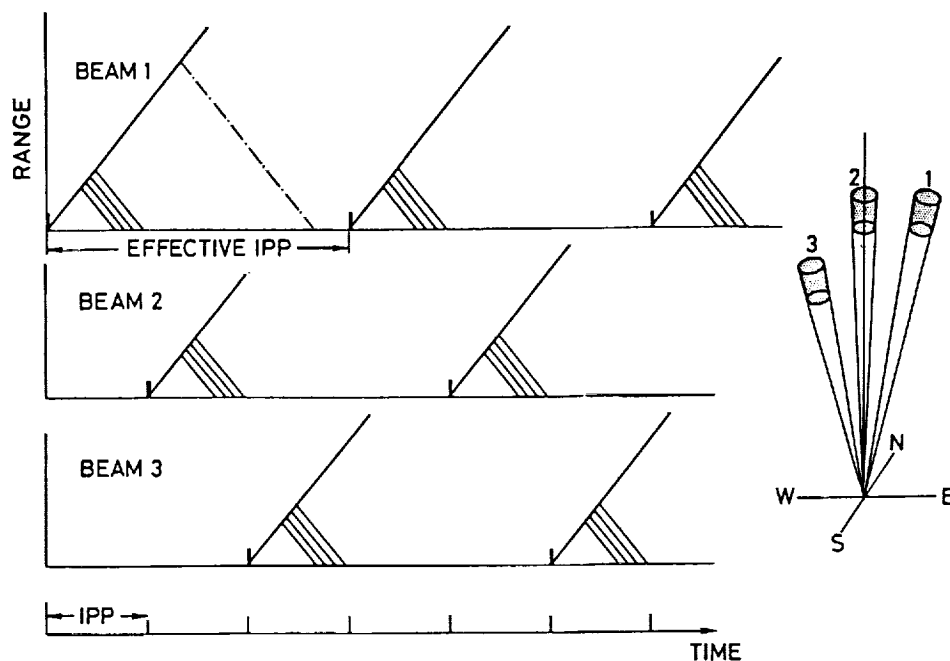


Fig. 6. Time-height chart for an MST radar whose antenna beam is steered every IPP into three directions as shown in the right panel.

For normal MST radar observations, clear air echoes are usually detected at heights lower than 100 km, which corresponds to $t_{IPP} = 667\mu\text{s}$. So, the IPP is usually set equal to less than 1 ms. Then, echoes scattered from the ionosphere would be received as shown in Fig. 5. These can be considered as a kind of multiple-time-around echoes, although characteristics of radar echoes are fairly different between the first and multiple-time-around echoes. The normal ionospheric echoes are much weaker than the clear air echoes and have much a broader spectral distribution, therefore, they may instead act as a white noise added to the normal cosmic noise. Although range-aliased ionospheric echoes increase the noise level, depending on the electron density, they do not usually present a large problem in estimating the spectral parameters of the Doppler spectra when the SNR is significantly large.

However, the intense radar echoes that are sometimes received from ionospheric irregularities such as sporadic E layers or meteor trails may seriously contaminate the clear air echoes. In such cases, t_{IPP} should be made large enough to remove the range aliasing.

Another way to weaken the effects of range aliasing is to change the antenna beam direction between every pulse. Fig. 6 shows the time-height chart for an MST radar that is steered sequentially into three directions, eastward, vertical and southward, denoted 1, 2 and 3. Thus, the effective IPP in each beam direction becomes three times the original IPP, which is usually large enough to remove the multiple-time-around echoes from the ionosphere. Of course, this technique can only be used with a directionally agile radar such as the MU radar [Kato et al., 1984].

6 RADAR SAMPLING VOLUME

Normal MST radar observations assume that the volume illuminated by the radar antenna beam is filled with scatterers. Fig. 7 schematically shows transmission and reception of a purely rectangular pulse with a width τ . The leading edge of the transmitted pulse covers distances from z_0 to $z_0 + c\tau/2$, while the tail end of the pulse goes from $z_0 - c\tau/2$ to z_0 . In total, the sampling volume extends from $z_0 - c\tau/2$ to $z_0 + c\tau/2$ with a thickness of $c\tau$. The right panel in Fig. 7 shows that the weighting function of the sampling volume has a triangular distribution partly overlapping the weighting function of the adjacent upper and lower sampling volumes. The range resolution is usually expressed as $c\tau/2$, which corresponds to the half power width of the weighting function.

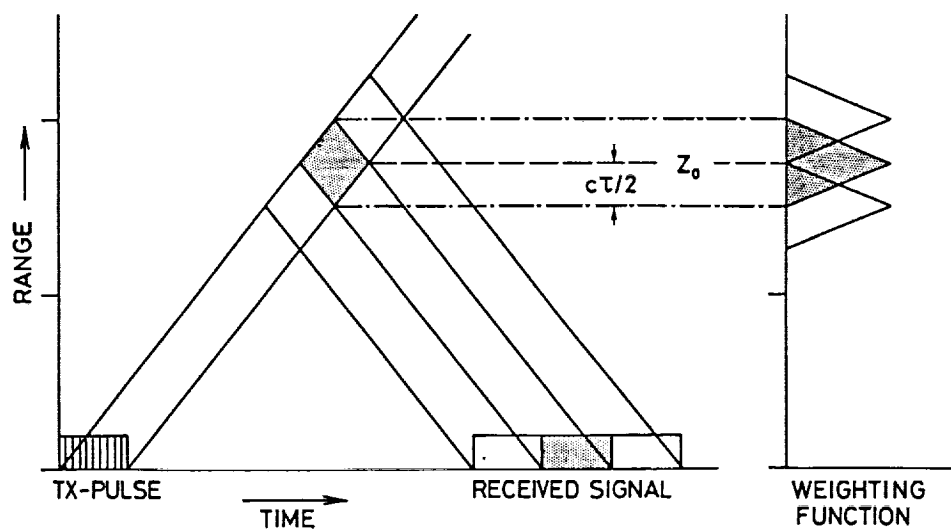


Fig. 7. Time-height chart and sampling weight when a rectangular pulse is transmitted.

The effective direction of radar echoes is usually assumed to be aligned with the antenna bore-sight direction. Therefore, the height of the radar sampling volume can be calculated by multiplying the range times $\cos \theta$ as shown in Fig. 8. In the vertical direction, the height resolution is the same as the range resolution. On the other hand, since the sampling volume for an oblique antenna beam is inclined to the horizon, the vertical distance between the highest and lowest points of the sampling volume is usually larger than the range resolution. That is, $\Delta R \cos \theta$ is not necessarily equal to ΔH as shown in Fig. 8.

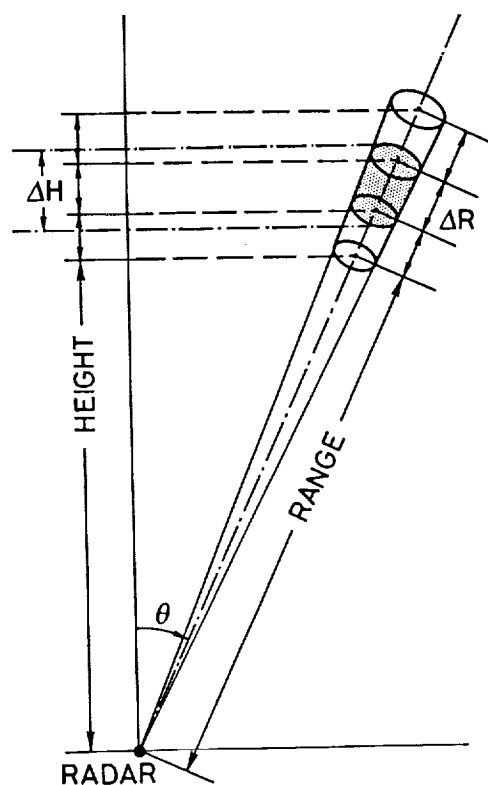


Fig. 8. The sampling volume for an oblique antenna beam.

The actual shape of the sampling volume depends on the exact shape of the transmitted pulse and antenna gain pattern. Fig. 9 shows an example of the weighting function at a range of 10 km when the pulse length and half-power, full-width antenna beam width are $1 \mu\text{s}$ and 3.7° , respectively. In order to optimize the range resolution, the pulse width should be as short as possible within the limitations of the radar system. However, the height resolution in oblique directions may not be improved by shortening the transmitted pulse width when the antenna beam is not narrow enough.

So far we have assumed that radar scatterers are uniformly distributed in the radar sampling volume. In the real atmosphere, scatterers are sometimes horizontally stratified in layers with thicknesses thinner than the sampling volume. When these thin layers are distributed unevenly in the sampling volume, the effective antenna direction becomes different from the antenna bore-sight direction, which causes an error in converting from range to altitude [e.g. Fukao et al., 1988; May et al., 1988].

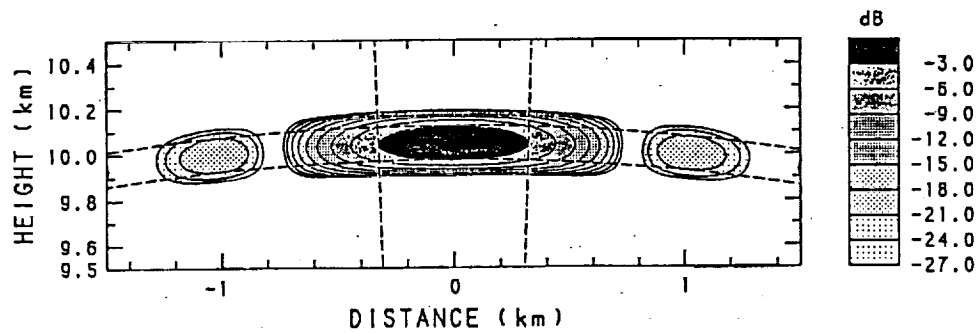


Fig. 9. The sampling weight for MU radar observations when the transmitted pulse width and half-power, full-width beam width are $1 \mu\text{s}$ and 3.7° , respectively.

In the lower stratosphere scattering from stratified layers is usually not isotropic, but has characteristics of specular reflection. In this case, the effective antenna direction is determined by the product of the antenna pattern and the angular distribution of the reflectivity. This usually biases the beam direction toward the zenith. [e.g., Röttger, 1981; Tsuda *et al.*, 1986].

7 COHERENT INTEGRATION

The detected quadrature signals are usually integrated for many pulses in order to increase the SNR. This digital signal processing is called a coherent integration, which requires that the phase of successively received signals be consistent with that of the local reference signal.

Before proceeding to a discussion of the effects of the coherent integration, it might be useful to review briefly the concept of a χ^2 -distribution, which is commonly used in expressing noise power characteristics. We first assume that a random variable x has a Gaussian probability distribution function, expressed as

$$a(x) = \frac{1}{\sqrt{2\pi}} \exp\left(-\frac{x^2}{2}\right) \quad (6)$$

where the mean value and standard deviation are assumed to be 0 and 1, respectively. When intensities of x are integrated M times as

$$y = x_1^2 + x_2^2 + x_3^2 + \dots + x_M^2 \quad (7)$$

it can be shown that y has a χ^2 -distribution given by

$$b(y) = \frac{(y/2)^{M/2-1} \exp(-y/2)}{2\Gamma(M/2)} \quad (8)$$

where $\Gamma(M/2)$ is defined as

$$\begin{aligned}\Gamma(M/2) &= \left(\frac{M}{2} - 1\right)! \quad (\text{when } M=\text{even integer}) \\ &= \left(\frac{M}{2} - 1\right)\left(\frac{M}{2} - 2\right) \dots \frac{1}{2} \sqrt{\pi} \\ &\quad (\text{when } M=\text{odd integer and } M \geq 3) \\ &= \sqrt{\pi} \quad (\text{when } M=1)\end{aligned}\tag{9}$$

The mean value μ and standard deviation σ of the χ^2 -distribution are

$$\begin{aligned}\mu &= M \\ \sigma &= \sqrt{2M}\end{aligned}\tag{10}$$

Therefore, when the square of a random variable is integrated M times, the resultant mean value is increased by M , where M is called the degrees of freedom of the χ^2 -distribution. It is noteworthy that the ratio between the standard deviation and mean value is

$$\frac{\sigma}{\mu} = \sqrt{\frac{2}{M}}\tag{11}$$

which means that after M of integrations, as in (7), the distribution about the mean becomes narrower.

Now we investigate the increase of the SNR after coherent integration. If N_c coherent signals with the same SNR are integrated, the resultant signal amplitude becomes N_c times that of a single value, therefore, the signal intensity is increased by N_c^2 .

On the other hand, when uncorrelated noise amplitudes are integrated over N_c samples, the resultant noise power can be expressed by (7). Because we can assume that the

noise amplitude has a Gaussian distribution, the noise power follows the χ^2 -distribution with degrees of freedom equal to N_c , so that the integrated noise power is increased by N_c . As a result, coherent integration over N_c pulses improves the SNR by N_c .

Coherent integration corresponds to digital filtering with a boxcar weighting in the time domain. The signal power spectrum after coherent integration becomes the product of the original IF-signal spectrum and a weighting function expressed as

$$\left(\sin\left(\frac{2\pi f}{2/\Delta t}\right)/\frac{2\pi f}{2/\Delta t}\right)^2 \quad (12)$$

where $\Delta t = N_c t_{IPP}$.

In order to increase the SNR, the number of coherent integrations should be selected to span the interval over which the received signals are phase coherent with each other. There are two effects that make the integration time finite: movement of the scatterers relative to each other within the radar sampling volume, and the mean motion of scatterers relative to the radar due to background wind fields.

The relative motion of the scatterers is estimated by the correlation time, which is defined as the half-power width of the auto-correlation function of the received signal. It depends on the radar wavelength, antenna beam width and altitude [Gossard and Strauch, 1983] and becomes of the order of 0.1 to 1 sec for MST radars operating at VHF or UHF (radar wavelengths ranging from 0.1 to 10 m).

As described later, the inverse of the coherent integration time corresponds to half of the maximum frequency range of the Doppler spectra. Therefore, the integration time should be short enough to determine unambiguously the maximum radial wind velocity. This condition usually puts a practical limit on the length of the coherent integration.

8 DOPPLER VELOCITY

As shown in Fig. 4 the main procedure of digital signal processing is Fourier transformation of the time series of the received signal constructed at each range gate after increasing the SNR by coherent integration.

For a monostatic radar, signals received from stationary targets have time independent phase $\psi = -2\pi(2R/\lambda) + \text{constant}$, where λ is the radar wavelength. If R increases with time because of the radial component V_R of the motion of the scatterer, the phase decreases and the time rate of change of phase becomes

$$\frac{d\psi}{dt} = -\frac{4\pi}{\lambda} \frac{dR}{dt} = -\frac{4\pi}{\lambda} V_R = -2\pi f_D \quad (13)$$

which appears as the Doppler shift from the carrier frequency of the scattered radiowave. The Doppler frequency shift is related to the radial Doppler velocity as

$$V_R = \frac{\lambda}{2} f_D \quad (14)$$

The shift is positive for motion toward the radar.

In the earth's atmosphere the horizontal wind velocity can range up to about 100 m/s near the peak of jet streams, while the vertical wind speed is only of the order of one tenth to a few m/s. Thus when radial wind velocities are sampled at zenith angles of 10 to 30°, they can be as large as 10 to 50 m/s. The Doppler spectrum should be constructed by taking into account the wind velocity resolution and the maximum unambiguous velocity.

9 DISCRETE FOURIER TRANSFORM

The Fourier transform $F(f)$ of an infinite time series $X(t)$ is defined as

$$F(f) = \int_{-\infty}^{\infty} X(t) e^{-i2\pi f t} dt \quad (15)$$

where f is the frequency. An actual signal processing system treats only a finite time series that is discretely sampled N times at intervals of Δt . Thus the total length of the time series is $T_m = N\Delta t$.

Fig. 10 shows three sinusoidal oscillations with slightly different frequencies. The vertical lines indicate sample timings. The oscillation plotted by the dashed curve has a frequency $f_N = 1/(2\Delta t)$, which is half of the sampling frequency. When an oscillation has a frequency lower than f_N , it can be detected if the sampling is continued long enough, while oscillations with frequencies higher than f_N cannot be correctly estimated. In order to specify completely a sinusoidal oscillation, at least two sampling points are needed within one cycle of the oscillation. Therefore, f_N , called the Nyquist frequency, is the highest frequency that can be unambiguously measured in a discretely sampled time series.

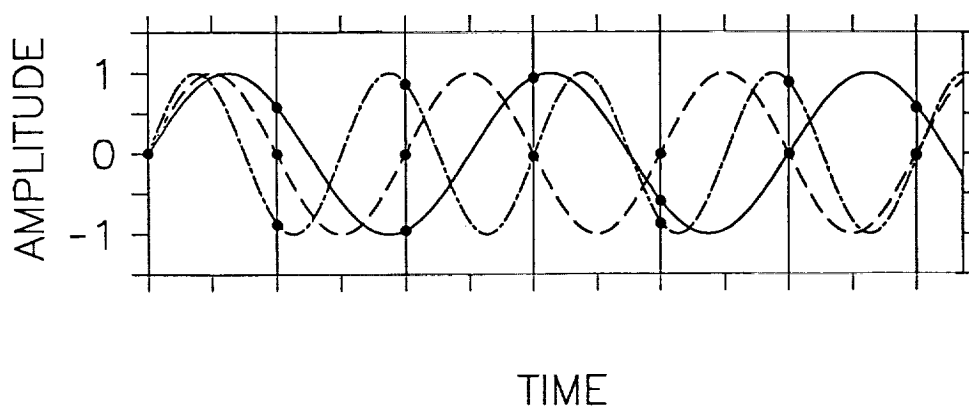


Fig. 10. Three sinusoidal signals with frequencies lower (solid), equal to (dash) and higher (dot-dash) than the sampling frequency. The sample timings are indicated by the thin vertical lines.

The Fourier transform of a discrete complex time series X_n ($n=0$ to $N-1$) is usually approximated by a finite series of harmonic functions, called a discrete Fourier transform. The coefficient of the k -th harmonic component F_k ($k=0$ to $N-1$) is defined as

$$F_k = \frac{1}{N} \sum_{n=0}^{N-1} X_n W^{nk} \quad (16)$$

while the time series of data X_n ($n=0$ to $N-1$) can be recomposed as

$$X_n = \sum_{k=0}^{N-1} F_k W^{-nk} \quad (17)$$

where

$$W = \exp\left(-\frac{i2\pi\Delta t}{T_m}\right) = \exp\left(-\frac{i2\pi}{N}\right) \quad (18)$$

Note that $F_{k+N} = F_{k-N} = F_k$, because $W^N = 1$; that is, the width of the unambiguous frequency range of a discrete Fourier transform is $2f_N$. Doppler spectra are usually plotted in a frequency range from $-f_N$ to f_N . The frequency resolution of a discrete Fourier transform then becomes $2f_N/N = 1/(N\Delta t) = 1/T_m$.

10 FREQUENCY ALIASING

We demonstrate in this section that a time series X_n sometimes cannot be related to a unique frequency because of the finite sampling resolution. We assume three oscillations with different frequencies. The dot-dash line in Fig. 11 shows an oscillation with a frequency of $0.8f_N$, while the solid and dash lines correspond to $2.8f_N$ and $-1.2f_N$, respectively, which differ by $2f_N$ in the frequency domain. When these three oscillations are sampled at the same timings indicated by the vertical lines, they produce the same data time series. This effect, which occurs when frequencies of signals are separated by an integer multiple of $2f_N$, is called a frequency aliasing.

If there are signals with frequencies outside of $\pm f_N$, they contaminate the signal within $\pm f_N$. However, because the weighting function of the coherent integration has the filter pass characteristics described by (12) and also plotted in the center panel in Fig. 12, the intensities of the components outside of $\pm f_N$ are significantly reduced, as shown in the bottom panel in Fig. 12. It should be noted that the power spectral density within $\pm f_N$ is also reduced because of the weighting. Note also that when the spectral width is large the mean Doppler shift is slightly shifted. This is due to the asymmetric weighting of the signal spectrum by the coherent integration.

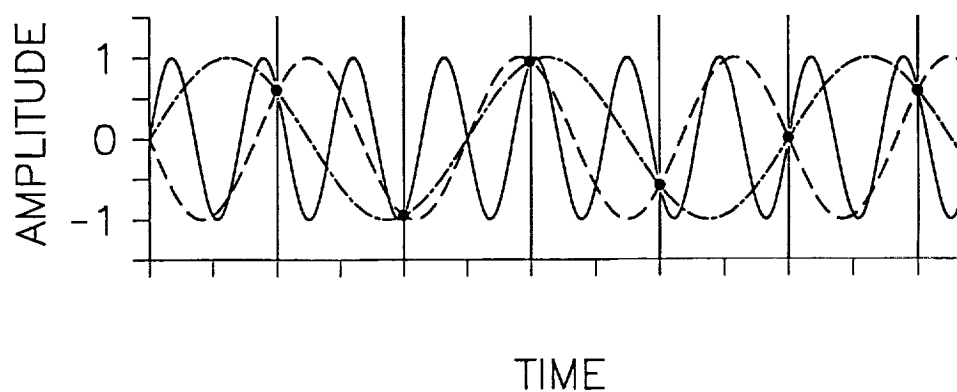


Fig. 11. The same as Fig. 10 except that the frequencies are at 0.8 (dot-dash), -1.2 (dash), and 2.8 (solid) times the Nyquist frequency (after Doviak and Zrnić, 1984).

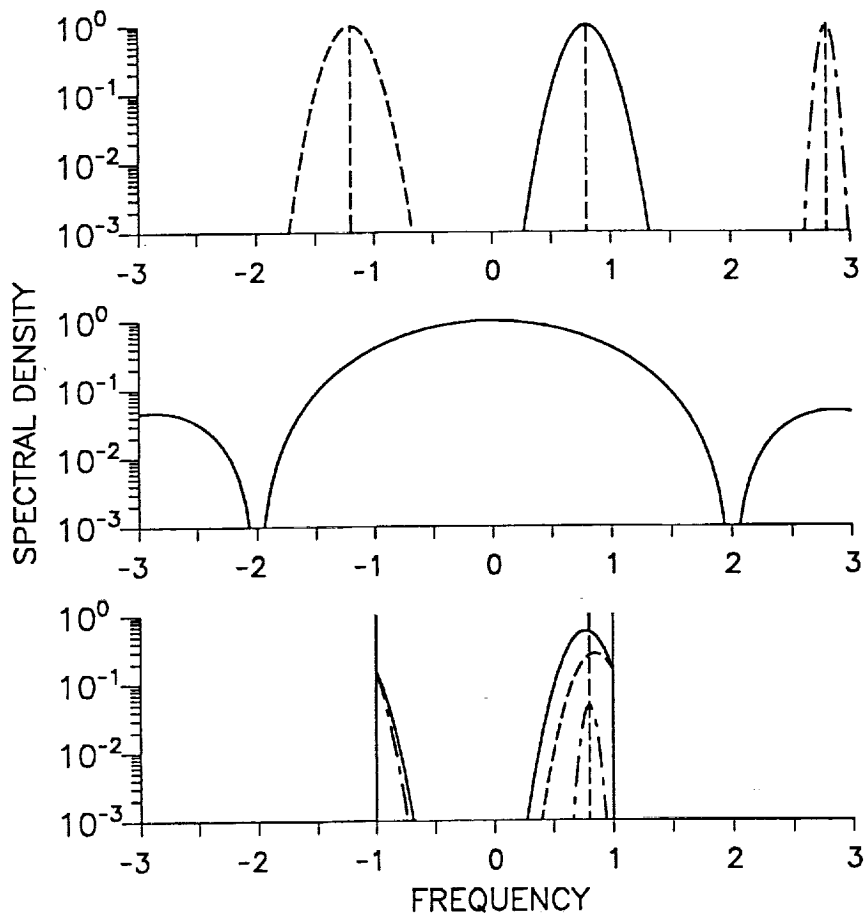


Fig. 12. Schematic diagram of frequency aliasing. The top panel shows Doppler spectra of three signals with center frequencies at $0.8f_N$ (solid), $-1.2f_N$ (dash) and $2.8f_N$ (dot-dash), where f_N is the Nyquist frequency. The center panel is the weighting function due to coherent integration, while the bottom panel shows the resultant spectrum. Vertical solid lines indicate the limits of the frequency range, while the dash line is at $0.8f_N$.

11 FAST FOURIER TRANSFORM (FFT)

Some recent MST radars have installed an array processor which is suitable for a large matrix calculations such as the discrete Fourier transform shown by Eq. (16). Most of them utilize a sophisticated technique called fast Fourier transform (FFT) [Singleton, 1967] in order to reduce computation time in analyzing the Doppler spectra.

Equation (16) indicates that N^2 multiplications are required to calculate a discrete Fourier transform. However, when N is a power of 2, part of the computation can be eliminated by using the characteristics of harmonic functions. For example, when $N = 8 = 2^3$, (16) becomes

$$\begin{aligned} NF_k &= X_0 + X_1W^k + X_2W^{2k} + X_3W^{3k} + X_4W^{4k} + X_5W^{5k} + X_6W^{6k} + X_7W^{7k} \\ &= (X_0 + X_2W^{2k} + X_4W^{4k} + X_6W^{6k}) + (X_1W^k + X_3W^{3k} + X_5W^{5k} + X_7W^{7k}) \\ &= (X_0 + X_2W^{2k} + X_4W^{4k} + X_6W^{6k}) + W^k(X_1 + X_3W^{2k} + X_5W^{4k} + X_7W^{6k}) \end{aligned} \quad (19)$$

which can be further rewritten as

$$F_k = \sum_{l=0}^{N/2-1} X_{2l}W^{2lk} + W^k \sum_{l=0}^{N/2-1} X_{2l+1}W^{2lk} = G_k + W^k H_k \quad (20)$$

Note that G_k and H_k are a matrix with a size of $N/2$. Therefore, total number of matrix computations becomes $2(N/2)^2$, which is reduced by a factor of 2 from (16). If $N/2$ is again a power of 2, then G_k and H_k can be further divided into smaller matrices to further reduce number of calculations. When N is a large power of 2, it can be shown that the total number of additions and multiplications to calculate an FFT increase approximately as $N \log_2 N$ and $\frac{1}{2}N \log_2 N$, respectively, which is significantly less than N^2 when N is large. The basic idea of the FFT can also be applied in cases when N is expressed by a mixed radix [Singleton, 1967].

12 INCOHERENT INTEGRATION AND DETECTABILITY

A typical Doppler velocity spectrum is shown in Fig. 13, which was observed by the MU radar in the lower atmosphere at a zenith angle of 10° . The horizontal axis corresponds to the radial wind velocity, while the vertical axis shows relative power spectral density.

The signal is the broad enhancement centered at about 9 m/s, and the peak signal spectral density is indicated by P_S . Random fluctuations spread in frequency ranges located at the left and right of the signal are due to white noise with a mean value and standard deviation of P_N and σ_N , respectively.

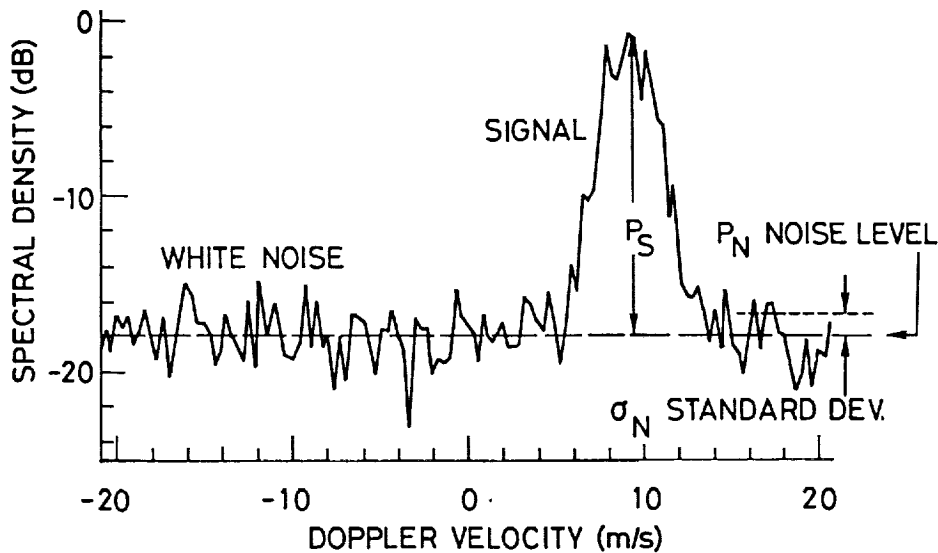


Fig. 13. A typical example of a Doppler velocity spectrum taken by the MU radar. The peak signal spectral density is indicated as P_S , while the noise level and standard deviation of noise are denoted as P_N and σ_N , respectively.

The detectability of a Doppler spectrum can be defined as

$$D = \frac{P_S}{\sigma_{S+N}} \quad (21)$$

where P_S is peak spectral density of the signal spectrum, and σ_{S+N} is standard deviation of spectral densities. When the fluctuation of the signal spectral densities is much smaller than that of the noise, (21) becomes

$$D = \frac{P_S}{\sigma_N} \quad (22)$$

which is more commonly used as a definition of the detectability [e.g., *Gage and Balsley, 1978; Balsley and Gage, 1980*].

The noise spectral density has a χ^2 -distribution with 2 degrees of freedom, because the noise spectral density is a summation of the squares of the real and imaginary components of the amplitude spectrum, which are assumed to have a Gaussian distribution.

For a single spectrum σ_N is equal to P_N . When Doppler spectra are integrated incoherently by averaging N_i times, the mean values of the spectral densities of both the signal and noise are not changed. But, σ_N/P_N becomes $1/\sqrt{N_i}$ according to (11), because N_i incoherent integration of the noise produces a χ^2 -distribution with $2N_i$ degrees of freedom. As a result, D is increased by $\sqrt{N_i}$.

Fig. 14 demonstrates the effects of incoherent integration by using a numerical simulation. The signal portion is not clearly recognizable in the spectrum plotted in the top panel in Fig. 14, which does not include any incoherent integration. On the other hand, the signal spectrum becomes easily visible in the bottom panel, which is the result of 20 incoherent integration. In normal MST radar observations, spectral parameter estimation can be done reasonably well when D is larger than about 3.

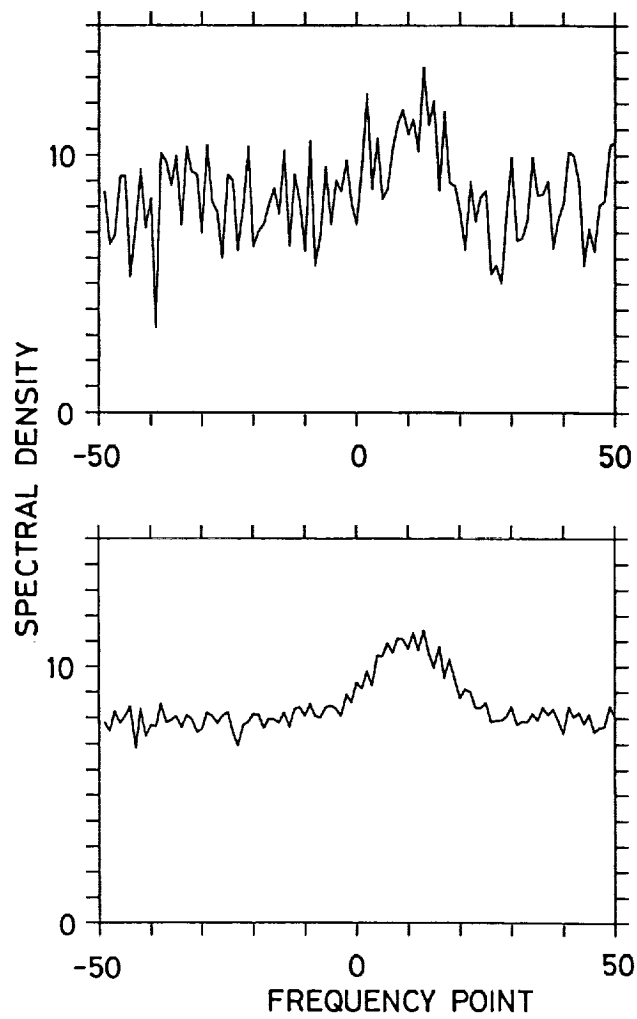


Fig. 14. Doppler spectra produced by a numerical simulation. The top panel shows a single spectrum, while the bottom panel shows a spectrum after 20 incoherent integrations.

13 NOISE LEVEL

In explaining Fig. 13 we have defined P_N as the mean value of the χ^2 -distribution of the noise spectral density. A correct estimate of P_N , commonly called the noise level, is important in determining SNR, from which the characteristics of the radar scatterers such as reflectivity or reflection coefficients are derived.

Since a χ^2 -distribution approaches a Gaussian distribution as its degrees of freedom becomes larger, a simple averaging of noise spectral densities might give an estimate of the noise level. However, the simple mean could be easily biased toward larger values due to spurious enhancements of the noise power by radio interference or airplane echoes.

Another estimate of the noise level can be obtained by taking the median values of the noise spectral densities. A median filter is more insensitive to spurious enhancements than simple averaging, and therefore it gives a more reliable estimate. Nevertheless, since calculation of the medians needs a large memory area and significant computation time, it cannot be practically realized in a real-time data processing systems.

We here introduce a convenient method to estimate the noise level, which can also be applied to determination of the echo power profile of incoherent scattering in the ionosphere [Sato *et al.*, 1988]. First, we need to pick up a portion of Doppler spectra that includes only noise, and separate it into K_m sub-sets each of which includes K_a spectral points. Second, in each sub-set the noise spectral densities for K_a data points are averaged. The resultant value follows a χ^2 -distribution with the degree of freedom of $2K_a$. Repeat this process K_m times for all of sub-sets and get a series of averaged noise spectral densities. Finally, among these K_m determinations we need to find the minimum value P_m .

For any distribution $Q(x)$ in order for α to be a minimum, the other K_m-1 events

must have a value larger than α , whose probability β becomes

$$\beta = K_m \left(\int_{\alpha}^{\infty} Q(x) dx \right)^{K_m-1} \quad (23)$$

where the factor K_m appears because we do not specify the order of occurrence of the events.

The expectation of the minimum value can be given by calculating the first moment as follows

$$e = \int_{-\infty}^{\infty} \alpha Q(\alpha) K_m \left(\int_{\alpha}^{\infty} Q(x) dx \right)^{K_m-1} d\alpha \quad (24)$$

When $Q(x)$ is a normalized Gaussian distribution with a mean value and standard deviation of 0 and 1, (24) can be simplified to

$$e = \int_{-\infty}^{\infty} \alpha Q(\alpha) K_m \frac{1}{2} (1 - \text{Erf}(\frac{\alpha}{\sqrt{2}})) d\alpha \quad (25)$$

where Erf is the error function defined as

$$\text{Erf}(y) = \frac{2}{\sqrt{\pi}} \int_0^y \exp(-t^2) dt \quad (26)$$

Note that e is always negative, since it is the expectation of the minimum value for the normalized Gaussian distribution with zero mean.

In our case $Q(x)$ is a χ^2 -distribution with $2K_a$ degrees of freedom, whose mean value and standard deviation are P_N and $P_N/\sqrt{K_a}$. However, when K_a is large enough, it can be approximated by a normalized Gaussian distribution. In this approximation, the x -axis must be normalized by the standard deviation and displaced by the mean value. In summary, e for the normalized Gaussian distribution can be related to P_m as

$$P_m = P_N - |e| \frac{P_N}{\sqrt{K_a}} \quad (27)$$

which is further modified to

$$P_N = \frac{P_m}{1 - |e|/\sqrt{K_a}} \quad (28)$$

Since the denominator of (28) is a constant for fixed K_m and K_a , P_N can be estimated by a simple computation when P_m is determined from observed Doppler spectra.

The SNR is defined as the ratio between the integrated signal and the noise power. If the signal spectrum is approximated by a Gaussian distribution with a peak value and standard deviation of P_S and σ_S , the SNR becomes

$$\text{SNR} = \frac{\sqrt{2\pi}\sigma_S P_S}{P_N B_D} \quad (29)$$

where B_D is the bandwidth of the Doppler spectra.

14 OBSERVATION PARAMETERS

We need to obtain a Doppler spectrum with large SNR and detectability in order to estimate easily the spectral parameters such as the SNR, mean Doppler shift and spectral width. Likewise, we need to take into account the effects of range or frequency aliasing so as to remove ambiguities in the range and velocity measurements.

Fig. 15 schematically shows the relations among observation parameters. The IPP is proportional to the maximum unambiguous range of the observation H_m . The time interval Δt of samples after coherent integration should be determined in order for the Doppler spectra to include the maximum radial wind velocity V_m expected in the observation height range. The number of coherent integrations N_{coh} , which is the ratio $\Delta t/IPP$, is required to be as large as possible to improve the SNR; that is, IPP should be as short as possible, and Δt should be as long as possible.

The velocity resolution ΔV of a Doppler spectrum in c/s is equal to the inverse of the maximum time length T_m of the data samples. The number of FFT points N_{FFT} , which is determined by dividing T_m by ΔT , needs to be a power of 2. Since ΔV does not

necessarily correspond to the velocity resolution of a spectral parameter estimation, ΔV could be adjusted in order to get an appropriate value of N_{FFT} .

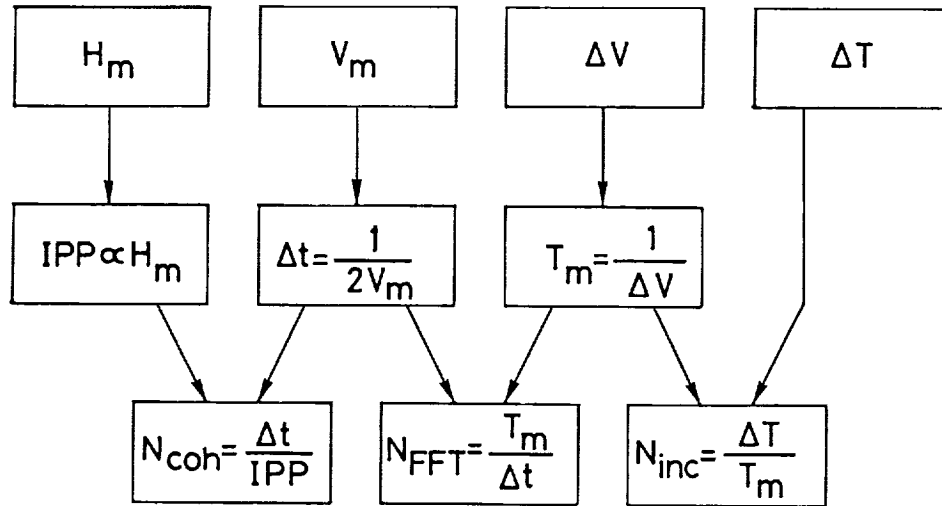


Fig. 15. The relations among observation parameters. H_m and V_m are the maximum range and radial velocity, respectively. Δt is the interval of data sampling. The minimum unit of the Doppler velocity spectrum is ΔV , while T_m is the total length of data samples. ΔT corresponds to a time resolution of Doppler spectra. N_{coh} , N_{FFT} and N_{inc} are the number of coherent integrations, FFT points and incoherent integrations, respectively.

The time resolution Δt of the spectral parameter estimation ranges from a few minutes to several hours, depending on the time scale of the phenomena to be detected by the MST radar observations. The number of incoherent integrations N_{inc} is the ratio of ΔT to T_m , which is required to be larger than about 10. Because the observation parameters are closely related to each other, we may need some experience to find a set of optimum observation parameters.

This chapter is concentrated on the description of basic concepts of the digital signal processing used in normal MST radar observations. The author hopes it will contribute to the understanding of Doppler spectra and stimulate further MST radar observations.

References

- Balsley, B. B., and K. S. Gage, The MST radar technique: Potential for Middle Atmosphere Studies, *Pure and Appl. Geophys.*, **118**, 452-493, 1980.
- Barton, D. K., *Radar System Analysis*, Artech House, Dedham, 1976.
- Bendat, J. S., and A. G. Piersol, *Random Data: Analysis and Measurement Procedures*, John Wiley & Sons, Inc., 1971.
- Cook, C. E., and M. Bernfeld, *Radar Signals, An Introduction to Theory and Applications*, Academic Press, New York, 1967.
- Doviak, R. J., and D. S. Zrnić, *Doppler Radar and Weather Observations*, Academic Press, Orlando, 1984.
- Fukao, S., T. Sato, P. T. May, T. Tsuda, S. Kato, M. Inaba, and I. Kimura, A systematic error in MST/ST radar wind measurement induced by a finite range volume effect, 1. Observational results, *Radio Sci.*, **23**, 59-73, 1988.
- Gage, K. S., and B. B. Balsley, Doppler Radar Probing of the Clear Atmosphere, *Bull. Amer. Met. Soc.*, **59**, 1074-1093, 1978.
- Gold, B., and C. M. Rader, *Digital Processing of Signals*, McGraw-Hill, Inc., 1969.
- Gossard, E. E., and R. G. Strauch, *Radar Observation of Clear Air and Clouds*, Elsevier Sci. Publ., Amsterdam, 1983.
- Kato, S., T. Ogawa, T. Tsuda, T. Sato, I. Kimura, and S. Fukao, The middle and upper atmosphere radar: First results using a partial system, *Radio Sci.*, **19**, 1475-1484, 1984.
- May, P. T., S. Fukao, T. Tsuda, T. Sato, and S. Kato, The effect of thin scattering layers on the determination of wind by Doppler radars, *Radio Sci.*, **23**, 83-94, 1988.

- Röttger, J., Investigations of lower and middle atmosphere dynamics with spaced antenna drift radars, *J. Atmos. Terr. Phys.*, **43**, 277-292, 1981.
- Sato, S., A. Ito, W. L. Oliver, S. Fukao, T. Tsuda, S. Kato, and I. Kimura, Ionospheric incoherent scatter measurements with the MU radar: Techniques and capability, *Radio Sci.*, in press, 1989.
- Skolnik, M. I., *Introduction to Radar Systems*, McGraw-Hill Inc., Tokyo, 1981.
- Singleton, R. C., On computing the fast Fourier transform, *Commun. ACM*, **10**, 647-654, 1967.
- Tsuda, T., T. Sato, K. Hirose, S. Fukao, and S. Kato, MU radar observations of the aspect sensitivity of backscattered VHF echo power in the troposphere and lower stratosphere, *Radio Sci.*, **21**, 971-980, 1986.

Chapter 6

SPECTRAL AND CORRELATION ANALYSIS WITH APPLICATIONS
TO MIDDLE-ATMOSPHERE RADARS

Prabhat K. Rastogi

Electrical Engineering and Applied Physics Department
Case Western Reserve University, Cleveland, Ohio 441061. Introduction

The first Doppler radar observations of waves and turbulence in the stratosphere and mesosphere were reported in VHF experiments conducted at Jicamarca, Perú by Woodman and Guillén [1974]. Doppler radars at frequencies near 450 and 50 MHz, and lately even at 2-3 MHz, continue to be used in extensive studies of middle-atmosphere dynamics. They are collectively called MST radars in view of their ability to probe parts of the Mesosphere-Stratosphere-Troposphere region [Balsley, 1981; Röttger, 1987]. Information about the dynamics of the medium - in terms of its bulk velocity (v) along the radar axis, spread (σ_v) in this velocity due to turbulence and background wind shears, and on the intensity of refractivity fluctuations (C_n^2) induced by turbulence - is obtained from the low-order moments of the power spectrum density of radar signals. The moments of the power spectrum density may also be obtained equivalently from its Fourier transform, the autocorrelation function, often with reduced computations. Indeed, the latter method was used in the early experiments at Jicamarca.

Nearly simultaneous Doppler observations along three or more beams allow measurements of the bulk velocity vector. The measured velocity perturbations are indicative of atmospheric wave-like phenomena. Velocities along coplanar beams, symmetrically offset from the vertical, provide a direct measurement of the vertical momentum flux in the middle atmosphere [Vincent and Reid, 1983]. Power spectrum density is once again of interest in data analysis of time series $\{v[k]; k=1,2,3...K\}$ of velocity components v , as it yields information about gravity-wave events [Rastogi and Woodman, 1974]

and on the almost turbulence-like ensemble of atmospheric waves [Balsley and Carter, 1982].

In this lecture we review the correlation and spectral analysis methods for uniformly-sampled stationary random signals, estimation of their spectral moments, and briefly address the problems arising due to nonstationarity. Some of these methods are already in routine use in atmospheric radar experiments. Others methods based on the maximum-entropy principle and time-series models have been used in analyzing data, but are just beginning to receive attention in the analysis of radar signals [Klostermeyer, 1986]. These methods are also briefly discussed.

We begin with a recapitulation of random signals (or processes) in Section 2. Several definitions used in the later sections are also introduced here. The nature of radar signals, with several different sampling time scales, and the contribution of unwanted components e.g. system noise and ground clutter, is outlined in Section 3. In Section 4, white Gaussian noise is used as a prototype to illustrate the salient statistical properties of the periodogram, obtained via the squared discrete Fourier transform (DFT). Use of the time-averaged periodogram to estimate the power spectrum density (PSD or power spectrum) of a wide-sense stationary signal is also discussed. In Section 5, methods for estimating the autocorrelation function (ACF) as lagged-product sums, and indirectly through the DFT, are introduced. We emphasize in Section 6 that, for nonstationary signals, the time-averaged periodogram may give a severely distorted estimate of the power spectrum and is not simply related to the true ACF via the Fourier transform. Use of windows or normalized weighting functions to improve the statistical properties of the PSD estimates is discussed in Section 7. The need for windowing and trend removal in spectral analysis of nonstationary signals, and the consequences of coherent integration are also discussed. Spectral parameters or moments can be estimated either directly, or by fitting an assumed shape (e.g. Gaussian or Lorentzian) to the spectral components by using a minimum mean squared error criterion. These fitting methods are discussed in Section 8. An efficient way of estimating the spectral moments from derivatives of the ACF at zero lag is discussed in Section 9. Limitations of this two-pulse technique, so called as a sequence of two closely-sampled

pulses suffices for obtaining the ACF derivatives, are also noted. Finally, high-resolution spectral-analysis methods based on maximizing the entropy for given ACF or data values, and through autoregressive moving-average models of the time series, are briefly introduced in Section 10.

2. Random Signals: Recapitulation and Definitions

In this section we review the salient concepts for wide-sense stationary random signals and introduce the definitions of the autocorrelation function (ACF), the power spectrum density (PSD) and spectral moments, and the notion of an estimate. An overall familiarity with the material of this section is assumed. The following recapitulation serves also the purpose of introducing the notation and other definitions used later. Further details may be found in standard engineering texts on random processes [e.g. Davenport and Root, 1958; Papoulis, 1983] and signal analysis [e.g. Stearns, 1975; Oppenheim and Willsky, 1983; Brigham, 1988].

Random Signals Suppose we perform some chance experiment E with outcomes and events defined as points (ζ) and subsets in a sample space S . A random signal or process $g(t, \zeta)$ is a mapping of these points ζ to real functions of some independent variable, usually taken as the time (t) or some spatial coordinate. The dependence on ζ is usually implied, hence $g(t, \zeta)$ is often written as $g(t)$. By a random process $g(t)$ we mean the ensemble of all time functions $\{g(t, \zeta)\}$ with chance outcomes ζ in the sample space S [see Fig. 2.1]. For a given t , $g(t)$ is merely a random variable. Associated with the random process $g(t)$ are the joint probability density functions of successive orders at times (t_1) , (t_1, t_2) , (t_1, t_2, t_3) etc.. This allows one to form statistical averages or moments of various products such as $g(t_1)$, $g(t_1)g(t_2)$, $g(t_1)g(t_2)g(t_3)$ etc.. Statistical averaging implies averaging over the entire sample space, i.e. over the ensemble $\{g(t, \zeta)\}$, with respect to an appropriate probability density function.

Stationarity An important class of processes that we deal with has joint densities and averages that do not depend on the choice of the time origin. Such random signals are called statistically stationary, or simply stationary. The statistical average or expectation $E[g(t)] = \mu_g(t) = \mu_g$ of a stationary process

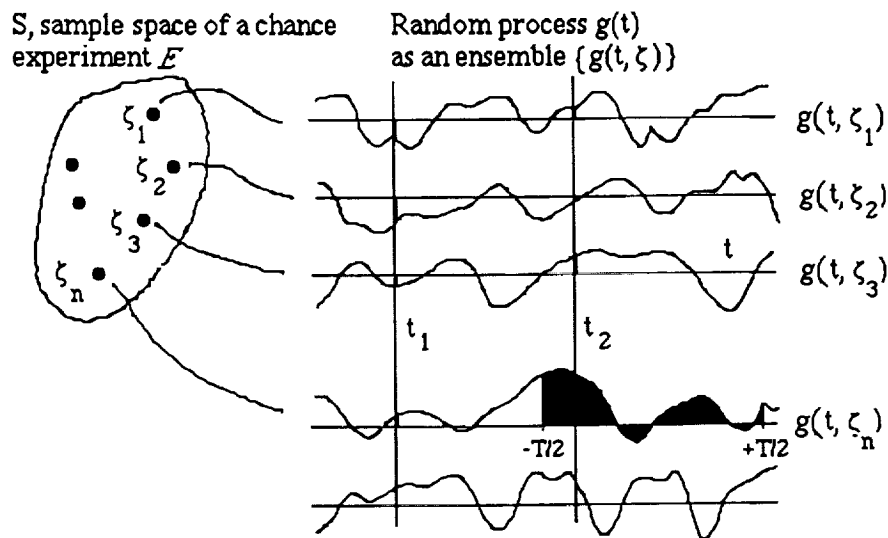


FIGURE 2.1. A random process $g(t)$ as an ensemble of time functions corresponding to the outcomes (ζ) in a sample space (S) for some chance experiment E . A suitable probability assignment is defined over S . Averages may be defined in two different ways as discussed further in the text. The time average $m(\zeta_n)$ of a realization $g(t, \zeta_n)$ is obtained by averaging it over a time window $(-T/2, T/2)$ which is eventually made infinitely wide. The ensemble average $\mu(t)$ is obtained by statistical averaging at some fixed time t over all realizations. If the process is stationary and ergodic, then $\mu(t)$ is independent of t , $m(\zeta_n)$ is independent of n , and the two averages are equal.

$g(t)$, evaluated with respect to the density function associated with it at time t , does not depend on t . Its ACF is the second moment defined as the expectation $R_g(t_1, t_2) = E[g(t_1)g(t_2)] = R_g(t_2 - t_1) = R_g(\tau)$ of the product $g(t_1)g(t_2)$ of its values at times t_1 and $t_2 = t_1 + \tau$, and it depends only on the time lag $\tau = t_2 - t_1$. In a strict sense, stationarity requires that similar conditions should hold for the joint probability densities and moments (or correlations) of all orders. We limit ourselves only to wide-sense stationary processes for which stationarity holds for any two times (t_1, t_2) , the average value μ_g is a constant, and the ACF $R_g(\tau)$ depends only on the time lag τ .

Time Averages and Ergodicity A single realization or sample function $g(t, \zeta)$ may be averaged in time over an interval $(-T/2, +T/2)$ or $(0, T)$ of duration T . In a time averaged sense, the mean value of $g(t, \zeta)$ may be obtained as $m_{g,T}(\zeta) = \langle g(t, \zeta) \rangle_T$ and its ACF as $r_{g,T}(\tau) = \langle g(t, \zeta)g(t + \tau, \zeta) \rangle_T$. Higher order averages may be similarly defined. The dependence on the interval duration T is removed by letting it become infinitely wide in the limit. In this limit, $\langle \rangle_T$ is denoted by $\langle \rangle$. We then find that the time averages $m_g(\zeta)$ and $r_g(\tau, \zeta)$ depend on the identity ζ of the realization. Do time averages equal statistical averages? Usually not, but if they do then we say that $g(t)$ is an ergodic process. An ergodic process must also be stationary. For an ergodic process, moments can be obtained as time averages over just one long (ideally, infinitely long) realization, as though different segments of the realization correspond to different members in the ensemble. The concept of ergodicity originated in statistical mechanics where it holds well for systems with a large number of molecules. Ergodicity is a useful assumption for atmospheric radar signals, but it is often quite difficult to verify.

Gaussian Processes A Gaussian process is one for which the first, second, and higher order probability density functions are jointly Gaussian. These processes are of interest for several reasons. First, it follows from the central limit theorem that a linear combination of many statistically independent identically distributed random variables tends to become Gaussian. In atmospheric radar experiments the scattered signal often arises from many small independent scatterers, hence its probability density functions approaches Gaussian. Exceptions occur when there are only few dominant components, due e.g. to coherent reflections from facets of turbulent layers

or from irregular terrain. Second, the joint probability density functions of any order for a Gaussian process can be expressed in terms of a correlation matrix \mathbf{R} , i.e. from a complete knowledge of its ACF. Finally, uncorrelated Gaussian variables are also statistically independent. This implies that if the ACF $R_g(\tau)$ of a zero-mean Gaussian random process $g(t)$ vanishes for $\tau > \tau_a$, then successive segments of a realization $g(t, \zeta)$ over windows $(0, T)$, $(T, 2T)$, ... etc of duration $T \gg \tau_a$ become uncorrelated, therefore statistically independent. In essence, a Gaussian process whose ACF has a finite support is also ergodic. Uncorrelatedness does not usually imply independence for non-Gaussian random variables and processes.

Complex Processes In radar experiments, the low-pass receiver output $z(t)$ following coherent detection is a complex signal in the following sense. It comprises an in-phase part $x(t)$ after demodulation the received signal with a reference carrier $\cos(2\pi f_0 t)$, and a quadrature component $y(t)$ after a similar demodulation with the orthogonal reference $-\sin(2\pi f_0 t)$. Since both $x(t)$ and $y(t)$ exhibit random fading, the signal $z(t) = x(t) + jy(t)$, where $j = \sqrt{-1}$, can be regarded as a complex random process [see e.g. Papoulis, 1983, or Miller, 1974]. The probability density of $z(t)$ is simply the joint density function of $\{x(t), y(t)\}$. Higher-order densities are similarly defined as joint densities of x and y at times (t_1, t_2) , (t_1, t_2, t_3) , etc. Statistical averages of a complex random process are defined with respect to these densities, but may also be evaluated as time averages under the ergodic assumption for a stationary process. Then the mean or average of the process $z(t)$ is a complex constant $(\xi + j\eta)$. The autocorrelation function may then be obtained in either of the following equivalent ways

$$R_z(\tau) = E\{z(t)z^*(t+\tau)\} = r_z(\tau) = \langle z(t, \zeta)z^*(t+\tau, \zeta) \rangle \quad [2.1]$$

R_z ensemble average (independent of t), r_z time average (independent of ζ)

where $*$ denotes the complex conjugate. Different ordering of the lagged term and conjugation gives three other forms, but we use the one above. The signal power P_z defined as $\langle z(t)z^*(t) \rangle$ is real, but the autocorrelation function $R_z(\tau)$ is generally complex. It may be expressed in the cartesian form as $R_z(\tau) = R_{zx}(\tau) + jR_{zy}(\tau)$, or in the polar form as $R_z(\tau) = |R_z(\tau)| \exp\{j\phi_z(\tau)\}$. It is readily seen that $R_z(\tau)$ has a Hermitian symmetry, i.e.

$$R_z(\tau) = R_z^*(-\tau) \quad [2.2]$$

which implies that its real part $R_{zx}(\tau)$ and magnitude $|R_z(\tau)|$ are even, but the imaginary part $R_{zy}(\tau)$ and phase $\phi_z(\tau)$ are odd in the time lag τ .

The Wiener-Khintchine theorem relates the ACF $R_z(\tau)$ and the PSD $S_z(f)$ of $z(t)$ as a Fourier transform pair (see e.g. Whalen, 1971; Miller, 1974),

$$S_z(f) = \mathfrak{F}\{R_z(\tau)\} = \int_{-\infty}^{\infty} R_z(\tau) \exp(-i2\pi f\tau) d\tau \quad [2.3]$$

$$R_z(\tau) = \mathfrak{F}^{-1}\{S_z(f)\} = \int_{-\infty}^{\infty} S_z(f) \exp(i2\pi f\tau) df \quad [2.4]$$

The signal power or variance $P_z = \langle z(t)z^*(t) \rangle = R_z(0)$ is obtained by integrating the PSD $S_z(f)$ over the entire frequency range. Since the power in each frequency band $(f, f+\delta f)$ must be real and non-negative, we infer that the PSD $S_z(f)$ must also be real and non-negative everywhere.

Periodogram Each realization of the complex random signal $z(t)$ is a deterministic signal. We assume that it has a Fourier transform $Z(f)$. Its energy spectrum is obtained as $E_z(f) = |Z(f)|^2$. By the Rayleigh energy theorem, the signal energy can be obtained either as the time integral of $|z(t)|^2$ or as the frequency integral of $|Z(f)|^2$. It follows that for signals of finite power P_z , the PSD $S_z(f)$ may alternatively be obtained as the time average of $|Z(f)|^2$ over an interval $(0, T)$ as T becomes infinite. Signals with infinite energy or power may be handled by including generalized functions e.g. the Dirac impulse. Consider now a truncated signal $z_T(t)$ which is zero outside the interval $(0, T)$. Then

$$T^{-1} \mathfrak{F}[z_T(t)]^2 = T^{-1} |Z_T(f)|^2$$

and the right hand side has properties similar to the PSD $S_z(f)$. It is called the periodogram or sample spectrum. The time-averaged periodogram is often used as an estimate of the power spectrum. The importance of periodogram in power-spectrum estimation of uniformly sampled signals is due mainly to

the availability of efficient Fast Fourier Transform (FFT) algorithms for computing the DFT [see e.g. Cooley et al. 1977; Brigham, 1988]. As we see later, the use of time-averaged periodogram as a power-spectrum estimate requires several assumptions which do not always hold for atmospheric radar signals and data.

Spectral moments Radar signals scattered from the atmosphere are slightly Doppler shifted due to bulk atmospheric motions, and also undergo a Doppler broadening due to local fluctuations in the bulk velocity. In the absence of other components in the complex signal $z(t)$ at the receiver output, the PSD $S_z(f)$ has a symmetric off-center peak. The area under the peak corresponds to the signal power P_z , its location or center frequency f_{cz} to the Doppler shift f_d , and its width σ_{fz} about the center frequency f_{cz} to the Doppler frequency spread σ_w . We note that, except for normalization to unit area, the PSD $S_z(f)$ shares all the properties of a probability density function. Hence the location parameters that we seek may be derived from spectral moments, defined almost identically to the moments $E\{Q^k\}$ of a random variable Q , with respect to its probability density function $f_Q(q)$.

The first few noncentral spectral moments of $z(t)$, denoted here by $s_z(0)$, $s_z(1)$, $s_z(2)$ are obtained by averaging f^0 , f^1 , and f^2 with respect to its PSD $S_z(f)$ over all frequencies. The zeroth moment $s_z(0)$ is the same as signal power P_z . $S_z(f)/P_z$ is then a probability density function. The location parameters f_{cz} and squared width $(\sigma_{fz})^2$ are obtained in the sense of mean and variance (or the second central moment) of $S_z(f)/P_z$. These may also be derived by transforming $s_z(1)$ and $s_z(2)$ as follows. First, $s_z(1)$ and $s_z(2)$ are normalized by dividing with $s_z(0)$ i.e.

$$s_z(1) \rightarrow s_z(1)/s_z(0) = f_{cz} \text{ and } s_z(2) \rightarrow s_z(2)/s_z(0).$$

Next $s_z(2)$ is modified as

$$s_z(2) \rightarrow [s_z(2) - \{s_z(1)\}^2] = (\sigma_{fz})^2.$$

A Doppler shifted peak of Gaussian shape $P_z N(f_{cz}, \sigma_{fz}^2)$ is fully specified by the (central) spectral moments P_z , f_{cz} , and σ_{fz}^2 as shown in Fig. 2.2.

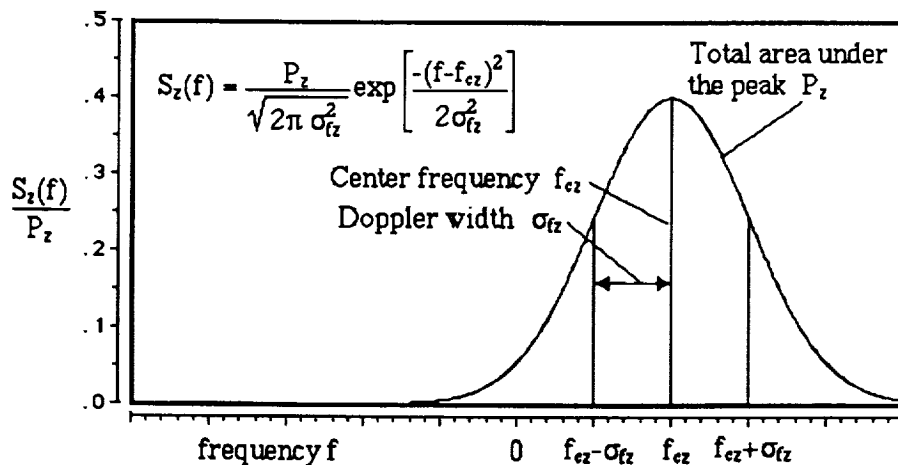


FIGURE 2.2. Power spectrum density and the corresponding spectral moments for an off-center Gaussian spectral peak. Parameters P_z , f_{cz} , and σ_{cz} define the shape of the peak through its area, center frequency and standard deviation. These parameters also correspond to the zeroth, first and second order normalized spectral moments $s_z^{(0)}$, $s_z^{(1)}$, and $s_z^{(2)}$ interpreted as signal power, Doppler frequency shift and Doppler frequency spread. Note that the frequency spread is σ_{cz} , whereas $s_z^{(2)}$ equals $(\sigma_{cz})^2$.

If the signal $z(t)$ at the receiver output contains components other than the scattered atmospheric signal, then extra steps may be necessary to relate P_z , f_{cz} , and σ_{fz}^2 to the signal power, Doppler shift and Doppler spread of the scattered signal. Finally, just as the moments of a random variable may be obtained from successive derivatives of its characteristic function at the origin, it is possible to infer the spectral moments via the autocorrelation function.

Estimation In statistical signal and data analysis we frequently estimate a random quantity θ by some function $\hat{\theta}(\theta_1, \theta_2, \dots, \theta_n)$ of n data points $\theta_1, \theta_2, \dots, \theta_n$. There can be many possible estimates of θ , e.g. $\hat{\theta}_1, \hat{\theta}_2, \dots, \hat{\theta}_m$ etc. We prefer those that satisfy some reasonable properties viz. unbiasedness, minimum variance, and consistency. An estimate $\hat{\theta}$ of θ is unbiased if the statistical average $E[\theta - \hat{\theta}]$ of the bias or error $e = \theta - \hat{\theta}$ is zero. An unbiased estimate $\hat{\theta}$, on the average, neither overestimates nor underestimates θ i.e. $E[\theta] = E[\hat{\theta}]$. Of all the available estimates, we also prefer the one(s) whose variance $\text{var } \hat{\theta}$ is minimum. It may often be justifiable to use a biased estimate, if it has lower variance. Finally, when the number m of data points is made infinite, we should expect $\text{var } \hat{\theta}$ to approach zero, otherwise taking more observations would be futile. In that case we say that the estimate $\hat{\theta}$ of θ is consistent. It is often possible to obtain a theoretical lower bound on the variance of an estimator using the Cramer-Rao inequality of statistics. An estimator that meets this bound is called an efficient estimator.

3. Nature of Radar Signals and Radar Data.

Essential statistical characteristics of sampled radar signals and time series of derived velocity data are summarized in this section. Choice of a suitable spectral-analysis scheme depends critically on these characteristics and the sampling time scales. We also take a first look at the rudiments of spectral-analysis methods using the DFT.

In radar experiments, an amplitude and/or phase modulated pulse train is transmitted in which each pulse has the form $p(t) \exp(i2\pi f_0 t)$ at a carrier frequency f_0 . The carrier term is removed in coherent demodulation, in

which the received signal is effectively multiplied with $\exp(-i2\pi f_0 t)$. The receiver should optimally have a bandpass frequency response to match the modulated pulse shape $p(t)$. Hence the receiver bandwidth B about f_0 is decided primarily by the correlation width T_p of the pulse shape $p(t)$. A simple way of defining T_p is as the distance between points at which the magnitude of the ACF $R_p(\tau)$, defined as $\langle p(t)p^*(t+\tau) \rangle$, becomes $1/2 R_p(0)$. Roughly, it corresponds to the smallest modulation time scale in $p(t)$. Then T_p is nearly equal to the pulse duration for amplitude-modulated pulse trains, but it is approximately equal to the baudlength T_b for binary phase-coded pulses used in high-resolution experiments. The receiver output is sampled in range with a time resolution T_r , which should be somewhat less than T_p to avoid undersampling. Typically, T_r is 1-10 μs for a nominal range resolution of 0.15-1.5 km.

The pulses $p(t)$ in the pulse train are repeated at an interval T_I , typically about one ms. The fading rate of the received signal is related to the nominal Doppler frequency shift. It is, nevertheless, very much smaller than the Nyquist frequency of ~ 500 Hz implied by T_I . The complex signal $z(t)$ is therefore coherently accumulated or integrated, range by range, over I successive pulses to obtain an effective sampling time $T=I.T_I$. Typical value of I may be 100 in VHF experiments and 10 for the UHF case. The receiver output signal is thus sampled in time as the function of two indices, j and i denoting range and time. After coherent integration, the index i is changed to k corresponding to the coarser time scale $T=I.T_I$. As the signals are analyzed separately for each range, in our subsequent analysis we need only consider a single complex time series $z[k]$. A range index j and a sampling time T are then implicit.

The complex series $z[k]$ not only includes the scattered atmospheric signal $s[k]$, it also comprises a wide-band noise component $n[k]$ due to the system and sky noise, a very slowly fading ground clutter term $c[k]$ due to sidelobe returns from terrain, vegetation, weather etc., a sporadic interference component $i[k]$ due to unwanted transmitters in the receiver passband, and possibly a residual d.c. or drift $d[k]$ due to slow changes in the receiver circuits. The drift term $d[k]$ is easily removed. Due to the intermittent and

sporadic nature of the unwanted interference, its identification and treatment is done on an ad-hoc basis. The only remaining terms are s , n , and c . The ground clutter component $c[k]$ is the most problematic of these as it is often nonstationary over the measurement interval.

The signal $z(t)$ is sampled in time as $z[k] = z(kT)$. The frequency range for its PSD $S_z(f)$ is then limited to the Nyquist interval $F = (-0.5T^{-1}, +0.5T^{-1})$. Any components of $S_z(f)$ outside F are aliased or folded back into it. The aliasing effect is most clear-cut for the wide-band noise component $n(t)$, originally limited by the receiver bandwidth $B \gg T^{-1}$. Hence the noise component is aliased many times over. The eventual effect is to impart a nearly flat or white-noise platform to $S_z(f)$, even when $n(t)$ is nonwhite. The slowly-fading ground clutter component should be manifest in $S_z(f)$ as a near d.c. or very low-frequency spike. This would be true if the measurement interval were either too small or too large compared to the typical fading-time for the clutter. We see later in section 6, that the clutter component usually appears as an f^{-2} platform in the PSD estimate.

Only a finite number K of signal samples $z[k]$ is generally available for spectral analysis. The limitation on K is due to finite memory or storage in the on-line processor. An intermediate step in estimating $S_z(f)$ is the K -sample discrete Fourier transform (DFT) of $z[k]$. The DFT pair is defined as

$$Z[m] = F_K\{z[k]\} = \sum_{k=0}^{K-1} z[k] e^{-i 2\pi km/K} \text{ where } m=0,1,\dots,[K-1] \quad [3.1]$$

$$z[k] = F_K^{-1}\{Z[m]\} = \frac{1}{K} \sum_{m=0}^{K-1} Z[m] e^{+i 2\pi km/K} \text{ where } k=0,1,\dots,[K-1] \quad [3.2]$$

The DFT converts K time samples of $z[k]=z(kT)$ to K samples of its Fourier transform $Z(f)$, evaluated at equispaced frequency points in the Nyquist frequency range F as $Z[m]=Z(m/KT)$. The effect of sampling in the time domain is to render $Z(f)$ periodic outside the Nyquist range. Conversely, due to sampling in the frequency domain, $z(t)$ is also treated as periodic, with a period KT . Thus both $z[k]$ and $Z[m]$ are periodic K -point sequences. Full implications of time and frequency sampling in the DFT pair, and its

equivalence to the continuous Fourier transform, has been discussed by Brigham(1988). The sampled signal $z[k]$ has a finite power, but infinite energy. It can be shown that the following form of Parseval's relation holds for $z[k]$ and $Z[m]$,

$$\sum_{k=0}^{K-1} |z[k]|^2 = \frac{1}{K} \sum_{m=0}^{K-1} |Z[m]|^2 \quad [3.3]$$

The use of DFT in estimating the PSD, $S_z(f)$, by time-averaged periodograms is examined in the next section.

Spectral analysis of derived parameters, e.g. the time series of a velocity component $v[k]$, is also of interest here. We note that $v[k]$ are samples of a real random process, and the index k denotes either the time or some spatial coordinate with a basic sampling interval. The power spectrum $S_v(f)$ often shows a power-law decay of the form $\alpha f^{-\beta}$ with a spectral index β . Here f may be a temporal or a spatial frequency. The power-law shape must be limited at the low-frequency end by some frequency f_L , else the power in $v(t)$ may become infinite for some β . Unless the frequency f_L is fully resolved, its effect is manifest in $v[k]$ as a non-stationary trend, similar to the ground-clutter component $c[k]$ in the radar signal $z[k]$. Implications of such trends in spectral analysis are discussed in Section 6.

4. Time Averaged Periodogram Analysis

The sample spectrum or periodogram $P_z(f)$ of a complex signal $z(t)$ has been briefly discussed in section 2. Suppose the signal $z(t)$ is first truncated over an interval of duration D , and $Z_D(f) = \mathcal{F}\{z_D(t)\}$ is the Fourier transform of the truncated signal $z_D(t)$. Then the periodogram $P_z(f)$ is defined as

$$P_z(f) = \frac{1}{D} |Z_D(f)|^2 \quad [4.1]$$

In the uniformly-sampled case, $z_D(t)$ is available at K sample points spaced an interval T apart over a total duration $D=KT$. For simplicity denote these sample values by the sequence $\{z[k], k=0,1,\dots,(K-1)\}$. The DFT $F\{z[k]\}$ of

this sequence is another complex sequence $\{Z[m], m=0,1,\dots,(K-1)\}$. The K points in $Z[m]$ have a frequency spacing $(KT)^{-1}$ or $(D)^{-1}$ over the entire Nyquist frequency interval $\pm 1/(2T)$. The rightmost point $Z[K]$ is excluded as it equals $Z[0]$ by periodicity. The periodogram in the sampled case is defined in analogy with eqn. [4.1] as

$$P_z[m] = \frac{1}{K} |Z[m]|^2 \quad [4.2]$$

The sum of $P_z[m]$ over all m , after scaling with the frequency spacing $(KT)^{-1}$, gives the signal power P_z . The distinction between the symbols used for the periodogram $P_z[m]$ and the signal power P_z should be noted.

In the limiting case we expect that the statistical average of the periodogram will approach the PSD. This actually gives a physically reasonable alternative definition for the PSD,

$$S_z(f) = E \left\{ \lim_{D \rightarrow \infty} \frac{1}{D} |Z_D(f)|^2 \right\} \quad [4.3]$$

The above asymptotic equality will not hold for periodogram estimated from samples of a single short realization. Hence we briefly state the statistical and sampling properties of the periodogram defined in equation [4.2] as a PSD estimator. Further details may be found in Blackman and Tukey(1958), Cooley et al. (1977), Koopmans (1974), Marple (1987), and Oppenheim and Schaffer(1975).

The periodogram can be computed at any continuous frequency f . The signal $z(t)$, however, has been truncated beyond the interval $(0,D)$ or, in effect, a rectangular window has been applied to it. Hence $Z_D(f)$ is obtained by the convolution of $Z(f)$ with the window transform $D \text{sinc}(fD)$. Then $|Z_D(f)|^2$ is similarly obtained by convolving $|Z(f)|^2$ with $D^2 \text{sinc}^2(fD)$. The convolving functions are modified slightly for K equispaced samples of $z(t)$; the sinc function is now replaced with the Dirichlet kernel $\sin(\pi fTK)/\sin(\pi fT)$. Those frequency component in $|Z(f)|^2$ that fall exactly at a sampled frequency point, when convolved with $\sin^2(\pi fTK)/\sin^2(\pi fT)$, produce a null response at

all other sampled frequencies. Hence the periodogram values at the sampled frequencies tend to be uncorrelated, provided that the signal $z(t)$ does not have significant intermediate frequency components that fall in-between two adjacent sampled frequencies. This fact has an important bearing in PSD estimation for signals with a strong clutter component, or with a power-law PSD. We also see later that this gives a singularly irregular appearance to the periodogram.

To simplify our discussion of the statistical properties of the periodogram, we assume that $z(t) = z_X(t) + j z_Y(t)$ is a zero-mean, complex Gaussian noise with variance σ^2 and a white or flat PSD. The signal power P_z then equals the variance σ^2 , and is divided evenly between the real and imaginary parts $z_X(t)$ and $z_Y(t)$ of $z(t)$. With samples at time spacing T , the PSD $S_z[m]$ should equal $\sigma^2 T$. Since the DFT $Z[m]$ is a linear combination of sample values $z[k]$, it follows that $Z[m]$ is also zero mean and Gaussian. From the definition of DFT given in eqn [3.1] and using uncorrelatedness of adjacent samples of white Gaussian noise, it can be verified that $\text{var}\{Z[m]\} = K\sigma^2$ and it is evenly divided between the real and imaginary parts $Z_X[m]$ and $Z_Y[m]$ of $Z[m]$. We are interested in the statistics of $|Z[m]|^2 = \{Z_X[m]\}^2 + \{Z_Y[m]\}^2$. We note that a chi-square random variable χ_n^2 with n degrees of freedom (d.o.f.) is obtained by quadratically adding n statistically independent zero-mean Gaussian random variables from a density $N(0, s^2)$. It has a mean ns^2 and variance $2ns^4$. It follows then that $|Z[m]|^2$ has simply a chi-square density with two d.o.f.. An alternative and simpler way of arriving at the same result is to note that $|Z[m]|$ has a Rayleigh density, hence $|Z[m]|^2$ has an exponential density, which is the same as the chi-square density with two d.o.f.. Hence $E\{|Z[m]|^2\} = K\sigma^2$ and $\text{var}\{|Z[m]|^2\} = K^2\sigma^4$. These results for the mean and variance of $|Z[m]|^2$ are only slightly modified when the convolutional effect of the Dirichlet kernel is properly considered, and are valid at least locally in the limit of large K .

With the sampling interval T included, and by noting that the area under the periodogram $P_z(f)$ must equal the signal variance $P_z = \sigma^2$, we see that $P_z[m]$ is an asymptotically unbiased estimate of PSD $S_z(f)$ at the sampled frequencies, with an average value $\sigma^2 T$ and a variance $\sigma^4 T^2$. As its variance remains

independent of the sample size, $P_z[m]$ is an inconsistent estimate of the PSD. The standard deviation of the periodogram is $\sigma^2 T$, same as its mean value. We recall that the periodogram values at adjacent sampled frequency points are nearly uncorrelated. However, as the sample size K increases, these points only come closer in frequency without any reduction in their standard deviation. Hence the periodogram usually shows large fluctuations, making it appear more and more jagged as the number K of sample points increases. Examples of this behavior may be found e.g. in Oppenheim and Schaffer (1975) and Marple (1987). These results are approximately valid for non-Gaussian noise, as for even modest K the central limit theorem warrants Gaussian statistics for $Z[m]$. As our analysis is localized in frequency, these results also nearly correct for signals with colored PSD. Then the periodogram $P_z[m]$ has its mean value and its standard deviation approach the local PSD $S_z[m]$ for large K .

For reasons discussed above the periodogram is perhaps the most maligned PSD estimator. Yet, the ease and efficiency with which it can be implemented through FFT algorithms also make it the most frequently used technique for spectral analysis. The FFT algorithms can work in place without additional storage, require only $\sim K \log_2 K$ complex multiply-adds instead of $\sim K^2$ for direct DFT evaluation, and are modular so that repetitive and computation intensive tasks such as bit reversal and sine-cosine computations can be detached from the main program (see e.g. Cooley et al., 1977). The periodogram $P_z[m]$ becomes a usable PSD estimate only after time averaging over many independent sequences of $z[m]$ of length K . We show below that its standard deviation is substantially reduced through averaging.

When M independent periodograms $P_{z[q]}[m]$ for $q=1,2,\dots$ are averaged, then each point in the averaged periodogram $Q_z[m]$ is obtained by quadratically adding $2M$ zero-mean Gaussian random variables with density $N(0, 0.5K\sigma^2)$. The sum is normalized by division with KM , and then multiplying it with T , to conserve the area under $Q_z[m]$ as the signal variance σ^2 . Hence the mean of the averaged periodogram $Q_z[m]$ becomes $\sigma^2 T$ and its variance, $\sigma^4 T^2/M$. The standard deviation of the time averaged periodogram is then just $\sigma^2 T/\sqrt{M}$. These results are approximate, but the approximations improve for larger K . For an arbitrary PSD $S_z[m]$, it follows that the averaged periodogram $Q_z[m]$

has a mean $\sim S_z[m]$ and a standard deviation $\sim S_z[m]/\sqrt{M}$. The variance of $Q_z[m]$ tends to vanish as the number M of periodograms averaged together increases. Hence the time-averaged periodogram is a consistent estimator of the PSD.

We close our discussion with a relevant example. In a typical UHF radar experiment with a 1 ms pulse repetition interval and coherent integration over 10 pulses, 64 complex samples may be gathered in 640 ms. About 64 sec of observations suffice for averaging over 100 periodograms. The time-averaged periodogram has a standard deviation that is $1/\sqrt{100}$ or 10% of the local PSD value. A Doppler shifted peak which occupies a sixth of the available frequency window, and is 50% above the background noise level, can be readily detected in the averaged periodogram. The total signal power is only about 0.04 of the total noise power for a hypothetical triangular peak. This corresponds to a detectable signal to noise ratio (SNR) of -14 dB with one minute of observations. This detectability criterion may often be difficult to attain in the presence of other dominant components. But the example does illustrate the basic considerations.

5. Estimation of the Autocorrelation Function

An alternative approach to estimating the PSD is through the ACF, using the Wiener-Khinchine relations stated in Section 2. These are readily modified for the discrete case using the DFT. The ACF cannot be usually recovered from the time-averaged periodogram estimates of PSD if the signal $z(t)$ has a nonstationary component, and if it does not satisfy certain ergodic conditions that constrain the ACF to a finite support [Papoulis, 1977 and 1983; Marple, 1987]. These conditions are further examined in Section 6 for the MST radar signals. Here we outline a direct and an indirect method of estimating the ACF from data. The use of these estimates in PSD estimation is discussed in Section 7.

As before, suppose $z(t)$ is a realization of a complex, ergodic, wide-sense stationary signal. Its samples $z[k]$ are available at times kT for $k=1,2..K$. Under the ergodic assumption, the ACF $R_z(\tau)$ can be estimated as a time average. Its estimates $R_z[n]$ are obtained at discrete time lags nT , for indices

$|n| \leq N < K$. The estimate $R_z[n]$ is evaluated as averaged lagged-products of the form $z[i] z^*[i+n]$, provided that the indices $[i]$ and $[i+n]$ do not exceed the bounds on k . We consider two different estimates $R^{[1]}[n]$ and $R^{[2]}[n]$ that differ only in the normalization :

$$R^{[1]}[n] = \frac{1}{K-n} \sum_{i=1}^{K-n} z[i] z^*[i+n], \quad n=0,1,\dots,N < K \quad [5.1]$$

$$R^{[2]}[n] = \frac{1}{K} \sum_{i=1}^{K-n} z[i] z^*[i+n], \quad n=0,1,\dots,N < K \quad [5.2]$$

The estimates for negative n may be obtained either by inter-changing the order of products in the summations, or by using the Hermitian symmetry (see eqn. 2.2) that $R_z[n] = R_z^*[n]$.

Only $[K-n]$ lagged products can be formed at a lag n . The estimate $R^{[1]}[n]$ normalizes the lagged-product sums by the their actual count $[K-n]$. The second estimate $R^{[2]}[n]$ normalizes these sums by the number K of data points. We may surmise that $R^{[1]}[n]$ should be an unbiased estimate of $R_z[n]$. Though $R^{[2]}[n]$ is biased, it becomes asymptotically unbiased as K becomes infinite. The variance of the unbiased estimate $R^{[1]}[n]$ increases with index n as there are fewer products averaged. For both the estimates, the variance decreases with increasing number K of data points, and eventually vanishes. Hence both the estimates are consistent. To ensure that a sufficient number of products has been averaged at each lag, we require $N/K \ll 1$, with the ratio K/N of ~ 10 or more usually desirable [Blackman and Tukey, 1958]. The two estimates have nearly identical properties under these conditions. The biased estimate $R^{[2]}[n]$ puts a triangular weight $1-|n|/K$ on the estimated values. This warrants for $R^{[2]}[n]$ the very desirable ACF property that $|R^{[2]}[n]| \leq R^{[2]}[0]$. The unbiased estimate $R^{[1]}[n]$ does not always satisfy the condition $|R^{[1]}[n]| \leq R^{[1]}[0]$. This condition may be readily violated for small K as the variance of $R^{[1]}[n]$ increases with n .

For a given maximum lag index N , the lagged product-sum scheme can be automated using two buffers of size N . New data is sequentially stored in a data buffer, at an address which wraps around the buffer. For each new data

point, all possible N lagged product sums are updated in the second buffer. Normalization can be done to obtain the ACF estimate, once the data buffer has been filled several times around. This scheme is readily adapted for real-time multi-channel signal processing. It was first used by R. M. Harper in 1974 for real-time data acquisition with the Jicamarca radar. The scheme has also been found quite effective for analysis of irregularly spaced data. Since an N -point history of the time-series is always available in the data buffer, the scheme is readily adapted for editing bad data points or outliers using e.g. mean, variance, median, and order statistics of the data.

An alternative and faster method of estimating the ACF is through the use of DFTs [see e.g. Cooley et al. 1977; Oppenheim and Schafer, 1975, Press et al. 1986]. We recall that the DFT of a K -point sequence $z[k]$ is another K -point sequence $Z[m]$, and convolution in time domain is equivalent to a product in the frequency domain. We also notice the similarity of ACF $R[n]$ with the discrete self-convolution $R_{\otimes}[n]$ of $z[n]$

$$R[n] = \langle z[i] z^*[i+n] \rangle$$

$$R_{\otimes}[n] = z[n] \otimes z[n] = \langle z[i] z[n-i] \rangle.$$

These operations yield $(2K+1)$ -point sequences with zero end values. The only difference between $R[n]$ and $R_{\otimes}[n]$ is that in convolution one of the terms is folded in the time index i , and in ACF one of the terms is conjugated. Hence ACF may be obtained as $R[n] = z[n] \otimes z^*[-n]$ using the convolution. In the frequency domain, the DFT of $R[n]$ is merely the product of $Z[m]$ with $Z^*[m]$. The only caution that needs be exercised is that $R[n]$, hence its DFT must be at least $2K$ -points long. The method then is to augment or extend the K -point sequence $z[n]$ with K zeros. The $2K$ -point DFT's of the extended $2K$ -point sequences $z_e[n]$ and $z_e^*[-n]$ are then multiplied point by point. Finally, the $2K$ -point inverse DFT gives the $2K$ -point periodic sequence $R[n]$. The estimate thus obtained is weighted by a triangle as for $R^{[1]}[n]$. The method can be readily extended to the cross-correlation function (CCF) $R_{xy}[n]$ of two complex K -point sequences $x[k]$ and $y[k]$. We merely note the following relations

$$R_{x\otimes y}[n] = x[n] \otimes y[n] = \langle x[i] y[n-i] \rangle.$$

$$R_{xy}[n] = \langle x[i] y^*[i+n] \rangle = x[n] \otimes y^*[-n] = F^{-1} [X[m] Y^*[m]]$$

which suggest that the K-point sequences $x[n]$, $y[n]$ must first be augmented with K zeros to get the 2K-point sequences $x_e[n]$ and $y_e[n]$, one of which is conjugated and inverted in time to get $y_e^*[-n]$, as was also tacitly done for the ACF. The CCF is obtained as the inverse DFT of the point by point product $X[m] Y^*[m]$ of the DFTs of these sequences. Averaging over several K-point data sequences is desirable to reduce the variance of ACF and CCF estimates.

This method has several advantages over the direct ACF estimation using lagged-product sums. The DFT (or FFT) computations can be carried out in-situ. When 2K is of the form 2^K , the number of complex multiplies and adds in the FFT can be made as small as $\sim 2K\kappa$. This computational advantage becomes quite significant even for short data sequences. The PSD estimate, moreover, is available as an intermediate step and it is related to the ACF estimate $R^{[2]}[n]$ by the DFT. However, augmenting the data sequence with zeros also doubles the storage requirements. It is perhaps for this reason that this method has not been used in real-time MST radar signal processing. The declining cost of computer memory certainly favors its use.

6. Nonstationarity and Spectral Distortion

In the foregoing discussion we have assumed that the complex signal $z(t)$ is a wide-sense stationary and ergodic random process. Usually several sets of K equispaced samples $z[k]$ at sample spacing T are available from a single realization $z(t, \zeta_0)$. The assumption of wide-sense stationarity implies that the low-order moments viz. the mean μ_z and the variance σ_z^2 of the process are constant, and its ACF $R_z(\tau)$ depends only on the time lag τ , irrespective of the time origin. The ergodic hypothesis is invoked to circumvent statistical averaging, by estimating these quantities as time averages over many statistically independent sub-sets from a single realization.

A constant mean value μ_z contributes a platform of fixed height $\mu_z \mu_z^*$ to the ACF, and a single spike of height $(TK) \mu_z \mu_z^*$ exactly at the zero frequency in the K-point PSD estimate. If the mean μ_z is indeed a constant, then it can be

effectively removed from $z[k]$, rendering it a zero-mean process in further analysis. The assumption of stationarity of mean is merely a convenient model for the signal time series $z[m]$. It is readily violated in situations described below making $\mu_z(t)$ a slowly varying function of time with discernible trends over the observation interval.

The ground clutter component $c(t)$ in radar experiments arises due to multiple paths to terrain seen through the antenna sidelobes. Its fading time varies from fraction of a second to minutes due to atmospheric refraction along the paths. When the same path is not traced back due to multiple reflections, $c(t)$ also has a very small Doppler shift. Fading time and Doppler shift of $c(t)$ critically depend on the radar frequency, radar location and on severe weather conditions. Nonstationarity of $c(t)$ is most serious for the ~ 450 MHz UHF radars. The same refractive multipath effects are nearly an order less severe and nearly insignificant for the ~ 50 MHz VHF radars. Coherent reflections at near vertical incidence from planar or slightly curved turbulent layers also produce a slowly fading component. Non-stationarity is also evident in the velocity data $v(t)$, especially when these are indicative of a power-law PSD, as slow trends at time scale of several hours to several days.

Removal of a nonstationary trend $\mu_z[k]$ from a single K -point sequence $z[k]$ is difficult unless K is very large or many contiguous K -point sequences are available. Subtracting the mean value $\langle z \rangle$ from the points $z[k]$ in a sequence does not remove the trend. Gottman(1985) describes simple methods for identifying and removing trends. These methods use averaging and differencing at several time scales to estimate parameters of an ad-hoc linear or quadratic trend model. Alternatively, the parameters of a low-order polynomial that models trend can be found by computation-intensive least-square methods [see e.g. Hamming, 1973, Press et al., 1986].

Nonstationary trends produce a severe distortion of time-averaged periodogram estimates obtained by DFT methods as convincingly discussed by Sato and Woodman (1982). Due to this distortion, ACF cannot generally be recovered from time-averaged periodogram estimates $Q_z[m]$ of the PSD. Suppose the N -point periodogram $P_z[m]$ is formed from an N -point sequence $z[k]$ using its N -point DFT $Z[m]$. From the same sequence a $(2N-1)$ -point

ACF estimate $R_z[n]$, for n ranging over $\pm(N-1)$, can be formed as $\langle z[i]z^*[i+n] \rangle$. A zero value can be added at either end. Now both $P_z[m]$ and its inverse DFT $P_z^{-1}[n]$ are periodic N -point sequences. We expect the periodic N -point sequence $P_z^{-1}[n]$ and the aperiodic $2N$ -point sequence $R_z[n]$ to be related. Thus $P_z^{-1}[n]$ is derived from $R_z[n]$ by wrapping it around a circle with N points indexed from 0 to $(N-1)$. If $R_z[n]$ is constant at all lags, or if it is zero for $|n| > N/2$, then $P_z^{-1}[n]$ unambiguously contains all the information about $R_z[n]$. However, if the support of $R_z[n]$ exceeds $\pm N/2$, then $P_z^{-1}[n]$ is severely distorted by wrap-around and its DFT, the periodogram $P_z[m]$, is no longer a reasonable PSD estimate. The problem can be alleviated with the use of a $2N$ -point DFT with N -point data (extended by zero-padding) to estimate both the PSD and triangular-weighted ACF estimate $R^{[2]}[n]$ as outlined in the previous section.

An alternative way to explain the periodogram distortion is to realize that the true PSD of the trends is a narrow spectral spike near, but not exactly at, the zero frequency. The use of a uniformly weighted N -point sequence $z[n]$ in periodogram estimation smooths this spike by convolution with a squared Dirichlet Kernel which can be approximated with $\text{sinc}^2(fT)$ for the continuous case. The contribution of the spike thus leaks or spills over all frequencies, and is evident at the sample points of the periodogram as an $\sim f^{-2}$ platform. Due to sampling in time at spacing T , tails of the $\sim f^{-2}$ platform are also aliased into the Nyquist window $(-0.5/T, +0.5/T)$. We discuss some ways of containing this leakage in the next section.

7. Windowing and Coherent Integration

The PSD $S_z[m]$ of an N -point sequence $z[n]$ sampled at time steps T can be estimated either directly from the N -point DFT $Z[m]$ via the periodogram $P_z[m]$, or as the DFT of an ACF estimate $R_z[n]$. Use of uniform weights or the default rectangular time window is equivalent to a circular convolution of $Z[m]$ or $R_z[n]$ with the Dirichlet kernel $\sin(\pi N f T)/\sin(\pi f T)$. A sinusoid of frequency f' is seen to leak at other frequencies f in the periodogram $P_z[m]$ as

$$\sin^2(\pi N(f' - f)T) / \sin^2\{\pi(f' - f)T\}.$$

This leakage eventually decays only as $\sim(f'-f)^{-2}$. In PSD estimates obtained as DFT of the ACF, the Dirichlet kernel produces undesirable negative ripples whose magnitude decreases as $\sim|(f'-f)|^{-1}$. These effects are similar to the familiar Gibbs phenomena in the Fourier reconstruction of signals near discontinuities. The PSD estimates can be improved by shaping the data $z[n]$ or ACF $R_z[n]$ with a suitable window. Since the sampling and aliasing effects in PSD estimation have already been considered in detail, window properties are discussed below in terms of the continuous variables t , τ , and f . The subscript z is also dropped for clarity.

In their classical monograph, Blackman and Tukey(1958) advocated the use of shaping the ACF $R(\tau)$ by multiplication with a window or weighting function $w(\tau)$ that depends on the lag τ . The windowed PSD estimate $S_w(f)$ is obtained by convolving the true PSD $S(f)$ with the window transform $W(f) = \mathcal{F}\{w(\tau)\}$. $S_w(f)$ has better statistical properties due to smoothing in frequency by $W(f)$. To conserve the signal power $R(0)$, lag windows $w(\tau)$ used with the ACF are normalized to have $w(0)=1$. Other desirable attributes of $w(\tau)$ are a smooth decaying shape as a function of time lag τ , an even symmetry about $\tau=0$, and negligible negative sidelobes in the transform $W(f)$. Good ACF windows are further selected to be well-behaved in frequency by requiring that the transform magnitude $|W(f)|$ has a small width, and a low sidelobe level that decays sufficiently steeply with f .

A data window $d(t)$ can be directly applied as a weighting function to the signal $z(t)$ before periodogram analysis. The windowed periodogram estimate $P_D(f)$ is now obtained by convolving $S(f)$ with the squared window-transform $|D(f)|^2$. Data windows share nearly all the properties of ACF windows, now stated in terms of $d(t)$ and $|D(f)|^2$. The only major differences are that $d(0)$ need not be 1, the PSD estimates with data windowing are always non-negative, and the signal power is modified because $z(t)$ is scaled by $d(t)$. Due to peaked shape of a data window $d(t)$, the values of $z(t)$ near the end points are not fully utilized. For this reason, as much as half of one set of K points of $z[m]$ can be used with the next set. This method of data windowing with partially overlapping data segments has been described by Welch (1967), who also discusses the statistical properties of the windowed time-averaged periodogram.

A very complete description of many windows, their transform properties, and criteria for their selection has been compiled by Harris (1978). Corrections to some of these are given by Nuttal(1981) who also discusses sidelobe properties of some preferred windows. Rabiner et al. (1979) give code for generating a few frequently used windows, including von Hann, Hamming, Kaiser and Dolph-Chebyshev. The Dolph-Chebyshev window attains a uniform sidelobe level and is described through its transform $W(f)$. The Kaiser window is a time-domain approximation to this window in terms of the modified Bessel function $I_0(x)$ of zeroth order. These windows are nearly ideal for data-processing applications.

Some of the simpler windows are given below as lag windows $w(t)$ for a support $(-0.5, +0.5)$ of t . The rate at which their sidelobes in $|W(f)|$ eventually decay with f is also indicated.

Hamming	$w(t) = 0.54 + 0.46 \cos(2\pi t)$	$\sim f^{-1}$
von Hann (or Hanning)	$w(t) = 0.50 + 0.50 \cos(2\pi t)$	$\sim f^{-3}$
Approximate Blackman	$w(t) = 0.42 + 0.50 \cos(2\pi t) + 0.08 \cos(4\pi t)$	$\sim f^{-3}$

The Hamming window minimizes the first sidelobe for a simple cosine shape but its transform decays as $\sim f^{-1}$ due to the rectangular platform of height 0.08. The von Hann and the approximate Blackman windows have a better sidelobe behavior. In the analysis of power-law PSD's, it may be desirable to use windows with a steeper side-lobe decay. The Blackman window can be modified by including higher-order cosine terms. The coefficients can be selected in such a way that with m cosinusoids, the frequency response decays at the rate $|f|^{-(2m+1)}$. Two examples of modified Blackman windows are given below.

Modified Blackman : order 2, highest term $\cos(4\pi t)$	
Coefficients (0.375, 0.500, 0.125)	$\sim f^{-5}$
Modified Blackman : order 4, highest term $\cos(8\pi t)$	
Coefficients(0.2734375, 0.4375000, 0.2187500, 0.0620000, 0.0078125)	$\sim f^{-9}$

The time-domain shape of these windows is shown in Fig. 7.1. The response of the modified fourth-order Blackman window is shown in Fig. 7.2 with its

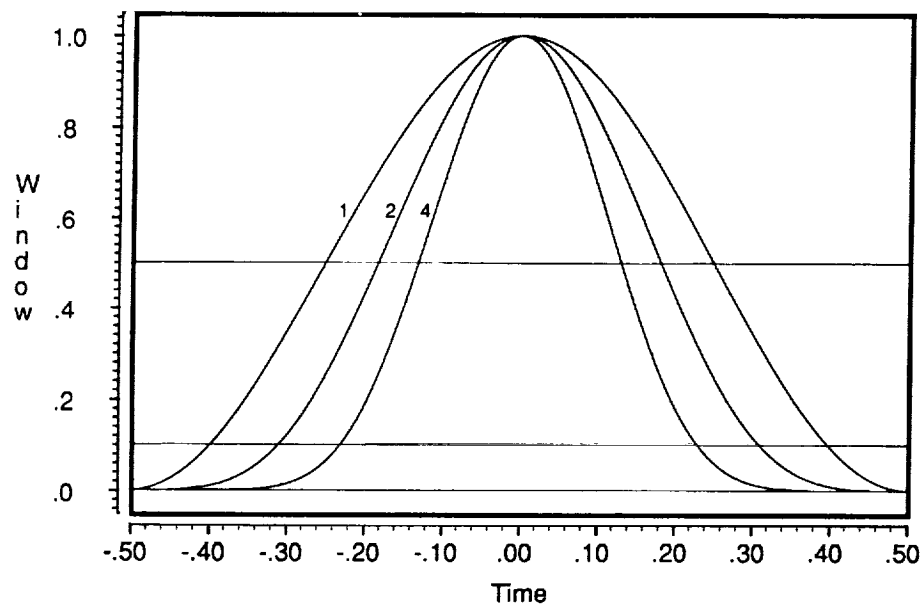


FIGURE 7.1. Time windows of order 1, 2 and 4 with good sidelobe behavior derived from the Blackman window are shown on a support $(-0.5, 0.5)$. The order 1 window is just the von Hann or Hanning window with a frequency response decaying at 60 dB/decade. The order 2 and 4 windows have a response decaying at 100 and 180 dB/decade respectively. The effective temporal width of these windows is one-half to one-fourth of their support. For a frequency resolution comparable to the rectangular, data length should then be two to four times longer.

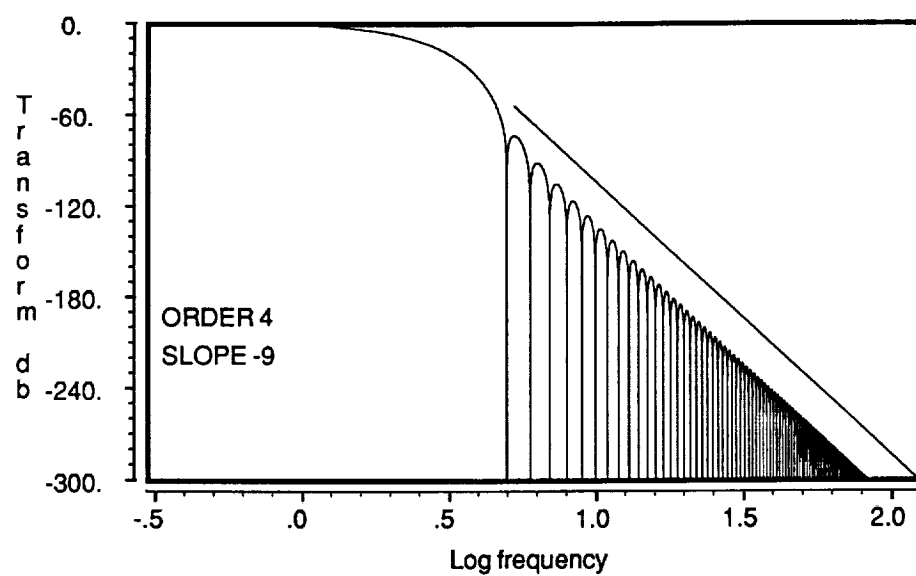


FIGURE 7.2. Frequency response of the fourth order window shown in Fig. 7.1 is shown to decay at 180 dB/decade. This and other windows with well-constrained side-lobe behavior may be useful in spectral analysis of velocity data with power-law spectra, and in suppressing the smearing of ground clutter in radar signal spectra by using longer record lengths.

$\sim f^{-9}$ decay rate. Simulations indicate that windows with well constrained sidelobes are effective in reducing the influence of trends, but require at least two to four times longer data segments. It may be surmised that the use of the modified Blackman windows, or any other suitable window, in the time-averaged periodogram method can contain the effect of fading ground clutter to near zero-frequencies.

We now briefly mention the effect of coherent integration of radar signals in PSD estimation with periodograms [Rastogi, 1983]. In coherent integration, I successive samples of $z[i]$ at a time spacing T_1 are averaged with uniform weights ($1/I$) and the averaged sequence $y[i]$ is re-sampled with time spacing $T=IT_1$. The periodogram $P_y(f)$ of $y[k]=y(kIT_1)=y(kT)$ is formed at K frequencies in the Nyquist interval $\pm 0.5(KT)^{-1}$ using the DFT.

The consequence of time averaging is to multiply the original periodogram $P_z(f)$ with a filter weighting function

$$|H(f)|^2 = \frac{1}{I^2} \frac{\sin^2(\pi f T_1 I)}{\sin^2(\pi f T_1)} \quad [7.1]$$

This filter function has maxima at multiples of $1/T_1$. Between any two maxima, there are $(I-2)$ secondary peaks with nulls at multiples of $1/(IT_1)$. The principle lobe at zero frequency, with adjacent nulls at $\pm 1/(IT_1)$, is twice as wide as the Nyquist interval. Echoes with Doppler shifts near the end points of the Nyquist interval are weighted down by nearly -4dB. A correction for this effect must be applied in spectral-moment estimation. Any components of $P_z(f)$ outside the Nyquist interval are weighted by the filter function of equation [7.1], and would then appear aliased in $P_y(f)$. Hence the coherent integration scheme is not very successful as an anti-aliasing filter.

Coherent integration does provides a computationally efficient means, through simple accumulation, of implementing a 'poor' matched filter for radar signals. Its principal advantage is in reducing the overall data rate by a factor I . The received signal $z(t)$ is originally constrained by the receiver bandwidth B . Sampling at interval $T_1 \gg B^{-1}$ aliases the entire received signal,

including noise and interference, into the frequency interval $\pm 0.5(T_1)^{-1}$. This frequency interval is further reduced to the Nyquist interval $\pm 0.5(IT_1)^{-1}$ through coherent integration. Obviously, the white-noise power outside the Nyquist interval is rejected by weighting with the filter function and its contribution is reduced by $\sim 1/I$. But within the Nyquist interval, the Doppler shifted signal peaks and white noise component are both weighted by the same filter function. Hence the detectability of spectral peaks, as discussed in Sec. 4, is not improved in any tangible way through coherent integration and there is definitely some impairment near the ends of the Nyquist interval.

8. Least Squares Estimation and Spectral Parameters

The general problem of estimating parameters from observations or data can only be examined within the frame work of a model. For any choice of parameter values, the model produces an output, which generally differs from observations. That choice of parameter values for which the model output matches the observations, in some statistical sense e.g. by minimizing the mean squared error (m.s.e.), can be said to agree with or derived from the observations. The behavior of m.s.e. as a function of model parameters may be visualized as an error surface. The best choice of parameters corresponds to the true or global minimum on this surface. An exhaustive search for the true minimum is impractical, so an acceptable local minimum is sought only within a limited region of parameter values.

With an initial guess of parameter values, it is possible to seek a local minimum in m.s.e. by using any of the several adaptive search strategies e.g. by changing parameters in the direction in which the m.s.e. changes most steeply. Excellent discussion of least mean square (l.m.s.) algorithms may be found in Alexander(1986), Bard(1974), and Widrow and Stearns(1985). Sato and Woodman(1982) have adapted Bard's formulation to spectral parameter estimation in radar experiments at Arecibo. Their approach is discussed below.

Suppose the observations $\mathbf{X} = x(k)$ represent an N-point vector. The model input is a parameter vector $\mathbf{P} = p(j)$ with J points. The model output $\mathbf{Y}(\mathbf{P}) = y(k, \mathbf{P})$ is an N-point vector that depends on \mathbf{P} . The error vector $\mathbf{e}(\mathbf{P}) =$

$\epsilon(k, \mathbf{P})$ varies with observation index k and depends on the choice of \mathbf{P} . Since $\epsilon(k, \mathbf{P})$ may be either positive or negative, we seek to minimize its accumulated square value (which divided by K is the m.s.e.)

$$e(\mathbf{P}) = \sum_{k=1}^N [y(k, \mathbf{P}) - x(k)]^2 \quad [8.1]$$

with respect to \mathbf{P} . Equating the derivative of $e(\mathbf{P})$ with respect to \mathbf{P} gives J conditions for each of its component $p(j); j=1,2,\dots,J$

$$\sum_{k=1}^N [y(k, \mathbf{P}) - x(k)] \frac{\partial y(k, \mathbf{P})}{\partial p(j)} = 0 \quad \text{for } j=1,2,\dots,J \quad [8.2]$$

Now J linear equations in as many unknowns can be solved by matrix methods, but eqns [8.2] contain nonlinear terms of the form $y \partial y / \partial p$. The equations may be linearized locally, about a parameter vector \mathbf{P}_0 , through a simple perturbation scheme. Then retaining linear terms in a Taylor series about \mathbf{P}_0 , gives $\mathbf{P} = \mathbf{P}_0 + \delta \mathbf{P}$. The model output $y(k, \mathbf{P})$ can now be written as

$$y(k, \mathbf{P}) = y(k, \mathbf{P}_0) + \sum_{i=1}^J \frac{\partial y(k, \mathbf{P}_0)}{\partial p(i)} \delta p(i) \quad \text{for } k=1,2,\dots,N \quad [8.3]$$

Substituting for $y(k, \mathbf{P})$ in the condition [8.2] for minimum m.s.e., we obtain the following J equations for each $j=1,2,\dots,J$

$$C(j) + \sum_{k=1}^N \sum_{i=1}^J \frac{\partial y(k, \mathbf{P}_0)}{\partial p(j)} \frac{\partial y(k, \mathbf{P}_0)}{\partial p(i)} \delta p(i) = 0 \quad \text{where } j=1,2,\dots,J \quad [8.4]$$

where the J constant terms $C(j)$ are given by

$$C(j) = \sum_{k=1}^N [y(k, \mathbf{P}_0) - x(k)] \frac{\partial y(k, \mathbf{P}_0)}{\partial p(j)} \quad \text{where } j=1,2,\dots,J \quad [8.5]$$

Eqn [8.4] can be more effectively written in the matrix form

$$C + D \delta P = 0 \quad [8.6]$$

$$\text{or } c(j) = \sum_{i=1}^K d(i,j) \delta p(i) \text{ where } j=1,2..J$$

Here C is a $[J \times 1]$ matrix defined in eqn [8.5], D is a $[J \times J]$ matrix denoting the product of derivatives of model output y in eqn [8.4], and δP is a $[J \times 1]$ matrix which denotes the desired change in P about P_0 to locally minimize the m.s.e. This equation can be inverted to yield,

$$\delta P = -D^{-1}C \quad [8.7]$$

where D^{-1} is the inverse of the $[J \times J]$ matrix D evaluated through any of the conventional numerical methods [see Press et al, 1986], since D does not have any special properties.

This gives the perturbation δP about P_0 to minimize the m.s.e. We are now at a new value of P_0 and the process can be iterated to find a parameter vector which either stabilizes the m.s.e. near a local bottom of the error surface, or brings it below an acceptable threshold corresponding to a 'good' estimate of parameter vector. It should be emphasized that the above scheme does not warrant a solution, though it often gives one for a reasonable initial guess P_0 , and it is extremely computation intensive.

In the m.s.e. spectral parameter scheme implemented for the 430 MHz Arecibo radar by Sato and Woodman (1982), the observation vector is the DFT of the time averaged periodogram sequence. The model output vector is then in the form of a distorted ACF sequence. In the model, MST radar signals $s(t)$ have one or two Doppler shifted components, each with three ACF or PSD parameters for an assumed Gaussian shape in the PSD. Fading ground clutter $c(t)$ also has three similar parameters. But due to its narrow, symmetric, and possibly unknown shape in the PSD, it is overspecified by the coefficients of a third order polynomial in $(\tau)^2$ and a small Doppler shift. With a noise platform included, the parameter vector has a length of 7(10) for 1(2) Doppler peaks. The distortion of ACF and PSD has been outlined in

Sec.6. The m.s.e. search is set about an initial guess of parameters obtained either by an ad-hoc analysis of spectra, or using the ACF method discussed in the next section. The m.s.e. implementation can routinely detect signals up to 50 dB below ground clutter, with a typical radial velocity uncertainty of 0.1-0.2 m/s.

The ad-hoc analysis, instead of estimating the parameters of ground clutter, merely removes it on the basis of its approximate symmetry in PSD estimates about zero Doppler shift. Estimates of Doppler shift and other parameters can be considerably improved by using time and range continuity of measured velocity, statistical editing of spectra, and by a statistical analysis of all the available data in several passes (Rastogi, 1984). These steps can be used to set a narrow range of parameters \mathbf{P} for the m.s.e. method. Adaptive processing of spectral records using the available prior statistical information, e.g. tracking Doppler peaks in range, searching for parameters near a median Doppler-shift profile, and even using 'future' data, may speed up spectral-moment processing.

9. Spectral Moment Estimation via Correlation Function

Consider a complex wide sense stationary process $z(t)$ with power P , PSD $S(f)$ and ACF $R(\tau)$. For simplicity z is omitted as a suffix. In as much as $S(f)/P$ has all the properties of a probability density function, and $S(f) = \mathfrak{F}\{R(\tau)\}$, the non-central moments of $S(f)$ and parameters derived from these are simply related to the successive derivatives of $R(\tau)$ at $\tau=0$. This method was originally used at Jicamarca for measuring the vertical motions in the F-region using the incoherent-scatter radar technique and later applied to the first middle-atmospheric radar experiments by Woodman and Guillén (1974). A complete statistical analysis of this approach has been independently given by Miller and Rochwarger (1972).

Details can be seen by considering $R(\tau) = \mathfrak{F}^{-1}\{S(f)\}$ as in eqn. [2.4]. Using the series expansion of $\exp(i2\pi f\tau)$ and evaluating the successive derivatives of $R(\tau)$ at $\tau=0$, we have

$$R(0) = \int_{-\infty}^{\infty} S(f) df = s^{(0)} \quad [9.1]$$

$$R'(0) = (j 2\pi) \int_{-\infty}^{\infty} f S(f) df = (j 2\pi) s^{(1)} \quad [9.2]$$

$$R''(0) = (j 2\pi)^2 \int_{-\infty}^{\infty} f^2 S(f) df = (j 2\pi)^2 s^{(2)} \quad [9.3]$$

We find that these derivatives are related to the successive spectral moments, $s^{(0)}$, $s^{(1)}$ and $s^{(2)}$. $s^{(0)}$ is merely the signal power P . The other two spectral parameters of interest are the center frequency or the Doppler shift f_c , and the spread σ_f of the PSD about it. As outlined in Sec. 2, these are related to the central moments of the PSD. In terms of the noncentral moments $s^{(1)}$ and $s^{(2)}$,

$$f_c = s^{(1)} / P \quad [9.4]$$

$$\sigma_f^2 = s^{(2)} / P - f_c^2 \quad [9.5]$$

which shows that uncertainties in a lower-order moment effects all higher-order parameters.

An interesting case arises when the Doppler-shifted component in the PSD is expressible through a simple shape such as the Gaussian. In terms of a normalized Gaussian function $N(f_c, \sigma_f^2)$ with mean f_c and variance σ_f^2 , the PSD becomes $S(f) = PN(f_c, \sigma_f^2)$. The ACF $R(\tau)$ is generally complex with a Hermitian symmetry. Its real part and magnitude are even, and the imaginary part and phase are odd functions of the lag τ . For the Gaussian PSD,

$$R(\tau) = P \exp(j 2\pi f_c \tau) \exp\{-\frac{1}{2}(2\pi)^2 \tau^2 \sigma_f^2\} \quad [9.6]$$

Comparing it with the polar form $|R(\tau)| \exp\{j \phi(\tau)\}$ of the ACF we see that the phase $\phi(\tau)$ increases linearly with lag τ and the mean frequency f_c . The magnitude $|R(\tau)|$ has a Gaussian shape which can be approximated by a

parabola for small τ . From just two ACF values at zero lag and a small lag τ , we find $P = R(0)$, and

$$(2\pi) f_c = \phi(\tau) / \tau \quad [9.7]$$

$$(2\pi)^2 \sigma_f^2 = 2 \tau^{-2} \{1 - |R(\tau)| / P\} \quad [9.8]$$

Fig. 9.1 shows how the spectral parameters are related for the ACF and PSD. The effect of two Gaussian components in signals scattered from two turbulent layers has been considered by Rastogi and Bowhill (1976).

The ACF approach provides a clever method for finding spectral parameters if $z(t)$ contains only an atmospheric component $s(t)$ conforming to the simple models just discussed. Otherwise spectral contributions to $z(t)$ from noise $n(t)$, ground clutter $c(t)$ and interference $i(t)$, are all included, by definition, in the ACF $R(\tau)$. We now use an appropriate suffix to identify these components. Corrections to remove their effect require ACF measurements at several lags.

An additive white noise $n(t)$, merely adds a spike of size P_n to $R_z(0)$ at zero lag. Then $P_s = P_z - P_n$. A correction for P_n can be applied by using two or more small non-zero lags of $R(\tau)$ to estimate and remove the noise spike $R_z(0)$. Ground clutter $c(t)$ has an effect on the estimation of f_c only through the error it introduces in the power estimate. It contributes a nearly constant platform R_c to $R_z(\tau)$ at small lags due to its long fading time. Its contribution may be effectively removed by d.c. subtraction from $z(t)$ [See Fig. 9.2].

Statistical errors in parameter estimates obtained by the ACF method are discussed in detail by Miller and Rochwarger (1972). The following analysis of the uncertainty in Doppler estimation is, however, quite instructive. Consider K samples of a complex, zero-mean Gaussian process $z(t) = x(t) + j y(t)$ with a sampling interval T . If the variance of $z(t)$ is σ^2 , identified also as its power P , then the signal power P_K estimated from K samples as $\langle z[k]z^*[k] \rangle$ has the statistics $E[P_K] = \sigma^2$ and $\text{var}[P_K] = \sigma^4/K$. Hence P_K is unbiased and its statistical error P/\sqrt{K} decreases with large K . Next we estimate $R(T)=R[1]$ at the first sampled lag index as $\langle z[k]z^*[k+1] \rangle$ using

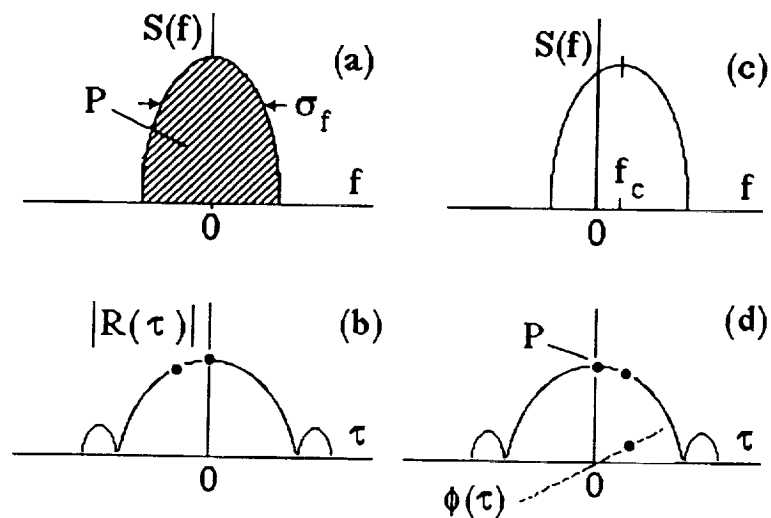


FIGURE 9.1 : A hypothetical PSD and the corresponding ACF for zero Doppler shift are shown in (a) and (b). The effect of a slight Doppler shift is shown in (c) and (d). The area under the PSD and the ACF at zero lag are equal to the signal power. The frequency width of the PSD and the relative value of ACF magnitude at a small lag are related. When the PSD is Doppler shifted by a small amount, the ACF becomes complex. Then the shift can be estimated from the ACF phase at a small lag.

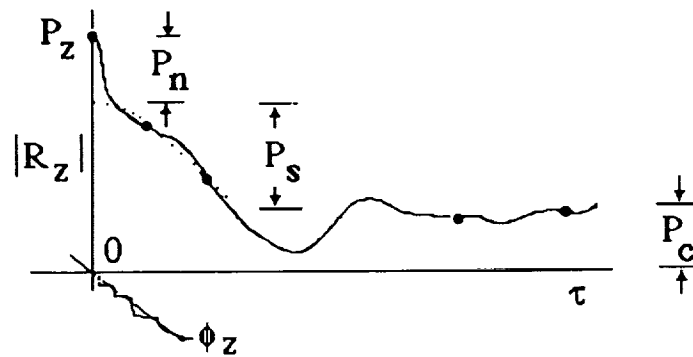


FIGURE 9.2 : The effect of noise and clutter on the shape of the ACF and their contribution to the total power. The effect of noise and clutter can be effectively removed from the total power using the ACF values measured at a few key points. The ACF phase still remains linear at small lags, but the Doppler shift is underestimated unless noise and clutter are removed from the total signal power. The spectral width is overestimated from the ACF value at a small lag, unless the noise spike at zero lag is removed.

either of the two estimates $R^{[1]}$ or $R^{[2]}$ given in eqns [5.1] and [5.2]. The biased estimate $R^{[2]}$ is preferable for reasons discussed earlier, but the use of $R^{[1]}$ is more convenient. For small T , the K sample estimate ϕ_K of ϕ is

$$\phi_K(T) \approx \tan \phi_K[1] = \{[K-1] P\}^{-1} \sum_{k=1}^{K-1} y[k] x[k+1] - x[k] y[k+1] \quad [9.9]$$

This estimate is unbiased due to the use of $R^{[1]}$. Its variance involves a moment of the form $E[abcd]$ of four zero-mean Gaussian variables. Using a result due to Isserlis and Hotelling (see e.g. Papoulis, 1983) the fourth moment reduces to $E[abcd] = E[ab] E[cd] + E[ac] E[bd] + E[ad] E[bc]$. The final result ,

$$\text{var}\{\phi_K(T)\} \approx \{P^2 - |R(T)|^2\} / 2 K |R(T)|^2 \quad [9.10]$$

shows that at small lags the uncertainty in phase estimate is quite sensitive to the relative magnitude of the ACF. The corresponding statistical error in the radial velocity for a radar wavelength λ in terms of the normalized autocorrelation magnitude ρ or $|R(T)/R(0)|$ is

$$\sigma_v \approx \frac{1}{\sqrt{2K}} \frac{\lambda_0}{4\pi T} \frac{\sqrt{1-\rho^2}}{\rho} \quad [9.11]$$

For a 50 MHz radar, with $T=0.25$ sec, $\rho=0.5$, and $K=100$, we find that the radial velocity can be measured with a standard deviation of 0.23 m/s. With $\rho=0.8$ the figure improves to 0.1 m/s.

The ACF method provides a relatively fast means of estimating the spectral moments for clean radar signals. Due to the ease of its implementation, it is suited to real time estimation of spectral moments. Statistical averages of these moments may also serve as an initial guess in the m.m.s.e. approach.

10. Spectral Analysis by Time Series Models and Maximum Entropy Method

Methods discussed so far for estimating the PSD $S(f)$ of a complex random process $z(t)$, from its uniformly-spaced samples $z[k]$, make some unrealistic

assumptions about extension of data or its ACF $R(\tau)$. The DFT assumes a periodic extension of data. In methods that use the ACF, windowing or truncation assumes zero correlation beyond a convenient maximum lag. J. P. Burg has proposed a method which circumvents these objections by seeking an extension of the ACF at measured lags that maximizes the entropy (in an Information-theoretic sense) of the observed process [see Childers, 1978]. Alternatively, one seeks to extend the process or its ACF from limited observations, using suitable time-series models. These are examined first.

Spectral analysis may be regarded as a filter design problem in which we seek coefficients $h[k]$ of a feedback filter excited by white noise $n[k]$, so that its output becomes the observed process $z[k]$. The filter output is taken as a linear combinations of the current input, q past inputs, and p past outputs. Such parametric representation of an observed process is called an autoregressive moving-average or ARMA model

$$z[k] = -\sum_{i=1}^p a[i] z[k-i] + \sum_{j=0}^q b[j] n[k-j] \quad \text{ARMA}(p,q) \text{ model [10.1]}$$

Recalling that shifting a signal s to the left by an interval iT amounts to multiplying its Fourier transform by $\exp(-i2\pi fT)$, the PSD $S(f)$ can be represented in terms of two polynomials (with $b[0]=1$),

$$A(f) = 1 + \sum_{i=1}^p a[i] \exp(-i2\pi fT) \quad \text{and} \quad B(f) = 1 + \sum_{j=1}^q b[j] \exp(-j2\pi fT)$$

and using the sampling interval T and noise variance σ^2 , as

$$S(f) = \sigma^2 T \frac{|B(f)|^2}{|A(f)|^2} \quad [10.2]$$

This representation has q zeros and p poles. Hence we expect the AR model to be more suitable for representing a process with sharp peaks in the PSD, and the MA process for a PSD with flat peaks. The ground clutter component $c(t)$ in radar experiments has a near-ideal representation as a pole. We surmise

that the Doppler shifted components should require an MA part. An ARMA(p,q) process can be overdefined in terms of an AR(p') or an MA(q') process with $p' \gg p$, $q' \gg q$. So a purely AR model, with $q=0$, may be adequate for representing PSD of radar signals $z(t)$.

For an AR(p) process $z(t)$, the ACF $R[k]$ is related for lags 0,1,...p through the Yule-Walker normal equations.

$$\begin{bmatrix} R[0] & R[-1] & & & R[-p] \\ R[1] & R[0] & & & R[-p+1] \\ & R[1] & R[-1] & & \\ & & R[0] & R[-1] & \\ R[p] & R[p-1] & R[1] & R[0] & \end{bmatrix} \begin{bmatrix} 1 \\ a[1] \\ a[2] \\ \\ a[p] \end{bmatrix} = \begin{bmatrix} \sigma^2 \\ 0 \\ 0 \\ 0 \\ 0 \end{bmatrix} \quad [10.3]$$

These linear equations involve the (p+1) ACF values arranged as a Toeplitz matrix. In this matrix form, the same elements appear along a diagonal. In addition, the elements along cross diagonals have Hermitian symmetry. The matrix can be inverted through Levinson's recursion in $\sim p^2$ operations. Programs for solving these equations may be found in Press et al. (1986) and Marple (1987). Note that the use of Wiener-Khintchine theorem to find the PSD $S(f)$ would require the ACF values $R[m]$ at all lags. But for an AR(p) process, the p coefficients suffice through eqn [10.2] for finding the PSD. The structure of these equations may also be discussed in terms of forward and backward linear-prediction filters, which given some values of data $z[k]$ extend these in the both directions. Further discussion may be found in several excellent papers in Childers(1978), and Marple (1987).

The modified Yule-Walker equations for MA and ARMA models are nonlinear and inherently difficult to solve for filter coefficients.

Entropy H of a random variable X with a probability density function f_x is defined as the expectation $E\{-\ln f_x(x)\}$. It is a measure of the randomness in the underlying chance experiment. Maximizing the entropy may yield a solution in some statistical situations. An interesting example is that of a

loaded die with an average face value of 3.5, instead of 4.5 for a fair one. There are infinitely many solutions to the probabilities p_i for the six faces. Maximizing the entropy H under the constraint of the given average value can be set up as a nice variational problem. Using the method of Lagrange multipliers, this gives p_i 's as a geometric series with a ratio r . The resulting equations for p_1 and r are nonlinear, but can be solved recursively from an initial guess. The solution is $p_1 = 0.05435$, $r = 1.44926$. This is not a unique solution, since changing any two p_i 's by a small amount $\pm\delta$ is also a solution.

For $(N+1)$ uniformly-spaced samples of a complex, zero-mean, Gaussian random process, the entropy H is obtained using the joint probability density function of $2(N+1)$ real Gaussian variables. This density involves the Toeplitz ACF matrix form given in eqn. [10.3], albeit of size $(N+1)$ instead of $(p+1)$. We denote this matrix by \mathbf{R}_N as it involves N distinct nonzero lags. It is also convenient to use the base $(2\pi)^{1/4}$ for the logarithm. Then the entropy H becomes $0.5 \log\{\det \mathbf{R}_N\}$ and it increases with N , eventually becoming infinite. We deal with the entropy rate h defined as $h = H/(N+1)$ which becomes $0.5 \log\{(\det \mathbf{R}_N)^{1/(N+1)}\}$. In the limiting case of infinite N , it can be shown from that for the Toeplitz form of \mathbf{R}_N , the entropy rate h reduces to

$$h = -0.5 \log T + 0.5T \int_{-0.5/T}^{0.5/T} \log S(f) df \quad [10.4]$$

where the integral is over the Nyquist interval. Complicated details leading to this result may be found e.g. in Smylie et al.(1973). We may expand $S(f)$ in a Fourier series using the ACF values $R[k]$. The entropy rate h may now be maximized with respect to the unknown ACF values $R[k]$ for $|k| > N$ under the constraints that the first $(N+1)$ values of ACF, including the zero lag, are known from the data. This difficult exercise, as in the loaded-die problem, does not warrant a unique solution. The final result expressed in the form of a PSD estimate is that

$$S(f) = \frac{T\sigma^2}{\left| 1 + \sum_{k=1}^p a[k] \exp(-j 2\pi f k T) \right|^2} \quad [10.5]$$

This result is exactly the same as the PSD of an AR(p) process given in eqn [10.2] with the moving-average order q set to zero and the numerator polynomial $|B(f)|^2 = 1$. The p coefficients $a[k]$ are the same as for the AR(p) model obtained by solving the Yule-Walker equations [10.3]. Hence the maximum entropy method (MEM) is equivalent to the AR(p) model for equispaced samples of a complex Gaussian process.

If the process is not Gaussian, then the final result in eqn [10.5] for entropy rate would not hold. MEM still will give a result, but it may not be a representative estimate of the PSD for the process. We also remark that though we have shown eqn [10.5] in the AR form, actual implementations of MEM are rather different and take the form of designing a linear-prediction filter. Computer programs for MEM may be found in Press et al. (1986) and in Marple (1987).

A fundamental problem in implementing the above methods is that of finding the order p of the process. Use of an incorrect order give larger statistical errors. The order must be found empirically for each class of processes. In a recent experimental and numerical study, Klostermeyer (1986) has compared the performance of periodogram, MEM and maximum likelihood method (MLM) for PSD estimation of ST signals observed with the 53.5 MHz SOUSY radar. It was found that for SNR of 0.3 to 10, MEM and MLM give better estimates of Doppler shift. The optimum order of the MEM filter is $\sim 3 \pm 1$ with a sampling time of 0.173 sec, and appears to decrease with the SNR. Similar studies with other atmospheric radar signals, and of their statistics, are needed for developing the use of MEM and AR PSD models.

References

- Alexander, S. T., *Adaptive signal processing - Theory and applications*, Springer-Verlag, New York, 197pp., 1986.
- Balsley, B. B., The MST technique - a brief review, *J. Atmos. Terres. Phys.*, **43**, 495-509, 1981.
- Balsley, B. B. and D. A. Carter, The spectrum of atmospheric velocity fluctuations at 8 km and 86 km, *Geophys. Res. Lett.*, **9**, 465-468, 1982.
- Bard, Y., *Nonlinear parameter estimation*, Academic, New York, 1974.
- Blackman, R. B. and J. W. Tukey, *The measurement of power spectra from the point of view of communications engineering*, Dover, New York, 190pp., 1958.
- Brigham, E. O., *The fast Fourier transform and its applications*, Prentice-Hall, Englewood Cliffs, 448pp., 1988.
- Childers, D. G., Ed., *Modern Spectral Analysis*, IEEE Press, New York, 334pp., 1978
- Cooley, J. W., P. A. W. Lewis, and P. D. Welch, *The fast Fourier transform and its application to time series analysis*, in *Statistical methods for digital computers*, Eds. K. Enslein et al., J. Wiley, New York, 377-423, 1977.
- Davenport, W. B. and W. L. Root, *An introduction to the theory of random signals and noise*, McGraw-Hill, New York, 393pp., 1958.
- Gottman, J. M., *Time-series analysis : A comprehensive introduction for social scientists*, Cambridge, New York, 400 pp., 1981.
- Hamming, R. W., *Numerical methods for scientists and engineers*, 2nd edition, Dover, New York, 721pp., 1973.

- Harris, F. J., On the use of windows for harmonic analysis with the discrete Fourier transform, *Proc. IEEE*, **66**, p.51-83, 1978.
- Klostermeyer, J., Experiments with maximum entropy and maximum likelihood spectra of VHF radar signals, *Radio Sci.*, **21**, 731-736, 1986.
- Koopmans, L. H., *The spectral analysis of time series*, Academic, New York, 366pp., 1974.
- Marple, S. L., *Digital spectral analysis with applications*, Prentice-Hall, Englewood Cliffs, 492pp., 1987.
- Miller, K. S., *Complex stochastic processes*, Addison-Wesley, Reading, Mass, 238pp., 1974.
- Miller, K. S., and M. M. Rochwarger, A covarinace approach to spectral moment estimation, *IEEE trans. Inf. Th.*, **IT-18**, 588-596, 1972.
- Nuttal, A. H., Some windows with very good sidelobe behavior, *IEEE trans. Audio, Speech and Sig. Proc.*, **ASSP-29**, p.84-91, 1981.
- Oppenheim, A. V. and R. W. Schafer, *Digital Signal Processing*, Prentice-Hall, Englewood Cliffs, 585pp., 1975.
- Oppenheim, A. V. and A. S. Willsky, *Signals and systems*, Prentice-Hall, Englewood Cliffs, 796pp., 1983.
- Papoulis, A., *Signal analysis*, McGraw-Hill, NewYork, 431pp., 1977.
- Papoulis, A., *Probability random variables and stochastic processes*, 2nd edition, McGraw-Hill, NewYork, 576pp., 1983.
- Press, W. H., B. P. Flannery, S. A. Teukolsky and W. H. Vetterling, *Numerical recipes : The art of scientific computing*, Cambridge, New York, 818pp., 1986.

- Rabiner, L. R., C. A. McGonegal and D. Paul, FIR windowed filter design program - WINDOW, in *Programs for Digital Signal Processing*, IEEE Press, New York, p. 5.2.1-5.2.19, 1979.
- Rastogi, P. K., A note on the use of coherent integration in periodogram analysis of MST radar signals, *Handbook for MAP*, v. 9, Ed. S. A. Bowhill and B. Edwards, SCOSTEP secretariat, Urbana, p. 509-512, 1983.
- Rastogi, P. K., Criteria and algorithms for spectrum parametrization of MST radar signals, *Handbook for MAP*, v. 14, Ed. S. A. Bowhill and B. Edwards, SCOSTEP secretariat, Urbana, p. 289-293, 1984.
- Rastogi, P. K. and S. A. Bowhill, Scattering of radio waves from the mesosphere 2. Evidence for intermittent mesospheric turbulence, *J. Atmos. Terres. Phys.*, **38**, 449-462, 1976.
- Rastogi, P. K. and R. F. Woodman, Mesospheric studies using the Jicamarca incoherent-scatter radar, *J. Atmos. Terres. Phys.*, **36**, 1217-1231, 1974.
- Röttger, J., VHF radar measurements of small-scale and meso-scale dynamical processes in the middle atmosphere, *Phil. Trans. Royal Soc. London, A* **323**, 611-628, 1987.
- Sato, T. and R. F. Woodman, Spectral parameter estimation of CAT radar echoes in the presence of fading clutter, *Radio Sci.*, **17**, p. 817-826, 1982.
- Smiley, D. E., G. K. C. Clarke, and T. J. Ulrych, Analysis of irregularities in the Earth's rotation, in *Methods in Computational Physics*, v. 13, eds. B. Alder et al, Academic, New York, p. 391-430, 1973.
- Stearns, S. D., *Digital signal analysis*, Hayden, Rochell Park, 280pp., 1975
- Vincent, R. A. and I. M. Reid, HF Doppler measurements of mesospheric gravity wave momentum fluxes, *J. Atmos. Sci.*, **40**, 1321-1333, 1983.

Whalen, A. D., *Detection of Signals in noise*, Academic Press, San Diego, 411pp, 1971.

Welch, P. D., The use of fast Fourier transform for the estimation of power spectra : A method based on time averaging over short, modified periodograms, *IEEE trans. Audio, Speech and Electroac.*, AU-15, p.70-73, 1967.

Widrow, B. and S. D. Stearns, *Adaptive signal processing*, Prentice-Hall, Englewood Cliffs, 474pp., 1985.

Woodman, R. F. and A. Guillén, Radar observations of winds and turbulence in the stratosphere and mesosphere, *J. Atmos. Sci.*, **31**, 493-505, 1974.

Chapter 7

TARGET PARAMETER ESTIMATION

W. K. Hocking¹Radio Atmospheric Science Center,
Kyoto University, Uji, Kyoto 611, JAPAN**Abstract**

The objective of any radar experiment is to determine as much about the entities which scatter the radiation as possible. This review discusses many of the various parameters which can be deduced in a radar experiment, and also critically examines the procedures used to deduce them. Methods for determining the mean wind velocity, the RMS fluctuating velocities, turbulence parameters (e.g. C_n^2 , ϵ , K_M), and the shapes of the scatterers are considered. Complications with these determinations are discussed. It is seen throughout that a detailed understanding about the shape and cause of the scatterers is important in order to make better determinations of these various quantities. Finally, some other parameters, which are less easily acquired, are considered. For example, it is noted that momentum fluxes due to buoyancy waves and turbulence can be determined, and on occasions radars can be used to determine stratospheric diffusion coefficients and even temperature profiles in the atmosphere.

1 Introduction

The ultimate aim of any radar experiment is of course to determine information about the structures which backscatter the radio waves, and the environment in which they exist. For example, it might be of interest to study the shape of the scatterers, or to differentiate different types of scatterers or reflectors. It might be of interest to determine the radar cross-section of the scatterers, or their spatial distribution over the sky. Other desired information might include the velocity of the scatterers, and information about the spatial and temporal variation of these velocities. If the radio scatter is due to the turbulence, it might be desirable to measure the intensity of the turbulence.

The purpose of this article is to discuss ways in which parameters like these can be determined, and how they can be interpreted. Some of the approximations used in determining these parameters are also critically examined. Some consideration will be given to experimental design, and then interpretation of the results. Studies of the parameters evaluated over long periods of time can give a considerable amount of additional information, over and above that which can be determined from a few discrete observations, but discussion of this aspect will not be considered in great detail, due to lack of space.

The paper is organized in such a way that the simplest parameters are discussed first, and parameters which are more difficult to extract are considered later.

2 Wind vector determination

One of the the simplest and yet most important parameters to determine is the wind speed, so we shall begin with a brief discussion of its determination, examining in detail some of the

¹On leave from Department of Physics and Mathematical Physics,
University of Adelaide, S.A., 5001 Australia

assumptions made in this evaluation.

There are at least two different approaches to the determination of the mean wind. One utilizes large antenna arrays with correspondingly narrow radiation patterns, and with the beams pointed in various directions to measure wind speeds; the Doppler shift of the backscattered signal is utilized for this calculation, and such techniques are called "Doppler Beam Swinging" (DBS) techniques. The second class of method, called spaced antenna methods, utilizes systems of separated (spaced) arrays; wind speeds are determined by using phase and time differences between signals received with the arrays. The sets of spaced antenna arrays usually have smaller physical dimensions than the antenna arrays used in the DBS mode. In some senses, the techniques which use time delays and the techniques which utilize phase delays can even be regarded as distinct techniques, and they will be considered somewhat independently in this paper; however they will both be considered as "spaced antenna" techniques. These various different approaches will now be discussed.

2.1 Doppler measurements

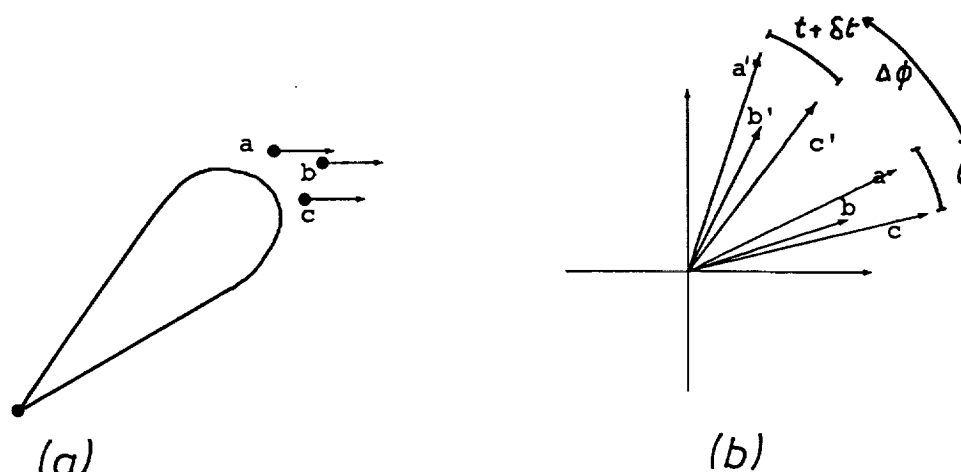


Fig. 1 Principle of Doppler method; off-vertical beam used to record rate of change of phase of scatterers.

The principle of Doppler determination of the wind speed is to utilize the change in the phase of scattered radio waves as a function of time. It is probably the most common procedure currently in use, so some time will be devoted to discussion of this technique.

2.1.1 Basic principles of the Doppler method

As the scatterers move, the path length between the transmitter, scatterer and receiver changes, and this shows as a change in phase (fig. 1a). We can think of this as the rotation of the vector in the argand plane (fig. 1b). For a monostatic radar, the mean rate of change of phase is a measure of the mean radial component of the velocity of the scatterers viz.

$$\langle v_{rad} \rangle = \frac{\lambda}{4\pi} \left\langle \frac{d\phi}{dt} \right\rangle \quad (1)$$

Here, $\langle \rangle$ represents the average value, averaged over the radar volume and the sampling time, v_{rad} is the radial component of the velocity, λ is the radar wavelength, ϕ is the phase, and $d\phi/dt$ is the rate of change of phase. Each scatterer causes its appropriate vector to rotate at a slightly different frequency, and we can represent this on a spectrum, where each line corresponds to a different scatterer (fig. 2). Of course it should be borne in mind that in a real spectrum, it may not be physical to think of each separate spectral line as due to such a scatterer, but for our purposes this is adequate.

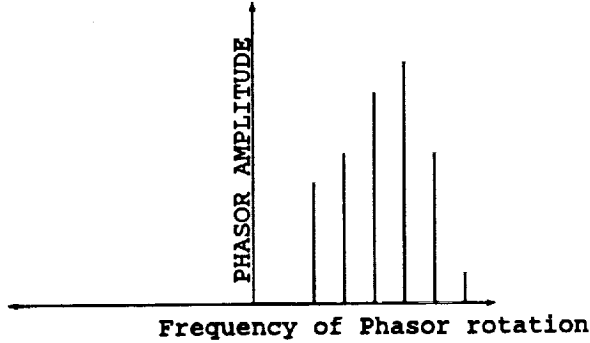


Fig. 2

We shall assume for simplicity that the spectral density and frequency of each line is invariant, so just the phase of the signal from each scatterer changes. If a single phasor at time t can be described by $\underline{a}_0 = a_0 e^{i\omega t}$, ($a_0 = |\underline{a}_0|$) then at time $t + \delta t$ it is given by $\underline{a}'_0 = a_0 e^{i\omega(t+\delta t)}$. Given the two phasors, the phase difference can be found by calculating $\underline{a}_0^* \cdot \underline{a}'_0$, where $(*)$ means complex conjugate. This calculation gives $a_0^2 e^{i\omega\delta t} = a_0^2 e^{i\Delta\phi}$. We actually seek $\langle \Delta\phi \rangle$ averaged over all the scatterers in the radar volume, but if the phasors all have equal amplitude, or even more generally the spectrum has a symmetric shape, then we can say that $\langle \Delta\phi \rangle = \arg\{\langle a^2 e^{i\Delta\phi} \rangle\}$, even for large values of $\Delta\phi$. In other words, summing the phasors and finding the rotation of the resultant gives the same result as averaging the angles of rotation of each phasor. This is also true even in the presence of a moderate amount of noise. Hence we will consider averages of $a_0^2 e^{i\Delta\phi}$. This mean value calculated for n phasors $\underline{a}_j e^{i\Delta\phi_j}$ ($j = 1$ to n) is

$$\langle a_0^2 e^{i\Delta\phi} \rangle = \frac{1}{n} \sum_{j=1}^n \underline{a}_j^*(t) \underline{a}_j(t + \delta t) \quad (2)$$

To improve the accuracy, imagine averaging over a reasonable length of time, say at N time steps $t_1, t_2, \dots, t_k, \dots, t_N$, where $t_k = k\delta t$. Then

$$\langle a_0^2 e^{i\Delta\phi} \rangle = \frac{1}{N} \sum_{k=1}^N \left[\frac{1}{n} \sum_{j=1}^n \underline{a}_j^*(t_k) \underline{a}_j(t_k + \delta t) \right] \quad (3)$$

We can write this as

$$\langle a_0^2 e^{i\Delta\phi} \rangle = \frac{1}{N} \sum_{k=1}^N \left[\frac{1}{n} \sum_{j=1}^n \underline{a}_j^*(t_k) \sum_{j'} \underline{a}_{j'}(t_k + \delta t) \right], \quad (4)$$

since the cross terms in the square brackets of (4) all involve terms like $e^{-i\omega_j t} e^{i\omega_{j'} t}$, where $\omega_j \neq \omega_{j'}$, and such terms sum to zero when summed over a period substantially longer than their beat period. In fact in the case that the time series is Fourier transformed by a discrete

Fourier transform, all frequencies are harmonically related and so these cross terms summed over the data length are all exactly zero. But the term $\sum_{j=1}^n a_j(t_k)$ is simply the value of the (complex) time series which would be recorded by the radar at time t_k , which we will denote as $\underline{f}(t_k)$, and so (4) can be written as

$$\langle a_0^2 e^{i\Delta\phi} \rangle = \frac{1}{N} \sum_{k=1}^N \underline{f}^*(t_k) \underline{f}(t_{k+1}) \quad (5)$$

which is simply the autocovariance function at the first lag, $\rho(\delta t)$ say. Thus the mean rate of change of phase can be found from

$$\langle \frac{d\Delta\phi}{dt} \rangle = \frac{1}{2\pi\delta t} \tan^{-1} \left\{ \frac{\text{Im}(\rho(\delta t))}{\text{Re}(\rho(\delta t))} \right\} \quad (6)$$

where Re means "the real part of" and Im means "the imaginary part of". This estimator of the rate of change of phase was introduced by WOODMAN and GUILLEN, (1974). Notice that the value of the autocovariance $\rho(\tau)$ at $\tau = \delta t$ can also be found from the power spectrum $P(f)$ as (Wiener-Kintchine theorem e.g BRACEWELL, 1978)

$$\rho(\delta t) = \sum_{j=1}^n P(f_j) e^{2\pi i f_j \delta t} \quad (7)$$

where $f_j = (j-1)/T$, T being the data length of the time series $\{\underline{f}(t_k)\}$.

Then

$$v_{rad} = \frac{\lambda}{4\pi} \langle \frac{\Delta\phi}{\delta t} \rangle = \frac{\lambda}{4\pi\delta t} \tan^{-1} \left\{ \frac{\text{Im}\{\sum_{j=1}^n P(f_j) e^{2\pi i f_j \delta t}\}}{\text{Re}\{\sum_{j=1}^n P(f_j) e^{2\pi i f_j \delta t}\}} \right\}. \quad (8)$$

Since $P(f)$ is real (by definition),

$$v_{rad} = \frac{\lambda}{4\pi} \langle \frac{\Delta\phi}{\delta t} \rangle = \frac{\lambda}{4\pi\delta t} \tan^{-1} \left\{ \frac{\sum_{j=1}^n P(f_j) \sin(2\pi f_j \delta t)}{\sum_{j=1}^n P(f_j) \cos(2\pi f_j \delta t)} \right\} \quad (9)$$

In the limit that the term in the right hand brackets $\{\}$ is $\ll 1$ and the $P(f_j)$ values are small for the larger $|f_j|$, this approximates to

$$v_{rad} \simeq \frac{\lambda}{2} \frac{\sum_{j=1}^n f_j P(f_j)}{\sum_{j=1}^n P(f_j)} \quad (10)$$

This last expression is one commonly employed as an estimator of the radial component of the velocity (eg GAGE and BALSLEY, 1978; ZRNIC, 1979). Nevertheless, notice it is only an approximation of the more exact expressions (6) and (9), and breaks down when the argument of the $\tan^{-1}\{\}$ expression in (9) becomes comparable to 1. This can happen particularly when the signal is noisy or when the spectral peak is close to the Nyquist frequency, and in these cases the approximation (10) can give erroneous estimates. In the case of high noise levels, the true radial velocity is underestimated. The more exact expressions (6) and (9) will work well in these cases, however.

Some workers extract the radial velocity from the spectrum not by using expressions like (6) - (10), but by fitting a particular spectral shape to the data. Usually a Gaussian function of the type

$$S(f) = N + \frac{P}{\sqrt{2\pi}\sigma} \exp \left[-\frac{(f - f_d)^2}{2\sigma^2} \right], \quad (11)$$

is used, where f is frequency and P , f_d and σ are echo power, mean Doppler shift and root mean square spectral width, respectively. N describes the noise contribution, and represents a constant offset of the spectrum since noise appears with equal spectral density at all frequencies. This method bypasses some of the problems involved in applying equation (10) (e.g. WOODMAN, 1985); its application is fairly straight-forward and it will not be discussed in any more detail here.

2.1.2 Practical problems with the DBS method

Having now determined the radial velocity, it is necessary to determine what it means in terms of atmospheric dynamics. It is generally true that the measured velocity really is the radial component of the mean velocity of the scatterers, but this is not always true, and cases can occur in which the measured velocity is an effective phase velocity of a moving patch. Such cases are rare, but should be born in mind. CROFT (1972) has given an excellent discussion of the Doppler technique, and some of its potential pitfalls.

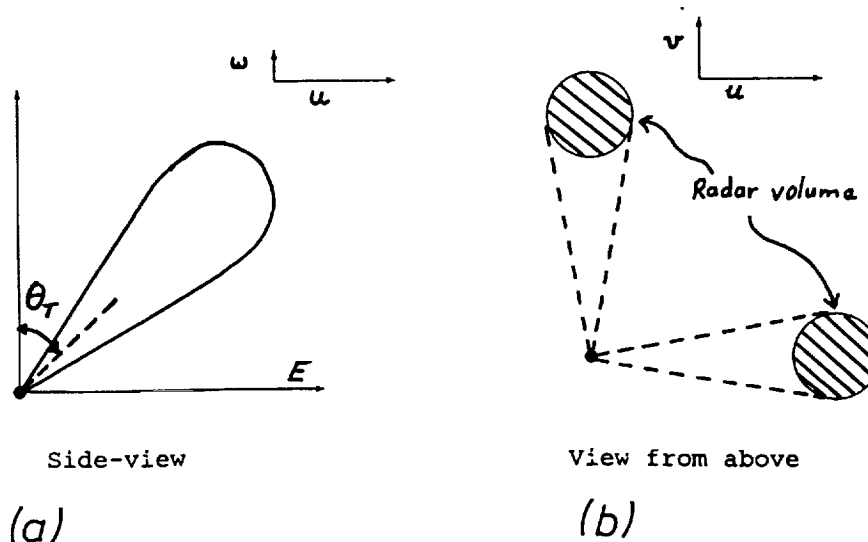


Fig. 3 DBS beam configuration (typical).

There are also many complicating features of a practical nature which arise in using the Doppler method to determine a mean wind (e.g. ROETTGER, 1981). It is sometimes assumed that the vertical wind component is zero, so that off vertical beams can be used to infer the horizontal wind. The situation is described in fig. 3, and if the vertical velocity w is zero then the component of the horizontal wind in the azimuthal direction of the radar v_{hor} can be found as

$$v_{hor} = \frac{v_{rad}}{\sin \theta_r} \quad (12)$$

By using orthogonal beams, one say pointing Northward and one Eastward, the total mean horizontal wind can be determined. However, the scatter recorded by each beam is received

from different regions of the sky (fig. 3b), and it is often desirable to know the wind vector at a single point in the sky. Provided that the wind does not vary too much spatially it is possible to assume that both components apply immediately above the radar, but sometimes the divergence of the wind field can be substantial. If the divergence is small, then it is also possible to correct for the vertical velocity, because one can determine the vertical speed w over the radar by using a vertical beam, and then when using an off vertical beam

$$v_{rad} = v_{hor} \sin \theta_T + w \cos \theta_T \quad (13)$$

so

$$v_{hor} = \frac{v_{rad} - w \cos \theta_T}{\sin \theta_T} \quad (14)$$

Nevertheless, the possibility of divergences in the wind field is a very real one, and must always be borne in mind when using these expressions.

Even without the problems of spatial variation of the wind field, the above simple assumptions can be in error. For example, if the scatterers are not isotropic, but are on average "stretched out" into horizontally aligned oval-type shapes, then they will have a nonisotropic backscatter polar diagram. Radio waves incident vertically will be more efficiently backscattered than those incident obliquely. Thus for an off vertical beam, strongest scatter will be received from angles nearer to the zenith than from the mean direction of tilt of the beam (e.g. ROETTGER 1981; HOCKING et al., 1986). We might parameterize the backscatter as

$$B(\theta) \propto e^{-\frac{\sin^2 \theta}{\sin^2 \theta_0}} \quad (15)$$

and then θ_0 is a parameter typifying the nature of the scatterers. For example, $\theta_0 = 90^\circ$ corresponds to almost isotropic scatter provided we are only interested in angles of θ out to 20° or so, and $\theta_0 = 0^\circ$ is for the case when reflection only occurs from overhead. (Some authors use the form $e^{-\frac{\theta^2}{\theta_0^2}}$ for $B(\theta)$.)

It can be shown that θ_0 relates to the ratio of the length to the depth of the scatterers (HOCKING, 1987a), and this relationship will be discussed in a later section. For the present, we will simply note (e.g. see appendix A) that in such cases one should replace the angles θ_T in equations (12) to (14) with the parameter θ_{eff} where

$$\sin \theta_{eff} = \sin \theta_T \left[1 + \frac{\theta_0^2}{\theta_T^2} \right]^{-1} \quad (16)$$

Here, it has been assumed that the radar two-way polar diagram has a Gaussian shape of the form $\exp\{-\sin^2 \theta / \sin^2 \theta_0\}$ (when aligned vertically), so that the half-power half-width of the beam is $\theta_{\frac{1}{2}} = \sqrt{\ln 2} \cdot \theta_0$. Even beyond this, however, there are still potential problems with Doppler determination of wind speeds. If there are a variety of shapes, for example, the simple theory of appendix A is not valid. If stratified reflecting steps exist as well as isotropic and anisotropic scatterers, then complications also arise.

The shapes of the scatterers can also affect determination of the vertical velocity. If, for example, the atmospheric scatterers are not aligned exactly horizontally, but have a small tilt, then the direction of preferred scatter will not be immediately overhead, but off to one side. The result is that the small vertical velocities will be contaminated with a small component of the horizontal wind. For example, if the effective tilt is only 1° , and the beam half-power half-width is say greater than about 3° , a horizontal wind of 50 ms^{-1} results in a contribution to the "vertical" velocity of $\sim 1 \text{ ms}^{-1}$. This is why most analyses of "vertical" velocity

" are made only by using long term means; it is hoped that such tilts average out to zero when averaged over long times, but even then some caution must be exercised. Indeed, a better radar configuration for estimates of the vertical velocity is a bistatic radar, with the transmitter and the receiver well separated (e.g. WATERMAN, 1983).

Other problems also exist; for example it is possible that erroneous wind speeds and wind shears will result if the scattering layers are much thinner in depth than the radar pulse-length (e.g. HOCKING, 1983a; FUKAO et al., 1988a, 1988b; MAY et al., 1988)

Despite all these potential problems, the Doppler method still remains a good way to get mean winds in the atmosphere, but any user must be aware of these limitations and bear them in mind during any experimental study.

2.2 Spaced antenna methods: FCA and Interferometer techniques

There are alternative approaches for determining atmospheric wind speeds, and these are the class of spaced antenna methods (e.g. see reviews by HOCKING, 1983c; BRIGGS, 1984; HOCKING et al., 1989). In this, one uses separate groups of antennas, spaced apart on the ground, to determine the wind speed. There are two main approaches; the first uses cross-correlation techniques to determine the time it takes for the diffraction pattern of the irregularities to cross between groups of antennas, and in its most sophisticated form is called Full Correlation Analysis, or FCA (BRIGGS, 1984). The second approach, originally introduced by PFISTER (1971) and later by FARLEY et al. (1981), ROETTGER and IERKIC (1985) and ADAMS et al. (1985) involves using the groups of antennas to form an interferometer. Briefly, such interferometer methods using phase differences between signals received at the groups of antennas to determine angles of arrival. Cross-spectral techniques are used for such angle-of-arrival determinations. Doppler methods are then used to determine the radial velocities associated with each separate scatterer. With such methods, it is possible to calculate the positions of the main scatterers in the sky, hence enabling more accurate determination of horizontal and vertical winds. The major disadvantage of this technique is that it requires that preferred regions of scatter, of narrow angular extent, do indeed exist, so that a direction can be determined. If scatter is diffuse, from a wide range of angles, the method breaks down; even though apparent directions of preferred scatter might still seem to result from the analysis in this case, they are not meaningful (e.g. BRIGGS, 1980).

These two techniques have been discussed extensively in HOCKING et al. (1989), and extensive discussions will not be entered into here. However, it is noted that they are viable and effective alternatives to the DBS method, and their use is growing.

2.3 Brief comments on the various techniques

There are advantages and disadvantages in all these methods. For example, correlation analysis techniques often use small groups of antennas, with corresponding wide polar diagrams. As a consequence, they often produce winds which are averaged over a large area of the sky. On the other hand, there is the advantage that both components of the wind speed are measured in the same volume, directly above the radar. Furthermore, even if the atmospheric scatterers have non-isotropic backscatter polar diagrams, correct estimates of the wind speed still result. The vertical wind speed is not measured, and Doppler methods must be used to determine this.

If isotropic scatterers are the main type of scatter, the spaced antenna and Doppler methods

are equivalent (BRIGGS, 1980). If there is a significant contribution from specular reflectors, it can result in enhanced scatter from the vertical, an advantage for the spaced antenna technique, since that method uses only vertically aligned beams. However, in the extreme that these specular reflector regions form a continuous blanket across the sky, with buoyancy waves causing undulations in this blanket, then the FCA and other simpler versions of the spaced antenna method can break down and effectively measure the phase speeds of the gravity waves. This is a problem for E region studies using MF and HF frequencies, but in the middle atmosphere it is rarely a problem (e.g. HOCKING et al., 1989).

As discussed, the major disadvantage of interferometer techniques is that they require that there are preferred regions of scatter in the sky, of narrow angular extent, so that a direction can be determined. If scatter is diffuse, from a wide range of angles, the method breaks down completely. On the other hand, if such discrete scatterers are present, interferometer methods enable high resolution studies of the scatterers.

It is clear from the preceding discussions that while the principles of estimation of wind speeds are simple, in practice there are many complicating features, and determination of perhaps the simplest target parameters, - their speeds, - is quite complex for the atmospheric case. To first order, all the methods are sound; but if one is interested in details about wind fluctuations, it is clear that it is necessary to know other features of the target, such as their "aspect sensitivity", their shape, the spatial distribution of the scatterers, and perhaps even the cause of the scatterers. In due course, we will address methods to determine such target parameters.

3 Spectral width estimates

So far we have concentrated on determination of mean winds. In the Doppler method, this relates largely to the mean frequency offset of the spectrum, whilst in the FCA method it relates to the time delay of the peak of the cross-correlation function. But there is more information in the signal. In the SA method, the width of the auto and cross-correlation functions holds extra information about the targets; in the Doppler method, the width of the spectrum contains the information. In some ways the second case is easy to visualize, so let us concentrate on this case.

A variety of methods can be used to determine this spectral width. One can utilize either the width of the autocorrelation function where it falls to one half of its value at zero lag, or the second lag of the autocorrelation function, or the second moment of the spectrum (e.g. see the discussion by WOODMAN, 1985). In all cases, one must be careful about the effects of noise, since noise can cause systematic errors. For example, noise produces a narrow spike at zero lag of the autocorrelation function, and this spike should be eliminated before proceeding with analysis. A procedure commonly used to determine the spectral width is least-squares fitting of a Gaussian-like function as in equation (11). In some cases, it is necessary to remove excessively large spikes from the spectra, a procedure which is especially necessary when there are "mirror-like" partial reflectors in the radar volume (e.g. HOCKING, 1983b). The details of these procedures will not be considered here; we are more concerned with the interpretation of the spectral width.

What then can cause the broadening of the spectrum? Perhaps the most obvious is random motion of the scatterers. If each scatterer has a velocity superimposed upon the mean speed, then each produces a line in the spectrum with a different frequency, as illustrated in the following diagram.

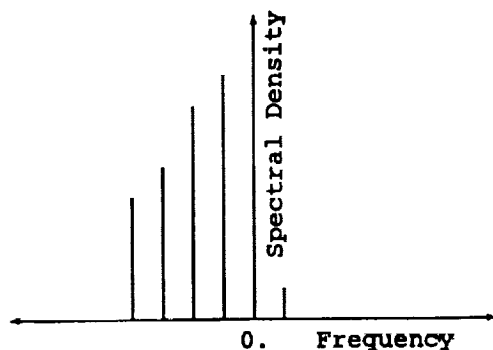


Fig. 4

If the scatterers have, for example, a Maxwellian distribution, then the vertical component of velocity (w) must have a Gaussian distribution, which is proportional to $\exp\{-w^2/(2w_{RMS}^2)\}$. Since for a vertical beam the Doppler shift from any scatterer is $f = \frac{2}{\lambda} \cdot w$, the spectrum will have a shape of the form $\exp\{-f^2/(2f_{RMS}^2)\}$, where $f_{RMS} = \frac{2}{\lambda} \cdot w_{RMS}$.

For some years in the early period of VHF middle atmosphere studies, it was assumed that this was the major cause of spectral broadening. However, for most VHF radars, this is not in fact the case. There are other causes of spectral broadening, which while understood by a few (e.g. ATLAS, 1964; SLOSS and ATLAS, 1968; ATLAS et al., 1969; HOCKING, 1983a, b), were not generally appreciated in the Middle Atmosphere community. Fortunately, this attitude has changed recently. These effects will now be discussed.

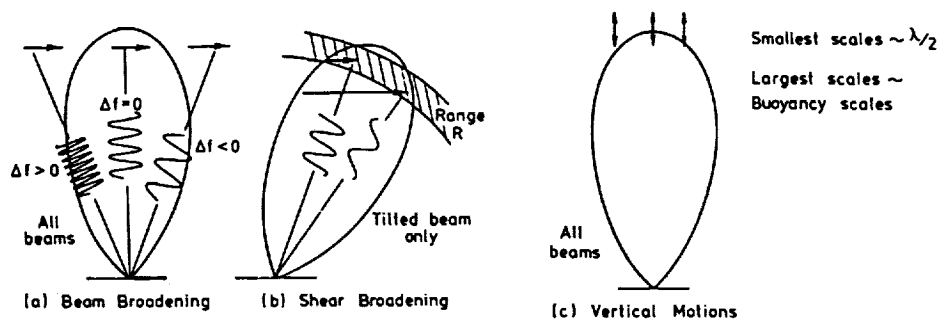


Fig. 5 Contributors to the spectral broadening at any instant.

For a vertically pointing beam, probably the main cause of the non-zero spectral width is

the so-called "beam broadening", which is illustrated in fig. 5a.

Even if all the scatterers are moving horizontally at the same velocity, each scatterer will produce a different Doppler shift. The nett result is a spectrum of finite width. This spectral broadening has been modelled by several workers (e.g. HITSCHFIELD and DENNIS, 1956; ATLAS, 1964; SLOSS and ATLAS, 1968; ATLAS et al., 1969; HOCKING, 1983a, b), and for relatively narrow beams (\leq about 5° half-power half-width), the spectral half-power half-width $f_{\frac{1}{2}b}$ obeys the approximate relation (in units of Hz)

$$f_{\frac{1}{2}b} = \frac{2}{\lambda}(1.0) |\underline{V}_{hor}| \theta_{\frac{1}{2}} \quad (17)$$

where $\theta_{\frac{1}{2}}$ is the two-way half-power half-width of the polar diagram in radians, and \underline{V}_{hor} is the TOTAL horizontal wind vector. The same approximation is also fairly accurate even for off-vertical beams, but it is important to note that the TOTAL wind speed should be used, and NOT just the component parallel to the tilt direction of the beam. This formula is based on the assumption that the scattering is statistically isotropic, an assumption which we will relax shortly. When one compares the spectral half-widths due to the non-fluctuating components of the wind-field to the experimental spectral half-widths measured with the vertical beam, one frequently finds that the two are very similar. For example, figure 6 from HOCKING (1983) shows an almost 1:1 relationship between the two parameters when spectra produced from 11s data sets were used.

This point cannot be emphasized too strongly:- the spectral widths are often dominated by so called beam broadening.

There are other effects which alter the spectral width, particularly if the beam is tilted from the vertical. Horizontal fluctuating motions will alter the spectral width (e.g. see fig. 7), and so will changes of the mean wind with height, as occurs for example in a wind shear (e.g. fig 5b). The former effect always broadens the spectrum, whilst the latter one can either reduce or increase the spectral width depending on the sign of the wind shear. These points are discussed in more detail by HOCKING (1983a), for example.

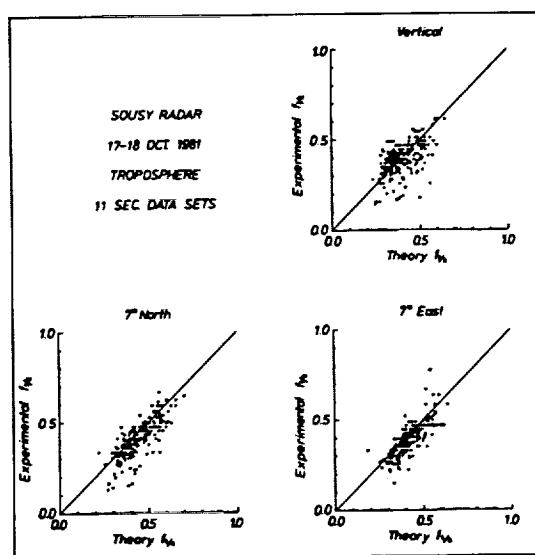


Fig. 6.

Scatter plots of experimental spectral half-power half-widths determined from 11 s data sets vs. the spectral half-width expected purely due to beam and wind-shear spectral broadening for the troposphere.

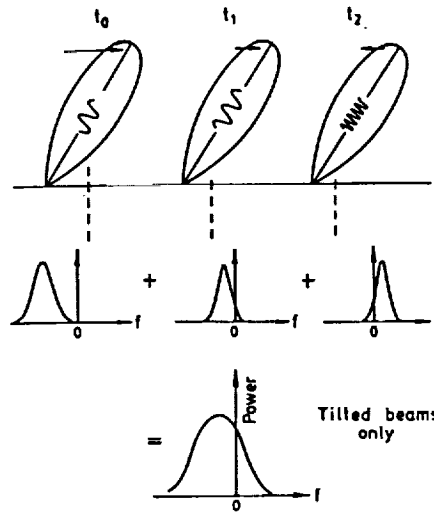


Fig. 7

Illustration of spectral broadening by variation of horizontal wind with time.

Of course the target parameter which is desired is the RMS fluctuating velocity of the scatterers, but this often contributes only a small fraction to the total spectral width. To determine the RMS fluctuating velocity, one should first use the measured mean wind speeds as a function of height, and the known polar diagram (radiation pattern) of the radar, to determine the spectral half-power half-width $f_{\frac{1}{2}nf}$ contributed by the non-fluctuating effects. Then the contribution from the fluctuating component f_{fluct} can be found through the relation

$$f_{fluct}^2 = f_{\frac{1}{2}expt}^2 - f_{\frac{1}{2}nf}^2 \quad (18)$$

This arises because the experimental spectrum is approximately a convolution between the spectrum which would be produced if there were no fluctuating components, and the spectrum due to the fluctuating components alone (at least for very narrow beams (\leq about 5° half-power half-width); the more general case has been modelled by HOCKING, 1983a).

To properly consider all the contributions from the mean wind including wind shear, a more accurate computer model needs to be used (eg HOCKING 1983a), but in many cases equation (17) serves as a useful approximation to obtain $f_{\frac{1}{2}nf}$.

Of course equation (17) is only a first-order estimate of the spectral half-width due to the non-fluctuating component, and it also assumes that the scatterers scatter isotropically. If the scatterers are anisotropic, as may be the case and as has been discussed previously, then the true contribution from non-fluctuating components will be less than that calculated with (17). That equation can still be used, but (see appendix A) $\theta_{\frac{1}{2}}$ must be replaced by $\theta'_{\frac{1}{2}} = R\theta_{\frac{1}{2}}$ where

$$R = \left[1 + \frac{\theta_{\frac{1}{2}}^2}{\theta_{s\frac{1}{2}}^2} \right]^{-\frac{1}{2}}, \quad (19)$$

$\theta_{\frac{1}{2}}$ being the true half-power half-width of the radar beam, and $\theta_{s\frac{1}{2}}$ is the half-power half-width of the polar diagram of backscatter due to the scatterers (i.e. $\theta_{s\frac{1}{2}} = \sqrt{\ln 2} \cdot \theta_s$, θ_s being defined by equation (15)). Notice that once again it is important to know the backscatter polar

diagram due to the scatterers, and it is becoming more and more important as we proceed through this text to know this parameter.

Having now determined the contribution due to non-fluctuating aspects of the wind field, and removed it from the experimentally determined spectral half-width, it is now necessary to decide what this residual contribution means, and how to interpret it. There are at least 3 possible contributions to this remaining contribution to the spectral width, namely the effects of fluctuations in the velocity due to turbulence, fluctuations due to buoyancy waves, and the decorrelation time associated with the decay of turbulent eddies. It is not always easy to separate out these terms.

In the case of a vertical beam, the most important effects are the vertical fluctuating component of the turbulent velocity, and both the vertical and horizontal components of the buoyancy-wave field. The horizontal component of the buoyancy field is important because although the beam is vertical, if the wave amplitudes are substantial the radial components of velocity fluctuations occurring near the edge of the beam may still contribute to the spectral broadening. This is especially true when wide beams are used, and is an argument for the use of narrow beams when studies of turbulence are made.

When off-vertical beams are used, both the vertical and horizontal fluctuating components of the turbulent velocity field are important. However, the horizontal components of the buoyancy-wave field become even more important in contributing to the spectral broadening; variations of velocity due to buoyancy waves occur both as a function of position within the radar beam and also as a function of time during the period of data collection. This latter effect can be quite dominant, and swamp the contribution due to the turbulence. For example, fig. 8, taken from HOCKING (1983b) illustrates this point, and shows the dramatic increase in spectral width recorded when an off-vertical beam is used as compared to a vertical beam. In this case the radar was an MF radar observing the mesosphere, and the beam-width was wider than for many VHF radars (about 4.5° half-width); data were collected for 12 mins in order to emphasize the effect. In normal VHF experiments the effect may not be so dramatic, but nevertheless occurs.

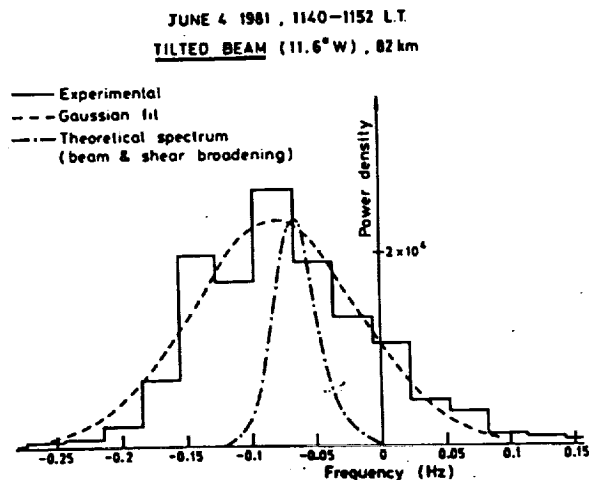


Fig. 8: The solid curve shows a spectrum recorded with the Buckland Park 1.98 MHz radar, using a 10 min data length and a beam tilted 11.6° off-vertical. The dash-dot curve shows the approximate shape of the spectrum recorded with a vertically pointing beam at the same time.

Thus measurements of turbulent energy dissipation rates are best made using a vertical beam. The contribution due to turbulence can be envisaged as follows, and is illustrated in fig. 9. Backscatter occurs predominantly from scatterers with scales of the order of the radar half-wavelength, but these scatterers are carried around by the larger scales. The mean square fluctuating velocity measured by the radar is then the integrated effect from scales of the order of the radar half-wavelength out to scales comparable with the radar volume (e.g SATO and WOODMAN, 1982; HOCKING, 1983a).

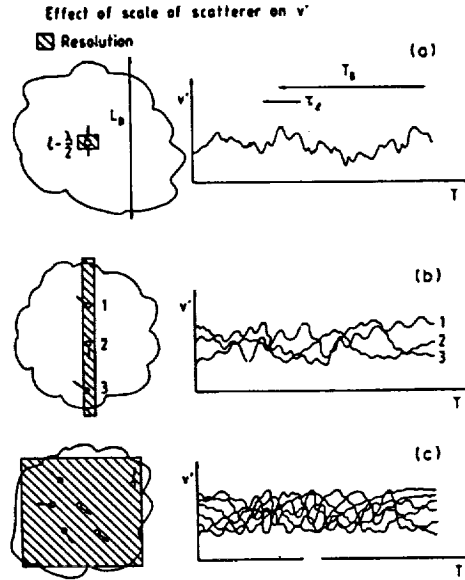


Fig. 9

For radars with pulse lengths and beam-widths comparable to the buoyancy scale of turbulence, scales even beyond the buoyancy scale may contribute to the mean square fluctuating velocity, although fortunately with reduced contributions. Let us say that the measured mean-square fluctuating velocity is due to a fraction F from scales within the inertial range of turbulence, and the remaining contribution comes from scales within the buoyancy range. The exact value of F depends on the radar configuration, sampling time, etc., and for the present we will not concern ourselves with its evaluation.

Then we may write (following HOCKING 1983a, 1986) that the velocity variance observed with the radar is

$$\overline{v^2} = \int \Theta_{11}(k_1) dk_1 \quad (20)$$

where $\Theta_{11}(k_1)$ is the longitudinal one-dimensional spectrum function (e.g. BATCHELOR, 1953, p.50) for the direction radial from the radar. The integration is performed over all scales which can affect the radar measurements, which for VHF radars means scales out to the radar pulse length or the buoyancy scale of turbulence, whichever is larger. For a radar pulse length of 600 m, say, this means that scales well into the buoyancy range will be effective, since the thicknesses of these layers is often well below 600 m (e.g. CRANE, 1980; BARAT, 1982) and

the inertial range-buoyancy range transition scale is usually several times less than the layer thickness (e.g. BARAT, 1982). If it is assumed that a fraction F of the measured velocity variance resides in the inertial range and the rest in the buoyancy range, we may write that the measured velocity variance $\overline{v^2}$ obeys the relation

$$\int_{-k_\lambda}^{-k_B} \Theta_{11}(k_1) dk_1 + \int_{k_B}^{k_\lambda} \Theta_{11}(k_\lambda) dk_1 = F.v^2 \quad (21)$$

where k_B is the wave number of the buoyancy scale (transition scale between the inertial and buoyancy ranges) and k_λ is the Bragg backscatter wave number. For Kolmogoroff, inertial-range turbulence, and defining the turbulent energy dissipation rate as ϵ , we may take

$$\Theta_{11}(k) = .1244 C_v^2 \epsilon^{2/3} |k|^{5/3} \quad (22)$$

and solve for ϵ in terms of k_B , k_λ , and $\overline{v^2}$. C_v^2 is well known from careful atmospheric experiments (e.g. CAUGHEY et al., 1978) to be close to 2.0.

This may then be used (e.g. HOCKING, 1983a) to derive

$$\epsilon = \epsilon_* L_B / \left(L_B^{2/3} - \left(\frac{\lambda}{2} \right)^{2/3} \right)^{3/2} \quad (23)$$

where

$$\epsilon_* = 2\pi \left(\frac{F}{.3732 C_v^2} \right)^{3/2} (\overline{v^2})^{3/2} / L_B. \quad (24)$$

If F is taken to be 0.5 and $C_v^2 = 2.0$, then we can write approximately that

$$\epsilon = 3.45 (\overline{v^2})^{3/2} / L_B. \quad (25)$$

WEINSTOCK (1978b) has suggested that the Buoyancy scale relates to the Brunt-Vaisala frequency and the energy dissipation rate through the relation

$$L_B = \frac{2\pi}{0.62} \epsilon^{1/2} \omega_B^{-3/2}$$

and using this relation with equation (24) gives

$$\epsilon = \left[\frac{12.24 F}{C_v^2} \right] \overline{v^2} f_B, \quad (26)$$

f_B being the Brunt-Vaisala frequency in Hz. Again taking $F = 0.5$ and $C_v^2 = 2.0$, we may write

$$\epsilon \simeq 3.1 \overline{v^2} f_B \quad (27)$$

Notice that this also means that

$$L_B \simeq 1.1 \frac{\overline{v^2}^{1/2}}{f_B},$$

a useful relation for making radar estimates of the Buoyancy scale.

Of course $\overline{v^2}$ can be found from the relation

$$\overline{v^2} = f_{fluct}^2 / (2 \ell n 2) \quad (28)$$

provided of course that f_{fluct} can be shown to be entirely due to the turbulence.

If F actually varies up to 1.0 or down to $1/4$, then the estimates represented by equations (25 and 27) will be incorrect by a factor of 2-3.

These formulae assume that the scattering scale $\lambda/2$ lies in the inertial range. However, it should be noted that if scatter occurs from the viscous range, as may at times happen in the mesosphere, the formulae are still largely valid. It will be noted from (21) that the mean square velocity is an integrated effect due to all scales between $\lambda/2$ and L_B and this integration is dominated by the large scales. A change in the spectral form from (22) within the viscous range will not greatly affect the integral; at worst, the $\lambda/2$ term in (23) may need to be replaced with the inertial range inner scale.

When the radar volume has dimensions less than the buoyancy scale of turbulence, the formula becomes slightly modified. The parameter L_B is replaced by the larger of the pulse length and the radar beam-width at the height of scatter (which we will denote as L_r), and the constant of proportionality changes slightly. In this case k_B in equation (21) is replaced by a Fourier scale representative of the range of Fourier components in the pulse (or the beam-width, whichever is larger). For example, if the pulse is Gaussian in shape with a half-power half-width L_r , then its Fourier transform has a half-width at half-power of about $0.44 \times 2\pi/L_r$. This different situation means that for $L_r \ll L_B$, the following relation applies (e.g. LABITT, 1979; BOHNE, 1982 (appendix C))

$$\epsilon \simeq 1.3 (\overline{v^2})^{3/2} / L_r. \quad (29)$$

The constant (1.3) has changed considerably compared to that in (24) and (25), and there are two main reasons for this. Firstly, the constant 1.64 assumes that there is no Buoyancy scale, and assumes that the $k^{-5/3}$ law applies over all scales; thus Fourier scales of small wavenumber, although only a small contribution to the pulse, make a large contribution to the integral in (21). As a result, (29) should not be applied even if L_r is less than but comparable to L_B ; in that case, the constant to be used should be considerably larger. The second reason relates to the different physical significances of L_r and L_B .

It should also be noted that even if $L_r \ll L_B$, if data lengths of a minute or so are used in forming the power spectra, equations (24) and (25) are better estimators of ϵ ; see fig. 9.

The relations (23-29) (whichever is applicable) may be used to determine the turbulent energy dissipation rate if one knows the contribution to the spectrum from turbulent fluctuations. However, we still must decide whether all the remaining spectral width is indeed due to turbulent fluctuations. Even when vertical beams are used to measure the spectrum, there may still be a small contribution due to buoyancy waves, (as has already been discussed), but it is possible to make at least some attempt to separate the turbulent and buoyancy wave effects. Use of procedures which involve least-squares fitting to a Gaussian shape like (11) help, because buoyancy-wave fluctuations of specular reflectors, for example, can produce fairly non-Gaussian spectra. Thus spectra dominated by buoyancy-wave fluctuations are often rejected by such procedures. Another possibility is that used by HOCKING (1988), who utilized the fact that the buoyancy-wave field tends to have only a small contribution (if at all) from oscillations with periods of less than 5 min. This is not to say, however, that using a data length of less than 5 mins eliminates the wave effects, since even a fraction of a wave cycle could cause significant contributions to the spectral width. However, one can predict how the spectral width might change as a function of data length in this case, and by comparing this prediction to the true variation in spectral width as a function of data length, can make some estimate of the relative contributions of buoyancy waves and turbulence. Such a process has some uncertainty associated with it, but is nevertheless of some value. An example was given in HOCKING (1988).

We have not yet addressed the contribution due to the decorrelation time associated with the finite lifetime of the eddies. In fact provided that the radar wavelength is substantially less than the buoyancy scale, this is not a major contribution, as will now be shown.

If the energy dissipation rate is again denoted ϵ , the typical eddy scale as ℓ and the velocity associated with such an eddy is denoted as v , then the typical lifetime τ of an eddy is

$$\tau \sim \frac{\ell}{v} \quad (30)$$

where

$$\epsilon \sim \frac{v^2}{\tau}. \quad (31)$$

Hence

$$\tau \sim \frac{v^2}{\epsilon} \sim \left(\frac{\ell}{\tau}\right)^2 \cdot \frac{1}{\epsilon} \quad (32)$$

so that

$$\tau \sim \ell^{\frac{2}{3}} \epsilon^{-\frac{1}{3}} \quad (33)$$

Thus the growth and decay of eddies produces an autocorrelation function with a half-width at a value of 0.5 of about τ , where τ is given by the above expression. If the autocorrelation function is taken to be Gaussian, then its Fourier transform is also Gaussian, with a half-power half-width of $0.22 / \tau$, and we will denote this as f_{dc} , where "dc" stands for "decorrelation". Thus

$$f_{dc} \simeq \frac{.22}{\tau} \sim .22 \ell^{-\frac{2}{3}} \epsilon^{\frac{1}{3}}, \quad (34)$$

where ℓ can be taken to be of the order $\lambda/2$.

Contrast this to the contribution due to fluctuating motions, which contribute out to scales of the order of the Buoyancy scale, L_B . In this case, we have already seen (equation 25) that if we take F as about 0.5, then

$$\epsilon \simeq 3.5 \frac{v_{RMS}^3}{L_B}. \quad (35)$$

Then the half-power half-width of the spectrum due to the fluctuating motion of the scatterers is given by

$$f_{fluct(m)} \simeq .8 \left(\frac{2}{\lambda}\right) \epsilon^{\frac{1}{3}} L_B^{\frac{1}{3}} \quad (36)$$

Hence the ratio of spectral half-widths due to the eddy motions and the decorrelation time of the eddies is

$$\frac{f_{fluct(m)}}{f_{dc}} \sim 4 \left[\frac{L_B}{\lambda/2} \right]^{\frac{1}{3}} \quad (37)$$

Physically this arises because the spectral width associated with the scatterer movement is related to the buoyancy scale L_B , (since we have seen that this width is due to the integrated effect of all scales up to L_B), whilst the decorrelation time depends only on the scale of the scatterers.

For a typical case with $\lambda/2$ equal to 3m, and L_B equal to say 200 m, the ratio is about 16. Since the total spectral width due to these two components combined is equal to the square root of the sum of the squares, the correction due to the decorrelation time in this case would be only a fraction of a percent. Thus provided the Buoyancy scale is greater than the Bragg

backscatter scale by a few times, the decorrelation time of the eddies is only a minor correction to the spectral width and can usually be ignored.

It was mentioned earlier that information about the level of turbulence also exists in the correlation functions, and can be obtained from the Full Correlation Analysis technique using spaced antennas. Indeed, one of the output parameters of the Full Correlation Analysis is a parameter which is usually denoted as T_1 and represents the correlation function half-width which would be measured with a radar which moved along the ground with the velocity of the mean wind in the scattering region. Spectral beam-broadening has been removed from this parameter, although the effects of wind-shear have not. Thus the parameter $f_1 = 0.22/T_1$ can be used in place of f_{fluct} in all the discussions above; the main potential problem is that there may be increased contributions from buoyancy waves if the polar diagram of the system is wide.

Provided the effects of gravity waves can be adequately separated, or even shown to be relatively unimportant, the procedures described above allows radars to be used to extract estimates of atmospheric turbulence.

It is also possible to infer the turbulent diffusion coefficient for a turbulent layer through the relation

$$K_M = c_2 \epsilon / \omega_B^2 \quad (38)$$

e.g. WEINSTOCK, 1978a, b; LILLY et al. 1974). The constant c_2 is quoted to have a variety of values in the literature, ranging from about 0.25 to 1.25. The most commonly accepted value seems to be 0.8 (WEINSTOCK, 1978). Ideally it is also necessary to know the Brunt-Vaisala frequency averaged over the turbulent layer, but unfortunately it is not always possible to find this. Some authors use climatological values, but it is better to use radio-sonde determinations where possible.

The method of determining ϵ described above has been used a few times, but is still largely unexploited; a much greater use of these procedures is to be actively encouraged.

4 Power Measurements

One simple but effective method for deducing information about the scatterers is to record the backscattered power. In many experiments powers are compared in a relative way; for example, power variations as a function of time and height are usually studied in most experiments. Even this simple process can give useful results, but it is even more effective if the radar can be calibrated in an absolute sense. This requires some careful work by the user, but if this is done it is then possible to convert the measured powers to effective reflection coefficients, backscatter cross-sections, or perhaps estimates of the turbulence intensity. (The parameter actually calculated depends largely on the scattering mechanism, and we will consider ways of determining this shortly.) Such calibration not only allows better comparisons to be made world-wide, but also allows better comparison with theory.

Before showing how this calibration can be done, however, it is a useful exercise to look in more detail at the mathematical formulation of the scattering process. We will begin by considering the simplest case, namely that of reflection from stratified steps.

4.1 Modelling the reflection and scattering processes

4.1.1 Horizontally stratified structure

Consider first, and for simplicity, a horizontally stratified atmosphere which has fluctuations in the refractive index in the vertical direction but none horizontally. In fact we will see later that this is not such an unreasonable model, and has some real applicability in the atmosphere. A pulse of the form $g_1(t - z/c)\cos[\omega_c(t - z/c)]$ is transmitted, where $f_c = \omega_c/(2\pi)$ is the carrier frequency. At $z = 0$, this is a pulse which varies in time as $g_1(t)\cos(\omega_c t)$. This can be written as $g(\xi) = g_z(\xi)\cos(k\xi)$ where $k = 2\omega/c = 4\pi/\lambda$ (λ being the radar wavelength) and $\xi = ct/2$ is a length coordinate which closely matches the height of the scatterers (e.g. HOCKING and ROETTGER, 1983). If the refractive index fluctuations are described by $n(z)$, then the radio-wave reflection coefficient profile is given approximately by $r(z) = \frac{1}{2}(dn/dz)$ (eg HOCKING and VINCENT, 1982a). The reflected complex amplitude as a function of height is then given by

$$a(z) = \left\{ \frac{r(z)}{z} \right\} \otimes g(z) \quad (39)$$

where \otimes stands for convolution. (e.g. HOCKING and ROETTGER, 1983, and references therein). (This expression is very accurate for VHF scatter, although if absorption is high or the pulse is significantly dispersive, more careful approaches are necessary, such those given by HOCKING and VINCENT (1982b), or even full-wave equations are necessary (e.g. BUDDEN, 1965).)

To begin, it is of interest to examine what happens when reflection occurs from a single step of some finite thickness. The easiest step to deal with is one of the type with

$$r(z) \propto e^{\{-\frac{(z-z_0)^2}{d^2}\}}. \quad (40)$$

In this case the refractive index profile is a step of finite thickness, as shown in the following diagram. Note that although d is a measure of the step depth, it is probably not the best measure of this depth. A better measure of the step depth might be the distance between the two points where the reflection coefficient falls to one half of its maximum value, or

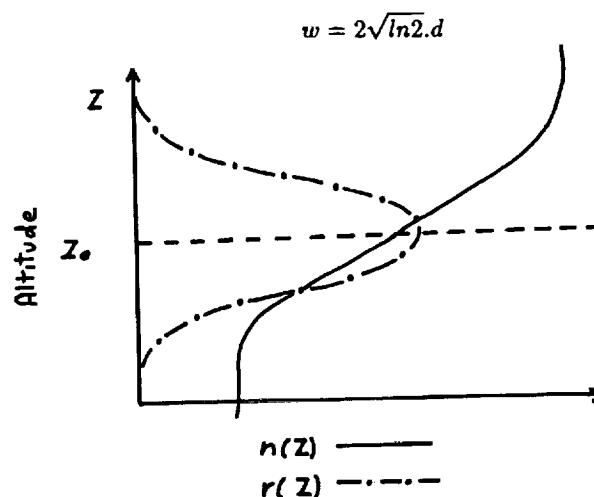


Fig. 10

The convolution can be done numerically, but it is instructive to examine the process using a slightly different approach. From Fourier theory (e.g. BRACEWELL, 1978) the convolution can be done by Fourier transforming each of $g(z)$ and $r(z)$, multiplying the Fourier transforms $G(k)$ and $R(k)$, and then re-Fourier transforming the product. The process is illustrated diagrammatically in the following diagram.

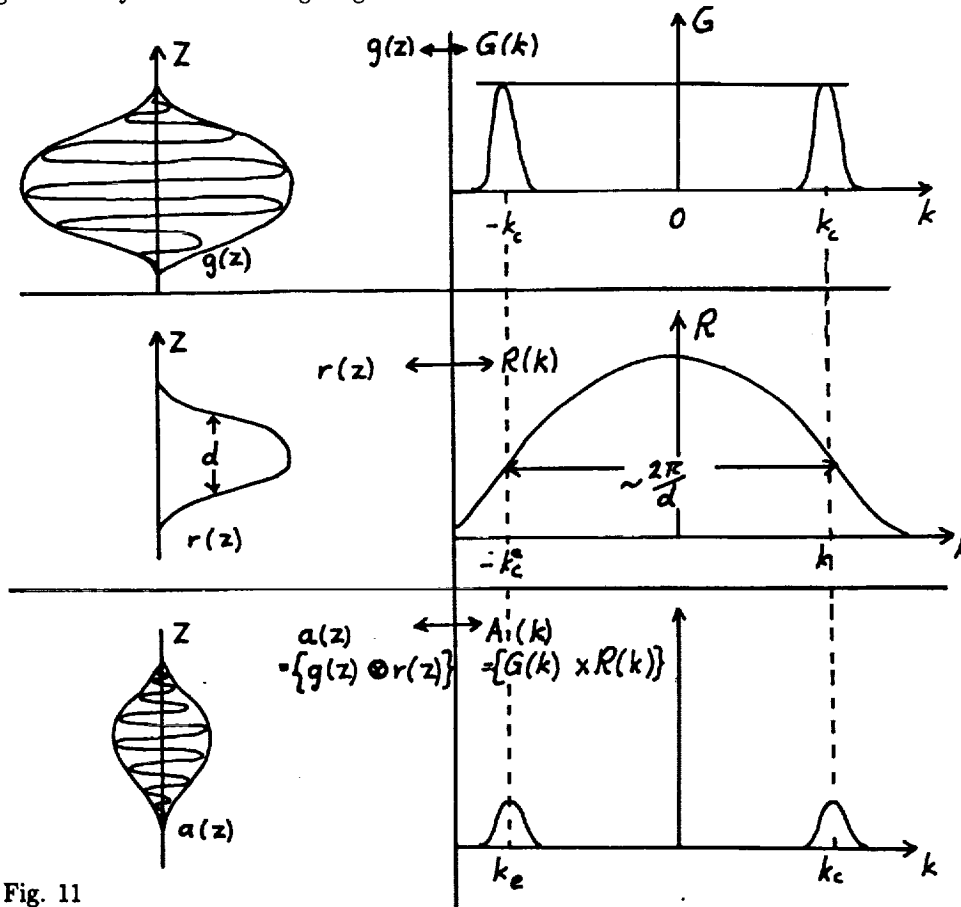


Fig. 11

Note that the Fourier transform $G(k)$ of $g(z)$ exists in a narrow band centred at $k_c = 4\pi/\lambda$. Notice also that the narrower the step (smaller d) the wider the function $R(k)$ and so the product of the Fourier transforms is larger. In fact the peak amplitude of the product is

$$A(k_c) \propto e^{-\frac{k_c^2 d^2}{4}} \propto e^{-\frac{4\pi^2 d^2}{\lambda^2}} \quad (41)$$

- so clearly once d exceeds λ , the backscattered power is very small. In fact even if $d = \lambda/4$ ($w = 0.42\lambda$), the reflected amplitude is 0.08 times that for a step of zero width (ie a sharp discontinuity). The power will therefore be reduced by 22 dB compared to a single step. Many authors have taken this to infer that only steps much less than about a quarter wavelength in thickness will ever be seen by radar, and this may well be true for say MF radars. However, with coherent integration and the greater sensitivity of modern radars, particularly VHF radars, it is not so easy to adopt this argument; VHF radars can often see such steps even if reduced in efficiency by 20 dB, and they are indeed capable of detecting layers with a depth d of about

$\lambda/4$. However, it is true that beyond this depth, the efficiency falls off remarkably quickly; for example, if $d = \lambda/2$, the power is reduced by 80 dB, and even VHF radars would not normally detect such a step. HOCKING (1987a) has discussed this point and suggests that some "specular reflectors" seen by VHF radars have typical depths with $2d = 3 - 4$ m, or w between 2.5 and 3 metres; in other words, the steps are right on the edge of the region of detectability.

Another useful model is that of "Fresnel Scatter", a model known for many years in D region MF studies, (eg AUSTIN et al., 1969; MANSON et al., 1969; GREGORY and VINCENT, 1970), but given renewed popularity by GAGE et al (1981) in respect to VHF studies. In this model, horizontal stratification is again assumed, but $n(z)$ is assumed to vary randomly, so the atmosphere can be thought of as a series of thin slabs sitting atop each other, each with slightly different refractive indices. Despite some initial controversy, it is relatively easy to show that in this case the backscattered power is proportional to the pulse length (HOCKING and ROETTGER 1983), and if one includes the decrease in reflected power as a function of height z then one finds that the power received by a radar takes the form

$$P_R = \frac{\alpha^2 P_t A_e^2}{4\lambda^2 z^2} [F(\lambda)\bar{M}]^2 (\Delta z) \quad (42)$$

where P_R is the received power, α is the array efficiency, P_t is the peak transmitted power, A_e is the array effective area, λ is the radar wavelength, z is the height of reflection, \bar{M} is the mean generalized refractive index gradient and $F(\lambda)$ is a "calibration constant" which must be determined empirically for each radar. The term Δz represents the radar pulse-length. In the case that \bar{M} varies substantially within one pulse-length this formula need some modification, as described by HOCKING and ROETTGER (1983). Later developments of this model have been discussed by GAGE et al., (1985) and GREEN and GAGE, (1985).

4.1.2 Three dimensional structures

The next extension to these models is to allow the scattering medium to have non-constant structure in the horizontal direction as well. An example might be fully developed isotropic turbulence, in which the refractive index has random fluctuations caused by the turbulent velocity field. In this case, the theory for relating the backscattered signal to the turbulence intensity has been fairly well developed (OTTERSTEN, 1969; VANZANDT et al, 1978; HOCKING, 1985). The backscattered power depends not only on the intensity of the turbulence, but also the mean refractive index gradient in which the turbulence exists. In the mesosphere, the latter term is largely determined by the electron density gradient, in the stratosphere by the temperature gradient, and in the troposphere by the temperature and humidity gradient. Expressions for these potential refractive index gradients are given below, but expressions for evaluation of the turbulence intensity from measurements of the absolute backscattered power will be left until after the following section on calibration of a radar.

In the unionized atmosphere, and for centimetre and metre radio waves, the potential refractive index gradient is given by (TATARSKI, 1961, p 57)

$$M = \frac{-79 \times 10^{-6}}{T^2} \cdot P \cdot \left[1 + \frac{15500}{T} q \right] \left[\frac{dT}{dz} + \Gamma_a - \frac{7800}{1 + \frac{15500}{T} q} \cdot \frac{dq}{dz} \right], \quad (43)$$

where P is the atmospheric pressure in units of millibars (hPa), T the temperature ($^{\circ}\text{C}$), Γ_a is the adiabatic lapse rate, and $q = e/(1.62P)$ is the specific humidity, e being the water vapour pressure.

In the ionosphere, the relevant potential refractive index gradient is given by (HOCKING, 1985)

$$M_e = \frac{\partial n}{\partial N} \left[N \frac{\omega_B^2}{g} - \frac{dN}{dz} + \frac{N}{\rho} \frac{d\rho}{dz} \right] \quad (44)$$

where N is the electron density, n is the refractive index, and ρ is the neutral density of the atmosphere. The Brunt-Vaisala angular frequency is represented by ω_B^2 , and g represents the acceleration due to gravity. Notice that this can also be written as (e.g. THRANE and GRANDAL, 1981)

$$M_e = \frac{\partial n}{\partial N} \left[\frac{N}{\gamma P} \frac{dP}{dz} - \frac{dN}{dz} \right] \quad (45)$$

where γ is the ratio of specific heats at constant pressure and constant volume.

For a VHF radar,

$$\frac{\partial n}{\partial N} = \frac{1}{2} \pi^{-1} r_e \lambda^2, \quad (46)$$

where r_e is the classical electron radius. At HF and MF, the relation between N and n becomes more complex (e.g. BUDDEN, 1965).

Let us now turn our attention to the subject of calibrating the radar, so we may then see how to use the above expressions to determine turbulence intensities.

4.2 Calibration of the radar

In order to calculate the parameters like backscatter cross-sections of the scatterers or the reflection coefficients of the reflectors, it is necessary to calibrate the radar. In this context, "calibration" refers to calculation of appropriate coefficients which enable conversion between the power received by the radar and reflection coefficients, back-scatter cross-sections etc (rather than determination of the polar diagram of the radar, for which the term "calibration" is also often used). Many radars world wide have still not been absolutely calibrated, which is a great pity.

One simple way of "calibrating" the measurements is to compare the signal received to the noise. For a VHF radar, the noise is predominantly sky-noise, due to extra-terrestrial sources. By measuring the ratio of the signal-to-noise (S/N), it is possible to get an approximate measure of the received power, provided the noise level is known (e.g. VANZANDT et al., 1978). Standard charts exist which may be used to give the noise level. However, this is not the best way to determine the signal power. For example, the true noise level has a diurnal variation, depending on the passage of noise sources through the beam, and of course radars at different locations have different dominant noise sources. It is also likely that the noise level may change as one changes the orientation of the beam. Furthermore, the procedure is of no use for MF and HF systems, in which noise depends on atmospheric phenomena like lightning. Therefore, other more accurate calibration procedures are to be preferred.

A moderately effective technique is to use a noise generator to calibrate the receiver. A noise generator is fed into the receivers at the point where the receiving antennas are normally connected, and the signal is recorded. Usually VHF radars employ coherent integration of the signal, and of course noise is incoherent, and this factor must be taken into account when the calibration is performed. For noise, the sum of N coherent integrations increases the total power by factor of N times, whilst for coherent signal it increases by a factor of N^2 . These differences are usually fairly easy to allow for, however, and calibration in this way is relatively simple (e.g. HOCKING et al., 1983). One simply determines what a particular level of receiver input power produces in terms of output units, and henceforth any measured receiver output

can be converted back to an input noise power. Standard radar equations may then be used to determine parameters like the scatterer cross-sections and reflection coefficients. For example, knowing the output power of the transmitter, P_t , the reflection coefficient of a scattered layer can be found through the relation

$$P_R = \frac{P_t e_t G}{4\pi(2z)^2} e_R A_R \overline{R^2} \quad (47)$$

where P_R is the received power, P_t is the power produced by the transmitter, G is the gain of the transmitting array, e_t and e_R are the efficiencies of the transmitting and receiving systems, (including the efficiencies of the respective arrays), A_R is the receiving area of the receiving array, and $\overline{R^2}$ is the mean square reflection coefficient. In the case that the same array is used both for transmission and reception, we may use the relation $A_R = G\lambda^2/(4\pi)$ to give

$$\overline{R^2} = \frac{P_R 64\pi^2 z^2}{P_t G^2 e_t^2 \lambda^2} \quad (48)$$

If the scatter is due to turbulence, an effective backscatter cross-section σ can be found. Here, σ is the power backscattered per unit solid angle, per unit incident power density, and per unit volume. σ is evaluated through the relation (e.g. HOCKING, 1985)

$$P_R = \frac{P_t e_R e_t G A_R}{4\pi z^4} \cdot \sigma \cdot \frac{V}{\ln 2}, \quad (49)$$

where V is the radar volume. For a monostatic radar, $V = \pi(z\theta_{\frac{1}{2}})^2 \Delta z$, where $\theta_{\frac{1}{2}}$ is the radar two-way half-power half-width and Δz is the pulse length ($= c\tau/2$, where τ is the transmitted pulse length in seconds and c is the speed of light in ms^{-1}).

The efficiency e is often hard to determine, but even if $\overline{R^2}$ or σ or C_n^2 can be determined to within a factor of 2 or 3, it is still useful. Various ways exist for calculating radar efficiencies, but lack of space prevents their discussion here. Examples include methods discussed by VINCENT et al., (1986) and MATHEWS et al., (1988).

At HF and MF, use can be made of the fact that the radio pulses are totally reflected from some part of the ionosphere. If a so called "second hop" echo occurs, (which arises when the pulse is totally reflected, returns to the ground, is re-reflected back to the ionosphere and returns), then the ratio of the strengths of the main and second hop echoes may be used to determine a calibration constant for the system. To see this, write that the power received from a reflecting layer at height z , and of reflection coefficient R is

$$P_{1R} = \kappa^{-2} \overline{R^2} z^{-2} P_t. \quad (50)$$

where κ is a calibration constant. In this case, P_t need not even be the actual transmitted power, but any value proportional to it. Then if a second-hop echo exists, the received power from it is

$$P_{2R} = \kappa^{-2} \overline{R^2}^2 (2z)^{-2} P_t. \quad (51)$$

Then squaring (50) and dividing through by (51) allows elimination of $\overline{R^2}$ and so

$$\kappa = \frac{2\sqrt{P_t}\sqrt{P_{2R}}}{zP_{1R}} \quad (52)$$

In this case, neither P_R nor P_t need to be known absolutely, and each can be a quantity which is simply proportional to the true received and transmitted powers. κ can be determined

as above, and then for any echo, whether it be strong enough to have a second hop or not, $\overline{R^2}$ can be evaluated through (50).

In VHF studies, there is no totally reflecting surface. It is possible to use artificial satellites, or even the moon (e.g. MATHEWS et al., 1988) to calibrate the system, provided that the backscatter cross-section of the target is known. In this case, the efficiency terms can also be evaluated.

The absolute calibration of radars by any of the means discussed above, or any other means, is to be actively encouraged, and will make comparisons between radars and between observations and theory much easier in the future.

4.2.1 Determination of turbulence intensities from measurements of received power

Once it can be ascertained that turbulence is the main cause of the radio wave scatterers, it is possible to convert the received powers to parameters which describe the turbulence. One key parameter is the "(potential) refractive index structure constant", usually denoted as C_n^2 . If the turbulence obeys the classical Kolmogoroff inertial spectrum, then the spectrum of refractive index fluctuations is given by (TATARSKI, 1961, 1971)

$$\phi_n(k_x, k_y, k_z) = 0.033 C_n^2 |k|^{-\frac{11}{3}} \quad (53)$$

where a normalization has been chosen such that $\int \int \int_{-\infty}^{\infty} \phi(k) d\mathbf{k} = \langle n^2 \rangle$. Thus C_n^2 is a parameter which indicates the level of refractive index fluctuation. C_n^2 can be determined from the cross-section defined above through the relation

$$\sigma = 0.00655 \pi^{\frac{4}{3}} C_n^2 \lambda^{-\frac{1}{3}} \quad (54)$$

(Note that sometimes a cross-section $\eta = 4\pi\sigma$ is used, in which case $\eta = 0.38 C_n^2 \lambda^{-\frac{1}{3}}$). When combined with the equations seen earlier, we see that for a monostatic radar

$$C_n^2 \approx 66. \frac{P_R z^2 \lambda^{\frac{1}{3}}}{P_t A_R \epsilon_t^2 \Delta z} \quad (55)$$

Appropriate relations can also be easily derived for the case in which the transmitter and receiver are separate systems (also see HOCKING, 1985).

C_n^2 is a useful parameter, but an even more useful one is of course the turbulent energy dissipation rate, ϵ . It is possible to relate C_n^2 to ϵ in the following way.

Starting from TATARSKI, 1961, (p44, equation 3.19), we have

$$C_n^2 = a^2 N \epsilon^{-\frac{1}{3}}, \quad (56)$$

where N is a parameter defined by

$$N = K_n M^2 \quad (57)$$

for a stratified environment. The constant a^2 has been measured to be about 2.8. Using the definition of the Prandtl number $P_r = K_M / K_n$, defining $\alpha' = P_r^{-1}$, and using the relation seen earlier that

$$K_M = c_2 \epsilon / \omega_B^2 \quad (58)$$

e.g. WEINSTOCK, 1978a, b; LILLY et al., 1974), we may see that

$$\epsilon = \left[\frac{C_n^2 \omega_B^2}{a^2 \alpha' c_2 M^2} \right]^{\frac{3}{2}} \quad (59)$$

These relations have also been derived by BLIX (private communication, 1988) ; a similar expression was derived by VANZANDT et al., (1978) and noted by HOCKING (1985), although a slightly different proof was used in the second case, with the result that

$$\epsilon = \left[\frac{C_n^2 \omega_B^2}{a^2 \alpha' M_n^2 \left[\frac{R_{i(c)}}{b^{\frac{2}{3}}} \right]} \right]^{\frac{3}{2}} \quad (60)$$

$R_{i(c)}$ is the critical Richardson number at which turbulence should develop, and b is yet another constant relating the energy dissipation rate to the mean windshear. In fact VANZANDT et al., (1978) and HOCKING (1985) took $b=1.0$, so b did not appear explicitly in their expressions, but with hindsight this was not wise. The first expression (59) is derived in a more fundamental way, and requires less assumptions, than the second (60), and it is better to use the former. The constant c_2 is quoted to have a variety of values in the literature, ranging from about 0.25 to 1.25. The most commonly accepted value seems to be 0.8 (WEINSTOCK, 1978b).

An extra complication arises if the turbulence does not fill the radar volume, and indeed this often appears to be the case. It appears that in the stratosphere and mesosphere, turbulence occurs in relatively thin layers with thicknesses ranging from a few tens of metres to perhaps a kilometre or so, but generally of the order of 100m. At any one instant, only a small fraction of the radar volume contains turbulence, and this should be taken into account when calculating ϵ . In other words, the calculated value of C_n^2 is actually too small by a factor F_t , where F_t is the fraction of the radar volume which is filled with turbulence at any one time. Thus one normally calculates

$$C_n^2(turb) = C_n^2(radar)/F_t, \quad (61)$$

where $C_n^2(radar)$ is the value determined from the radar measurements. VANZANDT et al. (1978, 1981) have developed models for the variation of F as a function of atmospheric conditions, enabling estimates of ϵ to be made. Furthermore, one is often interested in the mean value of ϵ averaged over the radar volume, so VANZANDT et al. suggested calculating the quantity

$$\bar{\epsilon} = F_t \epsilon_{turb} \quad (62)$$

GAGE et al. (1980) used a simplified model based on VanZandt's model, in which they showed that the parameter $F_t^{\frac{1}{3}} \omega_B^2$ could be determined to moderate accuracy from climatological data, so that the simplified expression

$$\bar{\epsilon} = \gamma [C_n^2(radar)]^{\frac{3}{2}} \left[\frac{T^3}{P} \right] \quad (63)$$

could be used, where $\gamma = 1.08 \times 10^{22}$ for a dry troposphere and $\gamma = 3.25 \times 10^{21}$ for the stratosphere. Here, P is in millibars, T in Kelvin, C_n^2 is in units of $m^{-\frac{2}{3}}$ and ϵ is in units of Wkg^{-1} . Variations on these principles have also been presented by CRANE (1980) and WEINSTOCK (1981).

Further complications arise if the turbulence is not isotropic, but we will not discuss these problems here, important though they are, due to lack of space.

5 Aspect sensitivity of the scatterers

We have seen several times throughout this text that a better understanding about the shapes of the scatterers is necessary in order to better interpret measurements of wind speed and turbulence intensities. It would also naturally help in understanding the cause of the scatterers.

The shape of the scattering irregularities has been the subject of active debate over many years. Models have ranged from flat, mirror-like partial reflectors to "pancake-like" scatterers to inertial-range isotropic turbulence, and in this review we will not dwell too much on these arguments. Rather, we will first describe the main models, and then concentrate on the sorts of techniques which might be, and have been, used to determine the shapes of the scatterers.

If it is assumed that the polar diagram of backscatter of the scatterers is of the form

$$B(\theta) \propto e^{-\frac{\sin^2 \theta}{\sin^2 \theta_s}} \quad (64)$$

, as assumed in equation (15), then θ_s gives a measure of how rapidly the backscattered power falls off as a function of zenith angle. If θ_s tends towards 90° , it indicates isotropic scatter, whilst if θ_s tends towards 0° then it indicates highly aspect-sensitive scatter.

There are a variety of models which have been advanced, but they basically fall into 2 categories. (e.g. LINDNER, 1975 a,b; BRIGGS and VINCENT, 1975; ROETTGER and LIU, 1978; GAGE and GREEN, 1978; HOCKING, 1979; FUKAO et al., 1980a, b; ROETTGER, 1980b; GAGE et al., 1981; DOVIK and ZRNIC, 1984; WATERMAN, 1985, amongst others).

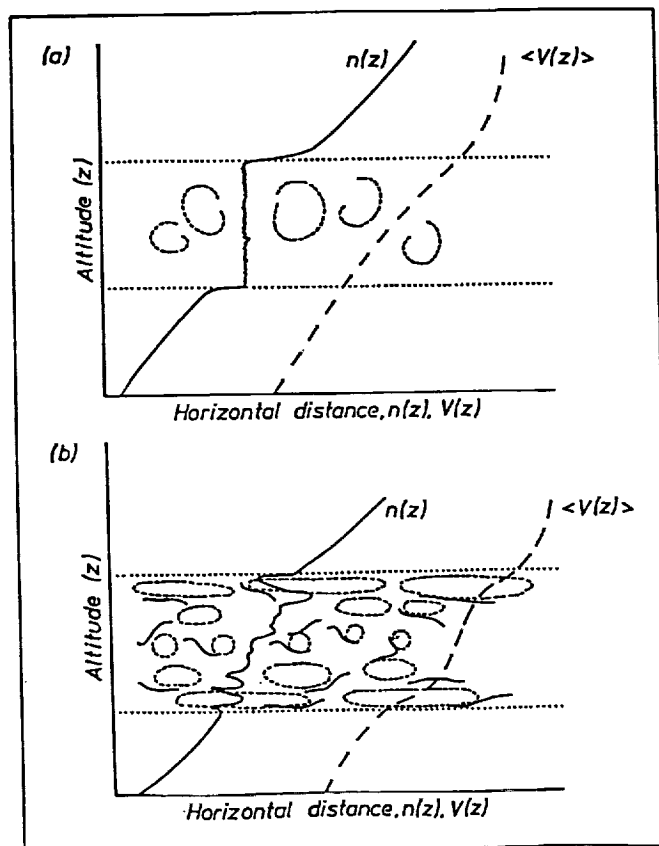
(A) The first class assumes that individual scatterers are (on average) ellipsoidal in shape, which may vary in their length to depth ratio as a function of scale. The extremes are spherical shapes (isotropic scatter) and highly elongated structures.

(B) The second class of model assumes a horizontally stratified atmosphere consisting of variations in refractive index in the vertical direction, so one can think of this as a series of "sheets" of different refractive index. Such structures, if truly stratified, would have $\theta_s = 0$, but if we imagine that these sheets are gently "wrinkled", then θ_s will become non-zero (e.g. RATCLIFFE, 1956). In this case, the range of θ_s values relates to the range of Fourier components necessary to describe the wrinkles.

Proponents of model B do not claim that the whole atmosphere is like this, but that it is like this in some places at some times, and use the model to describe particular observations.

Sometimes hybrids of the two models are invoked and other, more complicated, models have also been proposed, but they are generally based on the above models. To illustrate these later models, as well as give a feel for how they are explained physically, some examples of such more complicated models are shown below. The first (fig. 12a) is due to BOLGIANO (1968), and assumes that an intense turbulent layer might mix the layer so that the potential refractive index across the layer is constant, with sharp edges at the side. These edges might be able to explain the model B reflectors, for example, although doubts about the possibility of a turbulent layer maintaining sharp edges exist.

The second model in fig. 12 proposes that scatterers near the edges of a confined layer of turbulence are more anisotropic than in the centre. The model has been discussed by HOCKING et al. (1984), noted by HOCKING (1985), and also proposed independently by WOODMAN and CHU (1989). Such a model is physically likely because turbulent layers are often more stable near their edges (e.g. PELTIER et al., 1978; KLAASSEN and PELTIER, 1985), but for the purposes of this paper these models are simply noted as the type of extension to the simple models proposed above which should be borne in mind.



Idealized views of two models for turbulence in the atmosphere. The broken lines represent "eddies", and the solid lines represent scattering interfaces. The first graph represents an earlier proposal due to Bolgiano (1968), and the second represents a model discussed in the text.

Fig. 12

Another model which may give a physical basis to model B is the proposal that the specular reflectors might be damped gravity waves (e.g. VANZANDT and VINCENT, 1983; HOCKING, 1987a and references therein) or even viscosity waves, the latter being capable of existing at very short wavelengths (HOOKE and JONES, 1986).

Having now established that both models have some physical basis, let us concentrate on the simpler models, since these form an excellent basis for later discussion of any of the more complex models.

With regard to model A, it should be noted that θ_s gives a direct measure of the length to depth ratio of the scatterers. The following figure, from HOCKING (1987a), shows this relationship.

What techniques, then can be used to determine the nature of these scatterers?

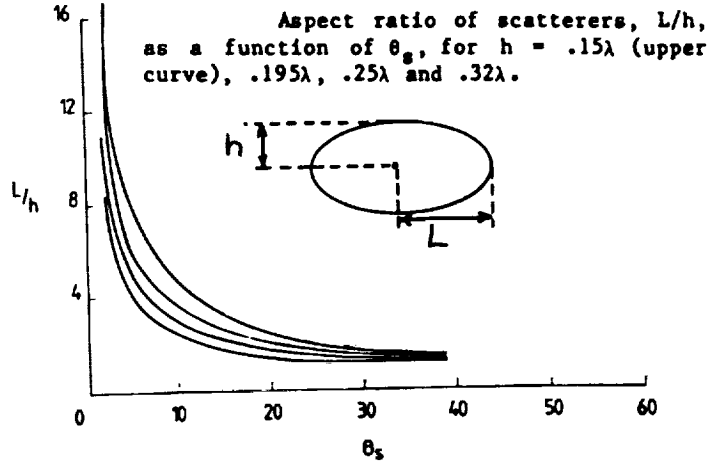


Fig. 13

5.1 Experimental techniques to determine the nature of the scatterers

In the following section a variety of techniques which may be used to determine information about the nature of the scatterers are described and some of the results obtained so far discussed. The list is not, however, exhaustive.

5.1.1 Methods utilizing different beam configurations

One of the simplest methods to investigate the aspect sensitivity of the scatterers is to simply point a narrow beam vertically, and then at several off-vertical angles. The variation in power P as a function of beam tilt angle θ , is then related to θ_s . In fact it can be shown that

$$P(\theta_T) \propto e^{-\left[\frac{(\theta_{eff} - \theta_T)^2}{\theta_0^2} + \frac{\theta_{eff}^2}{\theta_s^2}\right]} \quad (65)$$

where θ_{eff} is defined by equation (16), θ_T is the beam tilt direction from the vertical, and the polar diagram of the radar beam is assumed to be of the form $\exp\{-(\sin^2\theta)/(\sin^2\theta_0)\}$ [e.g. appendix A; HOCKING et al (1986); note that the derivation in appendix A corrects an error made in HOCKING et al 1986, in that the important term $\frac{\theta_{eff}^2}{\theta_s^2}$ was neglected in the exponent of e in that paper].

A typical experiment which might be performed is to compare the powers received with a vertical and an off-vertical beam, and use this to deduce θ_s . Utilizing equations (16) and (65) (or equivalently (A4) and (A10)), it is possible to derive the following simple relation between $P(\theta_T)/P(0)$, θ_T and θ_0 . If R is defined to be $\ln\{P(0)/P(\theta_T)\}$ (or $R = 0.23026 R_{dB}$, where R_{dB} is the ratio of $P(0)/P(\theta_T)$ expressed in dBs), then

$$\theta_s^2 = \frac{\theta_T^2}{R} - \theta_0^2$$

Typical variations of $P(\theta)$ show an approximately Gaussian fall-off out to about 5° - 10° , and then an approximately constant value beyond this, indicating possibly isotropic turbulence with more anisotropic scatterers either embedded or nearby (e.g. DOVIK and ZRNIC, 1984). Typical values of θ_s are often in excess of 8° in the troposphere, whilst in the stratosphere at VHF values can be as small as 3° - 4° . The following diagrams from HOCKING et al (1986) summarize some measurements made with the SOUSY radar in Germany (after correction for the error noted above). Note also the tendency for the scatterers to become more isotropic in the high stratosphere.

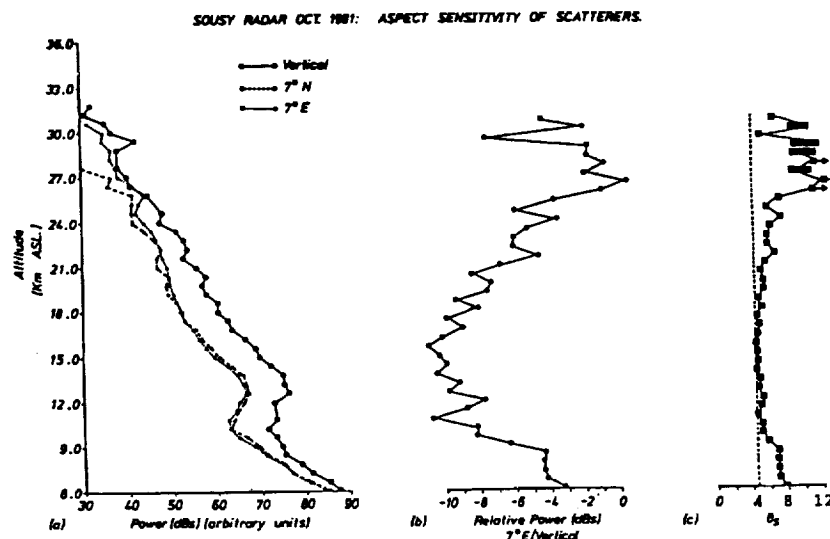


Fig. 14(a) Plots of 25 h mean powers as a function of altitude for the three beams. Noise has been subtracted. The noise was greatest on the north beam, because of the passage of Cassiopeia A through the beam, and so the signal disappeared into the noise at a lower height than for the other beams. The range effect on the powers has not been removed in this case. (b) Ratio of powers on the 7° E beam and the vertical beam. (c) Assuming that the scatterers had backscatter polar diagrams of the form $\exp(-\sin^2 \theta / \sin^2 \theta_s)$, this plot gives values of θ_s as a function of height. The vertical broken line shows the minimum θ_s measured. It is clear that above about 18 km, θ_s increased. The widths of each black rectangle gives the error in θ_s associated with a 1 dB increase in $P(7^\circ)/P(0^\circ)$. For θ_s values of greater than about 5° , a 1 dB uncertainty in $P(7^\circ)/P(0^\circ)$ implies a very large uncertainty in θ_s , and these squares with arrows indicate that the possible θ_s value may be as large as 90° for a 1 dB change in $P(7^\circ)/P(0^\circ)$ (i.e. the measurements are very insensitive for $\theta_s > 5^\circ$).

Fig. 14

In the mesosphere, θ_s is typically 4° for VHF scatter below 75 km, although on occasions isotropic scatter is also seen. Above 80 km, VHF measurements give θ_s to be about 6° - 8° . At MF, θ_s is typically 2° - 5° below 80 km, increasing to about 8° - 15° above 80 km (e.g. LINDNER, 1975a,b; VINCENT and BELROSE, 1978). REID (1989) has summarized the various mesospheric measurements.

An alternative means which may be used to determine θ_s is to utilize equation (16). By comparing wind speeds deduced using the DBS method for a beam pointed at say 5° off-zenith to one at say 15° off zenith, it is possible to deduce θ_s from (16), assuming that the value deduced with the 15° beam is the true wind speed. An alternative is to use spaced antenna methods to determine the true wind speed, and then comparisons with the DBS measurements may allow determination of θ_s .

Another interesting determination of θ_s was made by VINCENT and BELROSE (1978),

who compared the powers received on two beams of different polar diagram widths, and used the resultant ratios of powers to determine θ_s . The method yielded results consistent with determinations made by other techniques discussed in this section.

5.1.2 Spatial correlation methods

If one illuminates the sky from a transmitting array which has a very wide polar diagram, and monitors the electric field received at the ground, then the variation of electric field as a function of position is simply the diffraction pattern of the scattering irregularities. The spatial autocorrelation function over the ground can be determined by using an array of dipoles distributed over the ground, recording the signal on each dipole separately and then cross-correlating between dipoles. The spatial autocorrelation function so produced is simply the Fourier transform of the effective polar diagram (ie the combined polar diagrams of the radar beam and the scatterers). If the e^{-1} width of the effective polar diagram is θ_{sb} , then the spatial lag at which the amplitude of the complex autocorrelation function falls to 0.5 is approximately $12.0/\theta_{sb}$ radar wavelengths, where θ_{sb} is expressed in degrees (e.g. HOCKING et al., 1989).

Thus a useful technique for determination of the polar diagram of backscatter is to produce the spatial autocorrelation function in the manner described, and then Fourier transform it. Such a technique has been utilized by LINDNER (1975a, b) in order to study the aspect sensitivity of mesospheric scatterers at an MF frequency of 1.98 MHz. For example, Lindner found typical values for θ_s of about 2° to 5° below 80 km, and 10° to 15° above. These results are consistent with later observations using beam-swinging techniques (HOCKING, 1979). The method has not been greatly utilized, however, and deserves further attention.

5.1.3 Spectral methods

It was noted earlier in regard to discussions about extraction of turbulence from spectra that in many cases the main contribution to the spectral width was spectral-broadening due to the finite width of the polar diagram of the radar beam. At the time this was a nuisance, but now it can be turned to good effect. The effective polar diagram is the product between the polar diagram of the radar and the backscatter polar diagram of the scatterers. As seen in appendix A, if θ_{sb} is the e^{-1} half-width of the effective polar diagram (ie the product of the backscatter polar diagram and the radar beam polar diagram) then

$$\sin^{-2}\theta_{sb} = \sin^{-2}\theta_0 + \sin^{-2}\theta_s \quad (66)$$

But from equation (17) the beam-broadening of the spectral width is

$$f_{\frac{1}{2}b} = \frac{2}{\lambda}(1.0) |V_{hor}| \theta_{\frac{1}{2}} \quad (67)$$

The total spectral half-power-half-width is given approximately by

$$f_{\frac{1}{2}}^2 = f_{\frac{1}{2}b}^2 + f_{fluct}^2 \quad (68)$$

if we ignore the contribution due to wind-shear. (This last term can in fact reduce $f_{\frac{1}{2}}$, but it is usually fairly small.) Then we can apply our experimentally measured spectral widths to place upper limits on θ_s . That is, if we calculate

$$\theta'_{\frac{1}{2}} = \frac{\lambda}{2} \frac{f_{\frac{1}{2}}}{|V_{hor}|} \quad (69)$$

then this is a useful upper limit to $\theta_{\frac{1}{2}eff}$, the half-power half-width of the combined polar diagram of the scatterers and the radar beam. In the case that it can be shown that $f_{\frac{1}{2}} \gg f_{fluct}$, as often happens, then $\theta_{\frac{1}{2}}$ is a good estimate of $\theta_{\frac{1}{2}eff}$. Then $\theta_{ab} = \theta_{\frac{1}{2}eff}/\sqrt{\ln 2}$, and equation (66) can be used to deduce θ_s . In the special case that a relatively wide beam is used, so that $\theta_0 \gg \theta_s$, $\theta_{ab} = \theta_s$.

The above principles have been used by HOCKING et al., (1986), and HOCKING (1987a, b) to make estimates of backscatter polar diagram half-widths. The method of using fading times as a crude indicator of "specularity", as done by for example RASTOGI and ROETTGER (1982) may be also considered as a primitive special case of this method, although that procedure does not really pay proper consideration to the role of the mean wind in determining the fading time through beam-broadening. More recently WOODMAN and CHU (1989) have used similar techniques, but rather than just using the spectral width and assuming Gaussian polar diagrams as done here, they have used the whole spectrum and the one-to one correspondence between the polar diagram of backscatter and the spectrum to determine additional detail about the actual shape of the polar diagram of backscatter and so the irregularities themselves. Woodman and Chu also used a wide beam, but it should be noted that this procedure assumes azimuthal symmetry.

A procedure like this is very useful if there are several types of scatterers in the beam. For example, if scatterers and reflectors described by models A and B both exist in the same radar volume, the spectrum will not be Gaussian, but will comprise two portions; a narrow central component corresponding to the specular reflectors, and a wider component corresponding to the "model A" scatterers. As it turned out, WOODMAN and CHU (1989) saw no evidence of "model B" reflectors, but this is likely to be because their spectra were averaged over 45 min, whilst specular reflectors, if they exist, are likely to be relatively short-lived.

Indeed, evidence for the coexistence of the two types of scatterers coexisting in the same region of space has been given by HOCKING (1987a), and is illustrated in the following diagram. The data are presented because they show yet another useful means of determining information about the scatterers, as well as making the point that both specular reflectors and turbulent scatterers do seem to coexist.

These data were obtained using a hybrid of the beam-swinging and spectral approaches. Two beams were used, one vertical and one off-vertical. A strong signal of very narrow width was seen with the vertical beam, but nothing else, whereas on the off-vertical beam two separate contributions to the spectra were seen; first a broader component corresponding to isotropic backscatter received through the main lobe of the beam, and secondly the same narrow spectrum as seen with the vertical beam. Clearly the second component was due to leakage from overhead, and comparison of the powers in the specular component observed with the narrow beam and the more isotropic component show that the specular component is some 70 times stronger. The model discussed in Fig. 12 may apply in some cases, but certainly does not here, as it is unlikely that the anisotropic scatterers at the layer edges would be so much stronger than their counterparts in the centre of the layer. Thus this figure does indeed suggest the coexistence of both models, whilst at the same time demonstrating yet another useful technique to determine the aspect-sensitivity and nature of the scatterers.

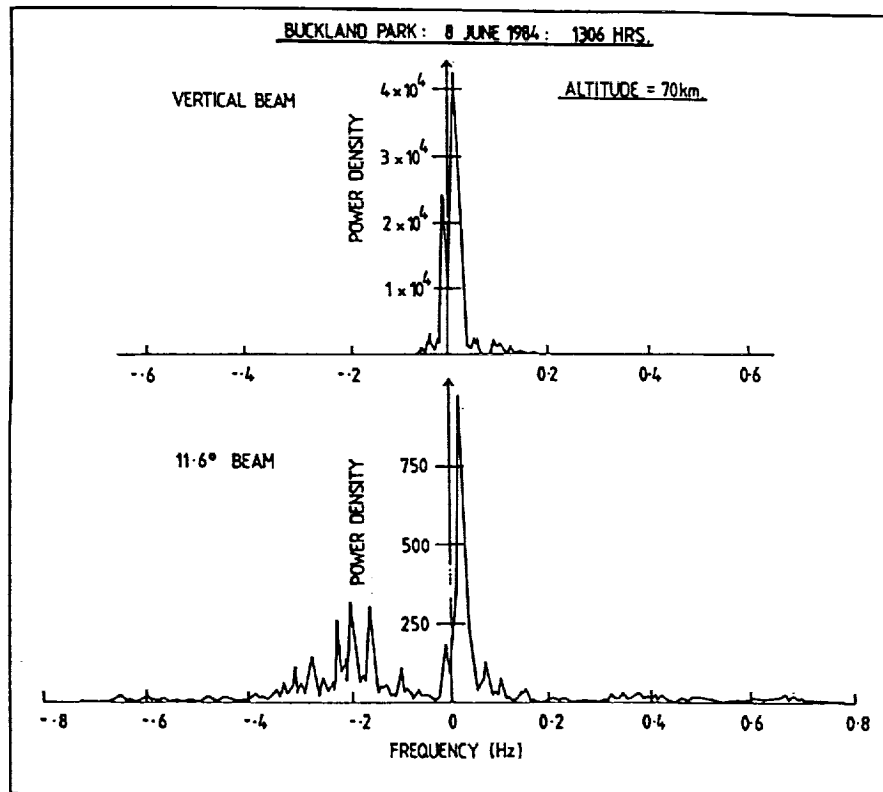


Fig. 15 Spectra recorded with vertical and off-vertical beams of the Buckland Park 2 MHz radar.

5.1.4 Amplitude distributions

The preceding techniques have been designed to make measurements of θ_s , and are particularly powerful if model A is valid. However, there is a useful method which allows the validity of model B to be tested, and which has been used with varying degrees of success in recent years. This is the use of amplitude distributions (e.g. VON BIEL, 1971, 1981; VINCENT and BELROSE, 1978; ROETTGER, 1980a; RASTOGI and HOLT, 1981; SHEEN et. al., 1985; HOCKING, 1987b; KUO et al., 1987 amongst others).

There are many variations of this technique, but only the simplest will be discussed here, in order to illustrate the method. If scatter is due to an ensemble of roughly similar scatterers, as might occur in a turbulent patch, then the amplitudes of the resultant distribution will have a so-called "Rayleigh distribution" (RAYLEIGH, 1894). If, however, there is also a much stronger single scatterer in addition to these weaker scatterers, the distribution changes to a so-called "Rice distribution" (RICE, 1944, 1945). The figure below shows how these distributions change as the specular component is made larger. Each curve is parameterized by a parameter called the "Rice parameter", which is a measure of the strength of the specular component divided by the RMS "random" component. For a Rayleigh distribution, this parameter is zero.

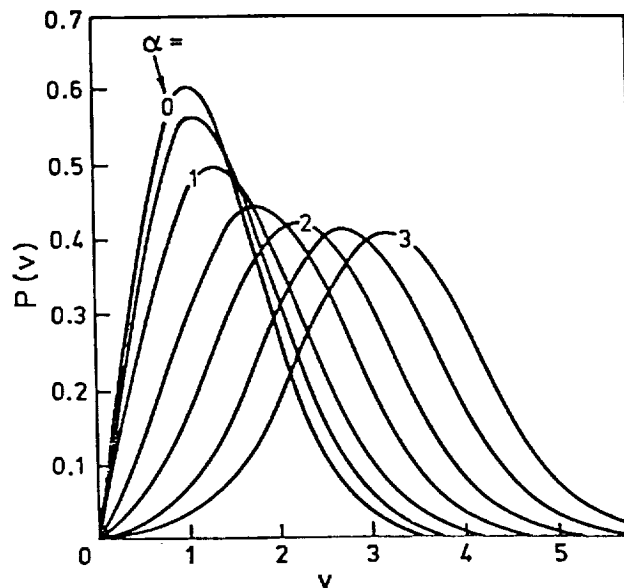


Fig. 16 Rice distributions in steps of $\alpha = 0.5$ as a function of $v = z/\sigma = \sqrt{2} \cdot z/k$, where z = received amplitude, k = RMS scattered power and σ = the standard deviation of each of the inphase and quadrature components of the scattered signal. These plots may also be regarded as the distribution of amplitudes for a constant RMS scatter component $k = \sqrt{2}$ and varying specular component.

Thus in principle, by making histograms of the amplitudes of the received signal and comparing them to the above curves, it is possible to determine if there is a single dominant scatterer within the radar beam. More complex variations on this process exist, including looking at the phase distributions (e.g. ROETTGER, 1980a) and using more complex distributions such as the Nakagami-M distribution (e.g. SHEEN et al., 1985; KUO et al., 1987). The latter generalization is particularly useful if the specular component has undulations on it and causes focussing and de-focussing of the reflected radiation.

Unfortunately, as with almost all techniques, complications exist. For example, if there is more than one specular reflector in the radar volume, then the amplitude distribution changes, and if there are more than about 4, the distribution begins to look almost Rayleigh-like again. Furthermore, if one uses relatively short data sets (less than about 10 mins of data), statistical effects can cause a set of scatterers which should produce a Rayleigh distribution to produce a Rice distribution, which wrongly suggests the existence of a specular component. To properly utilize the so-called Rice parameter one must look at the distributions of the Rice parameter itself; the calculation of several non-zero Rice parameters is not in itself evidence for a non-Rayleigh distribution. The correct interpretation of the Rice parameter is discussed by HOCKING, (1987b).

Nevertheless, the process can be useful, as illustrated by the many authors listed previously. An interesting example is shown in fig.17 below, which was taken from HOCKING (1987b).

17-18 OCT. 1981
SOUSY RADAR

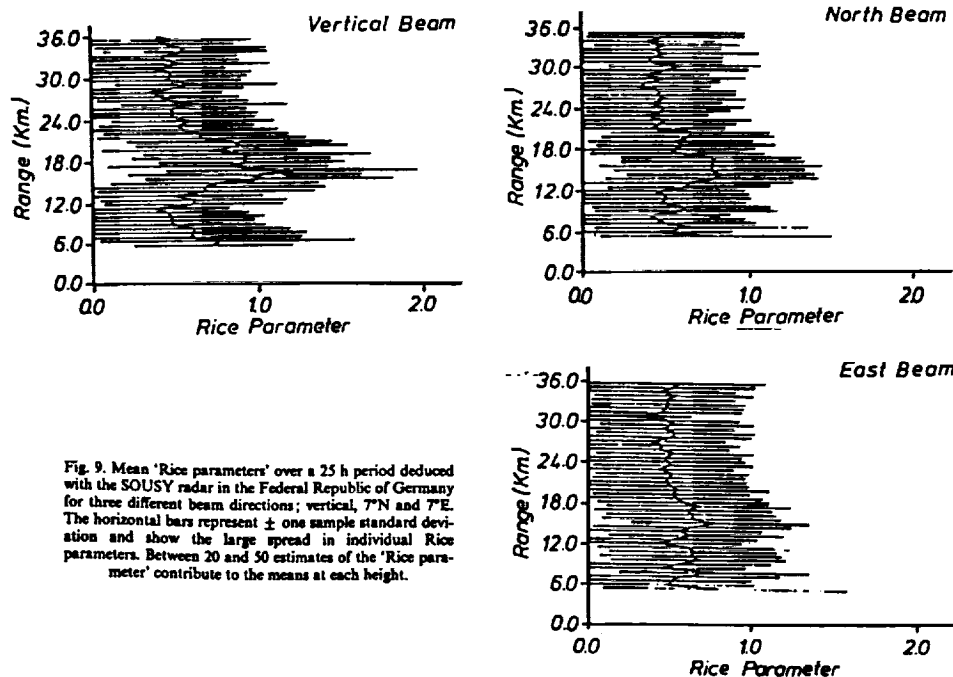


Fig. 17

This diagram shows the height profile of the mean Rice parameter ($\langle \alpha \rangle$) as a function of height measured with the SOUSY radar, using a vertical beam and two off-vertical beams, one directed at 7° off-vertical to the North, and one at 7° off-vertical to the East. Note the increase in $\langle \alpha \rangle$ just above the tropopause, when observing with the vertical beam, indicating the presence of a few dominant reflectors within the radar volume in the stratosphere. Notice also that there is still a non-Rayleigh character to the scattering process on the North beam, but on the East beam the mean Rice parameter is fairly constant with height and consistent with a Rayleigh process.

One possible interpretation of these results is that the scatterers are elongated in the Eastward direction compared to the Northward (ie aligned along the mean wind vector, which was predominately Eastward at the time). If such an elongation existed, then the polar diagram of backscatter would be narrower in the East-West direction, and so the half-power half-width may be substantially less than 7° and not show an effect on the 7° off-vertical beam; only the effects of the turbulent scatter are seen. In the North-South direction, the polar diagram would be wider, and some contribution from these scatterers may still show.

Alternatively, one might invoke model B, and speculate that flat specular reflectors exist with small wrinkles, but that there were a wider range of Fourier components in the North-South direction, causing a broadened polar diagram in this direction.

It is clear from the above techniques that there are a multitude of techniques available to enable the nature of the scatterers to be understood. However, there are still many unresolved

issues about these scatterers, and the application of the above procedures is to be actively encouraged, in the hope of eventually fully understanding the scattering and reflecting processes, and the parameters which describe them. The importance of knowing these characteristics has already been stressed.

6 Less easily determined target parameters

The discussion so far has concentrated on parameters which can be inferred fairly directly from the radar measurements. There are, however, other parameters which can be deduced with a little extra work. For example, VINCENT and REID (1983) showed how, by using two off-vertical beams, measurements of the gravity-wave and turbulent momentum fluxes could be calculated. The momentum flux is not actually a target parameter, and so has not been discussed here greatly, but it nevertheless is a parameter which affects the targets, and knowledge about is most desirable. Another example is the Brunt-Vaisala frequency. Normally this is very difficult to measure, but if the mean winds are light, then spectral analysis of the time series of velocity measurements can be used to measure the Brunt-Vaisala frequency. That is, the spectrum shows a cutoff at the Brunt-Vaisala frequency, and this in turn allows determination of the temperature gradient (e.g. ROETTGER, 1980b).

DEWAN (1981) and WOODMAN and RASTOGI (1984) have shown how careful measurements of the temporal and spatial distribution of the occurrence of thin turbulent layers can be used to infer the mean turbulent diffusion coefficient in the stratosphere, as distinct from the diffusion coefficient within a turbulent layer (the latter can be determined from equation (38)).

High resolution studies can also be used to infer something about the nature of the scatterers; for example ROETTGER and SCHMIDT (1979) used a resolution of 30m to observe cat's-eye structures in the stratosphere, confirming that at least some of the observed turbulent layers are due to dynamical instability. REID et al. (1987) have observed similar features in the mesosphere. Other studies which allow information about the nature of the scatterers to be obtained include, for example, those by KLOSTERMEYER and RUESTER (1980, 1981), and YAMAMOTO et al. (1987, 1988); in these studies relations between power bursts and buoyancy-wave oscillations were investigated.

By using radars in conjunction with other instruments, further information can be deduced. A good example is the use of acoustic waves to act as reflectors for VHF radar waves, as done with the RASS system at the MU radar in Japan. With this instrument, it is possible to measure temperature profiles in the atmosphere. The use of such hybrid systems in the future is likely to be of great benefit.

Of course, by using long time series of velocities, one can determine other characteristics of the scattering region, like the buoyancy wave spectra, tidal amplitudes, planetary wave amplitudes, and a whole host of dynamical quantities. In a broad sense one might like to think of these as "target parameters" of a sort, but these are beyond the scope of the current paper.

7 Conclusions

The main parameters which can be deduced directly from radar observations of the atmosphere have been discussed. It is clear that it is not possible to make best use of the observations without better understanding the scattering process, and the ways in which the scatterers are

formed. Methods for deducing more information about the scatterers have been described, as well as some procedures by which routine information like wind speeds, turbulence intensities, and scatterer shapes, can be deduced. The need for more observations of this sort is pressing.

Appendix A: Effective pointing angle and beamwidth for anisotropic scatter

As pointed out by ROETTGER (1981), an anisotropy in the scattering mechanism alters the effective pointing angles for an off-vertical radar. Such anisotropy also alters the effective beamwidth and this is important for the work in this paper. Let the polar diagram of backscatter for the scatterers be

$$P_s(\theta) \propto e^{-\frac{\sin^2 \theta}{\sin^2 \theta_s}}$$

and the two way polar diagram for a vertically pointing radar be (A1)

$$P_R(\theta) \propto e^{-\frac{\sin^2 \theta}{\sin^2 \theta_0}} \quad (A2)$$

Then for a radar pointed off-vertical by angle θ_T in the azimuth direction $\phi = 0$, the polar diagram at angle (θ, ϕ) is

$$P_{RT}(\theta, \phi) \propto e^{\left\{ - \left[\frac{(\sin \theta \sin \phi)^2 + (\sin \theta \cos \phi - \sin \theta_T)^2}{\sin^2 \theta_0} \right] \right\}} \quad (A3)$$

(Note that the expression $\exp[-\sin^2(\theta - \theta_T)/\sin^2 \theta_0]$ (which has in the past been used to represent a tilted beam) is NOT a good approximation, as that describes an annulus around the zenithal point at a mean angle θ_T .) When the effects of the polar diagram of the scatterers are included, the effective polar diagram is the product of (A1) and (A3). This is a maximum when the derivative of the exponent with respect to $\sin \theta$ is zero, or at

$$\sin \theta_{eff} = \sin \theta_T \left[1 + \frac{\sin^2 \theta_0}{\sin^2 \theta_s} \right]^{-1} \quad (A4)$$

For θ_0, θ_s less than about 10° , this approximates to

$$\sin \theta_{eff} = \sin \theta_T \left[1 + \frac{\theta_0^2}{\theta_s^2} \right]^{-1}$$

Thus the effective pointing angle is given by (A4), and horizontal wind speeds will be underestimated by the factor

$$R_1 = \left[1 + \frac{\theta_0^2}{\theta_s^2} \right] \quad (A5)$$

if one uses say equation (12) without any correction. This is in fact only approximate - to properly determine the actual measured radial velocity, equation (35) of HOCKING (1983a) should be integrated (including an aspect sensitivity for the scatterers) to produce the expected power spectrum; this will not have a maximum at the exact point described by (A4), but it will be close.

The half-width of the effective beam can be found by finding the angles (θ, ϕ) where the effective polar diagram [i.e. the product of (A1) and (A3)] falls to one half of the value at $(\theta, \phi) = (\theta_{eff}, 0)$. Consider only the line $\phi = 0$. Then the product of (A1) and (A3) gives

$$e^{\left\{ - \left[\frac{(\sin \theta - \sin \theta_T)^2}{\sin^2 \theta_0} + \frac{\sin^2 \theta}{\sin^2 \theta_s} \right] \right\}} \quad (A6)$$

and we seek the two angles $(\theta_{\frac{1}{2}})_{1,2}$ where this falls to one half of the value at $\theta = \theta_{eff}$. Some algebraic manipulation soon shows that a quadratic in $\sin\theta$ results, which has two roots at

$$(\theta_{\frac{1}{2}})_{1,2} = \sin\theta_{eff} \pm \sqrt{\ln 2} \cdot \sin\theta_0 \left[1 + \frac{\theta_0^2}{\theta_s^2} \right]^{-\frac{1}{2}} \quad (A7)$$

(for θ_0, θ_s less than about 10°), and this shows that the effective half-power half-width is

$$R_2 = \left[1 + \frac{\theta_0^2}{\theta_s^2} \right]^{-\frac{1}{2}} \quad (A8)$$

times the half-width of the radar alone. Notice that this ratio is independent of the radar tilt direction, at least out to angles of 10 - 15° .

Equivalently, we can write that the effective half-power half-width $\theta_{eff\frac{1}{2}}$ obeys the relation

$$\sin^{-2}(\theta_{eff\frac{1}{2}}) = \sin^{-2}(\theta_{\frac{1}{2}}) + \sin^{-2}(\theta_{s\frac{1}{2}}), \quad (A9)$$

where $\theta_{\frac{1}{2}}$ is the half power half width of the radar beam and $\theta_{s\frac{1}{2}}$ is the half-power half-width of the backscatter polar diagram of the scatterers.

Now let us address the issue of how the power received by the radar changes as a function of tilt angle θ_T . The power received by the vertical beam can be found by integrating over the beam, and for a Gaussian polar diagram this integral is proportional to $(\theta_{eff\frac{1}{2}})^2$ where $\theta_{eff\frac{1}{2}}$ is the effective half-power half-width of the combined polar diagrams of the radar and the scatterers. When the radar beam is phased to look at an off-vertical angle θ_T , the peak power will be reduced by a factor

$$f1 = e^{\left\{ -\frac{(\theta_{eff} - \theta_T)^2}{\theta_0^2} \right\}}$$

because the peak returned power is returned from θ_{eff} and not θ_T , and then by a further factor

$$f2 = e^{\left\{ -\frac{\theta_{eff}^2}{\theta_s^2} \right\}}$$

because of the reduction in power due to the polar diagram of backscatter of the scatterers.

Thus the total received power will be proportional to the product of $f1$ and $f2$, and then multiplied by the effective beam half-power half-width squared. Thus the received power on the off-vertical beam divided by that received on the vertical beam is equal to

$$\frac{f1 \cdot f2 \cdot (\theta_{eff\frac{1}{2}})^2}{(\theta_{eff\frac{1}{2}})^2}$$

or

$$\frac{P(\theta_T)}{P(0)} = \exp \left\{ - \left[\frac{(\theta_{eff} - \theta_T)^2}{\theta_0^2} + \frac{\theta_{eff}^2}{\theta_s^2} \right] \right\} \quad (A10)$$

Note that this final expression corrects an error in the original derivation of HOCKING et al, (1986), in which the factor $f2$ was neglected.

References

- Adams, G.W., D.P. Edwards and J.W. Brosnahn, The imaging Doppler interferometer; Data analysis, *Rad. Sci.*, **20**, 1481-1492, 1985.
- Atlas, D., *Advances in Geophysics*, vol 10, 317 pp, Academic New York, 1964.
- Atlas, D., R.C. Srevastava and P.W. Sloss, Wind shear and reflectivity Gradient effects on Doppler radar spectra, II, *J. Appl. Meteor.*, **8**, 384-388, 1969.
- Austin, G.L., R.G.T. Bennett, and M.R. Thorpe, The phase of waves partially reflected from the lower ionosphere, *J. Atmos. Terr. Phys.*, **31**, 1099-1106, 1969.
- Barat, J., Some characteristics of clear air turbulence in the middle stratosphere, *J. Atmos. Sci.*, **39**, 2553-2564, 1982.
- Batchelor, G.K., *The theory of homogeneous turbulence*, Cambridge University Press, New York, 1953.
- Bohne, A.R., Radar detection of turbulence in precipitation environments, *J. Atmos. Sci.*, **39**, 1819-1837, 1982.
- Bolgiano, R., Jr., *The general theory of turbulence - turbulence in the atmosphere*, in "Winds and turbulence in the stratosphere, mesosphere and ionosphere", ed K. Rawer, p371, North-holland, Amsterdam, 1968.
- Bracewell, R.N., *The Fourier Transform and Its Applications*, 444pp., McGraw-Hill, New York, 1978.
- Briggs, B.H., Radar observations of atmospheric winds and turbulence: a comparison of techniques, *J. Atmos. Terr. Phys.*, **42**, 823-833, 1980.
- Briggs, B.H., The analysis of spaced sensor records by correlation techniques, *Handbook for MAP*, vol. 13, Ground based techniques, 166-186, Univ. of Illinois, Urbana, 1984.
- Briggs, B.H. and R.A. Vincent, Some theoretical considerations on remote probing of weakly scattering irregularities, *Aust. J. Phys.*, **26**, 805-814, 1973.
- Budden, K.G., Effect of electron collisions on the formulas of magnetoionic theory, *Radio Sci.*, **69D**, 191-211, 1965.
- Caughey S.J., B.A. Crease, D.N. Asimakopoulos, and R.S. Cole, Quantitative bistatic acoustic sounding of the atmospheric boundary layer, *Q. J. R. Meteorol. Soc.*, **104**, 147-161, 1980.
- Crane, R.K., A review of radar observations of turbulence in the lower stratosphere, *Radio Sci.*, **15**, 177-194, 1980.
- Croft, T.A., Sky-wave backscatter: a means of observing our environment at great distances. *Revs. Geophys. Space Phys.*, **10**, 73-155, 1972.
- Dewan, E.M., Turbulent vertical transport due to thin intermittent mixing layers in the stratosphere and other stable fluids, *Science*, **211**, 1041-1042, 1981.
- Doviak, R.J., and D.S. Zrnic, Reflection and scatter formula for anisotropically turbulent air, *Radio Sci.*, **19**, 325-336, 1984.
- Farley, D.T., H.M. Ierick, and B.G. Fejer, Radar interferometry : a new technique for studying plasma turbulence in the ionosphere, *J. Geophys. Res.*, **86**, 1467-1472, 1981.
- Fukao, S., K. Wakasugi, and S. Kato, Radar measurement of short-period atmospheric waves and related scattering properties at the altitude of 13-25 km over Jicamarca, *Radio Sci.*, **15**, 431-438, 1980a.
- Fukao, S., T. Sato, R.M. Harper, and S. Kato, Radio wave scattering from the tropical mesosphere observed with the Jicamarca radar, *Radio Sci.*, **15**, 447-457, 1980b.

- Fukao, S., T. Sato, P.T. May, T. Tsuda, S. Kato, M. Inaba, and I. Kimura, A systematic error in MST/ST radar wind measurement induced by a finite range volume effect,1, Observational results, *Radio Sci.*, **23**, 59-73, 1988a.
- Fukao, S., M. Inaba, I. Kimura, P.T. May, T. Sato, T. Tsuda, and S. Kato, A systemic error in MST/ST radar wind measurement induced by a finite range volume effect,2, Numerical considerations, *Radio Sci.*, **23**, 74-82, 1988b.
- Gage, K.S., and Balsley, B.B., Doppler radar probing of the clear atmosphere, *Bull. Am. Meteorol. Soc.*, **59**, 1074-1093, 1978.
- Gage, K.S., and J.L. Green, Evidence for specular reflection from monostatic VHF radar observations of the stratosphere, *Radio Sci.*, **13**, 991-1001, 1978.
- Gage, K.S., J.L. Green, and T.E. VanZandt, Use of Doppler radar for the measurement of atmospheric turbulence parameters from the intensity of clear air echoes, *Radio Sci.*, **15**, 407-416, 1980.
- Gage, K.S., B.B. Balsley, and J.L. Green, Fresnel scattering model for the specular echoes observed by VHF radars, *Radio Sci.*, **16**, 1447-1453, 1981a.
- Gage, K.S., W.L. Ecklund, and B.B. Balsley, A modified Fresnel scattering model for the parameterization of Fresnel returns, *Radio Sci.*, **20**, 1493-1502, 1985.
- Green, J.L., and K.S. Gage, Observations of stable layers in the troposphere and stratosphere using VHF radar, *Radio Sci.*, **15**, 395-405, 1980.
- Green, J.L. and K.S. Gage, A Re-examination of the range resolution dependence of backscattered power observed by VHF radars at vertical incidence, *Radio Sci.*, **20**, 1001-1005, 1985.
- Gregory, J.B., and R.A. Vincent, Structure of partially reflecting regions in the lower ionosphere, *J. Geophys. Res.*, **75**, 6387-6389, 1970.
- Hitschfeld, W., and A.S. Dennis, *Measurement and calculation of fluctuations in radar echoes from snow*, Sci. Rep. MW-23, McGill Univ., Montreal, Canada, 1956.
- Hocking, W.K., Angular and temporal characteristics of partial reflections from the D-region of the ionosphere, *J. Geophys. Res.*, **84**, 845-851, 1979.
- Hocking, W.K., and R.A. Vincent, Comparative observations of D region HF partial reflections at 2 and 6 MHz, *J. Geophys. Res.*, **87**, 7615-7624, 1982a.
- Hocking, W.K. and R.A. Vincent, A comparison between HF partial reflection profiles from the D-region and simultaneous Langmuir probe electron density measurements, *J. Atmos. Terr. Phys.*, **44**, 843-854, 1982b.
- Hocking W.K., On the extraction of atmospheric turbulence parameters from radar backscatter Doppler spectra I, Theory, *J. Atmos. Terr. Phys.*, **45**, 89-102, 1983a.
- Hocking, W.K., Mesospheric turbulence intensities measured with a HF radar at 35°S, II, *J. Atmos. Terr. Phys.*, **45**, 103-114, 1983b.
- Hocking, W.K. The spaced antenna drift method, *Handbook for MAP*, vol.9, 171-186, Univ. of Illinois, Urbana, 1983c.
- Hocking, W.K., and J. Roettger, Pulse-length dependence of radar signal strengths for Fresnel backscatter, *Radio Sci.*, **18**, 1312-1324, 1983.
- Hocking, W.K., G. Schmidt, and P. Czechowsky, *Absolute calibration of the SOUSY VHF stationary radar*, Max-Planck-Institut für Aeronomie report MPAE-W-00-83-14, Katlenburg-Lindau, F.R.G., 1983.
- Hocking, W.K., R. Rueter and P. Czechowsky, *Observation and measurement of turbulence and stability in the middle atmosphere with a VHF radar*, University of Adelaide internal report ADP-335, University of Adelaide, Adelaide, S.A. Australia, 1984.

- Hocking, W.K., Measurement of turbulent energy dissipation rates in the middle atmosphere by radar techniques: a review, *Radio Sci.*, 20, 1403-1422, 1985.
- Hocking W.K., R. Ruester and P. Czechowsky, Absolute reflectivities and aspect sensitivities of VHF radio wave scatterers measured with the SOUSY radar, *J. Atmos. Terr. Phys.*, 48, 131-144, 1986.
- Hocking, W.K., Observation and measurement of turbulence in the middle atmosphere with a VHF radar, *J. Atmos. Terr. Phys.*, 48, 655-670, 1986.
- Hocking, W.K., Radar studies of small scale structure in the upper middle atmosphere and lower ionosphere, *Adv. Space Res.*, 7, 327-338, 1987a
- Hocking, W.K., Reduction of the effects of non-stationarity in studies of amplitude statistics of radio wave backscatter, *J. Atmos. terr. Phys.*, 49, 1119-1131, 1987b
- Hocking, W.K., Two years of continuous measurements of turbulence parameters in the upper mesosphere and lower thermosphere made with a 2-MHz radar, *J. Geophys. Res.*, 93, 2475-2491, 1988
- Hocking, W.K., May, P.T., and Roettger, J., Interpretation, reliability and accuracies of parameters deduced by the spaced antenna method in middle atmosphere applications, *Pure and Appl. Geophys.*, 1989, in press.
- Hooke, W.H., and R.M. Jones, Dissipative waves excited by gravity-wave encounters with the stably stratified Planetary Boundary Layer, *J. Atmos. Sci.*, 43, 2048-2060, 1986.
- Klaassen, G.P., and W.R. Peltier, Evolution of finite amplitude Kelvin-Helmholtz billows in two spatial dimensions, *J. Atmos. Sci.*, 42, 1321-1339, 1985.
- Klostermeyer, J. and R. Ruester, Radar observation and model computation of a jet stream-generated Kelvin-Helmholtz instability, *J. Geophys. Res.*, 85, 2841-2846, 1980.
- Klostermeyer, J. and R. Ruester, Further study of a jet stream-generated Kelvin-Helmholtz instability, *J. Geophys. Res.*, 86, 6631-6637, 1981.
- Kuo, F.-S., C.-C. Chen, S.I. Liu, J. Roettger, and C.H. Liu, Systematic behaviour of signal statistics of MST radar echoes from clear air and their interpretation, *Radio Sci.*, 22, 1043-1052, 1987.
- Labitt, M., *Some basic relations concerning the radar measurement of air turbulence*, Mass. Inst. of Technol., Lincoln Lab., Work. Pap. 46WP-5001, 1979.
- Lilly, D.K., D.E. Waco and S.I. Adelfang, Stratospheric mixing estimated from high-altitude turbulence measurements, *J. Appl. Meteorol.*, 13, 488 - 493, 1974.
- Lindner, B.C., The nature of D-region scattering of vertical incidence radio waves, I. Generalized statistical theory of diversity effects between spaced receiving antennas, *Aust. J. Phys.*, 28, 163-170, 1975a.
- Lindner, B.C., The nature of D-region scattering of vertical incidence radio waves, II., Experimental observation using spaced antenna reception, *Aust. J. Phys.*, 28, 171-184, 1975b.
- Manson, A.H., M.W.J. Merry, and R.A. Vincent, Relationship between the partial reflection of radio waves from the lower ionosphere and irregularities as measured by rocket probes, *Radio Sci.*, 4, 955-958, 1969.
- Mathews J.D., J.H. Shapiro and B.S. Tanenbaum, Evidence for distributed scattering in D-region partial-reflection processes, *J. Geophys. Res.* 78, 8266. 1973.
- Mathews, J.D., J.K. Breakall, and M.P. Sulzer, The moon as a calibration target of convenience for VHF-UHF radar systems, *Radio Sci.*, 23, 1-12, 1988.
- May, P.T., S. Fukao, T. Tsuda, T. Sato and S. Kato, The effect of thin scattering layers on the determination of wind by Doppler radars, *Radio Sci.*, 23, 83-94, 1988.
- Ottersten, H., Radar backscattering from the turbulent clear atmosphere, *Radio Sci.*, 12, 1251-1255, 1969.

- Peltier, W.R., J.Halle, and T.L.Clark, The evolution of finite-amplitude Kelvin-Helmholtz Billows, *Geophys. Astrophys. Fluid Dyn.*, **10**, 53-87, 1978.
- Pfister, W., The wave-like nature of inhomogeneities in the E-region, *J.Atmos.Terr.Phys.*, **33**, 999-1025, 1971.
- Rastogi P.K. and O. Holt, On detecting reflections in presence of scattering from amplitude statistics with application to D-region partial reflections, *Radio Sci.* **16**, 1431-1443, 1981.
- Rastogi, P.K. and J. Roettger, VHF radar observations of coherent reflections in the vicinity of the tropopause, *J. Atmos. Terr. Phys.*, **44**, 461-469, 1982.
- Ratcliffe, J.A., Some aspects of diffraction theory and their application in the ionosphere, *Rep. Prog. Phys.*, **19**, 188-267, 1956.
- Rayleigh, Lord(J.W.Strutt), *Theory of Sound*, vol.1, pp.35-42. Macmillan, New York, 1894.
- Reid, I.M., R. Rueter and G. Schmidt, *Nature*, **327**, 43, 1987.
- Reid, I.M., Radar observations of stratified layers in the mesosphere and lower thermosphere (50-100 km), *Adv. Space Res.*, 1989 (in press).
- Rice, S.O., Mathematical analysis of random noise, *Bell Syst. Tech.J.*, **23**, 282-332, 1944.
- Rice, S.O., Mathematical analysis of random noise, *Bell Syst. Tech.J.*, **24**, 46-156, 1945.
- Roettger, J., Reflection and scattering of VHF radar signals from atmospheric refractivity structures, *Radio Sci.*, **15**, 259-276, 1980a.
- Roettger, J., Structure and dynamics of the stratosphere and mesosphere revealed by VHF radar investigations, *Pure Appl. Geophys.*, **118**, 494-527, 1980b.
- Roettger, J., Investigations of lower and middle atmosphere dynamics with spaced antenna drifts radars, *J.Atmos.Terr.Phys.*, **43**, 277-292, 1981.
- Roettger, J., and C.H.Liu, Partial reflection and scattering of VHF radar signals from the clear atmosphere, *Geophys. Res. Lett.*, **5**, 357-360, 1978.
- Roettger, J. and G. Schmidt, High-resolution VHF radar soundings of the troposphere and stratosphere, *IEEE Trans. Geosci. Electron.*, **GE-17**, 182-189, 1979.
- Roettger, J. and H.M. Ierick, Postset beam steering and interferometer applications of VHF radars to study winds, waves and turbulence in the lower and middle atmosphere, *Radio Sci.*, **20**, 1461-1480, 1985.
- Sato, T., and R.F.Woodman, Fine altitude resolution observations of stratospheric turbulent layers by the Arecibo 430 MHz radar, *J.Atmos. Sci.*, **39**, 2553-2564, 1982.
- Sheen D.R., C.H. Liu and J. Roettger, A study of signal statistics of VHF radar echoes from clear air, *J. Atmos. Terr. Phys.*, **47**, 675-684, 1985.
- Sloss, P.W., and D. Atlas, Wind shear and reflectivity gradient effects on Doppler radar spectra, *J.Atmos.Sci.*, **25**, 1080-1089, 1968.
- Tatarski, V.I., *Wave propagation in a turbulent medium*, McGraw-Hill, New York, 1961.
- Tatarski, V.I., *The effects of the turbulent atmosphere on wave propagation*, Keter Press, Jerusalem, 1971.
- Thrane, E. V., and B. Grandal, Observations of finescale structure in the mesosphere and lower thermosphere, *J. Atmos. Terr. Phys.*, **43**, 179-189, 1981.
- VanZandt, T.E., J.L.Green, K.S.Gage, and W.L.Clark, Vertical profiles of refractivity turbulence structure constant: Comparison of observations by the Sunset radar with a new theoretical model, *Radio Sci.*, **13**, 819-829, 1978.

- VanZandt, T.E., K.S. Gage and J.M. Warnock, An improved model for the calculation of profiles of and in the free atmosphere from background profiles of wind, Temperature and humidity, paper presented at 20th Conference on Radar Meteorology, Am. Met. Soc., Boston, Mass., Nov. 30-Dec. 3, 1981.
- Van Zandt, T.E., and R.A. Vincent, Is VHF Fresnel reflectivity due to low frequency buoyancy waves?, *Handbook for MAP*, vol. 9, p 78-80, Univ. of Illinois, Urbana, 1983.
- Vincent, R.A., The interpretation of some observations of radio waves scattered from the lower ionosphere, *Aust. J. Phys.*, 26, 815-827, 1973.
- Vincent, R.A. and J.S. Belrose, The angular distribution of radio waves partially reflected from the lower ionosphere, *J. Atmos. Terr. Phys.*, 40, 35-47, 1978.
- Vincent, R.A., and I.M. Reid, HF Doppler measurements of mesospheric gravity wave momentum fluxes, *J. Atmos. Sci.*, 40, 1321-1333, 1983.
- Vincent, R.A., B. Candy and B.H. Briggs, Measurements of antenna polar diagrams and efficiencies using a phase-switched interferometer, *Handbook for MAP*, vol. 20, p409-409, Univ. of Illinois, Urbana, 1986.
- Von Biel, H.A., Amplitude distributions of D-region partial reflections, *J. Geophys. Res.*, 76, 8365-8367, 1971.
- Von Biel, H.A., A statistical assessment of synoptic D-region partial reflection data, *J. Atmos. Terr. Phys.*, 43, 225-230, 1981.
- Waterman, A.T., Techniques for measurement of vertical and horizontal velocities; monostatic vs. bistatic measurements, *Handbook for MAP*, vol 9, 164-169, Univ. of Urbana, 1983.
- Waterman, A.T., T.Z. Hu, P. Czechowsky and J. Roettger, Measurement of anisotropic permittivity structure of upper troposphere with clear-air radar, *Radio Sci.*, 20, 1580-1592, 1985.
- Weinstock, J., On the theory of turbulence in the buoyancy subrange of stably stratified flows, *J. Atmos. Sci.*, 35, 634-649, 1978a.
- Weinstock, J., Vertical turbulent diffusion in a stably stratified fluid, *J. Atmos. Sci.*, 35, 1022-1027, 1978b.
- Weinstock, J., Using radar to estimate dissipation rates in thin layers of turbulence, *Radio Sci.*, 16, 1401-1406, 1981.
- Woodman, R.F. and A. Guillen, Radar observations of winds and turbulence in the stratosphere and mesosphere, *J. Atmos. Sci.*, 31, 493-505, 1974.
- Woodman, R.F. and P.K. Rastogi, Evaluation of effective eddy diffusive coefficients using radar observations of turbulence in the , stratosphere, *Geophys. Res. Letts.*, 11, 243-246, 1984.
- Woodman, R.F., Spectral moment estimation in MST radars, *Radio Sci.*, 20, 1185-1195, 1985.
- Woodman, R.F. and Y-H Chu, Aspect sensitivity measurements of VHF backscatter made with the Chung-Li radar: plausible mechanisms, *Radio Sci.*, 1989 (accepted).
- Yamamoto, M., T. Tsuda, S. Kato, T. Sato, and S. Fukao, A saturated inertia gravity wave in the mesosphere observed by the middle and upper atmosphere radar, *J. Geophys. Res.*, 92, 11993-11999, 1987.
- Yamamoto, M., T. Tsuda, S. Kato, T. Sato, and S. Fukao, Interpretation of the structure of mesospheric turbulence layers in terms of inertia gravity waves, *Physica Scripta*, 37, 645-650, 1988.
- Zrnic, D.S., Estimation of spectral moments for weather echoes, *IEEE Trans. Geosci. Electron.*, GE-17, 113-128, 1979.

Chapter 8

GRAVITY WAVES AND INSTABILITIES IN THE LOWER AND
MIDDLE ATMOSPHERE

Jürgen Klostermeyer

Max-Planck-Institut für Aeronomie, 3411 Katlenburg-Lindau, FRG

1. INTRODUCTION

The atmosphere moves ceaselessly on scales ranging from the dimension of the earth down to the mean free path of individual air molecules. An understanding of atmospheric motions requires the study of very specific problems that have to be idealized to focus attention on the basic dynamical processes, and thus are not faithful in detail. MST radar observations comprise large-scale processes like longitudinally averaged wind fields, planetary and tidal waves, and synoptic weather disturbances, mesoscale processes like narrow jet streams, frontal zones and atmospheric gravity waves, and small-scale processes like Kelvin-Helmholtz instability and turbulence preferably at scales equal to half the radar wavelength. All these processes interact nonlinearly, e.g. winds can enhance gravity waves and gravity waves can accelerate winds (wave-mean flow interaction) or a gravity wave at a given wavelength and period can enhance gravity waves at other wavelengths and periods (wave-wave interaction). Idealizing a problem then means that some linear terms in the hydrodynamic equations are neglected to suppress unwanted types of motion and that nonlinear terms are neglected or simplified to study particular types of interaction with relatively simple mathematical tools.

It is clearly impossible to discuss the whole variety of atmospheric motions in this lecture, therefore we will confine ourselves to some basic aspects of mesoscale and small-scale gravity waves and instability mechanisms. These processes can be (and partly have been) investigated by single ST or MST radars rather than expensive networks of radars and other techniques that would be necessary to study details of large-scale processes (the physics of planetary waves, for example, depends strongly on the zonal flow averaged around a latitude circle and thus cannot be investigated by measuring only the time-averaged flow over a single radar station).

Internal gravity waves with wavelengths between ten and less than one kilometer and periods between several hours and several minutes appear to play a central role in atmospheric wavenumber and frequency spectra (VANZANDT, 1982). Therefore we discuss the propagation of gravity waves in simplified atmospheric models in Section 2. Their interaction with the wind, their mutual interaction and instability mechanisms based upon these processes will be treated in Sections 3 and 4. All sections stress the theoretical aspects but are completed by MST radar observations

showing the relevant hydrodynamic processes. Such a short treatment necessarily must be incomplete and sketchy but hopefully will stimulate further studies of dynamic processes by means of MST radars and other methods.

2. ATMOSPHERIC GRAVITY WAVES

To study atmospheric gravity waves it is convenient to consider an unbounded non-rotating model atmosphere without molecular viscosity and thermal conductivity. Thereby we eliminate unwanted types of dynamic processes like gyroscopic or inertial waves, viscosity waves and heat conduction waves resulting, respectively, from the Coriolis force and the dissipative terms in the equations of momentum and energy which play no role at the wavelengths and frequencies considered below. For further details of these wavetypes see VOLLAND (1969) and LEBLOND and MYSAK (1978). The remaining waves that can propagate through the model atmosphere fall into two categories: High-frequency acoustic waves due to the compressibility of the air and low-frequency internal gravity waves due to the gravitational force. The periods and wavelengths of acoustic waves are smaller than about 1 s and 300 m, respectively, whereas the corresponding values for internal gravity waves are larger than about 300 s and 300 m. The dispersion curves of both wave types thus are widely separated in the frequency-wavenumber plane and interactions can in general be neglected. We can therefore eliminate acoustic waves by assuming that the model atmosphere is incompressible so that the sound speed is infinite and the density cannot vary along the path of an air parcel:

$$\frac{d\rho}{dt} = 0 \quad (1)$$

where $d/dt = \partial/\partial t + \mathbf{u} \cdot \nabla$ and ρ and \mathbf{u} denote density and fluid velocity. It should be mentioned, however, that this approximation also filters out long-period Lamb waves which propagate horizontally at the speed of sound and sometimes play a dominant role in the atmospheric response to tropospheric excitations (KLOSTERMEYER, 1977; LIU et al., 1982).

Together with (1), the continuity equation and the Euler equation yield a closed set of equations for describing the dynamics of the model atmosphere:

$$\nabla \cdot \mathbf{u} = 0 \quad (2)$$

$$\rho \frac{d\mathbf{u}}{dt} + \nabla p - \rho \mathbf{g} = 0 \quad (3)$$

where p and \mathbf{g} denote pressure and gravitational acceleration.

Often it is useful to compare the actual atmospheric state with a reference state defined by hydrostatic equilibrium

$$\rho = \rho_0(z), \quad p = p_0(z), \quad \mathbf{u} \equiv 0 \quad (4)$$

satisfying (1) and (2) while (3) reduces to

$$p_{0z} = -\rho_0 g. \quad (5)$$

Here and in the following, the subscripts x, z and t denote partial derivatives with respect to horizontal and vertical coordinates and time, respectively. Equation (5) yields $p_0(z)$ for any given density distribution $\rho_0(z)$. An important quantity of the equilibrium state is the Väisälä-Brunt frequency N given by

$$N^2 = -g \frac{\rho_{0z}}{\rho_0}. \quad (6)$$

It will be shown below that N is the angular frequency of an air parcel when it is vertically displaced from its equilibrium position to a slightly higher or lower level. The period $2\pi/N$ is about 5 to 10 min in the earth's atmosphere. $N^2 < 0$ (convection) means that the air parcel would continue to rise or fall rather than oscillate around its equilibrium position. Such unstable situation in general cannot persist because this so-called static instability is eliminated by strong vertical mixing as fast as it forms.

Small departures from the basic state (4) can be described by the perturbation density ρ_1 , pressure p_1 and velocity \mathbf{u}_1 defined by

$$\rho = \rho_0 + \rho_1, \quad p = p_0 + p_1, \quad \mathbf{u} = \mathbf{u}_1. \quad (7)$$

Substituting into (1)–(3) and neglecting terms containing products of perturbation quantities yields

$$\rho_{1t} + w_1 \rho_{0z} = 0 \quad (8)$$

$$\nabla \cdot \mathbf{u}_1 = 0 \quad (9)$$

$$\mathbf{u}_{1t} + \frac{1}{\rho_0} \nabla p_1 - \frac{\rho_1}{\rho_0} \mathbf{g} = 0 \quad (10)$$

where w_1 is the vertical component of \mathbf{u}_1 . Equation (10) indicates that a reduced gravitational acceleration (or buoyancy) $\mathbf{g}\rho_1/\rho_0$ and a modified pressure p_1 act upon a displaced parcel. In a stably stratified atmosphere, buoyancy pulls back any parcel to its equilibrium position giving rise to internal wave oscillations. Linearization is primarily an approximation dictated by our inability to treat nonlinear problems with adequate mathematical tools. It is valid for wave motions of infinitesimal amplitude implying that the fluid velocity must be much smaller than the phase velocity, and clearly filters out all nonlinear interactions between waves of different wavelengths

and periods as well as self-interaction.

It is convenient to eliminate the variables ρ_1, p_1 and u_1 (the horizontal component of \mathbf{u}_1) yielding an equation for w_1 alone:

$$\nabla^2 w_{1tt} + N^2 \nabla_h^2 w_1 - \frac{N^2}{g} w_{1ztt} = 0 \quad (11)$$

where $\nabla_h = (\partial/\partial x, \partial/\partial y, 0)$. For constant Väisälä-Brunt frequency N , (11) has plane wave solutions of the form

$$w_1 = W_1 e^{i(lx + Mz - \omega t)}. \quad (12)$$

Then the dispersion relation

$$\left(1 - \frac{N^2}{\omega^2}\right) l^2 + \left(i \frac{N^2}{g} + M\right) M = 0 \quad (13)$$

must hold for a nontrivial solution.

The imaginary term in (13) is a consequence of the fact that for constant N , the unperturbed density ρ_0 decreases exponentially with height while the wave energy density should remain uniform in the absence of energy sources. Equation (6) in fact yields

$$\rho_0(z) = \rho_0(0) e^{-z/H} \quad (14)$$

where $H = g/N^2$ is the density scale height. To derive the perturbation energy density we note that the vertical displacement ζ of a fluid parcel from its equilibrium level is given by

$$\zeta_t = w_1 \quad (15)$$

so that integrating (8) with respect to time yields

$$\rho_1 = \frac{\rho_0}{H} \zeta. \quad (16)$$

From the scalar product of \mathbf{u}_1 with (10), and from (15) and (16) we then obtain

$$\left[\frac{\rho_0}{2} (\mathbf{u}_1^2 + N^2 \zeta^2) \right]_t + \nabla \cdot (p_1 \mathbf{u}_1) = 0 \quad (17)$$

where $\rho_0 \mathbf{u}_1^2/2$ and $\rho_0 N^2 \zeta^2/2$ are the kinetic and potential wave energy densities and $p_1 \mathbf{u}_1$ is the energy flux up to an arbitrary nondivergent contribution. The average kinetic and potential energy densities are equal, and the average wave energy density E varies as (ECKART, 1960)

$$E \propto \rho_0(z) |w_1|^2. \quad (18)$$

Constant E thus requires

$$\omega_1 \propto e^{\frac{z}{2H}}. \quad (19)$$

Indeed, with $M = \text{Re}M + i\text{Im}M$ we obtain from (13)

$$\text{Im}M = -\frac{1}{2H} \quad (20)$$

and with $m = \text{Re}M$

$$\omega^2 = \frac{l^2}{l^2 + m^2 + \frac{1}{4H^2}} N^2. \quad (21)$$

The frequency is zero for vertical phase propagation ($l = 0$) and equal to N for horizontal phase propagation ($m = 0$) if $l^2 \gg 1/4H^2$. For $\omega > N$, no waves are possible. The hyperbolae (dashed curves) in Figure 1a represent contours of constant ω in the wavenumber domain. The group velocity

$$\mathbf{c}_g = \left(\frac{\partial \omega}{\partial l}, \frac{\partial \omega}{\partial m} \right) \quad (22)$$

is normal to the contours always pointing away from the ordinate. It is typical of internal gravity waves that the vertical components of the phase and group velocities have different signs.

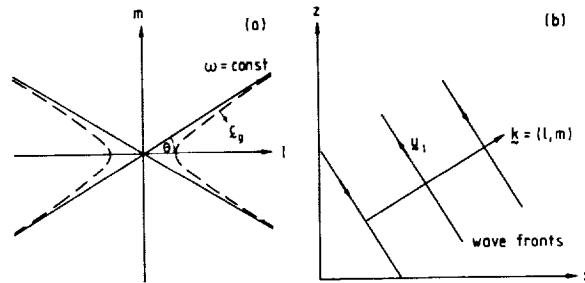


Fig. 1. (a) Contours of constant frequency in the wavenumber domain for internal gravity waves in an incompressible fluid (dashed lines) and in a Boussinesq fluid (continuous lines). The group velocity \mathbf{c}_g is normal to the contours. (b) Internal gravity waves are transverse with the fluid velocity parallel to the wave fronts.

For short wavelengths with $l^2 + m^2 \gg 1/4H^2$, (21) yields

$$\omega^2 = N^2 \cos^2 \theta \quad (23)$$

where without loss of generality, θ is the angle between the horizontal and the wavenumber vector $\mathbf{k} = (l, m)$ with $|\theta| \leq \pi/2$. The short wave dispersion equation (23) could have been obtained directly from the equations of motion by applying the Boussinesq approximation which consists of neglecting density variations in the inertia terms but retaining them in the buoyancy term. Then the last term on the left of (11) vanishes and (23) follows immediately. With the Boussinesq approximation, the hyperbolic contours $\omega = \text{const}$ in Figure 1a degenerate to linear asymptots of the hyperbolae including the angle θ with the l axis indicating that this approximation is the better the larger k .

From (9) and (10) we find that plane internal gravity waves are transverse with \mathbf{u}_1 in the $x - z$ plane parallel to the wave fronts (Figure 1b). Note that at $\theta = 0$, the phase propagation is horizontal and \mathbf{u}_1 vertical, showing that for small vertical displacements and $N^2 > 0$, an air parcel oscillates at the Väisälä-Brunt frequency.

A concise description of further details of the linearized theory of wave propagation such as wave energy, wave action, slowly varying wave trains in nonuniform media etc. is given by BRETHERTON (1971).

We will complete this chapter by showing MST radar observations that indicate the relevance and applicability of the foregoing to dynamic processes in the troposphere, stratosphere and mesosphere. Figure 2 contains contour lines of the power density of vertical velocities observed after the passage of a severe thunderstorm. Convective

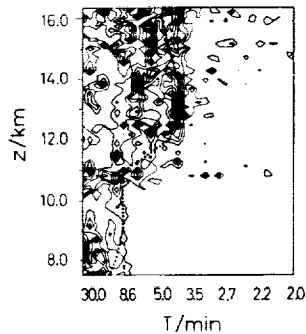


Fig. 2. Time-height contours of power spectra of vertical velocity measured with the SOUSY VHF Radar on 2 June 1978 after the passage of a thunderstorm. The peaks of the spectrogram correspond to a power of $1.1 \times 10^{-5} \text{ m}^2 \text{ s}^{-2}$. The dotted curve represents the height profile of the Väisälä-Brunt period obtained from radiosonde data (from RÖTTGER, 1980).

activity in the troposphere at times of thunderstorms should in particular excite internal wave motions in the stratosphere because rising columns of tropospheric air may penetrate a short distance through the tropopause and transfer kinetic energy to the stably stratified stratosphere (STULL, 1976). The spectrogram in Figure 2 demonstrates that oscillations with periods larger than $2\pi/N$ are observed at all heights with the strongest oscillations occurring above the tropopause at a height near 10 km. No oscillations are found at periods less than $2\pi/N$ so that it appears possible to derive mean potential temperature profiles from the cut-off period of gravity wave spectra (RÖTTGER, 1980).

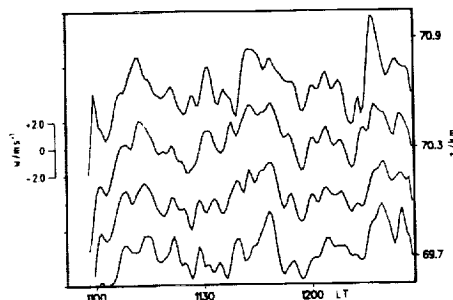


Fig. 3. Time variation of vertical velocity at four heights measured with the mobile SOUSY VHF Radar at Andenes (Norway) on 21 January 1984. Spectral analysis reveals significant peaks at periods near 5, 16 and 30 min (from RÜSTER, 1984).

Figure 3 shows the time dependence of the vertical velocity component of gravity waves measured in the arctic mesosphere. The spectra of the time series have three significant peaks at periods near 5, 16 and 30 min. Spectra with multiple peaks appear to be the rule rather than the exception at mesospheric heights. Almost all radar records show the presence of horizontally propagating waves with periods near $2\pi/N$ that must be generated by local sources rather than sources at lower atmospheric regions. Two possible source mechanisms, Kelvin-Helmholtz and parametric instabilities, will be addressed in the next two chapters. There seem to be no detailed case studies of the horizontal and vertical phase propagation of short-period gravity waves in the literature.

3. WAVE-MEAN FLOW INTERACTION

In the previous chapter we discussed linear gravity waves that do not interact. If interaction among waves or between waves and mean flow takes place, we can distinguish between weak and strong interactions. In weak interactions, the space

and time scales of energy exchange processes greatly exceed the typical wavelengths and periods so that the solutions of the equations of motion can be expressed as power series of small nondimensional parameters and can be found by perturbation methods (KEVORKIAN and COLE, 1981). An example will be given in the next chapter. Here we will study two types of strong wave-mean flow interaction characterized by energy exchanges occurring over scales comparable to the wavelength and period. The first type is the critical layer absorption of internal gravity waves losing their momentum to a vertically sheared mean flow, the second one is the stability of parallel flows to infinitesimal wave perturbations.

3.1. GRAVITY WAVE CRITICAL LEVEL

Besides being partially or totally reflected by a height dependent mean wind $u_0(z)$, an internal gravity wave can meet a critical level $z = z_c$ at which $u_0(z)$ is equal to its horizontal phase speed. In a continuously stratified shear flow, the Richardson number is defined by

$$Ri = \frac{N^2}{u_{0z}^2} \quad (24)$$

representing the ratio of the energy required to interchange vertically adjacent fluid parcels against the gravity acceleration to the available kinetic energy (e.g. CHANDRASEKHAR, 1961). For $Ri > 1/4$, ray theory describing the propagation of waves

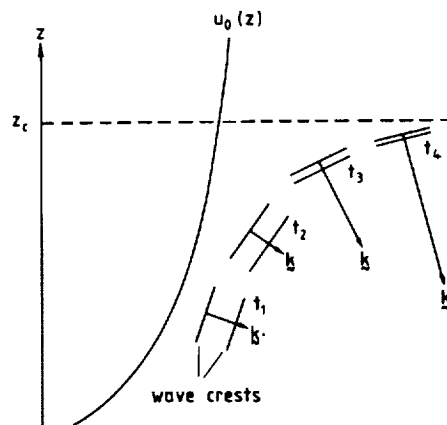


Fig. 4. Schematic of progression of a gravity wave packet propagating toward a critical level z_c at four different times. The horizontal component of k remains constant. The fluid velocity is parallel to the wave fronts.

in a slightly nonuniform medium can be used to study how an internal gravity wave packet approaches a critical level (BRETHERTON, 1966). The result is summarized in Figure 4 showing that the wavenumber increases and the perturbation velocity u_1 becomes more and more horizontally oriented as the packet comes closer to z_c . Moreover, the time required for the packet to reach z_c becomes infinite indicating that the packet would be effectively absorbed rather than reflected or transmitted.

Since ray theory becomes invalid at the critical level, the Frobenius method was used to determine the behaviour of an internal gravity wave at z_c (BOOKER and BRETHERTON, 1967). We again describe the perturbed state of the atmosphere by (7) but assume

$$\mathbf{u} = (u_0(z) + u_1, w_1) \quad (25)$$

considering only two-dimensional motions in the x - z plane. Substituting into (1)-(3), neglecting products of perturbation quantities and eliminating ρ_1, p_1 and u_1 yields under the Boussinesq approximation

$$\frac{d^2}{dt^2}(w_{1xx} + w_{1zz}) - \frac{d}{dt}(u_{0zz}w_{1x}) + N^2w_{1xx} = 0 \quad (26)$$

where $d/dt = \partial/\partial t + u_0\partial/\partial x$. Equation (26) reduces to the Boussinesq approximation of (11) for $u_0 = 0$, and with $N = \text{const}$, $u_0 = \text{const}$ and (12) yields the dispersion relation

$$\Omega^2 = N^2 \cos^2 \theta \quad (27)$$

where $\Omega = \omega - lu_0$ is the intrinsic (or Doppler-shifted) frequency. If u_0 is height dependent, there is a new restoring effect due to the vertical derivative of the mean vorticity u_{0z} . Assuming a solution of the form

$$w_1 = W_1(z)e^{il(x-ct)} \quad (28)$$

then gives the Boussinesq form of the Taylor-Goldstein equation

$$(u_0 - c)^2 W_1'' + [N^2 - (u_0 - c)u_0'' - (u_0 - c)^2 l^2] W_1 = 0 \quad (29)$$

with the prime denoting differentiation with respect to z . The original form of the Taylor-Goldstein equation obtained from (1)-(3) without Boussinesq approximation is

$$[\rho_0(u_0 - c)W_1']' - (\rho_0 u_0' W_1)' - \left[\frac{\rho_0' g}{u_0 - c} + \rho_0(u_0 - c)l^2 \right] W_1 = 0. \quad (30)$$

Besides containing the important special cases of internal gravity wave propagation and static instability for $u_0 = 0$, (29) is the starting point for analysing the effects of wind shear on gravity waves. For further studies of the critical level problem we note that at $z = z_c$, $u_0 - c = 0$ so that (29) has a singularity across which solutions have

to be joined. We assume that around $z = z_c, u_0$ and N can be expanded in power series

$$\begin{aligned} u_0 &= c + u'_0(z_c)(z - z_c) + \dots \\ N &= N(z_c) + N'(z_c)(z - z_c) + \dots \end{aligned} \quad (31)$$

with $u'_0(z_c) \neq 0$ and try to find a solution of the form

$$W_1 = \sum_{j=0}^{\infty} a_j (z - z_c)^{\alpha+j}, \quad a_0 \neq 0. \quad (32)$$

Substituting (31) and (32) into (29) yields

$$\alpha = \frac{1}{2} \pm i\mu, \quad \mu = (Ri(z_c) - \frac{1}{4})^{\frac{1}{2}} \quad (33)$$

requiring $Ri(z_c) \geq 1/4$ for real μ . Then the general solution near $z = z_c$ is

$$W_1 \approx A(z - z_c)^{\frac{1}{2}+i\mu} + B(z - z_c)^{\frac{1}{2}-i\mu}. \quad (34)$$

The foregoing analysis gives no indication how to join the solutions across $z = z_c$. A proper treatment requires some length (BOOKER and BRETHERTON, 1967) and is therefore beyond the scope of this lecture. One finds that for $u'_0(z_c) > 0$, the A -wave $W_{1A} = A(z - z_c)^{1/2+i\mu}$ is associated with upward propagating energy for $z < z_c$ and $z > z_c$ whereas the B -wave $W_{1B} = B(z - z_c)^{1/2-i\mu}$ is associated with downward propagating energy. For $u'_0(z_c) < 0$, the roles of both waves are reversed, and we obtain

$$\begin{aligned} |W_{1A}(z > z_c)| &= |W_{1A}(z < z_c)| e^{-\mu\pi \operatorname{sgn} u'_0(z_c)} \\ |W_{1B}(z > z_c)| &= |W_{1B}(z < z_c)| e^{\mu\pi \operatorname{sgn} u'_0(z_c)} \end{aligned} \quad (35)$$

indicating that both waves are severely attenuated as they cross z_c . The vertical flux of horizontal momentum is independent of height on each side of z_c but discontinuous across z_c with the attenuation factor $e^{-2\pi\mu}$ suggesting that there is significant horizontal momentum transfer to the mean flow at the critical level.

From (34) we find that near z_c ,

$$|w_1| \sim |z - z_c|^{\frac{1}{2}}, \quad |u_1| \sim |z - z_c|^{-\frac{1}{2}} \quad (36)$$

indicating that w_1 is well behaved whereas u_1 tends to infinity at z_c . The wave-associated shear tends to become infinite at an even higher rate:

$$|u_{1z}| \sim |z - z_c|^{-\frac{3}{2}}. \quad (37)$$

According to BOOKER and BRETHERTON (1967), these infinities are spurious in the sense that nature always generates wave packets of finite spectral width so that all Fourier components with infinitesimal amplitude encounter critical levels at

different heights and the infinities do not in fact occur in the total integrated disturbance. Nevertheless, gravity waves generated by sufficiently monochromatic sources may produce large-amplitude oscillations near critical levels so that one of the hitherto neglected mechanisms may become important: (1) Nonlinearities due to large perturbation amplitudes; (2) molecular dissipation due to strong vertical variations; (3) instability due to strong vertical shears.

3.2 KELVIN-HELMHOLTZ INSTABILITY

For illustrating some of the mechanisms and concepts of dynamic stability, we will work through a classic problem that was first addressed in 1868 by Helmholtz and in 1871 by Kelvin, and demands only little mathematics. We consider a basic flow of an incompressible inviscid two-layer fluid that has unlimited extent, constant densities ρ_I

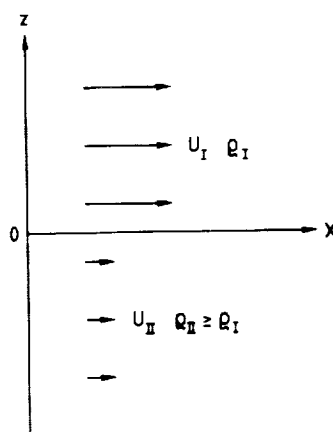


Fig. 5. Kelvin-Helmholtz flow configuration.

and ρ_{II} , and horizontal velocities U_I and U_{II} (Figure 5). We assume that the flow is disturbed by an infinitesimal perturbation displacing the interface between the two layers from $z = 0$ to

$$z = \zeta_1(x, t). \quad (38)$$

Since the model is discontinuous, the Taylor-Goldstein equation (30) must be solved separately in each layer, and both solutions must be matched across the interface $z = \zeta_1$ by two matching conditions.

(1) The interfacial displacement has to be continuous. To first order $w_1(+0) = \zeta_{1t} + U_I \zeta_{1x}$ and $w_1(-0) = \zeta_{1t} + U_{II} \zeta_{1x}$ at the upper and lower sides of the interface, respectively. For a travelling wave solution of the form (28) we then get

C-4

$$\frac{w_1(+0)}{U_I - c} = \frac{w_1(-0)}{U_{II} - c}. \quad (39)$$

(2) At $z = \zeta_1$, the total pressure must be continuous. Using Bernoulli's theorem (e.g. LAMB, 1945), we obtain

$$\rho_I \left[(U_I - c)w_1'(+0) - \frac{g}{U_I - c}w_1(+0) \right] = \rho_{II} \left[(U_{II} - c)w_1'(-0) - \frac{g}{U_{II} - c}w_1(-0) \right]. \quad (40)$$

The perturbation is further assumed to decay to zero for $|z| \rightarrow \infty$ yielding the boundary conditions

$$w_1 \rightarrow 0 \text{ as } z \rightarrow \pm\infty. \quad (41)$$

For the Kelvin-Helmholtz flow configuration (Figure 5), the Taylor-Goldstein equation (30) reduces to

$$W_1'' - l^2 W_1 = 0 \quad (42)$$

and must have a solution of the form

$$W_1 = \begin{cases} Ae^{-lz} & \text{at } z > 0 \\ Be^{lz} & \text{at } z < 0 \end{cases} \quad (43)$$

to satisfy the boundary conditions (41). Equations (39) and (40) then yield two homogeneous linear equations for A and B which are nontrivial only if

$$c = \frac{\rho_{II}U_{II} + \rho_I U_I}{\rho_{II} + \rho_I} \pm \left[\frac{\rho_{II} - \rho_I}{\rho_{II} + \rho_I} \frac{g}{l} - \frac{\rho_{II}\rho_I}{(\rho_{II} + \rho_I)^2} (U_{II} - U_I)^2 \right]^{\frac{1}{2}} \quad (44)$$

The first term on the right of (44) may be considered as the density-weighted mean velocity of the two fluid layers. The wave perturbation then travels with a velocity d given by

$$d^2 = d_0^2 - \frac{\rho_{II}\rho_I}{(\rho_{II} + \rho_I)^2} (U_{II} - U_I)^2 \quad (45)$$

relative to the mean velocity where

$$d_0 = \left(\frac{\rho_{II} - \rho_I}{\rho_{II} + \rho_I} \frac{g}{l} \right)^{\frac{1}{2}} \quad (46)$$

is the phase velocity in the absence of any basic flow. For

$$(U_{II} - U_I)^2 > \frac{\rho_{II}^2 - \rho_I^2}{\rho_{II}\rho_I} \frac{g}{l} \quad (47)$$

c is complex so that the wave perturbation grows and remains stationary with respect to the mean flow. For any given $U_{II} - U_I \neq 0$, the interface is unstable for sufficiently

small wavelengths. If $\rho_{II} = \rho_I$, it is unstable for all wavelengths indicating the stabilizing influence of a density change. Finally we note that for small density changes, $\rho_{II}^2 - \rho_I^2 \approx 2\rho_{II}(\rho_{II} - \rho_I)$. Then we can define a Richardson number by

$$Ri = \frac{\rho_{II} - \rho_I}{\rho_I(U_{II} - U_I)^2} \frac{g}{l} \quad (48)$$

so that $Ri > \frac{1}{2}$ ($< \frac{1}{2}$) for stability (instability).

The instability of the Kelvin-Helmholtz flow configuration at high wavenumbers is a consequence of the fact that vorticity is concentrated at a single height. A physically more realistic model together with the neutral stability curve obtained by DRAZIN (1958) is shown in Figure 6, where

$$u_0 = \Delta u \tanh\left(\frac{z}{d}\right), \quad \rho_0 = e^{-\frac{N^2}{g}z}, \quad Ri = \left(\frac{Nd}{\Delta u}\right)^2 \quad (49)$$

The flow is stable for $Ri > 1/4$. We note that the expression "Kelvin-Helmholtz instability" is also used for shear flow instability in models with continuous density and wind profiles.

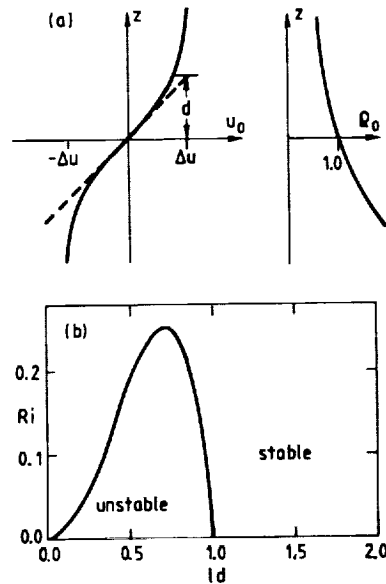


Fig. 6. (a) DRAZIN's (1958) model. (b) Neutral stability curve.

We conclude the theoretical part of this chapter by summarizing some general results on the stability of nonrotating stratified shear flows (for details cf. LE BLOND

and MYSAK (1978)).

(1) YIH's (1955) extension of SQUIRE's (1933) theorem: For each unstable three-dimensional disturbance in a stratified fluid, there is a more unstable two-dimensional one propagating parallel to the flow. For this reason we have considered only two-dimensional waves of the form (28).

(2) SYNGE's (1933) theorem: A necessary condition for instability is

$$[(U - c_r)^2 + c_i^2](\rho_0 U')' - 2(U - c_r)\rho_0 N^2 = 0 \quad (50)$$

somewhere in the field of flow. Here, $c_r = \text{Re}c$ and $c_i = \text{Im}c$. For $\rho_0 = \text{const}$, (50) yields $U'' = 0$ which is Rayleigh's inflection point theorem.

(3) MILES' (1961) stability condition: A sufficient condition for stability is $Ri \geq 1/4$ everywhere in the flow.

(4) HOWARD's (1961) semicircle theorem: The complex wave velocity c of an unstable wave with $c_i > 0$ lies in the semicircle

$$[c_r - (u_{0\text{max}} + u_{0\text{min}})/2]^2 + c_i^2 \leq [(u_{0\text{max}} - u_{0\text{min}})/2]^2. \quad (51)$$

There are characteristic streamline patterns of fluid motions near critical levels known as cat's eyes. For $N = 0$ and $u_0 - c \sim z - z_c$, Kelvin derived from (29) the cat's eye pattern shown in Figure 7a as seen by an observer moving with the wave velocity. The existence of closed streamline patterns is a purely kinematic consequence of a finite vertical velocity component at the critical level. In a stratified flow ($N > 0$), the cat's eye pattern becomes asymmetric as indicated by Taylor's cockeyed cat's eye in a three-layer model fluid (Figure 7b). According to HOWARD and MASLOWE (1973), also intermediate forms between Kelvin's and Taylor's cat's eye patterns are possible.

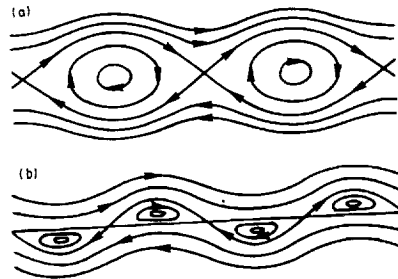


Fig. 7. (a) Kelvin's cat's eye streamline pattern. (b) Taylor's cockeyed cat's eye streamline pattern.

There is evidence that cat's eye structures occur in the time-height distributions of MST radar echo power both in the troposphere (RÖTTGER and SCHMIDT, 1979)

and in the mesosphere (REID et al., 1987) (Figures 8 and 9). The enhanced echo power is probably due to enhanced turbulence in thin layers surrounding the regions of closed streamlines (KELLY and MASLOWE, 1970).

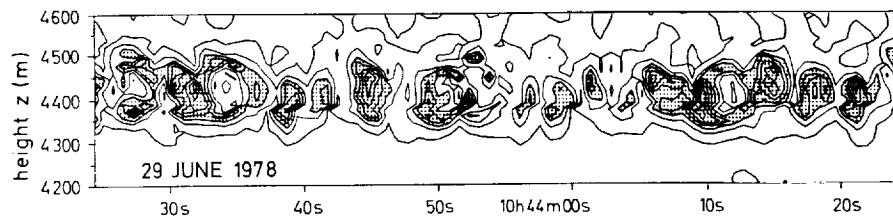


Fig. 8. Contour plot of constant MST radar echo power in the time-height plane indicating cat's eye structures (from RÖTTGER and SCHMIDT, 1979).

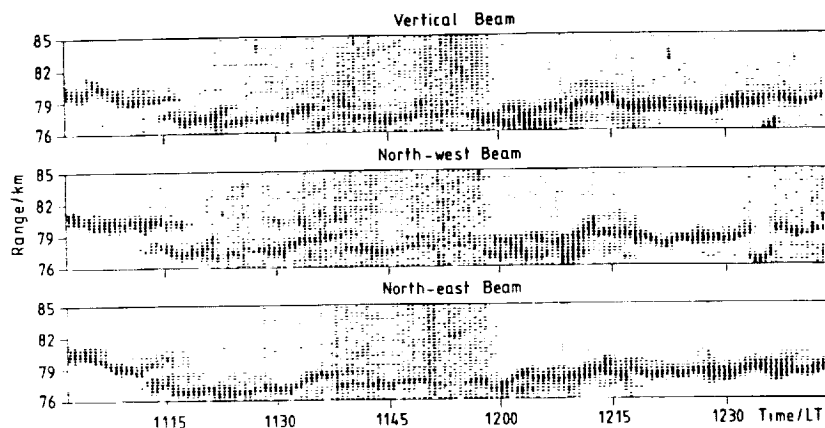


Fig. 9. Time-height intensity plot of MST radar echo power in three antenna beam directions. A cat's eye is visible between 11:55 and 12:10 LT (from REID et al., 1987).

Detailed investigations of cat's eye patterns observed by MST radars have not yet been performed, but there are three examples of Kelvin-Helmholtz instabilities that were analyzed and compared to numerical model computations (VANZANDT et al., 1979; KLOSTERMEYER and RÜSTER, 1980, 1981; RÜSTER and KLOSTERMEYER, 1983). Figure 10 shows the radial velocity oscillations associated with a Kelvin-Helmholtz instability at the bottom side of a polar jetstream and measured

with height and time resolutions of 150 m and 10 s, respectively. The oscillations reveal a period of about 4 min and amplitudes of the order of 1 m s^{-1} . The critical level

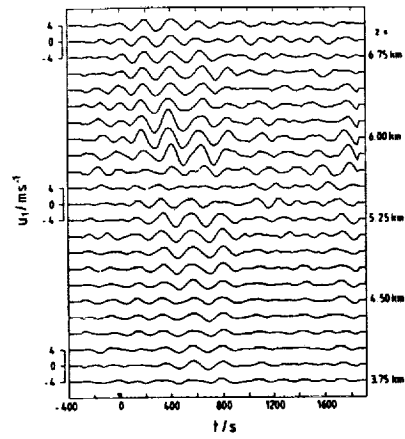


Fig. 10. Band pass-filtered time series of radial velocity oscillations associated with a Kelvin-Helmholtz instability and measured by the SOUSY VHF Radar on 11 April 1980 (from KLOSTERMEYER and RÜSTER, 1981).

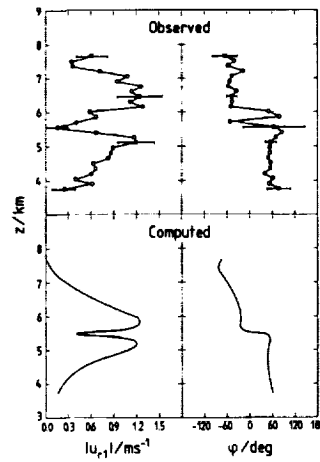


Fig. 11. Measured and computed height profiles of Kelvin-Helmholtz-associated velocity oscillations (from KLOSTERMEYER and RÜSTER, 1980).

is near $z = 5.55$ km and is indicated by a vanishing amplitude and a sudden phase jump of about 100° . Figure 11 shows a comparison between measured and computed height profiles of the amplitude and phase of the radial velocity oscillations. Further studies indicate that the growth of the observed Kelvin-Helmholtz instability is limited by the onset of static instability producing periodic radar echo power bursts (KLOSTERMEYER and RÜSTER, 1981).

4. WAVE-WAVE INTERACTION

Here we will investigate the general nature of weak resonant interaction between wave triplets and will always keep in mind that this is an oversimplification of natural processes which consist of resonant and forced energy transfer over continuous wavenumber and frequency domains. The actual wave spectrum thus is the result of a balance between the effects of sources, dissipation and redistribution due to nonlinear interaction. Moreover, the application of a weakly nonlinear theory which is based on perturbation methods, is restricted to small-amplitude waves. It should be mentioned, however, that the stability of a monochromatic internal gravity wave with arbitrary amplitude is closely related to weak resonant interactions. This so-called parametric instability provides a simple example for the instability of time dependent and spatially varying flows and will therefore be discussed in the second part of this chapter.

4.1. WEAK WAVE-WAVE INTERACTION

If we take into account the nonlinear terms that have been neglected in the previous chapters, we obtain a wave equation of the form

$$\mathcal{L}(w) + \mathcal{Q}(w, w) = 0 \quad (52)$$

where \mathcal{L} and \mathcal{Q} are differential operators which are linear and quadratic in w , respectively, and w represents any of the perturbation variables. We assume that there is a small nondimensional quantity ε characterizing the relative magnitude of the nonlinear term in (52). In a straight-forward perturbation procedure we expand w in powers of ε ,

$$w = \varepsilon w_1 + \varepsilon^2 w_2 + \dots \quad (53)$$

and solve the equations

$$\mathcal{L}(w_1) = 0, \quad (54)$$

$$\mathcal{L}(w_2) = -\mathcal{Q}(w_1, w_1) \text{ etc.} \quad (55)$$

Provided the expansion (53) converges we thus obtain a solution for (53) for waves of finite but small amplitudes (for details of perturbation methods cf. KEVORKIAN

and COLE (1981)). According to Chapter 2, (54) yields plane wave solutions in uniform atmospheric models so that

$$w_1 = \frac{1}{2} W_1 e^{i\mathbf{k}\cdot\mathbf{r} - \omega t} + \text{complex conjugate} \quad (56)$$

where the wavenumber vector \mathbf{k} and angular frequency ω satisfy a dispersion relation

$$\mathcal{D}(\mathbf{k}, \omega) = 0. \quad (57)$$

To second order in ε we get from (55) a nonhomogeneous linear equation for w_2 with a forcing term depending on w_1 . The process can be continued to any order of ε .

Now we consider the case that w_1 consists of two plane waves,

$$w_1 = w_a + w_b \quad (58)$$

both satisfying (54) and (57). Then (55) becomes

$$L(w_c) = -Q(w_a + w_b, w_a + w_b) \quad (59)$$

where $w_2 = w_c$ is the result of the interaction between w_a and w_b . Since the quadratic operator on the right of (59) produces plane waves with wavenumber vectors $\mathbf{k}_c = 0, \pm 2\mathbf{k}_a, \pm 2\mathbf{k}_b, \pm(\mathbf{k}_a \pm \mathbf{k}_b)$ and corresponding angular frequencies ω_c , w_c has the form

$$w_c = \frac{1}{2} \sum \frac{W_c e^{i(\mathbf{k}_c \cdot \mathbf{r} - \omega_c t)} + \text{complex conjugate}}{\mathcal{D}(\mathbf{k}_c, \omega_c)} \quad (60)$$

provided $\mathcal{D}(\mathbf{k}_c, \omega_c) \neq 0$. The summation is performed over all sign combinations resulting from the quadratic forcing term in (59). If $a = b$ and both signs are allowed for all wavenumbers and frequencies, all cases can be described by

$$\mathbf{k}_a + \mathbf{k}_b + \mathbf{k}_c = 0, \quad \omega_a + \omega_b + \omega_c = 0. \quad (61)$$

The forced wave $\varepsilon^2 w_c$ plays only a minor role in (53) as compared to $\varepsilon(w_a + w_b)$ unless $\mathcal{D}(\mathbf{k}_c, \omega_c) = 0$. Then resonance occurs so that the amplitude of w_c grows in space and time. Such a resonant wave is also called secular. It dominates the non-resonant waves after the interaction has lasted for some time and can therefore be considered as the most significant result.

It depends on the specific form of the dispersion relation whether three interacting waves can satisfy the resonance conditions (61) and (57). Clearly, if the waves are nondispersive, i.e. propagate at the same speed, all interactions are resonant. For internal gravity waves in a Boussinesq fluid with $N = \text{const}$, the resonance conditions may be written

$$\mathbf{k}_a \pm \mathbf{k}_b = \mathbf{k}_c, \quad \cos \theta_a \pm \cos \theta_b = \cos \theta_c \quad (62)$$

using (23). The loci of resonant triads can be calculated from simple geometrical considerations and are shown in Figure 12. It should be mentioned, however, that the Boussinesq approximation consists of neglecting terms of first and higher orders in the ratio of wavelength to density scale height (Chapter 2) and thus is only applicable if this ratio is much smaller than ϵ (LONG, 1965).

YEH and LIU (1985) pointed out that resonant wave interaction may play an important role in the evolution of the atmospheric wave spectrum. There are in particular three classes of resonant triads that can provide efficient energy transfer between separate parts of the gravity wave spectrum and have first been identified by MCCOMAS and BRETHERTON (1977) as elastic scattering, induced diffusion and parametric subharmonic instability (Figure 13). By elastic scattering, an upgoing

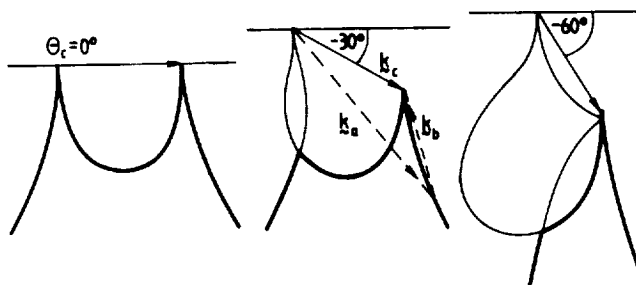


Fig. 12. Resonant interaction diagrams for internal gravity waves in a Boussinesq fluid for $\theta_c = 0^\circ, -30^\circ$ and -60° . Any point on a branch defines a resonant triad satisfying (62). The wavenumber vector with the least slope is always the vector sum of the other two. Thick (thin) branches indicate unstable (stable) triads (after PHILLIPS, 1969).

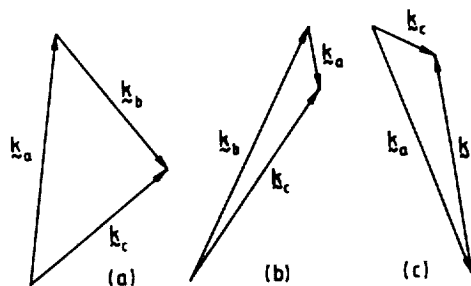


Fig. 13. Characteristic classes of resonant triads: (a) elastic scattering, (b) induced diffusion, (c) parametric subharmonic instability.

wave is scattered into a downgoing one by resonantly interacting with a low frequency, nearly vertically propagating wave with almost twice the vertical wavenumber of the other two waves. This process makes the atmospheric spectrum vertically symmetric if it is not so initially. The process of induced diffusion is responsible for the evolution of small-scale waves and consists of two almost identical waves which interact resonantly with a large-scale low-frequency wave propagating almost vertically. Finally, in the process of parametric subharmonic instability, two waves with nearly opposite large wavenumber vectors and almost identical frequencies resonate with a third wave having a much smaller wavenumber and twice the frequency. This mechanism provides energy transfer from an energetic large-scale wave to small-scale waves at subharmonic frequencies.

4.2. PARAMETRIC INSTABILITY

There is a close connection between the interaction of weak internal gravity waves and the parametric instability of a monochromatic internal gravity wave of arbitrary amplitude (MIED, 1976; KLOSTERMEYER, 1982, 1983). For studying parametric instability, it is useful to assume a uniformly stratified Boussinesq model and to introduce the stream function Ψ which describes the two-dimensional motion of an incompressible fluid in the $x - z$ plane by

$$\mathbf{u} = (\Psi_z, -\Psi_x) \quad (63)$$

and satisfies (2). We further introduce the buoyancy

$$B = -\frac{\rho - \rho_*}{\rho_*} g \quad (64)$$

where ρ_* is some suitable constant reference density used in the Boussinesq approximation to replace ρ in the inertia terms (e.g. LEBLOND and MYSAK, 1978). Buoyancy and Väisälä-Brunt frequency are related by

$$N^2 = B_z. \quad (65)$$

Equations (3) and (1) then yield

$$\nabla^2 \Psi_t + B_x = \Psi_x \nabla^2 \Psi_z - \Psi_z \nabla^2 \Psi_x \quad (66)$$

$$B_t - N^2 \Psi_x = \Psi_x B_z - \Psi_z B_x \quad (67)$$

We note that (66) results from the vorticity equation that is obtained by taking the curl of (3). The plane wave

$$\Psi = A \cos \varphi, \quad B = -N^2 l \omega^{-1} A \cos \varphi \quad (68)$$

with $\varphi = lx + mz - \omega t$ is a solution of (66) and (67) if the dispersion relation (23) is satisfied. The nonlinear terms are identically zero as a consequence of incompressibility.

We thus have the opportunity to investigate the stability of a finite-amplitude plane internal gravity wave by expressing the stream function and buoyancy fields as sums of the basic state (68) and a perturbation:

$$\Psi = A \cos \varphi + \psi, \quad B = -N^2 l \omega^{-1} A \cos \varphi + b. \quad (69)$$

We define nondimensional variables by

$$(\tilde{x}, \tilde{z}) = k(x, z), \quad \tilde{t} = Nt, \quad \tilde{\Psi} = k^2 N^{-1} \Psi, \quad \tilde{B} = k N^{-2} B, \quad M = k^2 (2N)^{-1} A \quad (70)$$

with $k = (l^2 + m^2)^{1/2}$ and introduce a rotated coordinate system (ξ, η) such that the η axis coincides with the direction of propagation of the basic wave (Figure 14).

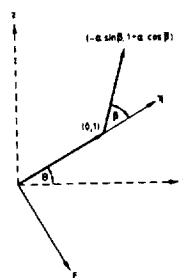


Fig. 14. Wavenumber vector of basic internal gravity wave, $(0, 1)$, and Floquet vector $(-\alpha \sin \beta, \alpha \cos \beta)$ in $\xi - \eta$ coordinates (from KLOSTERMEYER, 1982).

Substituting (69) into (66) and (67) and neglecting terms containing products of the perturbation quantities ψ and b then yields

$$\begin{aligned} \nabla^2 \psi_t + \sin \theta b_\xi + \cos \theta b_\eta &= 2M \sin \varphi (\psi_\xi + \nabla^2 \psi_\xi) \\ b_t - \sin \theta \psi_\xi - \cos \theta \psi_\eta &= 2M \sin \varphi (\psi_\xi + b_\xi) \end{aligned} \quad (71)$$

where the tilde of the nondimensional variables has been omitted and $\nabla^2 = \partial^2 / \partial \xi^2 + \partial^2 / \partial \eta^2$, $\varphi = \eta - \cos \theta t$. The terms on the right of (71) couple the perturbations with

the basic state via a periodic coefficient $2M \sin \varphi$ so that ψ and b take a parametric form dictated by Floquet theory (MIED, 1976):

$$(\psi, b) = e^{i(-\alpha \sin \beta \xi + \alpha \cos \beta \eta) + \lambda t} \sum_{j=-\infty}^{\infty} (\psi_j, b_j) e^{ij\varphi}. \quad (72)$$

As indicated in Figure 14, $|\alpha|$ can be considered as the magnitude of a Floquet vector forming an angle β with the basic wavenumber vector. Substitution of (72) into (71) yields a linear eigenvalue problem for the complex quantities λ and (ψ_j, b_j) ,

$$\begin{aligned} p_j^{(-1)} \psi_{j-1} + (p_j^{(0)} - \lambda) \psi_j + q_j^{(0)} b_j + p_j^{(1)} \psi_{j+1} &= 0 \\ r_j^{(-1)} \psi_{j-1} + s_j^{(-1)} b_{j-1} + r_j^{(0)} \psi_j + (s_j^{(0)} - \lambda) b_j + r_j^{(1)} \psi_{j+1} + s_j^{(1)} b_{j+1} &= 0 \end{aligned} \quad (73)$$

with $j = 0, \pm 1, \pm 2, \dots$ and constant coefficients p, q, r, s depending on $j, M, \theta, \alpha, \beta$ (cf. KLOSTERMEYER, 1982). Solutions can be obtained numerically for any given accuracy if the interaction equations (73) are truncated at $j = \pm J$ with J sufficiently large.

The numerical search for growing disturbances ($\text{Re} \lambda > 0$) is greatly facilitated by considering the case $M \rightarrow 0$. Then (73) yields for nontrivial solutions (ψ_j, b_j)

$$\text{Re} \lambda = 0, \quad j \cos \theta - \text{Im} \lambda = \frac{\alpha \cos(\theta + \beta) + j \cos \theta}{[(\alpha \sin \beta)^2 + (\alpha \cos \beta + j)^2]^{1/2}}. \quad (74)$$

From (72) and Figure 14, the nondimensional perturbation frequencies and wavenumbers in $x - z$ coordinates are

$$\begin{aligned} \omega_j &= j \cos \theta - \text{Im} \lambda \\ \mathbf{k}_j &= (\alpha \cos(\theta + \beta) + j \cos \theta, \alpha \sin(\theta + \beta) + j \sin \theta) \end{aligned} \quad (75)$$

so that with (74)

$$\omega_j = \cos \theta_j \quad (76)$$

where θ_j is the angle between \mathbf{k}_j and the horizontal. For $M \rightarrow 0$, the disturbances thus are freely propagating waves that satisfy the resonance conditions

$$\mathbf{k}_{j+1} - \mathbf{k}_j = \mathbf{k}, \quad \omega_{j+1} - \omega_j = \omega \quad (77)$$

for all j . Computations for $M > 0$ show in agreement with HASSELMANN's (1967) criterion for nonlinear wave stability that $\text{Re} \lambda > 0$ (i.e. instability) for resonant sum interactions and $\text{Re} \lambda = 0$ (i.e. stability) for resonant difference interactions. In Figure 12, the loci of unstable triads are indicated by the thick branches.

In a laboratory experiment, DAVIS and ACRIVOS (1967) demonstrated that an internal gravity wave propagating along a diffuse stratified interface between fluids of

different densities may become distorted by the growth of a three-wave resonance giving rise to local turbulent mixing. Their photographs are shown in Figure 15. MCEWAN and ROBINSON (1975) found good agreement between predicted and observed small-scale parametric instabilities in a cylindrical chamber. Although the potential

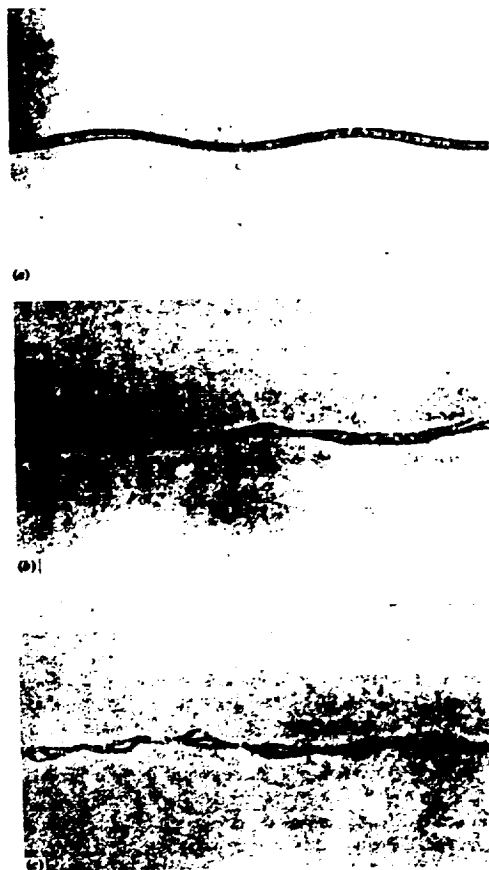


Fig. 15. Progressive distortion of an internal gravity wave by resonant wave-wave interaction (from DAVIS and ACRIVOS, 1967).

role of parametric instability in forming internal wave spectra in the atmosphere has been stressed by some authors (MCEWAN and ROBINSON, 1975; DRAZIN, 1977), there are only few atmospheric observations that have been interpreted in terms of resonant triads or parametric instability. Thus the power spectrum of a strong internal

ORIGINAL PAGE IS
OF POOR QUALITY

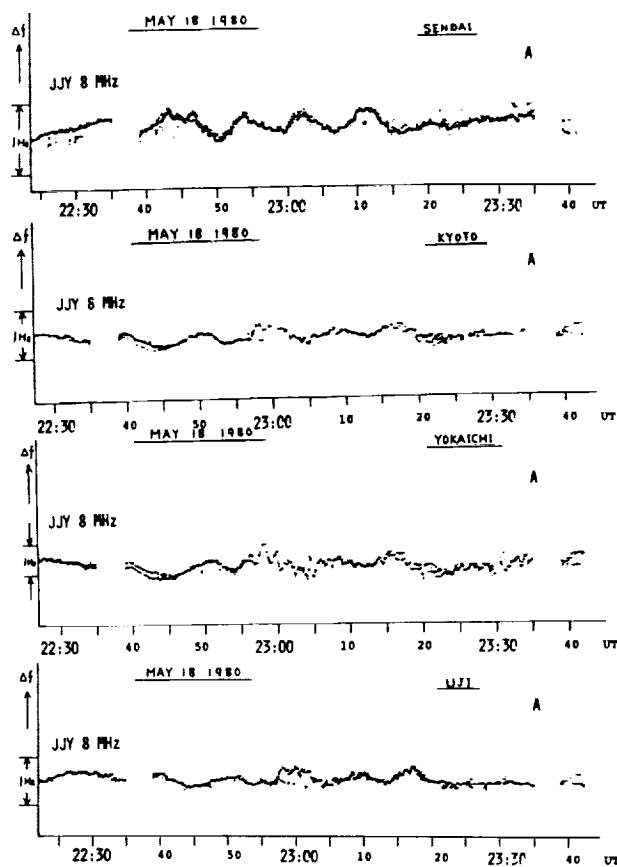


Fig. 16. Doppler shift of a 8 MHz continuous radio wave recorded at four Japanese stations after the eruption of Mount St. Helens on 18 May 1980. In the lower three records, an internal gravity wave with a period near the local Väisälä-Brunt period is strongly disturbed by short-period oscillations after 22:55 UT (from LIU et al., 1982).

gravity wave in the lower thermosphere which was generated by an eruption of Mount St. Helens, was explained in terms of parametric instability (KLOSTERMEYER, 1984). Figure 16 showing the Doppler shift of an 8 MHz radio wave reflected from the ionosphere near 200 km height, indicates strong high-frequency disturbances superposed on a gravity wave at Kyoto, Yokaichi and Uji after 2255 UT. Note a certain

resemblance of these records to Figure 15c.

RÖTTGER (1987) has noted that time series of spectra intensity plots obtained from MST radar measurements also show high-frequency oscillations superposed on low-frequency gravity waves. An example is seen in Figure 17 at 69.6 km after 1300 AST. Röttger further points out that the amplitude the low-frequency waves does not grow with increasing height (visible between 1200 and 1300 AST in the height

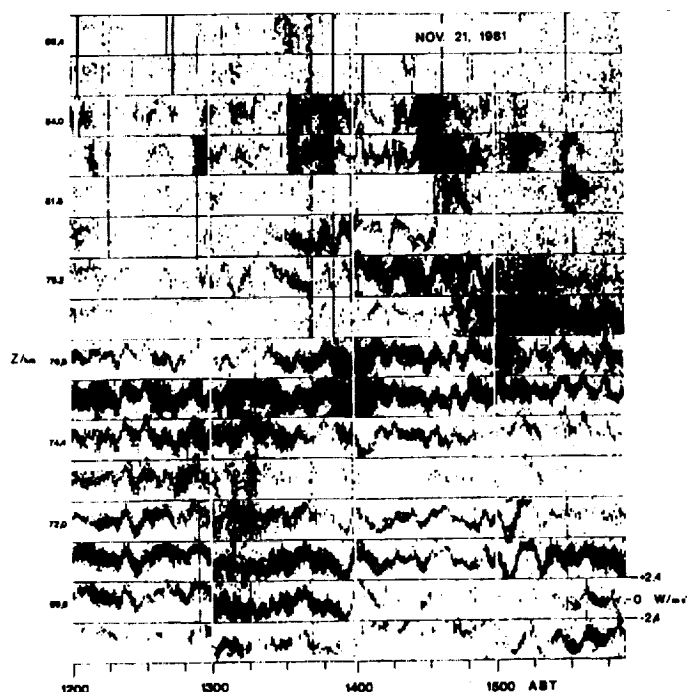


Fig. 17. Time series of spectra intensity plots measured with the mobile SOUSY VHF Radar at the Arecibo Observatory (from RÖTTGER, 1987).

interval from 69.6 to 76.8 km). Since wave breaking discernible from strong echo intensities does not occur some other saturation process such as parametric instability must be considered.

Short-period gravity waves with frequencies close to the local Väisälä-Brunt frequency occur frequently in mesospheric MST radar observations of vertical or near vertical radial velocities (HARPER and WOODMAN, 1976; MILLER et al., 1978).

ORIGINAL PAGE IS
OF POOR QUALITY

These waves do not show any vertical phase variation over height intervals of several kilometers indicating that they propagate horizontally and are generated in situ rather than in lower or higher atmospheric regions. Occasionally the local source mechanism is Kelvin-Helmholtz instability of a wind shear due to long-period inertial or tidal waves (KLOSTERMEYER and RÜSTER, 1984; YAMAMOTO et al., 1988). But in general the simultaneously observed wind shear is too weak for Kelvin-Helmholtz instability to set in. A numerical simulation of the wave motions shown in Figure 3 indicates that parametric instability could be another source candidate of the observed short-period waves. Figure 18a shows the same observations as Figure 3 but with very high-frequency noise and high-frequency waves removed by recursive Butterworth filters (continuous and dashed curves respectively). Figure 18b shows the numerical simulation where the dashed lines represent the finite-amplitude basic wave and the continuous lines the sum of the basic wave and the fastest growing parametric instability mode. Note that the height interval in Figure 18b is 75% of the basic vertical wavelength whereas in Figure 18a, it is only about 10%. The observed and computed short-period oscillations show good qualitative agreement. Both reveal in particular considerable temporal amplitude modulation, and the dominating period is not an integer multiple of the basic period. There is in general also no vertical phase variation. But the computed short-period oscillations show sudden phase reversals, e.g. at $Nt = 20$ and $kz = 4.8$. The loci of sudden phase reversals lie on basic wave

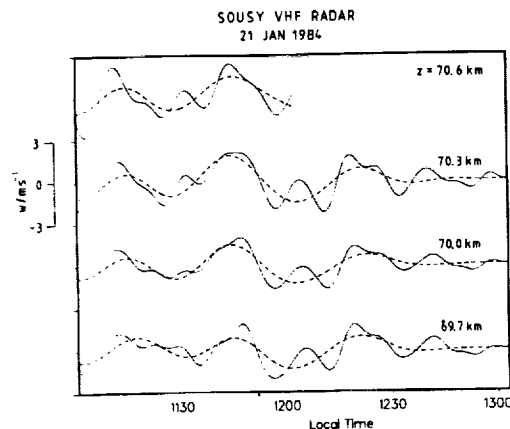


Fig. 18a. Same as Figure 3 but with noise and high-frequency waves removed (continuous and dashed curves, respectively). The time series at $z = 70.6$ km is not continued beyond 12 LT with regard to very small signal-to-noise ratios.

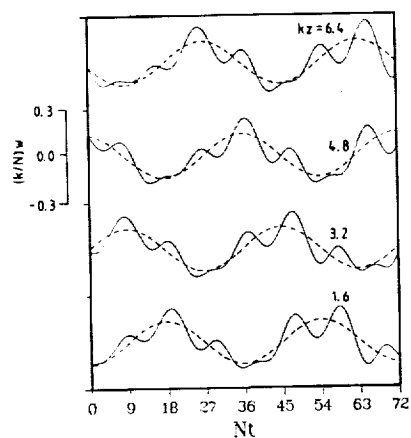


Fig. 18b. Numerical simulation of a parametric instability. The dashed and continuous lines represent the basic wave and the sum of basic wave and fastest growing instability mode, respectively. Time, height and vertical velocity component are normalized according to (70).

fronts. Whereas there is no clear evidence for phase reversals in Figure 18a (perhaps due to the small height interval) they become visible if velocity measurements can be obtained over larger height intervals (e.g. Figure 1 of MILLER et al. (1978)).

Acknowledgement. I thank Dr. Bernd Inhester for valuable comments and Mrs. Karin Peschke for carefully typing the manuscript.

REFERENCES

- Booker, J.R., and F.P. Bretherton, The critical layer for internal gravity waves in a shear flow, *J. Fluid Mech.*, **27**, 513-539, 1967.
- Bretherton, F.P., The propagation of groups of internal gravity waves in a shear flow, *Q.J.R. Meteorol. Soc.*, **92**, 466-480, 1966.
- Bretherton, F.P., The general linearized theory of wave propagation, In: *Mathematical Problems in the Geophysical Sciences* (W.H. Reid, ed.), 61-102, Am. Math. Soc., Providence, Rhode Island, 1971.
- Chandrasekhar, S., *Hydrodynamic and Hydromagnetic Stability*, Clarendon, Oxford, 1961.
- Davis, R.E., and A. Acrivos, The stability of oscillatory internal waves, *J. Fluid Mech.*, **30**, 723-736, 1967.
- Drazin, P.G., The stability of a shear layer in an unbounded heterogeneous inviscid fluid, *J. Fluid Mech.*, **4**, 214-224, 1958.
- Drazin, P.G., On the instability of an internal gravity wave, *Proc. R. Soc. Lond.*, **A356**, 411-432, 1977.
- Eckart, C., *Hydrodynamics of Oceans and Atmospheres*, Pergamon, Oxford, 1960.
- Harper, R.M., and R.F. Woodman, Preliminary multiheight radar observations of waves and winds in the mesosphere over Jicamarca, *J. Atmos. Terr. Phys.*, **39**, 959-961, 1977.
- Hasselmann, K., A criterion for nonlinear wave stability, *J. Fluid Mech.*, **30**, 737-739, 1967.
- Howard, L.N., Note on a paper of John W. Miles, *J. Fluid Mech.*, **10**, 509-512, 1961.
- Howard, L.N., and S.A. Maslowe, Stability of stratified shear flow, *Boundary-Layer Meteorol.*, **4**, 511-523, 1973.
- Kelly, R.E., and S.A. Maslowe, The nonlinear critical layer in a slightly stratified shear flow, *Stud. Appl. Math.*, **49**, 301-326, 1970.
- Kevorkian, J., and J.D. Cole, *Perturbation Methods in Applied Mathematics*, Springer, Berlin, 1981.
- Klostermeyer, J., Lamb waves originating in nongeostrophic disturbances: A case study, *J. Geophys. Res.*, **82**, 1441-1448, 1977.
- Klostermeyer, J., On parametric instabilities of finite-amplitude internal gravity waves, *J. Fluid Mech.*, **119**, 367-377, 1982.

- Klostermeyer, J., Parametric instabilities of internal gravity waves in Boussinesq fluids with large Reynolds numbers, *Geophys. Astrophys. Fluid Dyn.*, **26**, 85-105, 1983.
- Klostermeyer, J., Observations indicating parametric instabilities in internal gravity waves at thermospheric heights, *Geophys. Astrophys. Fluid Dyn.*, **29**, 117-138, 1984.
- Klostermeyer, J., and R. Rüster, Radar observation and model computation of a jet stream-generated Kelvin-Helmholtz instability, *J. Geophys. Res.*, **85**, 2841-2846, 1980.
- Klostermeyer, J., and R. Rüster, Further study of a jet stream-generated Kelvin-Helmholtz instability, *J. Geophys. Res.*, **86**, 6631-6637, 1981.
- Klostermeyer, J., and R. Rüster, VHF radar observation of wave instability and turbulence in the mesosphere, *Adv. Space Res.*, **4**, 79-82, 1984.
- Lamb, H., *Hydrodynamics*, 6th ed., Dover, New York, 1945.
- LeBlond, P.H., and L.A. Mysak, *Waves in the Ocean*, Elsevier, Amsterdam, 1978.
- Liu, C.H., J. Klostermeyer, K.C. Yeh, T.B. Jones, T. Robinson, O. Holt, R. Leiting, T. Ogawa, K. Sinno, S. Kato, T. Ogawa, A.J. Bedard, and L. Kersley, Global dynamic response of the atmosphere to the eruption of Mount St. Helens on May 18, 1980, *J. Geophys. Res.*, **87**, 6281-6290, 1982.
- Long, R.R., On the Boussinesq approximation and its role in the theory of internal waves, *Tellus*, **17**, 46-52, 1965.
- McComas, C.H., and F.P. Bretherton, Resonant interaction of oceanic internal waves, *J. Geophys. Res.*, **82**, 1397-1412, 1977.
- McEwan, A.D., and R.M. Robinson, Parametric instability of internal gravity waves, *J. Fluid Mech.*, **67**, 667-687, 1975.
- Mied, R.P., The occurrence of parametric instabilities in finite-amplitude internal gravity waves, *J. Fluid Mech.*, **78**, 763-784, 1976.
- Miles, J.W., On the stability of heterogeneous shear flows, *J. Fluid Mech.*, **10**, 496-508, 1961.
- Miller, K.L., S.A. Bowhill, K.P. Gibbs, and I.D. Countryman, First measurements of mesospheric vertical velocities by VHF radar at temperate latitudes, *Geophys. Res. Lett.*, **5**, 939-942, 1978.
- Phillips, O.M., *The Dynamics of the Upper Ocean*, University Press, Cambridge, 1969.

- Reid, I. M., R. Rüster and G. Schmidt, VHF radar observations of cat's-eye-like structures at mesospheric heights, *Nature*, **327**, 43-45, 1987.
- Röttger, J., Structure and dynamics of the stratosphere and mesosphere revealed by VHF radar investigations, *Pure Appl. Geophys.*, **118**, 494-527, 1980.
- Röttger, J., The relation of gravity waves and turbulence in the mesosphere, *Adv. Space Res.*, **7**, 10345-10348, 1987.
- Röttger, J., and G. Schmidt, High-resolution VHF radar sounding of the troposphere and stratosphere, *IEEE Trans. Geosci. Electron.*, **GE-17**, 182-189, 1979.
- Rüster, R., Winds and waves in the middle atmosphere as observed by ground based radars, *Adv. Space Res.*, **4**, 3-18, 1984.
- Rüster, R., and J. Klostermeyer, VHF radar observations of a Kelvin-Helmholtz instability in a subtropical jet stream, *Geophys. Astrophys. Fluid Dyn.*, **26**, 107-116, 1983.
- Squire, H.B., On the stability of three-dimensional disturbances of viscous flow between parallel walls, *Proc. R. Soc. Lond.*, **A142**, 621-628, 1933.
- Stull, R.B., Internal gravity waves generated by penetrative convection, *J. Atmos. Sci.*, **33**, 1279-1286, 1976.
- Synge, J.L., The stability of heterogeneous liquids, *Trans. R. Soc. Can.*, **27(III)**, 1-18, 1933.
- VanZandt, T.E., A universal spectrum of buoyancy waves in the atmosphere, *Geophys. Res. Lett.*, **9**, 575-578, 1982.
- VanZandt, T.E., J.L. Green, W.L. Clark, and J.R. Grant, Buoyancy waves in the troposphere: Doppler radar observations and a theoretical model, *Geophys. Res. Lett.*, **6**, 429-432, 1979.
- Volland, H., The upper atmosphere as a multiply refractive medium for neutral air motions, *J. Atmos. Terr. Phys.*, **31**, 491-514, 1969.
- Yamamoto, M., T. Tsuda, S. Kato, T. Sato, and S. Fukao, Interpretation of the structure of mesospheric turbulence layers in terms of inertia gravity waves, *Physica Scripta*, **37**, 645-650, 1988.
- Yeh, K.C., and C.H. Liu, Evolution of atmospheric spectrum by processes of wave-wave interaction, *Radio Sci.*, **20**, 1279-1294, 1985.
- Yih, C.S., Stability of two-dimensional parallel flows for three-dimensional disturbances, *Q. Appl. Math.*, **12**, 434-435, 1955.

Chapter 9

Applications of MST Radars: Meteorological Applications

M. F. Larsen

Department of Physics and Astronomy

Clemson University

Clemson, SC, USA 29631

1. Introduction

MST radars provide information about a broad range of scales. For example, wind measurements provide information about circulations ranging in size from the microscale to the synoptic or planetary scale; spectral width measurements contain information about microscale turbulence within the beam; and reflectivity measurements show the presence of small scale turbulence, as well as larger scale temperature gradients associated with the tropopause or frontal boundaries. In spite of the broad range of scales that can be investigated and the wide range of potential applications of MST radars, I will limit the discussion to those applications that are directly relevant to mesoscale meteorology since the radar technology seems to have found a natural niche in that area. The applications to mesoscale meteorology include using the radars either as research tools to improve our understanding of certain dynamical systems or as part of a network used to provide input data for weather forecasting. The goal of operational meteorology is twofold. The first is to forecast the weather over a variety of time scales, and the second is to monitor conditions so that we can assess the state of the atmosphere at a given time. Weather forecasting is probably one of the most commonly recognized tasks of operational meteorology since virtually all members of the public become users of such a service at one time or another. However, forecasting often includes more than a prediction of the chance of showers and the high and low temperature for the next day. User specific forecasts can include the air stagnation in a metropolitan area, winds aloft for routing aircraft, the strength of onshore winds and the associated beach erosion, or the strength and location of small-scale eddies and the effect of such eddies on chemical spraying in agriculture. The list goes on and on.

The workhorse of the operational observing network has been and still is the radiosonde balloon which provides measurements of pressure, temperature, humidity, and winds up to heights of 16-20 km, i. e., into the lower stratosphere. The average separation between radiosonde stations in the United States and Europe is ~150-500 km depending on the area. In addition to the radiosonde network, a much denser network of surface reporting stations cover the industrialized countries. The latter report the same quantities as the radiosonde provides, but only at the surface, and they also provide information about cloud cover, local precipitation, and tendencies, i. e., temporal changes, of the various quantities.

The station separation and measurement techniques used in the observing network lead to a natural emphasis on synoptic meteorology which is characterized by spatial scales of ~ 500 - 5000 km and time scales of $1/2$ to 5 days. Increasingly the interest of the national weather services is focusing on problems in mesoscale forecasting (see, e.g., Ray, 1986), first because we do not know very much about most mesoscale dynamical processes and second because most of the severe weather is associated with mesoscale phenomena. The mesoscale is characterized by spatial scales of ~ 1 - 500 km and time scales of $1/2$ to 12 hr. Satellites have provided important mesoscale data, particularly satellite photographs, but the thermodynamic and wind measurements that the satellites yield generally have poor vertical resolution which is unacceptable.

The seeds of MST radar technology have been sown on a fertile field. The radar wind profiler appears to solve many of the problems related to obtaining mesoscale observations needed for forecasting. The radars easily produce the time resolution, height resolution, and height coverage that are needed. A single radar still does not provide any extended spatial coverage, but the cost of the instruments is relatively low so that the possibility of deploying many of them still exists. The radars only provide direct measurements of the winds, which could be a drawback, but two factors operate in the radars' favor in this regard. The first is a result of geostrophic adjustment theory which predicts that at large scales, the wind field tends to adjust to the imposed pressure field, but at small scales the reverse happens. Therefore, if only one mesoscale quantity can be measured, the wind field is probably the best choice. The second factor again derives from the dynamic relationships and exploits the fact that the wind field is interrelated with the pressure and temperature fields through the balance equation and the vorticity equation. Thus, if the wind field is known over an extended horizontal region, information about the temperature and pressure fields can be derived. The accuracy and usefulness of these techniques still need to be carefully assessed but show great promise for the application of the radar technique to operational mesoscale forecasting.

My intent here is not to provide a complete review of the applications of MST radars to meteorological operations or research or to provide a complete literature review. Therefore, some important work will probably be slighted in my treatment. Rather, I hope to make the reader aware of some of the important issues presently being considered, and some of the potential of the technique for future applications. With this background, I will proceed to describe more specific aspects of the application of MST radar technology to meteorology. The next section deals with the characteristics of the horizontal wind measurements, Section 3 describes how the reflectivity measurements obtained from the radars can be used, Section 4 deals with the vertical velocity measurements from the radars, Section 5 describes quantities that are derived from the radar measurements, Section 6 deals with

special characteristics of an operational system, and Section 7 outlines some of the important open questions that remain about the usefulness of the technique.

2. Horizontal Velocity Measurement Capabilities

Interest in using MST radars for studies of mesoscale dynamics derives primarily from the possibility of measuring the horizontal winds over a large height range, with good height resolution and excellent time resolution. The time resolution, in particular, is the main advantage in using radars instead of balloons for horizontal wind measurements.

(a) Precision, Accuracy, and Errors

The wind profiler's capabilities for measuring the horizontal winds are the ones that have been explored most extensively to date. The first experiments that were carried out involved comparisons of the horizontal winds obtained from the radar measurements with the wind data from nearby radiosonde stations. An example of the type of agreement that can be expected is shown in Figure 1 which represents measurements made with the SOUSY-VHF-Radar located in the Harz Mountains in West Germany with wind data from the nearby Hannover radiosonde station (Röttger, 1983). The comparisons have shown good agreement from the outset and have led to a general acceptance of the radars' wind measurement capabilities. Two early studies attempted to quantify the comparisons by using longer time series and by making a better assessment of the magnitude of the errors that could be expected. The first was carried out by Fukao et al. (1982) and was based on 26 days of radar data obtained with the 430-MHz Arecibo radar and the corresponding radiosonde data from the San Juan station. Figure 2 shows the relative locations of the two sites and the trajectories of the balloons launched during the period. The figure also shows that the balloon measurements actually cover a large area during the ascent which can be a problem if small-scale flow features are of interest. The agreement was generally good, although errors varied between ~ 5 m/s in the troposphere and ~ 3 m/s in the lower stratosphere. The steady character of the flow in the subtropical region led to a nearly constant pattern in which the ascending balloons first traveled slightly to the east of San Juan, away from Arecibo, and then turned toward the west at higher altitudes. The authors argued that the differences in the lower stratosphere could be explained by errors in the radiosonde observations that occurred when the balloons were far from the launch site and therefore at low elevation angles. At least part of the difference between the two data sets in the troposphere, however, had to be due to variability in the flow.

Jasperson (1982a,b) has carried out numerous twin balloon experiments. Combinations of

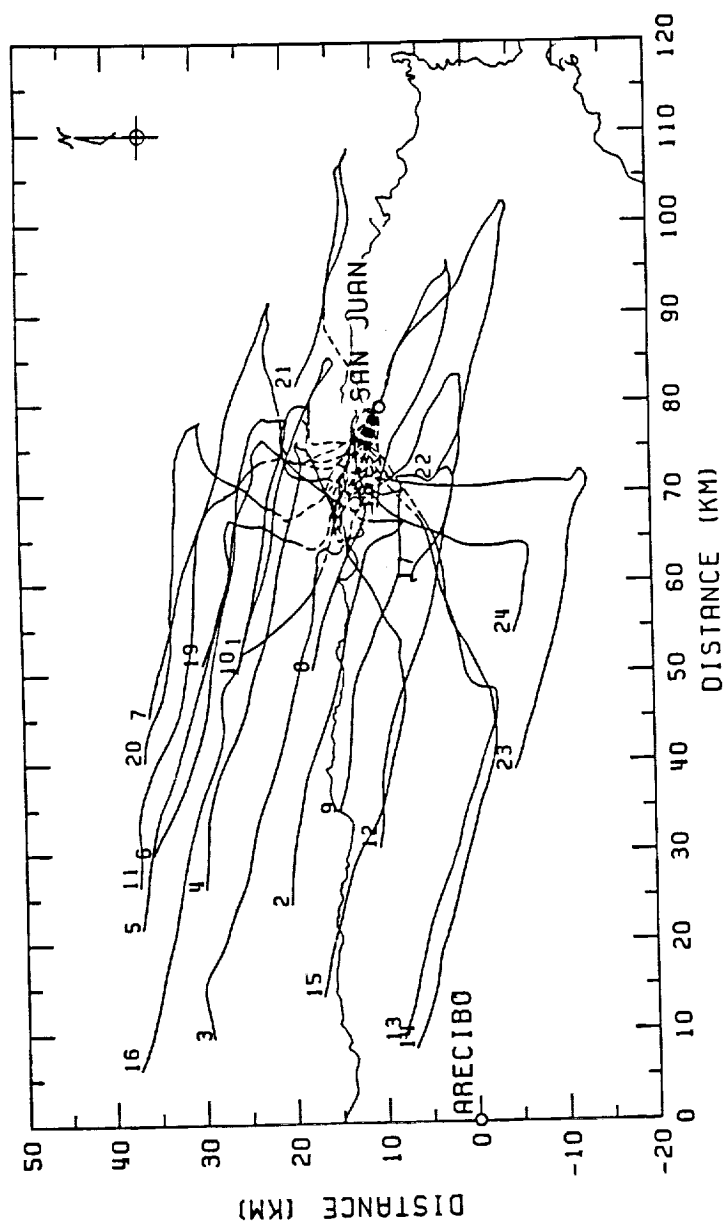


Figure 2. A map showing locations of Arecibo and San Juan, and trajectories of rawinsonde balloon ascents on 24 days in August and September 1977 when winds were also measured with the Arecibo 430-MHz radar.

spatially and temporally separated launches were carried out, and some launches from the same location at the same time were also made. The results provided an estimate of the errors attributable to the balloons and also the natural variability that occurs within the atmosphere as a function of temporal or spatial lag. Jasperson's data covered scales slightly different than the separation between San Juan and Arecibo but, when extrapolated to the appropriate scale, the natural variability could easily account for the differences between the radar winds and the radiosonde winds, without requiring large balloon errors, as pointed out by Larsen (1983).

Larsen (1983) compared data from the Poker Flat, Alaska, VHF radar to radiosonde data from nearby stations. Direct comparisons between the Poker Flat data and winds obtained with the Fairbanks radiosonde, only 30 km away, were made. Also, the radar and radiosonde winds were compared to the geostrophic winds calculated from the grid of radiosonde stations located closest to the radar. The 1-hr average radar and radiosonde winds were found to deviate from the geostrophic wind by about 5-6 m/s and they were found to deviate from each other by a smaller amount of ~ 2 -3 m/s. Thus, the accuracy of the two wind measurement techniques appears to be comparable. The differences between the two wind measurements were again explainable on the basis of the natural variability in the flow which is a function of the spatial separation. Röttger (1983) came to a similar conclusion based on the calculated auto- and cross-correlations between SOUSY radar data and winds measured by nearby radiosonde stations.

The Wave Propagation Lab in Boulder, Colorado, has carried out a series of experiments with a 5-beam 405-MHz wind profiler to assess the precision and accuracy of the measurements first during clear air conditions over a one-month period (Strauch et al., 1987) and then during periods when precipitation was in the beam (Wuertz et al., 1988). One beam was pointed toward the vertical, and the other four beams were pointed toward north, east, west, and south at a zenith angle of 15° . The differences in the east/west and north/south line-of-sight pairs could be combined to yield independent measures of the vertical velocity. The results in the form of scatter diagrams are shown in Figure 3. Figure 3a represents $(V_N - V_S)$ on the vertical axis and $(U_E - U_W)$ on the horizontal axis where the subscripts refer to the direction. Strauch et al. (1987) showed that deviations along an axis running at 45° from lower left to upper right includes both the measurement error and the vertical velocity contamination of the horizontal wind measurements. The axis running from lower right to upper left includes only the measurement error. Figure 3b shows a corresponding diagram in which the vertical beam measurements have been used to correct the horizontal wind measurements. In the latter case, the scatter in the plot is more nearly circular. The measurement error was found to be 1.7 m/s without the vertical beam correction and 1.3 m/s with the vertical beam correction. The study of the

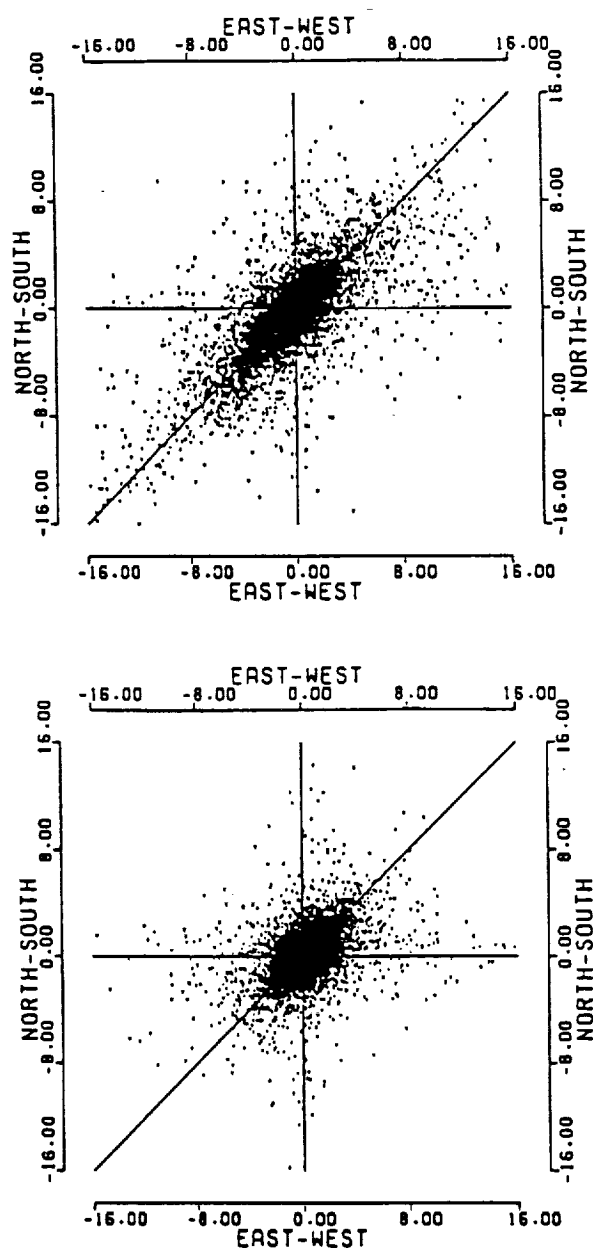


Figure 3. Scatter diagrams of $[V(\text{north})-V(\text{south})]$ vs. $[U(\text{east})-U(\text{west})]$ during February 1986 for the Platteville, Colorado, UHF profiler. The upper frame shows the values produced when no vertical velocity corrections were made. The lower frame shows the same data but with vertical velocity corrections applied.

precipitation cases carried out by Wuertz et al. (1988) showed that comparable measurement errors occurred when the precipitation was stratiform, i.e., spatially uniform, so that vertical velocity corrections could be made. The errors increased substantially when the precipitation was not uniform, however.

The radars not only provide better time resolution than the balloons but also overcome some other inherent limitations in the balloon technique, such as the problems that occur when balloons are launched during adverse conditions. Augustine and Zipser (1987) found that a series of balloons launched during a squall-line passage in Kansas during the Pre-STORM experiment did not reach heights much above the melting level. Wind profilers operating during the same period did not suffer from such problems. In fact, the conditions led to enhanced reflectivities that increased the signal-to-noise ratio during the period.

(b) Geostrophic Adjustment and Model Initialization

A good deal of the interest in using MST radars or wind profilers for mesoscale studies stems from the high time resolution and good temporal coverage afforded by the radars that will make it possible to study dynamical systems that have previously fallen between the "cracks" of the observational network. However, there is equally great interest in using a network of profilers as an observing system to provide the input for numerical forecast models, especially because geostrophic adjustment theory predicts that wind measurements are more useful when the scales of interest are small. The basic theory was worked out by Rossby (1937) and has been extended by numerous authors in various contexts. An excellent review is given by Blumen (1972). The theory predicts that the adjustment of the wind field and the mass field will be quite different depending on the ratio of the scale of the disturbance to the so-called Rossby radius of deformation. The Rossby radius L_R is defined as

$$L_R = \frac{C_N}{f} \quad (2)$$

where f is the Coriolis parameter and C_N is a characteristic velocity in the medium. In a shallow-water model that velocity becomes

$$C_N = \sqrt{gh} \quad (2)$$

where g is the acceleration of gravity and h is the fluid depth. Eq. 2 defines the gravity wave phase velocity in such a model. In a stratified atmosphere, the expression for C_N in a linearized treatment

becomes

$$C_N^2 = N^2 (N^2 c_s^{-2} + \Gamma^2 + m^2)^{-1} \quad (3)$$

where N is the Brunt-Vaisala frequency, c_s is the speed of sound, Γ is Eckart's coefficient which would vanish in the Bousinesq approximation, and m is the vertical wave number (Blumen, 1972). The Rossby radius varies substantially but typically has values in the range of 500-1000 km. The theory predicts that for scale sizes that are large compared to the Rossby radius, the wind field will tend to adjust to the pressure field. Therefore, if a synoptic scale perturbation pressure is induced in the flow, a wind that balances the pressure gradient will evolve over a time scale comparable to Γ^{-1} where f is the Coriolis parameter. If a large-scale perturbation in the wind field is induced, however, the energy input will be dissipated by gravity waves that propagate out of the region and carry the energy away. For small scales, the reverse situation holds, and a perturbation in the wind field will produce a pressure gradient that balances the wind geostrophically. A small-scale pressure perturbation, on the other hand, is dissipated by gravity waves that redistribute the energy.

A numerical model encompasses the same physics as the real atmosphere (or so we hope). Therefore, when observations of the pressure field at small scales are used to update the model, the effects of updated pressures are felt less. The situation is further worsened by the fact that gravity waves which are not handled well by the model are generated as part of the process of dissipating the pressure perturbation. Wind perturbations, on the other hand, tend to be maintained by the flow at small scales, and the pressure gradients needed to balance the flow develop with time. These considerations lead to an inherent preference for wind observations when small scales of motion are involved. Hoke and Anthes (1976), among others, have discussed these points in more detail, and Anthes (1983) has reviewed a number issues and strategies related to mesoscale models.

The wind profiler built and operated by NOAA's Aeronomy Lab at Christmas Island in the Pacific is the first facility to provide winds routinely by satellite transmission. After January 1987, the wind data was incorporated in the operational analysis of the National Meteorological Center and after April of that year the data was used in the European Centre for Medium-range Weather Forecasting's (ECMWF) operational analysis procedure. Gage et al. (1988) have described the results of a study designed to assess the improvement in the analysis procedure attributable to the profiler data. Before the data were incorporated in the analysis procedure, the standard deviations between the analysis and the observations was in the range of 3-5 m/s up to 250 mb. After the centers started using the profiler observations, the standard deviations decreased to 1-3 m/s. Figure 4 shows the deviations as a

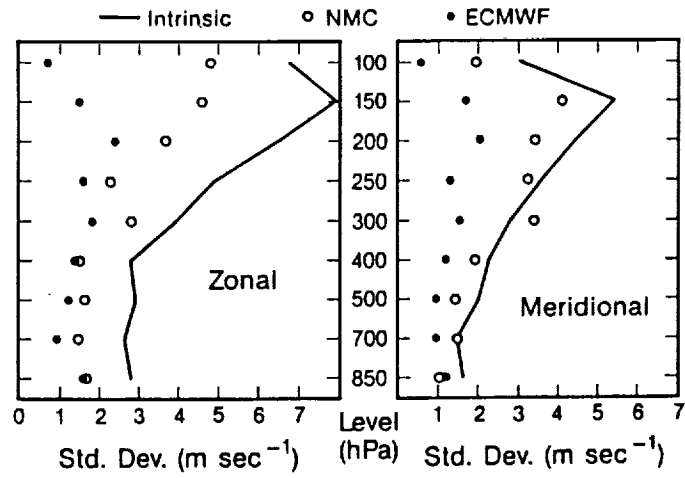


Figure 4. Standard deviations of Christmas Island winds compared to NMC and ECMWF analyses for May 1987.

function of height. The solid line indicates the variability in the profiler data alone and gives a reference by which the deviations between analysis and observations can be judged. In general, the NMC routine does a poorer job above 200-300 mb, apparently because less weight is assigned to this kind of data in carrying out the analysis. The study has shown the potential impact of wind profilers on initialization in remote areas. The minimal maintenance and unattended operation make the technique ideal for operation in isolated and remote locations. In the tropics, where the geostrophic relation is not applicable, direct observations of the winds are expected to be extremely important if significant improvements in forecasts are expected.

3. Reflectivity Data

Aside from the horizontal velocity components, the other parameter provided by all the radars is the reflectivity. The magnitude of the reflectivity is usually associated with the strength of the turbulence within the sampling volume, but strong gradients in the refractive index can also lead to enhanced reflectivities at longer wavelengths associated with what has become known as specular echoes or Fresnel reflection (see, e.g., Röttger and Larsen, 1988, or Gage, 1988). Whether the signal is due to Bragg or turbulent scatter or specular reflection, structure with a scale size comparable to the wavelength of the transmitted signal has to be present. In the former case, the structure is expected to be more microscopic in nature and characterized by shorter coherence times. In the latter case, the structure is expected to be more macroscopic in nature with longer coherence times. There is still considerable debate at meetings and in the literature about the dynamics associated with these two different kinds of scatter. Also, although we like to characterize the scatter as being of one type or the other, the actual scatter received in any real situation is likely to be the result of a combination of both effects.

These important questions need to be resolved in the future, but, in spite of the uncertainties about the details of the dynamics, we already know that in practice the result is an enhancement in the reflectivities observed at VHF at heights just below the radiosonde tropopause. Figure 5 shows an example of the reflectivities measured with the SOUSY-VHF-Radar, and the tropopause heights derived from the Hannover radiosonde data are shown by the arrows (Rastogi and Röttger, 1982). Gage and Green (1982a) have established objective criteria for locating the tropopause based on radar reflectivity data. They found that the errors were typically ± 270 m, although the authors expected the errors to increase slightly if the technique is used operationally. Gage et al. (1986) have extended the earlier work, and Sweezy and Westwater (1986) have compared different techniques for deriving the tropopause height from VHF radar data. Knowing the height of the tropopause can be valuable in

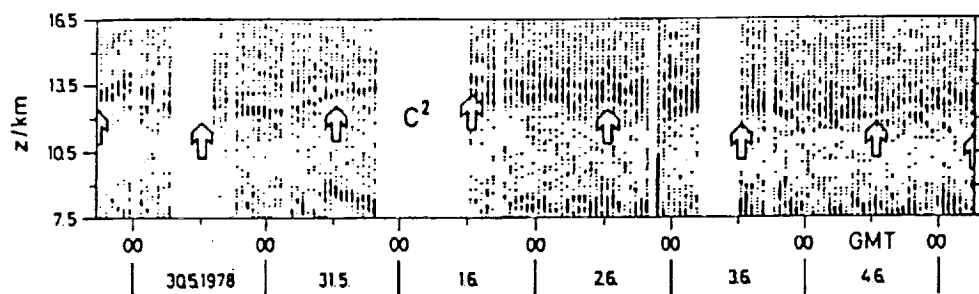


Figure 5. Plot of relative reflectivity indicating the fine structure of the tropopause region. The arrows show the tropopause height deduced from nearby radiosonde profiles.

fine-tuning the temperatures obtained from either satellite or ground-based microwave remote sensing data. Tropopause height information will not be available if UHF profilers are used since the shorter wavelengths are not sensitive to the aspect sensitivity effects that lead to the enhanced scatter from the tropopause region. Gage and Green (1982b) also pointed out that the measured radar reflectivity profiles could be used, in conjunction with information about the surface temperature, to provide an estimate of the temperature profile. Above the tropopause, the variations in reflectivity provided information about the temperature gradients. Below the tropopause, a constant lapse rate was assumed. Radiosonde profiles will be much more detailed and accurate than the profiles derived in this way, but temperature information derived from the radar data can be used as a supplement where no other information is available. Also, the potential improvements in microwave radiometer-derived temperature profiles when the two types of data are combined have not been fully explored (Hogg et al., 1983).

An effect related to the enhanced backscatter from the tropopause seen at VHF is the enhanced scatter from frontal boundaries. Röttger (1979) was the first to describe this effect based on analysis of data obtained with the SOUSY-VHF-Radar located in the Harz Mountains in West Germany. Larsen and Röttger (1982, 1983, 1985) have analyzed a series of frontal passage events using the same instrument. In essence, the enhanced reflectivities occur very close to the location of the frontal boundary as determined from radiosonde data. The boundaries usually slope either upward with time (cold frontal passage) or downward with time (warm frontal passage). An example is shown in Figure 6 which corresponds to the passage of a cold front indicated by the cross-hatched area followed by a warm front shown by the stippled areas during the period February 7-9, 1982. The tropopause heights measured by the Hannover radiosonde are shown by the crosses. On February 8 at 12 GMT, the passage of the front caused a very low tropopause height to be reported, in agreement with the radar reflectivity contours. The lower half of the figure represents the potential refractivity M^2 calculated from the radiosonde data for the same period. M given by

$$M = -77.6 \times 10^{-6} \left(\frac{P}{T} \right) \left(\frac{\partial \ln \theta}{\partial z} \right) \left[1 + 15500 \frac{q}{T} \left[1 - \frac{1}{2} \left(\frac{\partial \ln q}{\partial z} \right) \left(\frac{\partial \ln \theta}{\partial z} \right)^{-1} \right] \right] \quad (1)$$

Here P is the pressure in millibars, T is temperature in Kelvin, θ is the potential temperature, q is the specific humidity in grams per kilogram, and z is height in meters. The agreement in the gross features of both cross sections is evident. Recently, similar reflectivity structures have been observed with the Flatland radar in connection with frontal passages in Illinois (Nastrom, private communication, 1988). Larsen and Röttger (1982, 1983, 1985) made comparisons between calculated refractivities and

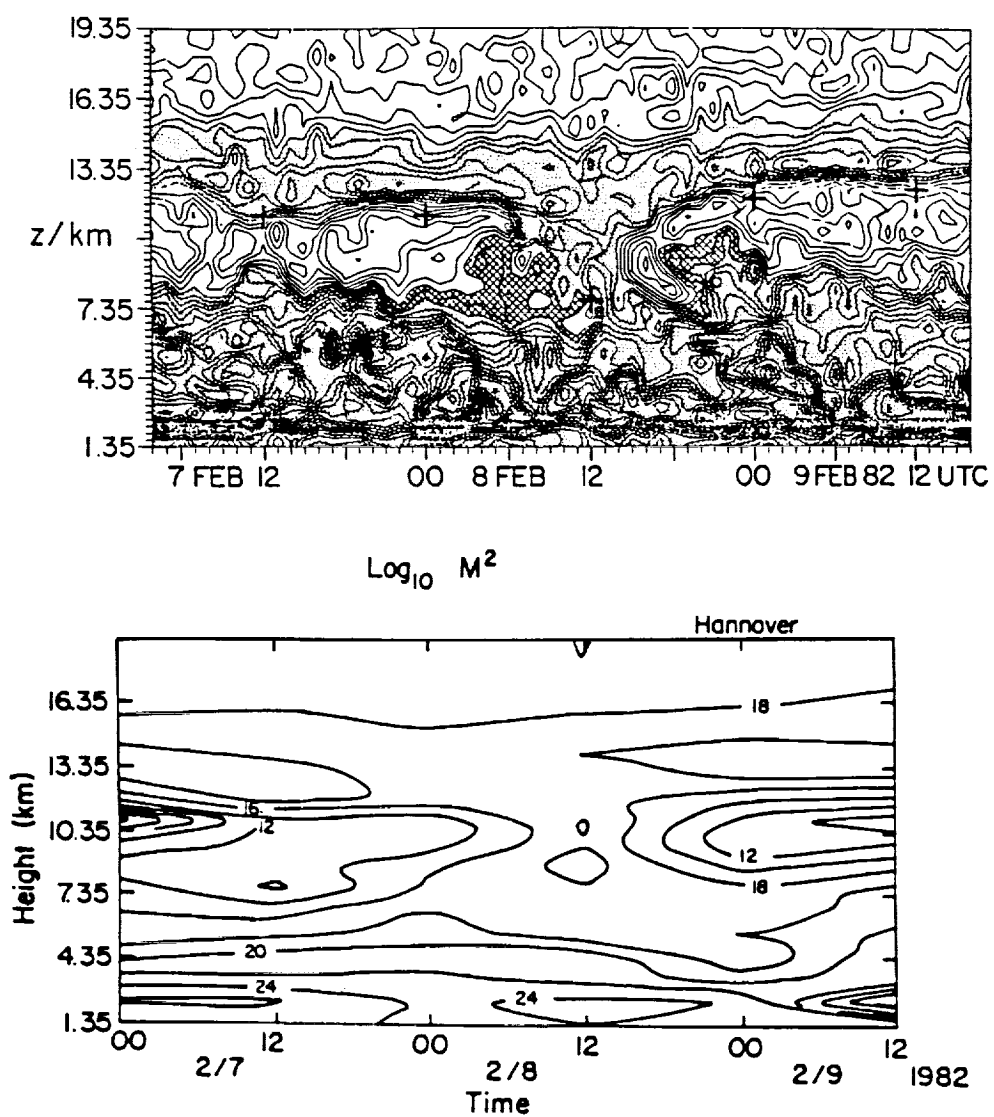


Figure 6. Top frame shows the reflectivities measured during February 1982. The stippled areas show highest reflectivities and the cross-hatched regions represent intermediate reflectivities. The lower frame shows the potential refractivity calculated from the Hannover radiosonde data for the same period.

observed reflectivities in a series of frontal passages. The agreement between the gross features of the two quantities was striking and indicated that the structure responsible for the scattering was being organized on a large scale. At least it persisted over the scale separating the radar and radiosonde which was approximately 90 km. An alternative hypothesis would have been that the enhanced reflectivities were generated by small-scale turbulence produced locally near the front. Some of the fine structure probably had this kind of source, but the larger organizing features were of mesoscale origin.

Some of the reflectivity data obtained with SOUSY has shown that the frontal boundary consists of smaller-scale filamented structure. Detailed reflectivity structure is shown in the gray-scale plot in Figure 7 for the March 6-7, 1981, warm-frontal passage. Presumably better height resolution would show even finer-scale structure. The dynamics of the upper level frontal zones are extremely important both in generating and enhancing tropospheric systems and in mixing constituents between the stratosphere and troposphere. The mixing that occurs during tropopause folding events was already documented by Danielsen (1968) in connection with experiments designed to study the transport of radioactivity and trace constituents through the tropopause region. It has become clear that the mixing between the troposphere and stratosphere is not steady and continuous but occurs discretely during certain special events, usually associated with frontal passages. We still know very little about the small-scale dynamics actually responsible for the mixing (see, e.g., Ray, 1986), but the radar reflectivities and radar measurements of velocities may provide us with more information about this aspect of the circulation.

4. Vertical Velocity Measurement Capabilities

The vertical velocity measurement capability of the MST radars has been one of the most intriguing as far as meteorological applications are concerned. Deployment of either an operational or a research network can be justified on the basis of the horizontal wind measurement capabilities alone, but vertical velocities have always had a special place in meteorology for a number of reasons. First, much of the effort in the field is devoted to predicting or understanding the vertical circulations that develop in the atmosphere. Clouds and precipitation are produced by upward vertical velocities; the large vertical gradients in density in the atmosphere lead to heating or cooling during adiabatic ascents or descents that produce significant temperature changes in competition with horizontal advection; and the vertical gradients in chemical constituent concentrations imply that vertical circulations will have a large effect on trace concentrations. In spite of the importance of the vertical velocity fields, the vertical circulation is almost always an inferred quantity. A few specialized techniques, such as aircraft measurements, exist for measuring vertical velocities, but for large-scale measurements, the vertical

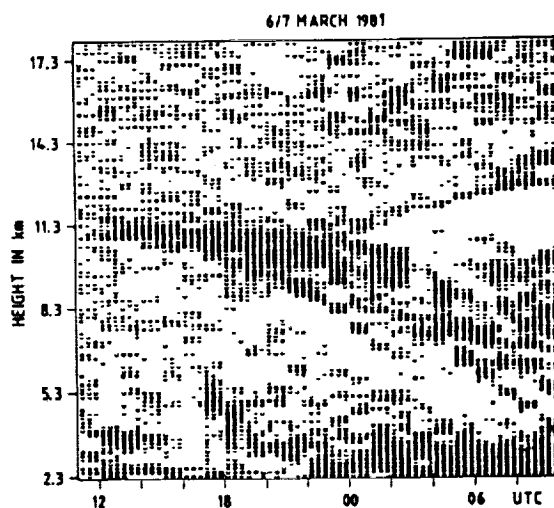


Figure 7. Reflectivities measured by the SOUSY VHF radar on March 6-7, 1981. The mean vertical reflectivity profile for the period has been subtracted from the individual profiles. Note the laminae near the tropopause and in the frontal band structure.

velocity is usually calculated from the divergence of the horizontal winds. Short-wavelength precipitation radars have been used to "measure" the vertical velocities in connection with special experiments, but the measurements usually amount to integrating the divergence over height to yield the vertical velocity. Since the radars are sensitive to precipitation, only the motion of the precipitation can be measured, and while the horizontal velocities of the precipitation and the air are expected to be the same, the vertical velocities are generally quite different.

Thus, with some reservations that I will explain later, we can say that the MST radars are the first instruments capable of providing vertical velocity measurements routinely over extended periods and over a large height range. Immediately the possibilities for verifying model forecasts of vertical velocities come to mind. Also, if the vertical velocity measurements can be trusted, the measurement of the vertical velocity can be inverted to provide us with information about the variation of divergence with height (Clark et al., 1986). The latter quantity would be extremely useful in initializing forecast models which generally use the horizontal wind field as part of the input parameters. Vertical velocity information would help the numerical models to develop realistic vertical circulations in a shorter time. Typically, the horizontal wind information is the only velocity input to the model, and it takes some time before realistic vertical circulations develop. The latter is not a problem if the ultimate goal is a 12-day forecast, but the problem is a serious one if a 2-3 hr forecast is sought. Finally, the vertical velocities may be characteristic of small-scale processes too small for the model to resolve, but even subgrid-scale momentum and heat fluxes are important in forcing the larger-scale dynamics. These fluxes are generally parameterized, but measurements of the vertical fluxes could be used to update the parameterization at the time of model initialization.

In spite of the clear need for and many potential uses of the radar vertical velocity measurements, there are still many uncertainties that need to be resolved before the potential can be realized. The first problem is related to the accuracy of the vertical velocity measurements. Although several different techniques have been used to measure horizontal velocities, including the Doppler method, the spaced antenna method, and the interferometer method, all the various techniques measure vertical velocities by the Doppler method. There seems to be general agreement that the signal received from the vertical direction is scattered by irregularities or sharp gradients in the refractive index, and that the Doppler shift of the received signal gives the line-of-sight, in this case vertical, velocity of the refractive index irregularities. The uncertainty relates to whether the irregularity velocity is the same as the air motion so that the Taylor hypothesis is valid.

A logical way to proceed in determining the accuracy of the vertical velocity measurements is to compare the measurements with vertical velocities obtained by some other technique, but in this

case no real basis for comparison exists. The next best approach is to compare the measured velocities with vertical velocities calculated from other data. The number of studies of this type is very limited so far. Nastrom et al. (1985) utilized data from the Platteville, Colorado, VHF radar obtained over a period of several weeks. A number of different methods for calculating the vertical velocity were applied to the gridded values produced by the NMC analysis for the surrounding region. The kinematic method was used to integrate the divergence to produce a vertical velocity profile, the thermodynamic method was used to calculate the vertical velocity based on temperature changes associated with adiabatic warming or cooling during ascent or descent, and the quasi-geostrophic omega equation was also used. Three examples of the profiles of calculated and observed vertical velocities from the study by Nastrom et al. (1985) are shown in Figure 8. The various methods for calculating the vertical velocities, indicated by letters, were found to yield comparable results, but large differences between the measured and calculated values were found throughout the period. Specifically, the radar measurements were generally 2-3 times larger than the calculated values, but there was better agreement between the signs of the velocities.

Larsen et al. (1988) compared vertical velocities obtained with the SOUSY-VHF-Radar located in the Harz Mountains in West Germany to the vertical velocities produced by the operational analysis procedure of the European Centre for Medium-range Weather Forecasting (ECMWF). The analysis uses a normal mode initialization procedure which is known to preserve more of the divergence in the horizontal velocity field than some of the other techniques. Therefore, larger and perhaps more realistic vertical velocities are expected from this type of calculation. The result of the study was that the magnitudes of the calculated and measured values were nearly the same. However, the agreement between specific features observed in connection with the passage of fronts, for example, was not as good. An example is shown in Figure 9 which represents contours of the upward vertical velocities measured with the radar over a two-week period in November 1981 in the upper panel and the operational analysis vertical velocities for the corresponding period in the lower panel. The same gross features are present in both the observed and calculated data sets. For example, 4-5 bands of upward velocity were seen in both data sets in connection with the passage of a cold front on November 6, but the timing of the passage of the bands varied by as much as 12 hr and one band that was present in the radar data after noon on November 6 was missing in the analysis. In some sense, discrepancies of this type are not surprising, but we need to be able to account for the discrepancies in the future before we can make use of the measurements for verification and initialization of models.

Gage and Nastrom (1986) compared vertical velocities obtained with the Platteville radar located in Colorado to precipitation data from the surrounding area. They concluded that there was a

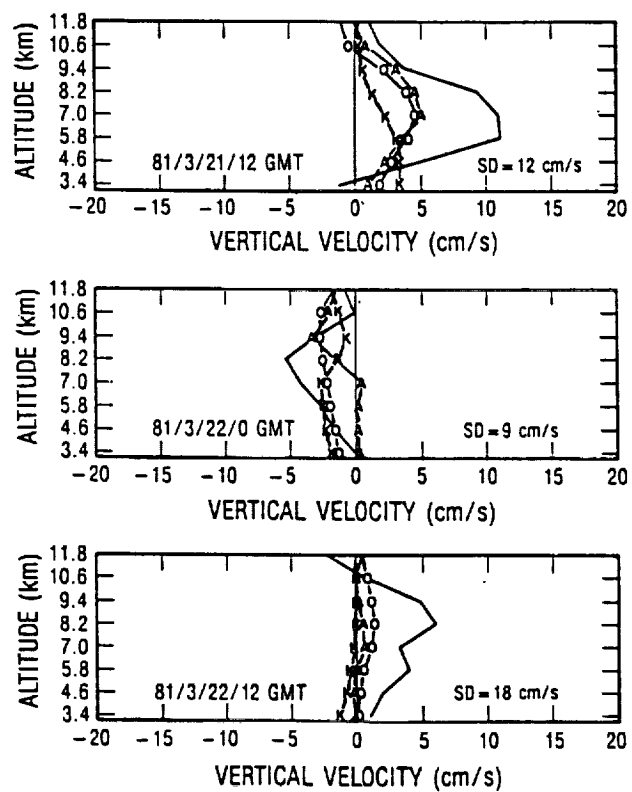


Figure 8. Profiles of the vertical velocity over Platteville, Colorado, from the ST radar (solid line) and the adiabatic (A), kinematic (K), and omega equation (O) methods.

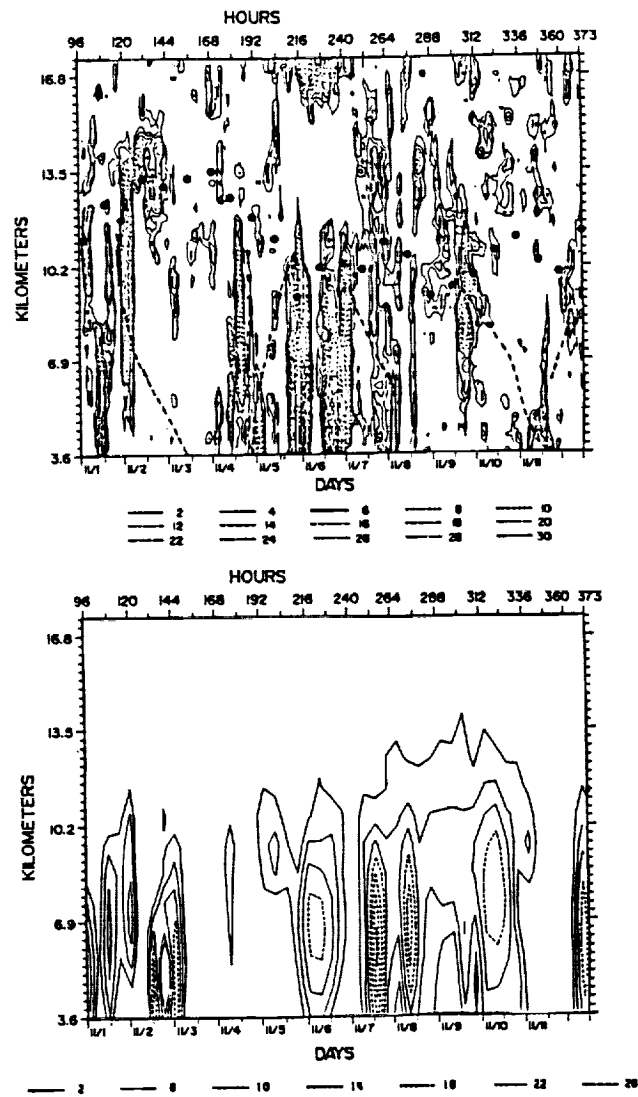


Figure 9. Contours of upward vertical velocities measured by the radar in the upper frame and produced by the ECMWF operational analysis in the lower frame for a two-week period in November 1981.

general relationship of the type that would be expected between the times when precipitation occurred downwind from the radar and the times when the radar showed a pattern of upward motion. Results of this type are encouraging, but more quantitative comparisons are difficult due to the large horizontal gradients and local variability in precipitation.

Wakasugi et al. (1985) measured the vertical velocities with the MU VHF radar during the passage of a cold front. A meteorological radar also provided data on the location of the precipitation during the period. Figure 10 is an example of the VHF data which shows the reflectivities at off-vertical incidence in the upper panel, the reflectivity at vertical incidence in the middle panel, and the circulation in the cross-frontal plane in the lower panel. The reflectivities clearly show the aspect sensitivity effects. The upward vertical velocities are strongest close to the time of the frontal passage, but a number of cells of alternating upward and downward velocities are evident before and after the passage. The times when precipitation occurred correlated well with the times when the updrafts were present, although not all updrafts produced precipitation. This type of data shows the potential for the observation of mesoscale systems and gives an indication of the insights that can be expected.

As mentioned above, an important question for the near future will be to determine the source of discrepancies between radar vertical velocity measurements and calculated values such as those produced by operational analysis. In comparing horizontal winds, a balloon can be launched immediately adjacent to the radar and a direct comparison can be made. Thus, the effects of small-scale gradients in the flow can be minimized. When the vertical velocities are calculated, usually from the divergence equation, at least three spatially separated wind profiles are needed. The result is that the derived vertical velocities represent a different quantity than the measured values since the derived values are effectively an average over the area defined by the area between the observing sites. The radar vertical velocities are representative of a single point within the domain. An attempt to reconcile the two values can be made by averaging the radar velocities in time. If the Taylor hypothesis is valid and the fluctuations are "frozen" within the flow, averaging in time should be equivalent to averaging in the spatial domain. There is some evidence that such an approach is valid (Brown and Robinson, 1979), but the two quantities will always be somewhat different. Some of these issues will likely be resolved when networks of wind profilers are deployed, such as the network proposed for the central United States as part of the STORM program (Augustine and Zipser, 1987).

Another potential problem is due to the effects of aspect sensitivity on the effective look angle of the radar beam. These effects will only be significant when longer wavelengths such as 6 m are used since the aspect sensitivity at 70 cm, for example, is negligible in virtually all but the most exceptional circumstances. Aspect sensitivity causes the largest signal to be received when the look direction is

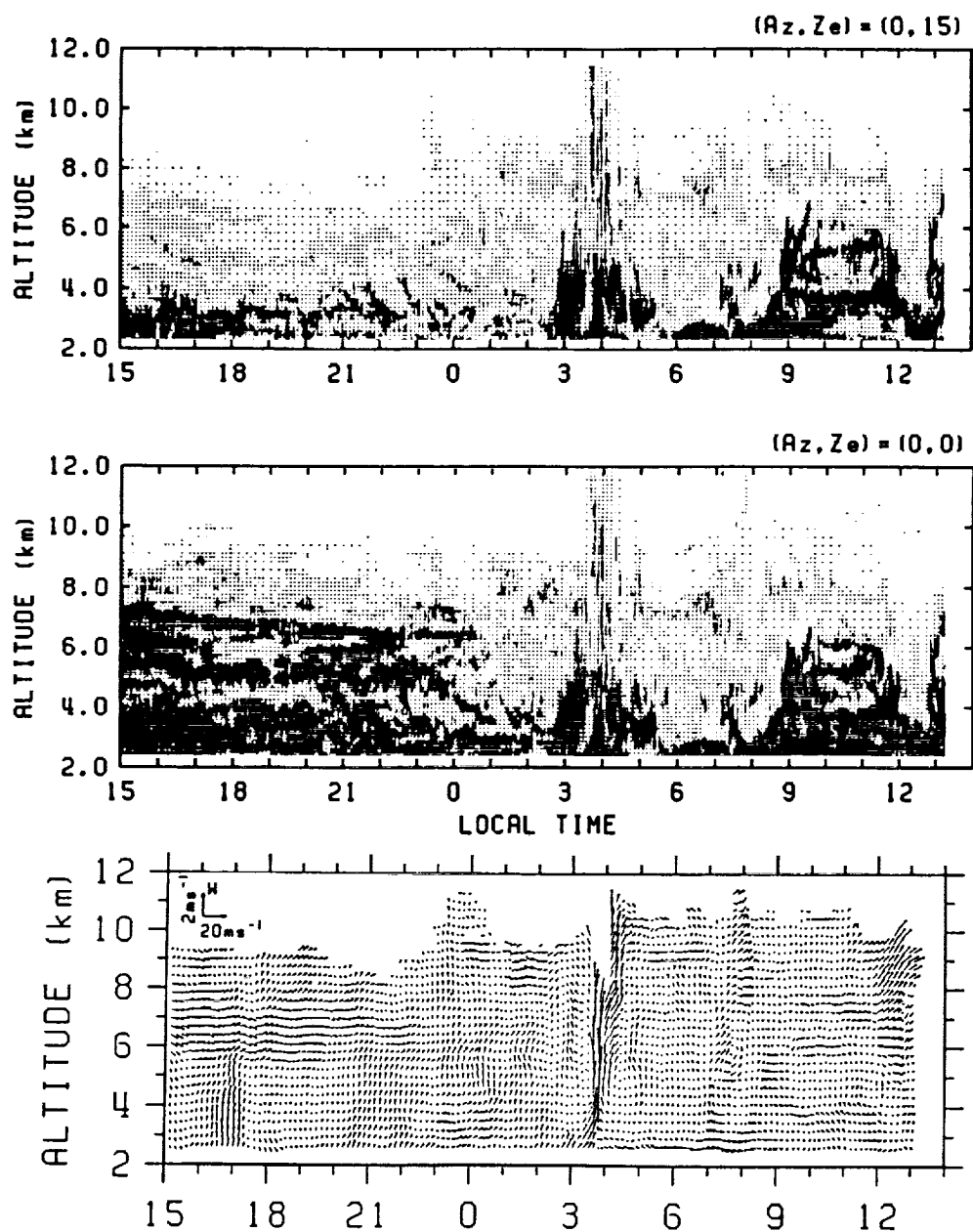


Figure 10. The upper frame shows the reflectivities measured by the MU radar in Japan at off-vertical incidence during a frontal passage in June 1984. The middle frame shows corresponding reflectivities at vertical incidence. The lower frame shows the circulation in the cross-frontal plane during the same period.

perpendicular to strong gradients in the refractive index associated with layers in the atmosphere. The layers are generally tilted by a few degrees, but except for the largest arrays, the tilt angle will be within the beamwidth. Thus, a beam that is nominally pointed in the vertical direction may receive the strongest signal from a look direction that is a degree or a few degrees off vertical. The measurement will then consist of the projection of the true vertical velocity on the effective look direction, which is usually a minimal error, plus the component of the horizontal velocity along the look direction. The latter can create errors of over 100%, i. e., even the sign of the apparent vertical velocity can be wrong in some instances. Röttger and Ierkic (1985) have described these problems and have shown that data from a spaced antenna array can be used to calculate the tilt angle of the layers in order to make the necessary corrections to the measured velocities. Very little analysis of this type of error has been carried out so far, but the effects need to be taken into account when VHF profilers are used. Such effects may be responsible for some of the discrepancies found in the studies by Nastrom et al. (1985) and Larsen et al. (1988) since both studies used data obtained with VHF radars.

Recently a VHF radar has been constructed near Champaign, Illinois, in one of the flattest portions of the central United States. The site has tremendous advantages for studies of the vertical velocities since almost no orographic effects are expected. Figure 11 from the article by Green et al. (1988) shows samples of the time series of vertical velocities obtained at the Flatland radar, at Platteville, Colorado, just east of the Rocky Mountains, and at Sunset, Colorado, in the mountains. The variability and amplitudes of the vertical velocities increase with proximity to the mountains. The active periods that occur with some regularity in the data sets taken near the mountains are due to generation of waves by the flow over the topography.

UHF radars are unlikely to suffer from the errors introduced by aspect sensitivity effects, but the shorter wavelengths are extremely sensitive to precipitation. Thus, if there is precipitation in the beam, the measured vertical velocity will be the fall velocity of the precipitation (see, e. g., Larsen and Röttger, 1987, and Wuertz et al., 1988). Periods of strong precipitation are easily distinguished in the data since the reflectivities increase significantly beyond the levels that can be accounted for by turbulent scatter. Periods of moderate precipitation may be more difficult to handle in practice. Eliminating all questionable data is not difficult but leads to a rather unsatisfactory solution since we will be deprived of data whenever the meteorological situation becomes interesting. More work is needed to determine the optimum approach that gives us the maximum usable information but eliminates the erroneous data.

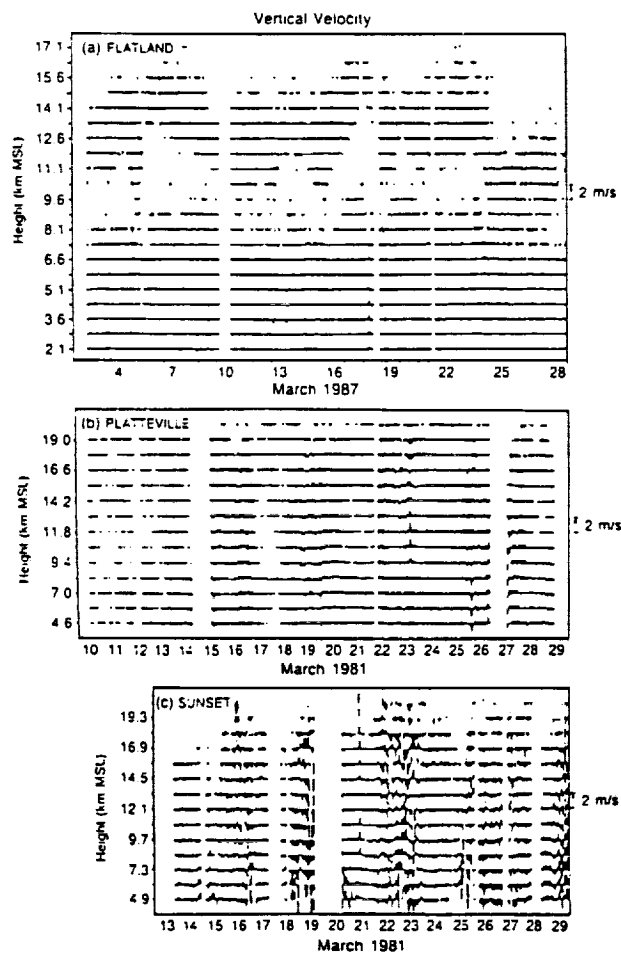


Figure 11. Radar vertical velocities averaged over fifteen-minute periods for Flatland in March 1987 in the upper frame, for Platteville during March 1981 in the middle frame, and for the Sunset radar during March 1981 in the lower frame.

5. Derivable Quantities or Parameters

(a) Pressure and Temperature Fields

The reflectivity data can be used to provide an estimate of the temperature profiles as described above, but the estimates are likely to be extremely coarse. However, there is a balance between the pressure and temperature fields and the winds imposed by the dynamical constraints. A simple example is the geostrophic relationship which relates the horizontal wind components and the horizontal pressure gradients. The balance equation is based on less limiting approximations than the geostrophic approximation and has been used in studies by Gal-Chen (1988) and by Kuo et al. (1987a,b) to determine how the wind information from a profiler network can be used to derive the temperature field. The input to the calculation is the observed wind field, and the output is a temperature field consistent with the wind field through the constraints imposed by the balance equation. The results to date have been very encouraging and show the potential for deriving parameters other than just the horizontal winds from the profiler observations.

(b) Divergence and Vorticity

Since the divergence is related to the vertical gradient of the vertical wind, the divergence can always be calculated once the vertical velocity profile is obtained (Clark et al., 1986). Alternatively, four off-vertical beams pointed along different azimuths can be combined to yield the divergence directly.

Ordinarily, a single radar cannot yield the vorticity in the flow since the radar measures the line-of-sight velocity and the vorticity is the circulation perpendicular to the look direction if the radar beam is cycled around in different azimuth directions. However, Smythe and Doviak (1987) have suggested that correlations of the signals obtained with the beams pointed in different directions can provide the cross-beam component of the flow. The procedure is similar, although not identical, to the spaced antenna method for obtaining the winds (e.g., Röttger and Vincent, 1978; Larsen and Röttger, 1988). The latter technique uses at least three vertically pointing but spatially separated beams. The cross-correlation between the signals in the various beams gives the time lag for the scatterers to move from one beam to the next. Thus, the cross-beam velocity component is derived. The spaced antenna set-up may be the most natural to use for obtaining the vorticity in the flow since the lags between the signals in the three beams are calculated anyway as part of the process of deriving the horizontal winds. The line integral of the inverse lags around the triangle defined by the receiving antennas divided by the area of the triangle will then be proportional to the vorticity.

The vorticity is an extremely important quantity in defining the properties of any

meteorological flow. The vorticity associated with frontogenetic flows would be a valuable parameter to measure. Observations of this quantity could be used to study the mixing that takes place near upper-level fronts in connection with tropopause folding and in the boundary layer in connection with convection, for example. Even if this type of measurement is shown to be feasible, we still have to determine how the microscale vorticity that is measured by the radar is related to the mesoscale vorticity. The problem is similar to the one that we face in determining how representative and useful the vertical velocity measurements will be for studies of mesoscale and synoptic scale dynamics.

(c) RASS

The RASS (Radar and Acoustic Sounding System) technique was introduced already in the 1960's. The system uses an acoustic generator to produce waves with half the wavelength used by the radar. The acoustic disturbances thus produce refractive index variations that cause strong Bragg scatter of the radar wave field. Measuring the velocity of the acoustic waves yields the temperature directly since the speed of sound is a function of the temperature. The early experiments used meteorological radars with relatively short wavelengths in the centimeter range, and the high frequencies made it difficult to obtain signals much above the boundary layer. Matuura et al. (1986) were the first to implement the technique at VHF with the MU radar in Japan. The longer wavelength of 3 m for the acoustic signal decreased the attenuation and made it possible to obtain temperature profiles well into the stratosphere.

The first experiments took over a day to carry out because of the problems associated with moving the acoustic source so that the sound waves would pass through the radar beam. Since the acoustic waves are blown around by the winds, the alignment problems can be severe. Obtaining the Doppler velocity which is then converted to temperature is a relatively quick process once the acoustic beam is within the radar beam. Placing an array of acoustic sources near the radar in more recent experiments has reduced the measurement time significantly to less than one hour. The radar beam still has to be steered, but the necessary calculations and movement of the beam can be carried out quickly.

The MU radar is rather special in the sense that it is extremely flexible and powerful compared to the wind profiler systems that are being deployed operationally. Therefore, it is not immediately obvious that the RASS technique can be applied with some of the simpler systems. However, the potential uses for the temperature data that could be obtained in this way are tremendous and will, no doubt, be explored in depth in the next 5-10 years. Work has already been carried out to test the application of the RASS technique with some of the systems developed at NOAA in the Aeronomy Lab

(Ecklund, private communication, 1988) and in the Wave Propagation Lab (Strauch, private communication, 1988). The work has produced at least some modest success.

(d) Momentum fluxes

Vincent and Reid (1983) have shown that two symmetrical off-vertical beams can be used to measure the vertical flux of horizontal momentum. Other beam configurations are possible, but the Vincent-Reid set-up appears to have some distinct advantages. Only a few studies of the momentum fluxes in the troposphere and lower stratosphere have been carried out so far. Cornish and Larsen (1984) used VAD data obtained with the 430 MHz Arecibo Observatory radar, Nastrom and Green (1986) obtained momentum flux data with the Sunset radar, and Fukao et al. (1988) calculated the momentum flux from MU radar data. The latter study also compared the three beam (one vertical, two off vertical) and four beam (four off vertical) methods for obtaining the momentum flux.

The momentum fluxes are extremely important in the dynamics of the atmosphere. Gravity waves serve as the agents for redistributing energy rapidly in the vertical direction. Wave dissipation results in a convergence of the momentum flux that causes an acceleration of the flow. In particular,

$$F_v = -\frac{1}{\rho} \frac{d}{dz} (\rho v' w') \quad (10)$$

and

$$F_u = -\frac{1}{\rho} \frac{d}{dz} (\rho u' w') \quad (10)$$

where ρ is the atmospheric density, z is height, and u' , v' , and w' are the fluctuating zonal, meridional, and vertical velocities, respectively. F_u and F_v are the accelerations induced in the flow in the zonal and meridional directions and are usually expressed in units of $\text{ms}^{-1}\text{day}^{-1}$. Nastrom and Green (1986) found values of $\sim 10^{-2} \text{ms}^{-2}$. There was considerable variability in the data, and the direction of the momentum flux changed over intervals of 1-6 hr. Fukao et al. (1988) found accelerations of $5\text{-}25 \text{ms}^{-1}\text{day}^{-1}$ for data averaged over a 4-day period. In the latter study, there was no evidence of large accelerations of the flow. Therefore, other processes must be balancing the induced accelerations. The study by Fukao et al. (1988) also found that the largest contribution to the momentum flux was from long period waves with periods of ~ 300 min.

Studies of the momentum fluxes have only begun to scratch the surface of the important dynamics associated with the vertical redistribution of energy effected by the higher frequency gravity

wave motions. It is likely that more studies of this type will help to clarify the important interconnections between orography and atmospheric dynamics and the mechanisms whereby energy generated in connection with dynamical processes is redistributed by the smaller-scale waves.

6. Special Operational Requirements

In certain instances, systems or networks of systems have been set up for meteorological experiments on a short-term campaign basis. However, the systems used for operational monitoring of the meteorological environment will have some special requirements in terms of strength of the system construction, reliability of the system, and accuracy.

(a) Construction and Reliability

When research systems such as the MU radar in Japan or the Flatland radar in the United States are deployed, the site is usually chosen carefully, and arrangements are made to have the site visited and maintained often. Large-scale networks generally do not afford such luxuries. Since extensive areas have to be covered by the instruments, relatively advantageous sites can be chosen, but often less than ideal choices will have to be made. Finally, the systems have to be capable of operating in a variety of weather conditions, and sometimes even in extreme weather. All of these requirements add up to the need for an exceptionally sturdy construction with a long mean time between failures.

(b) Accuracy and Precision

The required accuracy and precision are related quantities since the precision has to be at least as good as the accuracy, but the measurement error that can be tolerated is still unknown. Studies such as those of Kuo et al. (1987a, b) will help to establish the appropriate criteria. Meanwhile the systems deployed as part of the Colorado network (Strauch et al., 1987) appear to have measurement errors of about 1.5 m/s.

(c) Height Coverage

It is difficult to come up with a quantitative criteria for the height coverage required for a wind profiling system or network. In terms of the upper height limit, the more height coverage the better is probably a reasonable rule-of-thumb subject to various practical considerations. The Wave Propagation Lab in Boulder, Colorado, has compiled statistics on the height range coverage provided by systems with three different frequencies (Frisch et al., 1986). The prototype network has used a better height resolution at lower altitudes and poorer height resolution aloft, the rationale being that the larger-scale structure above still has a considerable effect on the flow closer to the surface, but the

small-scale structure aloft is less likely to influence the flow at lower levels. The increased pulse length at higher altitudes increases the signal-to-noise ratio in that part of the atmosphere where the signal usually becomes weaker. At least in some cases, we know that the small-scale structure aloft is crucial in the evolution of the larger scale flow, especially near frontal zones. Then the strategy may have disadvantages.

A major concern in the meteorological community has been the lack of coverage of the lower altitudes in the planetary boundary layer rather than poorer coverage of the upper troposphere or lower stratosphere. The boundary layer is the source of important fluxes of heat and moisture that fuel the systems in the free flow above the friction layer. Therefore, measurements of winds and momentum fluxes close to the surface but above the height covered by meteorological towers are extremely important. The Aeronomy Lab and Wave Propagation Labs of NOAA in Boulder, Colorado, have built special boundary layer radars (BLR's). Ecklund et al. (1988) have described one of the systems. These instruments use high frequencies that allow fast transmit/receive switches to be utilized. Since the signals in the boundary layer are relatively strong, small antenna sizes can be used. Already, these small specialized systems have shown good results, and the systems appear to provide good overlap with the larger profilers.

(d) Choice of Frequency

So far, only a few frequencies have been used in profiler applications. The popular choices to date have been near 50 MHz and 400 MHz. The ideal frequency, even for a particular application, is not known because the range of the frequency spectrum that has been explored is so limited. In practice, it may be almost impossible to choose any frequency but the 405 MHz frequency that is already allocated for meteorological use. The advantages of the 405 MHz band are that large bandwidths are easier to obtain, making it possible to operate with better height resolution, and faster T-R switches are generally available at the higher frequencies so that better coverage of the lower heights can be realized. The disadvantages include lack of aspect sensitivity, which eliminates the enhanced scatter from the tropopause or frontal boundaries, and the sensitivity to precipitation. Even low rainfall rates will result in the signal being dominated by the precipitation so that direct measurements of the vertical air motion become unreliable or impossible.

7. Remaining Questions

(a) Best Configuration for Networks

The prototype profiler network being deployed as part of the STORM program in the United

States is being established with an average spacing comparable to that of the radiosonde network, although a subgrid array with a smaller spacing will be embedded in the larger array. The plan seems reasonable, but it is still unclear whether this is an optimum spacing. We will need experience with the network to determine what characteristics of the various dynamical systems can be observed and whether important features are slipping between the cracks.

(b) Initialization of Models

There are still many important unanswered questions about how the profiler data can best be used to initialize numerical forecast models. Clearly, the straightforward input of profiler winds at the initial time step is a likely possibility, but various four-dimensional data assimilation schemes may also be useful, especially since the wind profilers have tremendous time resolution but provide limited spatial coverage.

(c) Usefulness of Vertical Velocity Measurements

We have already described some of the potential problems with the vertical velocity measurements with regard to the effect of small-scale variability on the representativeness of the measurements. In addition, we need to determine if the measurements can be used in model initializations in some way. Verifying model output with the vertical velocities is possible, but it may be that the implied divergence information can be used to generate more realistic vertical velocities at an earlier stage in the model run. The profile of vertical velocity can also be indicative of the latent heating associated with convection. Such information would be useful in parameterizing the heating and momentum fluxes generated by clouds. The errors introduced by the different types of scatter and by the effects of precipitation need to be determined more accurately in the future so that we can make the best use of the vertical velocity information.

(d) Usefulness of Small-Scale Turbulence Parameter Measurements

There is still disagreement about the dependence of the reflectivity and spectral width on the turbulent dissipation rate, although the work of Hocking (1983) has served to clarify a number of these issues. These small-scale fluxes can be extremely important in certain dynamical situations and can be potentially important in improving parameterizations of subgrid scale motions in numerical models. However, more comparisons between radar-derived values and observed quantities are needed to gain confidence in the turbulence data that can be obtained from the radar measurements. Also, Hocking et al. (1986) have shown that the spectral width measurements will be strongly contaminated by beam broadening and shears for any typical flows within the troposphere. We need to determine if other radar techniques can alleviate this problem and provide comparable information in a different way.

(e) Usefulness of Momentum Flux

The momentum fluxes measured by the Vincent-Reid (1983) technique appear to have a great potential for improving the parameterizations of small-scale dynamics used in virtually all of the forecast models. Again, the representativeness of fluxes measured at a single location will have to be determined. The possibility of updating the parameterizations based on flux-measurement input at initialization time should be explored.

(f) Advantages of Various Radar Techniques

So far, all the operational profiler applications have used the Doppler technique which involves two or more beams pointed in off-vertical directions. The combination of the line-of-sight velocities measured in the various beams produces the wind components. Alternative methods for measuring the winds include the spaced antenna method and the interferometer technique. The spaced antenna method has already been tested sufficiently so that we know that it can be used routinely. There are even various advantages of the technique for certain applications. The interferometer technique has not been tested extensively and its operational potential is unknown, but it provides some possibilities for measuring small scale structure in the flow that is impossible with other techniques, at least in the simplified implementations typical of the operational profilers.

REFERENCES

- Anthes, R. A., 1983: Regional models of the atmosphere in middle latitudes. *Mon. Wea. Rev.*, **111**, 1306-1335.
- Augustine, J. A., and E. J. Zipser, 1987: The use of wind profilers in a mesoscale experiment. *Bull. Amer. Meteor. Soc.*, **68**, 4-17.
- Blumen, W., 1972: Geostrophic adjustment. *Rev. Geophys. Space Phys.*, **10**, 485-528.
- Brown, P. S., Jr., and G. D. Robinson, 1979: The variance spectrum of tropospheric winds over Eastern Europe. *J. Atmos. Sci.*, **36**, 270-286.
- Clark, W. L., J. L. Green, and J. M. Warnock, 1986: The use of a vertical beam clear-air Doppler radar to measure horizontal divergence of the wind field. *Preprint Volume, 23rd Conference on Radar Meteorology*, American Meteorological Society, 38-40.
- Cornish, C. R., and M. F. Larsen, 1984: Use of the VAD technique and measurements of momentum flux in the stratosphere at Arecibo. *Handbook for MAP*, **14**, 208-210.
- Ecklund, W. L., D. A. Carter, and B. B. Balsley, 1988: A UHF wind profiler for the boundary layer: Brief description and initial results. *J. Atmos. Ocean. Tech.*, **5**, 432-441.

- Frisch, A. S., B. L. Weber, R. G. Strauch, D. A. Merritt, and K. P. Moran, 1986: The altitude coverage of the Colorado wind profilers at 50, 405, and 915 MHz. *J. Atmos. Ocean. Tech.*, **3**, 680-692.
- Fukao, S., T. Sato, N. Yamasaki, R. M. Harper, and S. Kato, 1982: Winds measured by a UHF Doppler radar and rawinsondes: Comparisons made on twenty-six days (August-September 1977) at Arecibo, Puerto Rico. *J. Appl. Meteor.*, **21**, 1357-1363.
- Fukao, S., T. Sato, T. Tsuda, S. Kato, M. Inaba, and I. Kimura, 1988: VHF Doppler radar determination of the momentum flux in the upper troposphere and lower stratosphere: Comparison between the three- and four-beam methods. *J. Atmos. Ocean. Tech.*, **5**, 57-69.
- Gage, K. S., 1988: The structure and dynamics of the free atmosphere as observed by VHF/UHF radar. To appear in *The Battan Memorial Volume on Radar Meteorology*, American Meteorological Society, Boston, Massachusetts.
- Gage, K. S., and J. L. Green, 1982a: A technique for determining the temperature profile from VHF radar observations. *J. Appl. Meteor.*, **21**, 1146-1149.
- Gage, K. S., and J. L. Green, 1982b: An objective method for determination of tropopause height from VHF radar observations. *J. Appl. Meteor.*, **21**, 1150-1154.
- Gage, K. S., and G. D. Nastrom, 1985: Relationship of precipitation to vertical motion observed directly by a VHF wind profiler during a spring upslope storm near Denver, Colorado. *Bull. Amer. Meteor. Soc.*, **66**, 394-397.
- Gage, K. S., W. L. Ecklund, A. C. Riddle, and B. B. Balsley, 1986: Objective tropopause height determination using low-resolution VHF radar observations. *J. Atmos. Ocean. Tech.*, **3**, 248-254.
- Gage, K. S., J. R. McAfee, W. G. Collins, D. Söderman, H. Böttger, A. Radford, and B. Balsley, 1988: A comparison of winds observed at Christmas Island using a wind-profiling Doppler radar with NMC and ECMWF analyses. *Bull. Amer. Meteor. Soc.*, **69**, 1041-1046.
- Gal-Chen, T., 1988: A theory for the retrievals of virtual temperature from remote measurements of horizontal winds and thermal radiation. *Mon. Wea. Rev.*, **116**, 1302-1319.
- Green, J. L., K. S. Gage, T. E. VanZandt, W. L. Clark, J. M. Warnock, and G. D. Nastrom, 1988: Observations of vertical velocity over Illinois by the Flatland radar. *Geophys. Res. Lett.*, **15**, 269-272.
- Hocking, W. K., 1983: On the extraction of atmospheric turbulence parameters from radar backscatter Doppler spectra - I. Theory. *J. Atmos. Terr. Phys.*, **45**, 89-102.
- Hocking, W. K., R. Rülster, and P. Czechowsky, (1986): Absolute reflectivities and aspect sensitivities of VHF radio wave scatterers measured with the SOUSY radar. *J. Atmos. Terr. Phys.*, **48**, 131-

144.

- Hogg, D. C., M. T. Decker, F. O. Guiraud, K. B. Earnshaw, D. A. Merritt, K. P. Moran, W. B. Sweezy, R. G. Strauch, E. R. Westwater, and C. G. Little, 1983: An automatic profiler of the temperature, wind, and humidity in the troposphere. *J. Atmos. Ocean. Tech.*, **22**, 807-831.
- Hoke, J. E., and R. A. Anthes, 1976: The initialization of numerical models by a dynamic-initialization technique. *Mon. Wea. Rev.*, **104**, 1551-1556.
- Jasperson, W. H., 1982a: The limiting accuracy of wind profiles obtained by tracking rising balloons. *J. Appl. Meteor.*, **21**, 816-822.
- Jasperson, W. H., 1982b: Mesoscale time and space wind variability. *J. Appl. Meteor.*, **21**, 831-839.
- Kuo, Y.-H., E. G. Donall, and M. A. Shapiro, 1987a: Feasibility of short-range numerical weather prediction using observations from a network of profilers. *Mon. Wea. Rev.*, **115**, 2402-2427.
- Kuo, Y.-H., D. O. Gill, and L. Cheng, 1987: Retrieving temperature and geopotential fields from a network of wind profiler observations. *Mon. Wea. Rev.*, **115**, 3146-3165.
- Larsen, M. F., and J. Röttger, 1982: VHF and UHF Doppler radars as tools for synoptic research. *Bull. Amer. Meteor. Soc.*, **63**, 996-1008.
- Larsen, M. F., and J. Röttger, 1983: Comparison of tropopause height and frontal boundary locations based on radar and radiosonde data. *Geophys. Res. Lett.*, **10**, 325-328.
- Larsen, M. F., and J. Röttger, 1985: Observations of frontal zone and tropopause structures with a VHF Doppler radar and radiosondes. *Radio Sci.*, **20**, 1223-1232.
- Larsen, M. F., and J. Röttger, 1988: The spaced antenna technique for radar wind profiling. Submitted to *J. Atmos. Ocean. Tech.*
- Larsen, M. F., J. Röttger, and T. S. Dennis, 1988: A comparison of operational analysis and VHF wind profiler vertical velocities. *Mon. Wea. Rev.*, **116**, 48-59.
- Matuura, N., Y. Masuda, H. Inuki, S. Kato, S. Fukao, T. Sato, and T. Tsuda, 1986: Radio acoustic measurement of temperature profile in the troposphere and stratosphere. *Nature*, **323**, 426-428.
- Nastrom, G. D., and J. L. Green, 1986: VHF radar measurements of the vertical momentum flux. *Preprint Volume, 23rd Conference on Radar Meteorology*, American Meteorological Society, 45 Beacon Street, Boston, Massachusetts, 41-43.
- Nastrom, G. D., W. L. Ecklund, and K. S. Gage, 1985: Direct measurement of large-scale vertical velocities using clear-air Doppler radars. *Mon. Wea. Rev.*, **113**, 708-718.
- Rastogi, P. K., and J. Röttger, 1982: VHF radar observations of coherent reflections in the vicinity of the tropopause. *J. Atmos. Terr. Phys.*, **44**, 461-469.
- Ray, P. S., (ed.), 1986: *Mesoscale Meteorology and Forecasting*, American

Meteorological Society, Boston, Massachusetts.

- Rossby, C.-G., 1937: On the mutual adjustment of pressure and velocity distributions in certain simple current systems. *J. Mar. Res.*, 1, 15-28.
- Röttger, J., 1979: VHF radar observations of a frontal passage. *J. Appl. Meteor.*, 18, 85-91.
- Röttger, J., 1983: The correlation of winds measured with a spaced antenna VHF radar and radiosondes. *Preprint Volume, 21st Conference on Radar Meteorology*, American Meteorological Society, Boston, Massachusetts, 97-99.
- Röttger, J., and R. A. Vincent, 1978: VHF radar studies of tropospheric velocities and irregularities using the spaced antenna technique. *Geophys. Res. Lett.*, 5, 917-920.
- Röttger, J., and M. F. Larsen, 1988: UHF/VHF radar techniques for atmospheric research and wind profiler applications. To appear in *The Battan Memorial Volume on Radar Meteorology*, American Meteorological Society, Boston, Massachusetts.
- Smythe, G. R., and D. S. Zrnic, 1983: Correlation analysis of Doppler radar data and retrieval of the horizontal wind. *J. Climate Appl. Meteor.*, 22, 297-311.
- Strauch, R. G., B. L. Weber, A. S. Frisch, C. G. Little, D. A. Merritt, K. P. Moran, and D. C. Welsh, 1987: The precision and relative accuracy of profiler wind measurements. *J. Atmos. Ocean. Tech.*, 4, 563-571.
- Sweezy, W. B., and E. R. Westwater, 1986: A comparison of methods for determining tropopause height from VHF radar observations. *J. Atmos. Ocean. Tech.*, 3, 324-332.
- Vincent, R. A., and I. M. Reid, 1983: HF Doppler measurements of mesospheric gravity wave momentum fluxes. *J. Atmos. Sci.*, 40, 1321-1333.
- Wakasugi, K., S. Fukao, S. Kato, A. Mizutani, and M. Matsuo, 1985: Air and precipitation particle motions within a cold front measured by the MU VHF radar. *Radio Sci.*, 20, 1233-1240.
- Wuertz, D. B., B. L. Weber, R. G. Strauch, A. S. Frisch, C. G. Little, D. A. Merritt, K. P. Moran, and D. C. Welsh, 1988: Effects of precipitation on UHF wind profiler measurements. *J. Atmos. Ocean. Tech.*, 5, 450-465.

INCOHERENT SCATTER RADAR OBSERVATIONS OF THE IONOSPHERE

Tor Hagfors

National Astronomy and Ionosphere Center
Cornell University, Ithaca, NY 14853

1. Introduction

Incoherent scatter radar (ISR) has become the most powerful means of studying the ionosphere from the ground. Many of the ideas and methods underlying the troposphere and stratosphere (ST) radars have been taken over from ISR. Whereas the theory of refractive index fluctuations in the lower atmosphere, depending as it does on turbulence, is poorly understood, the theory of the refractivity fluctuations in the ionosphere, which depend on thermal fluctuations, is known in great detail. The underlying theory is one of the most successful theories in plasma physics, and allows for many detailed investigations of a number of parameters such as electron density n_e , electron temperature T_e , ion temperature T_i , electron mean velocity v_e , ion mean velocity V_i as well as parameters pertaining to composition, neutral density and others.

Here we shall review the fundamental processes involved in the scattering from a plasma undergoing thermal or near thermal fluctuations in density. We shall relate the fundamental scattering properties of the plasma to the physical parameters characterizing it from first principles. We shall not discuss the observation process itself, as the observational principles are quite similar whether they are applied to a neutral gas or a fluctuating plasma. These observational principles are dealt with in other ISAR presentations.

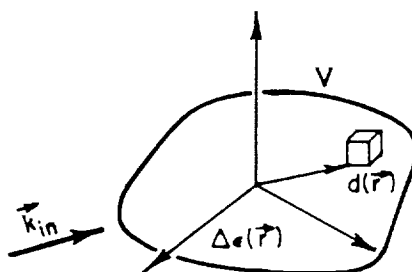


Figure 1. Volume element $d(\vec{r})$ in volume V illuminated by plane wave.

2. Volume Scattering from Random Irregularities. Continuum

In the neutral atmosphere the scattering is derived from the following consideration:

With an incoming wave: $\vec{E}_0 e^{-i\vec{k}_{in} \cdot \vec{r}}$ [note that $\exp(i\omega_0 t)$ is understood] and a dielectric constant in medium:

$$\epsilon = \epsilon_0 + \Delta\epsilon(\vec{r}),$$

the polarization of the medium becomes:

$$\vec{P}(\vec{r}) = \Delta\epsilon(\vec{r}) \cdot \vec{E}_o \cdot e^{-i\vec{k}_{in} \cdot \vec{r}} \quad (2)$$

This oscillating polarization acts as an equivalent current:

$$\vec{j}(\vec{r}) = i\omega_o \vec{P}(\vec{r}) = i\omega_o \Delta\epsilon \vec{E}_o \cdot e^{-i\vec{k}_{in} \cdot \vec{r}}, \quad (3)$$

and the vector potential at a point far from volume V is:

$$\vec{A}(\vec{r}) \simeq \frac{\mu_0}{4\pi} \cdot \frac{i\omega_o \vec{E}_o}{|\vec{r}|} \int \Delta\epsilon(\vec{r}') e^{-i\vec{k}_{in} \cdot \vec{r}'} \cdot e^{-ik|\vec{r}-\vec{r}'|} d(\vec{r}') \quad (4)$$

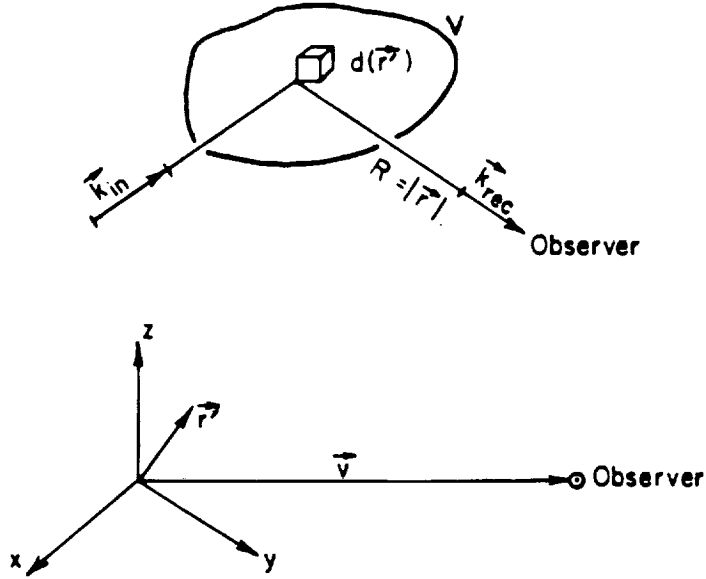


Figure 2. Scattering geometry to calculate vector potential at the observer.

with $|\vec{r} - \vec{r}'| \approx |\vec{r}| - \vec{n}_1 \cdot \vec{r}'$, where $\vec{n}_1 \approx \frac{\vec{k}_{rec}}{k}$

We obtain:

$$\vec{A}(\vec{r}) = \frac{\mu_0}{4\pi} \cdot \frac{i\omega_o \vec{E}_o}{|\vec{r}|} \cdot e^{-ik|\vec{r}|} \int_V \underbrace{\Delta\epsilon(\vec{r}') \cdot e^{-i\vec{r}' \cdot (\vec{k}_{in} - \vec{k}_{rec})}}_{\Delta\epsilon(\vec{k}_{in} - \vec{k}_{rec})} d(\vec{r}') \quad (5)$$

which means that the received field depends on the spatial Fourier component with wave vector $\vec{k} = \vec{k}_{in} - \vec{k}_{rec}$.

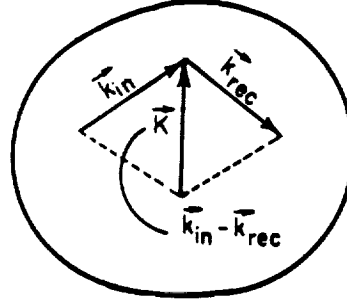


Figure 3. Relation between the wave vectors of the transmitted and revised waves and the spatial Fourier component of the dielectric fluctuation.

It is easy to show from this that for a plane incoming wave of flux (Poynting vector magnitude) S_{in} , the flux at the receiver is:

$$S_{rec} = \frac{\omega_o^4 \mu_0^2}{(4\pi)^2 R_1^2} \sin^2 \chi |\Delta \epsilon(\vec{k}_{in} - \vec{k}_{rec})|^2 S_{in} \quad (6)$$

$$\mu_0 = 4\pi \cdot 10^{-7} \text{ Henry/m}$$

$\sin \chi$ = polarization factor, see next section.

R_1 = distance between scattering volume and observer

In a plasma

$$\Delta \epsilon(\vec{r}) = -\frac{\Delta n(\vec{r}) \cdot e^2}{m \cdot \omega_o^2} \quad (7)$$

Where:

$\Delta n(\vec{r})$ = electron density fluctuation

$e = 1.602 \cdot 10^{-19}$ Coulomb = elementary charge

$m = 9.110 \cdot 10^{-31}$ kg = electronic mass

and one obtains by substitution:

$$S_{rec} = \left(\frac{\omega_o}{R_1}\right)^2 |\Delta n(\vec{k}_{in} - \vec{k}_{rec})|^2 \cdot \sin^2 \chi \cdot S_{in} \quad (8)$$

where r_o is the classical radius of the electron defined by

$$r_o = \frac{e^2}{4\pi mc^2 \cdot \epsilon_o}$$

$$\epsilon_o = 8.854 \cdot 10^{-12} \text{ F/m}$$

$$c = 2.998 \cdot 10^8 \text{ m/s}$$

3. Scattering from Individual Electrons, Discrete Particles

Let us recapitulate the derivation of the scattering by a free electron of electromagnetic waves impinging on it. It was originally thought that the scattering from a plasma could be considered a super-position of scattering from individual free electrons and that the strength and spectral broadening can be used to determine density and electron temperature. For the ionospheric plasma and for the frequency used in such scatter experiments, it turned out that the scattering could not usually be considered that simply and that the actual situation was more favorable from an experimental point of view. Nevertheless, even with the more complex theory of interacting electrons the scattering from an individual free electron forms an important and essential ingredient.

Assume as in Section 2 that the electric field set up at the position occupied by the electron is:

$$\vec{E}(t) = \vec{E}_o \cdot e^{+i\omega_o t} \quad (9)$$

where E_o is a complex electric field amplitude which allows for an arbitrary polarization. When we assume that $\omega_o \gg \Omega_e$, where Ω_e is the angular gyrofrequency of an electron, the equation of motion of the electron becomes:

$$-\vec{E}_o e^{+i\omega_o t} = m \cdot \ddot{\vec{v}}/e \quad (10)$$

Solving for $\vec{v}(t)$ with the substitution $\vec{v}(t) = \vec{v}_o e^{+i\omega_o t}$ one obtains:

$$\vec{v}_o = +i \frac{e}{m\omega_o} \vec{E}_o \quad (11)$$

Note that we have neglected the spatial variation of the external electric field and the fact that the electron moves in this field. We have also ignored the force caused by the motion of the electron in the magnetic field of the incoming wave. Both of these effects could contribute to a ponderomotive force which we ignore. We also note that the motion of the electron is considered undamped. This cannot be strictly true since the electron, even without collisions, is re-radiating because of the oscillation and hence, must experience damping.

The current density associated with the motion of this electron becomes:

$$\vec{j}(\vec{r}, t) = -e\vec{v}(t) \delta[\vec{r} - \vec{r}_e(t)] \quad (12)$$

where $\vec{r}_e(t)$ is the position of the electron and where $\delta(\vec{r})$ is a spatial deltafunction. With such an oscillating current at the origin we obtain as in the previous section:

$$\vec{A}(\vec{r}, t) = -i \frac{\mu_o e^2}{4\pi m \omega_o} \vec{E}_o e^{+i(\omega_o t - \vec{k} \cdot \vec{r})} \frac{1}{R_1} \quad (13)$$

The position of the observer \vec{r} may vary with time due to motion of the electron and we must substitute when necessary:

$$\vec{r} = \vec{r}'(t) = \vec{r} \left(t - \frac{|\vec{r}'|}{c} \right)$$

where $\vec{r}'(t)$ is the radius vector describing the position of the electron relative to the position of the observer at time t .

The Poynting flux vector at the receiver due to the radiation from this electron becomes:

$$S_{rec} = \frac{1}{2} \eta |\vec{H}|^2 = \frac{1}{2} \eta \left(\frac{e^2}{4\pi m \omega_o} \right)^2 \frac{|\vec{k}_{rec} \times \vec{E}_o|^2}{R_1^2} \quad (14)$$

where $\eta = \sqrt{\mu_o/\epsilon_o} = 376.7$ ohms. Introducing the polarization angle χ through

$$\sin \chi = \frac{|\vec{k}_{rec} \times \vec{E}_o|}{|\vec{k}_{rec}| \cdot |\vec{E}_o|} \quad (15)$$

and the power density incident on the electron, S_{in} by:

$$S_{in} = |E_o|^2 / \eta \cdot \frac{1}{2} \quad (16)$$

we obtain:

$$S_{rec} = (r_o/R_1)^2 \cdot \sin^2 \chi \cdot S_{in} = 10^{-28} \sin^2 \chi \cdot S_{in} \quad (17)$$

The usual radar cross section σ_s is defined by:

$$\sigma_s = 4\pi R_1^2 \cdot \frac{S_{rec}}{S_{in}} = 4\pi r_o^2 \sin^2 \chi \simeq 10^{-28} \sin^2 \chi (m^2) \quad (18)$$

In calculating the single electron scattering we have implicitly assumed that the driving electric field is linearly polarized and that the angle between the field and the direction of the receiver is χ . In actual fact the electron is often oscillating in two linearly polarized fields of arbitrary relative phase and amplitude. When this is the case the interpretation of $\sin^2 \chi$ is more complex and the amount of scattered energy available may only be received provided the receiver is properly "matched" to the scattered wave.

Consider a plane wave propagating along a positive z -axis. The complex amplitude \vec{E}_o may then be represented as;

$$\vec{E}_o = \xi_o (\cos \beta \cdot \vec{e}_x + e^{i\delta} \sin \beta \cdot \vec{e}_y) = \xi_o \begin{Bmatrix} \cos \beta \\ \sin \beta \cdot e^{i\delta} \end{Bmatrix} = \xi_o \vec{p} \quad (19)$$

A linear polarization along the x -axis corresponds to:

$$\vec{p} = \begin{Bmatrix} 1 \\ 0 \end{Bmatrix}$$

and along the y -axis:

$$\vec{p} = \begin{Bmatrix} 0 \\ 1 \end{Bmatrix}$$

Circular polarization is represented by:

$$\vec{p} = \frac{1}{\sqrt{2}} \begin{Bmatrix} 1 \\ -i \end{Bmatrix} \text{ right circular}$$

$$\vec{p} = \frac{1}{\sqrt{2}} \begin{Bmatrix} 1 \\ +i \end{Bmatrix} \text{ left circular}$$

It follows that the scattered field at the receiver can be expressed as follows:

$$\vec{E}_r(\vec{r}, t) = \frac{r_o}{R_1} \vec{n}_1 \times (\vec{n}_1 \times \vec{E}_o) e^{-i(\omega_o t - \vec{k}_{rec} \cdot \vec{r})} \quad (20)$$

where \vec{n}_1 is a unit vector along the direction of the scattered wave. In order to specify the polarization both of the transmitted and scattered wave we introduce the following two coordinate systems:

A. For the transmitted wave:

$$\vec{e}_z = \vec{n}_o = \vec{k}_{in}/|\vec{k}_{in}|$$

$$\vec{e}_y = \text{unit vector normal to plane defined by } \vec{k}_{in}; \vec{k}_{rec}$$

$$\vec{e}_x = \text{normal to both } \vec{e}_y \text{ and } \vec{e}_z \text{ in a right handed coordinate system.}$$

B. For the scattered wave:

$$\vec{e}_z = \vec{n}_1 = \vec{k}_{rec}/|\vec{k}_{rec}|$$

$$\vec{e}'_y = \vec{e}_y$$

$$\vec{e}'_x = \text{normal to } \vec{e}'_y \text{ and } \vec{e}_z \text{ in right handed coordinate system.}$$

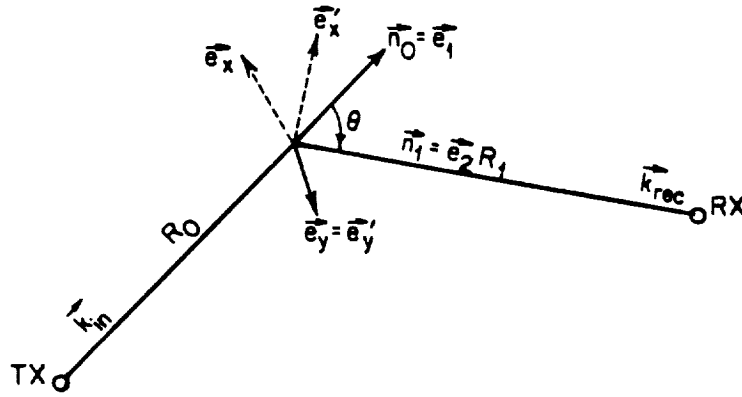


Figure 4. Relationship between polarization of incoming and scattered waves.

In terms of these two coordinate systems we may write:

$$\begin{Bmatrix} E'_{rx} \\ E'_{ry} \end{Bmatrix} = -\frac{r_0}{R_1} \xi_0 \begin{Bmatrix} \cos\theta & 0 \\ 0 & 1 \end{Bmatrix} \begin{Bmatrix} \cos\beta \\ \sin\beta \cdot e^{i\delta} \end{Bmatrix} e^{i(\omega_0 t - \vec{k}_{rec} \cdot \vec{r})}$$

or:

$$\xi_{r0} \begin{Bmatrix} \cos\beta' \\ \sin\beta' e^{i\delta'} \end{Bmatrix} = -\frac{r_0}{R_1} \begin{Bmatrix} \cos\theta & 0 \\ 0 & 1 \end{Bmatrix} \begin{Bmatrix} \cos\beta \\ \sin\beta e^{i\delta} \end{Bmatrix} \xi_0 \quad (21a)$$

This determines the relationship of the two fields. In particular we note that

$$\sin^2 \chi = \sin^2 \beta + \cos^2 \beta \cdot \cos^2 \theta \quad (22)$$

where θ is the angle between \vec{n}_0 and \vec{n}_1 .

It is now clear that one may express the relationship between scattered and incident electric field amplitudes as:

$$\xi_{r0} \vec{p}' = -\frac{r_0}{R_1} \xi_0 \Psi \vec{p} \quad (21b)$$

where:

$$\Psi = \begin{Bmatrix} \cos\theta & 0 \\ 0 & 1 \end{Bmatrix} (\text{geometry})$$

$$\vec{p} = \begin{Bmatrix} \cos\beta \\ \sin\beta e^{i\delta} \end{Bmatrix} (\text{transmitter})$$

$$\vec{p}' = \begin{Bmatrix} \cos\beta' \\ \sin\beta' e^{i\delta'} \end{Bmatrix} (\text{receiver})$$

4. The Scattering from a Collection of Electrons

When many scattering electrons are present inside a volume V rather than a single one the observed field is given by the sum

$$\vec{E}_r = -\frac{r_0}{R_1} \xi_0 \Psi \vec{p} \sum_{p=1}^N e^{i\vec{k} \cdot \vec{r}_p(t)} \quad (23)$$

where N is the total number of electrons within the volume V , where the polarization and geometry of all the electrons are the same so that we do not have to sum over different $\Psi \vec{p}'$'s. The previous distance between a scattering electron and the observer, R_1 , now represents the distance from an origin within the scattering volume and $\vec{r}_p(t)$ represents the position of electron number p within this volume. The vector $\vec{k} = \vec{k}_{rec} - \vec{k}_{in}$ comes about as follows:

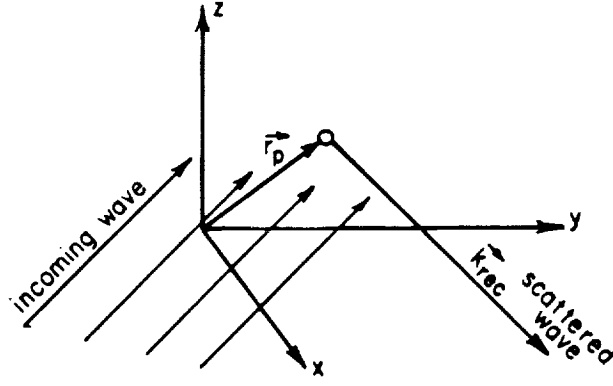


Figure 5. Scattering from electron at \vec{r}_p .

In the scattering volume, apart from a phase factor, the incoming wave has the form:

$$\vec{E}_{in}(\vec{r}, t) = \xi_o \vec{p} \cdot e^{i(\omega_o t - \vec{r} \cdot \vec{k}_{in})}$$

so that the field at electron number p is:

$$\vec{E}_{in}(\vec{r}_p, t) = \xi_o \vec{p} \cdot e^{i(\omega_o t - \vec{k}_{in} \cdot \vec{r}_p)} \quad (24)$$

From the previous section the field at the receiver due to electron p becomes

$$\vec{E}_r = -\frac{r_o}{R_1} \xi_o \Psi \vec{p} e^{i(\omega_o t - \vec{k}_{in} \cdot \vec{r}_p)} \cdot e^{-i\vec{k} R_{1p}} \quad (25)$$

If the distance from the receiver to the origin in the scattering volume is R_1 we have:

$$R_{1p} \approx R_1 - \vec{k}_{rec} \cdot \vec{r}_p$$

Substituting this into (25), ignoring an irrelevant phase factor ($e^{i\vec{k} R_1}$) and summing over all electrons gives eqn. (23) provided

$$\vec{k} = \vec{k}_{rec} - \vec{k}_{in}, \quad (26)$$

We next imagine the particle density to be expanded in a spatial Fourier series through:

$$n(\vec{r}, t) = \frac{1}{V} \sum_{\vec{k}} n(\vec{k}, t) e^{-i\vec{k} \cdot \vec{r}} \quad (27)$$

where

$$n(\vec{k}, t) = \int_V d(\vec{r}) n(\vec{r}, t) e^{+i\vec{k} \cdot \vec{r}} \quad (28)$$

Since the scattering electrons must be considered point particles at $\vec{r}_p(t)$, $p = 1, \dots, N$ the density is:

$$n(\vec{r}, t) = \sum_{p=1}^N \delta[\vec{r} - \vec{r}_p(t)]$$

with a spatial spectrum

$$n(\vec{k}, t) = \sum_{p=1}^N e^{+i\vec{k} \cdot \vec{r}_p(t)} = \sum_{p=1}^N n_p(\vec{k}, t) \quad (29)$$

A comparison with (23) shows that the observed scattered field from the electrons may be expressed as:

$$\vec{E}_r = -\frac{r_o}{R_1} \xi_o \Psi \vec{p} \cdot e^{i\omega_o(t-R_1/c)} \cdot n(\vec{k}, t) \quad (30)$$

The complex amplitude of the received signal is

$$\begin{aligned} A_r(t) &= \left| \frac{r_o}{R_1} \xi_o \Psi \vec{p} \right| \cdot n(\vec{k}, t) \\ &= A_o \cdot n(\vec{k}, t) \end{aligned} \quad (31)$$

$$\begin{aligned} \langle A_r^*(t) A_r(t+\tau) \rangle &= A_o^2 \langle n^*(\vec{k}, t) n(\vec{k}, t+\tau) \rangle \\ &= A_o^2 n_o \cdot V \langle n_p^*(\vec{k}, t) n_p(\vec{k}, t+\tau) \rangle \end{aligned} \quad (32)$$

where $\langle \dots \rangle$ denotes ensemble average, where individual particles are assumed to be independent, where n_o is the mean electron density and where:

$$\langle n_p^*(\vec{k}, t) n_p(\vec{k}, t+\tau) \rangle = \langle e^{i\vec{k} \cdot [\vec{r}_p(t+\tau) - \vec{r}_p(t)]} \rangle = \rho_p(\vec{k}, \tau) \quad (33)$$

is the autocorrelation of density fluctuations associated with a single electron.

Similarly, the power spectrum received is determined from the Wiener-Khinchine's theorem, and

$$P_{rec}(\omega) = n_o \cdot V \cdot P_{oe} \Phi_p(\vec{k}, \omega) \quad (34)$$

where P_{oe} is the power scattered by an individual electron under the same geometrical and external conditions and where:

$$\begin{aligned} \Phi_p(\vec{k}, \omega) &= \int_{-\infty}^{+\infty} \langle n_p^*(\vec{k}, t) n_p(\vec{k}, t+\tau) \rangle e^{-i\omega\tau} d\tau = \\ &= \int_{-\infty}^{+\infty} \langle e^{i\vec{k} \cdot [\vec{r}_p(t+\tau) - \vec{r}_p(t)]} \rangle \cdot e^{-i\omega\tau} d\tau \\ &= \int_{-\infty}^{+\infty} \rho_p(\vec{k}, \tau) e^{-i\omega\tau} d\tau \end{aligned} \quad (35)$$

We often need the integral:

$$G(\vec{k}, \omega) = \int_0^\infty \rho_p(\vec{k}, \tau) e^{-i\omega\tau} d\tau \quad (36)$$

With this function the spectrum of a particle becomes

$$P_{rec}(\omega) = n_o \cdot V \cdot P_{oe} \Phi_p(\vec{k}, \omega)$$

$$\Phi_p(\vec{k}, \omega) = 2 \cdot \text{Re}[G(\vec{k}, \omega)]. \quad (37)$$

It will become apparent in the next two sections that both the plasma response to an electric field as well as the thermal driving force can be described on the basis of the motion of non-interacting particles. It is, therefore, useful to study their motion in some detail.

We assume that the static magnetic field \vec{B}_0 is directed along the z -axis. It will be convenient to introduce "polarized" coordinates to describe the position of a particle:

$$\begin{array}{ll} \text{Cartesian:} & \text{Polarized:} \\ \vec{r} = \{x, y, z\} & \vec{r} = \{r_{+1}, r_{-1}, r_0\} \end{array} \quad (38)$$

The relationship between the two descriptions is

$$\begin{array}{ll} r_1 = \frac{1}{\sqrt{2}}(x + iy) & x = \frac{1}{\sqrt{2}}(r_1 + r_{-1}) \\ r_{-1} = \frac{1}{\sqrt{2}}(x - iy) & y = \frac{1}{\sqrt{2}}(r_1 - r_{-1}) \\ r_0 = z & z = r_0 \end{array} \quad (39)$$

The advantage of these polarized coordinates becomes evident when we state the equation of free motion of a particle:

$$\begin{aligned} \frac{dv_\alpha}{dt} &= -i\alpha\Omega v_\alpha & (\alpha = \pm 1, 0) \\ \Omega &= \frac{qB_0}{m} \end{aligned} \quad (40)$$

where q and m are the charge and the mass of the particle (electron or ion) respectively. From this we determine the relationship between the (past) velocity at time $t' = t - \tau$ in terms of the present velocity (at t)

$$\vec{v}(t - \tau) = \vec{\Gamma}(\tau) \vec{v}(t) \quad (41)$$

where $\vec{\Gamma}(\tau)$ is a diagonal matrix with elements.

$$[\vec{\Gamma}(\tau)]_{\alpha\alpha} = e^{i\alpha\Omega\tau} = g_\alpha(\tau) \quad (42)$$

The past particle position can be determined similarly in terms of present position and present velocity through

$$\vec{r}(t - \tau) = \vec{r}(t) - \Gamma(\tau) \vec{v}(t) \quad (43)$$

where $\Gamma(\tau)$ is a diagonal matrix which determines the particle helical motion. The elements are given by

$$[\Gamma(\tau)]_{\alpha\alpha} = \frac{e^{i\alpha\Omega\tau} - 1}{i\alpha\Omega} = g_\alpha(\tau) \quad (\alpha = \pm 1, 0) \quad (44)$$

The single particle autocorrelation, eqn. (33) now becomes:

$$\rho_p(\vec{k}, \tau) = \langle e^{i\vec{k} \cdot \vec{r}} \rangle \quad (45)$$

where

$$a_\alpha = k_\alpha \cdot g_{-\alpha} \quad (46)$$

The actual form of $\rho_p(k, \tau)$ depends on the statistical distribution of velocities, the magnetic field strength and the angle γ between \vec{k} and the magnetic field direction.

For a Maxwellian velocity distribution:

$$f_o(\vec{v}) = (2\pi)^{-3/2} v_{th}^{-3} e^{-v^2/2v_{th}^2} \quad (47)$$

where

$$v_{th}^2 = T/m$$

T = kinetic temperature (in energy units)

we obtain:

$$\rho_p(\vec{k}, \tau) = e^{-\frac{1}{2}v_{th}^2|\vec{k}|^2} - (kR)^2 \left\{ \left(\frac{\Omega\tau}{2} \right)^2 \cos^2\gamma + \sin^2\left(\frac{\Omega\tau}{2} \right) \sin^2\gamma \right\} \quad (48)$$

$= e$

The gyration radius R is defined as:

$$R = \frac{\sqrt{2}v_{th}}{\Omega} \quad (49)$$

It equals the ratio of the r.m.s. orbital velocity and the angular gyration frequency.

We note that for weak magnetic fields and arbitrary γ , or for $\vec{k} \parallel \vec{B}_o$ (i.e. $\gamma = 0$) and arbitrary magnetic field strength the autocorrelation becomes

$$\rho_p(\vec{k}, \tau) \rightarrow e^{-\frac{1}{2}(kv_{th}\tau)^2} \quad (50)$$

When \vec{k} is exactly perpendicular to the magnetic field, the autocorrelation for the plasma-density becomes periodic with period $T = 2\pi/\Omega$. The depth of modulation increases with R and decreases with the scale of the density fluctuation $\Lambda = 2\pi/k$, see Figure 6.

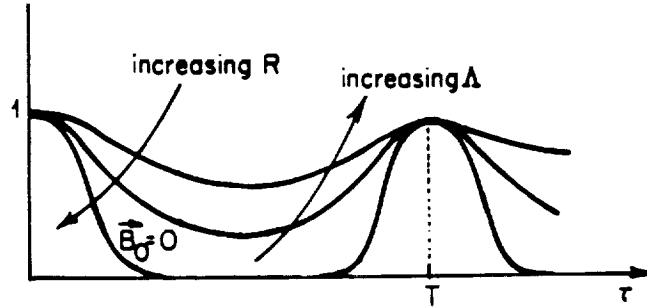


Figure 6. Autocorrelation of density fluctuation when $\vec{k} \perp \vec{B}_o$.

For intermediate angles between k and B_0 , the autocorrelation of the density fluctuation can be regarded a product of two factors, see (48).

$$\begin{aligned} \text{A)} \quad & e^{-(kR)^2 \left(\frac{\Omega\tau}{2}\right)^2 \cos^2\gamma} \\ \text{B)} \quad & e^{-(kR)^2 \sin^2\left(\frac{\Omega\tau}{2}\right) \cdot \sin^2\gamma} \end{aligned}$$

which are sketched in Figure 7.

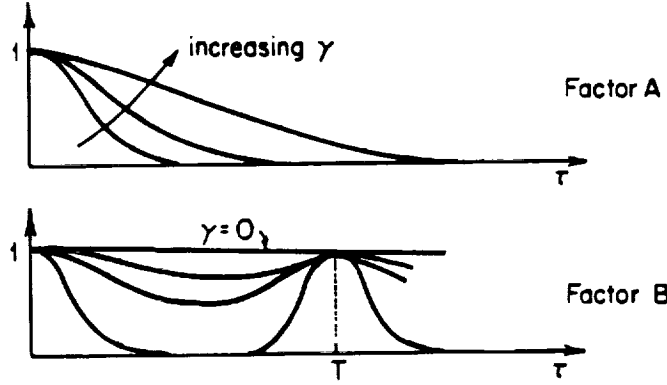


Figure 7. The two factors which in the autocorrelation of in the density fluctuation of non-interacting particles.

The spectral function $\phi(\vec{k}, \omega)$ becomes (see 37):

$$\phi_p(\vec{k}, \omega) = 2 \operatorname{Re} \left\{ G_p(\vec{k}, \omega) \right\} \quad (51)$$

where

$$G_p(\vec{k}, \omega) = \int_0^\infty e^{-\frac{1}{2} v_{th}^2 |\vec{a}_p|^2 - i\omega\tau} d\tau \quad (52)$$

The next section introduces particle interaction through a self-consistent electric field.

5. Response to a Field Particle. Electrostatic Interactions.

We now introduce particle correlations in the plasma components (electrons, various types of ions) by considering the particles smeared out into a continuum and by assessing the response of this continuum to each discrete particle separately.

The plasma response to an electric field $\vec{E}(\vec{r}, t)$ can be obtained by solving the Vlasov equation to first order in $\delta n(\vec{r}, \vec{v}, t)$ and $\vec{E}(\vec{r}, t)$. The perturbation solution for any of the species

is given by (see Appendix A)

$$\delta n(\vec{r}, \vec{v}, t) = -\frac{n_o q}{m} \int_{-\infty}^t \vec{E}(\vec{r}', t') \frac{\partial f'_o}{\partial \vec{v}'} dt' \quad (53)$$

Here $\vec{E}(\vec{r}, t)$ is a small electric field which we shall later assume set up by the fluctuating charges, often referred to as the self-consistent field. The integration is carried out along the unperturbed particle orbits which were studied previously. This is indicated by the primed quantities in the integrand.

We make the following substitutions:

$$\begin{aligned} t' &= t - \tau \\ \vec{E}(\vec{r}', t') &= \frac{1}{V} \sum_{\vec{k}} \vec{E}(\vec{k}, t - \tau) e^{-i\vec{k} \cdot \vec{r}'} e^{+i\vec{k} \cdot \Gamma(\tau) \vec{v}} \\ \frac{\partial f'_o}{\partial \vec{v}'} &= \dot{\Gamma}(\tau) \frac{\partial f_o(v')}{\partial \vec{v}} \end{aligned} \quad (54)$$

Integrating over all possible \vec{v} we obtain the induced density fluctuation:

$$n(\vec{k}, t) = \frac{n_o q}{m} \int_0^\infty d\tau \vec{E}(\vec{k}, t - \tau) \int d(\vec{v}) \dot{\Gamma}(\tau) \frac{\partial f_o(\vec{v}')}{\partial \vec{v}} e^{i\vec{k} \cdot \Gamma(\tau) \vec{v}} \quad (55)$$

We now take the Fourier transform with respect to time, and relate the electric field to the total electric charge fluctuation $Q(\vec{k}, \omega)$ by:

$$\vec{E}(\vec{k}, \omega) = \frac{i\vec{k}}{\epsilon_o k^2} Q(\vec{k}, \omega) \quad (56)$$

We, therefore, only include longitudinal electrostatic interactions. This is exact when there is no external magnetic field. When such a field is present the longitudinal and transverse modes are coupled and the electrostatic approximation breaks down particularly at very long wavelengths. In diagnostic experiments on the ionosphere only short wavelengths are used and the electrostatic approximation is adequate.

Substitution of (56) into (55) gives

$$n(\vec{k}, \omega) = -\frac{in_o q}{\epsilon_o m \cdot k^2} Q(\vec{k}, \omega) \int_0^\infty d\tau \cdot e^{-i\omega\tau} \int d(\vec{v}) \dot{\vec{a}}(\tau) \frac{\partial f_o}{\partial \vec{v}} e^{i\vec{a} \cdot \vec{v}} \quad (57)$$

For each of the species we now introduce

$$\frac{n_o q_\sigma^2}{\epsilon_o m_\sigma} = \omega_\sigma^2$$

and,

$$\chi_\sigma = +i \frac{\omega_\sigma^2}{k^2} \int_0^\infty d\tau e^{-i\omega\tau} \int d(\vec{v}) \dot{\vec{a}}_\sigma(\tau) \frac{\partial f_o}{\partial \vec{v}} e^{+i\vec{a}_\sigma \cdot \vec{v}} \quad (58)$$

Hence, we obtain for the fluctuation induced in species σ :

$$n_\sigma(\vec{k}, \omega) = -\frac{1}{q_\sigma} \chi_\sigma(\vec{k}, \omega) \cdot Q(\vec{k}, \omega) \quad (59)$$

We now have all the ingredients necessary to compute the density fluctuations in the plasma.

6. Calculation of the Fluctuation Spectrum

Let us now assume that we have a plasma of electrons and one type of singly charged ions.

For the electrons we substitute:

$$\begin{aligned}\omega_\sigma^2 &\rightarrow \omega_e^2 \\ q_\sigma &\rightarrow -e \\ m_\sigma &\rightarrow m \\ \vec{a}_\sigma &\rightarrow \vec{a}_e \\ f_{\sigma\sigma} &\rightarrow f_o \\ \chi_\sigma &\rightarrow \chi_e \\ n_\sigma &\rightarrow n\end{aligned}$$

For the ions we substitute:

$$\begin{aligned}\omega_\sigma^2 &\rightarrow \omega_i^2 \\ q_\sigma &\rightarrow +e \\ m_\sigma &\rightarrow M \\ \vec{a}_\sigma &\rightarrow \vec{a}_i \\ f_{\sigma\sigma} &\rightarrow F_o \\ \chi_\sigma &\rightarrow \chi_i \\ n_\sigma &\rightarrow N\end{aligned}$$

Consider first the fluctuation associated with a particular electron.

A. Intrinsic fluctuation $n_p(\vec{k}, \omega)$, See Section 4.

B. Induced electron fluctuation $n_e^1(\vec{k}, \omega) = +\frac{\chi_e}{e} Q_e(\vec{k}, \omega)$
(electron dressing on electron)

C. Induced ion fluctuation $N_e^1(\vec{k}, \omega) = -\frac{\chi_i}{e} Q_e(\vec{k}, \omega)$
(ion-dressing on electron)

The total charge fluctuation associated with this single electron is

$$Q_e(\vec{k}, \omega) = -e(n_p + \frac{\chi_e}{e} Q_e) + e(-\frac{\chi_i}{e} Q_e) \quad (60)$$

from which:

$$Q_e(\vec{k}, \omega) = \frac{-e \cdot n_p(\vec{k}, \omega)}{1 + \chi_e + \chi_i} \quad (61)$$

Since we are interested in the total electron-density fluctuation induced by electrons, not the charge fluctuation, we have:

$$\begin{aligned}n_e(\vec{k}, \omega) &= n_p(\vec{k}, \omega) + n_e^1(\vec{k}, \omega) \\ &= n_p(\vec{k}, \omega) + \frac{-\chi_e n_p(\vec{k}, \omega)}{1 + \chi_e + \chi_i} = \frac{n_p(\vec{k}, \omega)(1 + \chi_i)}{1 + \chi_e + \chi_i}\end{aligned} \quad (62)$$

The mean power spectrum associated with the thermal excitation by electrons is, therefore, found by averaging over the electron velocity distribution. If the velocity distribution is Maxwellian (47), then the independent electron spectrum is given by (51) and the result is

$$\langle |n_e(\vec{k}, \omega)|^2 \rangle = \frac{\langle |n_p(\vec{k}, \omega)|^2 \rangle |1 + \chi_i|^2}{|1 + \chi_e + \chi_i|^2} = \frac{\Phi_e(\vec{k}, \omega) |1 + \chi_i|^2}{|1 + \chi_e + \chi_i|^2} \quad (63)$$

where $\Phi_e(\vec{k}, \omega)$ is the independent single electron mean power spectrum discussed in Section 5.

Next consider the more important fluctuation arising from the thermal motion of an ion:

- A. Intrinsic fluctuation $N_p(\vec{k}, \omega)$, see Section 4.
- B. Induced electron fluctuation $n_i^1(\vec{k}, \omega) = +\frac{\chi_e}{\epsilon} Q_i(\vec{k}, \omega)$
(electron dressing on ion)
- C. Induced ion fluctuation $N_i^1(\vec{k}, \omega) = -\frac{\chi_i}{\epsilon} Q_i(\vec{k}, \omega)$

Solving for the charge fluctuation $Q_i(\vec{k}, \omega)$ we obtain:

$$Q_i(\vec{k}, \omega) = \frac{eN_p(\vec{k}, \omega)}{1 + \chi_e + \chi_i} \quad (64)$$

and the fluctuation induced in the electron density is given by:

$$n_i^1(\vec{k}, \omega) = \frac{\chi_e N_p(\vec{k}, \omega)}{1 + \chi_e + \chi_i} = n_i(\vec{k}, \omega) \quad (65)$$

The total electron density fluctuation in the plasma, therefore, can be expressed in terms of the independent particle spectra for electrons and ions and the response functions of the plasma as follows:

$$\begin{aligned} \langle |n(\vec{k}, \omega)|^2 \rangle &= [\langle |n_e(\vec{k}, \omega)|^2 \rangle + \langle |n_i(\vec{k}, \omega)|^2 \rangle] n_o V \\ &= \frac{|1 + \chi_i|^2 \Phi_e(\vec{k}, \omega) + |\chi_e|^2 \Phi_i(\vec{k}, \omega)}{|1 + \chi_e + \chi_i|^2} n_o V \end{aligned} \quad (66)$$

This is the form of the spectrum which has been widely used in the analysis of the incoherent scatter data, and which has remained valid for nearly 30 years!

Fluctuations in ion density, charge density, electric field, currents, etc. can all be obtained by an analogous procedure. An extension to a multi-ion plasma is relatively trivial. Different temperatures for electrons and ions are allowed.

Collisions have not been considered but can, in some cases, be taken into account by regarding the particle motion as a stochastic rather than a deterministic process, see Section 8.

7. Discussion of Results

The spectrum function contains the χ_e and χ_i together with Φ_e and Φ_i . All of these functions are related to the autocorrelation of independent particle fluctuations as follows:

Introduce for electrons (see 48):

$$\begin{aligned} \rho_o(\vec{k}, \tau) &= \rho_e(\vec{k}, \tau) = e^{-\frac{1}{2} v_{th}^2 |\vec{x}|^2} \\ v_{th}^2 &= \frac{T_e}{m} \\ a_{-\alpha} &= k_{-\alpha} \cdot g_{\alpha} \quad (g_{\alpha} \text{ computed with } \Omega = \Omega_e = -\frac{eB_o}{m}) \\ D_e^2 &= \frac{\epsilon_o T_e}{n_o \cdot e^2} \quad (\text{Debye length}) \end{aligned}$$

And for the ions:

$$\begin{aligned}\rho_o(\vec{k}, \tau) &= \rho_i(\vec{k}, \tau) = e^{-\frac{1}{2}v_{ih}^2|\vec{A}|^2} \\ V_{ih}^2 &= \frac{T_i}{M} \\ M &= \text{ionic mass} \\ A_{-\alpha} &= k_{-\alpha} \cdot g_{\alpha} \quad (g_{\alpha} \text{ computed with } \Omega = \Omega_i = +\frac{eB_o}{M}) \\ D_i^2 &= \frac{\varepsilon_o T_i}{n_o \cdot e^2}\end{aligned}$$

With these definitions we obtain:

$$\begin{aligned}\chi_e(\vec{k}, \omega) &= \left(\frac{1}{kD}\right)^2 [1 + \omega \cdot \text{Im} \{G_e(\vec{k}, \omega)\} - i\omega \cdot \text{Re} \{G_e(\vec{k}, \omega)\}] \\ \chi_i(\vec{k}, \omega) &= \left(\frac{1}{kD_i}\right)^2 [1 + \omega \cdot \text{Im} \{G_i(\vec{k}, \omega)\} - i\omega \cdot \text{Re} \{G_i(\vec{k}, \omega)\}]\end{aligned}\tag{67}$$

and:

$$\begin{aligned}\Phi_e(\vec{k}, \omega) &= 2 \cdot \text{Re} \{G_e(\vec{k}, \omega)\} \\ \Phi_i(\vec{k}, \omega) &= 2 \cdot \text{Re} \{G_i(\vec{k}, \omega)\}\end{aligned}$$

Here, from Section 4:

$$\begin{aligned}\text{Re} \{G_e(\vec{k}, \omega)\} &= \int_0^\infty e^{-\frac{1}{2}v_{ih}^2|\vec{A}|^2} \cos \omega \tau \, d\tau \\ \text{Im} \{G_e(\vec{k}, \omega)\} &= - \int_0^\infty e^{-\frac{1}{2}v_{ih}^2|\vec{A}|^2} \sin \omega \tau \, d\tau\end{aligned}$$

with similar definitions for the ions.

When there is no magnetic field or when $\vec{k}||B_o$ one obtains:

$$\omega \text{Re} \{G(\vec{k}, \omega)\} = \sqrt{\frac{\pi}{2}} Z e^{-\frac{1}{2}Z^2}\tag{68}$$

$$1 + \omega \text{Im} \{G(\vec{k}, \omega)\} = \begin{cases} 1 - Z^2 + \frac{1}{3}Z^4 - \frac{1}{15}Z^6 \dots Z \ll 1 \\ -\frac{1}{Z^3} - \frac{3}{Z^4} - \dots Z \gg 1 \end{cases}\tag{69}$$

where we have put

$$Z = \frac{\omega}{kv_{ih}} = \frac{v_\phi}{v_{ih}}$$

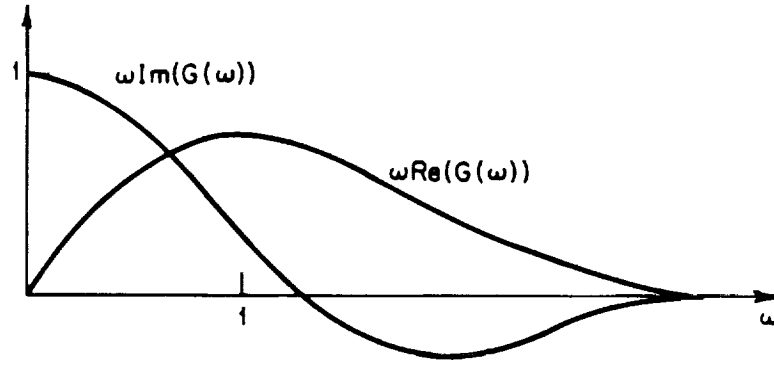


Figure 8. Plasma dispersion functions.

The only difference in the electronic and the ionic functions comes from the difference in thermal velocities.

For values of ω such that $\omega < kV_{th} \chi_i$ and χ_e are of the same order of magnitude.

However, $\Phi_e/\Phi_i \sim Re G_e/Re G_i \sim V_{th}/v_{th} \sim \sqrt{m/M}$

It follows that as long as kD_e and $kD_i \ll 1$ the dominant excitation of density waves at low frequencies must stem from the ion excitation, see the numerator of (66). In the denominator $\chi_e \simeq (\frac{1}{kD_e})^2$ whenever $\omega < kV_{th}$.

It follows that the low frequency part of the spectrum simplifies to:

$$\langle |n(\vec{k}, \omega)|^2 \rangle \approx 2n_0 V \frac{Re \{G_i(\omega, \vec{k})\}}{|1 + \frac{T_e}{T_i} [1 - i\omega G_i(\omega, \vec{k})]|^2} \quad (70)$$

For $T_e = T_i$ the factor multiplying $Re \{G_i(\omega, \vec{k})\}$ starts at $\frac{1}{4}$ at $\omega = 0$. As T_e/T_i increases above unity the depression near $\omega = 0$ increases and a near line spectrum develops, see Figure 9.

When kD_e and kD_i become much larger than unity, then the electronic part of the spectrum will dominate and we obtain a Gaussian spectrum with a width corresponding to the thermal motion of electrons.

A resonance occurs near the electron plasma frequency ω_e . This can be established by looking for a zero in the denominator of (66) near the plasma frequency. Since χ_i has vanished near ω_e we have:

$$1 + \left(\frac{1}{kD_e}\right)^2 \{1 + \omega Im(G_e) - i\omega Re(G_e)\} \equiv 0 \quad (71)$$

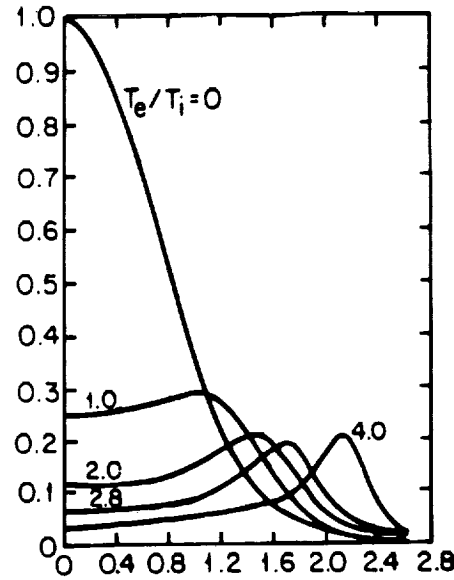


Figure 9. The ionic part of the fluctuation spectrum for various values of T_e/T_i .

As ω is close to ω_e the expansion of the plasma dispersion functions for large arguments can be used and we obtain

$$1 + \left(\frac{1}{kD_e} \right)^2 \left\{ -\frac{(kv_{th})^2}{\omega^2} - 3\frac{(kv_{th})^4}{\omega^4} \right\} = 0 \quad (72)$$

Where we have neglected the imaginary part. The solution is the familiar expression:

$$\omega^2 = \omega_e^2 [1 + 3(kD_e)^2] \quad (73)$$

the spectral peak associated with this oscillation is apparent in Figure 10. The peak can be strongly enhanced by the presence of photoelectrons or other suprathermal charged particles. The actual enhancement level involves the short-range Coulomb collisions as well as the angular distribution of the suprathermal electrons.

Let us now briefly turn to the effect of the magnetic field. As far as the ions are concerned the gyrofrequency Ω_i satisfies the relation:

$$kV_{th} \gg \Omega_i$$

This means that the correlation function

$$e^{-(kR)^2(\Omega_i^2)^2 \cos^2 \gamma}$$

becomes modulated with a periodicity $T_i = 2\pi/\Omega_i$.

In practice, however, these modulations are blurred out because of the diffusion of the ions away from their deterministic orbits. Very close to perpendicularity with the magnetic field (i.e. $\gamma = 90^\circ$) the spectrum may become very narrow if the radius of gyration of the

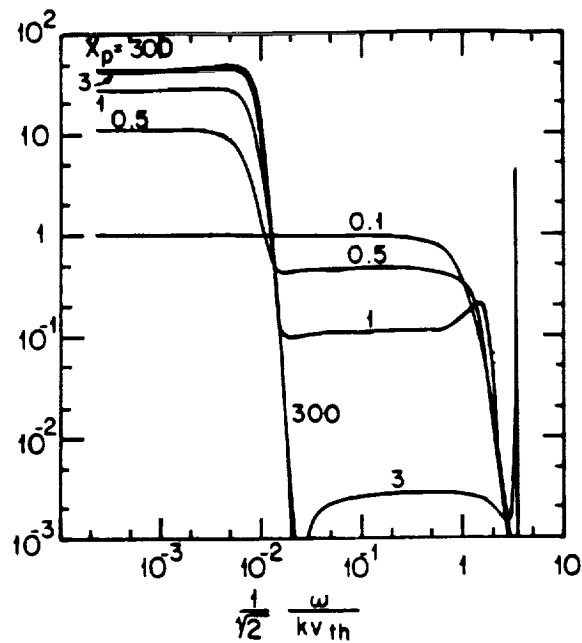


Figure 10. The fluctuation spectrum for $T_e/T_i = 1$ for varying Debye length D_e , $X_p = \frac{1}{\sqrt{2}} \cdot \frac{\omega_e}{kv_{th}}$.

electrons is so small that the electrons are prevented from participating in the fluctuations of the ions.

With a magnetic field the resonance associated with the plasma frequency becomes modified. When $\omega_e \gg \Omega_e$, when $kR < 1$ and when γ is not too close to 90° one obtains:

$$\omega^2 = \omega_p^2 [1 + 3(kD_e)^2] + \Omega_e^2 \cdot \sin^2 \gamma \quad (74)$$

An additional resonance, which can also be observed, arises because of the presence of the magnetic field. As $\gamma \rightarrow 90^\circ$:

$$\omega_h^2 = \Omega_e^2 (\omega_{pi}^2 + \Omega_i^2) / (\omega_e^2 + \Omega_e^2) \quad (75)$$

When $\omega_p^2 > \Omega_e^2$ one obtains:

$$\omega_h^2 = \Omega_e \Omega_i \quad (76)$$

which is sometimes referred to as the lower hybrid frequency. The strength of these lines depend on the relative magnitudes of plasma frequency and gyrofrequency, on the presence of suprathermal electrons (or ions) etc.

The total power residing in the electron plasma oscillation at thermal equilibrium is determined by integrating the spectrum through the electron lines with the result that

$$\int_{\text{electron line}} \Phi d\omega = \frac{(kD_e)^2}{1 + (kD_e)^2} \quad (77)$$

whereas the power in the ion line becomes:

$$\int_{ion} \Phi d\omega = \frac{1}{[1 + (kD_e)^2][1 + \frac{T_e}{T_i} + (kD_e)^2]} \quad (78)$$

Hence, whenever kD_e is small the ion contribution dominates.

Note that (78) $\rightarrow \frac{1}{2}$ when $(kD)^2 \rightarrow 0$ or more generally $\rightarrow \frac{1}{1+T_e/T_i}$ when $T_e \neq T_i$. Hence, the "ion-scattering" is half of the free electron scattering, which is obtained from (77). When $(kD)^2 \rightarrow \infty$ (77) $\rightarrow 1$.

8. The Effects of Collisions

Let us return to the solution of the inhomogeneous Vlasov first order equation:

$$\delta n(\vec{r}, \vec{v}, t) = -\frac{q m_o}{m} \int_0^\infty \vec{E}(\vec{r}', t - \tau) \frac{\partial f_o(\vec{v}')}{\partial \vec{v}} d\tau \quad (79)$$

Remember that the past \vec{R}, \vec{V} at time $t - \tau$ approach \vec{r}, \vec{v} at time t , and that the position/velocity travel back in time exactly as in deterministic orbit in accordance with the equations of motion of free particles.

Suppose that the particles suffer collisions. In this case, it is no longer possible to say for certain where they came from, because the previous history of the particle arriving at \vec{r}, \vec{v} at time t is a random process. If the collisions occur with like particles the process becomes difficult because pairs of particles have unrelated motions in this theory. However it is often the case that the collisions occur with particles of another kind with little dynamical mutual coupling. Important examples are:

ions in low ionosphere collide with neutral gas molecules which are much more numerous than the ions.

electrons deviating from their deterministic orbits because they have to move in the random field of near-stationary ions.

In cases such as the two quoted we introduce:

$$W_+(\vec{r}, \vec{v}, t | \vec{r} - \vec{R}, \vec{V}, t - \tau) = \begin{array}{l} \text{conditional probability density} \\ \text{of finding a particle at } \vec{r}, \vec{v} \\ \text{at time } t \text{ given that at time } t - \tau \text{ it was} \\ \text{at } \vec{r} - \vec{R}, \vec{V} \end{array}$$

The joint probability density of the two events (\vec{r}, \vec{v}, t) and $(\vec{r} - \vec{R}, \vec{V}, t - \tau)$ is

$$W_+(\vec{r}, \vec{v}, t | \vec{r} - \vec{R}, \vec{V}, t - \tau) f_o(\vec{V})$$

The individual probability of $\vec{r} - \vec{R}, \vec{v}, t - \tau$ given that the present coordinates are \vec{r}, \vec{v}, t is:

$$W_-(\vec{r} - \vec{R}, \vec{V}, t - \tau | \vec{r}, \vec{v}, t)$$

and the joint probability density of \vec{r}, \vec{v}, t and $\vec{r} - \vec{R}, \vec{V}, t - \tau$ is:

$$\begin{aligned}
W_-(\vec{r}-\vec{R}, \vec{V}, t-\tau|\vec{r}, \vec{v}, t)f_o(\vec{v}) = \\
= W_+(\vec{r}, \vec{v}, t|\vec{r}-\vec{R}, \vec{V}, t-\tau)f_o(\vec{V})
\end{aligned} \tag{80}$$

but,

$$W_-(-\vec{R}, \vec{V}, -\tau|o, \vec{v}, o)$$

clearly must equal

$$W_+(\vec{R}, \vec{V}, \tau|o, \vec{v}, o)$$

from the symmetry of the equations of motion.

Taking the spatial Fourier transform of the perturbation solution one obtains:

$$n(\vec{k}, \vec{v}, t) = -\frac{qn_o}{m} \int_0^\infty \vec{E}(\vec{k}, t-\tau) \cdot \frac{\partial f_o(\vec{v}')}{\partial \vec{v}'} \cdot e^{+i\vec{k} \cdot \vec{R}} > d\tau \tag{81}$$

where the average is taken over all the different particle orbits which lead to (\vec{r}, \vec{v}, t) .

Explicitly with $\frac{\partial f_o}{\partial \vec{v}'} = \frac{\partial f_o(\vec{V})}{\partial \vec{V}} = -\frac{\vec{V} \cdot \vec{m}}{T} \cdot f_o$:

$$n(\vec{k}, \vec{v}, t) = +\frac{\epsilon_o}{qD^2} \int_0^\infty \vec{E}(\vec{k}, t-\tau) \iint W_+(\vec{R}, \vec{V}, \tau|o, \vec{v}, o) \vec{V} \cdot e^{+i\vec{k} \cdot \vec{R}} d(\vec{R})d(\vec{V}) \cdot f_o(\vec{v}) \tag{82}$$

Hence, if we introduce:

$$f_o(\vec{v}) \iint d(\vec{R})d(\vec{V}) W_+(\tau) \vec{V} \cdot e^{+i\vec{k} \cdot \vec{R}} = \vec{A}(\vec{k}, \vec{v}, \tau) \tag{83}$$

we obtain:

$$n(\vec{k}, \vec{v}, t) = \frac{\epsilon_o}{qD^2} \int_0^\infty \vec{E}(\vec{k}, t-\tau) \cdot \vec{A}(\vec{k}, \vec{v}, \tau) d\tau \tag{84}$$

Let us formulate the modified scatter theory in terms of transition probability averaging.

Introducing as before:

$$\vec{E}(\vec{k}, \omega) = \frac{i\vec{k}}{\epsilon_o k^2} Q(\vec{k}, \omega) \tag{85}$$

and taking Fourier transforms, one obtains:

$$n(\vec{k}, \vec{v}, \omega) = i \frac{Q(\vec{k}, \omega)}{q(kD)^2} \int_0^\infty d\tau e^{-i\omega\tau} \vec{k} \cdot \vec{A}(\vec{k}, \vec{v}, \tau) \tag{86}$$

Integrating over all arrival velocities one finally obtains:

$$n(\vec{k}, \omega) = -\frac{1}{q} \chi(\vec{k}, \omega) \cdot Q(\vec{k}, \omega) \tag{87}$$

where now

$$\chi(\vec{k}, \omega) = -i \frac{1}{(kD)^2} \int_0^\infty d\tau e^{-i\omega\tau} \int d(\vec{v}) \cdot f_o(\vec{v}) \cdot \iint d(\vec{R}) d(\vec{v}) W_+(\vec{R}, \vec{v}, \tau | o, \vec{v}, o) (\vec{k} \cdot \vec{V}) e^{-i\vec{k} \cdot \vec{R}} \quad (88)$$

Similarly - studying independent particles - diffusing along as a result of collisions with another gas - but not exposed to an external field - one obtains the expression:

$$|n_p(\vec{k}, \omega)|^2 = 2 \int_0^\infty d\tau \cdot e^{-i\omega\tau} \int d(\vec{v}) f_o(\vec{v}) \cdot \iint d(\vec{R}) d(\vec{v}) W_+(\vec{R}, \vec{V}, \tau | o, \vec{v}, o) e^{-i\vec{k} \cdot \vec{R}} \quad (89)$$

So that what we previously referred to as G now takes the form:

$$G(\vec{k}, \omega) = \int_0^\infty d\tau e^{-i\omega\tau} \int d(\vec{v}) f_o(\vec{v}) \iint d(\vec{R}) d(\vec{V}) \cdot W_+(\vec{R}, \vec{V}, \tau | o, \vec{v}, o) e^{-i\vec{k} \cdot \vec{R}} \quad (90)$$

By properly manipulating the expression for $\chi(\vec{k}, \omega)$ we obtain

$$\chi(\vec{k}, \omega) = \frac{1}{(kD)^2} (1 + \omega \text{Im} G - i\omega \text{Re} G) \quad (91)$$

which is of the same form as before. Consider a model for $W(\vec{R}, v, \tau | o, \vec{v}, o)$:

Suppose the particle is moving as if in Brownian motion with an equation

$$\frac{d\vec{v}}{dt} = -\beta\vec{v} + \vec{A}(t) \quad (\text{Langevin's equation}) \quad (92)$$

(do not confuse with β in Section 2!)

Then, from Chandrasekhar's work:

$$W_+(\vec{R}, \vec{V}, \tau | \vec{v}) = \frac{1}{8\pi^3 (FG - H^2)^{3/2}} e^{-\frac{G \cdot \vec{R}_o^2 - 2\vec{H} \cdot \vec{R}_o \cdot \vec{S} + F \cdot \vec{S}^2}{2(FG - H^2)}} \quad (93)$$

$$\vec{R}_o = \vec{R} - \frac{\vec{g}}{\beta}(1 - e^{-\beta\tau})$$

$$\vec{S} = \vec{V} - \vec{v} \cdot e^{-\beta\tau}$$

$$F = \frac{T}{m\beta^2} [2\beta\tau - 3 + 4 \cdot e^{-\beta\tau} - e^{-2\beta\tau}]$$

$$G = \frac{T}{m} [1 - e^{-2\beta\tau}]$$

$$H = \frac{T}{m\beta} (1 - e^{-\beta\tau})^2$$

The correspondence for $\beta \rightarrow 0$

$$W_+(\vec{R}, \vec{V}, \tau | \vec{v}) = \delta(\vec{R} - \vec{v} \cdot \tau) \delta(\vec{V} - \vec{v}) \quad (94)$$

This is a formulation which preserves particles, momentum and energy (with the background). We shall now use it for a study of plasma line enhancement due to photoelectrons, or other energetic "tail" electrons, neglecting the magnetic field.

By substitution one obtains:

$$G(\vec{k}, \omega) = \int_0^\infty e^{-\frac{1}{2} \frac{k^2 v_{th}^2}{\beta^2} [\beta \tau - 1 + e^{-\beta \tau}]} \cdot e^{-i\omega \tau} d\tau \quad (95)$$

If we assume β to be small we obtain:

$$G(\vec{k}, \omega) \approx \underbrace{\int_0^\infty e^{-\alpha \tau^2 - i\omega \tau} d\tau}_{G_0(\vec{k}, \omega)} + \frac{\alpha \beta}{3} \int_0^\infty \tau^3 e^{-\alpha \tau^2 - i\omega \tau} d\tau \quad (96)$$

with $\alpha = \frac{k^2 v_{th}^2}{2}$

Hence: ✓friction term collision frequency

$$G(\vec{k}, \omega) = G_0(\vec{k}, \omega) - i \frac{\alpha \beta}{3} \frac{\partial^2}{\partial \alpha \partial \omega} G_0(\vec{k}, \omega) \quad (97)$$

The asymptotic expansion for $Im G$ for large $\frac{\omega}{kv_{th}} = Z$ is

$$\begin{aligned} & -\frac{1}{\omega} \{1 + Z^{-2} + 3Z^{-4} \dots\} \\ & = -\left\{ \frac{1}{\omega} + \frac{(kv_{th}^2)}{2\omega^3} \cdot 2 + \dots \right\} = -\left\{ \frac{1}{\omega} + 2 \frac{\alpha}{\omega^3} \dots \right\} \end{aligned} \quad (98)$$

Hence, we obtain approximately:

$$\begin{aligned} G(\vec{k}, \omega) & \approx G_0(\vec{k}, \omega) + \frac{\alpha \beta}{3} \cdot 2 \cdot 3 \cdot \frac{1}{\omega^4} \dots \\ & = G_0(\vec{k}, \omega) + \beta \cdot \frac{k^2 v_{th}^2}{\omega^4} + \dots \\ & \simeq G_0(\vec{k}, \omega) + \beta \cdot \frac{(kD)^2}{\omega^2} \end{aligned} \quad (99)$$

Turning to the fluctuation spectrum for electron plasma oscillations one obtains

$$\langle |n(\vec{k}, \omega)|^2 \rangle = \frac{\Phi_e}{|1 + \chi_e|^2} \quad (100)$$

Denominator:

$$\begin{aligned} 1 + \chi_e & = 1 + \left(\frac{1}{kD} \right)^2 [1 + \omega Im G - \omega Im G - i\omega Re G] \\ & \approx 1 - \frac{\omega_p^2}{\omega^2} - 3 \frac{(kv_{th})^2}{\omega^4} \omega_e^2 - \frac{i}{(kD)^2} \omega \cdot Re G \end{aligned}$$

$$\approx 1 - \frac{\omega_p^2}{\omega^2} - 3(kD)^2 \cdot \frac{\omega_e^2}{\omega^2} \quad (101)$$

Expand to first order in ω about $\omega = \omega_r$

$$\begin{aligned} 1 + \chi_e &\approx + \frac{2}{\omega_r}(\omega - \omega_r) - \frac{i}{(kD)^2} \omega \operatorname{Re} G \\ &= \frac{2}{\omega_r}(\omega - \omega_r) + \frac{i}{(kD)^2} \cdot \sqrt{\frac{\pi}{2}} \frac{d}{dz} (e^{-\frac{1}{2}z^2}) + \dots \end{aligned} \quad (102)$$

The power spectral shape in this approximation becomes:

$$\langle |n(\vec{k}, \omega)|^2 \rangle \simeq \frac{2n_o \operatorname{Re} G}{\frac{4}{\omega_r^2}(\omega - \omega_r)^2 + (\frac{1}{kD})^4 (\frac{d}{dz} \dots)^2} \quad (103)$$

This is a Lorentzian which can be integrated. If this is done one obtains for the intensity:

$$I \sim \frac{1}{2(kD)^2} \frac{f_m(v_\phi) + f_p(v_\phi) + \beta}{f_m(v_\phi) - T \frac{d}{dE_\phi} f_p(v_\phi) + \beta} \quad (104)$$

When electron-ion collisions dominate, β can be expressed approximation by as $\omega_p \frac{\ln \Lambda}{\Lambda}$ ($\Lambda \sim$ number of electrons in Debye sphere.)

$$v_\phi \sim \frac{\omega_e}{k}$$

$$f_m \sim n_m \left(\frac{m}{2\pi T} \right)^{1/2} a, e^{-mv_\phi^2/2T} \quad \text{background plasma}$$

$$f_p \sim \text{same for hot plasma.}$$

Collisions between ions and the neutrals cause the mobility of the ions to decrease. The collisions, therefore, effectively damps the ion-acoustic waves, which causes the frequency spectrum to narrow. Studies of the narrowing of the frequency spectrum with decreasing height can be used for studies of the neutral density at D and the E -region heights.

9. Summary and some final remarks

A summary of the application of the ion line of the incoherent scatter radar technique to ionospheric measurements can best be given in terms of the sketches shown in Figure 11.

The plasma line, in addition to providing information on suprathermal flux, see equation (104), also provides the possibility to determine the electron temperature and the electron density. Ignoring the geomagnetic field for simplicity we have, for the effective k -vectors \vec{k}_1 and $\vec{k}_2 (= \vec{k}_{in} - \vec{k}_{rec})$ the following plasma line frequency offsets apply, see equation (73):

$$f_{1R}^2 = f_e^2 [1 + 3(k_1 D)^2]$$

$$f_{2R}^2 = f_e^2 [1 + 3(k_2 D)^2]$$

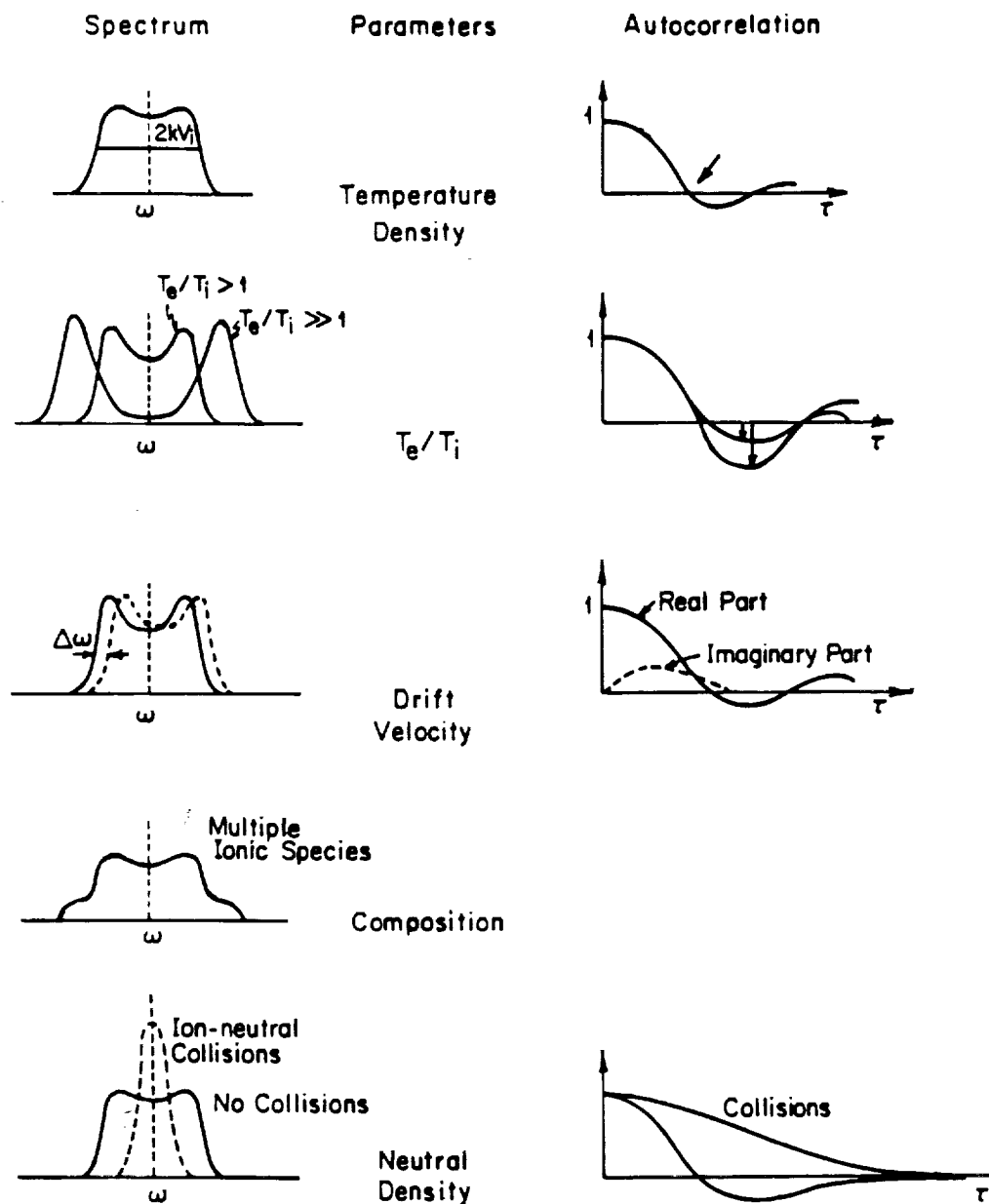


Figure 11. Sketches showing various observations leading to several plasma parameters.

If the two different k -vectors are generated by shifting the radar center frequency, the plasma line spectra at the two radar frequencies f_{01} and f_{02} will appear as shown in Figure 12. Different k -values can also be obtained by changing the geometry in a bistatic setup. In the case shown in Figure 12 we have:

$$(f_{2R} - f_{1R}) \underbrace{(f_{2R} + f_{1R})}_{\approx 2f_e} = 3D^2 \cdot f_e^2 (k_2 - k_1)(k_2 + k_1) \quad (107)$$

$$\begin{aligned} \delta f = f_{2R} - f_{1R} &= 3D^2 \cdot \frac{f_e}{2} \cdot \frac{4\pi(f_{02} - f_{01})4\pi(f_{02} + f_{01})}{e^2} = \\ &= 24\pi^2 \cdot \frac{v_{th}^2}{\omega_R^2} \cdot f_R \frac{f_{02}^2 - f_{01}^2}{e^2} = \frac{6}{f_R} \frac{T_e}{m} \frac{f_{02}^2 - f_{01}^2}{e^2} \end{aligned} \quad (108)$$

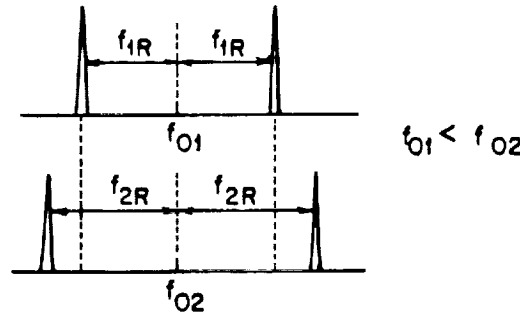


Figure 12. Plasma line spectra at radar frequencies f_{01} and f_{02} .

All of the quantities involved are well determined except for T_e which can be found this way.

Numerical example (EISCAT parameters)

$$\begin{aligned} T_e &\sim 2000^\circ K \\ f_{02} &= 933 MHz \\ f_{01} &= 224 MHz \quad \delta f \approx 335 kHz \\ f_e &= 5 MHz \end{aligned}$$

Hence, from a two-frequency plasma line experiment one can deduce the electron temperature accurately and independently.

In Section 2 of these lecture notes we started out considering the scattering from random irregularities in the dielectric function. Throughout the dielectric considered in this paper was a nearly lossless plasma. However, a neutral gas also exhibits random density fluctuations, and the curious reader might wonder whether they are detectable at radio wavelengths. In order to answer this question, consider a gas dense enough to support sound waves. The density fluctuation may, therefore, be considered as a superposition of thermally excited sound-waves of varying wavelength and direction. As in Section 4 we expand the parameters (velocity, density, temperature) associated with the acoustic wave-field in a spatial Fourier series:

$$n(\vec{r}, t) = \frac{1}{V} \sum_{\vec{k}} n(\vec{k}, t) \cdot e^{-i\vec{k} \cdot \vec{r}}$$

where n can be density, pressure, velocity etc. The wave-field amplitudes $n(\vec{k}, t)$ all must satisfy the wave-equation

$$\ddot{n}(\vec{k}, t) + k^2 c_s^2 n(\vec{k}, t) = 0 \quad (109)$$

where

$$c_s^2 = \frac{T}{M} \cdot \gamma \quad (110)$$

where T is the mean gas temperature in energy units, M the molecular mass and γ (1.4 for air) the ratio of specific heat at constant pressure and constant volume. From equipartition arguments (assuming minute losses to insure equipartition) as used in deriving specific heat of solids we find that

$$\langle |n(k\omega)|^2 \rangle = \frac{n_0 \cdot V}{2\gamma} [\delta(\omega - kc_s) + \delta(\omega + kc_s)] \quad (111)$$

From Toru Sato's lecture, his equation 2, we see that for dry, nonionized air:

$$\begin{aligned} \Delta\epsilon(k) &= \epsilon_0 \cdot \frac{1.55 \cdot 10^{-9} v(k)(mb)}{T(^{\circ}K)} = \\ &= \epsilon_0 \cdot \frac{1.55 \cdot 10^{-7} v(k)(N/m^2)}{T(^{\circ}K)} = \\ &= \epsilon_0 \cdot 1.55 \cdot 10^{-7} \delta \cdot \kappa \cdot n(k) \end{aligned} \quad (112)$$

where

$$\kappa = \text{Boltzmann's constant} = 1.38 \cdot 10^{-23} J/^{\circ}K$$

combining 111 and 112, one obtains:

$$\langle |\Delta\epsilon(k)|^2 \rangle = \epsilon_0^2 \gamma \cdot \kappa^2 \cdot n_0 \cdot V \cdot 2.4 \cdot 10^{-14} \quad (113)$$

The radar cross section per unit volume of the gas is formed by combining equations (6) and (18) to give:

$$\sigma = \frac{k_0^4}{4\pi} 3.73 \cdot 10^{-60} n_0 (m^2/m^3)$$

As a specific numerical example, take the Arecibo S-band wavelength and the atmospheric number density at sea level:

$$\lambda_0 = 0.125 m$$

$$n_0 = 2.688 \cdot 10^{25} m^{-3}$$

This gives for the troposphere:

$$\sigma_{trop} \approx 5 \cdot 10^{-26} m^2/m^3$$

As a comparison the cross section per unit volume in the F-region is typically:

$$\sigma_F \approx 10^{-18} \text{ m}^2/\text{m}^3$$

If the Arecibo beam could be focused at lower altitude, if full advantage could be taken of the reduced distance and the reduced bandwidth of scattering one might be able to make up for the nearly seven orders of magnitude discrepancy in specific radar cross section. It is probably a much more practical approach to excite low frequency sound waves as done with the Shigaraki MV radar system, and scatter from them.

BIBLIOGRAPHY

- [1] Beynon, W.J.B. and Williams, P.J.S., Incoherent Scatter of Radio Waves from the Ionosphere, *Rep. Prog. Phys.*, **41**, 909, 1978.
- [2] Bowles, K., Observation of Vertical-Incidence Scatter from the Ionosphere at 41 Mc/sec, *Phys. Rev. Lett.*, **1**, 454, 1958.
- [3] Budden, K.G., *The Propagation of Radio Waves*, Cam. U. Press, 1985.
- [4] Chandrasekhar, S., Stochastic Problems in Physics and Astronomy, *Revs. Mod. Phys.*, **15**, 1, 1942.
- [5] Dougherty, J.P. and Farley, D.T., A Theory of Incoherent Scattering of Radio Waves by a Plasma, *Proc. R. Soc. A*, **259**, 79, 1960.
- [6] Evans, J.V., Theory and Practice of Ionosphere Study by Thomson Scatter Radar, *Proc. IEEE*, **57**, 496, 1969.
- [7] Farley, D.T., Faraday Rotation Measurements Using Incoherent Scatter, *Radio Sci.*, **4**, 143, 1969.
- [8] Fejer, J.A., Scattering of Radio Waves by an Ionized Gas in Thermal Equilibrium, *Can. J. Phys.*, **38**, 1114, 1960.
- [9] Hagfors, T., Density Fluctuations in a Plasma in a Magnetic Field, with Applications to the Ionosphere, *J. Geophys. Res.*, **66**, 1699, 1961.
- [10] Hagfors, T., Birkmeyer, W. and Sulzer M., A New Method for Accurate Ionospheric Electron Density Measurements by Incoherent Scatter Radar, *J. Geophys. Res.*, **89**, 6841, 1984.
- [11] Hagfors, T. and Lehtinen, M., Electron Temperature Derived from Incoherent Scatter Radar Observations of the Plasma Line Frequency, *J. Geophys. Res.*, **86**, 119, 1981.
- [12] Moorcroft, D.R., On the Determination of Temperature and Ionic Composition by Electron Backscattering from the Ionosphere and Magnetosphere, *J. Geophys. Res.*, **69**, 955, 1964.
- [13] Petit, M., Mesures de températures, de densité électronique et de composition ionique dans l'ionosphère par diffusion de Thomson, *Annls Geophys.*, **24**, 1, 1968.
- [14] Rishbeth, H. and Williams, P.J.S., The EISCAT Ionospheric Radar: the System and its Early Results, *Q.J.R. Astr. Soc.*, **26**, 478, 1985.
- [15] Salpeter, E.E., Scattering of Radio Waves by Electrons Above the Ionosphere, *J. Geophys. Res.*, **65**, 1851, 1960.
- [16] Yngvesson, K.O. and Perkins, F.W., Radar Thomson Scatter Studies of Photoelectrons in the Ionosphere and Landau Damping, *J. Geophys. Res.*, **73**, 97, 1968.

APPENDIX A

Notes on Vlasov's Equation.

$$n(\vec{r}, \vec{v}, t) \cdot d(\vec{r})d(\vec{v}) \sim \# \text{ particles } \begin{pmatrix} \text{ions} \\ \text{electrons} \\ \text{atoms} \\ \text{molecules} \end{pmatrix}$$

in "volume" $d(\vec{r})d(\vec{v})$

Equation of motion for $n(\vec{r}, \vec{v}, t)$:

$$\begin{aligned} n(\vec{r}, \vec{v}, t) \cdot d(\vec{r})d(\vec{v}) \\ = n(\vec{r}', \vec{v}', t + \Delta t) \cdot d(\vec{r}')d(\vec{v}') \quad \text{particles preserved!} \end{aligned} \quad (A1)$$

$$n(\vec{r}', \vec{v}', t + \Delta t) = n(\vec{r}, \vec{v}, t) + \left(\frac{\partial n}{\partial \vec{r}'} \Big|_{\vec{r}'=\vec{r}} \cdot \Delta \vec{r} + \frac{\partial n}{\partial \vec{v}'} \Big|_{\vec{v}'=\vec{v}} \cdot \Delta \vec{v} + \frac{\partial n}{\partial t} \cdot \Delta t \right) + \dots \quad (A2)$$

$$\Delta \vec{r} = \vec{v} \cdot \Delta t$$

$$\Delta \vec{r} = \vec{a} \cdot \Delta t = \frac{\vec{F}}{m} \cdot \Delta t$$

Hence

$$n(\vec{r}', \vec{v}', t + \Delta t) = n(\vec{r}, \vec{v}, t) + \left(\frac{\partial n}{\partial t} + \vec{v} \cdot \frac{\partial n}{\partial \vec{r}} + \frac{\vec{F}}{m} \cdot \frac{\partial n}{\partial \vec{v}} \right) \cdot \Delta t + \dots \quad (A3)$$

But from Liouville's theorem: incompressible flow in phase space:

$$d(\vec{r})d(\vec{v}) = d(\vec{r}')d(\vec{v}')$$

Which means that:

$$\frac{\partial n}{\partial t} + \vec{v} \cdot \frac{\partial n}{\partial \vec{r}} + \frac{\vec{F}}{m} \cdot \frac{\partial n}{\partial \vec{v}} = 0 \quad (A4)$$

This is only true provided the particles are conserved and are allowed to travel along their dynamical orbits. There are several reasons why this might not be the case. For instance:

- A) Collisions with particles not in the same phase-space volume will remove particles from this volume or:
- B) Collisions between particles outside this volume $d(\vec{r})d(\vec{v})$ causing particles to appear inside volume.
- C) Reaction or loss due to chemical or physical processes.

With $\frac{D}{Dt} = \frac{\partial}{\partial t} + \vec{v} \cdot \frac{\partial}{\partial \vec{r}} + \frac{\vec{F}}{m} \cdot \frac{\partial}{\partial \vec{v}}$

One obtains:

$$\frac{D}{Dt}n = \left. \frac{\partial n}{\partial t} \right|_{\text{collisions}} + \left. \frac{\partial n}{\partial t} \right|_{\text{chemical reaction}} \quad (\text{Boltzmann's equation}) \quad (\text{A5})$$

When collisions are ignored, and reactions are ignored, one obtains:

$$\frac{D}{Dt}n = 0 \quad (\text{Vlasov's equation}) \quad (\text{A6})$$

For gas of charged particles we have:

$$\vec{F} = \frac{q}{m} (\vec{E} + \vec{v} \times \vec{B}) \quad (\text{A7})$$

so that:

$$\frac{Dn}{Dt} = \frac{\partial n}{\partial t} + \vec{v} \cdot \frac{\partial n}{\partial \vec{r}} + \frac{q}{m} (\vec{E} + \vec{v} \times \vec{B}) \cdot \frac{\partial n}{\partial \vec{v}} \quad (\text{A8})$$

First order perturbation:

$$n = n_o + n_1$$

$$\vec{E} = \vec{E}_1 \quad (\text{small})$$

$$\vec{B} = \vec{B}_o + \vec{B}_1$$

$$\begin{aligned} & \frac{\partial n_o}{\partial t} + \vec{v} \cdot \frac{\partial n_o}{\partial \vec{r}} + \frac{q}{m} (\vec{v} \times \vec{B}_o) \cdot \frac{\partial n_o}{\partial \vec{v}} \\ & + \frac{\partial n_1}{\partial t} + \vec{v} \cdot \frac{\partial n_1}{\partial \vec{r}} + \frac{q}{m} \left(\vec{E}_1 \cdot \frac{\partial n_o}{\partial \vec{v}} + (\vec{v} \times \vec{B}_1) \cdot \frac{\partial n_o}{\partial \vec{v}} + \vec{v} \times \vec{B}_o \cdot \frac{\partial n_1}{\partial \vec{v}} \right) = 0 \end{aligned} \quad (\text{A9})$$

For n_o independent of t and \vec{r} and with a velocity distribution which is isotropic about \vec{B}_o , the zero order terms vanish and one obtains:

$$\frac{\partial n_1}{\partial t} + \vec{v} \cdot \frac{\partial n_1}{\partial \vec{r}} + \frac{q}{m} (\vec{v} \times \vec{B}_o) \cdot \frac{\partial n_1}{\partial \vec{v}} = -\frac{q}{m} \vec{E}_1 \cdot \frac{\partial n_o}{\partial \vec{v}} \quad (\text{A10})$$

A solution of the inhomogeneous equation may be obtained by Green's function:

$$G(t, \vec{r}, \vec{v}; t', \vec{r}', \vec{v}')$$

which has the property

$$\frac{D}{Dt} G(\vec{r}, \vec{v}, t; \vec{r}', \vec{v}', t') = \delta(t - t') \delta(\vec{r} - \vec{r}') \delta(\vec{v} - \vec{v}') \quad (\text{A11})$$

It is then clear that a solution of the inhomogeneous equation is:

$$n_1(\vec{r}, \vec{v}, t) = -\frac{q}{m} \int \dots \int d(\vec{r}') d(\vec{v}') dt' G(\vec{r}, \vec{v}, t; \vec{r}', \vec{v}', t') \cdot \vec{E}_1(\vec{r}', t) \cdot \frac{\partial n_o(\vec{v}')}{\partial \vec{v}'} \quad (A12)$$

The Green function required clearly is given by:

$$G(\vec{r}, \vec{v}, t; \vec{r}', \vec{v}', t') = \delta[(\vec{r} - \vec{R}(t, \vec{r}', \vec{v}', t'))] \delta[\vec{v} - \vec{V}(t, \vec{r}', \vec{v}', t')] D(t - t') \quad (A13)$$

where

$\vec{R}(t, \vec{r}', \vec{v}', t')$ = position of particle at time t which at time t' had coordinates \vec{r}', \vec{v}'

$\vec{V}(t, \vec{r}', \vec{v}', t')$ = velocity of particle at time t which at time t' had coordinates \vec{r}', \vec{v}'

$D(t - t')$ = unit step function

$$\left(D(t - t') = 1 \quad \text{when } t > t' \right. \\ \left. = 0 \quad \text{when } t < t' \right)$$

From Section 4 we have:

$$\vec{V}(t, \vec{r}', \vec{v}', t') = \dot{\Gamma}(t' - t) \vec{v}'(t') \quad (A14)$$

$$\vec{R}(t, \vec{r}', \vec{v}', t') = \vec{r}'(t') - \Gamma(t' - t) \vec{v}'(t')$$

The use of these orbits to construct the Green function explains our preoccupation with the orbits of non-interacting particles.

Finally, we must prove that $\frac{D}{Dt} G = \delta(t - t') \delta(\vec{r} - \vec{r}') \delta(\vec{v} - \vec{v}')$

$$\begin{aligned} \frac{\partial}{\partial t} G &= \delta(t - t') \delta(\vec{r} - \vec{r}') \delta(\vec{v} - \vec{v}') - \frac{\partial \vec{R}}{\partial t} \cdot \frac{\partial G}{\partial \vec{r}} - \frac{\partial \vec{V}}{\partial t} \cdot \frac{\partial G}{\partial \vec{v}} \\ &= \delta(t - t') \delta(\vec{r} - \vec{r}') \delta(\vec{v} - \vec{v}') - \vec{v} \cdot \frac{\partial G}{\partial \vec{r}} - \vec{a} \cdot \frac{\partial G}{\partial \vec{v}} \end{aligned} \quad (A15)$$

The two last terms cancel and:

$$\frac{D}{Dt} G = \delta(t - t') \delta(\vec{v} - \vec{V}) \delta(\vec{r} - \vec{R}) \quad (A16)$$

Hence, when integrating \vec{r}', \vec{v}', t' contribution can only be obtained for such \vec{r}', \vec{v}' , at time t' which can cause \vec{R} and \vec{V} to equal \vec{r} and \vec{v} at time t . Hence, by substitution we obtain

$$n_1(\vec{r}, \vec{v}, t) = \delta n(\vec{r}, \vec{v}, t) = -\frac{qn_o}{m} \int_{-\infty}^t \vec{E}(\vec{R}, t) \frac{\partial f_o(\vec{V})}{\partial \vec{V}} \cdot dt' \quad (A17)$$

CUMULATIVE LISTING FOR THE MAP HANDBOOK

<u>Volume</u>	<u>Contents</u>	<u>Publication Date</u>
1	National Plans, PMP-1, PMP-2, PMP-3 Reports, Approved MAP Projects	June 1981
2	Symposium on Middle Atmosphere Dynamics and Transport	June 1981
3	PMP-5, MSG-1, MSG-2, MSG-3 Reports, Antarctic Middle Atmosphere Project (AMA), EXOS-C Scientific Observations, WMO Report No. 5., Updated Chapter 2 of MAP Planning Document, Condensed Minutes of MAPSC Meetings	November 1981
4	Proceedings of MAP Assembly, Edinburgh, August 1981 Condensed Minutes of MAPSC Meetings, Edinburgh, Proceedings of MAP Open Meeting, Hamburg, August 1981.	April 1982
5	A Catalogue of Dynamic Parameters Describing the Variability of the Middle Stratosphere during the Northern Winters	May 1982
6	MAP Directory	November 1982
7	Acronyms, Condensed Minutes of MAPSC Meetings, Ottawa, May 1982, MAP Projects, National Reports, Committee, PMP, MSG, Workshop Reports, Announcements, Corrigendum	December 1982
8	MAP Project Reports: DYNAMICS, GLOBUS, and SSIM, MSG-7 Report, National Reports: Czechoslovakia, USA	July 1983
9	URSI/SCOSTEP Workshop on Technical Aspects of MST Radar, Urbana, May 1983	December 1983
10	International Symposium on Ground-Based Studies of the Middle Atmosphere, Schwerin, May 1983	May 1984
11	Condensed Minutes of MAPSC Meetings, Hamburg, 1983, Research Recommendations for Increased US Participation in the Middle Atmosphere Program, GRATMAP and MSG-7 Reports	June 1984
12	Coordinated Study of the Behavior of the Middle Atmosphere in Winter (PMP-1) Workshops	July 1984
13	Ground-Based Techniques	November 1984
14	URSI/SCOSTEP Workshop on Technical Aspects of MST Radar, Urbana, May 1984	December 1984
15	Balloon Techniques	June 1985
16	Atmospheric Structure and its Variation in the Region 20 to 120 km: Draft of a New Reference Middle Atmosphere	July 1985
17	Condensed Minutes of MAPSC Meeting, Condensed Minutes of MAP Assembly, MAP Project, MSG, and National Reports	August 1985
18	MAP Symposium, Kyoto, November 1984	December 1985
19	Rocket Techniques	March 1986
20	URSI/SCOSTEP Workshop on Technical and Scientific Aspects of MST Radar, Aguadilla, October 1985	June 1986
21	MAPSC Minutes, ATMAP Workshop, Atmospheric Tides Workshop, MAP/WINE Experimenters Meetings, National Reports: Coordinated Study of the Behavior of the Middle Atmosphere in Winter	July 1986
22	Middle Atmosphere Composition Revealed by Satellite Observations	September 1986
23	Condensed Minutes of MAPSC Meetings, Toulouse, June/July 1986	December 1986
24	MAP Directory	May 1987
25	First GLOBMET Symposium, Dushanbe, August 1985	August 1987
26	MAPSC Minutes, Abstracts and Report of Workshop on Noctilucent Clouds, Boulder,	June 1988
27	COSPAR Symposium 6, The Middle Atmosphere After MAP, Espoo, July 1988, MAPSC Minutes, Espoo, July 1988; Workshop on Noctilucent Clouds, Tallinn, July 1988	October 1985 April 1989
28	URSI/SCOSTEP Workshop on Technical and Scientific Aspects of MST Radar, Kyoto, November/December 1988	August 1989
29	International Symposium on Solar Activity Forcing of the Middle Atmosphere, Liblice, Czechoslovakia, April 1989; MASH Workshop, Williamsburg, April 1986	September 1989
30	International School on Atmospheric Radar, Kyoto, November 1988	October 1989

CONTENTS

Part 1

Overview	1
----------------	---

Part 2

Radar System, Control and Signal Processing	19
---	----

Part 3

Theory, Practice and Applications	269
---	-----